NIMS Monographs

Yutaka Wakayama
Katsuhiko Ariga *Editors*

System-Materials Nanoarchitectonics

National Institute for Materials Science

Springer

NIMS Monographs

National Institute for Materials Science

NIMS publishes specialized books in English covering from principle, theory and all recent application examples as NIMS Monographs series. NIMS places a unity of one study theme as a specialized book which was specialized in each particular field, and we try for publishing them as a series with the characteristic (production, application) of NIMS. Authors of the series are limited to NIMS researchers. Our world is made up of various “substances” and in these “materials” the basis of our everyday lives can be found. Materials fall into two major categories such as organic/polymeric materials and inorganic materials, the latter in turn being divided into metals and ceramics. From the Stone Ages - by way of the Industrial Revolution - up to today, the advance in materials has contributed to the development of humankind and now it is being focused upon as offering a solution for global problems. NIMS specializes in carrying out research concerning these materials. NIMS: http://www.nims.go.jp/eng/index.html

More information about this series at https://link.springer.com/bookseries/11599

Yutaka Wakayama · Katsuhiko Ariga
Editors

System-Materials Nanoarchitectonics

Springer

Editors
Yutaka Wakayama
National Institute for Materials Science,
Tsukuba, Ibaraki, Japan

Katsuhiko Ariga
National Institute for Materials Science,
Tsukuba, Ibaraki, Japan

ISSN 2197-8891 ISSN 2197-9502 (electronic)
NIMS Monographs
ISBN 978-4-431-56911-4 ISBN 978-4-431-56912-1 (eBook)
https://doi.org/10.1007/978-4-431-56912-1

This Springer imprint is published by the registered company Springer Japan KK part of Springer Nature. The registered company address is: Shiroyama Trust Tower, 4-3-1 Toranomon, Minato-ku, Tokyo 105-6005, Japan

Preface

Nanoarchitectonics is a new term for a new concept beyond nanotechnology. In nanoarchitectonics, nanoscale materials are assembled in systematic ways to generate new functionalities, which cannot be attained solely by each material. The materials are well designed and synthesized. However, synergetic effects are key factors for device performance rather than the properties of individual materials. That is, each material works as a building block as a member of a nanoscale architecture. We refer to such research concept as "nanoarchitectonics."

To explore this new research field, the International Center for Materials Nanoarchitectonics (WPI-MANA) was founded in 2007 as one of the first five research centers within the framework of the World Premier International Research Center Initiative (WPI), which is sponsored by Japan's Ministry of Education, Culture, Sports, Science and Technology. In this project, we have produced nanoscale components and integrated them into various dimensional systems that exhibit cutting-edge functions. Here, we expect that these efforts will lead to scientific breakthroughs and technological innovations.

In this book, we present the state-of-the-art achievements of the material architects in MANA, including supramolecules, one- or two-dimensionally controlled semiconductors, optically and catalytically active nanomaterials, atomic switches, and molecular assemblies for electronic applications. We hope that this book will arouse a feeling of curiosity and provide an excellent springboard for young materials scientists in particular.

Tsukuba, Japan — Yutaka Wakayama

Contents

What is Nanoarchitectonics?

What is Nanoarchitectonics?

Katsuhiko Ariga and Masakazu Aono

1 Initiation of Nanoarchitectonics

These days, scientists and engineers are requested to solve many problems including how to save resources, how to create energy, how to reduce emissions, how to reduce environmental impact, and how to efficiently handle information. All these problems can be solved with one common concept, control of NANO and the related functional structures. Developing functional materials and systems rationally fabricated with nanoscale structural precision can save resources, create energy, reduce emissions, reduce environmental impact, and efficiently handle information. In the coming days, human society will be supported by science and technology capable of regulating nanoscale structures. The corresponding methodology started as nanotechnology and has now evolved to nanoarchitectonics.

It is said that the term nanotechnology was initially proposed by Richard Feynman, who foresaw huge possibilities for science and technology in nanoscale spaces [1]. The social impacts of nanotechnology were again brought up in the 2001 declaration, the National Nanotechnology Initiative, made by the US president Bill Clinton, in order to promote the nanotechnological approach in industrial developments. Such social and political flows have, of course, been supported by various innovations in instrumental developments for nanoscale observation, such as the invention of the scanning tunneling microscope (STM) and other scanning probe microscopes, as well as rapid developments in micro- and nanofabrication. Scientists are now capable of directly watching and handling nanoscale objects.

K. Ariga (✉) · M. Aono
International Center for Materials Nanoarchitectonics (WPI-MANA), National Institute for Materials Science (NIMS), 1–1 Namiki, Tsukuba 305-0044, Ibaraki, Japan
e-mail: ARIGA.Katsuhiko@nims.go.jp

K. Ariga
Graduate School of Frontier Sciences, The University of Tokyo, 5-1-5 Kashiwanoha, Kashiwa 277-8561, Chiba, Japan

Y. Wakayama and K. Ariga (eds.), *System-Materials Nanoarchitectonics*,
NIMS Monographs, https://doi.org/10.1007/978-4-431-56912-1_1

Another conceptually important proposal was made by Kim Eric Drexler, who described the possibilities in the formation of functional structures through bottom-up molecular organization in his book entitled *Nanosystems: Molecular Machinery, Manufacturing and Computation* [2]. This concept was also supported in actual developments of science and technology, as seen in various methodologies such as layer-by-layer assemblies of biomolecules and the programed organization of DNA origami. However, these scientific movements were separately and rather independently developed before Masakazu Aono initiated the novel concept of nanoarchitectonics to unify these potentially complementary scientific disciplines into a single methodology in 2000 [3, 4]. It can be roughly said that under the nanoarchitectonics concept, functional materials and systems are architected by organizing nanoscale units into larger functional objects, similar to the way a carpenter builds things.

Around the same time as the initiation of the nanoarchitectonics concept, that is, the end of the twentieth century and the beginning of the twenty-first century, people realized the importance of architectonics on the nanoscale. In 1999, Heath and coworkers (University of California Los Angeles, UCLA) published an article entitled Architectonic Quantum Dot Solids [5]. In this article, the term architectonics was described as "having an organized and unified structure that suggests an architectural design" (Merriam-Webster's WWW dictionary), as suggested by R. S. Williams, Hewlett-Packard Labs [1]. The novel conceptual term, nanoarchitectonics, was first used in the title of a scientific conference, the 1st International Symposium on Nanoarchitectonics Using Suprainteractions, held in Tsukuba, Japan, in 2000 and led by Masakazu Aono [6, 7]. This can be regarded as the initiation of the conceptual term, nanoarchitectonics (a fusion of nano and architectonics), in the scientific community. In 2001, the National Institute of Advanced Industrial Science and Technology (AIST) started a research center under the name of Interfacial Nanoarchitectonics, led by Toshimi Shimizu, also in Tsukuba city. In 2003, UCLA established a research center named Functional Engineered Nano Architectonics (FENA). The first paper with nanoarchitectonics in the title, "Welding, organizing, and planting organic molecules on substrate surfaces—Promising approaches towards nanoarchitectonics from the bottom up", was published by Stefan Hecht (Freie Universität Berlin) in the same year [8]. Aono named the World Premier International Research Center in the National Institute for Materials Science (NIMS) the Research Center for Materials Nanoarchitectonics (WPI-MANA) in 2007. In 2017, RESEARCH FRONTS 2017, prepared by the Chinese Academy of Sciences (CAS) and Clarivate Analytics designated nanoarchitectonics as one of the key hot research frontiers in chemistry and materials science [9].

2 Outline of Nanoarchitectonics

Prior to summarizing nanoarchitectonics, the essence of nanoarchitectonics is described herein. In addition to the above historical background, nanoarchitectonics

has scientific innovations over the well-known microtechnology. We must realize the fundamental difference between micro and nano.

From building constructions to small plastic models, visible-size macroscopic objects are manufactured exactly according to their design drawings and blueprints, as we well know. This fact can actually be applied to structural fabrication on the micrometer scale. Even very small structures on the microscale can be exactly fabricated by advanced lithographic techniques in accordance with what is previously designed. Therefore, microfabrication (microtechnology) can be said to be a highly advanced version of macroscopic craftwork. In contrast, fabrications on the nano- and sub-nanoscales are completely different from those observed on the macroscopic and microscopic scales. Materials fabrication and structural construction in the nanoscale or mesoscale region are not always definitive and are sometimes difficult to achieve in accordance with their design drawings. In the nanoscale region, uncontrollable and unexpected disturbances and fluctuations, such as thermal fluctuations, statistical distributions, and quantum effects, cannot be avoided. In addition, mutual component interactions significantly affect entire materials systems on the nanoscale. Outcomes such as materials structures and properties are not a result of simple summation in many cases, and may be the consequence of numerous controllable and uncontrollable interactions. Materials architectonics with nanoscale components having nanoscale dimensions are developed on the basis of techniques for atom/molecule fabrication, self-assembly/self-organization, field-controlled organization, microfabrication, and biological processes and their integration.

The ways in which nanoarchitectonics is used to create functional materials and systems can be summarized as below.

(i) Reliable nanomaterials or nanosystems are created by organizing nanoscale structures (nanoparts) even though there may be some unavoidable unreliability.
(ii) The main players are not the individual nanoparts but their interactions, which cause new functionalities to emerge.
(iii) Unexpected emergent functionalities can result from assembling or organizing a huge number of nanoparts.
(iv) A new theoretical field where conventional first-principles computations are combined with novel bold approximations can be explored.

These nanoarchitectonics strategies can be applied to a wide range of sciences and technologies including the production of functional materials and systems. Therefore, the nanoarchitectonics concept has been accepted by various research fields including structural fabrication, materials production, device, energy, environment, catalyst, biological, and biomedical applications, as will be discussed in the following chapters in this book.

References

1. Roukes M (2001) Plenty of room, indeed. Sci Am 285:48
2. Eric Drexler K (1992) Nanosystems: molecular machinery, manufacturing, and computation. Wiley, New York
3. Ariga K, Ji Q, Nakanishi W, Hill JP, Aono M (2015) Nanoarchitectonics: a new materials horizon for nanotechnology. Mater Horizons 2:406
4. Aono M, Ariga K (2016) The way to nanoarchitectonics and the way of nanoarchitectonics. Adv Mater 28:989
5. Markovich G, Collier CP, Henrichs SE, Remacle F, Levine RD, Heath JR (1999) Architectonic quantum dot solids. Acc Chem Res 32:415
6. Ariga K, Ji Q, Hill JP, Bando Y, Aono M (2012) Forming nanomaterials as layered functional structures toward materials nanoarchitectonics. NPG Asia Mater 4:e17
7. Ariga K, Aono M (2016) Nanoarchitectonics. Jpn J Appl Phys 55:1102A6
8. Hecht S (2003) Welding, organizing, and planting organic molecules on substrate surfaces—promising approaches towards nanoarchitectonics from the bottom up. Angew Chem, Int Ed 42:24
9. RESEARCH FRONTS 2017 by Institutes of Science and Development, Chinese Academy of Sciences, The National Science Library, Chinese Academy of Sciences, and Clarivate Analytics (2017). https://clarivate.com.cn/research_fronts_2017/2017_research_front_en.pdf

Nanostructured Materials and Their Construction

Synthesis of Semiconductor Nanowires

Ken C. Pradel and Naoki Fukata

1 Introduction

Research interest in semiconducting nanowires has exploded in the past two decades. Because of their high aspect ratio and small dimensions, it is possible to observe some unique effects and enhanced properties. In order to push these materials from a simple curiosity to something of practical usage, one must go through three steps: synthesis, characterization and application. The first step is crucial as a stable, reproducible, and controllable means of synthesis is needed to produce material with acceptable levels of yield. This point will be the primary focus of this chapter. For characterization, there are a number of tools at one's disposal. Microscopy techniques like scanning and transmission electron microscopy (SEM & TEM) can give information about the nanowire's physical and crystalline properties [1, 2]. Meanwhile, techniques like Raman and photoluminescence spectroscopy can be used to probe the material's electrical properties [3, 4]. Numerous works throughout the years have shown considered their applicability by looking at features such as biological compatibility, [5–7] in particular how cells grow and survive in the their presence, and how nanowires can be used as a tool to probe them. On the side of optoelectronics, nanowires can be used to enhance the efficiency of photovoltaics [8] by reducing reflection, improving light trapping and allowing for band gap tuning.

While a number of viable techniques to synthesize nanowires exist, the scope of this chapter will be limited to two main ones, vapor–liquid-solid (VLS) and solution-based techniques. VLS growth will be focused on owing to its long and interesting history, which dates back over 50 years to when Wagner and Ellis first demonstrated this technique with the growth of "Si whiskers." [9] Solution methods are of interest as they provide a low-temperature, low-cost, and high-yield means of producing

K. C. Pradel · N. Fukata (✉)
International Center for Materials Nanoarchitectonics (WPI-MANA), National Institute for Materials Science (NIMS), 1-1 Namiki, Tsukuba 305-0044, Ibaraki, Japan
e-mail: FUKATA.Naoki@nims.go.jp

Y. Wakayama and K. Ariga (eds.), *System-Materials Nanoarchitectonics*,
NIMS Monographs, https://doi.org/10.1007/978-4-431-56912-1_2

nanowires, making them a strong candidate for applications in commercial devices. In this chapter, when multiple materials are discussed at length in association with VLS and solution growth, the focal point of each technique will be silicon (Si) and zinc oxide (ZnO), respectively, and doping techniques to give them added functionality. The former needs little introduction as Si is, without a doubt, the most widely studied and best understood semiconductor and is the basis of so much of the technology we use today. ZnO, on the other hand, has many exciting properties but has seen limited applicability owing to the lack of a stable *p*-type dopant. In the section focusing on ZnO, particular attention will be paid to the growth and applications of antimony (Sb)-doped ZnO grown via solution methods.

2 Si and Ge Nanowires

2.1 VLS Growth

Using VLS growth, various pure and compound semiconductor nanowires can be grown [10]. A variety of techniques for nanowire growth all fall under the umbrella term of VLS. Breaking down the term into its component terms, the process generally involves gaseous Si (vapor) dissolving into a gold (Au) catalyst droplet (liquid) and freezing out at the interface with the substrate (solid). The more specific names of such techniques generally come from how the Si vapor is formed, with the more common ones being chemical vapor deposition (CVD), molecular beam epitaxy (MBE), and laser ablation. Later, the pros and cons of each of these techniques will be compared among each other. Before that, it is important to discuss in detail what occurs during the VLS process.

The most commonly used catalyst for the VLS process is Au, which can be explained by the Si-Au binary phase diagram (Fig. 1) [11]. The key feature of this phase diagram is the eutectic point at 19 at.% Si and 590 K, which is much lower than the melting points of pure Si and Au. By heating the system to above this point and introducing a constant supply of Si to the system, one can push the system across the liquidus line into the Si+ liquid region, which results in the Si precipitating out into the substrate. Part of what makes Au such an ideal catalyst is that it has a high solubility of Si at the eutectic point, indicating that the energy needed to dissolve Si is not very high. Furthermore, Au has a low vapor pressure below 800 °C, removing concerns over evaporation of the seed layer during growth.

Despite these advantages, there is active research being performed on replacing Au as the catalyst in this process. The primary reason is that Au is known to create deep-level defects in Si, which could act as charge-carrier recombination centers, decreasing the carrier mobility, lifetime, and diffusion length. This could kill the material's effectiveness in applications such as photovoltaics. When considering alternative catalysts, there are a few factors to consider. The first is the absence of a silicide phase. To properly precipitate out Si nanowires, it is important to avoid

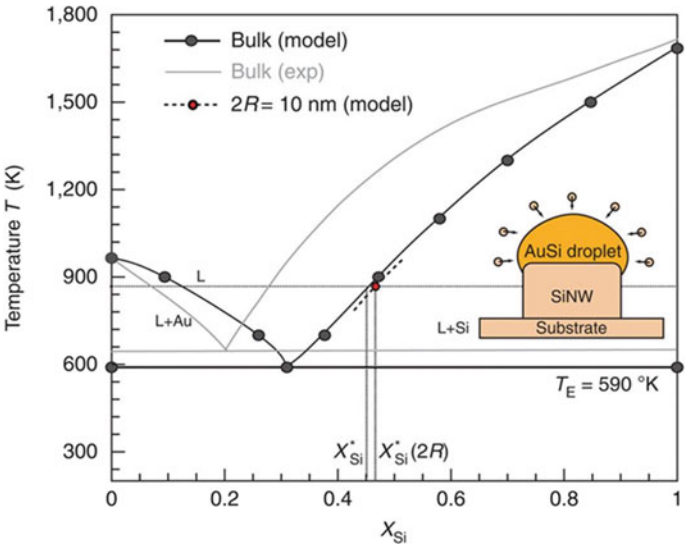

Fig. 1 Au–Si phase diagram illustrating differences in the position of the liquidus line based on the size of the Au droplets. Reprinted from [3] by The Author(s) licensed under CC BY-NC-ND 3.0 with permission from Nature

extraneous phases. A high Si solubility in the metal at the eutectic point is also highly desirable. Of the possible catalysts, the one that has received the most attention is aluminum (Al) due to the Al-Si phase diagram being similar to that of Au–Si. One group found that by performing growth from 430 to 490 °C, which is below the eutectic temperature (577 °C), vapor–solid-solid (VSS) growth of Si nanowires with an Al catalyst could be achieved, although all the wires showed some tapering [12]. Another group expanded on this work and found that in this temperature range it was possible to achieve controllable morphology and nanowire density [13]. However, the growth was highly dependent on the quality of the Al seed layer, and special care was needed to avoid oxidation, an issue that does not concern Au seeds.

2.2 Si Nanowire Growth Techniques

As mentioned earlier, there are several popular techniques for treating the material source. Interestingly, many of these techniques are commonly used for depositing semiconductor films but have found applications in nanowire growth with a metal contaminant acting as a seed. Here are a few examples involving Si nanowires. CVD starts with a gaseous Si gas source, such as a silane gas, which is broken down into its component parts at an elevated temperature, resulting in growth [14]. To avoid forming SiO_2, a good vacuum is needed. One advantage of this method is that because gaseous sources are used, the doping concentration can be controlled

in situ by adjusting the partial pressure of the dopant gas, allowing controlled doping profiles along the axis of the nanowires. However, one downside of this method is that it is occasionally difficult to control the orientation of the nanowires, especially for diameters below 50 nm.

MBE involves heating up a high-purity Si source until the Si begins to evaporate. The gaseous beam of Si is directed at the substrate surface, where nanowires are catalyzed and grown [15]. MBE offers excellent controllability in terms of orientation and doping as beams of different elements can be easily switched on and off. However the nanowire diameter is more difficult to control due to the Gibbs–Thomson effect. Furthermore, an ultrahigh vacuum is needed and the growth rate is low compared with CVD.

Laser ablation is a somewhat unusual technique as it forgoes many of the conventions of the previous two reviewed growth techniques [16, 17]. A quartz tube is placed inside a tube furnace with a target made from pressed Si powder mixed with a small amount of a catalyst such as iron (Fe) or nickel (Ni). Argon (Ar) gas is flowed through the tube furnace, which is heated to 1200 °C. An excimer laser ablates Si off the target, which flows down the tube and is collected on a cooled piece of copper (Cu), forming a spongy mesh of tangled nanowires, unlike CVD and MBE, in which the nanowires grow aligned on a Si substrate. The growth rate for these nanowires is quite high, from 10 to 80 μm/h, and very thin nanowires can be formed with diameters of less than 10 nm. The proposed growth model is that the Si and Fe vapors condense into Si-rich nanoclusters as they cool through the buffer gas. Because of the elevated temperature of the tube furnace, the nanoclusters stay in a liquid state and nanowires precipitate out of the liquid as it continues to collect more Si vapor. Eventually, growth stops when the nanowires leave the hot zone of the tube furnace and are collected on a Cu cold finger. Doping can be controlled by changing the composition of the target used for ablation, and the doping concentration has been estimated to be on the order of 10^{19} cm^{-3} using electron spin resonance (ESR) and Raman spectroscopy [18, 19].

2.3 Si Nanowire Doping

The ability to easily dope semiconductors is part of what makes them such an integral part of our modern lives. As mentioned when discussing the previous growth techniques, the various VLS techniques for synthesizing Si nanowires can control the doping in the wires, with the most commonly used dopants for *p*- and *n*-type Si being boron (B) and phosphorus (P), respectively. In order to effectively apply these doped wires, it is imperative to develop techniques to characterize them. Raman spectroscopy was found to be effective for characterizing B doping in Si nanowires grown via laser ablation [20]. Si is defined by an intense peak around 520.1 cm^{-1}, which is due to its optical phonon peak (Fig. 2a). However, in B-doped samples, additional peaks are observed around 618 and 640 cm^{-1}, which match the positions and intensities of local vibrational peaks in B-doped bulk samples [21] (Fig. 2b).

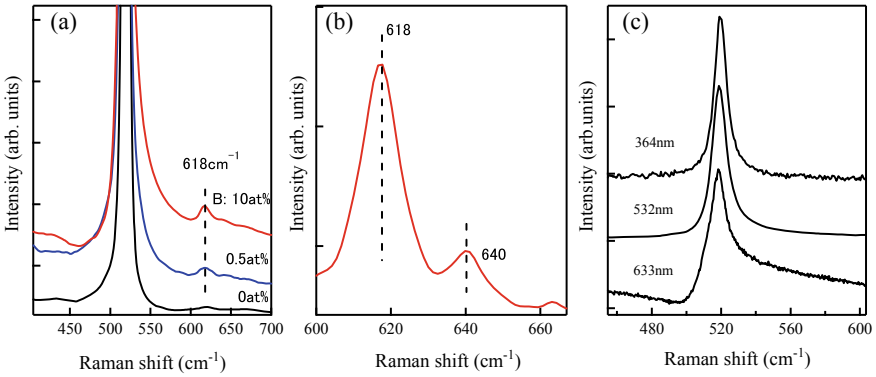

Fig. 2 **a** Raman peaks for Si nanowires grown via laser ablation using targets with 0.5 and 10% B. **b** Magnification of the Raman peaks corresponding to the bonds between Si and ^{11}B and ^{10}B isotopes. (c) Dependence of the Raman peak shape on the excitation wavelength [20]

Furthermore, Fano broadening, the coupling between discrete optical phonons and the continuum of interband hole excitations [22], is observed, causing the optical phonon peak to broaden due to the presence of free holes. To confirm that this is caused by the Fano effect, three different excitation wavelengths are used (Fig. 2c). At higher wavenumbers, the amount of broadening increases with increasing excitation wavelength, which is characteristic of the Fano effect induced by heavy B doping. While it is possible to accurately deduce the free hole concentration in bulk Si using Raman spectroscopy based on the degree of peak broadening and previous results from the literature, this is more challenging for nanowire samples owing to phonon confinement by the nanowire structure. In previous works [20], the doping level was estimated by comparing the Raman spectrum with that of B-ion-implanted bulk Si, and from the much higher intensity of the B local vibrational peaks and the increased Fano broadening, it was confirmed that the B concentration was over 10^{19} cm^{-3}.

While Raman spectroscopy can also be used to characterize *p*-type doping in Si nanowires, it is not the most appropriate technique for *n*-type doping (it is worth noting that it can be used to characterize both kinds of doping in germanium (Ge) nanowires (Fig. 3) [23]). Transmission electron microscopy (TEM) techniques such as energy-dispersive X-ray spectroscopy (EDX) can give rough estimates of doping concentrations but do not reveal how much of the dopant is electrically active (Fig. 4a). Electron paramagnetic resonance (EPR), also known as electron spin resonance (ESR) and electron magnetic resonance (EMR), is a technique for characterizing unpaired electrons and can be used in both solid and liquid materials [24]. By deconvoluting the signal in Fig. 4b, g values of 1.998 and 2.006 are obtained, the former only being observed for the P-doped sample. This corresponds to conduction electrons in Si, showing that *n*-type doping was successful. The common signal at 2.006 is likely due to the surface state of the nanowires and originates from the native oxide. From the linewidth of the ESR signal, the doping concentration can be

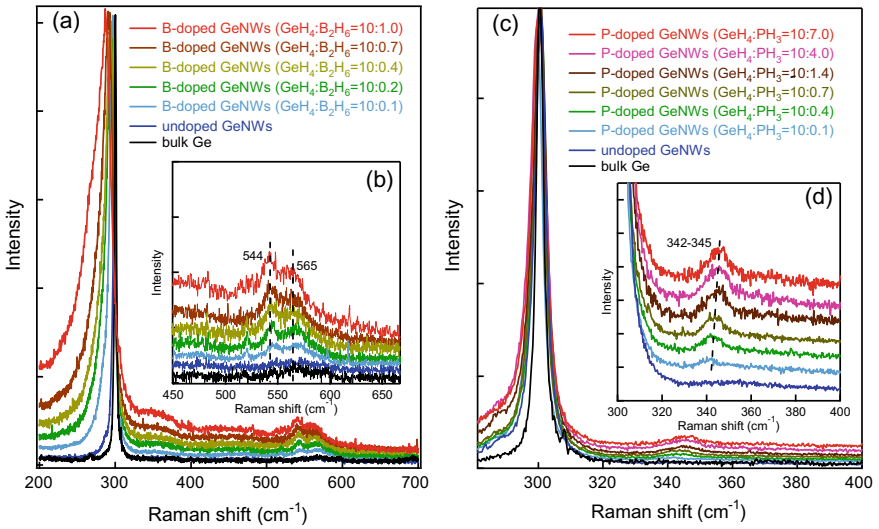

Fig. 3 Raman spectra of (**a**) B-doped *p*-type and (**c**) P-doped *n*-type Ge nanowires. The insets (**b**) and (**d**) highlight the characteristic local vibrational peaks of their respective dopants

estimated by comparing it with other values from the literature (Fig. 4c). From this, the authors concluded that the P concentration in the Si nanowires was about 10^{19} cm^{-3}.

3 Oxide Nanowires

3.1 ZnO and Solution Growth

There is a wide variety of techniques for synthesizing ZnO nanowires, each with their own strengths and weaknesses. Similarly to the case of Si, VLS and VSS techniques have been studied [27], but they have the same limitation of requiring high temperatures of over 900 °C to perform growth. MBE has also been used to produce high-purity single-crystalline ZnO nanorods [28]. However, it is a costly and slow process and requires a high vacuum to operate properly. The hydrothermal method has proven to be a viable alternative to these methods and has several advantages over them [29]. First, it has a low cost as the precursors are readily available, and no specialized equipment is needed. Next, it can be performed on a number of different substrates, most importantly polymers, owing to the low growth temperature (65–95 °C), allowing applications in flexible and implantable devices. Wafer-scale growth has also been demonstrated, showing the scalability of this method [30]. Finally,

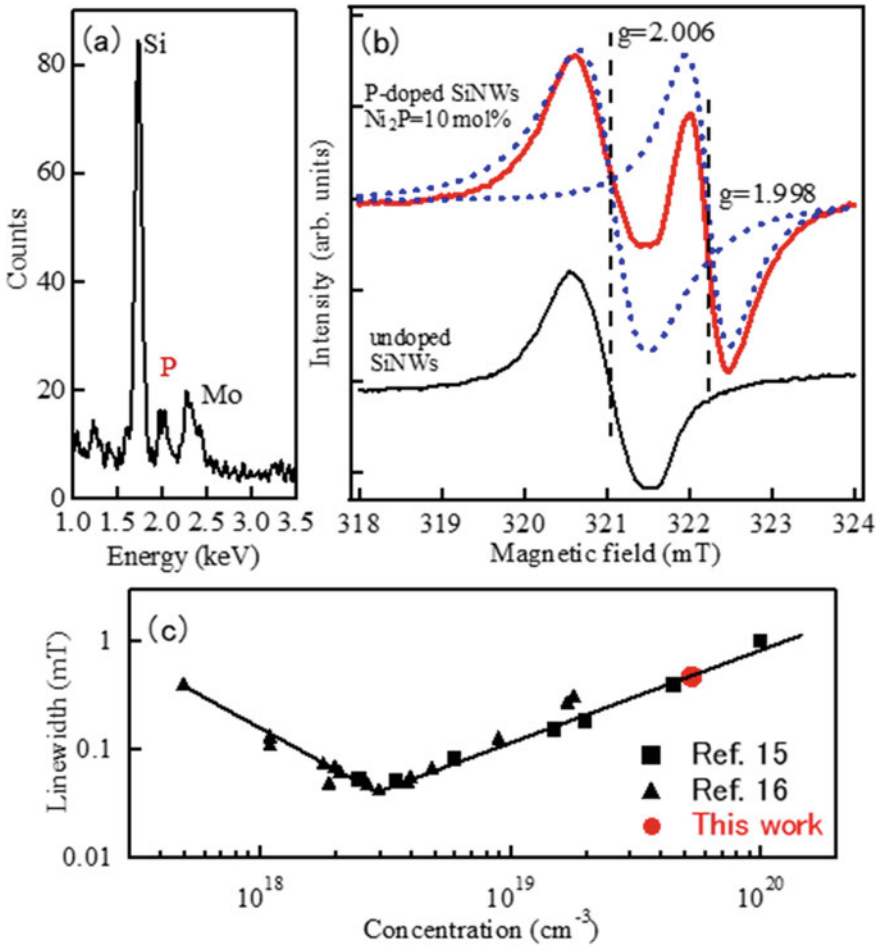

Fig. 4 **a** EDX spectra for Si nanowires doped with P grown via laser ablation. **b** ESR spectra of undoped and doped Si nanowires, with the signal from the doped sample deconvoluted into two components. **c** Correlation of ESR linewidth with P concentration in bulk P-doped Si. Refs. 15 and 16 refer to the work by Maekawa and Kinoshita [25] and Quirt and Marko [26], respectively [20]

adjusting growth parameters such as temperature, time, and precursor concentrations enables effective tuning of the nanowire dimensions [31].

In its simplest form, the hydrothermal synthesis of ZnO nanowires is performed by mixing a zinc salt, such as zinc nitrate or zinc chloride, with an equal molar part of hexamethylenetetramine (HMTA) in water. A substrate with a seed layer is placed in the solution, and the solution is heated for several hours. HMTA acts as a weak base, which slowly hydrolyzes water to provide oxygen as shown in the following reactions [32]:

$$(CH_2)_6N_4 + 6H_2O \leftrightarrow 4NH_3 + 6HCHO \quad (1)$$

$$NH_3 + H_2O \leftrightarrow NH_3 \cdot H_2O \quad (2)$$

$$NH_3 \cdot H_2O \leftrightarrow NH_4^+ + OH^- \quad (3)$$

The resulting OH^- anions react with the Zn^{2+} cations from the salt to form ZnO as follows:

$$Zn^{2+} + 2OH^- \leftrightarrow Zn(OH)_2 \quad (4)$$

$$Zn(OH)_2 \leftrightarrow ZnO + H_2O \quad (5)$$

The growth rate is highly dependent on the pH of the solution, and one group demonstrated that it reaches a maximum at a pH of 10.6 [33]. At higher pH values, it is believed that secondary reactions, such as the dissolution of ZnO, slow down growth. No additional additives are required as ZnO naturally forms nanowires. These nanowires grow preferentially along the [0001] direction [34], as doing so minimizes the total surface area by reducing the area of the high-energy (0001) surface.

To encourage aligned growth, a seed layer is added to the substrate. Some commonly used seed layers are gallium nitride (GaN), Au, and ZnO. GaN produces nicely aligned vertical nanowires due to good lattice matching [36]. When combined with a mask defined using an electron beam [37] or laser interference lithography [35, 38], large patterned arrays of wires are produced (Fig. 5). However, sapphire substrates coated with GaN are expensive and rigid, limiting the scalability. While Au can be sputtered onto a variety of substrates, and it can double as an electrode for electronic applications, thermal annealing is required to improve the crystallinity of the surface to promote growth [39]. Despite this, the growth density remains low. ZnO deposited through physical vapor deposition is an effective seed layer as it naturally has the same lattice as the subsequent nanowires [40]. The seed layer thickness and doping have also been shown to affect the nanowire growth rate and alignment [41]. Growing a thicker seed layer also causes the ZnO grains to become larger, allowing higher-diameter wires at the cost of density. Larger grains also increase the surface roughness, which causes the wire alignment to deteriorate.

As mentioned previously, the growth environment plays a large role in determining the wire dimensions [31]. Temperature was found to perhaps be the most important factor. At very high or low temperatures, the growth density of the nanowires decreases due to the basic kinetics of nucleation and growth. At low temperatures, the Zn ions cannot easily diffuse in solution, resulting in the formation of larger but fewer nuclei. Conversely, at high temperatures, the precursor material has a higher affinity to existing nuclei, resulting in increased growth, but at the cost of nucleation events. Increasing the concentration of zinc nitrate and HMTA leads to increased deposition density until a saturation point is reached, which can be explained by nucleation and

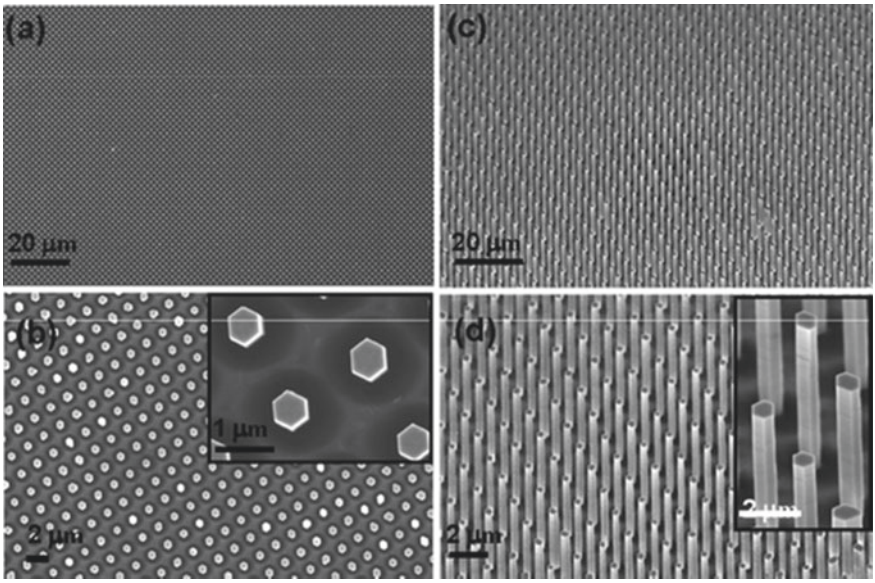

Fig. 5 **a** & **b** Top and **c** & **d** 45°-tilted view of large-scale ZnO nanowire arrays grown on a GaN substrate patterned via laser interference lithography. The nanowire diameter and length are uniform over the large arrays with few observable defects [35]

growth kinetics. At a higher concentration, more nucleation is needed to balance out the increased chemical potential. However, once the saturation point is passed, the growth of existing nanowires is more likely than a new nucleation event. By studying the effect of the growth time, one can observe the process flow of nanowire growth [42]. At first, lateral growth dominates, which is followed by axial growth while the nanowire diameter remains constant. Eventually, growth continues in both directions, causing the wire to become longer and wider. The growth rate in each of these directions can be controlled through additives. Sodium citrate can be used to promote lower-aspect-ratio nanowires [43]. This is attributed to the citrate ions binding preferentially to the (0001) surface, which inhibits lateral growth in favor of axial growth, forming stacked ZnO plates at a sufficiently high concentration instead of nanowires. Using zinc chloride or acetate as the Zn source has been shown to have a similar effect, and ZnO nanosheets [44] and films [45] have been produced with these chemicals, respectively. Polymer additives such as polyvinyl alcohol (PVA) [46] and polyethylenimine (PEI) [30] have the opposite effect as they bind to the $(01\bar{1}0)$ and $(2\bar{1}\bar{1}0)$ faces, promoting higher-aspect-ratio nanowires. When used in conjunction with ammonium hydroxide, PEI can be used to grow ultrahigh-aspect-ratio nanowires [47]. During growth, most of the precursor is lost to homogeneous nucleation and precipitates in the solution container rather than growing on the substrate surface. While increasing the pH should cause ZnO to precipitate out, the ammonia groups form a complex with the Zn^{2+} ions, inhibiting nucleation [48]. As the solution is

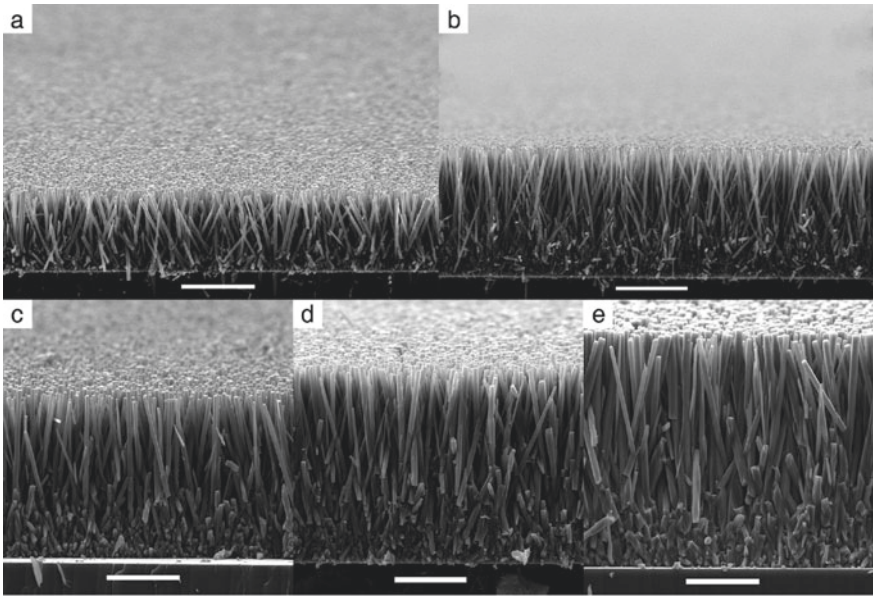

Fig. 6 Long ZnO nanowires grown with the assistance of ammonium hydroxide and PEI. The scale bar is 5 μm for all images. The nanowire lengths are **a** 11, **b** 17, **c** 22, **d** 27, and **e** 33 μm [47]

heated, the ammonia slowly evaporates, releasing Zn^{2+} and allowing the reaction to progress, which has enabled the realization of nanowire arrays with nanowires having a length of over 30 μm (Fig. 6) [47].

3.2 P-*Type Doping of ZnO*

The successful *p*-type doping of ZnO has remained a controversial field of study for several years [49, 50]. As-synthesized ZnO is naturally *n*-type due to the formation of point donor defects such as Zn [51] or hydrogen [52] interstitials. Previously, oxygen vacancies were also thought to be a cause of *n*-type conduction in ZnO due to their low formation energy, but first-principles calculations have disproven this; oxygen vacancies act as a deep donor instead [53]. Further *n*-type doping can be achieved through doping elements such as Al [54], and heavily Al doped ZnO has been proposed as a potential replacement for indium-doped tin oxide (ITO) as a transparent conductor in the ever growing number of flat panel displays [55, 56]. For a II-VI semiconductor, group I or V elements should act as *p*-type dopants in ZnO. However, with the addition of acceptor dopants comes the risk of inadvertently introducing compensating donor defects. MBE and VLS nanowire growth have been used to achieve *p*-type ZnO [50, 57–62] but, as mentioned previously, here we focus on solution-based methods.

Group I elements such as lithium (Li) have been used to produce hydrothermally grown *p*-type ZnO nanowires [63] due to their low acceptor energy. In the as-grown nanowires, Li ions were found to primarily form interstitial defects. While Li should act as an acceptor in Zn sites (Li_{Zn}^{1-}), it is more likely to form an interstitial due to its smaller atomic radius, making it act as a donor (Li_{i}^{1+}). By annealing the sample in oxygen at 500 °C, the Li ions can migrate to the Zn sites, producing *p*-type conductivity. By growing the nanowires on an *n*-type seed layer, a *p*-*n* homojunction was produced and the expected rectification behavior was observed.

Potassium (K) has also been used to produce *p*-type ZnO nanorod films [64, 65]. When a small concentration of dopant was added during the growth, Hall effect measurement was successfully used to detect *p*-type conduction. However, increasing the dopant concentration caused the free hole concentration to decrease until the sample became *n*-type again. At lower dopant concentrations, most of the K ions entered the Zn sites, forming acceptors. However, as more K was added, more of them formed interstitials, which canceled out and eventually overwhelmed the acceptor dopants. By annealing the ZnO to outdiffuse hydrogen and K interstitials, a higher hole concentration was eventually achieved [65].

Group V elements such as P [66, 67] have also been used to achieve *p*-type conduction in ZnO using ammonium phosphate ($NH_4H_2PO_4$) as the dopant source. It has been theorized that P is doped through the formation of $Zn_3(PO_4)_2$, which is incorporated into the nanorods during growth [66]. Annealing the sample causes P atoms to be released, which form P_{Zn}-$2V_{Zn}$ acceptor complexes. A later study showed that the dopant concentration was improved by adding ammonium hydroxide to the solution [67]. As $Zn_3(PO_4)_2$ is more soluble than ZnO in a basic solution, increasing the solution pH allows more P ions to be released. In both cases, homojunction structures were produced by growing a layer of *p*-type nanorods on top of a layer of *n*-type nanorods, and the rectification behavior was measured.

Among the group V elements, Sb has shown the highest level of stability as a *p*-type dopant in ZnO. As Sb has a much larger atomic radius than oxygen, one theory suggests that the Sb enters the Zn site instead of oxygen, forming a Sb_{Zn}-$2V_{Zn}$ complex and realizing *p*-type doping [68]. Sb atoms can be incorporated into the ZnO lattice through their coordination with glycolate ligands. During growth, antimony glycolate is absorbed onto the growth surface of the nanowires, and the glycolate ligands desorb, leaving the Sb ions behind, while normal ZnO growth continues [69]. Single-wire field-effect transistors show *p*-type conduction in doped wires, even without annealing. While similar carrier concentrations were observed for unannealed and annealed samples, the annealed sample had an improved carrier mobility, increasing from 0.03 to 1.2 cm^2V^{-1} s^{-1}. A follow up study used scanning transmission electron microscopy (STEM) to show the formation of head-to-head basal plane inversion domain boundaries as well as voids inside the nanowires [70]. ZnO naturally grows much faster along the positive c-axis than along the negative c-axis, so the inversion domain boundary slows down growth in that direction in that region, leading to the rest of the nanowire growing around it, forming voids. From density functional theory calculations, this group [70] determined that an extra basal plane of oxygen atoms acted as electron acceptors and were the true source of the

nanowires' *p*-type characteristics. A recent study on the void structures found that they migrate and impinge upon each other when the nanowires are annealed, resulting in the larger voids observed in these works (Fig. 7) [71]. Furthermore, microelectron diffraction was used to identify the phase below the voids as a Zn–Sb alloy in the form of $Zn_7Sb_2O_{12}$ rather than simply a planar precipitate of Sb (Fig. 7c). Before annealing, these voids also contained water, which shows the possibility of trapping other aqueous materials inside them. This solution-based technique has been the subject of a number of other studies as ZnO nanowires grown by this technique have shown stable *p*-type conductivity for an unprecedented 18 months [70], making it one of the more promising doping methods for *p*-type ZnO nanowires.

The Wang group from Georgia Tech followed up on this solution-based Sb doping technique and found numerous improvements and advancements for the system. First, they found that by adding ammonium hydroxide to the solution, nanowires up to 60 μm in length could be grown while still maintaining the *p*-type conduction and void structures observed in previous work [72]. Wires of this size were necessary for them to demonstrate the piezotronic effect [73], a strain-based sensing technique that combines the piezoelectric and semiconducting properties of ZnO. Furthermore, in this work they were able to demonstrate that a simple piezoelectric nanogenerator [74] with an output of about 3 V could be fabricated. To further prove the viability of this material, homojunctions with *n*-type ZnO were fabricated. An axial junction was produced by growing densely packed nanowire films on top of each other [75]. By forming a *p*–*n* junction, the piezoelectric output was enhanced because the formation of the depletion region lowered the free charge carrier concentration in the bulk material, which had a deleterious effect on the nanogenerator performance. Ultimately, the nanogenerator was integrated into flexible silicone rubber that was mounted on a human wrist to detect hand gestures based on the movement of the tendons controlling the fingers.

To show the potential of Sb doping for optoelectronic devices, core–shell homojunctions [76] and heterojunctions with Si nanowires [77] were fabricated. For the homojunction wires, an array of 50 nm nanowires was grown, followed by a shell

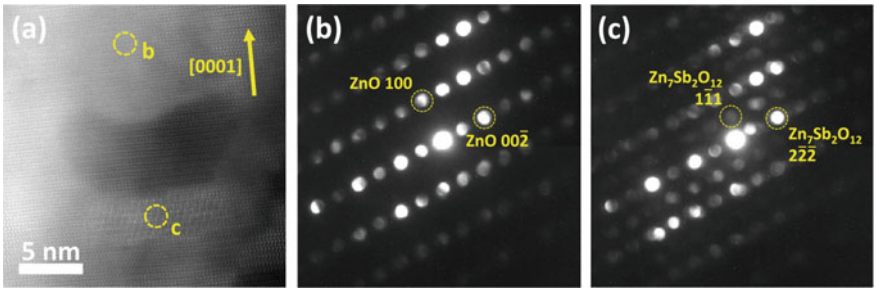

Fig. 7 **a** HAADF STEM image of a void in solution-grown Sb-doped *p*-type ZnO nanowires. The areas where nanobeam electron diffraction was performed are circled in yellow. **b** NBD pattern of the area above the void showing that only ZnO is present. **c** NBD pattern of the phase under the void with overlapping ZnO and $Zn_7Sb_2O_{12}$ phases present [71]

layer of the opposite doping type, so that both *p*-core and *n*-shell nanowires and *n*-core and *p*-shell nanowires could be grown. By using a high-concentration growth solution for the shell layer, the shell was densely packed, forming a bulk homojunction with a higher surface area than a typical planar structure. Using TEM, the aforementioned void structures were observed exclusively in the *p*-type region, confirming successful doping. The successful formation of a *p*–*n* junction was confirmed by using a UV lamp with wavelengths of 365 and 254 nm to measure the photoresponse of the device, and responses of 0.425 and 0.318 A/W, respectively, were observed at a reverse bias of 5 V, the same order of magnitude as a commercial Si-based photodiode.

The formation of a heterojunction structure was especially significant as it showed that *p*-type ZnO can interact sufficiently with other semiconductors, expanding its practical applications beyond simple ZnO-only systems. For this structure [77], Si nanowires were first formed from an *n*-type substrate using nanoimprint lithography and the Bosch process (Fig. 8a) [78]. *p*-type ZnO wires were subsequently grown, completely backfilling the space between the Si nanowires (Fig. 8b, c). ZnO nanowires grew perpendicularly from the surface of the substrate and also from the sides of the nanowires as observed via SEM and confirmed with XRD. Because the latter wires grew parallel to the substrate, a distinct (110) peak was observed, which

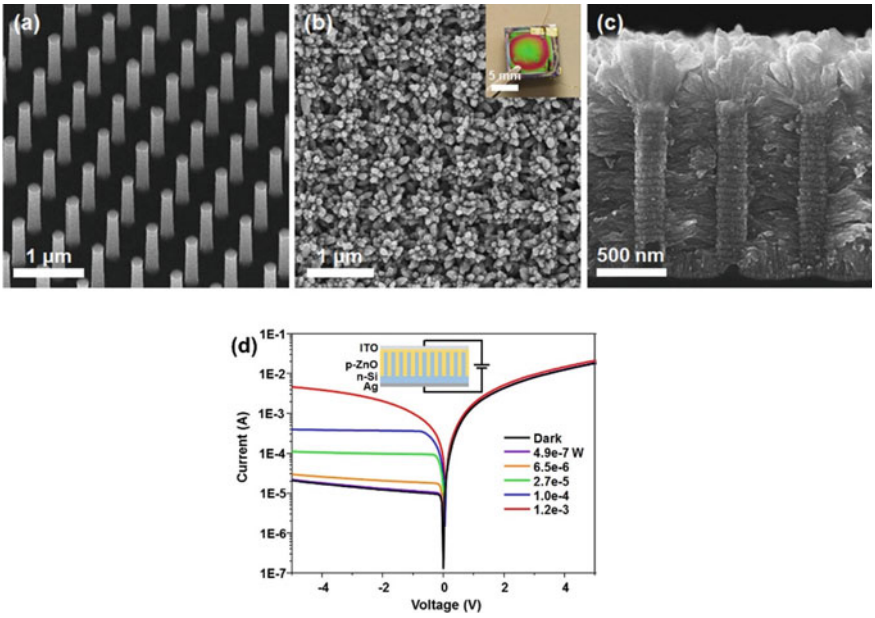

Fig. 8 **a** n-Si nanowires formed via nanoimprint lithography and the Bosch process. **b** Top and **c** side views of p-ZnO/n-Si nanowire heterojunction structures formed by solution growth. The inset in (b) shows a photograph of the sample. **d** Photoresponse IV curves of the nanowire heterojunction irradiated by a 442 nm laser at different power levels [77]

is associated with the sides of the ZnO nanowires. The photoresponse was measured using a 442 nm laser under different power levels ranging from 0.5 μW to 1.2 mW (Fig. 8d). The response time of the photodetector was less than 10 ms, which was the detection limit of the authors' characterization setup. The current varied with the laser power, as expected, but the overall responsivity at a driving voltage of 1 V was about the same, 1.02 A/W, which is much higher than that in previous reports on ZnO/Si heterojunction structures [79–81].

4 Summary and Outlook

In conclusion, a look back at the research done on these two materials has yielded an overwhelming number of results, which have only been examined to a limited extent here. Hopefully, this review can serve as a starting point, which will inspire the reader to look into synthesis techniques for materials more closely related to their interest. Naturally, much of what has been covered here for Si can also be applied to other group IV semiconductors such as Ge, which has also been subject to a large amount of research in its own right. The case of ZnO is an interesting one as stable *p*-type ZnO is still relatively new, so some fundamental measurements to determine its carrier type, such as Hall effect measurements, still have not been done. Thus, while some applications have been demonstrated, there are still large gaps in our knowledge about ZnO. There is still much fundamental work to be done with this material before research with concrete applications in mind can hopefully be carried out.

References

1. Ding Y, Wang ZL (2004) Structure analysis of nanowires and nanobelts by transmission electron microscopy. J Phys Chem B 108:12280–12291
2. Wang C-M, Xu W, Liu J, Zhang J-G, Saraf LV, Arey BW, Choi D, Yang Z-G, Xiao J, Thevuthasan S, Baer DR (2011) In situ transmission electron microscopy observation of microstructure and phase evolution in a SnO_2 nanowire during lithium intercalation. Nano Lett 11:1874–1880
3. Piscanec S, Cantoro M, Ferrari AC, Zapien JA, Lifshitz Y, Lee ST, Hofmann S, Robertson J (2003) Raman spectroscopy of silicon nanowires. Phys Rev B 68:241312
4. Qi J, Belcher AM, White JM (2003) Spectroscopy of individual silicon nanowires. Appl Phys Lett 82:2616–2618
5. Kim W, Ng JK, Kunitake ME, Conklin BR, Yang P (2007) Interfacing Silicon nanowires with mammalian cells. J Am Chem Soc 129:7228–7229
6. Yan R, Park J-H, Choi Y, Heo C-J, Yang S-M, Lee LP, Yang P (2011) Nanowire-based single-cell endoscopy. Nat Nanotechnol 7:191
7. Prinz CN (2015) Interactions between semiconductor nanowires and living cells. J Phys: Condens Matter 27:233103
8. Garnett EC, Brongersma ML, Cui Y, McGehee MD (2011) Nanowire solar cells. Annu Rev Mater Res 41:269–295

9. Wagner RS, Ellis WC (1964) Vapor-liquid-solid mechanism of single crystal growth. Appl Phys Lett 4:89–90
10. Schmidt V, Wittemann JV, Senz S, Gösele U (2009) Silicon nanowires: a review on aspects of their growth and their electrical properties. Adv Mater 21:2681–2702
11. Wang H, Zepeda-Ruiz LA, Gilmer GH, Upmanyu M (2013) Atomistics of vapour–liquid–solid nanowire growth. Nat Commun 4:1956
12. Wang Y, Schmidt V, Senz S, Gösele U (2006) Epitaxial growth of silicon nanowires using an aluminium catalyst. Nat Nanotechnol 1:186
13. Wacaser BA, Reuter MC, Khayyat MM, Wen C-Y, Haight R, Guha S, Ross FM (2009) Growth system, structure, and doping of aluminum-seeded epitaxial silicon nanowires. Nano Lett 9:3296–3301
14. Kamins TI, Williams RS, Chen Y, Chang Y-L, Chang YA (2000) Chemical vapor deposition of Si nanowires nucleated by $TiSi_2$ islands on Si. Appl Phys Lett 76:562–564
15. Schubert L, Werner P, Zakharov N, Gerth G, Kolb F, Long L, Gösele U, Tan T (2004) Silicon nanowhiskers grown on <111> Si substrates by molecular-beam epitaxy. Appl Phys Lett 84:4968–4970
16. Morales AM, Lieber CM (1998) A laser ablation method for the synthesis of crystalline semiconductor nanowires. Science 279:208–211
17. Zhang YF, Tang YH, Wang N, Yu DP, Lee CS, Bello I, Lee ST (1998) Silicon nanowires prepared by laser ablation at high temperature. Appl Phys Lett 72:1835–1837
18. Fukata N, Chen J, Sekiguchi T, Okada N, Murakami K, Tsurui T, Ito S (2006) Doping and hydrogen passivation of boron in silicon nanowires synthesized by laser ablation. Appl Phys Lett 89:203109
19. Fukata N, Matsushita S, Okada N, Chen J, Sekiguchi T, Uchida N, Murakami K (2008) Impurity doping in silicon nanowires synthesized by laser ablation. Appl Phys A 93:589–592
20. Fukata N (2009) Impurity doping in silicon nanowires. Adv Mater 21:2829–2832
21. Herrero CP, Stutzmann M (1988) Microscopic structure of boron-hydrogen complexes in crystalline silicon. Phys Rev B 38:12668–12671
22. Fano U, Effects of configuration interaction on intensities and phase shifts. Phys Rev 124:1866–1878 (1961)
23. Fukata N, Sato K, Mitome M, Bando Y, Sekiguchi T, Kirkham M, Hong J-I, Wang ZL, Snyder RL (2010) Doping and Raman characterization of boron and phosphorus atoms in germanium nanowires. ACS Nano 4:3807–3816
24. Eaton SS, Eaton GR (2002) Electron paramagnetic resonance spectroscopy. Charact Mater
25. Maekawa S, Kinoshita N (1965) Electron spin resonance in phosphorus doped silicon at low temperatures. J Phys Soc Jpn 20:1447–1457
26. Quirt J, Marko J (1972) Absolute spin susceptibilities and other ESR parameters of heavily doped n-type silicon. I. metallic samples. Phys Rev B 5:1716
27. Pan ZW, Wang ZL (2001) Nanobelts of semiconducting oxides. Science 291:1947–1949
28. Heo YW, Varadarajan V, Kaufman M, Kim K, Norton DP, Ren F, Fleming PH (2002) Site-specific growth of ZnO nanorods using catalysis-driven molecular-beam epitaxy. Appl Phys Lett 81:3046–3048
29. Greene LE, Law M, Goldberger J, Kim F, Johnson JC, Zhang Y, Saykally RJ, Yang P (2003) Low-temperature wafer-scale production of ZnO nanowire arrays. Angew Chem Int Ed 42:3031–3034
30. Greene LE, Yuhas BD, Law M, Zitoun D, Yang P (2006) Solution-grown zinc oxide nanowires. Inorg Chem 45:7535–7543
31. Xu S, Adiga N, Ba S, Dasgupta T, Wu CFJ, Wang ZL (2009) Optimizing and improving the growth quality of ZnO nanowire arrays guided by statistical design of experiments. ACS Nano 3:1803–1812
32. Xu S, Lao C, Weintraub B, Wang ZL (2008) Density-controlled growth of aligned ZnO nanowire arrays by seedless chemical approach on smooth surfaces. J Mater Res 23:2072–2077
33. Song J, Baek S, Lee J, Lim S (2008) Role of OH− in the low temperature hydrothermal synthesis of ZnO nanorods. J Chem Technol Biotechnol 83:345–350

34. Li WJ, Shi EW, Zhong WZ, Yin ZW (1999) Growth mechanism and growth habit of oxide crystals. J Cryst Growth 203:186–196
35. Wei Y, Wu W, Guo R, Yuan D, Das S, Wang ZL (2010) Wafer-scale high-throughput ordered growth of vertically aligned ZnO nanowire arrays. Nano Lett 10:3414–3419
36. Le HQ, Chua SJ, Koh YW, Loh KP, Fitzgerald EA (2006) Systematic studies of the epitaxial growth of single-crystal ZnO nanorods on GaN using hydrothermal synthesis. J Cryst Growth 293:36–42
37. Xu S, Wei Y, Kirkham M, Liu J, Mai W, Davidovic D, Snyder RL, Wang ZL (2008) Patterned growth of vertically aligned ZnO nanowire arrays on inorganic substrates at low temperature without catalyst. J Am Chem Soc 130:14958–14959
38. Yuan D, Guo R, Wei Y, Wu W, Ding Y, Wang ZL, Das S (2010) Heteroepitaxial patterned growth of vertically aligned and periodically distributed ZnO nanowires on GaN using laser interference ablation. Adv Func Mater 20:3484–3489
39. Ji L-W, Peng S-M, Wu J-S, Shih W-S, Wu C-Z, Tang IT (2009) Effect of seed layer on the growth of well-aligned ZnO nanowires. J Phys Chem Solids 70:1359–1362
40. Song J, Lim S (2006) Effect of seed layer on the growth of ZnO nanorods. The J Phys Chem C 111:596–600
41. Ghayour H, Rezaie HR, Mirdamadi S, Nourbakhsh AA (2011) The effect of seed layer thickness on alignment and morphology of ZnO nanorods. Vacuum 86:101–105
42. Baruah S, Dutta J (2009) Hydrothermal growth of ZnO nanostructures. Sci Technol Adv Mater 10:013001
43. Tian ZR, Voigt JA, Liu J, McKenzie B, McDermott MJ, Rodriguez MA, Konishi H, Xu H (2003) Complex and oriented ZnO nanostructures. Nat Mater 2:821–826
44. Zhang W, Yanagisawa K (2007) Hydrothermal synthesis of zinc hydroxide chloride sheets and their conversion to ZnO. Chem Mater 19:2329–2334
45. Sun K, Wei W, Ding Y, Jing Y, Wang ZL, Wang D (2011) Crystalline ZnO thin film by hydrothermal growth. Chem Commun 47:7776–7778
46. Zhang H, Yang D, Li D, Ma X, Li S, Que D (2005) Controllable growth of ZnO microcrystals by a capping-molecule-assisted hydrothermal process. Cryst Growth Des 5:547–550
47. Xu C, Shin P, Cao L, Gao D (2009) Preferential growth of long ZnO nanowire array and its application in dye-sensitized solar cells. The J Phys Chem C 114:125–129
48. Wang L, Tsan D, Stoeber B, Walus K (2012) Substrate-free fabrication of self-supporting ZnO nanowire arrays. Adv Mater 24:3999–4004
49. Lu M-P, Lu M-Y, Chen L-J (2012) p-Type ZnO Nanowires: from synthesis to nanoenergy. Nano Energy 1:247–258
50. Fan JC, Sreekanth KM, Xie Z, Chang SL, Rao KV (2013) p-type ZnO materials: theory, growth, properties and devices. Prog Mater Sci 58:874–985
51. Zhang SB, Wei SH, Zunger A (2001) Intrinsic n-type versus p-type doping asymmetry and the defect physics of ZnO. Phys Rev B 63:075205
52. Van de Walle CG (2000) Hydrogen as a cause of doping in zinc oxide. Phys Rev Lett 85:1012–1015
53. Janotti A, Van de Walle CG (2005) Oxygen vacancies in ZnO. Appl Phys Lett 87
54. Lv Y, Zhang Z, Yan J, Zhao W, Zhai C (2018) Al doping influences on fabricating ZnO nanowire arrays: enhanced field emission property. Ceram Int 44:7454–7460
55. Minami T, Oohashi K, Takata S, Mouri T, Ogawa N (1990) Preparations of ZnO:Al transparent conducting films by D.C. magnetron sputtering. Thin Solid Films 193–194:721–729
56. Kim H, Horwitz JS, Qadri SB, Chrisey DB (2002) Epitaxial growth of Al-doped ZnO thin films grown by pulsed laser deposition. Thin Solid Films 420–421:107–111
57. Yuan GD, Zhang WJ, Jie JS, Fan X, Zapien JA, Leung YH, Luo LB, Wang PF, Lee CS, Lee ST (2008) p-type ZnO nanowire arrays. Nano Lett 8:2591–7
58. Lu M-P, Song J, Lu M-Y, Chen M-T, Gao Y, Chen L-J, Wang ZL (2009) Piezoelectric nanogenerator using p-type ZnO nanowire arrays. Nano Lett 9:1223–1227
59. Cao BQ, Lorenz M, Rahm A, Wenckstern HV, Czekalla C, Lenzner J, Benndorf G, Grundmann M (2007) Phosphorus acceptor doped ZnO nanowires prepared by pulsed-laser deposition. Nanotechnology 18:455707

60. Look DC, Reynolds DC, Litton CW, Jones RL, Eason DB, Cantwell G (2002) Characterization of homoepitaxial p-type ZnO grown by molecular beam epitaxy. Appl Phys Lett 81:1830–1832
61. Sun JW, Lu YM, Liu YC, Shen DZ, Zhang ZZ, Li BH, Zhang JY, Yao B, Zhao DX, Fan XW (2006) The activation energy of the Nitrogen acceptor in p-type ZnO film grown by plasma-assisted molecular beam epitaxy. Solid State Commun 140:345–348
62. Xiang B, Wang P, Zhang X, Dayeh SA, Aplin DPR, Soci C, Yu D, Wang D (2006) Rational synthesis of p-type zinc oxide nanowire arrays using simple chemical vapor deposition. Nano Lett 7:323–328
63. Lee J, Cha S, Kim J, Nam H, Lee S, Ko W, Wang KL, Park J, Hong J (2011) p-type conduction characteristics of lithium-doped ZnO nanowires. Adv Mater 23:4183–4187
64. Tay CB, Chua SJ, Loh KP (2010) Stable p-type doping of ZnO film in aqueous solution at low temperatures. The J Phys Chem C 114:9981–9987
65. Tay CB, Tang J, Nguyen XS, Huang XH, Chai JW, Venkatesan VT, Chua SJ (2012) Low temperature aqueous solution route to reliable p-type doping in ZnO with K: growth chemistry, doping mechanism, and thermal stability. The J Phys Chem C 116:24239–24247
66. Fang X, Li J, Zhao D, Shen D, Li B, Wang X (2009) Phosphorus-doped p-type ZnO nanorods and ZnO nanorod p−n homojunction LED fabricated by hydrothermal method. The J Phys Chem C 113:21208–21212
67. Hwang S-H, Moon K-J, Lee TI, Lee W, Myoung J-M (2014) Controlling Phosphorus doping concentration in ZnO nanorods by low temperature hydrothermal method. Mater Chem Phys 143:600–604
68. Limpijumnong S, Zhang SB, Wei S-H, Park CH (2004) Doping by large-size-mismatched impurities: the microscopic origin of arsenic- or antimony-doped p-type zinc oxide. Phys Rev Lett 92:155504
69. Wang F, Seo JH, Bayerl D, Shi JA, Mi HY, Ma ZQ, Zhao DY, Shuai YC, Zhou WD, Wang XD (2011) An Aqueous solution-based doping strategy for large-scale synthesis of Sb-doped ZnO nanowires. Nanotechnology 22
70. Yankovich AB, Puchala B, Wang F, Seo JH, Morgan D, Wang XD, Ma ZQ, Kvit AV, Voyles PM (2012) Stable p-type conduction from Sb-decorated head-to-head basal plane inversion domain boundaries in ZnO nanowires. Nano Lett 12:1311–1316
71. Pradel KC, Jun U, Toshiaki T, Tadakatsu O, Kazuhiro H, Naoki F (2018) Investigation of nanoscale voids in Sb-doped p-type ZnO nanowires. Nanotechnology 29:335204
72. Pradel KC, Wu WZ, Zhou YS, Wen XN, Ding Y, Wang ZL (2013) Piezotronic effect in solution-grown p-type ZnO nanowires and films. Nano Lett 13:2647–2653
73. Zhou J, Gu Y, Fei P, Mai W, Gao Y, Yang R, Bao G, Wang ZL (2008) Flexible piezotronic strain sensor. Nano Lett 8:3035–3040
74. Xu S, Qin Y, Xu C, Wei Y, Yang R, Wang ZL (2010) Self-powered nanowire devices. Nat Nanotechnol 5:366
75. Pradel KC, Wu W, Ding Y, Wang ZL (2014) Solution-derived ZnO homojunction nanowire films on wearable substrates for energy conversion and self-powered gesture recognition. Nano Lett 14:6897–6905
76. Pradel KC, Ding Y, Wu W, Bando Y, Fukata N, Wang ZL (2016) Optoelectronic properties of solution grown ZnO np or pn core-shell nanowire arrays. ACS Appl Mater Interfaces 8:4287–4291
77. Pradel KC, Jevasuwan W, Suwardy J, Bando Y, Fukata N, Wang ZL (2016) Solution derived p-ZnO/n-Si nanowire heterojunctions for photodetection. Chem Phys Lett 658:158–161
78. Keith JM, Gregory N, Shufeng B, Stephen YC (2008) Wafer-scale patterning of sub-40 nm diameter and high aspect ratio (>50:1) silicon pillar arrays by nanoimprint and etching. Nanotechnology 19:345301
79. Sun K, Jing Y, Park N, Li C, Bando Y, Wang D (2010) Solution synthesis of large-scale, high-sensitivity ZnO/Si hierarchical nanoheterostructure photodetectors. J Am Chem Soc 132:15465–15467
80. Liu D, Shen X, Song T, Hu J, Sun B (2013) Low temperature solution-processed high performance photodiode based on Si–ZnO core–shell structure. Phys Chem Chem Phys 15:4970–4974

81. Al-Hardan NH, Jalar A, Abdul Hamid MA, Keng LK, Ahmed NM, Shamsudin R (2014) A wide-band UV photodiode based on n-ZnO/p-Si heterojunctions. Sens Actuators A: Phys 207:61–66

Nanoparticle Biomarkers Adapted for Near-Infrared Fluorescence Imaging

Naoto Shirahata

1 Introduction

The development of biocompatible nanoparticles adapted for *in-vitro* and *in-vivo* fluorescence imaging is a research area that is currently attracting considerable interest across a wide range of fundamental studies and biomedical disciplines [1, 2]. For *in-vivo* imaging, the use of fluorescent materials having excitation and emission bands in the near-infrared (NIR) spectral region, especially in the first (NIR-I) and second (NIR-II) biological windows (see Fig. 1), is of vital importance because of a lack of endogenous absorbers in this spectral range [3, 4]. Human tissues are made up of several organic molecules that naturally absorb (DNA, collagen, elastin, proteins, nicotinamide adenine dinucleotide (NADH), and flavin adenine dinucleotide (FAD)) and emit (NADH, FAD, proteins, and DNA) light in the ultraviolet (UV) to visible wavelength region, yielding auto-fluorescence from the tissues, which is strong in the 400–600 nm range and weak in the 700–1700 nm range (see Fig. 2) [5–7]. To avoid auto–fluorescence that interferes with the clear imaging of tissues, optical communication in the NIR spectral range is necessary. However, the organic dyes including fluorescent proteins available for NIR fluorescence imaging are rather limited, and their poor photostability also hinders their application for long-term *in-vitro* and *in-vivo* bioimaging [8].

Fluorescent inorganic nanocrystals offer substantial advantages over organic dyes such as efficient NIR emission, broad absorption spectra coupled to narrow and size-tunable emissions, and exceptional resistance to both photobleaching and chemical degradation. The clinical translation of these nanocrystals has been impeded owing to concerns regarding the biodegradability of such materials, the toxicity of degradation by-products, and/or the toxic characteristics of the nanomaterials themselves

N. Shirahata (✉)
International Center for Materials Nanoarchitectonics (WPI-MANA), National Institute for Materials Science (NIMS), 1–1 Namiki, Tsukuba 305-0044, Ibaraki, Japan
e-mail: SHIRAHATA.Naoto@nims.go.jp

Y. Wakayama and K. Ariga (eds.), *System-Materials Nanoarchitectonics*,
NIMS Monographs, https://doi.org/10.1007/978-4-431-56912-1_3

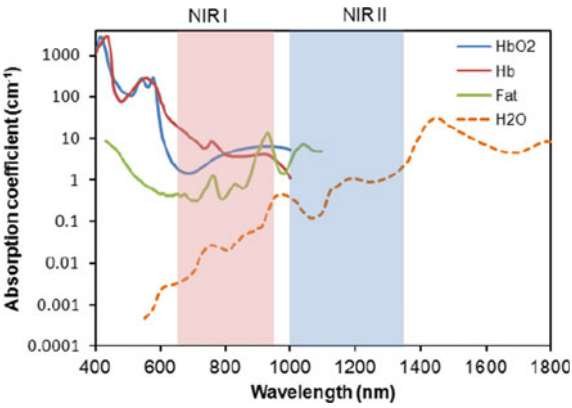

Fig. 1 Absorption coefficients (on a log scale) of oxygenated blood, deoxygenated blood, fatty tissue, and water as a function of wavelength. Reprinted from [4], Copyright 2012, with permission from MDPI

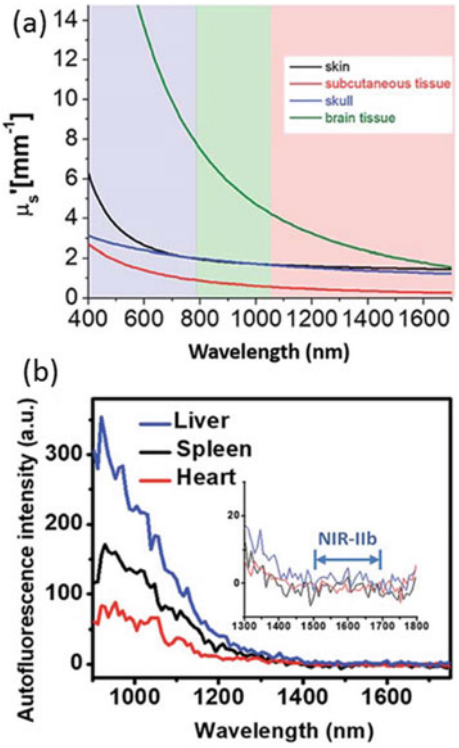

Fig. 2 **a** Reduced scattering coefficient, ms, plotted as a function of wavelength in the range of 400–1700 nm for various tissue types including the skin (black), brain (green), skull (blue) and subcutaneous tissue (red). **b** Auto-fluorescence spectrum of ex vivo mouse liver, spleen and heart tissue. Reprinted from [4], Copyright 2012, with permission from MDPI

[9–12]. Therefore, the use of NIR-emitting inorganic nanocrystals including metal nanoclusters, semiconductor quantum dots (QDs), rare-earth (RE)-doped ceramics

and perovskite nanoclusters has attracted a great deal of attention for optical communication in the biological window [13, 14]. In this chapter, recent advances in NIR-light-emitting, water-borne nanoparticles of inorganic crystals with low cytotoxicity towards biomedical applications including fluorescence imaging are demonstrated.

2 Nanoparticles

Fluorescent inorganic nanocrystals are the main component of the nanoparticle biomarkers described in this article. In principle, bioimaging can be achieved by the detection of light emission from the inorganic nanocrystals involved in the biomarkers using a confocal fluorescence microscope or a photoacoustic effect microscope. Hence, the inorganic nanocrystals have to exhibit two important characteristics, i.e., optical absorption and emission. The bandgap energy of the crystal must be designed to achieve a sufficiently high absorption coefficient for the light used for excitation. Simultaneously, high luminescence efficiency enabling detection through the microscopes has to be achieved. In this article, two different light emission mechanisms are considered: one is the radiative recombination of photoexcited carriers and the other is light emission from active centers that are excited by energy transfer (ET) from photoexcited carriers. The luminescence wavelength is determined by the energy band structure of the matrix in the former case and by the electronic structure of the active center in the latter case. Regardless of the luminescence mechanism, one of the most important issues is the termination of nonradiative recombination to obtain high luminescence efficiency.

Inorganic nanocrystals are usually insoluble in water owing to a lack of surface polarity. A typical molecular design giving water solubility and targetability is presented in Fig. 3. Water solubility is given by the chemical modification of the nanocrystal surface with amphipathic molecules or self-assembled monolayers. Self-assembled monolayers with terminal carboxyl or amine groups are conventionally used. It is known that a self-assembly of amphipathic molecules forms a micelle in water or an inverted micelle in a nonpolar organic solvent. By taking advantage of self-assembly, chemists have prepared a biomarker with a nanocrystal/monolayer/inverted-micelle core/shell/shell structure. Furthermore, in some cases, the polar surfaces are functionalized with biomolecules including an antibody, DNA aptamer or proteins as illustrated in Fig. 3. This section reviews two types of nanoparticles with RE-doped nanocrystals and colloidal QDs working as cores that can be used as emission source.

2.1 Rare-Earth-Doped Nanoparticles

Nanoparticles with RE dopant are a new class of fluorescent biomarkers that work in the NIR wavelength range. The abundant energy-level structures in 4f configurations

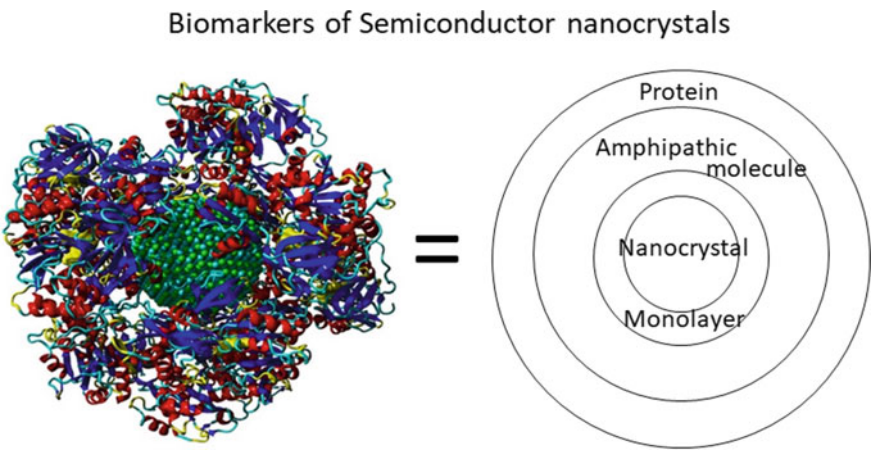

Fig. 3 A typical biomarker consisting of core/multi-shell nanostructures, and its cross-section view

and Laporte-forbidden f-f electronic transitions of RE ions result in a large Stokes shift between optical absorption and emission, sharp emission bandwidths, long PL decay time (~microsecond scale), tunable PL spectra and good photostability, which render them particularly useful for bioimaging applications [15–17]. The concept of optical communication in the biological window was reported in 2008 by Prasad and colleagues [18]. Since then, nanoparticles doped with the Tm^{3+}–Yb^{3+} couple have been widely adopted to achieve ~800 nm emission by upconversion (UC) ET from Yb^{3+} upon excitation using low-cost 980 nm laser diodes [19–24]. It is known that the nonradiative ET of RE ions, on the one hand, facilitates the effective sensitization of some RE ions by others (e.g., in the case of the Tm^{3+}–Yb^{3+} couple) but, on the other hand, greatly reduces the emission yields (i.e., concentration quenching and nonradiative cross-relaxation of RE ions). As a result, a careful design of the doping routes of RE ions in the targeted material systems is important to suppress the energy losses caused by electronic transitions between RE ions, especially when the performance characteristics of RE-ion-doped materials are approaching their physical limits. Zhou et al. reported simultaneous UC and down-shifting (DS) NIR emissions within the same nanoparticle [25]. In their study, a hexagonal-phase $NaGdF_4$ crystal (see Fig. 4a) was chosen as the host structure for RE ion doping owing to its outstanding properties including a photon energy as low as that of $NaYF_4$. As illustrated in Fig. 4b, a pair of Tm^{3+} and Yb^{3+}, which is efficient for UC NIR-to-NIR emission was doped in the host structure. On the other hand, Nd^{3+} was doped for DS NIR-to-NIR emission because of its characteristic emission peak at ~1060 nm when excited at 740 nm. Interestingly the emission intensities based on UC and DS were very low for the tri-doped nanoparticles (NTY in Fig. 4b) because the Tm^{3+} UC luminescence is quenched in the nanoparticle, suggesting that the quenching of the Tm^{3+} luminescence is strongly correlated with the presence of Nd^{3+} ions. According to the energy level diagrams of Nd^{3+}, Tm^{3+} and Yb^{3+}, ET occurs as a result of the

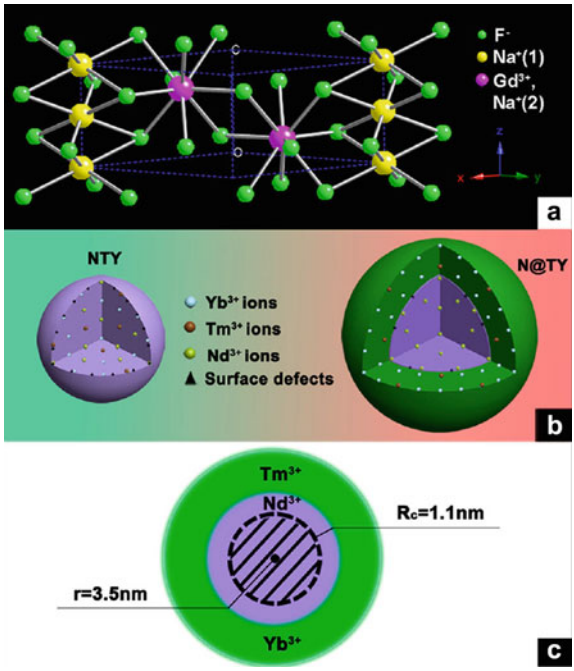

Fig. 4 **a** Crystal structure of β-NaGdF4. **b** Illustration of the spatial structure of NTY and N@TY. **c** Cross section of the core − shell structure with spatial doping. Reprinted from [25], Copyright 2013, with permission from American Chemical Society

high population density in the donor level (Tm^{3+}) and the strong absorption transition in the acceptor-level (Nd^{3+}). In the case of the DS mode, the quenching of Nd^{3+} emission is not solely due to the ET from Nd^{3+} to Yb^{3+}, but it is also a result of the inverse process of the ET mentioned above, that is, from Nd^{3+} to Tm^{3+}. As a result, efficient emission was not observed. Achieving efficient emission requires dopants of Tm^{3+} and Yb^{3+} ions which are spatially separated from Nd^{3+} in a single nanoparticle. To achieve the spatial separation, the core–shell nanostructure illustrated in Fig. 4b (N@TY) is used. Simultaneous UC and DS with high PL intensities were observed for the core–shell nanoparticles with Tm^{3+} and Yb^{3+} doped in the shell and Nd^{3+} doped in the core (see Fig. 4c).

In general, inorganic UC is a powerful technique for optical communication in the biological window [26]. Four UC processes are shown in Fig. 5. In the panels, the length of the violet arrow corresponds to the energy gap for UC emission. Panel (a) illustrates excited state absorption (ESA). ESA occurs under the sequential absorption of two or more photons by a single optically active lanthanide ion (e.g., Er^{3+}, Nd^{3+} or Tm^{3+}) with ladder-like energy levels. Typically, electrons are promoted to an intermediate energy state positioned between the ground state and the upper energy level as illustrated in panel (a). The electrons transit from the intermediate energy state to the upper energy state by absorbing more photon energy. The radiative relaxation of electrons yields UC emission. Panel (b) illustrates energy transfer upconversion (ETU). This process is similar to ESA in terms of photon energy absorption in the intermediate energy state, while it differs from ESA in that it occurs by ET between

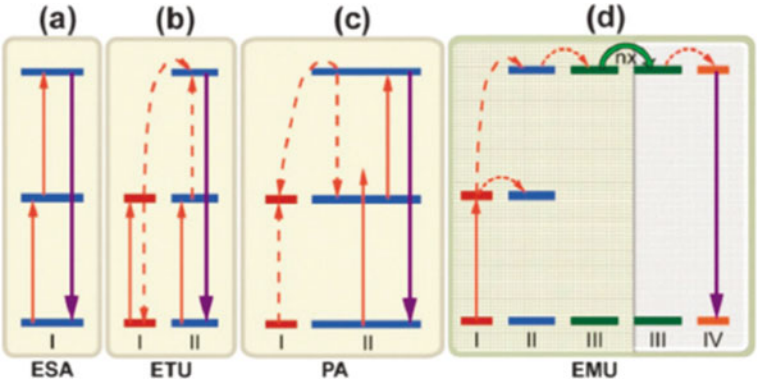

Fig. 5 Proposed typical UC processes: **a** excited state absorption (ESA); **b** energy transfer UC (ETU); **c** photon avalanche (PA). **d** Energy migration-mediated UC (EMU) involving the use of four types of lanthanide ions and a core–shell design. Reprinted from [27] Copyright 2015, with permission from Royal Society of Chemistry

two neighboring lanthanide ions. In this process, ions (I) and (II) illustrated in the panels absorb the same photon energy for the transition to the intermediate state. By nonradiative energy-transfer between the ions, one of the excited electrons (ion II) is promoted to a higher energy state for UC emission, while the other electron (ion I) relaxes back to the ground state. Panel (c) illustrates photon avalanche (PA), which is widely known as an unconventional process for UC emission. The PA process is based on the combination of the two mechanisms mentioned above. It requires an excitation power exceeding a certain threshold for pumping. Panel (d) illustrates energy-migration-mediated UC (EMU). This process does not take advantage of the intermediate energy state of a lanthanide ion. It involves the use of four types of lanthanide ions and a core–shell structure. The ions without long-lived intermediate energy states ($Ln^{3+} = Eu^{3+}$, Tb^{3+}, Dy^{3+} and Sm^{3+}) become activators to generate efficient UC luminescence in the core–shell nanoparticles, which benefit from the energy migration effect of a dopant located in the host lattice [27]. A high concentration of dopant ions seems to be necessary for efficient UC phenomena, but the intensity of optical absorption, the critical distance between the donor and the acceptor, and the radiative efficiency are dependent on the dopant concentration. Therefore, a high concentration of dopants usually results in PL quenching. For example, the optimum concentration of Tm^{3+} dopant in the $NaYF_4$ host structure has been found to be in the range of ~0.2–0.5 mol% at excitation irradiance below 100 W cm^{-2} (with ~20–40 mol% Yb^{3+}) [27].

2.2 *Quantum Dots*

QDs of semiconductors are an attractive class of fluorescent biomarkers owing to their superior optical properties including narrow PL spectra without long emission tails, continuous tunability over the NIR-I (λ_{em} = 700–950 nm) and NIR–II (λ_{em} = 1000–1700 nm) windows, PL quantum yields exceeding 30%, and PL lifetimes longer than that of autofluorescence. Furthermore, the development of water-soluble QDs adapted for multi-photon excitation opens the way towards minimal tissue absorbance and a large penetration depth for *in-vivo* study. This subsection describes the *in-vitro* and *in-vivo* imaging of NIR-emitting QDs in the region of 650–900 nm and 1000–1450 nm. The optical performance characteristics of the QDs of group I-VI, I-III-VI_2, III-V and IV semiconductors shown in Table 1 are highlighted. The PL wavelengths used for cellular imaging are tuned in the NIR-I and/or NIR-II range by taking advantage of the effects of quantum confinement (QC). The surfaces of the QDs are functionalized with organic ligands to give them solubility in water. For this purpose, chemists have usually used an amphiphile, which is a chemical compound having both hydrophilic (water-affinity, polar) and lipophilic (fat-affinity, less nonpolar) properties. In particular, polyethylene glycol (PEG) forms a micelle in water and completely envelops assemblies of QDs to give them solubility in water.

2.2.1 Group I-VI QDs

As an example of a group I-VI semiconductor QD, silver sulfide (Ag_2S) has been broadly studied. Ag_2S QDs exhibit size-dependent PL bands peaking in the NIR-I and NIR-II regions [28]. Gui, et al. reported the cation exchange between visible-light-emitting QDs of cadmium sulfide and Ag^+ ions [29]. The hydrophilic Ag_2S QDs prepared by Javidi et al. showed low cytotoxicity to both human A549 and Hep G2 cell lines at concentrations of 6.25–200 μg/mL [33]. As Ag_2S QDs have low ability to produce reactive oxygen species, low cytotoxicity and good biocompatibility are observed [30]. According to a study by Zhang et al., Ag_2S QDs, which demonstrates low toxicity in terms of cell proliferation, apoptosis and necrosis, ROS, and DNA damage, have good potential for *in-vivo* imaging, disease finding, and cancer diagnosis with clearance from the body [39]. According to blood biochemistry, hematological analysis, and histological examinations, PEGylated-Ag_2S QDs administrated to mice for up to 2 months at doses (of 15–30 mg/kg body weight show low toxicity) [40]. Qin et al. reported a fluorescence-CT dual-mode biomarker developed using DSPE-PEG2000-FA and other amphiphilic molecules to coat Ag_2S QDs and iodinated oil nanoparticles simultaneously. Their *in-vivo* experiments revealed that the biomarker has a rather long circulation time (blood half-life of 5.7 h), and histopathological tissue tests indicated that it is not damaging to the normal function of essential organs [41]. Tan et al. produced NIR fluorescent Ag_2S QDs in cultured HepG2 cancer cells [36]. QD precursors were delivered into the cells, where they reacted to produce QDs under the action of endogenous glutathione [36]. As a result

Table 1 Summary of representative QDs and their surface modifications, PL peak positions, and biomedical applications. Reproduced from [12] Copyright 2019 The Author(s) under CC BY 4.0. Published by Informa UK Limited, trading as Taylor & Francis Group

Types of QDs	Surface coating	PL peak (nm)	Applications	Ref
I-VI Group				
Ag_2Se	polyethylene glycol (PEG)	1300	Blood Clearance and bio-distribution	[31]
Ag_2Se	Multidentate polymer	950–1250	In-vivo fluorescence images	[38]
Ag_2Se	C_{18}-PMH-PEG	1300	In-vivo imaging of live mice	[93]
Ag_2S	Glutathiose	1015	Nitric oxide delivery and fluorescence imaging	[36]
Ag_2S	Dihydrolipoic acid	1000 - 1400	Early stage tumor diagnosis	[94]
Ag_2S	carboxylic acid group	825	EGFR targeted tumor imaging	[95]
I-III-VI Group				
$CuInS_2$	RNase A capped $CuInS_2$	700–800	In-vivo imaging	[44]
$AgInS_2$	multidentate polymer	820	In-vivo imaging	[96]
III-V Group				
InAs core–shell	Phospholipid Nanosomes Composite particles	1280 1300 1280	Multicolor imaging Quantitative metabolic imaging Blood flow maps	[50]
InAs/InP/ZnSe	MPA	800	Tumor detection in living mice	[51]
IV Group				
Carbon	S, Se-codoped	731 & 820	Fluorescence imaging and photothermal therapy	[90]
Carbon	Poly(vinylpyrrolidone)	750	In-vivo NIR fluorescence imaging	[91]

(continued)

Table 1 (continued)

Types of QDs	Surface coating	PL peak (nm)	Applications	Ref
Carbon	PEG-800	600–900	Photothermal cancer therapy	[97]
Carbon	Fluorescein isothiocyanate	683	Two-photon fluorescence bio-imaging	[88]
Si	Pluronic F127	650	Two-photon fluorescence cell imaging	[52]
Si	4,7-di(2-thienyl)-2,1,3-benzothiadiazole	900	Two-photon Absorbing Antenna	[75]
Si	Boron (B) and phosphorus (P) - codoped	600–1200	Time-gated fluorescence imaging in the second near-infrared window	[76]

of the QD precursors delivered into cultured hepatoma carcinoma cells, QDs with sufficient emission efficacy for *in-vivo* imaging were effectively synthesized with the aid of endogenous glutathione in the cells. A study of multiple nanodiagnostics and multicolor imaging in an *in-vivo* environment was reported by Jiang et al. who synthesized emission-tunable Ag_2S QDs ($\lambda_{em} = 690–1227$ nm) by controling their diameters from below 1.5 nm to 4.6 nm [99].

Silver selenide (Ag_2Se) also works as a fluorescent biomarker ($\lambda_{em} = 1000 - 1400$ nm). Figure 6 shows the typical PL tunability of Ag_2Se QDs at room temperature in the NIR-II region [38]. Ge et al. studied the biodistribution and clearance of Ag_2Se QDs in mice [37]. According to their paper, ICP-MS studies and biodistribution fluorescent images of the QDs in mouse organs confirmed that they could be cleared rapidly from the mouse body, typically by renal excretion, without accumulation. Furthermore, they claimed that pathological and biochemical analyses, and body weight results also showed that the QDs do not cause significant toxicity in the *in-vivo* environment. PEGylated Ag_2Se QDs exhibit blood clearance, distribution, transformation, excretion, and low toxicity in mice after intravenous injection [31]. These QDs preferentially accumulate in the spleen and liver although they are almost completely transformed and cleared within 1 day. Ag^+ ions liberated from the QDs are excreted as waste products such as in the feces and/or urine, whereas Se^{2-} ions are excreted at a low-rate, resulting in the low toxicity of PEGylated Ag_2Se QDs [32].

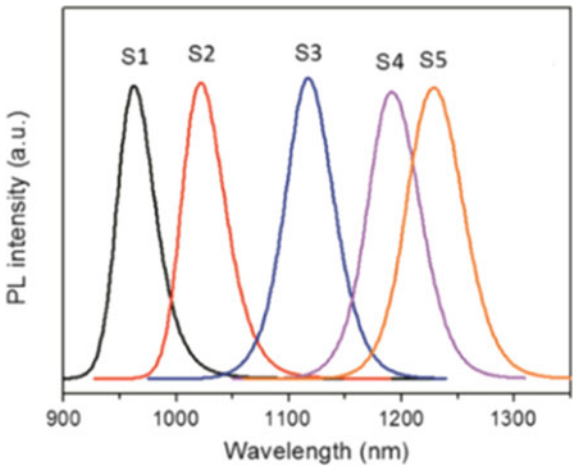

Fig. 6 PL spectra of MDP-capped Ag_2Se QDs synthesized with different reaction times (S1-S5), corresponding to 0.5, 1, 1.5, 2 and 3 h. Reprinted from [38], Copyright 2014, with permission from American Chemical Society

2.2.2 Group I-III-VI_2 QDs

Group I-III-VI_2 QDs include $CuInS_2$ $Cu(InGa)Se_2$ and $AgInS_2$. These ternary compounds consist of environmentally benign elemental components and show potential for biomedical use because of their low toxicity [11, 42]. Moreover, the band structures of these QDs can be conveniently modified through alloying. For example, NIR-emitting $AgInS_2$/ZnS QDs can be synthesized by heating a Ag/In/Zn/S solution and ending the reaction at 165 °C [43]. This paper showed that the zinc concentration and temperature strongly influence the structural parameters of QDs including the crystallinity and defect density. Cytotoxicity tests of $AgInS_2$, AgZnInS, $AgInS_2$/ZnS and AgZnInS/ZnS QDs show their use for clinical diagnosis [34]. Ag_2Te and Ag_2Te/ZnS core–shell QDs work as biomarkers with low toxicity which are available in the 900–1300 nm range [35]. As shown in Fig. 7, $CuInS_2$ QDs exhibiting the tunability of PL peak energies in the NIR-I range are good luminescent biomarkers for the gastrointestinal system [44]. Cu-doped Zn–In–S (CZIS) QDs with a ZnS shell were subjected to a cytotoxicity test to confirm their nontoxicity [45]. Fahmi and Chang. prepared $AgInS_2$-ZnS QDs and showed their high dispersity in water by covering their surfaces with oleylamine without any surfactant or polymer for cancer cell staining [46]. The addition of folic acid for conjugation with the oleylamine-capped QDs provides targeting capability for HeLa and MCF7 cancer cell staining.

2.2.3 Group III-V QDs

Indium arsenide (InAs) and indium phosphide (InP) are included in this category. Highly crystalline, surface-passivated, and monodispersed InAs QDs have superior PL spectra to other QDs in the NIR range ($\lambda_{em} = 700$–1400 nm). Such InAs QDs were

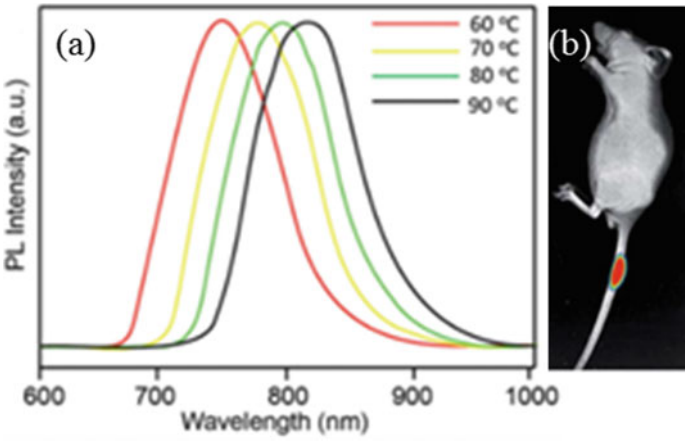

Fig. 7 **a** PL spectra of RNase A-$CuInS_2$ QDs at different reaction temperatures. **b** Mouse after treatment with the RNase A-$CuInS_2$ QDs. Reprinted from [44], by The Author(s) licensed under CC BY-NC 3.0 with permission from Royal Society of Chemistry

synthesized through self-focusing of the size distribution. Several papers showed the high optical performance of InAs QDs. For example, the maximum value of their PL quantum yields (QYs) was close to 90%, and they exhibited photostability. Furthermore, the narrow PL spectral linewidths observed are preferred for *in-vivo* multifunction imaging. Cu-doped InP QDs were synthesized by the epitaxial growth of a ZnSe diffusion barrier for the dopants. Although InP/ZnSe QDs are visible-light-emitters, they change into NIR emitters upon impurity doping. For example, Cu-doped InP/ZnSe QDs can cover the NIR spectral range (λ_{em} = 650–1100 nm) as shown in Fig. 8. As expected, PL tunability was achieved by varying the size of the InP core [47]. Allen et al. prepared water-soluble InAs (ZnCdS) QDs with bright and stable PL bands peaking in the NIR region [48]. Group III-V QDs do not contain toxic elements such as Pb, Hg and Cd, and exhibit superior optical performance for light emission on the basis of the QC effect. However, studies of III-V QDs are limited owing to complications in their synthesis. InP QDs are good fluorescence biomarkers for bio-imaging [49]. According to Bruns et al. InAs-based core–shell

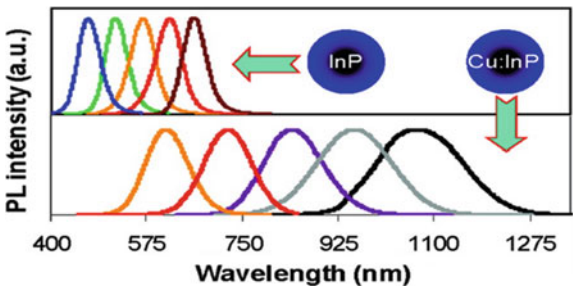

Fig. 8 PL spectra of InP and Cu-doped InP QDs. Reprinted from [47], Copyright 2009, with permission from American Chemical Society

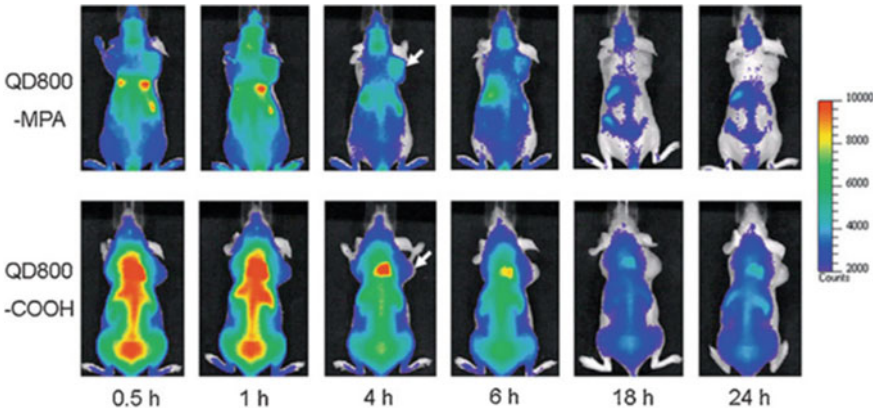

Fig. 9 In-vivo NIR fluorescence imaging of 22B tumor-bearing mice (arrows) injected with QD800-MPA and QD800-COOH. Reprinted from [51], Copyright 2010, with permission from Wiley

and core–shell–shell QDs are a flexible class of materials for functional biological imaging in the short-wave IR (SWIR) range [50]. Moreover, InAs-based QDs display a high QY and stable PL compared with the previously reported SWIR biomarkers. Gao et al. reported the use of 22B and LS174T tumor xenograft models, and *in-vivo* and ex-vivo imaging studies showed that a large amount of QD800-MPA is accumulated in the tumor part, which is essential for tumor detection in living mice as shown in Fig. 9 [51].

2.2.4 Group IV QDs

Group IV QDs include carbon dots, graphene dots, silicon (Si) nanocrystals and germanium (Ge) nanocrystals. Bulk crystalline Si is an environmentally friendly semiconductor with a room-temperature bandgap of 1.14 eV. It is highly recyclable and has been used as a fundamental material of semiconductor integrated circuits, which support our modern, highly sophisticated information society. However, since Si has an indirect transition-type band structure, its PL QY is extremely low (<~0.0001%). The effects of QC lead to the relaxation of the momentum conservation by the uncertainty principle ($\Delta\chi\,\Delta\rho \geq \hbar/2$), which allows zero-phonon optical interband transitions. This theory predicts the appearance of PL peaks with a tail on the low energy side. This tail continues until ~1.1 eV, which is equal to the bulk bandgap for crystalline Si. However, most of the NIR PL spectra reported recently show a homogeneous and Gaussian-like shape without long emission tails [52]. Although the PLQYs of hydrogen-terminated Si QDs are as low as ~5%, merely substituting the surface hydrogen atoms with alkyl chains, which yields a covalent carbon–silicon linkage, increases the PL QY up to ~60% [53]. Furthermore, the PL peak energy in the NIR-I range can be tuned even after the substitution of surface ligands [52]. Presently, the high PL QY is postulated to arise from an increase in

radiative recombination rate [54], a marked reduction in the number of non-radiative channels [55, 56], or a bandgap modulation from indirect to direct transitions [57]. Impurity doping into the diamond cubic Si lattice enables PL tunability in the NIR-II range [58]. A long PL lifetime on the microsecond scale, which is characteristic of the diamond cubic Si lattice structure, overcomes the shortcoming of auto-fluorescence [59]. NIR-emitting Si QDs have been prepared by the non-thermal plasma or thermal disproportionation of hydrogen silsesquioxane ($HSiO_{1.5}$), followed by hydrofluoric acid etching to liberate the Si QDs from the oxide matrix [60–65]. In most of the studies, $HSiO_{1.5}$ purchased from Dow Corning (trade name FOx-17) was used for QD synthesis [62, 66], but a similar compound has been derived from the hydrolysis of trichlorosilane or triethoxysilane [63, 67]. Wang et al. reported the first ever biomedical use of Si QDs as a fluorescence label for DNA [68]. Since then, Swihart and co-workers have further studied Si QD biomarkers [69]. It has been reported that cell cytotoxicity is strongly influenced by surface terminal groups [70, 71]. In particular, a low cell viability is known for an amine-terminated surface, while a carboxyl-terminated surface exhibits less toxicity to cells than amine-terminated one because most living cells are charged in minus. In many cases, amphiphilic molecules such as Pluronic F127 or PEG are employed to encapsulate the core of Si QDs owing to their electronically neutralized surfaces, yielding high hydrophilicity and biocompatibility [52, 72, 73]. Si QDs exhibit low absorption efficiency to red-to-NIR light. Therefore, it is difficult to achieve NIR–NIR excitation–emission bio-imaging in a single-photon excitation environment. To overcome this difficulty, He et al. reported the possible compatibility of the multiphoton excitation technique with Si QDs [74]. Chandra et al. developed water-borne Si QDs adapted for two-photon excitation and used them to provide the first direct evidence of NIR-to-NIR excitation–emission imaging [52]. Furthermore, HiLyte Fluor 750 amine was linked via an amide link to Si QDs prepared with Pluronic-F127-COOH as the first demonstration of a functional NIR-emitting water-dispersible biomarker of Si QDs [52]. Ravotto et al. presented a light-harvesting two-photon antenna using the emission of Si QDs [75]. This result revealed their potential for bioimaging applications, such as deep tissue imaging with –high resolution, and low photodamage– coupled with the bright, long-lived, and oxygen-insensitive NIR luminescence of Si QDs [75]. By taking advantage of the microsecond-scale PL lifetime, time-gated fluorescence imaging in the NIR-II window has also been investigated for the observation of biological tissues tagged with Si QDs [76]. Si exhibits high chemical affinity for covalent linkages with carbon, oxygen, and nitrogen, which can produce various organic derivatives hybridized at the molecular level [77]. A well-designed ligand working as a molecular wire is expected to decrease the magnitude of the potential energy barrier between NCs and monolayers, leading to efficient electronic conduction.

Bulk Ge crystal is also a typical indirect–bandgap semiconductor with a narrow bandgap of 0.67 eV at room temperature. As predicted, Ge QDs exhibit poor optical performance because of their indirect-bandgap character. However, photogenerated carriers confined in a tiny Ge crystal with a diameter smaller than the bulk exciton Bohr radius (~11.6 nm) induce a change in energy structure for light emission. This situation allows the overlapped wavefunctions of spatially confined carriers, leading

to zero-phonon optical interband transitions for recombination as a result of the relaxation of the k-selection rule due to the Heisenberg uncertainty relation [78]. Since the discovery of yellow fluorescent Ge QDs in 1993, there have been many papers showing that size-controlled structures result in emission tunability over the whole visible-wavelength range [79, 80]. In contrast, a few papers reported the colors of fluorescence in the NIR wavelength region [81–83]. Ruddy et al. reported Ge QDs ($2.3 - 11.3$ nm) synthesized by the reduction of GeI_4/GeI_2 mixtures [84]. Their QDs exhibited NIR absorption ($1.60 - 0.70$ eV) and corresponding band-edge emissions on the basis of QC effects [84]. To date, continuous tunability in a biological window in the $\lambda_{em} = 900$–1600 nm range has been achieved, but the QYs of these NIR emissions are too low (~5%) for the QDs to be adapted for fluorescent biomarkers.

Carbon QDs (CQDs) show good PL properties [85–87]. CQDs that exhibit strong absorption at around 600 to 900 nm while emitting NIR light are suitable for *in-vivo* imaging, favored uptake, and accumulation at tumors [88]. The NIR-emitting CQDs adopted for two-photon excitation exhibit high water solubility, low-cytotoxicity, a narrow spectral emission, and a PL QY as high as 16.8% [89]. Biomimetic synthesis is used to obtain CQDs. For example, NIR-emitting CQDs ($\lambda_{em} = 680$ nm, PLQY = 15%) synthesized from spinach as a precursor are excellent labeling agents for lung cancer cells (A549) excited at 543 nm [90]. Impurity doping sometimes enhances the photothermal performance. S-, and Se-codoped CQDs exhibit PL bands peaking at 731 and 820 nm, and a photothermal conversion efficiency of ~58% [90]. The CQDs have a two-photon absorption cross-section (~30,045 GM). From these results, it was claimed that CQDs are useful for phototheranostic agents, and for the two-photon excitation fluorescence imaging, and photothermal therapy of cancer cells. As CQDs show band-edge emission character, optical communication in the NIR range can be achieved on the basis of a single photon excitation technique. Furthermore, more recently, Li et al. have observed multiphoton-induced fluorescence in dimethyl sulfoxide (DMSO) under the excitation of light peaking in the NIR-II window [91]. In their paper, poly(vinylpyrrolidone) (PVP) modified CQDs were used for the *in-vivo* imaging of the stomach of a living mouse.

3 Toxicological Studies

The biomedical use of inorganic nanocrystals has raised concern about their toxicity within living organisms. Table 2 shows a summary of typical toxicological studies on different QDs [92]. Various *in-vivo* models were demonstrated for each assessment. As expected, QDs containing Cd and Pb show high toxicity in every case. The high cytotoxicity of Ag_2Se QDs is unexpected, although they show good NIR PL performance based on the effect of QC. The advantageous PL performance offered by the QDs cannot outweigh the potential risk associated with the accumulation of their constituent elements in the human body. PbSe QDs exhibit nontoxicity to cells up to a concentration of 100 μg/mL. It is predicted that PbS QDs will also show similar toxicity. On the other hand, PbS/SiO_2 core − shell QDs are nontoxic up to a

Table 2 Different types of quantum dots used for in-vivo toxicity studies in various animal models. Reprinted from [92] Copyright 2013, with permission from Royal Society of Chemistry

Type of QD	Cells	Zebrafish	Xenopus embryo	Mouse	Rat	Macaque
CdSe	Toxic after oxidation, ~0.0625 mg ml^{-1}	–	–	–	–	–
CdSe–ZnS[a]	Toxic after exposed to UV irradiation, ~1 mg ml^{-1}	LC_{50} values: 7–42 μM	Non-toxic at $4.2X10^9$ particles per cell	Non-toxic at 360 pmol - 6 nmol	Non-toxic at 15 nmol	–
CdSe–CdS–ZnS[b]	LC_{50}: ~0.7 μM	–	–	Non-toxic at 125 nmol	Non-toxic at 3 nmol	Non-toxic at 25 mg kg^{-1}
CdSe–CdS	LC_{50}: 50–100 nM	–	–	Non-toxic at 48 pmol	–	–
CdTe	LC_{50}: ~40 μg/mL	–	–	–	–	–
CdTe–ZnSe	Non-toxic at 1 mg ml^{-1}	–	–	Non-toxic at 5 mg kg^{-1}		
CdTe–ZnTe	Relatively Non-toxic at 150 μg ml^{-1}	–	–	Non-toxic at 5 mg kg^{-1}	–	–
CdTe–CdS–ZnS	Non-toxic at 3.0 μM	–	–	–	–	–
CdHgTe–ZnS	Adopted for cell imaging, no toxicity study was performed	–	–	–	–	–
CdSe–CdTe	Non-toxic at 1–10 μg ml^{-1} loaded in PLGA nanospheres	–	–	Sentinel lymph node mapping in mouse (dosage ~ 0.01 nmol) and pig (dosage ~ 0.4 nmol), no toxicity study was performed	–	–
$CdTe_xSe_{1-x}$ -CdS	Non-toxic at 200 μM	–	–	Nontoxic at 5 mg kg^{-1}	–	–

(continued)

Table 2 (continued)

Type of QD	Cells	Zebrafish	Xenopus embryo	Mouse	Rat	Macaque
InP–ZnS	Non-toxic at 100 mg ml^{-1}	–	–	Intratumor administration of 74 μg for imaging, no toxicity study was performed	–	–
Mn:ZnSe	Non-toxic at 1.2 μM	–	–	–	–	–
ZnS:Mn–ZnS	Non-toxic at 400 μg ml^{-1}	–	–	Non-toxic at 0.5 mg	–	–
Mn:$CdSe_xTe_{1-x}$ –CdS	Non-toxic at 800 μg ml^{-1}	–	–	Non-toxic at 10 mg Kg^{-1}	–	–
$InAs_xP_{1-x}$ –InP–ZnSe	–	–	–	Non-toxic at 150 pmol	–	–
InAs–ZnSe	–	–	–	Used for imaging, no toxicity study was performed	Sentinel lymph node imaging, no toxicity study was performed	–
InAs–InP–ZnSe	LC_{50}: ~ 100 nmol L^{-1}	–	–	Non-toxic at 0.5 nmol	–	–
$CuInSe_2$	–	–	–	Sentinel lymph node imaging, no toxicity study was performed	–	–
$CuInS_2$	LC_{50}: ~ 300 mg ml^{-1}	–	–	Non-toxic at 0.1–0.2 μmol (based on Cu atoms), or 0.5 mg	–	–
Ag_2Se	Non-toxic at 47.4 μg ml^{-1}	–	–	Non-toxic at 0.15 mg	–	–

(continued)

Table 2 (continued)

Type of QD	Cells	Zebrafish	Xenopus embryo	Mouse	Rat	Macaque
PbSe	Non-toxic at 100 μg ml^{-1} SiO_2 coated	–	–	–	–	–
PbS	Non-toxic at 220 μg ml^{-1}	Caused malformations above 40 μg ml^{-1}	–	Non-toxic at 25 mg kg^{-1} or 0.3 mg	–	–
ZnS	Non-toxic at 100 μM	–	–	–	–	–
Si	Non-toxic at 0.2 mg ml^{-1}	–	–	Non-toxic at 380 mg kg^{-1} or 60 nmol	–	–
CdSe–CdS Quantum rods	LC_{50}: less than 500 μM	–	–	–	–	–
CdSe–CdS–ZnS Quantum rods	Non-toxic at 500 μM and 2.8 μg ml^{-1}	–	–	Non-toxic at 1 mg	–	–

[a]Core–shell structure. [b]Core–shell–shell structure

concentration of 220 μg/mL in a cell culture owing to the presence of a nontoxic shell (i.e., SiO_2), and this concentration is as high as that of Si QDs. However, contrasting results were obtained for toxicity between PbSe/SiO_2 and Si when mice were used for the test. The concentration of PbS/SiO_2 core–shell QDs (~25 mg/kg body weight) when used as a nontoxic biomarker was very low in a nonhuman primate study of QD toxicity. However, Si QDs demonstrate non-toxicity even at 380 mg/kg body weight, which is 15 times larger than the limitation of PbS/SiO_2 QDs (~25 mg/kg body weight). This comparison indicates that covering toxic cores with less-toxic materials could not be the answer to the toxicity problems. In addition, the presence of heavy-metals in these QDs makes them a potential risk to the environment as their use increases and the products reach their end of life. Pb-based QDs also emit high intensity light up to the NIR-II region, which researchers used at a low concentration for bio-imaging after surface modification. Because of the limitations of QDs working in the NIR-II wavelength range, it is desirable to improve the PL performance for Ag-based QDs. There are many papers reporting the cellular cytotoxicity of Ag_2S QDs being lower than those of Cd-, Pb-, and Hg-based QDs. It has also been reported that $CuInS_2$ and $AgInS_2$ QDs are more biocompatible than other toxic QDs such as HgTe, CdHgTe, CdTeSe, CdTeSe/CdS, PbS, and Au/PbS QDs. InAs-based core–shell QDs do not show high cytotoxicity and are rapidly eliminated through renal clearance which reduces their potential toxicity to the body. Si and Ge QDs are non-toxic to the human body and they emit light in the NIR region. For Si QDs, the drawback is a low photoabsorption coefficient because of their energy structure, which retains the indirect bandgap nature observed for bulk crystals. Surface chemistry allowing efficient fluorescence resonance ET between surface ligands working as absorbers and Si QDs is expected to solve this problem.

4 Summary

This chapter showed the recent progress in the development of NIR-emitting biomarkers of inorganic nanocrystals towards fluorescence imaging for therapy. The tremendous efforts invested in the colloidal synthesis and further functionalization of water-borne NIR-emitting QDs with different chemical compositions was described. Nanoclusters of metals including gold are also accessible to the biological window, but the present chapter omits their discussion to focus on the advantages of semiconductor QDs and RE-doped ceramics nanoparticles. By controlling (i) the size of the QDs and/or (ii) the compositional ratio of alloys, the accessible emission wavelengths could be extended to the NIR-I and NIR-II windows. Furthermore, the QDs have unique optical properties such as a large multiphoton absorbance cross section, yielding the multiphoton absorption of NIR light and resulting in successful multiphoton imaging and upconverted emission imaging. According to this scenario, QDs with optical absorption maxima in the UV range have acquired similar importance to the NIR-to-NIR excitation—emission fluorescent biomarkers.

Group IV QDs have the potentials to be used as nontoxic and biocompatible biomarkers. Unlike the QDs of compound semiconductors, the QDs of Si and Ge exhibit a high chemical affinity with carbon to form a covalent linkage with an organic ligand (i.e., C-Si or C-Ge bonds). The covalent linkage results in high dispersity in aqueous media or organics, enabling them to be purified by various column chromatographic processes. Biochemists can avoid the problem of autofluorescence, which disturbs high-resolution imaging, by using biomarkers of Si or Ge QDs because they exhibit slow PL decay relaxation at a microsecond scale. The disadvantage in their use as biomarkers is that these QDs require UV light for excitation which exhibits a high phototoxicity. In other words, Si and Ge QDs must have a low light absorption coefficient in the visible—NIR wavelength range. Therefore, the use of a two- or three-photon excitation technique is one way to avoid the use of UV light [52]. Recently, by taking advantage of surface ligand chemistry, Ceroni and co-workers achieved efficient NIR-emission with a single photon under visible—light excitation conditions [98]. In their proposed molecular system, the strong absorption of visible light is responsible for the attachment of the organic ligand to the QD surface. The efficient ET from the ligand to the QD allows the radiative recombination to achieve the strong fluorescence. Thus, the fluorescence resonance energy transfer (FRET) mechanism is also an attractive photoexcitation method for group IV QDs. These distinguishing features observed for the NIR-emitting QDs described herein will expand their use to various pathways for bright imaging with high contrast, including photothermal cellular imaging under *in-vitro* and *in-vivo* environment.

References

1. Michalet X, Pinaud FF, Bentolila LA, Tsay JM, Doose S, Li JJ, Sundaresan G, Wu AM, Gambhir SS, Weiss S (2005) Quantum dots for live cells, in-vivo imaging, and diagnostics. Science 307:538–544
2. Resch-Genger U, Grabolle M, Cavaliere-Jaricot S, Nitschke R, Nann T (2008) Quantum dots versus organic dyes as fluorescent labels. Nat Methods 5:763–775
3. Weissleder RA (2001) Clearer vision for in-vivo imaging. Nat Biotechnol 19:316–317
4. Quek C, Leong KW (2012) Near-infrared fluorescent nanoprobes for in-vivo optical imaging. Nanomaterials 2:92–112
5. Liu TM, Conde J, Lipiński T, Bednarkiewicz A, Huang CC (2016) Revisiting the classification of NIR-absorbing/emitting nanomaterials for in-vivo bio applications. NPG Asia Mater 8:295
6. He S, Song J, Qu J, Cheng Z (2018) Crucial breakthrough of second near-infrared biological window fluorophores: design and synthesis toward multimodal imaging and theranostics. Chem Soc Rev 47:4258–4278
7. Ding F, Zhan Y, Lu X, Sun Y (2018) Recent advances in near-infrared II fluorophores for multifunctional biomedical imaging. Chem Sci 9:4370–4380
8. Eggeling C, Widengren J, Rigler R, Seidel CAM (1998) Photobleaching of fluorescent dyes under conditions used for single-molecule detection: evidence of two-step photolysis. Anal Chem 70:2651–2659
9. Reiss P, Carrière M, Lincheneau C, Vaure L, Tamang C (2016) Synthesis of semiconductor nanocrystals, focusing on nontoxic and earth-abundant materials. Chem Rev 116:10731–10819
10. Xu G, Zeng S, Zhang B, Swihart MT, Yong K, Prasad PN (2016) New generation cadmium-free quantum dots for biophotonics and nanomedicine. Chem Rev 116:12234–12327

11. Coughlan C, Ibáñez M, Dobrozhan O, Singh A, Cabot A, Ryan KM (2017) Compound copper chalcogenide nanocrystals. Chem Rev 117:5865–6109
12. Chinnathambi S, Shirahata N (2019) Recent advances on fluorescent biomarkers of near-infrared quantum dots for in-vitro and in-vivo imaging. Sci Technol Adv Mater 20:337–355
13. Gao XH, Cui YY, Levenson RM, Chung LM, Nie SM (2004) In-vivo cancer targeting and imaging with semiconductor quantum dots. Nat Biotechnol 22:969–976
14. He Y, Zhong YL, Su YY, Lu YM, Jiang ZY, Peng F, Xu TT, Su S, Huang Q, Fan CH et al (2011) Water-dispersed near-infrared-emitting quantum dots of ultrasmall sizes for in-vitro and in-vivo imaging. Angew Chem Int Ed 50:5695–5698
15. Chen GY, Ohulchanskyy TY, Kachynski A, Agren H, Prasad PN (2011) Intense visible and near-infrared upconversion photoluminescence in colloidal $LiYF_4$: Er^{3+} nanocrystals under excitation at 1490 nm. ACS Nano 5:4981–4986
16. Wang F, Deng RR, Wang J, Wang QX, Han Y, Zhu HM, Chen XY, Liu XG (2011) Tuning upconversion through energy migration in core-shell nanoparticles. Nat Mater 10:968–973
17. Ostrowski AD, Chan EM, Gargas DJ, Katz EM, Han G, Schuck PJ (2012) Controlled synthesis and single-particle imaging of bright, sub-10 nm lanthanide-doped upconverting nanocrystals. ACS Nano 6:2686–2692
18. Nyk M, Kumar R, Ohulchanskyy TY, Bergey EJ, Prasad PN (2008) High contrast in-vitro and in-vivo photoluminescence bioimaging using near infrared to near infrared up-conversion in Tm^{3+} and Yb^{3+} doped fluoride nanophosphors. Nano Lett 8:3834–3838
19. Zhou J, Sun Y, Du XX, Xiong LQ, Hu H, Li FY (2010) Dual-modality in-vivo imaging using rare-earth nanocrystals with near-infrared (NIR-to-NIR) upconversion luminescence and magnetic resonance properties. Biomaterials 31:3287–3295
20. Cao TY, Yang Y, Gao Y, Zhou J, Li ZQ, Li FY (2011) High-quality water-soluble and surface-functionalized upconversion nanocrystals as luminescent probes for bioimaging. Biomaterials 32:2959–2968
21. Zhan QQ, Qian J, Liang HJ, Somesfalean G, Wang D, He SL, Zhang ZG, Andersson-Engels S (2011) Using 915 nm laser excited Tm^{3+}/Er^{3+}/Ho^{3+}-doped $NaYbF_4$ upconversion nanoparticles for in-vitro and deeper in-vivo bioimaging without overheating irradiation. ACS Nano 5:3744–3757
22. Dong NN, Pedroni M, Piccinelli F, Conti G, Sbarbati A, Ramírez-Hernández JE, Maestro LM, Iglesias-de la Cruz MC, Sanz-Rodriguez F, Juarranz A, Chen F, Vetrone F, Capobianco JA, Solé JG, Bettinelli M, Jaque D, Speghini A (2011) NIR-to-NIR two-photon excited CaF_2: Tm^{3+}, Y^{b3}+ nanoparticles: multifunctional nanoprobes for highly penetrating fluorescence bio-imaging. ACS Nano 5:8665–8671
23. Xing HY, Bu WB, Ren QG, Zheng XP, Li M, Zhang S, Qu H, Wang Z, Hua Y, Zhao K, Zhou L, Peng W, Shi J (2012) A $NaYbF_4$: Tm^{3+} nanoprobe for CT and NIR-to-NIR fluorescent bimodal imaging. Biomaterials 33:5384–5393
24. Chen GY, Shen J, Ohulchanskyy TY, Patel NJ, Kutikov A, Li Z, Song J, Pandey RK, Agren H, Prasad PN, Han G (2012) (-NaYbF4:Tm^{3+})/CaF_2 core/shell nanoparticles with efficient near-infrared to near-infrared upconversion for high-contrast deep tissue bioimaging. ACS Nano 6:8280–8287
25. Zhou J, Shirahata N, Sun HT, Ghosh B, Ogawara M, Teng Y, Zhou S, Gui SCR, Fujii M, Qiu J (2013) Efficient dual-modal NIR-to-NIR emission of rare earth ions codoped nanocrystals for biological fluorescence imaging. J Phys Chem Lett 4:402–408
26. Lyu L, Cheong H, Ai X, Zhang W, Li J, Yang H, Lin J, Xing B (2018) Near-infrared light-mediated rare-earth nanocrystals: recent advances in improving photon conversion and alleviating the thermal effect. NPG Asia Mater 10:685–702
27. Zhou J, Xu S, Zhanga J, Qiu J (2015) Upconversion luminescence behavior of single nanoparticles. Nanoscale 7:15026–15036
28. Hong G, Robinson JT, Zhang Y, Diao S, Antaris AL, Wang Q, Dai H (2012) In-vivo fluorescence imaging with Ag_2S quantum dots in the second near-infrared region 51:9818–9821
29. Gui R, Sun J, Liu D, Wang Y, Jin H (2014) A facile cation exchange-based aqueous synthesis of highly stable and biocompatible Ag_2S quantum dots emitting in the second near-infrared biological window. Dalton Trans 43:16690–16697

30. Zamberlan F, Turyanska L, Patane A, Liu Z, Williams HEL, Fay MW, Clarke PA, Imamura Y, Jin T, Bradshaw TD, Thomas NR, Grabowska AM (2018) Stable DHLA-PEG capped PbS quantum dots: from synthesis to near-infrared biomedical imaging. J Mater Chem B 6:550–555
31. Tang H, Yang ST, Yang YF, Ke DM, Liu JH, Chen X, Wang H, Liu Y (2016) Blood clearance, distribution, transformation, excretion, and toxicity of near-infrared quantum dots Ag_2Se in mice. ACS Appl Mater Interf 8:17859–17869
32. Durmusoglu EG, Turke Y, Acar HY (2017) Green synthesis of strongly luminescent, ultrasmall PbS and PbSe quantum dots. J Phys Chem C 121:12407–12415
33. Javidi J, Haeri A, Shirazi FH, Kobarfard F, Dadashzadeh S (2017) Synthesis, characterization, in-vivo imaging, hemolysis, and toxicity of hydrophilic Ag_2S near-infrared quantum dots. J Cluster Sci 28:165–178
34. Song J, Ma C, Zhang W, Li X, Zhang W, Wu R, Cheng X, Ali A, Yang M, Zhu L, Xia R, Xu X (2016) Bandgap and structure engineering via cation exchange: from binary Ag_2S to ternary $AgInS_2$, quaternary AgZnInS alloy and AgZnInS/ZnS core/shell fluorescent nanocrystals for bioimaging. ACS Appl Mater Interf 8:24826–24836
35. Chen C, He X, Gao L, Ma N (2013) Cation exchange-based facile aqueous synthesis of small, stable, and nontoxic near-infrared Ag_2Te/ZnS core/shell quantum dots emitting in the second biological window. ACS Appl Mater Interf 5:1149–1155
36. Tan L, Wan A, Li H (2013) Conjugating nitrosothiols with glutathiose stabilized silver sulfide quantum dots for controlled nitric oxide release and near-infrared fluorescence imaging. ACS Appl Mater Interf 5:11163–11171
37. Ge XL, Zhang ZL, Xie ZX, Cui R, Pang DW (2017) Revealing the biodistribution and clearance of Ag_2Se near-infrared quantum dots in mice. New J Chem 41:12721–12725
38. Tan L, Wan A, Zhao T, Huuang R, Li H (2014) Aqueous synthesis of multidentate-polymer-capping Ag_2Se quantum dots with bright photoluminescence tunable in a second near-infrared biological window. ACS Appl Mater Interf 6:6217–6222
39. Zhang Y, Hong G, Zhang Y, Chen G, Li F, Dai H, Wang Q (2012) Ag_2S quantum dot: a bright and biocompatible fluorescent nanoprobe in the second near-infrared window. ACS Nano 6:3695–3702
40. Zhang Y, Zhang Y, Hong G, He W, Zhou K, Yang K, Li F, Chen G, Liu Z, Dai H, Wang Q (2013) Biodistribution, pharmacokinetics and toxicology of Ag_2S near-infrared quantum dots in mice. Biomaterials 34:3639–3646
41. Qin MY, Yang XQ, Wang K, Zhang XS, Song JT, Yao MH, Yan DM, Liu B, Zhao YD (2015) In-vivo cancer targeting and fluorescence-CT dual-mode imaging with nanoprobes based on silver sulfide quantum dots and iodinated oil. Nanoscale 7:19484–19492
42. Kolny-Olesiak J, Weller H (2013) Synthesis and application of colloidal $CuInS_2$ semiconductor nanocrystals. ACS Appl Mater Interf 5:12221–12237
43. Mao B, Chuang C, McCleese C, Zhu J, Burda C (2014) Near-infrared emitting $AgInS_2$/ZnS nanocrystals. J Phys Chem C 118:13883–13889
44. Xi Y, Yang J, Ge Y, Zhao S, Wang J, Li Y, Hao Y, Chen J, Zhu Y (2017) One-pot synthesis of water-soluble near-infrared fluorescence RNase A capped $CuInS_2$ quantum dots for in-vivo imaging. RSC Adv 7:50949–50954
45. Jiang T, Song J, Wang H, Ye X, Wang H, Zhang W, Yang M, Xia R, Zhu L, Xu X (2015) Aqueous synthesis of color tunable Cu doped Zn- In-S/ZnS nanoparticles in the whole visible region for cellular imaging. J Mater Chem B 3:2402–2410
46. Fahmi MZ, Chang JY (2016) Potential application of oleylamine-encapsulated $AgInS_2$-ZnS quantum dots for cancer cell labeling. Procedia Chem 18:112–121
47. Xie R, Peng X (2009) Synthesis of Cu-doped InP nanocrystals (d-dots) with ZnSe diffusion barrier as efficient and color-tunable NIR emitters. J Am Chem Soc 131, 10645–10651
48. Allen PM, Liu W, Chauhan VP, Lee J, Ting AY, Fukumura D, Jain RK, Bawendi MG (2010) InAs (ZnCdS) quantum dots optimized for biological imaging in the near-infrared. J Am Chem Soc 132:470–471
49. Liu Z, Kumbhar A, Xu D, Zhang J, Sun Z, Fang J (2008) Coreduction colloidal synthesis of III-V nanocrystals: the case of InP. Angew Chem Int Ed 120:3596–3598

50. Bruns OT, Bischof TS, Harris DK, Franke D, Shi Y, Riedemann L, Bartelt A, Jaworski FB, Carr JA, Rowlands CJ, Wilson MWB, Chen O, Wei H, Hwang GW, Montana DM, Coropceanu I, Achorn OB, Koepper J, Heeren J, So PTC, Fukumura D, Jensen KF, Jain RK, Bawendi MG (2017) Next-generation in-vivo optical imaging with short-wave infrared quantum dots. Nat Biomed Eng 1:0056
51. Gao J, Chen K, Xie R, Xie J, Lee S, Cheng Z, Chen X (2010) Ultrasmall near-infrared non-cadmium quantum dots for in-vivo tumor imaging. Small 6:256–261 (2010)
52. Chandra S, Ghosh B, Beaune G, Nagarajian U, Yasui T, Nakamura J, Tsuruoka T, Baba Y, Shirahata N, Winnik FM (2016) Functional double-shelled silicon nanocrystals for two-photon fluorescence cell imaging: spectral evolution and tuning. Nanoscale 8:9009–9019
53. Ghosh B, Yamada H, Chinnathambi S, Özbilgin ING, Shirahata N (2018) Inverted device architecture for enhanced performance of flexible silicon quantum dot light-emitting diode. J Phys Chem Lett 9:5400–5407
54. Mastronardi ML, Laier-Flaig F, Faulkner D, Henderson EJ, Kübel C, Lemmer U, Ozin GA (2012) Size-dependent absolute photoluminescence quantum yields for size-separated colloidally-stable silicon nanocrystals. Nano Lett 12:337–342
55. Ghosh B, Hamaoka T, Nemoto Y, Takeguchi M, Shirahata N (2018) Impact of anchoring monolayers on the enhancement of radiative recombination in light emitting diodes based on silicon nanocrystals. J Phys Chem C 122:6422–6430
56. Ghosh B, Takeguchi M, Nakamura J, Nemoto Y, Hamaoka T, Chandra S, Shirahata N (2016) Origin of the photoluminescence quantum yields enhanced by alkane-termination of freestanding silicon nanocrystals: temperature-dependence of optical properties. Sci Rep 6:36951
57. Dohnalová K, Poddubny AN, Prokofiev AA, de Boer WDAM, Umesh CP, Paulusse JMJ, Zuihof H, Gregorkiewicz T(2013) Surface brightens up Si quantum dots: direct bandgap-like size-tunable emission. Light Sci Appl 2:e47
58. Chandra S, Masuda Y, Shirahata N, Winnik FM (2017) Transition metal doped NIR emitting silicon nanocrystals. Angew Chem Int Ed 56:6157–6160
59. Ghosh B, Shirahata N (2014) Colloidal silicon quantum dots: synthesis and luminescence tuning from the near-UV to the near-IR range. Sci Technol Adv Mater 15:014207
60. Kortshagen UR, Sankaran RM, Pereira RN, Girshick SL, Wu JJ, Aydil ES (2016) Nonthermal plasma synthesis of nanocrystals: fundamental principles, materials, and applications. Chem Rev 116:11061–11127
61. Priolo F, Gregorkiewicz T, Galli M, Krauss TF (2014) Silicon nanostructures for photonics and photovoltaics. Nat Nanotechnol 9:19–32
62. Dasog M, Kehrle J, Rieger B, Veinot JGC (2015) Silicon nanocrystals and silicon-polymer hybrids: synthesis, surface engineering, and applications. Angew Chem Int Ed 54:2–20
63. Ghosh B, Masuda Y, Wakayama Y, Imanaka Y, Inoue J, Hashi K, Deguchi K, Yamada H, Sakka Y, Ohki S, Shimizu T, Shirahata N (2014) Hybrid white light emitting diode based on silicon nanocrystals. Adv Funct Mater 24:7151–7160
64. Fujii M, Sugimoto H, Imakita K (2016) All-inorganic colloidal silicon nanocrystals- surface modification by boron and phosphorus co-doping. Nanotechnology 27:262001
65. Dohnalová K, Gregorkiewicz T, Kůsová K (2014) Silicon quantum dots: surface matters. J Phys: Condens Matter 26:173201
66. Hessel CM, Reid D, Panthani MG, Rasch MR, Goodfellow BW, Wei J, Fujii H, Akhavan V, Korgel BA (2012) Synthesis of ligand-stabilized silicon nanocrystals with size-dependent photoluminescence spanning visible to near-infrared wavelengths. Chem Mater 24:393–401
67. Sun W, Qian C, Mastronardi ML, Wei M, Ozin GA (2013) Hydrosilylation kinetics of silicon nanocrystals. Chem Commun 49:11361–11363
68. Wang L, Reipa V, Blasic J (2004) Silicon nanoparticles as a luminescent label to DNA. Bioconjugate Chem 15:409–412
69. Erogbogbo F, Yong K, Roy I, Hu R, Law WC, Zhao W, Ding H, Wu H, Kumar R, Swihart MT, Prasad PN(2011) In-vivo targeted cancer imaging, sentinel lymph node mapping and multi-channel imaging with biocompatible silicon nanocrystals. ACS Nano 5:413–423

70. Ruizendaal L, Bhattacharjee S, Pournazari K, Rosso-Vasic M, de Haan LH, Alink GM, Marcelis ATM, Zuilhof H (2009) Synthesis and cytotoxicity of silicon nanoparticles with covalently attached organic monolayers. Nanotoxicology 3:339–347
71. Alshgarif NH, Berger CEM, Varanasi SS, Chao Y, Horrocks BR (2009) Alkyl-capped silicon nanocrystals lack cytotoxicity and have enhanced intercellular accumulation in the malignant cells via cholesterol-dependent endocytosis. Small 19:221–228
72. Chinnathambi S, Chen S, Ganesan S, Hanagata M (2014) Silicon quantum dots for biological applications. Adv Healthcare Mater 3:10–29
73. Hessel CM, Rasch MR, Hueso JL, Goodfellow BW, Akhavan VA, Puvanakrishnan P, Tunnel JW, Korgel BA (2010) Alkyl passivation and amphiphilic polymer coating of silicon nanocrystals for diagnostic imaging. Small 6:2026–2034
74. He GS, Zheng Q, Yong KT, Erogbogbo F, Swihart MT, Prasad PN (2008) Two- and three-photon absorption and frequency upconverted emission of silicon quantum dots. Nano Lett 8:2688–2692
75. Ravotto L, Chen Q, Ma Y, Vinogradov SA, Locritani M, Bergamini G, Negi F, Yu Y, Korgel BA, Ceroni P (2017) Bright long-lived luminescence of silicon nanocrystals sensitized by two-photon absorbing antenna. Chem 2:550–560
76. Sakiyama M, Sugimoto H, Fujii M (2018) Long-lived luminescence of colloidal silicon quantum dots for time-gated fluorescence imaging in the second near infrared window in biological tissue. Nanoscale 10:13902–13907
77. Shirahata N (2011) Colloidal Si nanocrystals: A controlled organic-inorganic interface and its implications of color-tuning and chemical design toward sophisticated architectures. Phys Chem Chem Phys 13:7284–7294
78. Carolan D (2017) Recent advances in germanium nanocrystals: synthesis, optical properties and applications. Prog Mater Sci 90:128–158
79. Shirahata N, Hirakawa D, Masuda Y, Sakka Y (2013) Size-dependent color-tuning of efficiently luminescent germanium nanoparticles. Langmuir 29:7401–7410
80. Ghosh B, Sakka Y, Shirahata N (2013) Efficient green-luminescent germanium nanocrystals. J Mater Chem A 1:3747–3751
81. Karatutlu A, Song M, Wheeler AP, Ersoy O, Little WR, Zhang Y, Puech P, Boi FS, Luklinska Z, Sapelkin AV (2015) Synthesis and structure of free-standing germanium quantum dots and their application in live cell imaging. RSC Adv 5:20566–20573
82. Lee DC, Pietryga JM, Rovel I, Werder DJ, Schaller RD, Klimov VI (2009) Colloidal synthesis of infrared-emitting germanium nanocrystals. J Am Chem Soc 131:3436–3437
83. Ghosh B, Ogawara M, Sakka Y, Shirahata N (2014) Reductant-free colloidal synthesis of NIR emitting germanium nanocrystals: role of primary amine. J Nanosci Nanotechnol 14:2204–2210
84. Ruddy DA, Johnson JC, Smith ER, Neale R (2010) Size and bandgap control in the solution-phase synthesis of near-infrared-emitting germanium nanocrystals. ACS Nano 4:7459–7466
85. Xu Q, Liu Y, Gao C, Wei J, Zhou H, Chen Y, Dong C, Sreeprasad TS, Li N, Xia Z (2015) Synthesis, mechanistic investigation, and application of photoluminescent sulfur and nitrogen co-doped carbon dots. J Mater Chem C 3:9885–9893
86. Xu Q, Kuang T, Liu Y, Cai L, Peng X, Sreeprasad TS, Zhao P, Yu Z, Li N (2016) Hetero atom doped carbon dots: synthesis, characterization, properties, photoluminescence mechanism and biological applications. J Mater Chem B 4:7204–7219
87. Ding H, Yu SB, Wei JS, Xiong HM (2015) Full-color light emitting carbon dots with a surface-state-controlled luminescence mechanism. ACS Nano 10:484–491
88. Pan L, Sun S, Zhang L, Jiang K, Lin H (2016) Near-infrared emissive carbon dots for two-photon fluorescence bio imaging. Nanoscale 8:17350–17356
89. Li L, Zhang R, Lu C, Sun J, Wang L, Qu B, Li T, Liu Y, Li S (2017) In situ synthesis of NIR-light emitting carbon dots derived from spinach for bio-imaging applications. J Mater Chem B 5:7328–7334
90. Lan M, Zhao S, Zhang Z, Yan L, Guo L, Niu G, Zhang J, Zhao J, Zhang H, Wang P, Zhu G, Lee CS, Zhang W (2017) Two-photon-excited near-infrared emissive carbon dots as multifunctional agents for fluorescence imaging and photothermal therapy. Nano Res 10:3113–3123

91. Li D, Jing P, Sun L, An Y, Shan X, Lu X, Zhou D, Han D, Shen D, Zhai Y, Qu S, Zboril R, Rogach AL (2018) Near-infrared excitation/emission and multiphoton-induced fluorescence of carbon dots. Adv Mater 30:1705913
92. Yong K, Law W, Hu R, Ye L, Liu L, Swihart MT, Prasad PN (2013) Nanotoxicity assessment of quantum dots: from cellular to primate studies Chem Soc Rev 42:1236–1250
93. Dong B, Li C, Chen G, Zhang Y, Deng M, Wang Q (2013) Facile synthesis of highly photoluminescent Ag_2Se quantum dots as a new fluorescent probe in the second near-infrared window for in vivo imaging. Chem Mater 25:2503–2509
94. Gu YP, Cui R, Zhang ZL, Xie ZH, Pang DW (2012) Ultrasmall near-infrared Ag_2Se quantum dots with tunable fluorescence for in vivo imaging. J Am Chem Soc 134:79–82
95. Torimoto T, Kameyama T, Kuwabata S (2014) Photofunctional materials fabricated with chalcopyrite-type semiconductor nanoparticles composed of $AgInS_2$ and its solid solutions. J Phys Chem Lett 5:336–347
96. Tan L, Liu S, Li X, Chronakis IS, Shen Y (2015) A new strategy for synthesizing $AgInS_2$ quantum dots emitting brightly in near-infrared window for in vivo imaging. Coll Surf B Biointerf 125:222–229
97. Zheng M, Li Y, Liu S, Wang W, Xie Z, Jing X (2016) One-pot to synthesize multifunctional carbon dots for near infrared fluorescence imaging and photo thermal cancer therapy. ACS Appl Mater Interf 8:23533–23541 (2016)
98. Ravotto L, Chen Q, Ma Y, Vinogradov SA, Locritani M, Bergamini G, Negri F, Yu Y, Korgel BA, Ceroni P (2017) Bright long-lived luminescence of silicon nanocrystals sensitized by two-photon absorbing antenna. Chem 2:550–560
99. Jiang P, Tian ZQ, Zhu CN, Zhang ZL, Pang DW (2012) Emission-tunable near infrared Ag_2S quantum dots. Chem Mater 24:3–5

Frontiers in Mesoscale Materials Design

Yusuke Ide, Joel Henzie, Kenya Kani, and Yusuke Yamauchi

1 Mesoporous Materials

1.1 Background

Porous materials including zeolites and activated carbons have been utilized as adsorbents and separation membranes owing to their large specific surface areas derived from the numerous pores inside these materials. They are classified into three categories depending on their pore size (diameter), namely, microporous, mesoporous, and macroporous, which possess <2 nm, 2–50 nm, and >50 nm pores, respectively [1]. Macroporous materials are highly accessibile even for large molecules, but have a small surface area. Meanwhile, microporous materials have a large pore density with a narrow pore size distribution, but they cannot provide high accessiblity to large molecules. Therefore, mesoporous materials with intermediate pore sizes have attracted much interest and have been utilized as catalysts (and their supports) [2–5], drug delivery systems (DDSs) [6, 7], and adsorbents [8, 9].

Mesoporous materials can be produced by surfactant-based synthesis with electrochemical methods. Since the first synthesis of ordered mesoporous silica was reported in the 1990s, a number of studies on mesoporous silica [10, 11], carbon [12, 13], and metal oxides [14, 15] have been reported. Furthermore, several approaches have been developed for the orientation control of tubular nanochannels. The macroscopic-scale control of nanochannels is important for innovative applications such as molecular-scale devices and electrodes with enhanced diffusion of guest species [16]. Among

Y. Ide · J. Henzie (✉)
International Center for Materials Nanoarchitectonics (WPI-MANA), National Institute for Materials Science (NIMS), 1-1 Namiki, Tsukuba 305-0044, Ibaraki, Japan
e-mail: HENZIE.Joeladam@nims.go.jp

K. Kani · Y. Yamauchi
School of Chemical Engineering and Australian Institute for Bioengineering and Nanotechnology (AIBN), The University of Queensland, Brisbane, QLD 4072, Australia

Y. Wakayama and K. Ariga (eds.), *System-Materials Nanoarchitectonics*,
NIMS Monographs, https://doi.org/10.1007/978-4-431-56912-1_4

the mesoporous materials, mesoporous metals have been considered to be the most promising materials since they have the advantages of both mesoporous structures and metallic properties, such as a robust framework and superior thermal/electrical conductivity. Owing to their metallic frameworks, mesoporous metals with high electroconductivity and high surface areas hold promise for a wide range of electrochemical applications [17]. A high specific surface area derived from numerous pores is the most advantageous trait of mesoporous metals, leading to the improved mass activity of metal catalysts, which is crucial especially in the use of precious metals. Previous studies have shown that there are abundant catalytically active sites on the surface of mesoporous metals. Thus, mesoporous metals have been widely used as promising catalysts for energy applications.

There are two methods of synthesizing mesoporous metals [17]. One is a hard-templating method where inorganic materials, silica in most cases, are used as a sacrificial template. The other is a soft-templating method where self-assembled molecules act as a pore-directing agent. In particular, the soft-templating method with the use of lyotropic liquid crystals (LLCs) has traditionally been employed to generate 2D hexagonal-ordered mesoporous structures. However, the highly viscous LLC solution restricts its wide and flexible application to various reaction systems, and the pore diameter is also relatively small. Recently, our group has proposed a new concept on the synthesis of mesoporous metals. We use a low-concentration solution of block polymer micelles so that we can easily handle and control the system. Furthermore, the pore diameter can be controlled by tuning the molecular weight of the initial block polymer. To date, a number of mesoporous metal nanoparticles and films have been synthesized by chemical reduction and electrochemical deposition, respectively. On the other hand, the possible compositions are limited to noble metals or their alloys with other metals that can be relatively easily reduced. In this section, we summarize a recent advance in this emerging research area of mesoporous materials.

1.2 Traditional Ways of Preparing Mesoporous Metals

Templating methods are the main route for the preparation of mesoporous metals, and there are two types of methods. One is called the hard-templating method where inorganic materials, especially silica, are used as templates. In this method, metals are deposited in the confined space of structured templates, and after removing the templates, replicas of the original templates can be obtained (Fig. 1). As one of the pioneering works, Ryoo et al. reported a network of interconnected Pt nanowires obtained by flowing H_2 to reduce Pt precursors in the spaces of mesoporous silica (MCM-41) [18]. In this method, the final structure is an inverted replica of the original hard template, and so far, various kinds of nanostructure including nanoparticles, nanowires, and nanowire networks have been generated with structured silica such as MCM41, SBA-15, KIT-6, MCM-48, and nanoparticles [19–23]. While the structure can be controlled by tuning the morphology of the templates, this method requires a

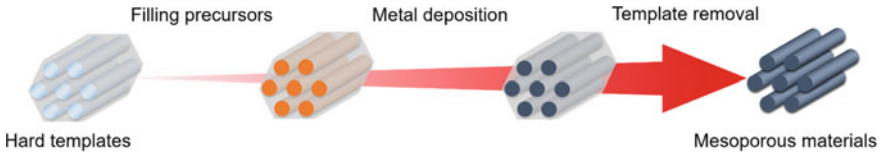

Fig. 1 Hard-templating synthesis of mesoporous materials

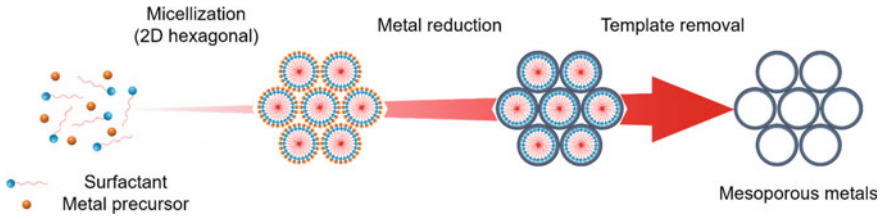

Fig. 2 Traditional soft-templating synthesis of mesoporous metals

multistep process involving the preparation of a hard template. Moreover, irregular-shaped mesoporous metals are formed because of the difficulty of controlling the metal deposition inside the template.

On the other hand, the soft-templating method, which uses self-assembled micelles as a template, is a simple process where the micelle formation and metal deposition can be carried out in the same pot. In this method, metal precursors are attached on the hydrophilic unit of micelles and reduced by reducing agents or external power sources, followed by the removal of the template to obtain the final mesoporous metal (Fig. 2). The traditional self-templating method employed surfactants such as Brij 56 and CTAB for a soft template with a high concentration (above 30 wt.%). 2D hexagonal-arrayed LLCs (Lyotropic Liquid Crystals) can be formed in such a high-concentration solution; hence, ordered mesoporous structures can be obtained. Attard et al. reported the first synthesis of mesoporous metals (Pt nanoparticles) by the soft-templating method [24], and this method has been applied to many other compositions with various shapes [25–28]. However, the relatively small pore diameter (~10 nm) and the highly viscous solution have hampered the wide-range application and easy control of the reaction system, respectively.

1.3 New Discovery in the Syntheses of Mesoporous Metal Nanoarchitectures

To overcome the limitation of pore diameter and easily handle the reaction solutions, our group has recently proposed a new method of synthesizing mesoporous metals using block polymers as a template at a low concentration. Block polymers consisting of hydrophilic and hydrophobic units can act as surfactants and form

micelles. The pore diameter can exceed 10 nm and can be controlled by tuning the molecular weight of the initial block polymers. To date, our group has studied many mesoporous metal nanoparticles [29, 30] and films [31–35] by chemical reduction and electrochemical deposition, respectively. In the former process, metal precursors are reduced around the micelle by a reducing agent, which is followed by nucleation, growth, and template removal (Fig. 3a). On the other hand, the latter uses external electrical power to reduce the metal precursors (Fig. 3b). Therefore, it is much easier to control the reaction kinetics by adjusting the potential, temperature, pH, and so on, and even non-noble metal frameworks can be attained. We believe that this concept of synthesizing mesoporous metals with a large pore size can open a new field in energy and environment catalysts such as fuel cells, supercapacitors, CO_2 conversion, and toxic gas remediation.

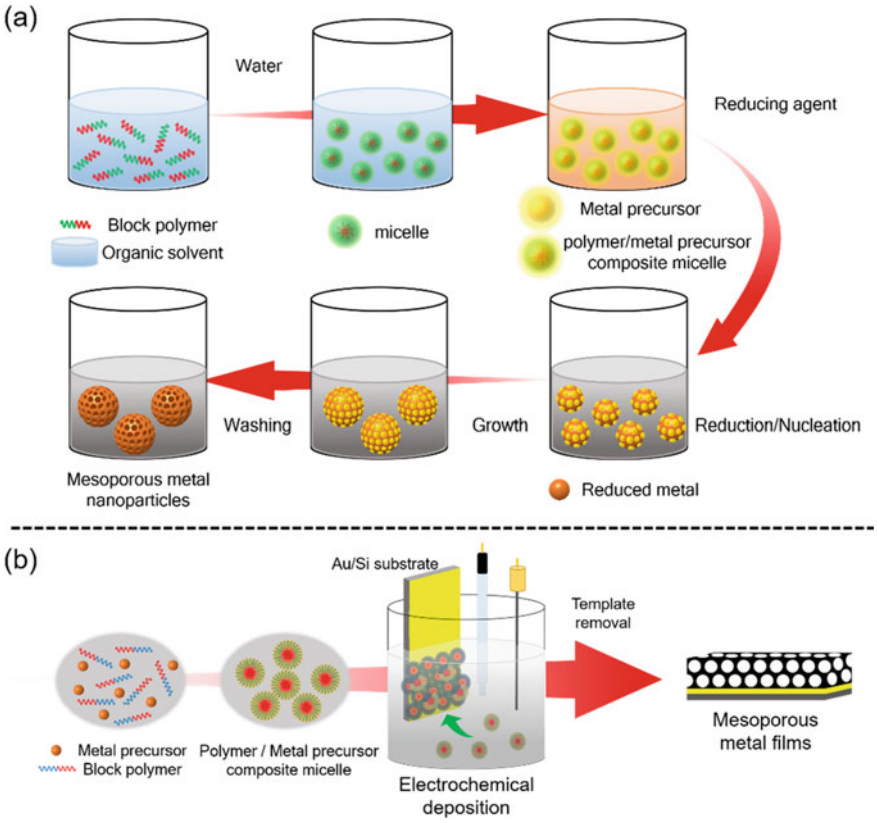

Fig. 3 Syntheses of mesoporous metal **a** nanoparticles by chemical reduction and **b** films by electrochemical deposition

2 Layered Inorganic Solids

2.1 Introduction

Layered inorganic solids including layered clay minerals are part of a class of porous materials that generate expandable 2D interlayer nanospaces that accommodate ions and molecules. These materials have high chemical and thermal stability and are inexpensive and relatively easy to synthesize or process; thus, they have long been used as ion exchangers, adsorbents, and catalysts since the 1960s. Layered inorganic solids have also been used as scaffolds to design porous materials via different intercalation methods [36–44]. On the other hand, during the past 20 years, other classes of porous materials such as zeolites and metal–organic frameworks (MOFs) that employ diverse materials and materials design techniques have been burgeoning.

Recently, our group has developed new methods of generating porous materials from layered inorganic solids such as silicates and titanates [45–61]. These new kinds of porous material are interesting because they exhibit properties and functions that are not achievable with conventional porous materials. Here, we present three good examples.

2.2 Zeolitic Magadiite But with Unique Open Micropores Within the Layers

Magadiite is a layered silicate that was originally discovered in Lake Magadi, Kenya in 1967 [62]. It is one of the most frequently used/investigated layered silicates because it can be easily prepared using simple, scalable hydrothermal reactions. However, its properties have remained mysterious, in part because its crystal structure has never been solved. We have recently reported the first known crystal structure of magadiite [52]. This structure is highly interesting because it possesses unique zeolite-like microchannels within the silicate layers. In this section, we will describe some of the details of the experiments used to solve the structure, and explain its implications for applications.

The original form of magadiite containing Na cations (called Na-magadiite) was purchased from Nippon Chemical Industrial and used without further treatments. The protonated form of the material (called H-magadiite) was generated by treating Na-magadiite with dilute HCl. We succeeded in solving the local-to-medium-range structure of Na-magadiite and H-magadiite through analysis of the X-ray pair distribution function (PDF) with the aid of other characterization methods including compositional analysis, X-ray diffraction (XRD), and solid-state nuclear magnetic resonance (NMR) spectroscopy. The unit cell was derived from the XRD pattern, while the crystal structure was solved by the real-space method using the network structure obtained by the PDF analysis.

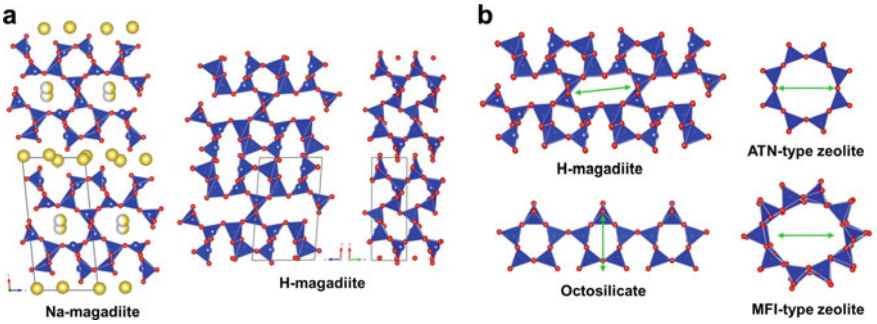

Fig. 4 **a** Structures of Na-magadiite and H-magadiite. **b** Single-layer structures of H-magadiite and octosilicate, and channel structures of 8-membered rings and 10-membered rings in ATN-type zeolite and MFI-type zeolite, respectively. Color coding: red = O, yellow = Na, blue = Si. The lengths of the arrows are identical, showing the unique shapes and sizes of micropores in H-magadiite

The structure of Na-magadiite consists of ~1.2-nm-thick silicate layers, along which microchannels are filled with Na^+ cations coordinated by H_2O molecules (and OH^- to compensate for the positive charge of Na^+) (Fig. 4a). Treating the structure with acid removes the Na^+ cations, generating open elliptical channels within the layers of H-magadiite (Fig. 4a). The silicate layer of H-magadiite is ~1.2 nm thick, which is thicker than other layered silicates such as octosilicate (also called RUB-18). This was suggested previously and is reasonable owing to the existence of microchannels defined by eight-membered rings of SiO_4 tetrahedra networks. Compared with octosilicate and other many layered silicates composed of smaller rings (e.g., four-, five-, and six-membered rings), the eight-membered ring channels are unique. The channels are accessible to certain molecules and ions as the channels are formed by Na^+ cations coordinated by H_2O molecules.

The interlayer spaces of magadiite also generate unique physiochemical properties. The interlayer space is formed by silicate surfaces covered with silanol groups like those of other protonated layered silicates, while the surface of the H-magadiite layers is covered with a large number of silanol groups, twice as many as those on protonated octosilicate. This leads to relatively strong hydrogen bonding interactions between layers in H-magadiite (this is supported by solid-state ^1H NMR experiments). The strong interactions between layers of H-magadiite suggest that aprotic solvents and hydrophobic molecules are difficult to intercalate into the interlayer space.

Indeed, the experimental data revealed that aromatic compounds dissolved in an aprotic solvent (acetonitrile) adsorbed to the micropores of H-magadiite but not to the interlayer space. This allows H-magadiite to separate aromatic compounds, which cannot be achieved with conventional zeolites containing channels with 8- and 10-membered rings [52, 53]. This specific adsorption ability must originate from the unique shape of the elliptical 8-membered ring channels (Fig. 4b). For example,

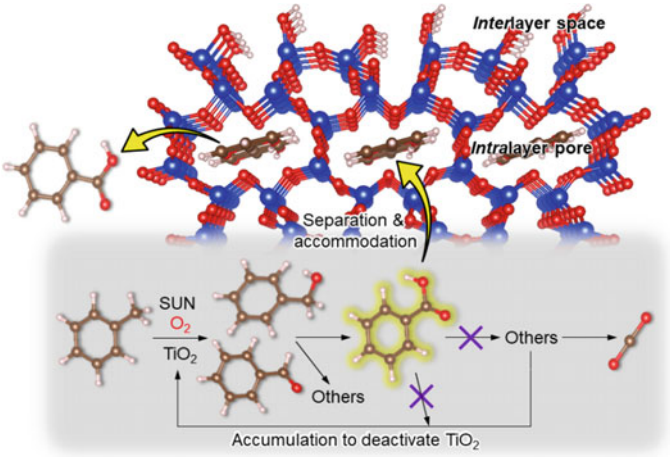

Fig. 5 Schematic representation of the effective and selective synthesis of benzoic acid from toluene by TiO_2 photocatalysis with the aid of magadiite additive

owing to the specific adsorption ability toward benzoic acid over toluene, benzaldehyde, and benzyl alcohol, magadiite could be used as an additive of TiO_2 photocatalytic systems to oxidize toluene to selectively synthesize benzoic acid (Fig. 5) [52].

2.3 Intercalation and Alignment of 1D Coordination Polymer to Create Well-Defined Janus Pores

Pillaring of layered inorganic solids with inorganic nanoparticles or organic molecules is a way of designing microporous hybrid materials with unique porous structures in layered materials. A good example of these structures is the so-called "pillared layered clays", where the interlayer space of layered clay minerals is pillared with metal oxide nanoparticles or bulky organic molecules. However, compared with zeolites and MOFs, well-defined pores still remain difficult to form in these microporous hybrids.

In addition to pillaring, the intercalation of polymers into layered inorganic solids has long been sought for many applications. However, little attention has been paid to the alignment/packing of the intercalated polymers. Here, we report on a new type of microporous hybrid obtained by packing certain kinds of one-dimensional (1D) polymer into 2D materials (Fig. 6) [54].

As the polymer component, we selected a 1D coordination polymer (CP) composed of zinc paddle-wheel units typically observed in MOFs such as MOF-2 [Zn(bdc), where bdc is 1,4-benzenedicarboxylate]. As the layered solid component, we selected the layered silicate HUS-2 $[(C_5H_{14}NO)_4\{Si_{20}O_{40}(OH)_4\}$, where

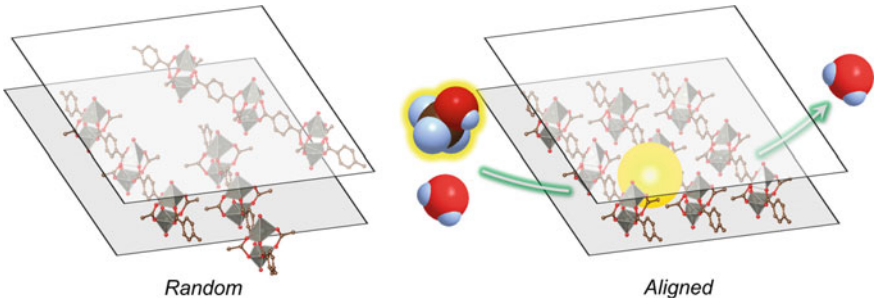

Fig. 6 *Left*: Random distribution of intercalated 1D coordination polymers. *Right*: Aligning and packing of intercalated 1D coordination polymers to create well-defined micropores (indicated by a yellow sphere), which is useful for separations including methanol/water separation

$C_5H_{14}NO$ is the interlayer choline cation] [63]. HUS-2 was pre-intercalated with zinc(II) acetylacetonate [Zn(acac)], which interacts with its surface silanol groups. Thus, the CPs were expected to form exclusively in the interlayer spaces of HUS-2 when the precursor solutions of MOF-2 were added to the reaction.

X-ray PDF analysis was used to determine the local structure of CP/HUS-2 because the crystals were not large enough to measure by single-crystal XRD analysis. This data was further analyzed by other characterization methods such as XRD and solid-state NMR spectroscopy. Figure 7a shows that CP/HUS-2 is composed of 2D-packed layers containing 1D CPs with zinc paddle-wheel units $[Zn_2(ac)_2(bdc)_2(H_2O)_2]$ (ac: acetate). The interlayer silanol groups interact with the associated H_2O of $[Zn_2(ac)_2(bdc)_2(H_2O)_2]$, forming a 3D structure with the chemical formula $[Zn_2(ac)_2(bdc)_2(H_2O)_2][Si_{15}O_{33}H_6]_{0.77}$ (Fig. 7b).

To measure the permanent porosity of CP/HUS-2, the N_2 adsorption/desorption isotherms were measured after the evacuation of the remaining organics such as solvents. As shown in Fig. 7c, CP/HUS-2 is microporous with a narrow pore size distribution, similar to zeolites and MOFs. The BET area (710 $m^2\ g^{-1}$) and micropore volume (0.36 $cm^3\ g^{-1}$) are considerably larger than those of pillared layered clays and comparable to those of zeolites. These results indicate the permanent porosity of CP/HUS-2. Considering that the intercalated CPs are densely packed next to each other and the parent HUS-2 scarcely shows porosity, the permanent microporosity must originate from the void space surrounded by the hydrophilic silicate layers, which have plenty of silanol groups, in addition to the hydrophobic benzene and methyl groups from the CPs. Thanks to these micropores, CP/HUS-2 exhibited the efficient and selective adsorption of methanol vapor owing to the cooperative interactions between the hydrophilic/hydrophobic surfaces of the adsorbent and the hydroxy/methyl groups of methanol. Also, CP/HUS-2 was successfully used as an adsorbent for the separation of methanol/water mixtures (Fig. 6), a strongly required but as-yet challenging technology for energy-effective biofuel purification.

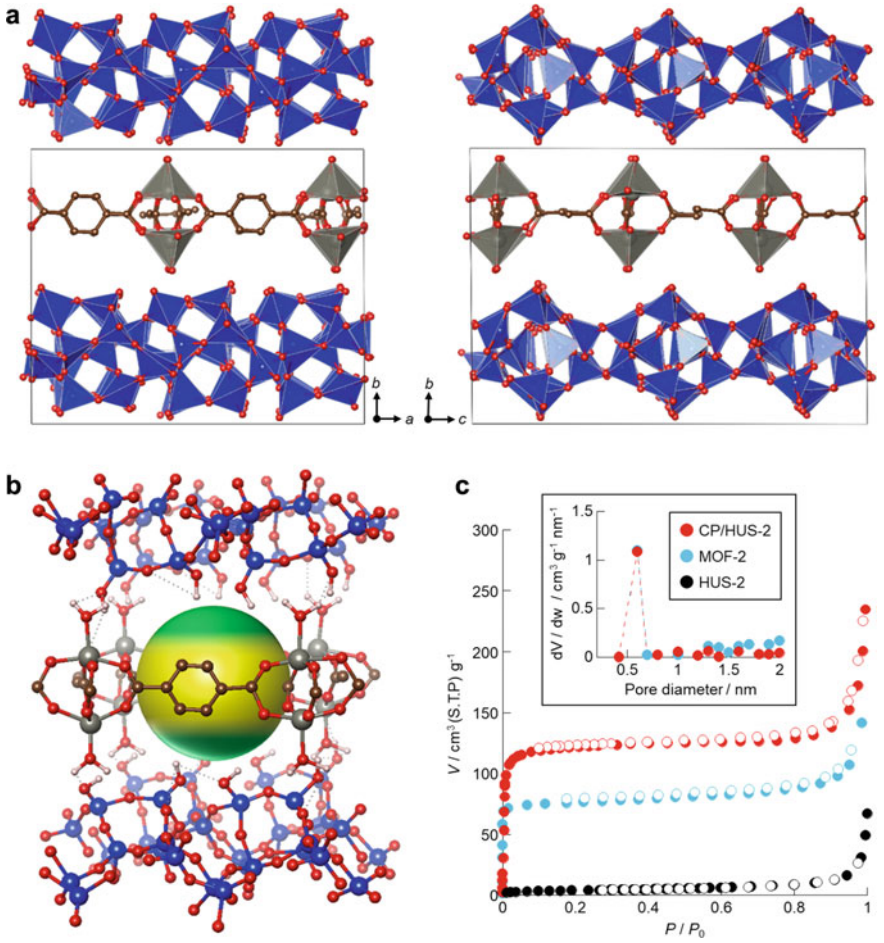

Fig. 7 **a** Local structure determined by PDF simulation and **b** calculated solvent-accessible void spaces of CP/HUS-2. Color coding: Zn = gray, Si = blue, O = red, C = brown, H = white. The void space is represented by the colored ball, and the pores have two types of faces that are exposed to hydrophobic (yellow) and hydrophilic (green) environments. The dotted lines indicate relatively strong hydrogen bonds between the silicate layers and CPs. **c** N_2 adsorption/desorption isotherm of CP/HUS-2, together with those of HUS-2 and MOF-2. The inset shows their pore size distributions

2.4 Conversion Through Nanoparts

Interzeolite conversion has been considered as an effective method of designing new kinds of zeolites. In this hydrothermal reaction, the zeolite starting materials are decomposed into small segments (so-called nanoparts) that have the same structures as the local ones of the starting zeolites. Recrystallization changes the structures and

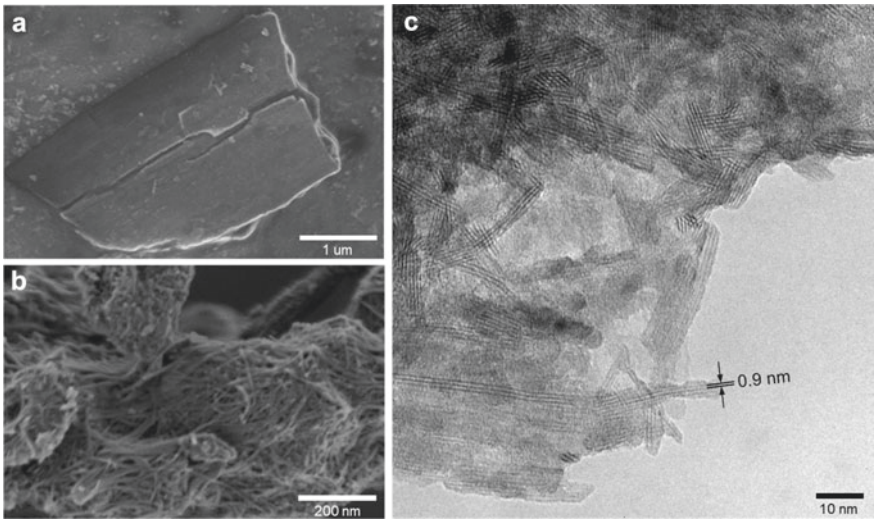

Fig. 8 **a** SEM image of the starting $K_2Ti_2O_5$. **b** SEM and **c** HRTEM images of MPTNF

new types of configuration are adopted. Inspired by this method, we have strategically converted different nanomaterials, including layered inorganic solids, into new materials, including porous materials [55–61].

A good example is the conversion of a layered titanate, $K_2Ti_2O_5$, into a new microporous TiO_2 material, microporous titanate nanofiber (MPTNF) [55]. As shown in Fig. 8, MPTNF has a nanofibrous morphology (~10 nm diameter and ~1 μm length) and contains numerous microchannels within each nanofiber (unlike a nanotube, which has only one channel). The BET is up to 240 $m^2\ g^{-1}$, which is comparable to that of state-of-the-art TiO_2 nanostructured materials. Considering the similarity in the local structure between $K_2Ti_2O_5$ and the product, we concluded that MPTNF formed via nanoparts, as suggested for interzeolite conversion.

The MPTNF material has two advantageous properties, namely, a relatively low refractive index (n) and little to no photocatalytic activity (Fig. 9a). Thanks to these properties, MPTNF can be used as a UV-absorbing transparent coating. To evaluate its UV-absorbing ability, the MPTNF was embedded in polycaprolactam ($n = 1.53$) and placed on top of a film containing a highly UV-sensitive organic dye (Rhodamine 101). This sample was then irradiated with intense UV light from the MPTNF/polycaprolactam side (Fig. 9b). The MPTNF film substantially suppressed the photodegradation of the organic dye as expected, whereas a similar film containing TiO_2 (P25) led to much more photodegradation of the UV-sensitive dye. TiO_2 has a much higher refractive index ($n \sim 2.7$) than the polymer matrix and high photocatalytic activity. So far, TiO_2 has been extensively used in sunscreen products (mainly as a UV-blocking material rather than a UV-absorbing one). For such applications, however, the photocatalytic activity of TiO_2 must be suppressed by appropriate surface modification. Also, the high refractive index of

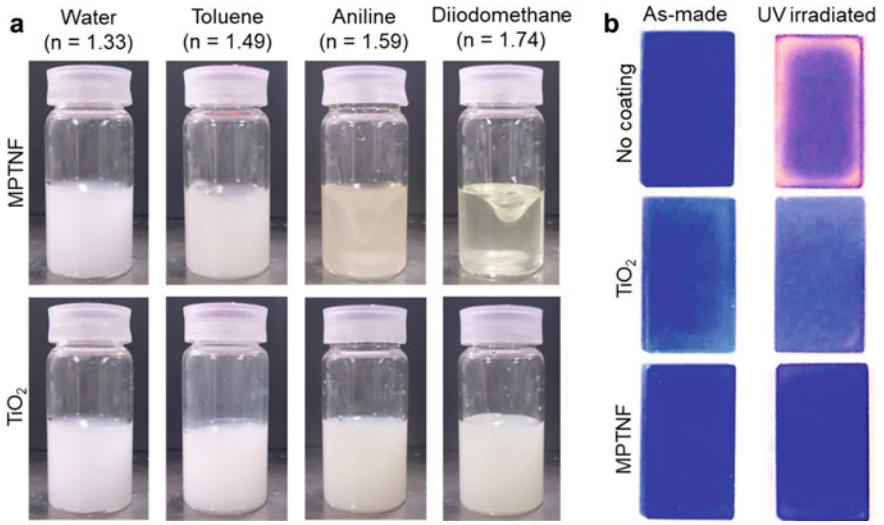

Fig. 9 **a** Immersion tests to estimate the refractive index of MPTNF. MPTNF was almost transparent when dispersed in diiodomethane ($n = 1.74$). This is due to so-called refractive index matching and means that the refractive index of MPTNF is around 1.7. **b** Color change upon UV light irradiation of Rhodamine 101 films versus the same films that were coated with polycaprolactam films containing either MPTNF or P25

TiO_2 seriously limits its application as a UV-shielding transparent coating in optical devices because the aggregate of TiO_2 particles is not transparent. Thus, MPTNF has potential as a more versatile and reliable type of UV-shielding material.

Another example is the conversion of a well-studied layered niobate, $K_4Nb_6O_{17} \cdot 3H_2O$, to a rare niobite, $K_6Nb_{10.8}O_{30}$ (Fig. 10) [61]. This niobite has 1D microchannels occupied with K^+ cations, while the properties have remained mysterious owing, at least partially, to the lack of methods to synthesize this material. The obtained $K_6Nb_{10.8}O_{30}$ is unique because its size is smaller and its aspect ratio is higher than those of $K_6Nb_{10.8}O_{30}$ prepared by a conventional complicated method. As expected, this $K_6Nb_{10.8}O_{30}$ exhibited significantly enhanced adsorption properties.

We can use many layered inorganic solids with different local structures for this type of hydrothermal reaction. In other words, we can create a variety of nanoparts and assemble them. Therefore, our series of studies show the potential of the strategic design of porous materials from layered inorganic solids.

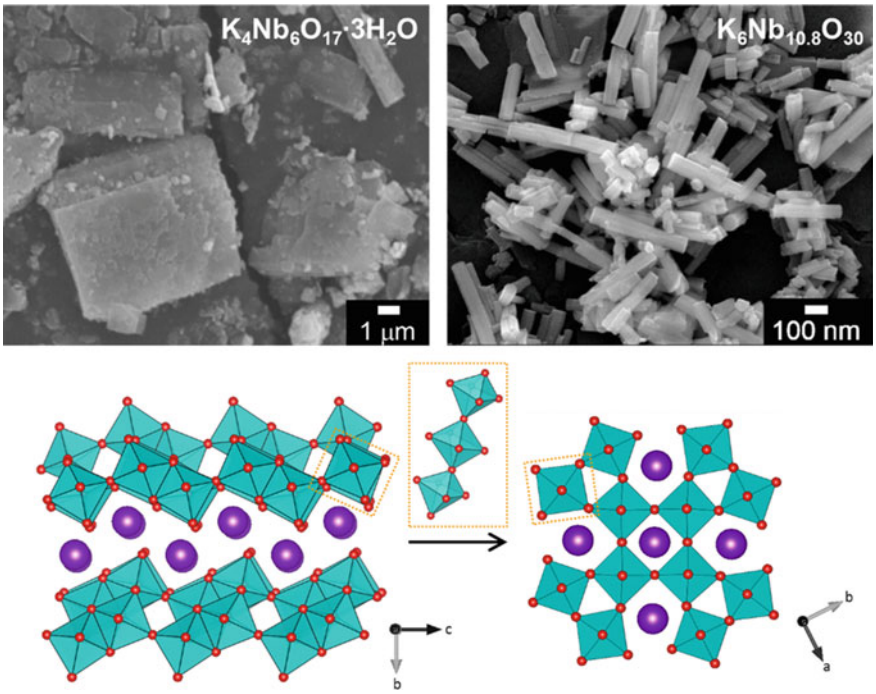

Fig. 10 Scheme for conversion of $K_6Nb_{10.8}O_{30}$ from $K_4Nb_6O_{17} \cdot 3H_2O$ through nanoparts, 1D small segments composed of NbO_6 octahedra (indicated by yellow dashed lines). The starting 2D $K_4Nb_6O_{17} \cdot 3H_2O$ is composed of platy particles, while $K_6Nb_{10.8}O_{30}$ is composed of rodlike particles reflecting the channel structure. Color coding: Nb = green, K = purple, O = red

3 Nanocrystals and Nanoparticles

3.1 Background

Devices that use electrochemical reactions to generate and/or store energy such as fuel cells [64], types of capacitor [65], and water splitting systems [66, 67] require high-surface-area porous electrodes to efficiently drive electrochemical reactions. Electrocatalysts that use precious metals are currently favored in these technologies, but their high cost and scarcity limit their large-scale adoption. Researchers have been developing new types of transition-metal catalyst that are Earth-abundant while combining good performance with low economic cost. Nanoparticles and nanocrystals have high surface areas and controllable facets that expose numerous active sites for catalysis and electrocatalysis. Our goal in this research area is to understand the nanoscale crystal chemistry of manganese oxides and learn how to create composite mesoscale 3D architectures for (photo)electrocatalysis.

3.2 α-Mn_2O_3 and the Creation of a Phase Pure Material

Minerals such as manganese oxides have emerged as catalysts owing to their high abundance in Earth's crust [68, 69]. Manganese oxides containing Mn^{3+} metal cations such as α-Mn_2O_3 possess surface $Mn^{3+}O_6$ octahedral sites with an electron in the e_g orbital and conductive metal–oxygen bonds. Researchers have demonstrated that transition metal oxide materials including mixed metal perovskites support these properties and can exhibit high electrocatalytic activities for the oxygen evolution reaction (OER) and the oxygen reduction reaction (ORR) [70–72].

Bixbyite α-Mn_2O_3 may be viewed as an intermediate step between simple oxide-based minerals and the more complex mixed metal perovskite oxides used in technological applications. It has an 80-atom unit cell with magnetic Mn ions and electron correlation between the Mn *d*-orbitals. Its crystal structure has been studied for more than 50 years, in part because it has an interesting and very subtle orthorhombic → cubic phase change at ~27 °C [73]. This phase change is also sensitive to small amounts of dopants, which tend to drive it toward the cubic phase [74]. The lack of good crystal structures and the complexity of the unit cell made it difficult to predict its electronic and magnetic properties [75]. Developing new methods to synthesize high-purity α-Mn_2O_3 is necessary to understand the properties of this prototype transition metal binary oxide. Recently, researchers have succeeded in measuring the neutron diffraction patterns of both the cubic and orthorhombic phases of α-Mn_2O_3 and solved its magnetic ground state [76]. The impact of this phase transition on the electronic band structure is still unknown, but it will affect all of its applications since it is near the operation temperature of devices.

We have recently developed two different synthetic wet-chemical methods to generate high-purity α-Mn_2O_3 nanocrystals in order to understand their fundamental electronic properties and then use them as porous electrodes in fuel cells and LIBs [77, 78]. The first method uses a phenomenon called "cation-bridging" to enable docusate anions to drive the dissolution of $LiMn_2O_3$ powder and then assist in recrystallizing the material into high-purity {100} bound α-Mn_2O_3 prisms (Fig. 11a). Figure 11b shows an SEM image of the $LiMn_2O_3$ starting material (**left**) and facetted α-Mn_2O_3 prisms (**right**). We found that the prisms were crystalline with nicely defined lattice fringes, and the edge had little to no amorphous surfaces. Initial powder X-ray diffraction (PXRD) results showed a tiny peak at ~28°, which matched the crystal structure of orthorhombic-phase α-Mn_2O_3 (Fig. 11c**; right**). Heating the prisms to a high temperature in air caused this peak to disappear, indicating that heating it caused the material to transform into the cubic phase. We used pair distribution XRD to closely examine the bonding arrangements of the as-prepared prisms and prisms that had been heated to generate their crystal structures. These results show how the structural change from orthorhombic → cubic α-Mn_2O_3 relieves Jahn–Teller distortions on the $Mn^{3+}O_6$ octahedral sites to make the material more symmetrical (Fig. 11c**; left**).

This subtle change in bonding arrangement presents a unique opportunity to study how the electronic structure of the material impacts its electrocatalytic activity. Previously, Gorlin and Jaramillo showed that electrochemically deposited α-Mn_2O_3 films

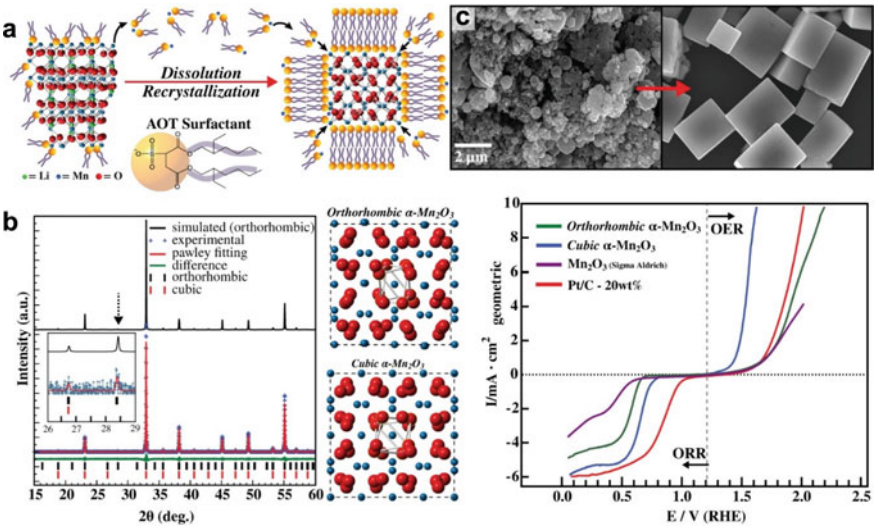

Fig. 11 **a** Scheme describing the low-temperature hydrothermal synthesis of α-Mn_2O_3 prisms from $LiMn_2O_4$ powder. The AOT surfactant assists in the dissolution and recrystallization of the prisms. **b** SEM images showing the $LiMn_2O_4$ powder precursor (**left**) and α-Mn_2O_3 product (**right**). The scale bar applies to both SEM images. **c** X-ray structural analysis of the orthorhombic-phase α-Mn_2O_3 prisms. The PXRD patterns of the newly synthesized prisms (blue dots) were analyzed with a Pawley fitting (red curve) and then compared with a simulated pattern based on the orthorhombic α-Mn_2O_3 structure. The calculated Bragg peak reflections of orthorhombic- and cubic-phase α-Mn_2O_3 are shown at the bottom. The inset pattern shows that an orthorhombic reflection occurs in the pattern that is not in the cubic phase. Crystal structures of the orthorhombic- and cubic-phase α-Mn_2O_3 prisms obtained with X-ray pair distribution function (PDF) analysis show that the cubic phase has less Jahn–Teller distortion. **d** LSVs showing the ORR and OER activities of as-prepared orthorhombic α-Mn_2O_3 prisms (green curve), cubic-phase prisms (blue curve), commercial α-Mn_2O_3 powder (purple curve), and commercial platinum catalyst (red curve)

can serve as efficient electrocatalysts in oxygen electrochemistry [79, 80]. We developed an electrochemical setup to examine the performance of α-Mn_2O_3 prisms in both OER and ORR. Figure 11d shows the linear sweep voltammetry (LSV) curves and Tafel plots for the heated and unheated α-Mn_2O_3 prisms compared with those of commercial Mn_2O_3 as well as a Pt catalyst. We estimated the overall oxygen electrode activity (OEA) of the catalysts by taking the voltage difference between the ORR at -3 mA·cm^{-2} and the OER at 10 mA·cm^{-2}. The cubic-phase α-Mn_2O_3 prisms are 79% more active than commercial Mn_2O_3 and have roughly the same activity as the Pt catalyst. Interestingly, they are ~30% more active than the unheated α-Mn_2O_3 prisms. We attribute this improvement in part to the orthorhombic → cubic transition, which likely affects the electronic properties of the material. We are currently studying how such a subtle change in the bonding arrangement caused by the phase change affects its electronic band structure.

3.3 Creation of Monodisperse α-Mn_2O_3 for Porous Electrodes

The performance of porous electrodes is limited by the size, shape, and material inhomogeneities of the materials used to construct them [81]. This lack of control is particularly important in the context of LIBs because it will affect the transport, adsorption, and intercalation of ions, which ultimately determine both the performance and safety of batteries in portable devices. Additionally, achieving better control of porous materials is the next big step in the creation of more complex hierarchical nanostructured materials whose properties and functions depend on the ordering of materials at multiple length scales.

α-Mn_2O_3 is an important alternative anode material in lithium ion batteries because it can support a high theoretical capacity. Therefore, we developed a new method of synthesizing monodisperse α-Mn_2O_3 octahedra using an approach inspired by the way organisms generate minerals in nature. In biomineralization processes, living organisms use a two-step process to precipitate a poorly crystalline product and then use ordered molecular matrices to initiate the annealing and growth of high-quality crystalline crystals. We searched for various polymers that would be a suitable molecular matrix to generate high-quality monodisperse α-Mn_2O_3 crystals. Polyvinylpyrrolidone (PVP) is a non-ionic polymer that is frequently used in shape-controlled nanoparticle synthesis methods. It also enables reversible interactions with polarizable anions and cations. So we developed a simple and inexpensive method using PVP to make monodisperse α-Mn_2O_3 octahedra on the multigram scale [78]. Figure 12a shows a scheme of the synthesis. The PVP polymer acts as a nanoscale reactor to recruit the NO_3 oxidizing agent from a solution to drive the oxidation of the Mn^{+2} precursor. The synthesis goes through two stages, first generating $Mn^{(+2,+3)}{}_3O_4$ tetragonal bipyramids that eventually undergo a topotactic reaction to generate $Mn^{(+3)}{}_2O_3$. Figure 12b shows an SEM image of the particles removed in the middle of this process, showing that the elongated bipyramids eventually transform into octahedra. After the synthesis ended, we observed monodisperse octahedral particles with an average edge length of ~300 nm (Fig. 12c).

We took the α-Mn_2O_3 octahedra samples and made porous electrodes for Li-ion half-cells, which had a total specific capacity of 831 $mA{\cdot}h{\cdot}g^{-1}$ after the first charge profile. The half-cell had a voltage plateau of ~1.25 V with a shoulder at 2.25 V matching the oxidation of Mn into MnO/MnO_x. This reaction follows the Mn^{2+}/Mn^0 redox coupling mechanism thus the practical specific capacity of the cell is limited to 832 $mA{\cdot}h{\cdot}g^{-1}$ rather than the theoretical capacity of α-Mn_2O_3 (1018 $mA{\cdot}h{\cdot}g^{-1}$). The formation of the initial surface electrolyte interface (SEI) and the partial reversibility of Li_2O formation result in a capacity loss of 44% in the first cycle. Figure 12d shows the electrochemical rate capability of the α-Mn_2O_3 electrodes when subjected to charge–discharge at increasing current densities (100, 200, 400, 800, 1600, and 3200 $mA{\cdot}g^{-1}$). The cell exhibited reversible discharge capacities of 791, 682, 646, 618, 560, and 435 $mA{\cdot}h{\cdot}g^{-1}$, respectively. After 100 galvanostatic charge–discharge cycles at a current density of 100 $mA{\cdot}g^{-1}$, it achieved a stable specific capacity of

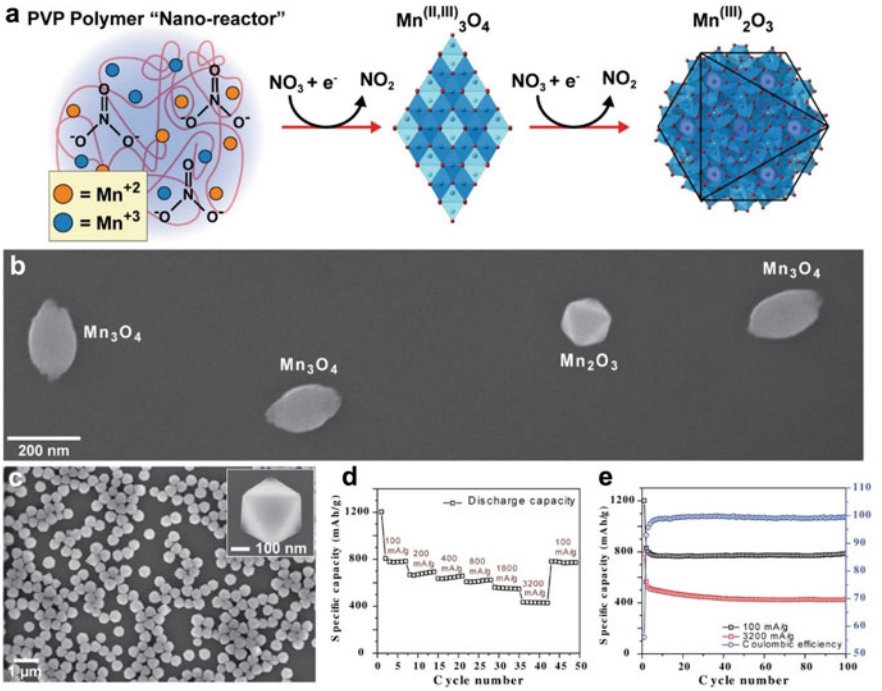

Fig. 12 **a** Scheme describing the polymer-mediated oxidation of the Mn precursor and growth of Mn_3O_4 bipyramids that ultimately form monodisperse α-Mn_2O_3 octahedra. **b** SEM image of particles taken at the transition from Mn_3O_4 to α-Mn_2O_3. **c** SEM image of the final product with monodisperse octahedra. The zoom-in image shows an individual α-Mn_2O_3 octahedron. **d** Electrochemical rate performance of monodisperse and polydisperse α-Mn_2O_3. **e** Galvanostatic cycling performance at various current densities of monodisperse octahedral α-Mn_2O_3 single crystals

780 mA·h·g^{-1} (Fig. 12e). Even after extended cycling at 3.2 A·g^{-1}, the α-Mn_2O_3 anodes retained a capacity of 425 mA·h·g^{-1}. We examined the α-Mn_2O_3 anodes by SEM after 100 lithiation–delithiation cycles, and the particles were roughly the same shape. This shows that the single-crystal α-Mn_2O_3 octahedra can accommodate a huge volume change (>200%) without fracturing or pulverizing. The homogeneity of the particles reduces the occurrence of hot spots and other heterogeneities that could lead to device failure.

Heterogeneity greatly affects the performance of porous electrodes. At the microscale level, heterogeneity in porosity leads to structural instability after extended galvanostatic cycling. Generating porous electrodes with microscale homogeneity increases performance while limiting the possibility of damage due to hot spots. At the nanoscale level, nonuniform surface terminations make lithium insertion and extraction vary from particle to particle, resulting in a nonuniform state of charge (SOC). Our nanocrystals have identical facets that ensure identical insertion/extraction dynamics. The synthetic methods described in this chapter

enable the scalable and inexpensive synthesis of high-purity α-Mn_2O_3 particles with notable performance in both LIBs and fuel cells. These methods are part of a new thrust in research and technology to generate a class of hierarchically organized nanostructured materials that are completely assembled from the bottom up.

References

1. Malgras V, Ji Q, Kamachi Y, Mori T, Shieh F, Wu KCW, Ariga K, Yamauchi Y (2015) Templated synthesis for nanoarchitectured porous materials. Bull Chem Soc Jpn 88:1171–1200
2. Shang L, Bian T, Zhang B, Zhang D, Wu LZ, Tung CH, Yin Y, Zhang T (2014) Graphene-supported ultrafine metal nanoparticles encapsulated by mesoporous silica: robust catalysts for oxidation and reduction reactions. Angew Chem Int Ed 53:250–254
3. Maiyalagan T, Alaje TO, Scott K (2012) Highly stable Pt–Ru nanoparticles supported on three-dimensional cubic ordered mesoporous carbon (Pt–Ru/CMK-8) as promising electrocatalysts for methanol oxidation. J Phys Chem C 116:2630–2638
4. Kuo CH, Mosa IM, Poyraz AS, Biswas S, Sawy AME, Song W, Luo Z, Chen S-Y, Rusling JF, He J, Suib SL (2015) Robust mesoporous manganese oxide catalysts for water oxidation. ACS Catal 5:1693–1699
5. Tao Y, Ju E, Ren J, Qu X (2014) Bifunctionalized mesoporous silica-supported gold nanoparticles: intrinsic oxidase and peroxidase catalytic activities for antibacterial applications. Adv Mater 27:1097–1104
6. Li Y, Li N, Pan W, Yu Z, Yang L, Tang B (2017) Hollow mesoporous silica nanoparticles with tunable structures for controlled drug delivery. ACS Appl Mater Interfaces 9:2123–2129
7. Chen L, Zhou X, Nie W, Zhang Q, Wang W, Zhang Y, He C (2016) Multifunctional redox-responsive mesoporous silica nanoparticles for efficient targeting drug delivery and magnetic resonance imaging. ACS Appl Mater Interfaces 8:33829–33841
8. Naushad M, Ahamad T, Al-Maswari BM, Alqadami AA, Alsheri SM (2017) Nickel ferrite bearing nitrogen-doped mesoporous carbon as efficient adsorbent for the removal of highly toxic metal ion from aqueous medium. Chem Eng J 330:1351–1360
9. Niu M, Yang H, Zhang X, Wang Y, Tang A (2016) Amine-impregnated mesoporous silica nanotube as an emerging nanocomposite for CO_2 capture. ACS Appl Mater Interfaces 8:17312–17320
10. Zhao D, Sun J, Li Q, Stucky GD (2000) Morphological control of highly ordered mesoporous silica SBA-15. Chem Mater 12:275–279
11. Che S, Liu Z, Ohsuna T, Sakamoto K, Terasaki O, Tatsumi T (2004) Synthesis and characterization of chiral mesoporous silica. Nature 429:281–284
12. Liang C, Li Z, Dai S (2008) Mesoporous carbon materials: synthesis and modification. Angew Chem Int Ed 47:3696–3717
13. Liang C, Dai S (2006) Synthesis of mesoporous carbon materials via enhanced hydrogen-bonding interaction. J Am Chem Soc 128:5316–5317
14. Ren Y, Ma Z, Bruce PG (2012) Ordered mesoporous metal oxides: synthesis and applications. Chem Soc Rev 41:4909–4927
15. Yang P, Zhao D, Margolese DI, Chmelka BF, Stucky GD (1999) Block copolymer templating syntheses of mesoporous metal oxides with large ordering lengths and semicrystalline framework. Chem Mater 11:2813–2826
16. Wu KC-W, Jiang X, Yamauchi Y (2011) New trend on mesoporous films: precise controls of one-dimensional (1D) mesochannels toward innovative applications. J Mater Chem 21:8934–8939
17. Malgras V, Ataee-Esfahani H, Wang H, Jiang B, Li C, Wu KCW, Kim JH, Yamauchi Y (2016) Nanoarchitectures for mesoporous metals. Adv Mater 28:993–1010

18. Ryoo R, Joo SH, Jun S (1999) Synthesis of highly ordered carbon molecular sieves via template-mediated structural transformation. J Phys Chem B 103:7743–7746
19. Wang D, Zhou WL, McCaughy BF, Hampsey JE, Ji X, Jiang YB, Xu H, Tang J, Schmehl RH, O'Connor C, Brinker CJ, Lu Y (2003) Electrodeposition of metallic nanowire thin films using mesoporous silica templates. Adv Mater 15:130–133
20. Liu Z, Sakamoto Y, Ohsuna T, Hiraga K, Terasaki O, Ko CH, Shin HJ, Ryoo R (2000) TEM studies of platinum nanowires fabricated in mesoporous silica MCM-41. Angew Chem Int Ed 39:3107–3110
21. Takai A, Doi Y, Yamauchi Y, Kuroda K (2010) Soft-chemical approach of noble metal nanowires templated from mesoporous silica (SBA-15) through vapor infiltration of a reducing agent. J Phys Chem C 114:7586–7593
22. Doi Y, Takai A, Sakamoto Y, Terasaki O, Yamauchi Y, Kuroda K (2010) Tailored synthesis of mesoporous platinum replicas using double gyroid mesoporous silica (KIT-6) with different pore diameters via vapor infiltration of a reducing agent. Chem Commun 46:6365–6367
23. Guo XJ, Yang CM, Liu PH, Cheng MH, Chao KJ (2005) Formation and growth of platinum nanostructures in cubic mesoporous silica. Cryst Growth Des 5:33–36
24. Attard GS, Corker JM, Göltner CG, Henke S, Templer RH (1997) Liquid-crystal templates for nanostructured metals. Angew Chem Int Ed 36:1315–1317
25. Elliott JM, Birkin PR, Bartlett PN, Attard GS (1999) Platinum microelectrodes with unique high surface areas. Langmuir 15:7411–7415
26. Takai A, Yamauchi Y, Kuroda K (2010) Tailored electrochemical synthesis of 2D-hexagonal, lamellar, and cage-type mesostructured Pt thin films with extralarge periodicity. J Am Chem Soc 132:208–214
27. Bartlett PN, Pletcher D, Esterle TF, Low CJ (2013) The deposition of mesoporous Ni/Co alloy using cetyltrimethylammonium bromide as the surfactant in the lyotropic liquid crystalline phase bath. J Electroanal Chem 688:232–236
28. Theplaew J, Therdthianwong S, Kucernak A, Therdthianwong A (2012) Electrocatalytic activity of mesoporous binary/ternary PtSn-based catalysts for ethanol oxidation. J Electroanal Chem 685:41–46
29. Jiang B, Li C, Tang J, Takei T, Kim JH, Ide Y, Henzie J, Tominaka S, Yamauchi Y (2016) Tunable-sized polymeric micelles and their assembly for the preparation of large mesoporous platinum nanoparticles. Angew Chem Int Ed 55:10037–10041
30. Kang Y, Jiang B, Alothman ZA, Badjah AY, Naushad M, Habila M, Wabaidur S, Henzie J, Li H, Yamauchi Y (2019) Mesoporous PtCu alloy nanoparticles with tunable compositions and particles sizes using diblock copolymer micelle templates. Chem Eur J 25:343–348
31. Li C, Dag Ö, Dao TD, Nagao T, Sakamoto Y, Kimura T, Terasaki O, Yamauchi Y (2015) Electrochemical synthesis of mesoporous gold films toward mesospace-stimulated optical properties. Nat Commun 6:6608
32. Iqbal M, Li C, Wood K, Jiang B, Takei T, Dag Ö, Baba D, Nugraha AS, Asahi T, Whitten AE, Hossain MSA, Malgras V, Yamauchi Y (2017) Continuous mesoporous Pd films by electrochemical deposition in nonionic micellar solution. Chem Mater 29:6405–6413
33. Li C, Jiang B, Wang Z, Li Y, Hossain MSA, Kim JH, Takei T, Henzie J, Dag Ö, Bando Y, Yamauchi Y (2016) First synthesis of continuous mesoporous copper films with uniformly sized pores by electrochemical soft templating. Angew Chem Int Ed 55:12746–12750
34. Iqbal M, Kim J, Yuliarto B, Jiang B, Li C, Dag Ö, Malgras V, Yamauchi Y (2018) Standing mesochannels: mesoporous PdCu films with vertically aligned mesochannels from nonionic micellar solutions. ACS Appl Mater Interfaces 10:40623–40630
35. Nugraha AS, Malgras V, Iqbal M, Jiang B, Li C, Bando Y, Alshehri A, Kim J, Yamauchi Y, Asahi T (2018) Electrochemical synthesis of mesoporous Au–Cu Alloy films with vertically oriented mesochannels using block copolymer micelles. ACS Appl Mater Interfaces 10:23783–23791
36. Okada T, Ide Y, Ogawa M (2012) Organic–inorganic hybrids based on ultrathin oxide layers: designed nanostructures for molecular recognition. Chem -Asian J 7:1980–1992
37. Sangian D, Ide Y, Bando Y, Rowan AE, Yamauchi Y (2018) Materials nanoarchitectonics using 2D layered materials: recent developments in the intercalation process. Small 14:1800551

38. Ide Y, Ogawa M (2003) Surface modification of a layered alkali titanate with organosilanes. Chem Commun 1262–1263
39. Ide Y, Fukuoka A, Ogawa M (2007) Preparation of Au nanoparticles in the interlayer space of a layered alkali silicate modified with alkylthiol groups. Chem Mater 19:964–966
40. Ide Y, Ogawa M (2007) Interlayer modification of a layered titanate with two kinds of organic functional units for molecule-specific adsorption. Angew Chem Int Ed 46:8449–8451
41. Ide Y, Matsuoka M, Ogawa M (2010) Efficient visible-light-induced photocatalytic activity on gold-nanoparticle-supported layered titanate. J Am Chem Soc 132:16762–16764
42. Ide Y, Nakasato Y, Ogawa M (2011) Molecular recognitive photocatalysis driven by the selective adsorption on layered titanates. J Am Chem Soc 132:3601–3604
43. Fuse Y, Ide Y, Ogawa M (2010) Hybridization of epoxy resin with a layered titanate and UV light durability and controlled refractive index of the resulting nanocomposite. Polym Chem 1:849–853
44. Ide Y, Ochi N, Ogawa M (2011) Effective and selective adsorption of Zn^{2+} from seawater on a layered silicate. Angew Chem Int Ed 50:654–656
45. Ide Y, Kagawa N, Itakura M, Imae I, Sadakane M, Sano T (2012) Effective and selective bisphenol a synthesis on a layered silicate with spatially arranged sulfonic acid. ACS Appl Mater Interfaces 4:2186–2191
46. Hattori H, Ide Y, Ogo S, Inumaru K, Sadakane M, Sano T (2012) Efficient and selective photocatalytic cyclohexane oxidation on a layered titanate modified with iron oxide under sunlight and CO_2 atmosphere. ACS Catal 2:1910–1915
47. Ide Y, Torii M, Tsunoji N, Sadakane M, Sano T (2012) Molecular recognitive adsorption of aqueous tetramethylammonium on the organic derivative of Hiroshima University Silicate-1 with a silane coupling reagent. Chem Commun 48:7073–7075
48. Ide Y, Kagawa N, Sadakane M, Sano T (2013) Precisely designed layered silicate as an effective and highly selective CO_2 adsorbent. Chem Commun 49:9027–9029
49. Weng Q, Ide Y, Wang X, Wang X, Zhang C, Jiang X, Xue Y, Dai P, Komaguchi K, Bando Y, Golberg D (2015) Design of BN porous sheets with richly exposed (002) plane edges and their application as TiO_2 visible light sensitizer. Nano Energy 16:19–27
50. Ide Y, Liu F, Zhang J, Kawamoto N, Komaguchi K, Bando Y, Golberg G (2014) Hybridization of Au nanoparticle-loaded TiO_2 with BN nanosheets for efficient solar-driven photocatalysis. J Mater Chem A 2:4150–4156
51. Tsunoji N, Ide Y, Yagenji Y, Sadakane M, Sano T (2014) Design of layered silicate by grafting with metal acetylacetonate for high activity and chemoselectivity in photooxidation of cyclohexane. ACS Appl Mater Interfaces 6:4616–4621
52. Ide Y, Tominaka S, Kono H, Ram R, Machida A, Tsunoji N (2018) Zeolitic intralayer microchannels of magadiite, a natural layered silicate, to boost green organic synthesis. Chem Sci 9:8637–8643
53. Ide Y, Torii M, Sano T (2013) Layered silicate as an excellent partner of a TiO_2 photocatalyst for efficient and selective green fine-chemical synthesis. J Am Chem Soc 135:11784–11786
54. Ide Y, Tominaka S, Okuyama T, Tsunoji N, Ohara K, Mitome M, Sano T, Bando Y, Golberg D (2019) Microporous materials formed via intercalation of ultrathin coordination polymers in a layered silicate. Nano Energy 59:162–168
55. Hattori H, Ide Y, Sano T (2014) Microporous titanate nanofibers for highly efficient UV-protective transparent coating. J Mater Chem A 2:16381–16388
56. Ide Y, Komaguchi K (2015) A photocatalytically inactive microporous titanate nanofiber as an excellent and versatile additive to enhance the TiO_2 photocatalytic activity. J Mater Chem A 3:2541–2546
57. Ide Y, Inami N, Hattori H, Saito K, Sohmiya M, Tsunoji N, Komaguchi K, Sano T, Bando Y, Golberg D, Sugahara Y (2016) Remarkable charge separation and photocatalytic efficiency enhancement through interconnection of TiO_2 nanoparticles by hydrothermal treatment. Angew Chem Int Ed 55:3600–3605
58. Ide Y, Shirae W (2017) Hydrothermal conversion of layered niobate $K_4Nb_6O_{17}{\cdot}3H_2O$ to rare microporous niobate $K_6Nb_{10.8}O_{30}$. Inorg Chem 56:10848–10851

59. Saito K, Tominaka S, Yoshihara S, Ohara K, Sugahara Y, Ide Y (2017) Room-temperature rutile TiO_2 nanoparticle formation on protonated layered titanate for high-performance heterojunction creation. ACS Appl Mater Interfaces 9:24538–24544
60. Al-Attafi K, Nattestad A, Wu Q, Ide Y, Yamauchi Y, Dou SX, Kim JH (2018) The effect of amorphous TiO_2 in P25 on dye-sensitized solar cell performance. Chem Commun 54:381–384
61. Ide Y, Shirae W, Takei T, Mani D, Henzie J (2018) Merging cation exchange and photocatalytic charge separation efficiency in an anatase/$K_2Ti_4O_9$ nanobelt heterostructure for metal ions fixation. Inorg Chem 57:6045–6050
62. Eugster HP (1967) Hydrous sodium silicates from lake magadi, Kenya: precursors of bedded chert. Science 157:1177–1180
63. Tsunoji N, Ikeda T, Ide Y, Sadakane M, Sano T (2012) Synthesis and characteristics of novel layered silicates HUS-2 and HUS-3 derived from a SiO_2–choline hydroxide–NaOH–H_2O system. J Mater Chem 22:13682–13690
64. Dresselhaus MS, Thomas IL (2001) Alternative energy technologies. Nature 414:332–337
65. Li W, Shao J, Liu Q, Liu X, Zhou X, Hu J (2015) Facile synthesis of porous Mn_2O_3 nanocubics for high-rate supercapacitors. Electrochim Acta 157:108–114
66. Gray HB (2009) Powering the planet with solar fuel. Nat Chem 1:7
67. Kanan MW, Nocera DG (2008) In Situ formation of an oxygen-evolving catalyst in neutral water containing phosphate and Co^{2+}. Science 321:1072–1075
68. U.S. Geological Survey (2002) USGC Fact Sheet 087–02 Rare earth elements: critical resources for high technology. https://doi.org/10.3133/fs08702
69. Stoerzinger KA, Risch M, Han B, Shao-Horn Y (2015) Recent insights into manganese oxides in catalyzing oxygen reduction kinetics. ACS Catal 5:6021–6031
70. Suntivich J, May KJ, Gasteiger HA, Goodenough JB, Shao-Horn Y (2011) A perovskite oxide optimized for oxygen evolution catalysis from molecular orbital principles. Science 334:1383–1385
71. Suntivich J, Gasteiger HA, Yabuuchi N, Nakanishi H, Goodenough JB, Shao-Horn Y (2011) Design principles for oxygen-reduction activity on perovskite oxide catalysts for fuel cells and metal–air batteries. Nat Chem 3:546–550
72. Fabbri E, Habereder A, Waltar K, Kötz R, Schmidt TJ (2014) Developments and perspectives of oxide-based catalysts for the oxygen evolution reaction. Catal Sci Technol 4:3800–3821
73. Geller S (1971) Structure of α-Mn_2O_3, $(Mn_{0.983}Fe_{0.017})_2O_3$ and $(Mn_{0.37}Fe_{0.63})_2O_3$ and relation to magnetic ordering. Acta Crystallogr B 27:821–828
74. Grant RW, Geller S, Cape JA, Espinosa GP (1968) Magnetic and crystallographic transitions in the α-Mn_2O_3-Fe_2O_3 system. Phys Rev 175:686–695
75. Franchini C, Podloucky R, Paier J, M. Marsman M, Kresse G (2007) Ground-state properties of multivalent manganese oxides: density functional and hybrid density functional calculations. Phys Rev B 75:1–11
76. Cockayne E, Levin I, Wu H, Llobet A (2013) Ground-state properties of multivalent manganese oxides: density functional and hybrid density functional calculations. Phys Rev B 87:195128
77. Jahan M, Tominaka S, Henzie J (2016) Phase pure α-Mn_2O_3 prisms and their bifunctional electrocatalytic activity in oxygen evolution and reduction reactions. Dalton Trans 45:18494–18501
78. Henzie J, Etacheri V, Jahan M, Rong H, Hong CN, Pol VG (2017) Biomineralization-inspired crystallization of monodisperse α-Mn_2O_3 octahedra and assembly of high-capacity lithium-ion battery anodes. J Mater Chem A 5:6079–6089
79. Gorlin Y, Jaramillo TF (2010) A bifunctional nonprecious metal catalyst for oxygen reduction and water oxidation. J Am Chem Soc 132:13612–13614
80. Gorlin Y, Jaramillo TF (2012) Investigation of surface oxidation processes on manganese oxide electrocatalysts using electrochemical methods and ex situ x-ray photoelectron spectroscopy. J Electrochem Soc 159:H782–H786
81. Harris SJ, Lu P (2013) Effects of inhomogeneities—nanoscale to mesoscale—on the durability of li-ion batteries. J Phys Chem C 117:6481–6492

Wavelength-Selective Photothermal Infrared Sensors

Tadaaki Nagao, Dao Duy Thang, Doan Tung Anh, Satoshi Ishii, and Toshihide Nabatame

1 Introduction

By designing the size and geometry of dielectric and metallic materials in the nanometer scale, one can control thermal emission and infrared (IR) absorption with desired spectral features. In particular, objects that exhibit 100% optical absorptivity are often referred to as "perfect absorbers" and can constitute important building blocks for thermal detectors and thermal emitters that exhibit an ultra-narrowband spectral response or emission peaks at the desired wavelength. Recently, spectrally selective thermal detection has become of crucial importance for diverse modern spectroscopic applications, such as multi-wavelength pyrometry, nondispersive IR gas sensing, biomedical analysis, flame detection, and thermal imaging. Spectrally selective IR detectors that are based on resonant cavity enhanced (RCE) photodetectors exhibit excellent spectral sensitivity and fast responses [1–5]. However, the requirement for cryogenic cooling makes them bulky, heavy, excessively costly, and complicated for some applications. On the other hand, pyroelectric and thermopile detectors have the advantages of room-temperature operation and sharp spectral responses with flexible tenability in a wide wavelength range. Conventional spectrally selective uncooled detectors typically use passband filters mounted in front of

The original version of this chapter was revised: Figure 1 copyright information has been included and Figure 10c citation has been corrected as "9c". The correction to this chapter is available at https://doi.org/10.1007/978-4-431-56912-1_20

T. Nagao (✉) · D. D. Thang · D. T. Anh · S. Ishii · T. Nabatame
International Center for Materials Nanoarchitectonics (WPI-MANA), National Institute for Materials Science (NIMS), 1-1 Namiki, Tsukuba 305-0044, Ibaraki, Japan
e-mail: NAGAO.Tadaaki@nims.go.jp

T. Nagao · D. T. Anh
Department of Condensed Matter Physics, Hokkaido University, Kita 10, Nishi-8, Kita-ku, Sapporo 060-0810, Hokkaido, Japan

Y. Wakayama and K. Ariga (eds.), *System-Materials Nanoarchitectonics*, NIMS Monographs, https://doi.org/10.1007/978-4-431-56912-1_5

the sensing element to filter out signals at wavelengths not of interest, resulting in bulky designs and limited wavelength tunability.

Over the last two decades, the advent of plasmonic metamaterials, which are artificially structured materials with subwavelength structural units, has offered great freedom to tailor absorption spectra [6–8]. The absorption wavelength can be precisely controlled and manipulated by carefully designing the geometrical parameters of the unit cells. The absorbed thermal radiation is converted into heat, which is converted into electrical signals by thermal transducers, such as pyroelectric, bolometric, and thermoelectric transducers.

Figure 1 shows a schematic illustration of such photothermal IR detectors, which are often referred to as "uncooled IR detectors." These devices are in contrast to photoconductivity-type IR detectors, such as quantum well infrared photodetectors (QWIPs), which are composed of narrow-gap semiconductor quantum wells and require low-temperature operation to supress unwanted background signals. The spectral responsivity of QWIPs is predetermined by the electronic sub-band structure of the quantum well detectors, and tunability of the detection wavelength is not easy to realize. However, the absorption wavelength and bandwidth of the photothermal-type IR detectors can be flexibly designed using the artificial nanostructure of the photothermal module. That is, in photothermal detectors, wavelength selection is separately carried out using the photothermal module, and then the selected light is converted into heat to be detected by the thermal detector, which does not have any

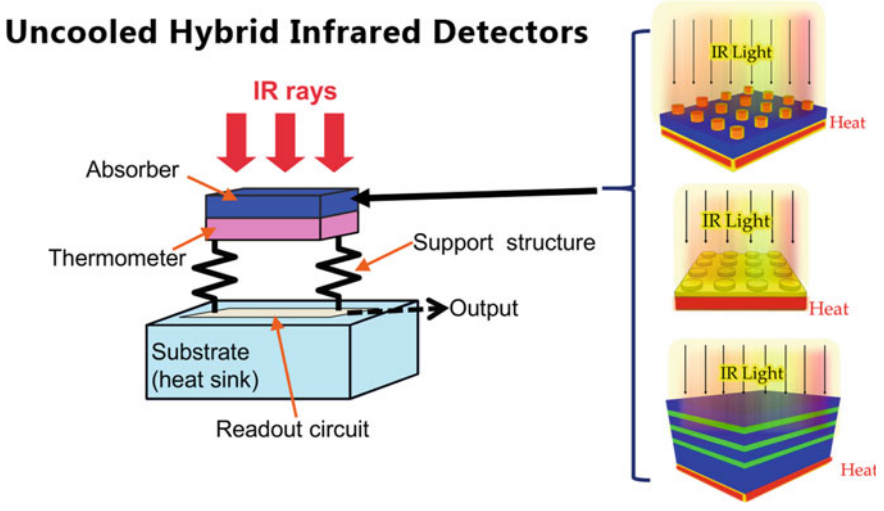

Fig. 1 Schematic of thermally isolated uncooled mid-IR wavelength detectors with high wavelength selectivity. Three different wavelength-selective perfect absorber designs are shown on the right-hand side. IR light with a specific wavelength is absorbed by the perfect absorber and heat is generated in it. Then, the heat is transferred to the thermal detectors (Thermometers) beneath the absorbers and detected as an electrical signal. Part of this figure is reproduced from Figure 1 in S. Ogawa, M. Kimata, Materials 10(5), 493 (2017)

spectral selectivity. In our work, we take advantage of a photothermal detector to flexibly design the wavelength selectivity by the nanoarchitectonics approach. As shown in Fig. 1, the photothermal light–heat converter structure can be varied depending on the use to provide high wavelength resolution, high directivity, or a wide acceptance angle. Owing to the rapid advances in the field of micro-electromechanical systems (MEMS), plasmonic perfect absorbers can be directly integrated on micromachined pyroelectric transducers to create compact, high-performance yet low-cost multiwavelength detectors that operate at room temperature.

In this chapter, we introduce different types of uncooled IR detectors operative in the mid-IR region [9, 10]. Firstly, on the basis of metal–insulator–metal (MIM) plasmonic metamaterial perfect absorbers, we have developed a quad-wavelength (four detection-wavelength) IR detector with sub-micrometer wavelength resolution and a wide detection angle. The wavelength-selective sensing modules were designed as floating membranes above a void space to minimize thermal conduction, thereby improving the responsivity of the detector [10]. The incident thermal radiation at the resonance wavelengths generated heat on the upper surface of the zinc oxide layer, which exhibits high pyroelectricity in thin-film form. Owing to the pyroelectric effect, a signal voltage was generated at the resonance wavelengths for each absorber providing a multicolored signal outputs. Secondly, we have developed an uncooled IR sensor with ultrahigh wavelength resolution and high directivity. The proposed light–heat converter for the device, which is based on Wood's anomaly absorption from a two-dimensional plasmonic square lattice, shows a narrowband polarization-independent resonance (quality factor Q of 73) with a nearly perfect absorptivity of as high as 0.99 at normal incidence. The developed IR sensors exhibit four different narrowband spectral responses at normal incidence in the mid-IR wavelength region. Finally, a design of a perfect absorber with a 1D layered cavity structure is introduced, which is designed to dissipate the incident light field energy in a Gires–Tournois (GT) etalon into the inherent losses of the metal back layer to obtain ultra-narrowband absorption in the IR region.

These devices can be applied for practical spectroscopic applications, such as non-dispersive IR sensors, IR chemical imaging devices, pyrometers, and spectroscopic thermography imaging. In particular, the on-chip design of the proposed quad-wavelength pyroelectric detector demonstrated the feasibility of integrating microdetectors of different selective wavelengths into arrays with high CMOS compatibility. This opens the possibility of developing miniaturized and robust multicolor spectroscopic sensors for next-generation perceptive devices contributing to Society 5.0.

2 MEMS-Based Architecture of On-Chip Quad-Wavelength Pyroelectric Infrared Detectors

Here, we exemplify a quad-wavelength pyroelectric detector with four distinct plasmonic absorbers to selectively detect light in the mid-IR region. For non-dispersive infrared (NDIR; fixed-wavelength infrared) multigas sensing applications, the four resonance wavelengths were determined as 3.3, 3.7, 4.1, and 4.5 μm, which correspond to the centers of the absorption bands of CH_4, H_2S, CO_2, and N_2O [11, 12]. Spectral selectivity was achieved by coupling incident IR light to resonant modes of Al-disk-array/Al_2O_3/Al perfect absorbers with various disk diameters. The top-patterned resonators were hexagonal arrays of disks used to achieve wide-angle acceptance and polarization insensitivity, which are highly desirable for many sensing applications. We chose Al as the plasmonic base metal because it is abundant on Earth and it is industry-compatible while still exhibiting low-loss plasmonic properties in the IR region similar to those of noble metals such as Au and Ag [13]. The model of the Al-disk-array/Al_2O_3/Al perfect absorber was simulated and optimized using the commercial rigorous coupled-wave analysis (RCWA) package and the FullWAVE package from Synopsys Rsoft, which is a highly sophisticated tool for studying the interaction of light and photonic structures, including integrated wavelength-division multiplexing (WDM) devices [14, 15], as well as nanophotonic devices such as metamaterial structures [16, 17] and photonic crystals [18]. The sensing areas were designed as suspended membranes in free space to minimize heat flow, thereby improving the responsivity of the thermal detector. The electromagnetic energy at the resonance wavelengths generated heat on the upper surface of the zinc oxide layer, which we used as a pyroelectric detector in this device. Owing to the pyroelectric effect, a signal voltage was generated at the resonance wavelengths for each absorber. The on-chip design of the proposed quad-wavelength pyroelectric detector demonstrated the feasibility of integrating microdetectors of different selective wavelengths into arrays with good CMOS compatibility. This opens the possibility of developing miniaturized and robust multicolor spectroscopic devices.

The schematic diagram in Fig. 2a illustrates the design layout of the proposed quad-wavelength detector. Four individual sensing elements were directly integrated on the same complementary metal–oxide–semiconductor (CMOS) platform of 0.5 × 1.0 cm^2 size to selectively detect IR radiation at four resonant wavelengths of 3.3, 3.7, 4.1, and 4.5 μm. The structural design of a single sensing element is illustrated in Fig. 2b. From top to bottom, it consisted of an Al-disk-array/Al_2O_3/Al perfect absorber structure with an active area of 200 × 200 μm^2, a 300-nm-thick pyroelectric zinc oxide thin film sandwiched between the Al back plate of the absorber and a 100 nm Pt/10 nm Ti bottom electrode, and a membrane-based CMOS substrate. A 300-nm-thick layer of silicon nitride was deposited on both sides of the silicon substrate to ensure sufficient mechanical strength of the membrane structure. The silicon wafer was 380 μm thick. The width and length of the supporting arms were 20 and 400 μm, respectively. The cross-sectional profile of the unit cell is shown in Fig. 2c. The Al-disk-array/Al_2O_3/Al perfect absorber consisted of an Al disk array

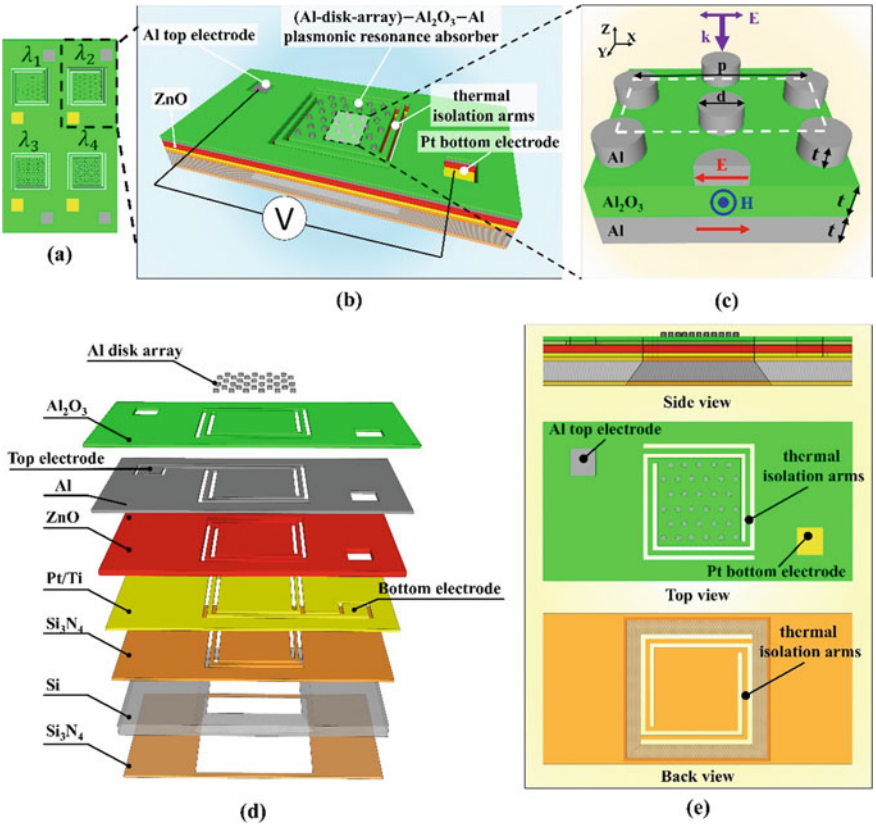

Fig. 2 **a** Schematic illustration of the proposed quad-wavelength detector. **b** Illustration of the structural design of a single sensing element. **c** Illustration of the plasmonic perfect absorber with the indicated field lines at resonance (electric field E, red arrows; magnetic field H, blue arrows). **d** Exploded view of a single sensing element. (**e**) Side, top, and bottom views of a single sensing element

as the resonator, an Al_2O_3 layer as the middle insulator, and an Al film as the back reflector. The thicknesses of the three layers were identical and are denoted as t. The Al disks of diameter d were arranged in a periodic hexagonal array of periodicity p. After some numerical computations based on RCWA analysis, the optimized geometrical dimensions for the perfect absorbers were taken as $p = 2.0\ \mu m$, $t = 100$ nm, and $d = 0.97, 1.25, 1.35$, and $1.60\ \mu m$ for the individual sensing elements at resonance wavelengths of 3.3, 3.7, 4.1, and 4.5 μm, respectively. When incident IR radiation impinged on the top surface of the device, its external oscillating electric field induced electric dipoles inside the Al disks, which excited anti-parallel currents between the disk array and the back reflector. These circular currents produced a magnetic flux opposing the external magnetic field, resulting in magnetic resonance. By adjusting the geometrical parameters of the Al disk array, we could tailor the

electromagnetic response of the structure to the external electromagnetic field to achieve selective absorption.

The exploded view of a single sensing element is shown in Fig. 2d. It was shown that the bottom layer of the plasmonic metamaterial perfect absorber was also utilized as the top electrode of the pyroelectric detector. In this design, the zinc oxide layer was stacked below and in intimate contact with the photothermal plasmonic absorber to fully exploit the spectrally selective absorption. It is also worth noting that we chose zinc oxide as the pyroelectric material owing to its advantages of nontoxicity and compatibility with the semiconductor process. This design is also applicable to other pyroelectric materials, such as lead zirconate titanate, lithium tantalate, lithium niobate, barium strontium titanate, and deuterated triglycine sulfate. The side, top, and back views of the single sensing elements are shown in Fig. 2e, indicating the micromachined floating membrane design of the sensing element.

To tailor and optimize the spectrally selective absorption, the optical properties of the plasmonic absorbers were simulated by implementing RCWA (DiffractMOD, Synopsys Rsoft). Figure 3a shows the simulated reflectivity, transmissivity, and absorptivity characteristics of the two Al-disk-array/Al_2O_3/Al perfect absorbers, which had diameters of 1.25 and 1.6 μm, respectively. As the optimal parameters, the unit cells had periodic dimensions of 2.0 μm, and the thicknesses of the Al disks, Al_2O_3 dielectric spacer, and Al back reflector were all 100 nm. Since the continuous metal back reflector was sufficiently thick to block light transmission, the transmissivity was zero across the investigated wavelength range. With disk diameters of 1.25 and 1.6 μm, the simulated absorptivities at normal incidence were resonantly enhanced up to 0.99 and 0.94 at the resonance wavelengths of 3.72 and 4.05 μm, with full widths at half maximum (FWHMs) of 0.44 and 0.63 μm, respectively.

3 Electromagnetic Simulations for Wavelenght-Selective Photothermal Converter: An Example for an MIM Perfect Absorber

To optimize the resonant behavior of the Al-disk-array/Al_2O_3/Al perfect absorber and adopt it for a wavelength-selective photothermal converter, a full-wave simulation based on the finite-difference time-domain (FDTD) method (using FullWAVE) was performed at the resonance wavelength of 3.72 μm. The simulated electric field distribution in the x direction (Fig. 3b) shows that the electric field was localized at the edges of the Al disks, indicating the generation of induced electric dipoles. The magnetic field was intensively confined under the center of the top resonator (Fig. 3c), for which the antiparallel currents were excited in the top Al disks and the bottom Al reflector (Fig. 3d).

The dependence of the absorption wavelength of the plasmonic absorber as a function of disk diameter is illustrated in Fig. 4a. The absorption peak was found to shift almost linearly with the disk diameter. Meanwhile, the resonance wavelength

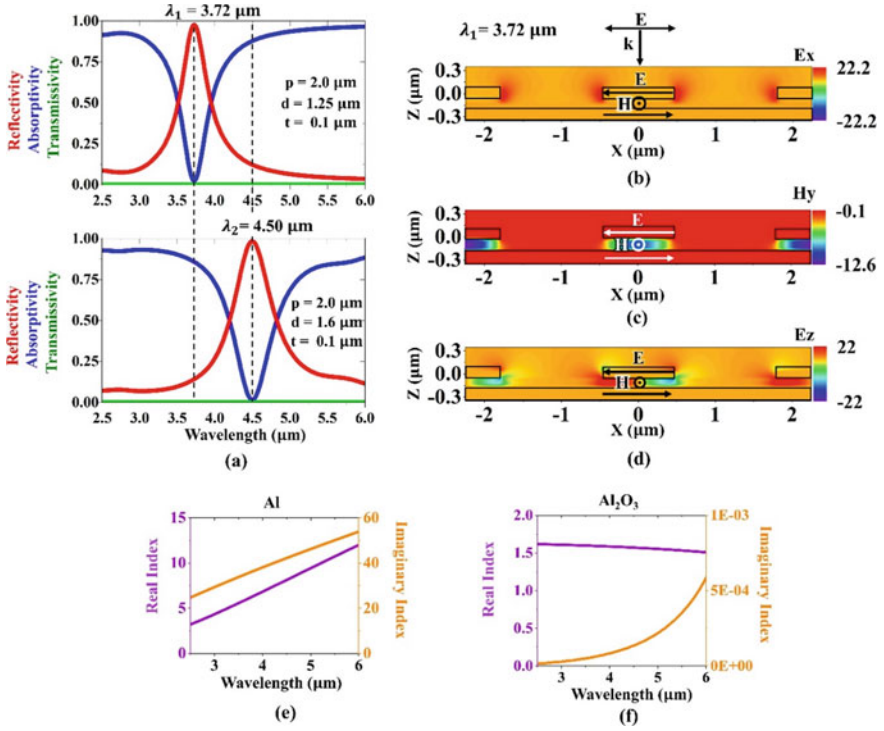

Fig. 3 **a** Reflectivity, absorptivity, and transmissivity characteristics of the plasmonic perfect absorber at the resonance wavelengths of 3.72 and 4.50 μm. The simulated amplitude plots of the **b** electric field in the x direction, **c** magnetic field in the y direction, and **d** electric field in the z direction at the resonance wavelength of 3.72 μm illustrate the highly localized characteristics of the plasmonic perfect absorber. The refractive index dispersion data of (**e**) Al and **f** Al_2O_3 used in the simulations were taken from the literature [19]. The figures and the corresponding discussion are reproduced from ref [20] with permission

was not significantly affected by the variation in the periodicity of the unit cells (Fig. 4b). Owing to this robust tunability with respect to the disk size, the electromagnetic responses of these Al-disk-array/Al_2O_3/Al structures were engineered to achieve resonant absorption at multiple desired wavelengths.

Figure 5a shows the simulated incident-angle-dependent absorptivity with the geometrical parameters p = 2.0 μm, d = 1.25 μm, and t = 0.1 μm. The simulation results showed that the absorptivity of the proposed plasmonic perfect absorber was almost completely independent of the incident angle. The absorption still remained near unity when the incident angle was increased to as large as 85°. Figure 5b shows the polarization-dependent absorptivity with the geometrical parameters p = 2.0 μm, d = 1.25 μm, and t = 0.1 μm. The resonances of the plasmonic absorber were almost unchanged when the polarization angle changed from 0 to 90°. The symmetrical design typically resulted in wide-angle acceptance and polarization independence, which are desirable for most sensing applications.

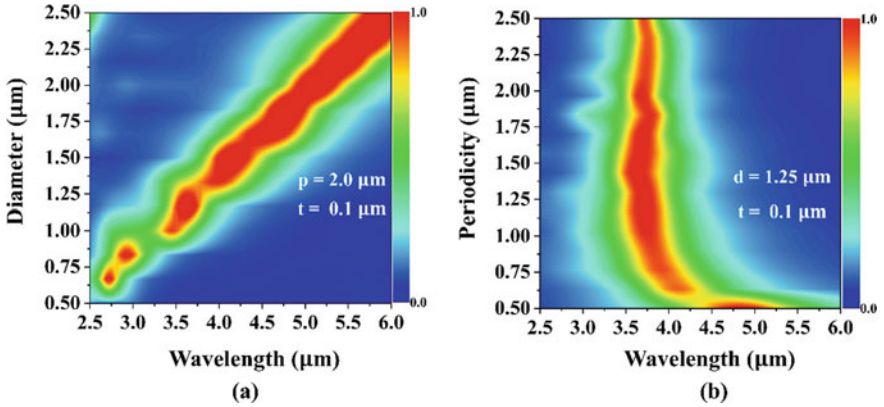

Fig. 4 **a** Periodicity dependence with p changed from 0.5 to 2.5 μm while keeping the diameter and insulator thickness unchanged at 1.25 and 0.1 μm, respectively. **b** Diameter dependence with d changed from 0.5 to 2.5 μm while keeping the periodicity and insulator thickness unchanged at 2.0 and 0.1 μm, respectively. The figures and the corresponding discussion are reproduced from ref [20] with permission

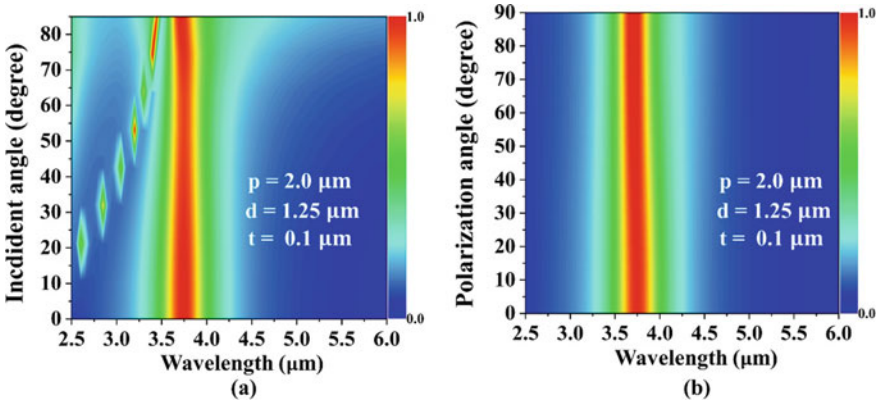

Fig. 5 Simulated absorptivity spectrum as a function of **a** incident angle and **b** polarization angle for an absorber with p = 2.0 μm, d = 1.25 μm, and t = 0.1 μm. The figures and the corresponding discussion are reproduced from ref [20] with permission

4 CMOS-Compatible Fabrication Process of a Pyroelectric Infrared Sensor

Here, we show an example of the fabrication process of our photothermal IR detector, which involves standard photolithography with dry and wet etching techniques. The microfabrication process of the MEMS-based hybrid plasmonic–pyroelectric detector is shown in Fig. 6. The device was fabricated on commercial double-

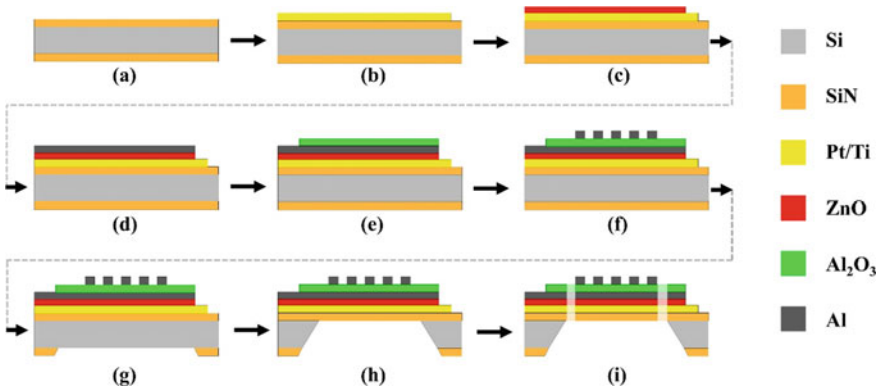

Fig. 6 CMOS-compatible microfabrication process: **a** Rapid thermal oxidation of the silicon wafer and deposition of Si_3N_4 on both sides; **b** deposition and lift-off of the Pt bottom electrode; **c** deposition and lift-off of ZnO; **d** deposition and lift-off of Al; **e** deposition and lift-off of Al_2O_3; **f** E-beam lithography of the Al disk; **g** dry etching of back side of Si_3N_4; **h** wet etching of Si by KOH; **i** dry etching of Si_3N_4. The figures and the relevant discussion in the text are reproduced from ref [20] with permission

side-polished *n*-type silicon prime wafers with <100> orientation in cleanroom facilities.

First, an 80-nm-thick SiO_2 insulator was formed by dry thermal oxidation of the silicon wafer. This was followed by depositing a 300-nm-thick silicon nitride (Si_3N_4) layer onto both sides of the silicon substrate by radio frequency (RF) reactive sputtering using a boron-doped p-type Si target processed in ambient N_2 as a reactive gas with a flow rate of 20 sccm (!-Miller, Shibaura, Tokyo, Japan) (Fig. 6a). This silicon nitride layer isolates the thermal conduction to the substrate, which enhances the pyroelectric signal and the overall responsivity of the device. Then the silicon nitride layer was subjected to rapid thermal annealing at 1000 °C for 1 min. After that, laser direct writing lithography (μPG 101 Heidelberg Instruments) was performed to pattern the bottom electrode on top of the silicon nitride layer with a double layer of resists. The 100 nm Pt/10 nm Ti bottom electrodes were deposited in an electron beam evaporator at ambient temperatures, followed by a lift-off process in acetone (Fig. 6b). Then, the sputter deposition of the 300-nm-thick zinc oxide layer was followed by laser direct writing lithography with a positive photoresist combined with reactive ion etching (RIE) using CF_4 gases (ULVAC CE-300I) (Fig. 6c). Next, the sputter deposition of the 100-nm-thick Al top electrode was followed by laser direct writing lithography with a positive photoresist and RIE using BCl_3/Cl_2 gases (Fig. 6d). After exposing and developing the pattern, a 100-nm-thick Al_2O_3 film was sputtered and then patterned by direct laser writing lithography combined with an RIE step using CF_4 gas (Fig. 6e). The 100-nm-thick Al disk array was patterned by E-beam lithography and lift-off process (Fig. 6f). The Si_3N_4 back layer serving as an RIE mask for the wet etching process of Si was patterned by RIE with CHF_3 gas using a photoresist mask formed by direct laser writing lithography (Fig. 6g). Then,

wet alkaline etching was implemented on the back side as follows (Fig. 6h). A thin polymeric ProTEK®B3 protective coating was spun on the front side of the structure to provide temporary wet-etch protection for the patterned Al-disk-array/Al_2O_3/Al resonator during alkaline etching. The Si layer from the back side of each sensor was completely released by anisotropic wet etching by immersing the structure in a deep reactive KOH 40% aqueous solution and heating at 60 °C for 10 h. Then, the polymeric protective coating was removed by immersing it in acetone. Finally, the RIE of Si_3N_4 was carried out to form the supporting arms (Fig. 6i). The Si_3N_4/SiO_2 composite layer was used as the membrane to support the zinc oxide pyroelectric film and absorber. Each sensing element was wire-bonded to the Cu electrodes attached on a glass plate. The materials and fabrication process of the detector were fully compatible with the CMOS process.

5 Fabrication and Demonstration of a Quad-Wavelength Pyroelectric MIM Sensor

Figure 7a shows a photo of a fabricated MEMS-based quad-wavelength hybrid plasmonic–pyroelectric detector, which had a width of 0.5 cm and a length of 1 cm. It clearly demonstrates that multiple hybrid plasmonic–pyroelectric sensing elements were easily integrated on a standard CMOS platform to achieve multiband selectivity without using any additional bulky optical filters. Figure 7b shows optical microscopy images of the top and bottom of a single sensing element with an active area of 200 × 200 μm. It verifies that the sensing area was suspended by the long thermal isolation arms. The suspended area remained flat without any additional stress-reducing process.

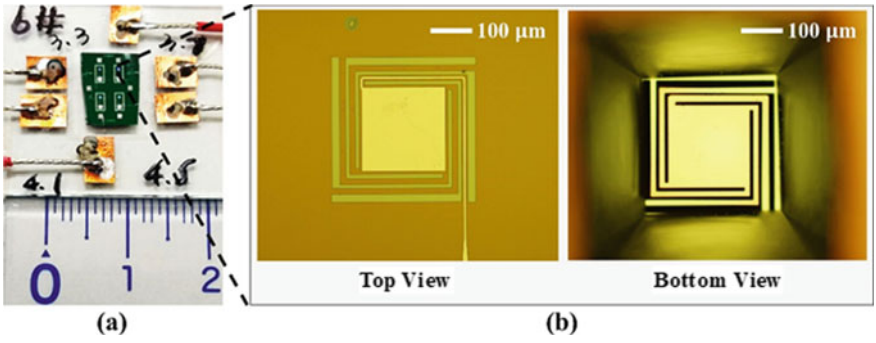

Fig. 7 **a** Photo of a fabricated MEMS-based hybrid plasmonic–pyroelectric detector. **b** Microscopy images of the top and bottom of the fabricated sensing element. The figures and relevant discussion in the text are reproduced from ref [20] with permission

While the thicknesses of the sputtered layers could be precisely controlled by establishing optimum sputtering conditions and deposition rates, the process of transferring the shape and size of the Al disk arrays poses further challenges owing to the complex multistage photolithography of the submicron patterning. The residual photoresist and nonuniformity may result in degradation from the expected performance. Figure 8a–d show scanning electron microscopy (SEM) images of the hexagonal arrays of the Al disk resonators with diameters of 0.97, 1.25, 1.35, and 1.60 μm. The Al disk arrays fabricated on top of the membrane structures were well-defined and homogeneously distributed, indicating that the patterning process was effectively implemented. The Al disk arrays were patterned using electron-beam lithography with sub-10 nm resolution, and there was a tolerance of a few nm (5–10 nm) in the diameter of the disks.

The reflectance spectrum of each sensing element was measured using a Fourier transform infrared (FTIR) spectrometer (Thermo Scientific Nicolet iS50, Thermo Fisher Scientific), coupled with a microscope (Nicolet Continuum FTIR Microscope, Thermo Nicolet). The reflectance spectra were normalized by the reflectance from a gold film. Given that the transmittance was zero for the thick back reflector, the absorptivity spectra were calculated using the formula $A = 1 - R$, where A is the

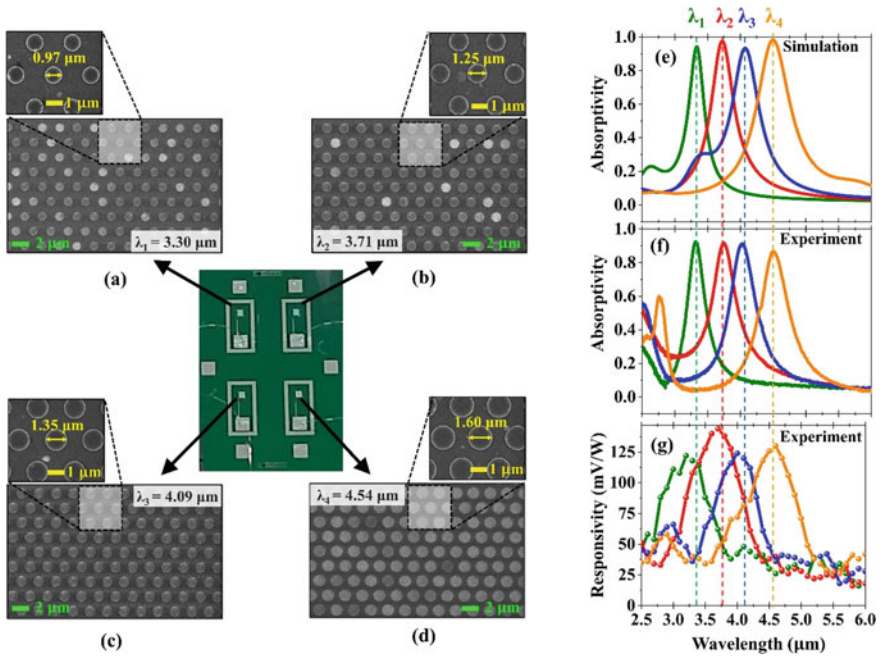

Fig. 8 **a–d** Scanning electron microscopy (SEM) images of the fabricated disk array patterns at four resonance wavelengths. **e**, **f** Simulated and measured absorptivity of the perfect absorbers at four resonance wavelengths. **g** Measured responsivity of the quad-wavelength detector. The figures and relevant discussion in the text are reproduced from ref [20] with permission

absorptivity and R is the reflectivity. The simulated and measured absorptivity spectra are respectively shown in Figs. 8e and f. The reflectance spectra were normalized by the reflectance from a gold film. The four sensing elements exhibited absorptivity peaks of 0.92, 0.93, 0.85, and 0.87 at 3.32, 3.74, 4.06, and 4.51 μm, respectively, which were highly consistent with the corresponding simulated absorptivity peaks of 0.94, 0.99, 0.94, and 0.98 at 3.33, 3.72, 4.05, and 4.50 μm, respectively. The precise pattern transfer in the fabrication process resulted in small shifts of only a few tens of nm and slightly lower magnitudes of the absorption peaks. The FWHMs of the measured absorptivity curves were 0.35, 0.45, 0.49, and 0.68 μm, compared with those of the simulated curves of 0.30, 0.44, 0.47, and 0.63 μm. Together with the defined patterns and uniformity observed in the SEM images, the excellent agreement between the simulated and experimentally measured absorptivity proved the quality of the optimized fabrication method.

The performance of the detector was evaluated by measuring its spectral responses to IR radiation in the range of 2.5–6.0 μm. A wavelength-tunable pulsed laser system was used with the IR laser beam guided to the sensing area of the detector with a pulse width of 104 fs and a repetition rate of 1 kHz. The output electrical signal was detected by demodulating the signal with a lock-in amplifier after amplifying it with a preamplifier. The spectrally selective absorption of laser pulses at resonant wavelengths was due to the excitation of highly localized magnetic and electric dipole resonances, which was evidenced by the simulated field distributions (see Figs. 3b–d). Such strong resonances efficiently confined the electromagnetic energy and provided sufficient time to convert it into resistive heat within the Al disks and the continuous Al back plate. Al_2O_3 exhibited almost no loss in the mid-IR region (see Fig. 3f), which reflects the negligible dielectric losses in the spacer layer at the mid-IR frequencies of interest. The heat at the continuous Al back plate, which is associated with spectrally selective absorption, was directly transferred to the zinc oxide thin film, which was among the materials that were electrically polarized owing to their c-axis-oriented textured crystal structure [21–24]. The zinc oxide film consequently became electrically polarized with changes in temperature, and the electrically polarized zinc oxide film hence produced a voltage between the Al and Pt electrodes. Pt was chosen as the bottom electrode because it has been reported that the hexagonal arrangement of atoms in the (111) plane of Pt facilitates the nucleation and growth of hexagonal zinc oxide oriented along the [0001] direction [16]. In Fig. 8g, the measured spectral responsivity curves of the four sensing elements are plotted. The spectral responses of the four sensing elements were 125, 150, 126, and 128 mV/W at 3.30, 3.71, 4.09, and 4.54 μm, respectively. The excellent measured spectral responses proved that the detector exhibited low thermal drift and thermal noise owing to the low mass of the membrane-based design. The measured FWHMs of the spectral responses were 0.94, 1.02, 1.10, and 1.20 μm, respectively, which were approximately two times larger than those of the absorptivity measured using the FTIR spectrometer. The broadened spectra was partly attributed to the spectral bandwidth and the beam stability of the IR pulsed laser that we used. These experimental results clearly demonstrated that the proposed multispectral hybrid plasmonic–pyroelectric detectors can be fabricated and easily integrated into existing IR spectroscopic devices, such as miniature NDIR

sensors, chemical and biological sensors, photoacoustic imaging systems, and thermographic cameras. As an example, on-chip multispectral IR detectors may offer an opportunity to develop miniaturized and robust photoacoustic computed tomography [25, 26]. Specifically, in all-optical photoacoustic imaging systems, shifts in the wavelengths of light can be detected and analyzed using an array of multispectral microdetectors.

6 Design of a Quad-Wavelength Pyroelectric Wood's Anomaly Sensor

In this section, we present an ultra-narrowband absorber based on the interacton between surface plasmon polaritons and a metallic grating (Wood's anomaly) in a two-dimensional plasmonic square lattice. To discuss and demonstrate the advantage of a Wood's anomaly metallic-grating-based absorber, we simulated the absorptivity and field distribution of three configurations: a plasmonic dipole resonator-based absorber, a tiny-gap resonator-based absorber, and a Wood's grating absorber.

The essential requirements to construct a wavelength-selective absorber are high-quality resonance and gradual losses of the medium. In this regard, plasmonic resonators consisting of a lossless dielectric and a low-loss metallic layer, which are similar to the MIM structure in Sect. 3, are the most widely investigated structures for perfect absorbers [3, 27].

Figure 9 demonstrates three different perfect absorbers that can be integrated with thermal detectors of many transducer platforms, such as pyroelectric, bolometric or thermoelectric materials for an on-chip IR spectroscopic instrument. As can be seen in Fig. 9a, an MIM absorber with a plasmonic dipole resonator array exhibits a perfect resonant absorption peak with a Q-factor of approximately 10. In this design, the thermal radiation is absorbed and converted into heat in both the top resonant antenna and the bottom metal mirror. Figure 9b presents another perfect absorber configuration utilizing near-field confinement in a periodically arranged tiny-gap array with a comparable Q-factor and absorptivity. This design has an advantage of conductive heat transfer from the absorber to the thermal transducer platforms. Unfortunately, this absorber design requires that the gaps are very tidy, approximately a few tens of nanometers in width and 500 nm in height. This poses a serious challenge to the fabrication process. Moreover, it is clear that the resonant bandwidth of these absorbers (Fig. 9a, b) is much larger than that of the absorption spectra of molecular vibrations, which severely limits their application in spectroscopic sensor devices.

Absorbers with periodic metallic gratings based on Wood's anomaly absorption can significantly reduce the resonance bandwidth. Figure 9c presents Wood's anomaly absorption in a 1D metallic grating structure that exhibits ultra-narrowband resonance with a Q-factor as high as 150, which can be used to distinguish most molecular vibrations in the solid state [28].

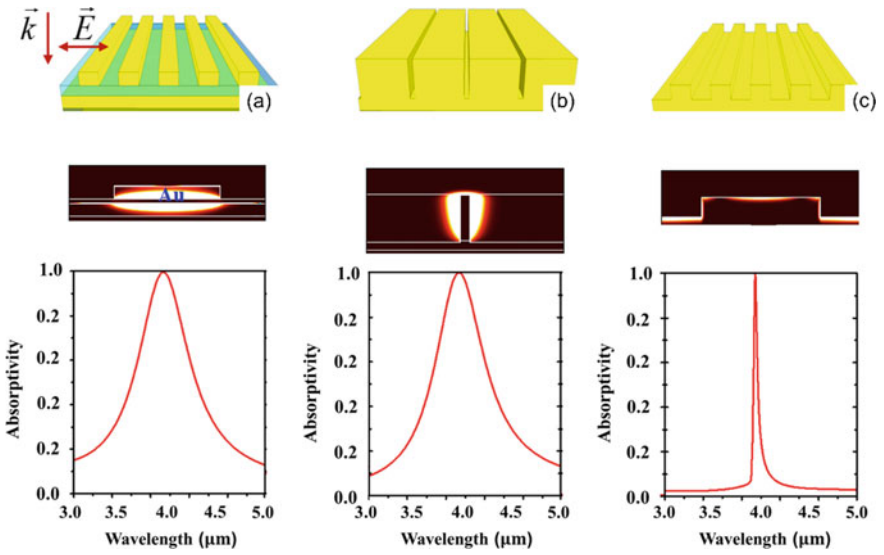

Fig. 9 Comparison of three different perfect absorbers with resonances at around 3.7 μm. From top to bottom: device structures, simulated absorption maps, and absorptivity spectra of the three absorbers. **a** Metal dipole antenna–insulator–metal absorber. **b** Tiny-gap plasmonic resonator array exhibiting unity absorption peak with Q-factor of about 10. **c** Wood's anomaly (grating-coupled SPP) exhibiting a much narrower unity absorption peak with a Q-factor as high as ~150. The figures and relevant discussion in the text are reproduced from ref [28] with permission

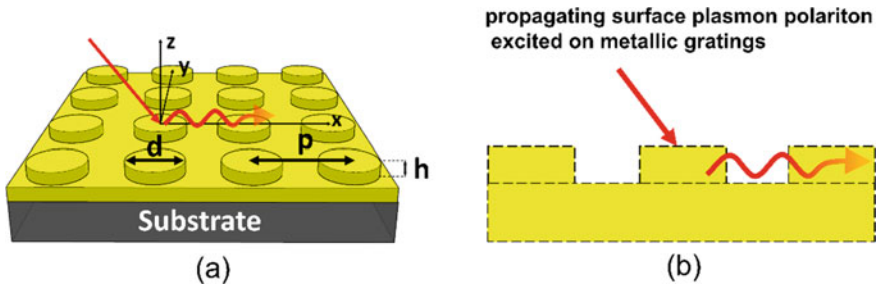

Fig. 10 **a** Schematic illustration of a two-dimensional metallic grating. **b** The ultra-narrowband absorption is achieved by the surface-wave resonance condition between the surface plasmon polariton and the metallic gratings. The figures and relevant discussion in the text are reproduced from ref [28] with permission

Ultra-narrowband absorption can be attained by the surface-wave resonance excitation between the surface plasmon polariton and metallic gratings. Selective perfect absorption is achieved by engineering the depth and height of the unit cell structure, and its resonance absorption wavelengths and angles can be flexibly tuned by changing the periodicity. These fascinating features make the Wood's anomaly absorber more advantageous than the other two absorbers. However, the absorber in

Fig. 9c is polarization-dependent. Polarization-independent absorbers can be readily accomplished by extending the design into a two-dimensional periodic array.

A Wood's anomaly absorber is illustrated in Fig. 10. In this design, a two-dimensional periodic disk array made of Au serves as a narrowband perfect absorber to absorb IR radiation at a resonant wavelength. The resonance of the absorber depends on the diameter d, height h, and periodicity p of the disk.

The resonant absorption of Wood's anomaly metallic gratings can be elucidated in terms of the surface plasmon polariton–photonic coupling in a two-dimensional periodic plasmonic lattice. For a plasmonic square lattice, surface plasmon polaritons at the metal–air interface are described by the wave vector

$$\left|\overrightarrow{k}_{spp}\right| = k_0\sqrt{\frac{\varepsilon_m}{\varepsilon_m + 1}}, \tag{1}$$

where ε_m is the complex permittivity of the grating metal and $k_0 = 2\pi/\lambda$. Surface plasmon polaritons are excited with the condition that the momentums of the plasmons match the momentum of the incident photons:

$$\vec{k}_{sp} = \vec{k}_{||} + i\vec{G}_x + j\vec{G}_y \tag{2}$$

where $\left|\overrightarrow{k}_{\parallel}\right| = k_0\sin\theta$ is the projection of the momentum of the excited photons with an incident angle of θ on the metallic surface, $\overrightarrow{G}_x$ and $\overrightarrow{G}_y$ are two primitive lattice vectors, and i and j are integers. In the case that $\overrightarrow{k}_{\parallel}$ is oriented along $\overrightarrow{G}_x$ ($\Gamma - \mathrm{X}$ direction), Eq. (2) can be expressed as

$$\left|\overrightarrow{k}_{spp}\right|^2 = \left|\left(\overrightarrow{k}_{||} + i\overrightarrow{G}_x\right) + j\overrightarrow{G}_y\right|^2 = (k_0\sin\theta + iG_x)^2 + \left(jG_y\right)^2. \tag{3}$$

From Eq. (3) and under the condition $\left|\overrightarrow{G}_x\right| = \left|\overrightarrow{G}_y\right| = 2\pi/p$, the angular-dependent dispersion relation of surface plasmon polaritons for a square lattice along the $\Gamma - \mathrm{X}$ direction is expressed as

$$\frac{\varepsilon_m}{\varepsilon_m + 1} = \sin^2\theta + \left(\frac{2i}{p}sin\theta\right)\lambda + \left(\frac{i^2 + j^2}{p^2}\right)\lambda^2. \tag{4}$$

For normal incidence, the resonant wavelength is solely calculated from the formula $\lambda = \frac{p}{\sqrt{i^2+j^2}}\sqrt{\frac{\varepsilon_m}{\varepsilon_m+1}}$. As a result, the resonant wavelength at normal incidence of the Wood 's anomaly absorber can be easily tailored by changing the periodicity p since the height and diameter of the disk only change the resonance strength. Owing to the photonic-structure-coupled nature of plasmonic surface waves, the resonance in the two-dimensional Wood's anomaly absorber is much narrower than the localized plasmon resonance in MIM absorbers.

Figure 11a, b respectively show an illustration of the two-dimensional Wood's anomaly absorber with a thin Au-covered Si disk array together with the simulated optical spectra with a periodicity of 3.7 μm and a disk height of 0.34 μm with normal incidence. Note that we employed a thin Au-covered layer on a patterned silicon disk array instead of using entire homogeneous Au disks. This practice shows the advantage of acquiring similar optical properties while avoiding the use of a large amount of expensive gold compared with the conventional design using homogeneous Au disks.

As can be seen from Fig. 11, the plasmonic dipole resonator-based absorber with 3.7 μm periodicity exhibits a nearly perfect absorptivity (~0.99) resonant peak at 3.722 μm with a narrow bandwidth of 51 nm (with an equivalent *Q*-factor of 73). Owing to the symmetrical geometry of the two-dimensional plasmonic square lattice employed here, the Wood's anomaly absorber does not depend on the polarization.

To further elucidate the surface plasmon polariton–photonic coupling in the two-dimensional Wood's anomaly absorber, E-field distributions in the plasmonic structure were calculated using a full-wave simulation based on the FDTD method.

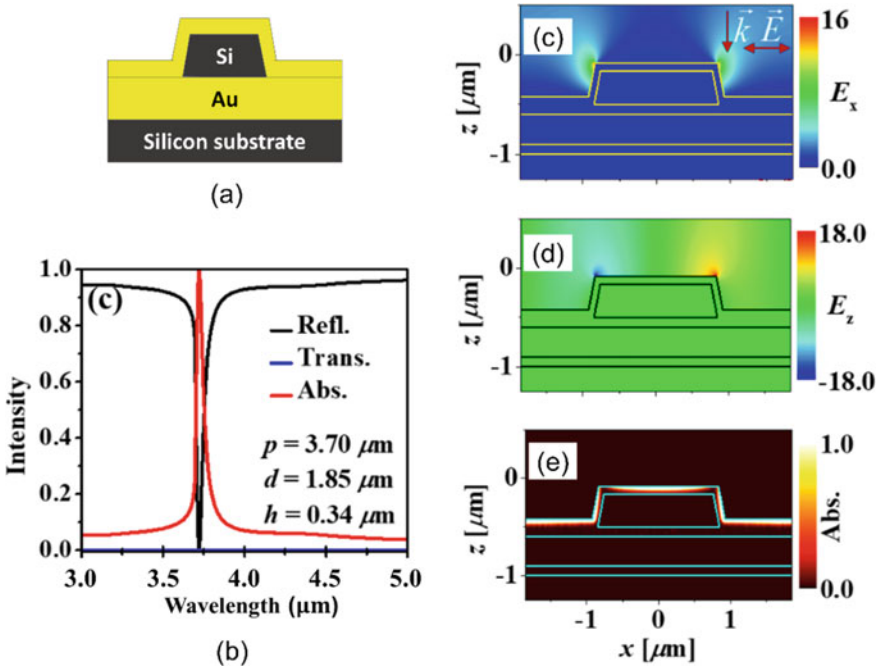

Fig. 11 **a** Schematic illustration of the two-dimensional Wood's anomaly absorber with a thin Au film covering a patterned silicon disk array instead of using a submicron-thick entire Au disk array. **b** The simulated reflectance, transmittance, and absorptivity of a 3.7 μm periodicity absorber indicate ultranarrow and perfect absorption. (c)–(e) Simulated electric fields and absorption excited at a resonance of a two-dimensional plasmonic array absorber. The figures and relevant discussion in the text are reproduced from ref [28] with permission

Figure 11c, d show the simulated electric field distributions (E_x and E_z) of a 3.722 μm resonant absorber based on Wood's anomaly. The fields are excited at the resonance under normal incidence. We can clearly observe the existence of strong electric near-fields converging at the edges of the metallic disks. Likewise, the induced electric field E_z (Fig. 11d) resulting from the coupling between the incident photons and the two-dimensional periodic metallic lattice exposes a strongly coupled near-field enhancement with phases alternating along the x-axis. This provides evidence that surface plasmon polariton waves are excited and propagate horizontally along the patterned metallic surface. The surface plasmon polaritons are then effectively damped via moderate metallic losses (Fig. 11e) as the surface plasmon polariton wave propagates at the Au surface, resulting in ultranarrow absorption as shown in Fig. 11b. The coupling of the highly selective excitation of grating-coupled surface waves and plasmonic damping is an effective mechanism for achieving perfect absorption with very high wavelength selectivity.

7 Fabrication and Demonstration of a Quad-Wavelength Pyroelectric Wood's Anomaly Sensor

To fabricate the proposed two-dimensional Wood's anomaly absorber, multiple steps of direct laser writing lithography, including film deposition, lift-off, and RIE, were adopted [28]. The fabrication procedure is illustrated in Fig. 12. The absorber was fabricated on commercial silicon wafers with <100> orientation by nanolithography processes. First, we sputtered an 80-nm-thick Au layer on a clean silicon substrate, followed by the deposition of a 340 nm Si film. Then, we spin-coated a thin positive photoresist (AZ5214E) layer at 5000 rpm in 60 s, then performed prebaking at 90 °C for about 3 min. Next, laser direct writing lithography was performed to transfer the geometric patterns on the photoresist layer. The transferred geometric patterns were developed using an NMD-3 solution in approximately 50 s. RIE was performed to detach the Si layer at the designed gap position using CF_4 gas (ULVAC CE-300I). The remaining photoresist layer was removed using a PG remover solution. Finally, an 80-nm-thick Au film was deposited on patterned silicon disk array structures.

Figure 13 shows the morphological characterization of the Wood's anomaly absorber. A top-view SEM image of the Wood's anomaly absorber is presented in Fig. 13a, which exhibits well-defined and uniform patterns. The cross-sectional tilted view in Fig. 13b clearly shows that a Au-shell disk supported by a Si-core template was well constructed using the proposed fabrication process described above.

The measured performance of the fabricated device exhibited the world's highest wavelength and angular resolution, with a wavelength resolution as high as 51 nm (quality factor of 73) and directivity better than ±1°, as well as compatibility with multiband IR sensors mounted on a single chip. Figure 14 shows an example of such fabricated on-chip sensor arrays with quad-wavelength detection, which can be a prototype device for IR multicolor imaging. This device can lead to the realization

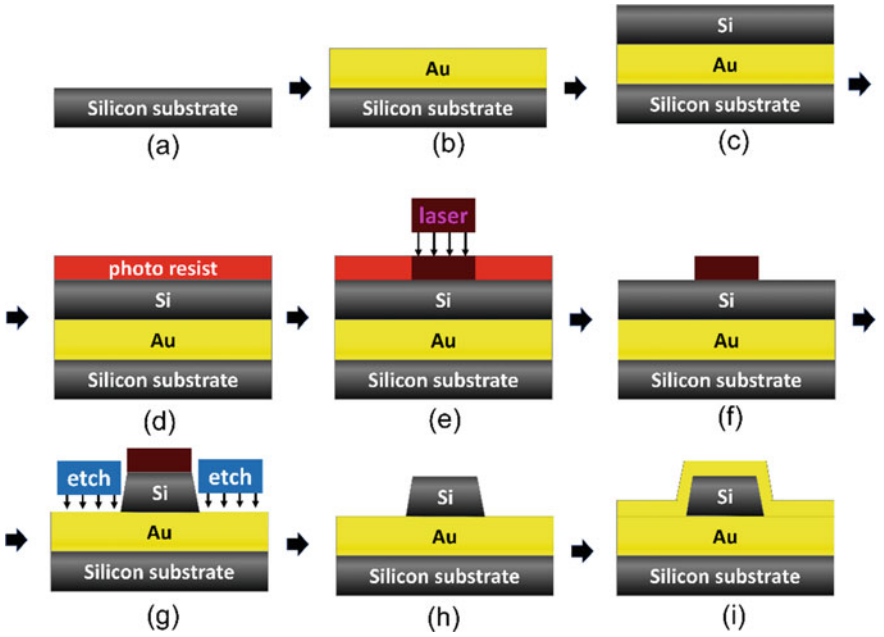

Fig. 12 CMOS-compatible microfabrication process: **a** preparation of silicon wafer; **b** sputtering of Au bottom layer; **c** sputtering of Si layer; **d** spin coating with photoresist; **e** laser lithography of disk pattern; **f** development of transferred patterns; **g** dry etching of Al; **h** removal of remaining photoresist; **i** sputtering of Au layer. The figures and relevant discussion in the text are reproduced from ref [28] with permission

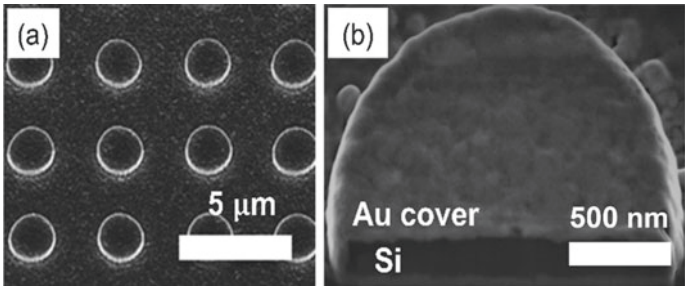

Fig. 13 **a** Top-view SEM image of the fabricated 3.7 μm periodic resonance Wood's anomaly absorber. **b** Cross-sectional tilted-view SEM image of the Wood's anomaly absorber. Thickness of the Au cover is 80 nm. The figures and relevant discussion in the text are reproduced from ref [28] with permission

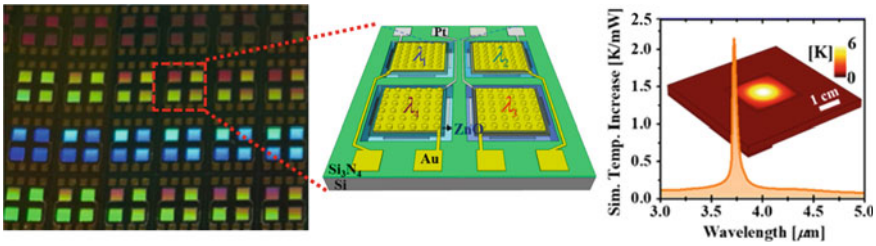

Fig. 14 *Left*: Fabricated array of on-chip quad-wavelength IR sensor array. *Middle*: Magnified schematic view of a single quad-wavelength IR sensor with four Wood's anomaly absorbers with different resonance wavelengths. *Right*: Simulation result of wavelength-dependent photothermal heat generation in one absorber module. The figures and relevant discussion in the text are reproduced from ref [28] with permission

of a range of new products, including miniature spectroscopic IR devices for true-temperature pyrometry, gas imaging, position and motion sensing with high angular resolution, material-specific imaging, and environmental sensing.

8 Conclusions

In this chapter, we have described two different types of IR sensor based on photothermal pyroelectric detection mounted on a MEMS platform. Their high wavelength resolution is achieved by IR perfect absorbers with an MIM metamaterial trilayer structure or with a plasmonic lattice structure that exhibits narrowband IR photothermal conversion. The former offers sub-1 μm wavelength resolution with a wide acceptance angle. The latter offers ultra-narrowband wavelength resolution as high as 50 nm together with high directivity better than $\pm 1^{\circ}$. Both devices are realized as on-chip multiband (multicolor) mid-IR sensors mounted on MEMS platforms to achieve high wavelength resolution as well as sensitivity. The photothermal uncooled IR sensors demonstrated in this study are limited to pyroelectric sensors, but other types of photothermal transducers, such as bolometers and thermopiles, are also possible [29, 30]. These will also be incorporated in a similar MEMS platform to realize higher sensitivity. The high spectral selectivity and good thermal responsivity of such multiwavelength detectors offer a low-cost yet robust platform for diverse applications, such as temperature measurement, biosensing, gas sensing, and hyperspectral imaging.

Acknowledgements This work is partially supported by JSPS KAKENHI (JP16H06364) and CREST "Phase Interface Science for Highly Efficient Energy Utilization" (JPMJCR13C3) from the Japan Science and Technology Agency.

References

1. Boboridis K, Obst AW (2003) A high-speed four-channel infrared pyrometer. AIP Conf Proc 684:759–764
2. Dinh T-V, Choi I-Y, Son Y-S, Kim J-C (2016) A review on non-dispersive infrared gas sensors: improvement of sensor detection limit and interference correction. Sens Actuators, B 231:529–538
3. Hodgkinson J, Smith R, Ho WO, Saffell JR, Tatam RP (2013) Non-dispersive infra-red (NDIR) measurement of carbon dioxide at 4.2 μm in a compact and optically efficient sensor. Sens Actuators, B 186:580–588
4. Hasan D, Lee C, Hasan D, Lee C (2018) Hybrid metamaterial absorber platform for sensing of CO_2 gas at Mid-IR. Adv Sci 5:1700581
5. Hodgkinson J, Tatam RP (2013) Optical gas sensing: a review. Meas Sci Technol 24:012004
6. Tan Q, Zhang W, Xue C, Xiong J, Ma Y, Wen F (2008) Design of mini-multi-gas monitoring system based on IR absorption. Opt Laser Technol 40:703–710
7. Wang L, Mizaikoff B (2008) Application of multivariate data-analysis techniques to biomedical diagnostics based on mid-infrared spectroscopy. Anal Bioanal Chem 391:1641–1654
8. Wang H, Wang L (2013) Perfect selective metamaterial solar absorbers. Opt Express 21:A1078
9. Felice RA (2003) The spectropyrometer—a practical multi-wavelength pyrometer. AIP Conf Proc 684:711–716
10. Boebel FG, Möller H, Hertel B, Grothe H, Schraud G, Schröder S, Chow P (1995) In situ film thickness and temperature control of molecular beam epitaxy growth by pyrometric interferometry. J Cryst Growth 150:54–61
11. Korotchenkov GS (2013) Handbook of gas sensor materials: properties, advantages and shortcomings for applications. New trends and technologies, vol 2. Springer, New York Heidelberg Dordrecht London
12. Esler MB, Griffith DW, Wilson SR, Steele LP (2000) Precision trace gas analysis by FT-IR spectroscopy. 1. Simultaneous analysis of CO_2, CH_4, N_2O, and CO in air. Anal Chem 72:206–215
13. Dao TD, Chen K, Ishii S, Ohi A, Nabatame T, Kitajima M, Nagao T (2015) Infrared perfect absorbers fabricated by colloidal mask etching of Al-Al_2O_3-Al Trilayers. ACS Photonics 2:964–970
14. Malka D, Danan Y, Ramon Y, Zalevsky Z, Malka D, Danan Y, Ramon Y, Zalevsky Z (2016) A photonic 1×4 power splitter based on multimode interference in silicon–gallium-nitride slot waveguide structures. Materials 9:516
15. Shoresh T, Katanov N, Malka D (2018) 1×4 MMI visible light wavelength demultiplexer based on a GaN slot-waveguide structure. Photonics Nanostruct Fundam Appl 30:45–49
16. Dao TD, Ishii S, Yokoyama T, Sawada T, Sugavaneshwar RP, Chen K, Wada Y, Nabatame T, Nagao T (2016) Hole srray perfect absorbers for spectrally selective midwavelength infrared pyroelectric detectors. ACS Photonics 3:1271–1278
17. Yokoyama T, Dao TD, Chen K, Ishii S, Sugavaneshwar RP, Kitajima M, Nagao T (2016) Spectrally selective mid-infrared thermal emission from molybdenum plasmonic metamaterial operated up to 1000 °C. Adv Opt Mater 4:1987–1992
18. Khorasaninejad M, Zhu AY, Roques-Carmes C, Chen WT, Oh J, Mishra I, Devlin RC, Capasso F (2016) Polarization-insensitive metalenses at visible wavelengths. Nano Lett 16:7229–7234
19. Palik ED (1998) Handbook of optical constants of solids. Academic Press, Cambridge, Massachusetts. ISBN 9780125444156
20. Doan AT, Yokoyama T, Dao TD, Ishii S, Ohi A, Nabatame T, Wada Y, Maruyama S, Nagao T (2019) A MEMS-based quad-wavelength hybrid plasmonic–pyroelectric infrared detector. Micromachines 10:413
21. Heiland G, Ibach H (1966) Pyroelectricity of zinc oxide. Solid State Commun 4:353–356
22. Hsiao C-C, Huang K-Y, Hu Y-C, Hsiao C-C, Huang KY, Hu Y-C (2008) Fabrication of a ZnO pyroelectric sensor. Sensors 8:185–192

23. Hsiao C-C, Yu S-Y, Hsiao C-C, Yu S-Y (2012) Improved response of ZnO films for pyroelectric devices. Sensors 12:17007–17022
24. Mirica E, Kowach G, Evans P, Du H (2003) Morphological evolution of ZnO thin films deposited by reactive sputtering. Cryst Growth Des 4:147–156
25. Yao J, Xia J, Maslov KI, Nasiriavanaki M, Tsytsarev V, Demchenko AV, Wang LV (2013) Noninvasive photoacoustic computed tomography of mouse brain metabolism in vivo. Neuroimage 64:257–266
26. Wissmeyer G, Pleitez MA, Rosenthal A, Ntziachristos V (2018) Looking at sound: optoacoustics with all-optical ultrasound detection. Light Sci Appl 7:53
27. Diem M, Koschny T, Soukoulis CM (2009) Phys Rev B 79:033101
28. Dao TD, Ishii S, Doan AT, Wada Y, Ohi A, abatame T, Nagao T (2019) On-chip quad-wavelength pyroelectric sensor for infrared spectroscopy. Adv Sci 6:1900579
29. Dao TD, Doan AT, Ngo HD, Chen K, Ishii S, Tamanai A, Nagao T (2019) Selective thermal emitters with infrared plasmonic indium tin oxide working in the atmosphere. Opt Mater Express 9:2534–2544
30. Dao TD, Doan AT, Ishii S, Yokoyama T, Handegård Sì Ngo HD, Ohki T, Ohi A, Wada Y, Niikura C, Miyajima S, Nabatame T, Nagao T (2019) MEMS-based wavelength selective bolometers. Micromachines 10:416

Functional Molecular Liquids

Edward A. Neal and Takashi Nakanishi

1 Introduction

A substance in the solvent-free liquid state has several advantages over one in the solid state in terms of molecular dispersal, including the flow of units past each other, the potential to dissolve other species and the ability of interacting species to collide. Many molecules have photophysical properties, form complex architectures through dynamic self-assembly or may form (photo)conducting materials under certain conditions. However, many functional molecules are held in a rigid but fragile solid state by a variety of intermolecular attractions, often resulting in the quenching of fluorescence, a lack of molecular flow for self-assembly components to meet prior to interaction and brittle materials that seldom have use as photo- or semiconductors. As such, these individual molecules usually only exhibit these properties when the rigidifying interactions are disrupted in the solution state. As a consequence, solvent and concentration effects will also alter molecular dispersal and therefore how these functions manifest themselves to the research scientist and material end-user alike.

Under solution conditions, the bulk medium selected (be it a single solvent or mixture thereof), cofactors, such as additives or salts, and the concentration of the functional molecule in that system will alter the properties observed, including the formation of gel states in cases, potentially impairing the reliability of the material. This may be in potentially harmful and hazardous organic solvents or in water, which society is under increasing pressure to conserve. The presence of solvent can dramatically change the properties of the molecule in question. The bulk properties will be altered owing to the disruption of its solid packing [1], which may affect photophysical properties such as excimer fluorescence, depending on the distance

E. A. Neal · T. Nakanishi (✉)
Frontier Molecules Group (FMG), International Center for Materials Nanoarchitectonics (WPI-MANA), National Institute for Materials Science (NIMS), 1-1 Namiki, Tsukuba 305-0044, Ibaraki, Japan
e-mail: NAKANISHI.Takashi@nims.go.jp

Y. Wakayama and K. Ariga (eds.), *System-Materials Nanoarchitectonics*,
NIMS Monographs, https://doi.org/10.1007/978-4-431-56912-1_6

between two monomer units such as pyrenes [2]. In addition to this, the dispersal of the molecule in solution exposes it to reactions, beneficial or deleterious.

This presents a challenge: how can nanoscale functional molecules be made liquid without solvent or high melting temperatures? One approach is to use *ionic* liquids, which have been extensively covered elsewhere, yet by their very nature remain as charged species, which may not always be desirable [3].

Herein, we present an alternative approach to converting π-conjugated and other functional molecules to fluid materials: uncharged, covalently bonded functional molecular liquids (FMLs).

2 Molecular Design Principles of Functional Molecular Liquids

To explain the rationale behind the design of an FML, it is important to identify the function of the molecule and its intermolecular interactions, as well as the potential modifications required to render it in a liquid state in the absence of counterions (Fig. 1). Such functions may include the fluorescent responses of conjugated π-systems, host–guest properties of macrocycles or the optoelectronic effects within fullerenes, as will be examined in later chapters.

The addition of flexible alkyl chains, whether aliphatic or with various degrees of branching, introduces disorder to the system, as well as an isolating distance between the functional cores. This spacing is similar to that in a solution without the need of external solvent, but still allows cofactors to be dissolved in the neat liquid

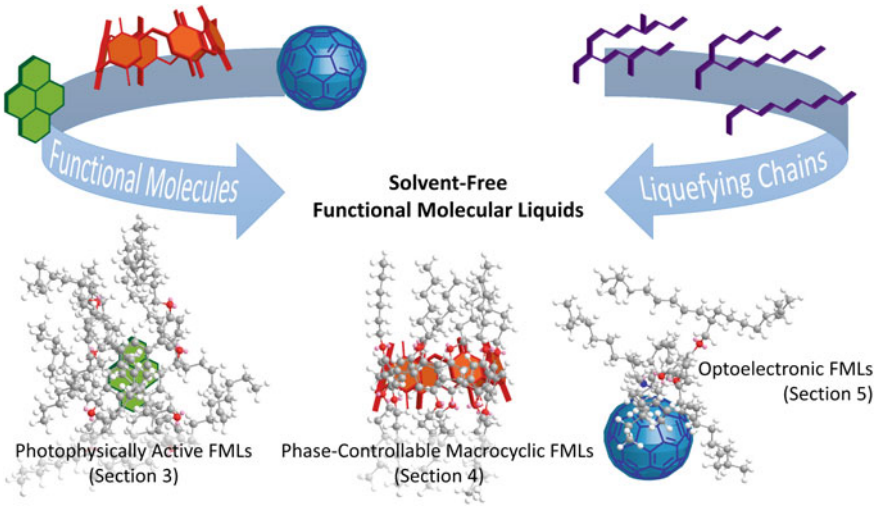

Fig. 1 Functional molecular liquids (FMLs): design philosophy and applications

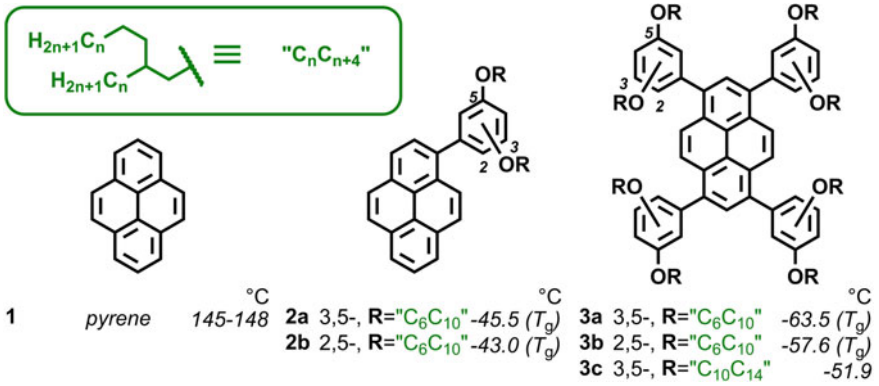

Fig. 2 Design of photoemissive pyrene liquids with high quantum yield through the disruption of the solid state with disordered "C_nC_{n+4}" alkyl chains. Melting points or glass transition temperatures (T_g) are given where available

itself. The variation in chain length and branching in Guerbet-type alcohol-derived "C_nC_{n+4}" groups (Fig. 2, inset) [4] to render a range of nanocarbons, fluorophores and conjugated polymers as liquids will be described, but has already been covered in more detail [5]. The FML design philosophy could be applied to many molecules with different functions besides these provided the structural and functional characteristics of the starting molecule are borne in mind: different starting functional entities will require different extents and natures of functionalization to lower the phase transition temperatures below room temperature and so produce a liquid.

By means of illustration, consider pyrene (**1**): a planar-aromatic molecule with functional fluorescence, prone to π-stacking with a high melting point. This can be peripherally modified, while crucially leaving the fluorophore intact, *preserving* the function of the original molecule (Fig. 2) [6]. By decorating the molecule with dihydroxyphenyl units functionalized with branched alkyl chains (**2** and **3**), many new degrees of freedom are introduced, increasing the disruption of π-stacking and entropically lowering the melting point (m.p.) or glass transition temperature (T_g) of the system to *below room temperature*. This also serves to prevent aggregation-based fluorescence quenching, enhancing the function of the molecule [7]. During development, no birefringent texture was observed by polarized optical microscopy (POM), confirming that therefore, no long-range order was present in the liquid examples. Signals in small- and wide-angle X-ray scattering (SWAXS) were also broadened, further confirming the disruption of the stacking interactions normally present in unfunctionalized pyrene. The fluorescence properties of the pyrene center differed in a fashion commensurate with the disruption of excimer formation from overlapping pyrene centers; this will be discussed in more detail later.

Besides simply disrupting the solid state, other factors must be considered to ensure the material remains in an amorphous state with reliable function. It was recently discovered that unusual supercooling behavior could arise in an anthracene-based FML (**4a–f**), wherein the system would stay as a liquid for several weeks or

months, then crystallize (Fig. 3) [8]. Such solid materials are fragile, have altered (usually worsened) photophysical properties due to the proximity of other units and may expose the central functional motif—in this case, a π-conjugated core—to unwanted oxidation, photolysis or other deleterious reactions. Through disruption of the symmetry of the anthracene, using a bulkier core less prone to stacking and/or adjusting the length of alkyl units, this unwanted supercooling behavior could be screened for beforehand through differential scanning calorimetry (DSC) tests on preannealed samples, then avoided altogether.

For the practical use of FMLs, large amounts of sample are required (at least several grams). The large-scale synthesis of FMLs may result in by-products from E2 reactions during the S_N2 alkylation step, presenting a challenge at purification. This can be addressed simply with *tert*-butoxide treatment to eliminate the remaining reagent to form further alkene, which is then susceptible to hydrogenation or hydroboration for enhanced separation from the unaffected target product (Scheme 1) [9].

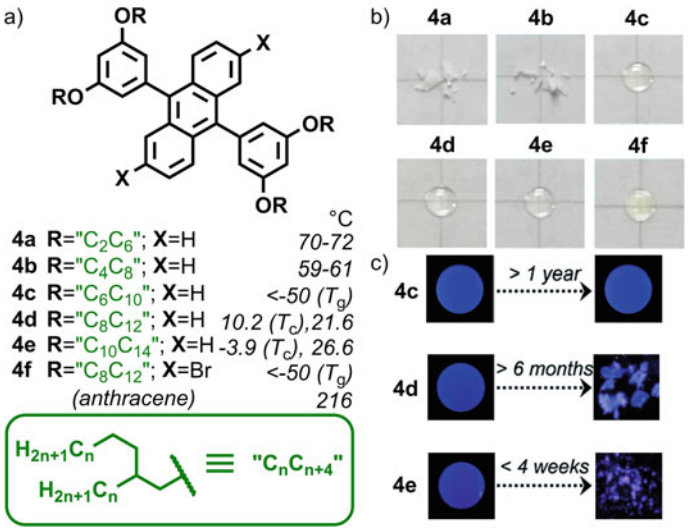

Fig. 3 **a** Chemical structures of diphenylanthracenes **4a–e** with different chain length and dibrominated **4f**. Melting points or glass transition temperatures (T_g) are given where available. **b** Photographs of freshly synthesized **4a–f** in daylight at 20 °C, with a drop of fluid or powder of solid on a glass plate. **c** Photographs of **4c**, **4d** and **4e** as fresh (left) and after long-term aging at ambient temperature (right) taken under irradiation of a UV lamp (365 nm). Figures b and c adapted from Ref. 8 with permission from the Royal Society of Chemistry (2018)

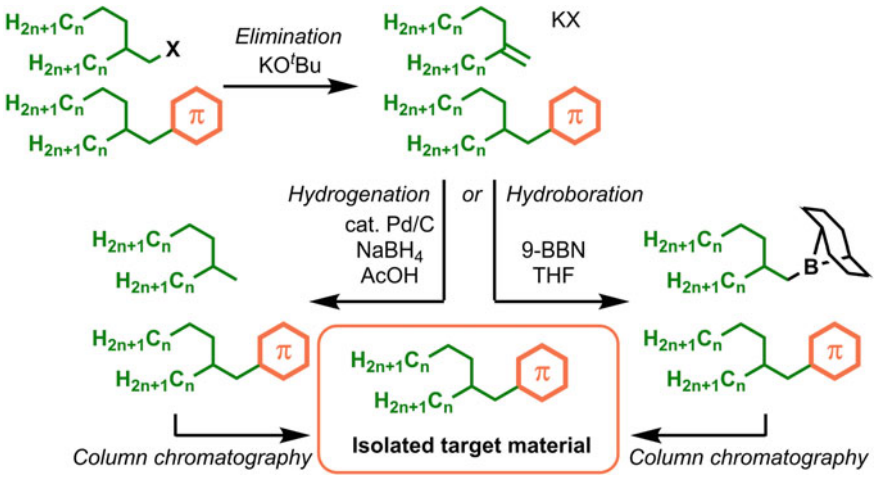

Scheme 1 Three-step treatment for the improved separation of by-products from FMLs (n = 2 or 6)

3 Aromatic Functional Liquids for Photophysical Applications

Smaller aromatic molecules have long been known to have photophysical properties but—prior to the advent for FMLs—have only been measured in solution, as crystalline solids directly or as cast films through solvent evaporation. The addition of liquefying groups allows these properties to be accessed without solvent through interfering with the intermolecular π-π interactions described above. This results in an enhancement of monomeric photophysical properties but may interfere with excimer formation, as seen in the examples below.

3.1 Naphthalene Liquids

Naphthalene, m.p. 80 °C, can be incorporated into an FML through the alkylation of 1- and 2-naphthol with Guerbet-type alcohol-based branched alkyl chains (**5a–f**, Fig. 4) [10]. This affords a set of FMLs with chain length-dependent viscosity and an interesting difference in fluorescence properties between the two positions: 1-substituted naphthalenes (**5a–c**) preferring excimeric emission despite the alkyl chains, with the 2-substituted naphthalene series (**5d–f**) exhibiting monomer-rich luminescence. It is worth noting that 1-naphthol (95–96 °C) and 2-naphthol (121–123 °C) have higher melting points than naphthalene, making their liquid state more remarkable.

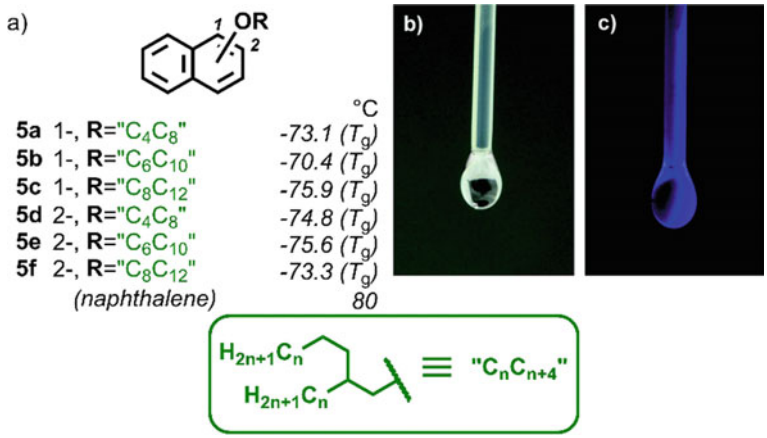

Fig. 4 **a** Chemical structures of regioisomeric liquid naphthalenes **5**. **5a–c** represent the 1-regioisomers and **5d–f** the 2-regioisomers. Melting points or glass transition temperatures (T_g) are given where available. Photographs of **5a** dropping down through a PTFE needle under ambient light (**b**) and UV (254 nm) light (**c**). Figures **b** and **c** reproduced from Ref. 10 with permission from the PCCP Owner Societies

3.2 Anthracene Liquids

Anthracene-derived systems have highly tunable photophysical properties that, as an FML, have improved stability to photodegradation (Fig. 5).

Anthracene itself, m.p. 216 °C, has been known to be liable to photodimerization for over 150 years [11] and photooxidation for at least 50 years; [12] both of these reactions pose challenges to the formation of higher acenes, for which the interested reader is referred to a review by Anthony [13]. The functionalization of the central rings with sp- or sp^2-hybridized entities—such as with alkynes or aryls—prevents these deleterious reactions yet also modifies their photophysical properties. As such, the addition of liquefying groups to these pendant units provides photochemical FMLs with high photostability (Fig. 5a).

The addition of 3,5-functionalized aryl units to the 9- and 10- positions of anthracene produces UV-active liquids **6** photostable to four hours of irradiation at 365 nm with a 100 Wm^{-2} Xe lamp, compared with 9,10-diphenylanthracene cast as a film, which withstood only two hours. Doping these systems with 9,10-di(phenylethylenyl)anthracene **D1** – itself designed to resist dimerization/oxidation – allows tunable luminescence wavelengths (Fig. 5b, c) [14]. Adding 0.3 and 0.5 mol% **D1** resulted in red-shifts of the blue emission in **6(i)** to paler blue **ii** and green **iii** respectively. A further increase to 2.0 mol% produced yellow-emitting **iv**, which can be rendered darker yellow (**v**) at 5.0 mol%. Europium complex **D2** blue-shifted the emissions, producing light and dark purple **vi** and **vii** at 2.0 and 5.0 mol%. A thermoresponsive composite of **iii** and **vii** containing **D1** and **D2** in different proportions

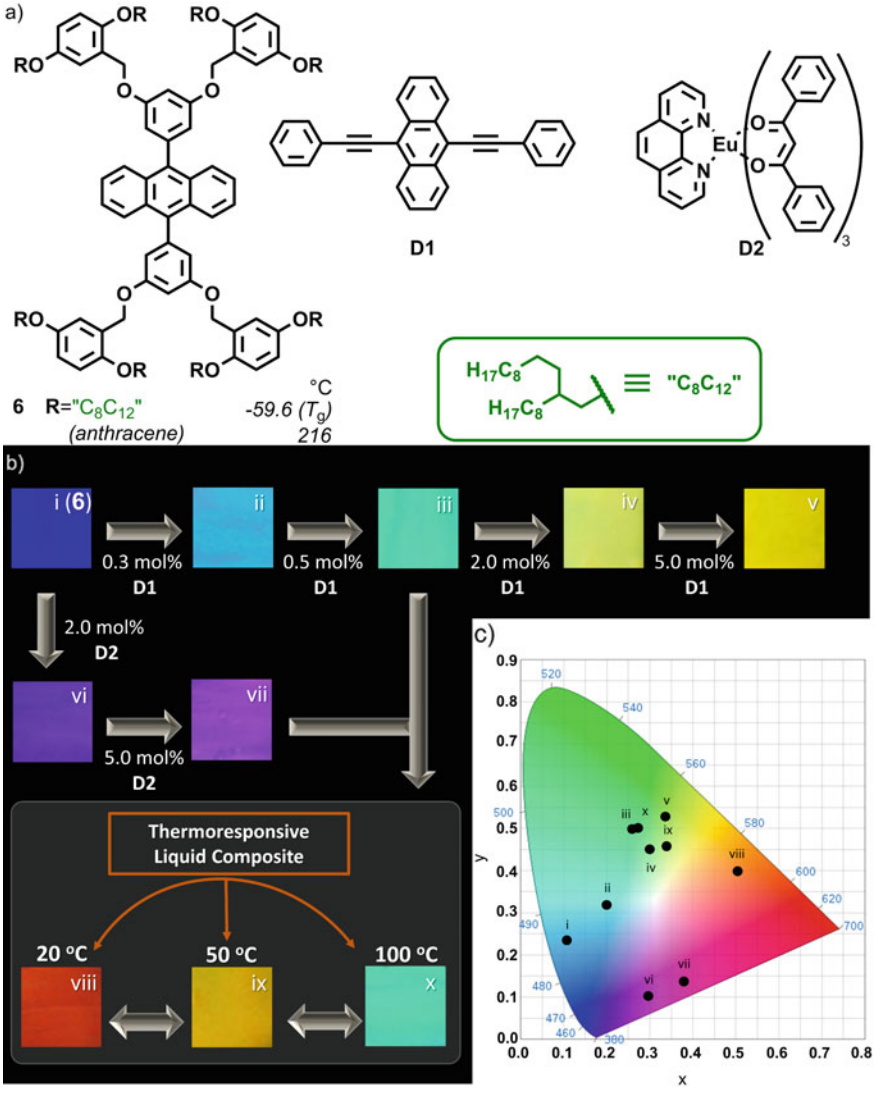

Fig. 5 a Chemical structures of anthracene-based FML **6** and two dopants, 9,10-di(phenylethynyl)anthracene **D1** and [(phenanthrolino)Eu(III)(dbm)$_3$] **D2** (dbm = dibenzoylmethane). **b** Color changes resulting from addition of the dopants and temperature variations. **c** Commission International de l'Éclairage coordinate values of the overall color tunability achieved by the doping of **6** with **D1** and/or **D2**, as well as temperature variation. The **i-x** represent different blends and temperatures derived from **i** (**6**) as shown in figure b. Figures b and c adapted (merging (**b**), numbering (**c**)) from Ref. 14 published by Springer Nature under the CC-BY-3.0 license

was also made and tested, affording a thermochromic composite material going from red (**viii**, 20 °C) via ochre (**ix**, 50 °C) to turquoise at 100 °C (**x**).

Such mixtures have the drawback of being inhomogeneous owing to the presence of solid dopant molecules diffusing through the anthracene FML. It was recently shown that modifications to the anthracene backbone *directly* can also alter the color observed, while providing improved uniformity and steadiness of emission [15].

3.3 Pyrene Liquids

Pyrene, m.p. 145–148 °C, is the smallest *peri*-fused polycyclic aromatic hydrocarbon. As such, it provides a large conjugated π-network that does not oxidize as readily as the larger linear acenes but has a greater contact face for π-π interactions.

Functionalizing pyrene with 3,5-dialkyloxyphenyl units (as with the anthracenes), or their 2,5-dialkyloxyphenyl isomers, results in a class of FMLs with different emissions based on the alkyl chain length and whether the pyrene is substituted solely in the 1-position (**2**, Fig. 2) or tetrasubstituted (**3**, Fig. 2). The difference in the number of alkyl chains and their length affects the ability of the pyrene cores to overlap, resulting in materials shifting from excimeric to monomeric emissions with increasing barriers to stacking. These were probed by picosecond time-resolved fluorescence spectroscopy and femtosecond time-resolved near-IR (TRNIR) to not only characterize these emissions in themselves but also use them as a tool for investigating local order within these amorphous substances. Even with the range of emissions produced from different local arrangements, all exhibit high fluorescence quantum yields (Φ_{FL}, 57–85%) in a range of blue emission wavelengths (Table 1) [6].

An alkane-substituted pyrene also forms a highly excimeric fluorescent solvent-free liquid with a 65% fluorescent quantum yield. In addition, the liquid pyrene can form micelles with monododecyl hexaethylene glycol in water to give fluorescent emissions depending on the concentration of the pyrene: high concentrations in the micelles increase excimer-derived emission, resulting in a redshift [16].

Table 1 Photochemical properties of liquid pyrene derivatives **2** and **3**: Solvent-free fluorescence emissions and quantum yields (Φ_{FL}). Data taken from ref. 6

Compound	Aryl Substitution	Chain	λ_{max} / nm	Φ_{FL}
2a	3,5-	"C_6C_{10}"	472	0.72
2b	2,5-	"C_6C_{10}"	467	0.66
3a	3,5-	"C_6C_{10}"	456	0.67
3b	2,5-	"C_6C_{10}"	441	0.57
3c	3,5-	"$C_{10}C_{14}$"	456	0.85

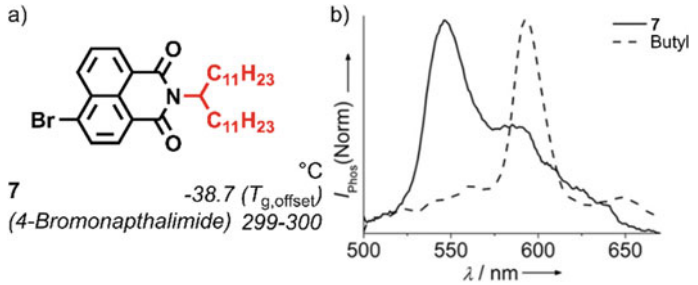

Fig. 6 **a** A chemical structure of bromonaphthalimide-based FML **7**. Glass transition temperatures (T_g) are given where available. **b** Normalized phosphorescence spectra of **7** at 25 °C in air (λ_{ex} = 345 nm). Figure **b** adapted (numbering) from Ref. 17 with permission from John Wiley and Sons

3.4 Bromonaphthalimide FMLs

Bromonaphthalimide is a rhylene dye with a singlet–triplet gap conducive to phosphorescence. Use of a symmetrical branched alkyl chain to *N*-substitute the bromonaphthalimide to tune this gap afforded a highly desirable room-temperature phosphorescent FML **7** with a 5.7 ms phosphorescence lifetime (Fig. 6) [17].

The luminescence intensity of **7** was further enhanced by the use of terephthaldehyde and 1,3,5-triformylbenzene as phosphors partially dissolved therein. Noteworthily, the singlet–triplet energy level gap, ΔE_{ST}, was found to be 0.13 eV by density functional theory (DFT) calculations, similar to that of a simpler butyl-functionalized analog (0.12 eV). This demonstrated that the liquefying modification did not significantly affect the phosphorescent properties of the bromonaphthalimide core.

3.5 Conjugated Oligomeric Liquids

Functional liquids can also be made from conjugated systems, which may be of use for future electronic devices [18]. A *p*-di(phenylenedivinylene)benzene, when tetrafunctionalized with branched alkyl chains, affords a liquid OPV **8**, which on doping with tris(8-hydroxyquinolinato)aluminium (Alq3) and 5,6,11,12-tetraphenyltetracene (rubrene) produces a white-emitting liquid under stimulation at 365 nm (Fig. 7a) [19].

Shinohara et al. have recently demonstrated a range of conjugated 9,9-Guerbet-difunctionalized fluorene copolymer materials, where the nature of the second monomer unit and its alkylation affect the physical state (Fig. 7b) [20]. A copolymer with a 9,9-dioctylated monomer units afforded viscoelastic substances **9a**, with further soft, deformable materials afforded from *alt*-copolymers incorporating thiophenes (**9b**) and thiophene-benzothiadiazole-thiophene motifs (**9c**). These three

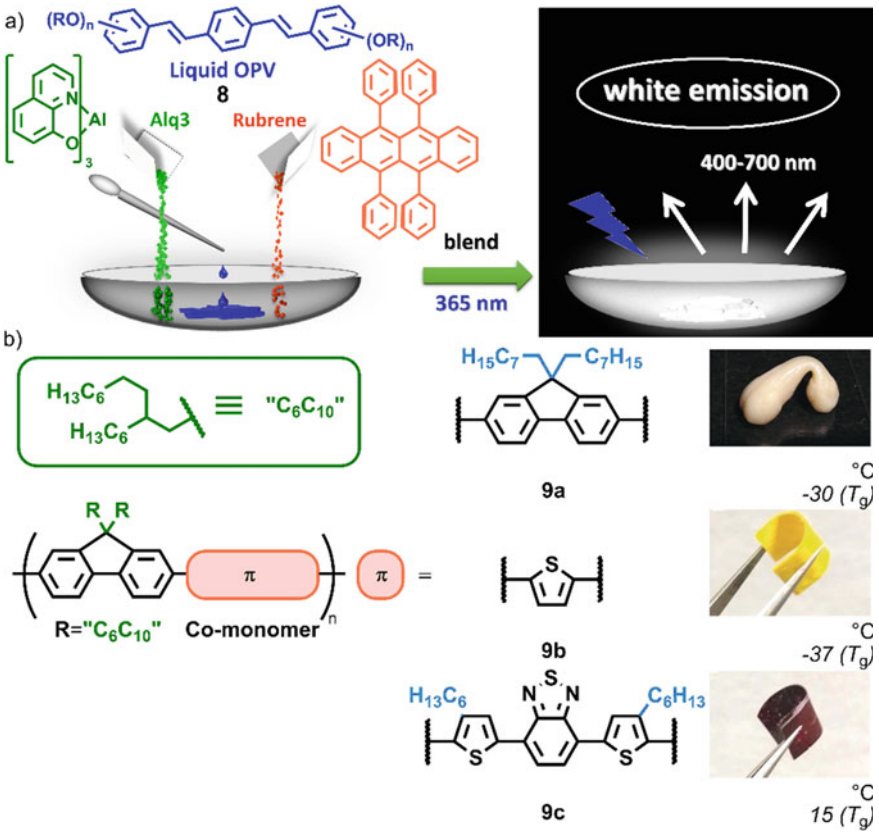

Fig. 7 **a** Illustration of the preparation of a solvent-free white-emitting liquid composite from **8**. **b** Viscoelastic polymers **9a**, **9b** and **9c**. Glass transition temperatures (T_g) are given where available. Figure a reproduced from Ref. 19 with minor reformatting and figure b (photographs) reproduced from Ref. 20 with permission from John Wiley and Sons

materials produced blue, green/yellow and red fluorescence respectively with good quantum yields. Upon blending, the composite materials produced demonstrated dynamic miscibility, leading to mechanochromic fluorescence variation with phase segregation clearly visible under fluorescence microscopy, yet with full restorability.

While these two systems demonstrate the potential for soft optoelectronic devices, it is possible that such advances will underpin future fluid-cast soft electronic devices.

4 Macrocyclic Functional Molecular Liquids

Large cyclic systems with cavities, known as macrocycles, can receive guest entities that suit the chemistry and size of the pocket. Such host–guest interactions underpin

the field of supramolecular chemistry and much of the wide array of sensory and interlocked systems therein: the interested reader is directed to an introductory text by Steed and Atwood [21]. These interactions may be ion–ligand, hydrophobic or hydrophilic in nature but, as before, many of the systems so far reported are dependent on the solution state for the dispersal of host and guest to permit interaction. Some examples of FMLs that obviate the need for solvent are discussed below.

4.1 Phthalocyanine Functional Molecular Liquids

Phthalocyanine macrocycles are tetradentate ligands with two displaceable hydrogens, well-suited to divalent cations. The addition of eight (2-dodecyloxyphenyl) substituents produced a dark green sticky macrocyclic FML **10** (Fig. 8a) [22]. Both before and after the complexation of Cu^{2+} cations—an inherent property of the molecule unaffected by liquefication—the UV/Vis spectra and polar optical microscopy of sheared or pushed samples showed a lack of order between subunits. The zero-shear viscosities of the two systems were comparable (both on the order of 10^4) but *decreased* with temperature and strain (Fig. 8b, c).

A phthalocyanine FML functionalized with 2-octyldecylthio units is also a suitable sandwich ligand for lanthanide metals, affording a liquid spin-active, electrochromic Lu complex **11** with a hole delocalized over the ligands (Fig. 8d) [23]. The disruption of quenching π-π stacking was confirmed by SWAXS through the interference of the solubilizing chains.

4.2 Porphyrin Functional Molecular Liquids

Porphyrins are similar in structure to phthalocyanines and, owing to their applications in sensing, liquid crystals, nanoelectronics and optics, they are extensively researched, with low-melting derivatives being highly desirable [24]. They differ from phthalocyanines in having sp^2 carbon linkers between the pyrrole ring units instead of nitrogen, so they may be functionalized at these *meso* positions on the central ring, rather than modifying fused benzene ring positions, as in phthalocyanine. Porphyrin FMLs were reported independently by Maruyama et al. [25] and Nowak-Król et al. [26] in 2010, both showing distinct single phase transitions at temperatures depending nonlinearly on alkyl chain length. Solid porphyrins have been tested for their ability to form complexes, such as that of Koszlewski et al., in which interesting optical property variations were found [27].

The most recent development in FMLs is a material composed of tetraphenylporphyrins alkylated with Guerbet chains, which has only recently been reported [28]. The central porphyrin ring was determined to be distorted, based on magnetic circular dichroism measurements and an unusual order of absorption band intensities in the UV–visible region. As a consequence of this distortion and the insulation of

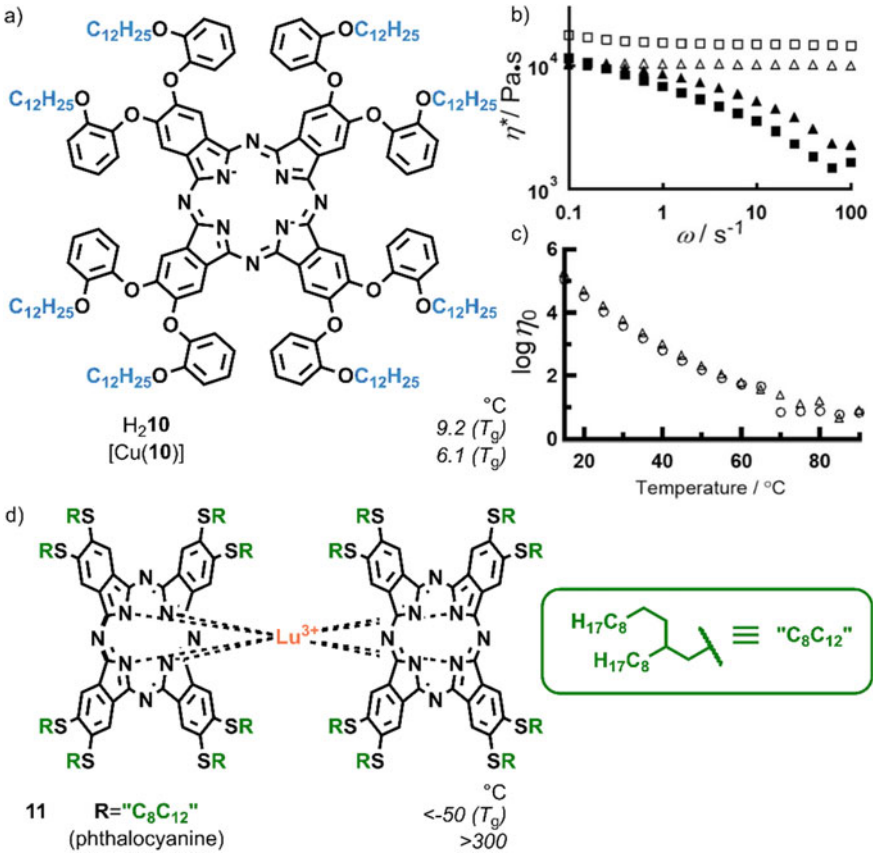

Fig. 8 **a** A chemical structure of phthalocyanine-based FML **10**. **b** Complex viscosity (η^*) versus ω on double logarithmic scale: □ H_2**10** ($\gamma = 0.1\%$), ■ H_2**10** ($\gamma = 50\%$), Δ [Cu(**10**)] ($\gamma = 0.1\%$), ▲ [Cu(**10**)] ($\gamma = 50\%$). **c** Plots of log η_0 vs temperature at $\gamma = 0.1\%$ for H_2**10** (Δ) and [Cu(**10**)] (○). **d** A chemical structure of spin-active electrochromic double-decker lutetium phthalocyanine-based FML **11**. Melting points or glass transition temperatures (T_g) are given where available. Figures **b** and **c** reproduced from Ref. 22 with permission from the Chemical Society of Japan

the core from both air and electrostatic interactions by the alkyl units, these systems have excellent charge retention compared with the unfunctionalized core and free branched alcohol. Such *electret* materials have useful mechanoelectrical and electroacoustic functions, as demonstrated in a polyurethane-textile sandwich electrode device, rendered pressure-sensitive upon impregnation with the liquefied porphyrin. These applications are only possible owing to the aforementioned insulation and mobility of the core in this FML material.

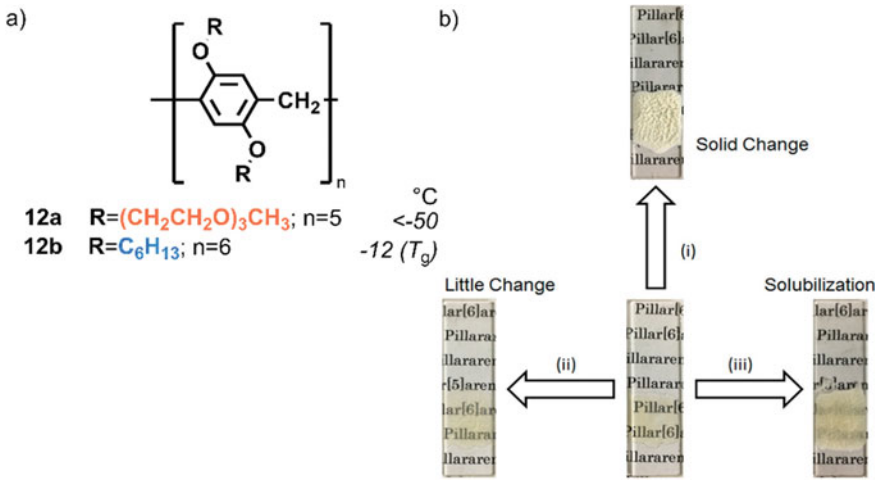

Fig. 9 **a** A chemical structure of pillararene cyclic host liquids **12a** and **12b**. Melting points or glass transition temperatures (T_g) are given where available. **b** Structural liquid-to-solid state change of **12b** after exposure to (i) 1,4-dioxane vapor (solidification), (ii) methanol vapor (little change), (iii) chloroform vapor (solubilization). Figure **b** reprinted with permission from Ref. 34. Copyright 2019 American Chemical Society

4.3 Pillararene Cyclic Host Liquids

Macrocycles capable of hosting organic guests rather than metal cations have also been converted to FMLs. The pillararene macrocycles of Ogoshi et al. are formed from methylene-bridged hydroquinone units—usually five—which can be alkylated with a variety of functionalities; the interested reader is directed to a recent review and a book [29, 30]. Through alkylation with a methyl triethylene glycol entity, cyclic host liquids **12a** were developed from such a pillar[5]arene, producing a liquid macrocycle with an aromatic hydrophobic cavity suitable for a range of guests (Fig. 9a) [31]. These systems gave rise to latter supra- and macromolecular systems, such as rotaxane generation [32] and a polyrotaxane "topological gel" [33].

Hydrophobic structural liquid variants **12b** have been recently developed. Assemblies of perhexylated pillar[6]arenes afforded functional liquids with a cavity suited to 1,4-dioxane; all other alkylations tested afforded solids at room temperature [34]. Upon exposure to 1,4-dioxane vapor, the liquid assembly promptly solidified, with methanol causing little change and chloroform solubilizing the material (Fig. 9b).

5 Optoelectronically Active Fullerene Liquid Materials

Fullerenes are large spherical or spheroidal structures of conjugated carbons of great interest to supramolecular chemistry and materials science alike [35].

Fullerene FMLs **13a**, **13b** and **13d** were first developed in 2006 from C_{60}, a tris(alkyloxy)benzyldehyde and *N*-methylglycine under reflux, with viscosities dependent on the length of their saturated *linear* chains and the electrochemical properties of the C_{60}-base unit unaffected (Fig. 10a) [36]. The chain length dependence of their transition temperatures was further explored for **13a–e** alongside an octyl analog and found to be nonlinear (Fig. 10b). Three examples of C_{70} were also tested

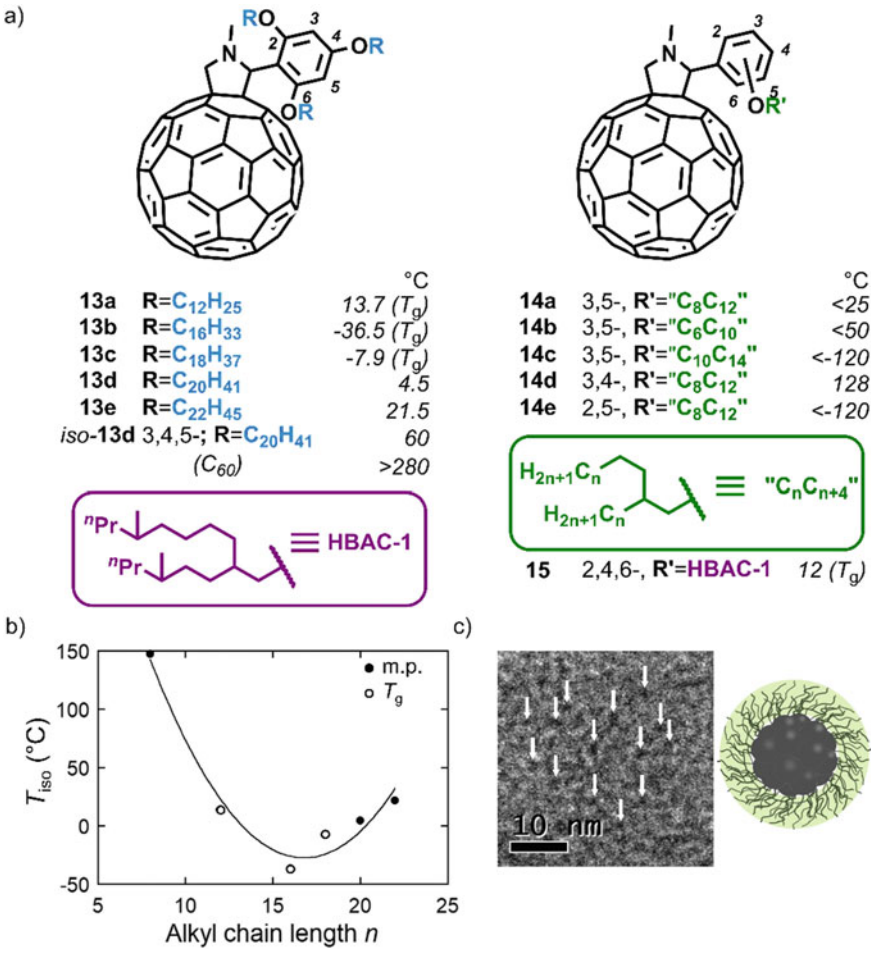

Fig. 10 **a** Chemical structures of fullerene-based FMLs **13**–**15**. **b** Variation of isotropic transition point temperature with linear chain length in **13a-13e** (and octyl analog; melting points as full circles, glass transition points as hollow circles). **c** Cryo-TEM image of micelles of **14c** in *n*-decane, with illustration of the arrangement of alkylated-C_{60} units. The dark regions indicated by white arrows are the C_{60}-rich cores of the micelles. Figure **b** reprinted with permission from Ref. 37. Copyright 2013 American Chemical Society. Figure **c** (part) reproduced from Ref. 40 with permission from Springer Nature

(not shown) [37]. Later, *branched* series **14** demonstrated liquid crystalline or liquid properties at ambient temperature (except **14d** which requires heating to 128 °C), whereas *hyperbranched* liquid **15** was found to have a relatively high viscosity of 1.28×10^5 Pa s [38].

The photoelectrochemical properties of C_{60} are not simply preserved as an alkylated "alk-C_{60}" FML but are also open to enhancement through cofactors in the liquid state. Doping the liquid with CdSe nanocrystals sensitizes the system to visible light through charge transfer, resulting in photoelectrochemical properties [39]. Even the addition of simple *n*-hexane solvent can affect these systems profoundly, driving the formation of micelles from **14c** through minimizing C_{60}-alkane interactions in a manner analogous to a surfactant (Fig. 10c) [40]. Liquid fullerene systems have been shown to have a broad array of assemblies with various properties, and interested readers are referred to a recent account of their development [41].

6 Conclusions

Throughout this chapter, we have shown a variety of functional molecular liquid materials developed over the past decade. From simple aromatic cores such as naphthalene up to larger π-systems such as spherical fullerenes, suitably selected bulky and flexible alkyl chains with various extents of branching reliably liquefy the substance. This not only eliminates the need for solvent, but gives both photophysical advantages and ease of fabrication independent of the shape and geometry of devices. The liquid physical properties can be tuned through modification of these chains and host–guest interactions in particular systems. This demonstrates the versatility of the functional molecular liquid design philosophy in producing materials of a wide array of viscosities that respond to light, pressure, chemical stimulus or charge: in all senses, the future of functional molecular liquids is bright.

References

1. Yao Z-F, Wang J-Y, Pei J (2018) Control of π–π stacking via crystal engineering in organic conjugated small molecule crystals. Cryst Growth Des 18:7–15
2. Bains GK, Kim SH, Sorin EJ, Narayanaswami V (2012) The extent of pyrene excimer fluorescence emission is a reflector of distance and flexibility: analysis of the segment linking the LDL receptor-binding and tetramerization domains of apolipoprotein E3. Biochemistry 51:6207–6219
3. Dong K, Liu X, Dong H, Zhang X, Zhang S (2017) Multiscale studies on ionic liquids. Chem Rev 117:6636–6695
4. Guerbet M (1909) Condensation de L'Alcool Isopropylique avec son Dérivé Sodé; Formation du Méthylisobutylcarbinol et du Diméthyl-2.4-heptanol-6. Comptes Rendus Hebd Séances Académie Sci 149:129–132
5. Hollamby MJ, Nakanishi T (2013) The power of branched chains: optimising functional molecular materials. J Mater Chem C 1:6178–6183

6. Lu F, Takaya T, Iwata K, Kawamura I, Saeki A, Ishii M, Nagura K, Nakanishi T (2017) A guide to design functional molecular liquids with tailorable properties using pyrene-fluorescence as a probe. Sci Rep 7:3416
7. Beddard GS, Porter G (1976) Concentration quenching in chlorophyll. Nature 260:366–367
8. Lu F, Jang K, Osica I et al (2018) Supercooling of functional alkyl-Π molecular liquids. Chem Sci 9:6774–6778
9. Okamoto K, Lu F, Nakanishi T (2018) Posttreatment technique for S_N2 alkylation of aromatics with alkyl halides: aiming toward large-scale synthesis of building blocks for soft π-molecular materials. Bull Chem Soc Jpn 91:1258–1263
10. Narayan B, Nagura K, Takaya T et al (2018) The effect of regioisomerism on the photophysical properties of alkylated-naphthalene liquids. Phys Chem Chem Phys 20:2970–2975
11. Bouas-Laurent H,Desvergne J-P, Castellan A, Lapouyade R (2000) Photodimerization of anthracenes in fluid solution: structural aspects. Chem Soc Rev 29:43–55
12. Sugiyama N, Iwata M, Yoshioka M, Yamada K, Aoyama H (1969) Photooxidation of anthracene. Bull Chem Soc Jpn 42:1377–1379
13. Anthony JE (2008) The larger acenes: versatile organic semiconductors. Angew Chem Int Ed 47:452–483
14. Babu SS, Hollamby MJ, Aimi J et al (2013) Nonvolatile liquid anthracenes for facile full-colour luminescence tuning at single blue-light excitation. Nat Commun 4:1969
15. Lu F, Hagiwara K, Yoshizawa M, Nagura K, Ishihara S, Nakanishi T (2019) Luminescence tuning with excellent colour homogeneity and steadiness using fluorescent molecular liquids. J Mater Chem C 7:2577–2582
16. Hollamby MJ, Danks AE, Schnepp Z, Rogers SE, Hart SR, Nakanishi T (2016) Fluorescent liquid pyrene derivative-in-water microemulsions. Chem Commun 52:7344–7347
17. Goudappagouda MA, Wakchaure VC, Ranjeesh KC, Das T, Vanka K, Nakanishi T, Babu SS (2019) Paintable room-temperature phosphorescent liquid formulations of alkylated bromonaphthalimide. Angew Chem Int Ed 58:2284–2288
18. Junkers T, Vandenbergh J, Adriaensens P, Lutsen L, Vanderzande D (2012) Synthesis of Poly(*p*-Phenylene Vinylene) materials via the precursor routes Polym Chem 3:275–285
19. Santhosh Babu S, Aimi J, Ozawa H, Shirahata N, Saeki A, Seki S, Ajayaghosh A, Möhwald H, Nakanishi T (2012) Solvent-free luminescent organic liquids. Angew Chem Int Ed 51:3391–3395
20. Shinohara A, Pan C, Guo Z, Zhou L, Liu Z, Du L, Yan Z, Stadler FJ, Wang L, Nakanishi T (2019) Viscoelastic conjugated polymer fluids. Angew Chem Int Ed 58:9581–9585
21. Steed JW, Atwood JL (2009) Supramolecular Chemistry, 2nd ed. https://doi.org/10.1002/9780470740880
22. Chino Y, Ghosh A, Nakanishi T, Kobayashi N, Ohta K, Kimura M (2017) Stimuli-responsive rheological properties for liquid phthalocyanines. Chem Lett 46:1539–1541
23. Zielinska A, Takai A, Sakurai H, Saeki A, Leonowicz M, Nakanishi T (2018) A Spin-active, electrochromic, solvent-free molecular liquid based on double-decker lutetium phthalocyanine bearing long branched alkyl chains. Chem—Asian J 13:770–774
24. Henriques CA, Pinto SMA, Canotilho J, Ermelinda M, Eusébio S, Calvete MJF (2016) Synthesis of low melting point porphyrins: a quest for new materials. J Porphyr Phthalocyanines 20:843–854
25. Maruyama S, Sato K, Iwahashi H (2010) Room temperature liquid porphyrins. Chem Lett 39:714–716
26. Nowak-Król A, Gryko D, Gryko DT (2010) Meso-substituted liquid porphyrins. Chem—Asian J 5:904–909
27. Koszelewski D, Nowak-Król A, Drobizhev M et al (2013) Synthesis and linear and nonlinear optical properties of low-melting Π-extended porphyrins. J Mater Chem C 1:2044–2053 (2013)
28. Ghosh A, Yoshida M, Suemori K et al (2019) Soft chromophore featured liquid porphyrins and their utilization toward liquid electret applications. Nat Commun 10:4210
29. Ogoshi T, Yamagishi T, Nakamoto Y (2016) Pillar-shaped macrocyclic hosts pillar[n]arenes: new key players for supramolecular chemistry. Chem Rev 116:7937–8002

30. Ogoshi T (2016) Pillararenes, 1st ed. https://doi.org/10.1039/9781782622321
31. Ogoshi T, Shiga R, Yamagishi T (2012) Reversibly tunable lower critical solution temperature utilizing host-guest complexation of pillar[5]arene with triethylene oxide substituents. J Am Chem Soc 134:4577–4580
32. Ogoshi T, Aoki T, Shiga R, Iizuka R, Ueda S, Demachi K, Yamafuji D, Kayama H, Yamagishi TA (2012) Cyclic host liquids for facile and high-yield synthesis of [2]rotaxanes. J Am Chem Soc 134:20322–20325
33. Ogoshi T, Aoki T, Ueda S, Tamura Y, Yamagishi T (2014) Pillar[5]arene-based nonionic polyrotaxanes and a topological gel prepared from cyclic host liquids. Chem Commun 50:6607–6609
34. Ogoshi T, Maruyama K, Sakatsume Y, Kakuta T, Yamagishi TA, Ichikawa T, Mizuno M (2019) Guest vapor-induced state change of structural liquid pillar[6]arene. J Am Chem Soc 141:785–789
35. Shen Y, Nakanishi T (2014) Exotic Self-Organized Fullerene Materials Based on Uncommon Hydrophobic-Amphiphilic Approach. In: Fuller, Carbon-Rich Nanostructures. Springer, New York. pp. 1–22
36. Michinobu T, Nakanishi T, Hill JP, Funahashi M, Ariga K (2006) Room temperature liquid fullerenes: an uncommon morphology of C_{60} derivatives. J Am Chem Soc 128:10384–10385
37. Michinobu T, Okoshi K, Murakami Y, Shigehara K, Ariga K, Nakanishi T (2013) Structural requirements for producing solvent-free room temperature liquid fullerenes. Langmuir 29:5337–5344
38. Li H, Babu SS, Turner ST, Neher D, Hollamby MJ, Seki T, Yagai S, Deguchi Y, Möhwald H, Nakanishi T (2013) Alkylated-C_{60} based soft materials: regulation of self-assembly and optoelectronic properties by chain branching. J Mater Chem C 1:1943–1951
39. Kramer TJ, Babu SS, Saeki A, Seki S, Aimi J, Nakanishi T (2012) CdSe nanocrystal/C60-liquid composite material with enhanced photoelectrochemical performance. J Mater Chem 22:22370–22373
40. Hollamby MJ, Karny M, Bomans PHH et al (2014) Directed assembly of optoelectronically active alkyl–Π-conjugated molecules by adding N-alkanes or Π-conjugated species. Nat Chem 6:690–696
41. Lu F, Neal EA, Nakanishi T (2019) Self-assembled and nonassembled alkylated-fullerene materials. Acc Chem Res 52:1834–1843

Devices and Computation by Nanoarchitectonics

Ionic Nanoarchitectonics: Creation of Polymer-Based Atomic Switch and Decision-Making Device

Kazuya Terabe, Tohru Tsuruoka, and Takashi Tsuchiya

1 Introduction

Although today's information and communication technology has made rapid progress owing to the high performance of semiconductor devices mounted in computers, a concern is that the performance improvement by conventional miniaturization and high integration is approaching its limit. Therefore, in addition to promoting further research and development of conventional semiconductor devices, it is necessary to proactively develop new functions and high-performance devices beyond this limit. Such innovative devices will operate on different principles from conventional semiconductor devices. One type of device operated on a new principle is devices that utilizes not only electron transport phenomena but also ion transport phenomena. These devices, achieved by controlling the migration of ions within solids, can be referred to as solid state ionic devices because they operate on the principle of solid-state ionics [1].

The movement speed of ions in solids is slow compared with that of electrons, so the operation speed of solid-state ionic devices has been considered to be low. However, with the recent advancement of nanotechnology, it has become possible to construct solid-state ionic devices capable of controlling ion migration at the nanoscale and even the atomic scale, and operate at a relatively high speed. Recently, such nanoscale solid-state ionic devices (nanoionic devices) have attracted renewed attention in information and communication technologies as a means of overcoming the above serious defect.

In nanoionic devices, as a unique feature that cannot be obtained in semiconductor devices utilizing electron and hole transport phenomena, it is possible to move ions (atoms) forming material frames on the nanoscale and atomic scale. The

K. Terabe (✉) · T. Tsuruoka · T. Tsuchiya
International Center for Materials Nanoarchitectonics (WPI-MANA), National Institute for Materials Science (NIMS), 1–1 Namiki, Tsukuba 305-0044, Ibaraki, Japan
e-mail: TERABE.Kazuya@nims.go.jp

Y. Wakayama and K. Ariga (eds.), *System-Materials Nanoarchitectonics*,
NIMS Monographs, https://doi.org/10.1007/978-4-431-56912-1_7

control of local ion migration allows the reconstruction of any internal and surface nanostructures of materials, as well as heterointerface nanostructures. Namely, it is a nanoarchitecture of materials achieved by the control of ion migration (referred to as ionic nanoarchitectonics). So far, we have created nanoionic devices with diverse functions by using the ionic nanoarchitectonics [2]. Figure 1 shows an example of created nanoionic devices. Figure 1a shows a two-terminal device with functions such as atomic switch, quantized conductance, and an artificial synapse [3–6]. These functions are obtained by controlling the atomic point contact of a metal filament by utilizing the migration and redox reaction of metal ions in an ionic conductor. Figure 1b shows two-terminal devices with functions such as rectification and memory. These functions are obtained by modulating the Schottky-like barrier

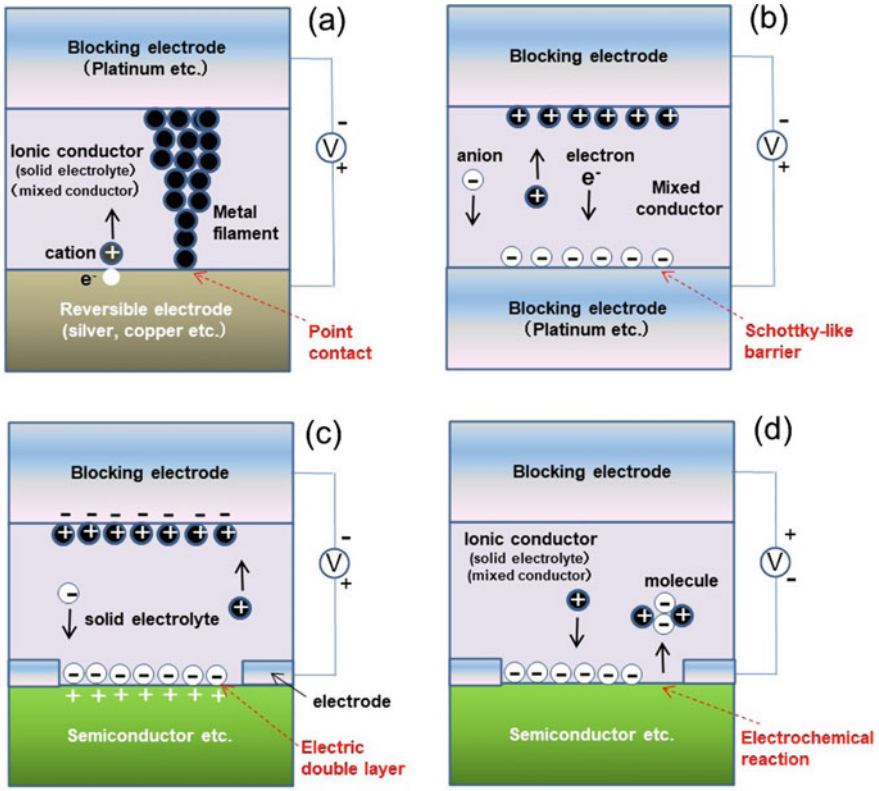

Fig. 1 Schematic diagram of functional devices creation by ionic nanoarchitectonics utilizing ion migration in solids. **a** Devices with functions such as atomic switch, an artificial synapse, and nonvolatile memory using a point contact. **b** Devices with functions such as rectification and volatile memory using Schottky-like barrier modulation. **c** Devices with functions such as resistance change and superconducting transition temperature change using an electric double layer. **d** Devices with functions such as resistance change, magnetic change, and decision-making using electrochemical reactions. Reproduced from [2] by The Author(s) licensed under CC BY NC 3.0, published by The Royal Society of Chemistry

generated by moving ions at the heterointerface between the blocking electrode and the mixed conductor of ions and electrons [7]. In Fig. 1c, an electric double layer is formed by moving ions in a solid electrolyte (pure ionic conductor) to an interface with an electrode such as a semiconductor. Through the high-density carrier doping caused by using the electric double layer, it is possible to control physical properties such as electrical, optical, and magnetic properties [8, 9]. Three-terminal devices with various novel functions were fabricated by utilizing these properties. In Fig. 1d, an electrochemical reaction is caused by ion migration in the vicinity of the interface between an ionic conductor and an electrode such as a semiconductor, whereby ions are injected into the electrode or are detached from the electrode. By utilizing the ion injection and detachment, it is possible to control the physical properties of electrode materials, and high performance three-terminal devices were created by using these properties [10–12].

In the following sections, as representative examples of nanoionic devices created by using the ionic architectonics method, an atomic switch utilizing the migration of silver ions in a solid polymer electrolyte (SPE) and a decision-making device utilizing the proton migration in an ion conductor polymer are demonstrated. The polymer-based atomic switch operates by controlling an atomic point contact by utilizing the growth and shrinkage of a metal filament, as shown in Fig. 1a. The decision-making device operates by utilizing the electric potential difference among several electrodes caused by the injection and detachment of different numbers of ions. The ion injection and desorption are controlled by utilizing ion migration and an electrochemical reaction as shown in Fig. 1d.

2 Atomic Switch Operation Based on Solid Polymer Electrolytes

In 2011, we found that an atomic switch can be realized using an SPE. Owing to its mechanical flexibility, higher ionic conductivity, compatibility with various substrates, and low fabrication cost, an SPE is considered as a possible substitute for inorganic solid electrolytes such as sulfides [3, 4] and metal oxides [13]. Ag-salt incorporated polyethylene oxide (Ag-PEO) was used as the ion conducting medium, and the fabricated Ag/Ag-PEO/Pt device exhibited bipolar resistive switching behavior under bias voltage sweeping [14]. We subsequently succeeded in fabricating the device on a plastic substrate using an inkjet-printing technique, and obtained stable switching behavior even when the substrate was bent [15].

Understanding the correlation between the resistance change and filament growth has been the subject of much recent attention owing to its effectiveness in controlling switching behavior and its promising memory performances. It is significant that the high ionic conductivity of an SPE enables us to directly observe filament formation even in micrometer-scaled devices. Here, we describe the kinetic factors determining the filament growth from the results of scanning electron microscopy

(SEM) on a planar structure. In addition to bi-stable resistive switching, one of the unique characteristics of the atomic switch is conductance quantization. A quantized conductance was reported for atomic switches using sulfides [3, 4, 16], superionic conductors [17], and metal oxides [18]. We found highly reproducible quantized conductance in a PEO-based atomic switch.

2.1 *Kinetic Factors Dominating the Filament Growth*

We performed in situ optical microscopy and ex situ SEM observations of the growth behavior of conducting filaments in planar SPE-based atomic switches, in which Ag (or Pt) and Pt electrodes are opposed with a gap ranging from 0.5 to 8 μm [19, 20]. The experimental setup is illustrated in Fig. 2a. A typical resistive switching characteristic is shown in Fig. 2b. Figure 2c, e show the typical current–voltage (*I–V*) curves at the first voltage scan, which corresponds to the forming process of conducting filaments, for Ag/PEO/Pt and Ag/Ag-PEO/Pt devices with a 1 μm gap, respectively. The forming process was terminated when the current reached the compliance level (100 nA), and then the morphology of the device was observed by SEM. In order to avoid damage to devices by a large current when the device is switched to a low-resistance state, the current compliance function of the measurement system is often used in *I-V* measurements. Usually, the compliance level ranging from μA to mA is

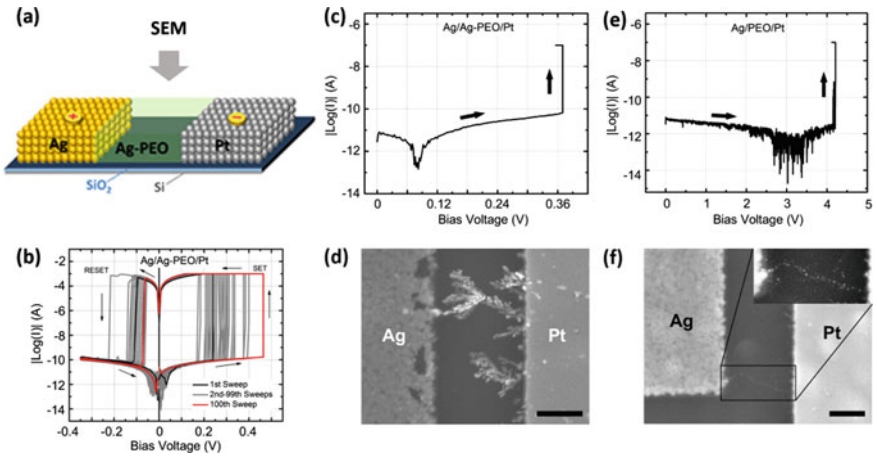

Fig. 2 **a** Schematic of filament growth observation in a planar atomic switch. **b** Typical resistive switching behavior of a Ag/Ag-PEO/Pt atomic switch. **c**, **e** and **d**, **f** *I–V* curves and SEM images taken after the forming process in Ag/Ag-PEO/Pt and Ag/PEO/Pt atomic switches, respectively. The inset of **f** shows a magnified view of the filament consisting of Ag clusters. The scale bar is 500 nm. Reproduced from [20] by The Author(s) licensed under CC BY NC 3.0, published by The Royal Society of Chemistry

applied. Here, the low compliance current was set to stop the initial stage of filament growths.

The SEM images taken after the forming process are shown in Fig. 2d, f. The Ag/Ag-PEO/Pt device exhibits dendritic filament morphologies starting from the Pt electrode. Voids created in the Ag electrode provide evidence of the oxidation of Ag under voltage bias. The dendritic growth can be observed for gaps larger than 2 μm. In the Ag/Ag-PEO/Pt device, both Ag^+ oxidized from the Ag electrode and pre-dissolved Ag^+ in the PEO matrix migrate toward the Pt electrode under voltage bias. Once precipitation takes place on Pt, precipitated Ag atoms grow by incorporating Ag^+ distributed in the PEO matrix, forming dendritic morphologies with three-branch structures. In contrast, the Ag/PEO/Pt device shows very narrow filaments, consisting of a number of small Ag clusters, as shown in the inset of Fig. 2f. For larger gaps, complete filaments did not form even up to an applied bias voltage of ~10 V. Pure PEO is a highly crystalline polymer, in which long-range Ag^+ transport is significantly hindered, resulting in lowered ionic conductivities. Hence, unidirectional filament growth is likely to occur with small Ag clusters rather than continuously connected structures. It was also found that the density of filament structures is proportional to the compliance current.

In general, the filament growth processes can be explained by the standard electrochemical metallization (ECM) model [21]. In devices with inorganic solid electrolytes, such as chalcogenides, the growth process occurs with a large number of metal ions moving through the electrolyte and they are reduced at the inert cathode, resulting in a filament growing toward the active anode [22]. However, in some oxides such as Al_2O_3, filament growth is limited by lower conductivity of metal ions, giving rise to the reduction of metal ions inside the electrolyte before they reach the inert cathode, resulting in filaments growing from the active anode [23]. In our observations, filament growth always initiated from the Pt electrode, even for devices with pure PEO, which has a lowered ionic conductivity. This means that the ECM model is applicable to the filament formation scheme in a PEO-based atomic switches. The filament formation behavior in a PEO-based atomic switch is determined by the properties of the polymer matrix, the device structure, and the experimental parameters.

2.2 Quantized Conductance of an Atomic Point Contact

We also found that a PEO-based atomic switch exhibits conductance quantization, where the atomic point contact is formed by the electrochemical oxidation and reduction of Ag atoms in the polymer matrix [24, 25]. Such atomic point contact gives a construction in the transverse direction which represents a resistance to the motion of electrons. Applying voltage V across the point contact induces a current flow, given by $I = GV$, where G is the conductance of the contact. This formula resembles Ohm's law for macroscopic resistors. However, in the small system size which requires a quantum mechanical analysis, the transverse motion cannot vary continuously, but

has to be one of a series of discrete modes. As a consequence, the total conductance is given by $G = nG_0$. Here G_0 corresponds to the conductance of a single atomic point contact given by $G_0 = 2e^2/h$, where e is the electron charge and h is the Planck's constant.

Figure 3a shows typical I–V and the corresponding conductance–voltage (G–V) curves of a Ag/PEO/Pt atomic switch, measured under bias sweeping. As the bias voltage was swept in the positive direction, the device conductance reached larger integer multiples of G_0 with increasing in a stepwise fashion. Figure 2b shows a conductance state histogram evaluated from a number of G–V curves with various stop voltages in the bias sweep. In addition to large peaks at integer multiples, distinct peaks appear at half-integer multiples of G_0, and fractional conductance variations are also observed.

First-principles density functional theory simulations were used to examine the role of the atomic configurations in determining the conductance state of an atomic point contact. We considered an atomic point contact composed of different numbers (10–12) of Ag atoms between Ag electrodes (consisting of a linked nine atom chain), as illustrated in Fig. 3c. The structures were optimized so as to minimize the total energy. Consequently, the 10-atom chain forms a single-atom contact and exhibits a conductance of almost $1G_0$ at the Fermi energy (E_F), while the 11- and 12-atom chains form two-atom contacts with conductance values lower and higher than $2G_0$

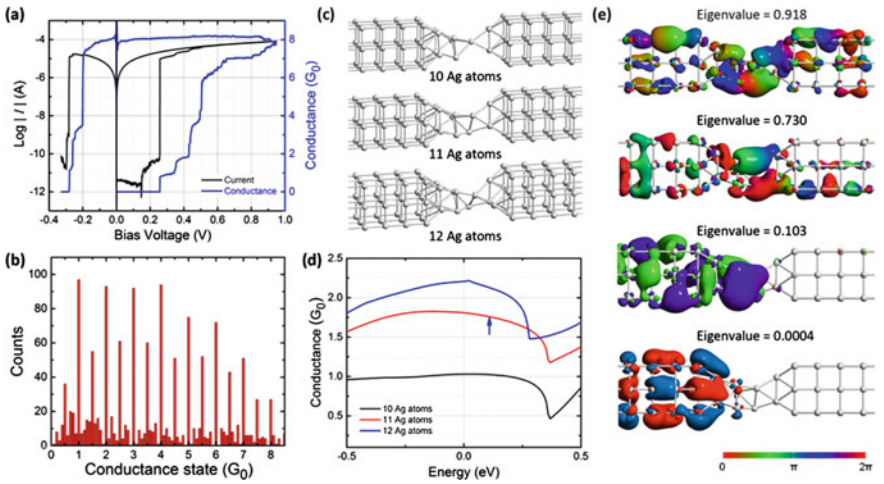

Fig. 3 **a** I–V and the corresponding G–V curves measured for a Ag/PEO/Pt atomic switch. **b** Conductance histogram in G_0 evaluated from G–V curves. **c** Geometrically optimized configurations of different numbers of Ag atoms between nine-Ag-atom electrodes. **d** Energy-dependent conductance plot for different Ag atom chains. **e** Transmission eigenstates of 11-atom chains forming a two-atom contact, calculated for the highest four eigenstates at 0.12 eV. The isovalue is 0.05, which corresponds to the magnitude of the wave function. The phase is used to color the isosurface. From [24] Copyright © 2017 by John Wiley Sons, Inc. Reprinted by permission of John Wiley & Sons, Inc

at E_F, respectively, as shown in Fig. 3d. From the transmission channel analysis, it was revealed that eight conducting channels are possible at 0.12 eV above E_F for the 10-atom chain. However, only the first three channels, with eigenvalues higher than 0.1, contribute to the total conductance, as shown in Fig. 3e. This indicates that the conductance of an atomic point contact is dominated by the atomic configuration and its slight rearrangement can generate half-integer multiples and fractional variations of the conductance state.

In neuroscience, synaptic plasticity is known as the ability of biological synapses to strengthen and weaken over time, in response to increases or decreases in their activity. Since memories are postulated to be represented by vastly interconnected neural circuits in the brain, the synaptic plasticity is one of the important neurochemical foundations of learning and memory. It was found that SPE-based atomic switches also exhibit this plasticity in memory behaviors in response to input voltage pulses, which are characterized by short-term memory and long-term memory [6]. This suggests that the functions of the brain can be mimicked by constructing self-assembled Nano systems consisting of SPE-based atomic switches. The synaptic behavior, as well as the conductance quantization of SPE-based atomic switches, is realized by the reversible control of an atomic point contact based on ionic nanoarchitectonics. The redox reactions, ion transport, and filament formation at the nanoscale can precisely be tuned via the applied bias voltage. Our findings are expected to contribute to the development of new multilevel memories, quantum information processing, and neuromorphic systems.

3 Decision-Maker Based on Proton Conducting Polymers

There is an urgent need for artificial intelligence (AI) systems capable of quickly making optimum selections in response to environmental changes, in fields such as information and communications technology (ICT), medical diagnosis, manufacturing, and economic activities. Efforts in recent years have focused on the development of AI systems based on conventional computations using a central processing unit (CPU), memory, and algorithms (software programs). While the usefulness of CPU-based computing in mimicking intelligent human behavior has been verified, one critical weak point is inherent in this method: i.e. the amount of computational resources required for processing the vast streams of information required increases exponentially. Such conventional methodology for computations is hence reaching its limit, and breakthrough computational methodologies have been intensively explored [26–36].

The ionic decision-maker, a state-of-the-art derivative of the atomic switch [3, 4], overcomes the limitations of CPU-based computing through its decision-making functions, which are realized by the use of ionic nanoarchitectonics in solid electrochemical systems [37]. Specifically, it utilizes nanoionic phenomena in the vicinity of a solid/solid interface, which phenomena includes electric double layer charging and electrochemical reactions [8–12]. The ionic decision-maker, based on proton

conducting polymers, uses the inherent nonlinearity observed in the voltage-charge relationships in nanoionic devices, which in turn is caused by modulation of the local proton and gas (*e.g.* hydrogen, oxygen) concentration, in order to achieve excellent decision-making abilities related to mathematic problems with stochastic events and is adaptable to changes in the computational environmental.

3.1 Operating Principle of the Ionic Decision-Maker for Solving Dynamic Multiarmed Bandit Problems

Various problems are solved, by both human beings and computers, through decision-making related to subsequent actions. In many cases, the problems can be interpreted as multiarmed bandit problems (MBPs) with stochastic events [38–40]. The MBP is a mathematical problem in which a gambler facing many slot machines with various reward probabilities has to determine, on the basis of his experience (trials), which machines to play so as to maximize the total reward [41, 42]. Figure 4a illustrates a typical MBP situation. MBPs are long-standing mathematical problems that relate to adaptive human behavior in various situations (*e.g.* medical diagnosis, ICT, manufacturing, economic activities) [38–42].

In this work, the MBP is discussed in a scenario where the user of a busy communications network needs to choose the most appropriate channels from among the available channels in order to maximize the efficient transmission of information packets. The situation can be handled in the framework of the channel model proposed by Lai et al. [43, 44]. Figure 4b illustrates the channel model for one user and two channels, where the user can choose only a single channel at any given time. Suppose that at a certain time (t), the user chooses either channel A or B, which are open with probabilities P_A and P_B and occupied with probabilities 1- P_A and 1- P_B, respectively. In advance of the trials, the user has zero knowledge of the value of P_A and P_B. When channel A is open with P_A, one packet is transmitted; this situation is hereinafter referred to as "transmitted". With a probability of 1-P_A, the packet will

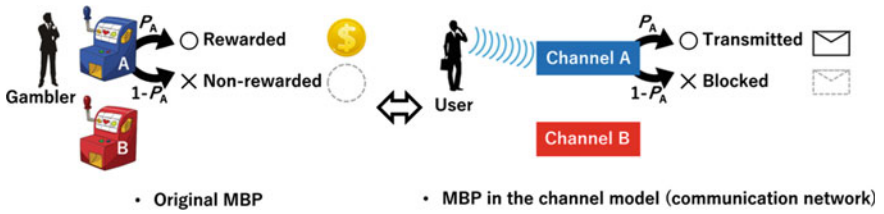

Fig. 4 **a** The original MBP (slot machines and a gambler). **b** MBP in the channel model (communication network and a user). Reprinted from [37]. © The Authors, some rights reserved; exclusive licensee American Association for the Advancement of Science. Distributed under a Creative Commons Attribution NonCommercial License 4.0 (CC BY-NC) http://creativecommons.org/licenses/by-nc/4.0/

not be transmitted, which situation is hereinafter referred to as "blocked". A series of trials gives three types of possible result for each trial; (i) a channel was selected and the packet was transmitted, (ii) a channel was selected and the packet was blocked, or (iii) no channel was selected. The results are used to calculate the correct selection rate, which is the main concern of this study and which will be discussed in Sect. 3.2. The model is suitable for a discussion of dynamic MBPs (DMBPs), in which the reward probabilities are dynamic.

Our ionic decision-maker can efficiently solve DMBPs, with excellent solvability and adaptability, which are useful for handling the temporal dynamics of practical problems. Figure 5a illustrates the operating principle of the device for a case where (P_A, P_B) is (0.6, 0.4). Figure 5b shows the dynamic variation in the voltage V measured during operation of the device.

First, in the open circuit condition, the sign V is judged (indicated by small black arrows). When V is positive (negative), channel A (B) with P_A (P_B) is used to send the packets. In accordance with the results [transmitted or blocked, as illustrated in Fig. 4b], a pulse current of 500 nA, or -500 nA, is applied to electrode A for 500 ms. The circuit is then opened, and V is measured (indicated by large green arrows). The sequence of these steps (from one black arrow to the next black arrow) is defined as one channel selection. As shown in Fig. 5b, repeated selections resulted in a digital-like V variation, which leads to a correct decision on the basis of tug-of-war (TOW) dynamics, which resembles the TOW game in which two persons, A and B, pull against each other at opposite ends of a rigid rope [45–48].

This behavior corresponds to a variation in the concentration distribution of chemical species in the electrolyte, which is caused by EDL formation and/or redox reactions related to protons (e.g. reduction of protons to hydrogen gas, oxidation of water). Because it is an electrochemical cell in which electrical charges are consumed by the

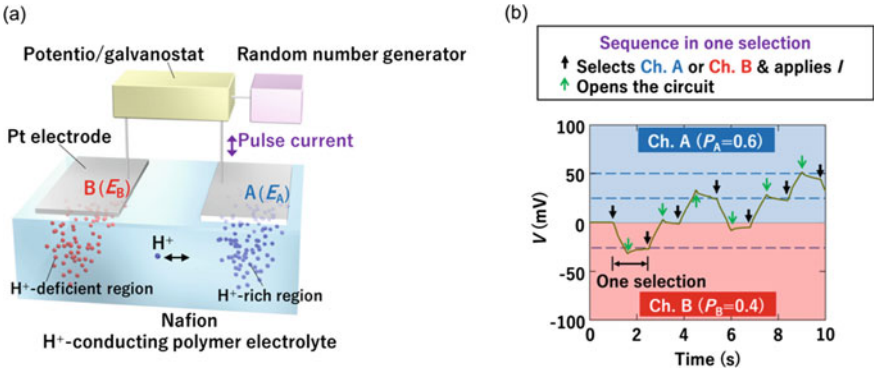

Fig. 5 **a** Illustration of the ionic decision-maker for solving MBPs with two channels. **b** Variation in V during operation of the device. Reprinted from [37]. © The Authors, some rights reserved; exclusive licensee American Association for the Advancement of Science. Distributed under a Creative Commons Attribution NonCommercial License 4.0 (CC BY-NC) http://creativecommons.org/licenses/by-nc/4.0/

redox reactions, the Q–V relationship deviates significantly from the ideal (linear) seen in capacitors (indicated by the dashed lines in Fig. 5b). Such a deviation from an ideal linear relationship, in which charges are completely preserved after current application, is of great importance for the adaptive operation of our device.

3.2 *Learning Properties of the Ionic Decision-Maker in Relation to Environmental Changes*

To investigate the ability of our ionic decision-maker device to solve dynamic MBPs, the variation in the correct selection rate (CSR) was investigated. Correct selection means that the channel with the highest probability (P_i) was selected, regardless of whether a packet was transmitted or not. CSR can be calculated using V variation with time (e.g., Fig. 5b). Please refer to the reference [37] for details of the CSR calculations.

Figure 6 shows the variation in CSR of our ionic decision-maker device. The experiment started from the initial condition $(P_A, P_B) = (0.9, 0.1)$. During the experiment, P_i inversions were applied [e.g., (0.9, 0.1) was inverted to (0.1, 0.9)]. At the beginning of the experiment (i.e., the number of selections was zero), CSR was about 0.5. This was reasonable because the device had no information about channels A and B; the ionic decision-maker randomly selected channels. However, as the number of selections increase, CSR showed a gradual increase toward 1.0, which is indicative of empirical learning on the basis of the results of selections. The learning process corresponds to an electrical response of the cell, in which repetition of selections made V take a positive or negative value. The V variation is caused by modulation

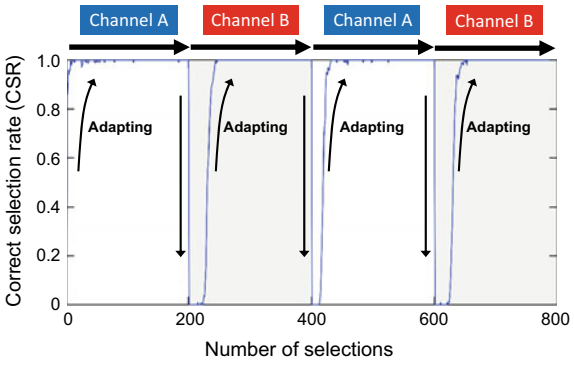

Fig. 6 Variations in CSR of the ionic decision-maker for solving DMBP under the initial condition $(P_A, P_B) = (0.9, 0.1)$. Reprinted from [37]. © The Authors, some rights reserved; exclusive licensee American Association for the Advancement of Science. Distributed under a Creative Commons Attribution NonCommercial License 4.0 (CC BY-NC) http://creativecommons.org/licenses/by-nc/4.0/

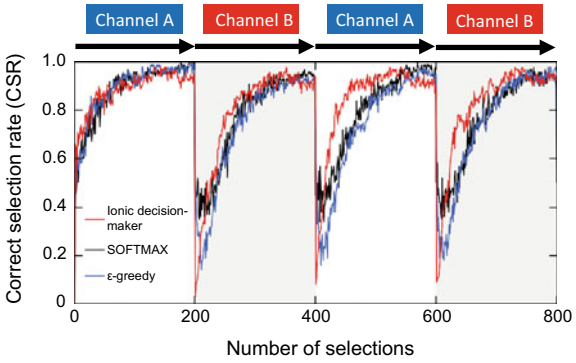

Fig. 7 Comparison of the performance between the ionic decision-maker, SOFTMAX and ε-greedy algorithms for solving DMBP under the initial condition $(P_A, P_B) = (0.6, 0.4)$. Reprinted from [37].

in the concentration distribution of proton, gas and water molecule near electrodes A and B.

P_i inversion was applied at every 200th selection to assess the adaptability of the device to a dynamic environment, which adaptability is essential for practical use. After each P_i inversion, immediate drop of CSR was observed because the correct channel had changed from A to B or vice versa. The steep increase of CSR toward 1.0 after P_i inversions indicates that our device possesses good adaptability.

To evaluate the efficiency of our ionic decision-maker, performance of the device was compared with conventional CPU-based computations using ε-greedy and SOFTMAX algorithms, which are typical algorithms for solving MBPs. Figure 7 shows a comparison of the performance among the three for solving DMBP under the initial condition $(P_A, P_B) = (0.6, 0.4)$. The ionic decision-maker and the other two computations all showed good adaptability, although CSR did not reach 1.0 within the 200th selections because the DMBP under the present condition is much more difficult to solve due to the very close P_i. It is quite surprising that the ionic decision-maker, operating on the basis of simple repetitions of pulse current application, exhibited performance that was so closely equivalent to conventional computations, which were achieved by complex processing using CPU and memory. Whereas a typical personal computer consumes 15 mW while solving a DMBP, the ionic decision-maker consumes only 7.5 μ W in the cell. Such excellent efficiency is realized by utilizing the inherent electrochemical properties of nanoionic systems for processing and storing information, both of which functions are handled by CPUs and memory in conventional computers.

The ionic decision-maker introduced here was created on the basis of the ionic nanoarchitectonics in solid state devices. It achieved outstanding solvability and adaptability with a combination of TOW dynamics and the ionic motion found in the nanospaces in the vicinity of solid/solid interfaces. The ionic decision-maker is

opening new avenues in the "nanoelectronics achieved by ions" paradigm, invented at MANA as the atomic switch, for "materials decision-making" in which the inherent properties of materials are used to realize low power consumption AI technologies.

4 Summary

In the future advanced information society, it will be increasingly important to collect and analyze huge amounts of data as rapidly as possible, and act on the basis of appropriate judgments. AI development has been actively conducted worldwide as a technology that enables to realize social demands. Currently, the core of this technology is software, and hardware is simply responsible for storing and computing data. However, in order to efficiently process and judge ever-increasing amounts of data, it is also important to develop AI technologies with new concepts. As one of them, the development of a brain-type computer is expected. Nanoionic devices based on ionic nanoarchitectures such as polymer-type atomic switches and decision-making devices will further develop as essential elements for brain-type computers and AI systems.

References

1. Kudo K, Fueki K (1990) Solid state ionics. VCH
2. Terabe K, Tsuchiya T, Yang R (2016) Nanoionics devices enabling a multitude of new features. Nanoscale 8:13873–13879
3. Terabe K, Hasegawa T, Nakayama T, Aono M (2001) Quantum point contact switch realized by solid electrochemical reaction. RIKEN Rev 37:7
4. Terabe K, Hasegawa T, Nakayama T, Aono M (2005) Quantized conductance atomic switch. Nature 433:47
5. Terabe K, Hasegawa T, Liang C, Aono M (2007) Control of local ion transport to create unique functional nanodevices based on ionic conductors. Sci Technol Adv Mater 8:536–542
6. Ohno T, Hasegawa T, Tsuruoka T, Terabe K, Gimzewski JK, Aono M (2011) Short-term plasticity and long-term potentiation in single Ag_2S inorganic synapse. Nat Mater 10:591
7. Yang R, Terabe K, Liu G, Tsuruoka T, Hasegawa T, Gimzewski JK, Aono M (2012) On-demand nanodevice with electrical and neuromorphic multifunction realized by local ion migration. ACS Nano 6:9515–9521
8. Tsuchiya T, Terabe K, Aono M (2013) All-solid-state electric-double-layer transistor based on oxide ion migration in Gd-doped CeO_2 on $SrTiO_3$ single crystal. Appl Phys Lett 103:073110
9. Tsuchiya T, Moriyama S, Terrabe K, Aono M (2015) Modulation of superconducting critical temperature in niobium film by using all-solid electric-double-layer transistor. Appl Phys Lett 107:013104
10. Tsuchiya T, Terabe K, Ochi M, Higuchi T, Osada M, Yamashita Y, Ueda S, Aono M (2016) In situ tuning of magnetization and magnetoresistance in Fe_3O_4 thin film achieved with all-solid-state redox device. ACS Nano 10:1655–1661
11. Tsuchiya T, Tsuruoka T, Terabe K, Aono M (2015) In situ and nonvolatile photoluminescence tuning and nanodomain writing demonstrated by all-solid-state devices based on graphene oxide. ACS Nano 9:2102–2110

12. Tsuchiya T, Terabe K, Aono M (2014) In situ and non-volatile bandgap tuning of multilayer graphene oxide in an all-solid-state electric double-layer transistor. Adv Mater 26:1087–1091
13. Tsuruoka T, Terabe K, Hasegawa T, Aono M (2010) Forming and resistive mechanisms of a cation-migration-based oxide resistive memory. Nanotechnology 21:425205
14. Wu S, Tsuruoka T, Terabe K, Hasegawa T, Hill JP, Ariga K, Aono M (2011) A polymer-electrolyte-based atomic switch. Adv Funct Mater 21:93
15. Mohapatra SR, Tsuruoka T, Hasegawa T, Terabe K, Aono M (2012) Flexible resistive switching memory using inkjet printing of a solid polymer electrolyte. AIP Adv 2:022144
16. Nayak A, Ohno T, Tsuruoka T, Terabe K, Hasegawa T, Gimzewski JK, Aono M (2012) Controlling the synaptic plasticity of a Cu_2S atomic switch. Adv Funct Mater 22:3606
17. Tappertzhofen S, Valov I, Waser R (2012) Quantum conductance and switching kinetics of AgI-based microcrossbar cells. Nanotechnology 23:145703
18. Tsuruoka T, Hasegawa T, Terabe K, Aono M (2012) Condutance quantization and synaptic behavior of a Ta_2O_5-based atomic switch. Nanotechnology 23:435705
19. Krishnan K, Tsuruoka T, Mannequin C, Aono M (2016) Mechanism for conducting filament growth in self-assembled polymer thin films for redox-based atomic switches. Adv Mater 28:640
20. Krishnan K, Aono M, Tsuruoka T (2016) Kinetic factors determining conductive filament formation in solid polymer electrolyte based planar devices. Nanoscale 8:13976
21. Valov I, Waser R, Jameson JR, Kozicki MN (2011) Electrochemical metallization memories—fundamentals, application, prospects. Nanotechnology 22:1844
22. Waser R, Aono M (2007) Nanoionics-based resistive switching memories. Nat Mater 6:833
23. Yang Y, Gao P, Gaba S, Chang T, Pan X, Lu W (2012) Observation of conducting filament growth in nanoscale resistive memories. Nat Commun 3:732
24. Krishnan K, Muguganathan M, Tsuruoka T, Mizuta H, Aono M (2017) Highly reproducible and regulated conductance quantization in a polymer-based atomic switch. Adv Funct Mater 27:1605104
25. Krishnan K, Muguganathan M, Tsuruoka T, Mizuta H, Aono M (2017) Quantized conductance operation near a single-atom point contact in a polymer-based atomic switch. Jpn J Appl Phys 56:06GF02
26. Kim S-J, Naruse M, Aono M (2016) Harnessing the computational power of fluids for optimization of collective decision making. Philosophies 1:245–260
27. Rozenberg G, Back T, Kok J (2012) Handbook of natural computing. Springer
28. Adleman LM (1994) Molecular computation of solutions to combinatorial problems. Science 266:1021–1024
29. Lipton RJ (1995) DNA solution of hard computational problems. Science 268:542–545
30. Ursin R, Tiefenbacher F, Schmitt-Manderbach T, Weier H, Scheidl T, Lindenthal M, Blauensteiner B, Jennewein T, Perdigues J, Trojek P, Ömer B, Fürst M, Meyenburg M, Rarity J, Sodnik Z, Barbieri C, Weinfurter H, Zeilinger A (2007) Entanglement-based quantum communication over 144 km. Nat Phys 3:481–486
31. Nakagaki T, Yamada H, Tóth A (2000) Maze-solving by an amoeboid organism. Nature 407:470
32. Tero A, Takagi S, Saigusa T, Ito K, Bebber DP, Fricker MD, Yumiki K, Kobayashi R, Nakagaki T (2010) Rules for biologically-inspired adaptive network design. Science 327:439–442
33. Kim S-J, Aono M (2014) Amoeba-inspired algorithm for cognitive medium access. NOLTA 5:198–209
34. Kim S-J, Naruse M, Aono M, Ohtsu M, Hara M (2013) Decision maker based on nanoscale photo-excitation transfer. Sci Rep 3:2370
35. Naruse M, Nomura W, Aono M, Ohtsu M, Sonnefraud Y, Drezet A, Huant S, Kim S-J (2014) Decision making based on optical excitation transfer via near-field interactions between quantum dots. J Appl Phys 116:154303
36. Naruse M, Berthel M, Drezet A, Huant S, Aono M, Hori H, Kim S-J (2015) Single-photon decision maker. Sci Rep 5:13253
37. Tsuchiya T, Tsuruoka T, Kim S-J, Terabe K, Aono M (2018) Ionic decision-maker created as novel, solid-state devices. Sci Adv 4:eaau2057

38. Fudenberg D, Levine DK (1998) The theory of learning in games. The MIT Press, Cambridge, MA, USA
39. Marden JR, Young HP, Arslan G, Shamma J (2009) Payoff based dynamics for multiplayer weakly acyclic games. SIAM J Control Optim 48:373–396
40. Garivier A, Capp´e O (2011) The KL-UCB algorithm for bounded stochastic bandits and beyond. In: Conference on Learning Theory, COLT
41. Robbins H (1952) Some aspect of the sequential design of experiments. Bull Am Maths Soc 55:527–535
42. Weber R (1992) On the Gittins index for multiarmed bandits. A Appl Probability 2:1024–1033
43. Lai L, Jiang H, Poor HV (2008) Medium access in cognitive radio networks: a competitive multi-armed bandit framework. In: Proceedings of the IEEE 42nd Asilomar Conference on Signals, System and Computers Pacific Grove, CA, USA, 26–29 October 2008, pp 98–102
44. Lai L, Gamal HE, Jiang H, Poor HV (2011) Cognitive medium access: exploration, exploitation, and competition. IEEE Trans Mob Comput 10:239–253
45. Kim S-J, Aono M, Hara M (2010) Tug-of-war model for multi-armed bandit problem. In: Calude CS, Hagiya M, Morita K, Rozenberg G, Timmis J (ed) Unconventional computation; LNCS 6079. Springer, Berlin/Heidelberg, Germany, pp 69–80
46. Kim S-J, Aono M, Hara M (2010) Tug-of-war model for two-bandit problem: nonlocally correlated parallel exploration via resource conservation. BioSystems 101:29–36
47. Kim S-J, Aono M, Nameda E (2015) Efficient decision-making by volume-conserving physical object. New J Phys 17:083023
48. Kim S-J, Tsuruoka T, Hasegawa T, Aono M, Terabe K, Aono M (2016) Decision maker based on atomic switches. AIMS Mater Sci 3:245–259

Oxoporphyrinogens: Novel Dyes Based on the Fusion of Calix[4]pyrrole, Quinonoids and Porphyrins

Jonathan P. Hill and Jan Labuta

1 The Birth of the 'OxP' Chromophore

Porphine [1] is universally recognized as one of the most important known chromophore compounds [2]. It exists as the colored moieties of hemoglobin (where its function as its iron(II) complex is to bind oxygen destined for use in respiration) and chlorophyll (where it is largely responsible for the collection and sequestration of light energy for photosynthesis). Cytochromes are another type of chromophore containing porphines [3], whose function (among others) is to mediate electron transfer in the terminal electron transport chain. Hence, it can be seen that the functionality of porphine (esp. its metal complexes) is critical even for our existence. Therefore, these molecules have been intensively investigated in related applications, and a large community of scientists have dedicated their careers to studying the synthetic chemistry and properties of these compounds [4]. This account commences with a porphine molecule bearing very specific substituents whose synthesis is shown in Fig. 1. The condensation of 3,5-di-*t*-butyl-4-hydroxybenzaldehyde with pyrrole in refluxing propionic acid yields tetrakis(3,5-di-*t*-butyl-4-hydroxyphenyl)porphyrin (**TD*t*BHPP**), which can be converted to tetrakis(3,5-di-*t*-butyl-4-oxocyclohexadien-2,5-yl)porphyrinogen by oxidation under basic conditions [5]. Tetrakis(3,5-di-*t*-butyl-4-oxocyclohexadien-2,5-yl)porphyrinogen is a rather cumbersome term to be generally applied so we have applied the abbreviation '**OxP**'. **OxP** denotes the fact that the basic structure of these molecules is an oxoporphyrinogen. Porphyrinogens are tetrapyrrole compounds obtained by condensing pyrrole with aldehydes under acidic conditions. These compounds generally contain saturated carbon atoms at their meso-positions (positions between or connecting the pyrrole groups), although the pyrrole units may also be joined by ketone groups. Compounds of the latter

J. P. Hill (✉) · J. Labuta
International Center for Materials Nanoarchitectonics (WPI-MANA), National Institute for Materials Science (NIMS), 1-1 Namiki, Tsukuba 305-0044, Ibaraki, Japan
e-mail: Jonathan.HILL@nims.go.jp

Y. Wakayama and K. Ariga (eds.), *System-Materials Nanoarchitectonics*,
NIMS Monographs, https://doi.org/10.1007/978-4-431-56912-1_8

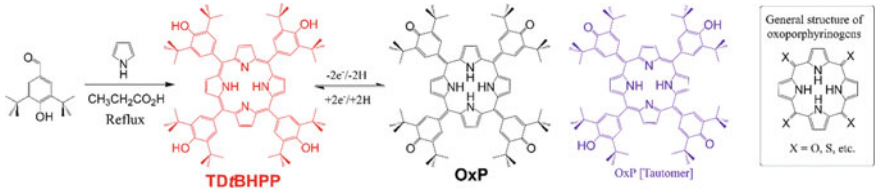

Fig. 1 Synthesis and chemical structures of **TD*t*BHPP** and **OxP** [5]. OxP can also exist in a minor tautomeric form (purple). General structure of oxoporphyrinogens is shown at right. Note that alkyl groups other than *t*-butyl are not useful in studies of the compounds due to the requirement of antioxidant activity of the phenyl substituents in the transformation from **TD*t*BHPP** to **OxP**

type belong to the family of oxoporphyrinogens (see right side of Fig. 1). More generally, 'oxo' denotes unsaturation at meso-positions while 'porphyrinogen' is a less commonly used term for calix[4]pyrrole. In the context of this chapter, the abbreviation '**OxP**' denotes only the oxoporphyrinogen tetrakis(3,5-di-*t*-butyl-4-oxocyclohexadien-2,5-yl)porphyrinogen.

As shown in Fig. 1, the **TD*t*BHPP** molecule also contains 2,6-butylated phenol (analogous with butylated hydroxy toluene, BHT) groups that are better known for their antioxidant activity [6] (i.e., as a food additive or other preservative). The breakthrough finding in this case was that **TD*t*BHPP** can be elaborated by the introduction of further functional groups at its central nitrogen atoms [7]. This is as a result of 2-electron oxidation to its **OxP** form, which has a nonplanar saddle-like structure also illustrated in Fig. 2. This point for synthetic modification has led to the preparation of a wide range of molecules with functions based on their photochemistry and sensing properties. **TD*t*BHPP** (Fig. 2a) is substituted with 2,6-butylated phenol groups that confer antioxidant activity, i.e., oxidizability, on the molecule. This ultimately manifests as a 2-electron oxidation of the molecule, which is promoted by deprotonation of its phenol groups. The deprotonation of those groups of **TD*t*BHPP** results in a shift of electron density onto its porphyrin macrocycle and leads to an increasing propensity for reaction with dioxygen. The mechanism of the oxidation has been the subject of previous investigations [8] and will not be discussed here. Oxidation of **TD*t*BHPP** to **OxP** does, however, introduce several features within the scope of this chapter. First, the **TD*t*BHPP** to **OxP** transformation (see Fig. 2a, b) involves redistribution of the electronic network of the molecule over the entire conjugated part of the molecule including the *meso*-substituents, which are reconstituted as hemiquinonoid groups. This is significant since it shifts the main electronic absorption of the compound from UV (i.e., the narrow, intense Soret or B band of the porphyrin at 420 nm) to visible (i.e., a broad absorption centered around 500 nm, which covers most of the visible region and extends into the NIR region). Also, while the **TD*t*BHPP** porphyrin is formally aromatic, the electronic structure of **OxP** is such that it is non-aromatic. Second, the electronic conjugation with *meso*-substituents leads to puckering of the now non-aromatic tetrapyrrole core so that it adopts a saddle-shape with pyrrole groups pointing alternately above and below the plane of the macrocycle. Thus, the conformation of **OxP** is now essentially similar

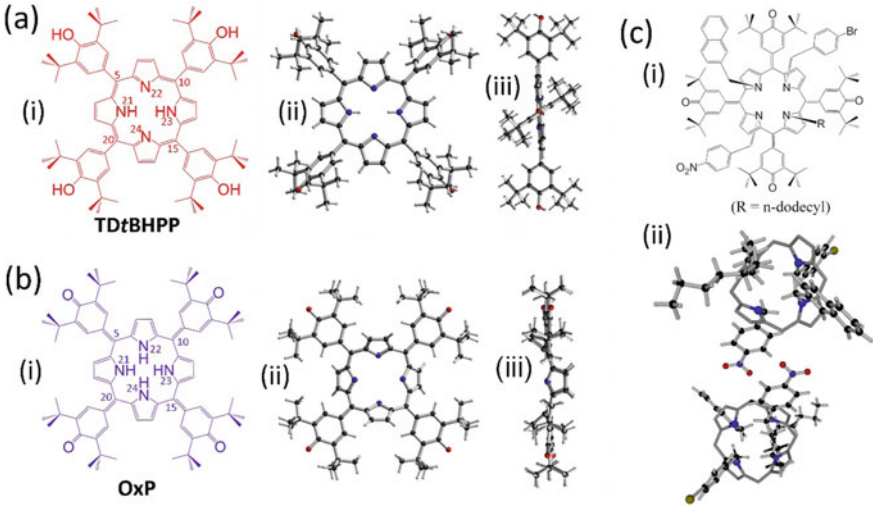

Fig. 2 Chemical formulae (i) and X-ray crystal structures (ii, iii) of **a TD*t*BHPP**, **b OxP**, and **c** asymmetrically substituted derivative of **OxP**. (ii) Top views and (iii) edge-on views (not shown for **c**). Panel **c**(ii) shows the unit cell of the compound in **c**(i) containing both enantiomers of the racemic mixture and with meso substituents removed for clarity. Panel **c** reprinted from [11], Copyright 2010, with permission from Elsevier

to calix[4]pyrrole [9], a well-known type of macrocycle which has been exploited extensively due to its guest binding interactions at pyrrole NH groups. This is the birth of '**OxP**' which can be seen as the preparation of a highly electronically conjugated (and so highly colored) version of the calix[4]pyrrole motif. **OxP** has several advantages over the calix[4]pyrrole class in that its high color presents excellent opportunities for its application as a chromogenic probe, pyrrole groups are available for regioselective modification, and the whole-molecule electronic conjugation rigidifies the system as a nanomolecular construct.

OxP derivatives may accommodate alkyl substituents at their central nitrogen atoms N_{21}-N_{24}. N-alkylation occurs without changing the conformation of the macrocycle and is regioselective. N_{21} and N_{23} are N-alkylated first, then N_{22}, N_{24}. For reasons of simplicity, only positions of N-alkylation are mentioned and, since the compounds are stable with respect to oxidation state once N-alkylated, presence of NH at a non-alkylated pyrrole group can be assumed. Also, **OxP**-type compounds have so far only been obtained where 3,5-di-*t*-butyl-4-hydroxyphenyl has been used as the substituents so that only *t*-butyl groups are present in the phenol/hemiquinone substituents.

It is a relatively simple matter to obtain crystal structures of **OxP**-type molecules [10] because of their good solubilities and well-defined forms. In addition, synthetic flexibility in this case lies in the possibility of introducing different groups to the **OxP** core, and even chiral derivatives have been prepared (Fig. 2c) where four different functional groups have been introduced [11]. The stepwise introduction

of substituents also allows tuning of the electrochemical and optical properties of the compounds [12].

The porphyrin precursor of **OxP**, namely **TD*t*BHPP**, is of some interest in its own right because of its oxidation state fluxionality [13] (a symptom of its phenolic substituents) and because, like other porphyrins, it can mediate the generation of reactive oxygen species in processes involving reactive radical species [14]. The latter subject is complex and will not be discussed here, but the existence of different oxidation states has permitted the observation of oxidation-state-dependent self-assembly structure variation on metal surfaces [15]. **TD*t*BHPP** is similar to other tetraphenylporphyrin compounds in that it contains a planar tetrapyrrole with phenyl substituents subtending an angle of 60° with the plane of the macrocycle [15]. In contrast, the 2-electron-oxidized, nonaromatic derivative **OxP** has alternating dihedral angles of ±48° between the planes of the pyrrole groups and the macrocyclic least-squares plane [16]. A surprising feature of the latter molecule is the approximate coplanarity of its *meso*-substituents with the macrocyclic least-squares plane and the conjugated π-electron system extends across the entire molecule.

Prior to the description of the properties of **OxP** derivatives, it is worth setting the scene in the current area of chromophore research with respect to these compounds. Organic chromophores (e.g., porphyrins, phthalocyanines, fullerenes, etc.) are important as light absorbing pigments. This is true in naturally occurring photosynthetic systems and also in manmade artificial systems to mimic nature for the harvesting of light energy for various purposes. Porphyrins, and by extension **OxP**, are critical in these systems since they provide a means to absorb significant quantities of incident sunlight energy. Incorporation of these chromophores into light harvesting arrays could allow the redirection of absorbed light for specific purposes rather than its aimless re-emission or loss as heat. Furthermore, highly colored compounds that can vary their hues in response to some environmental cue can be used for sensing applications. In relation to this, colorless calix[4]pyrroles have a long history of being used to demonstrate interactions that might be also used for sensing. Thus, **OxP**, being a highly colored calix[4]pyrrole, is an excellent candidate for such applications including the aforementioned light-harvesting type uses.

2 Nanometric OxP Derivatives

TD*t*BHPP behaves similarly to other analogously substituted porphyrins that have been reported previously to adopt a 'saddle' structure when deposited on metal substrates [17], presumably owing to improved van der Waals contacts between the molecules' *t*-butyl groups and the metal surface. This saddle form is remarkably similar to that found in **OxP** derivatives (mentioned above), suggesting that **OxP** derivatives might also form stable monolayers and be used to functionalize metal surfaces. This was realized when N_{21},N_{23}-disubstituted **OxP** derivatives (Fig. 3) were deposited on Au(111), where it was found that the **OxP** unit is always in contact with the surface regardless of the identity of N-substituents.

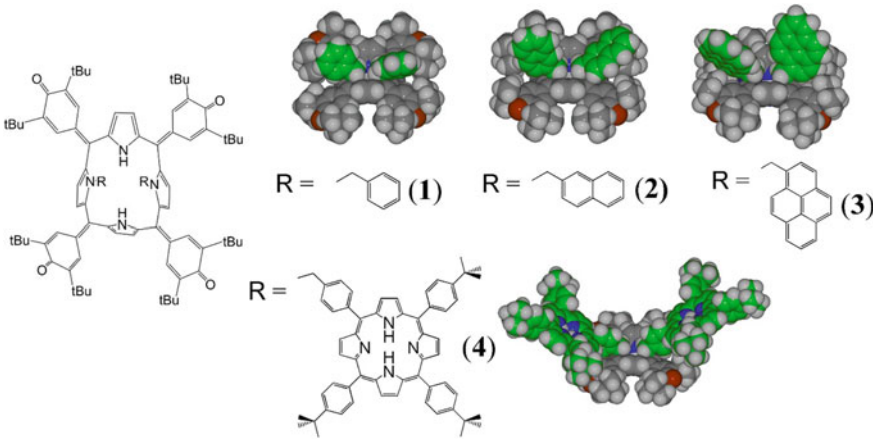

Fig. 3 Molecular structures of **1** – **4**; for **OxP**, R = H. **1**, **2**: X-ray crystallography or **3**, **4**: MM2 energy minimization. Carbon atoms of N-substituents are highlighted in green otherwise atoms are shown as C (grey), N (blue), O (red)

Even the addition of large porphyrinic N-substituents such as those contained in compound **4** yielded only monolayers with the **OxP** unit adsorbed at the surface and porphyrin substituents deflected away. This provides a method for the selective modification of metal (or other) surfaces by using **OxP** as an anchoring unit because of the preference of the unsubstituted face of the **OxP** moiety for the Au(111) surface [18]. As shown in Fig. 4a–c), molecules of compound **4** form monolayer structures with porphyrin substituents facing away from the substrate.

OxP can also be adapted for appending to surfaces by the introduction of sulfur atoms, which allows selective binding on gold substrates. This has facilitated the observation of through-molecule conductance properties of **OxP**. In particular, the core of **OxP** is essentially a calix[4]pyrrole macrocycle, which is known to possess substantial flexibility especially with respect to its interaction with anionic species [19]. In the **OxP** system, we had observed that different N-substituents and substitution patterns lead to varying dihedral angles for the pyrrole groups, suggesting that the flexibility of calix[4]pyrrole remains in **OxP**. Therefore, we were interested in determining whether (a) **OxP** actually remains flexible despite its conjugated structure and (b) what effect would the distortion of the molecule have on its through-molecule conductance properties. For this purpose, we prepared a derivative containing thiomethyl groups so that it could be applied in mechanically controlled break junction (MCBJ) experiments in which the properties of molecules contained in single-molecule junction device configurations can be investigated. These investigations revealed that the single-molecule conductance in the **OxP** molecular system can be modulated by the stretching of the molecules in situ in the MCBJ device, a feature permitted by the flexibility of the **OxP** macrocycle system illustrated using X-ray crystallographic and density functional theory (DFT) calculations shown in Fig. 5 [20]. Several crystal structures of N_{21},N_{23}-disubstituted **OxP** derivatives reveal

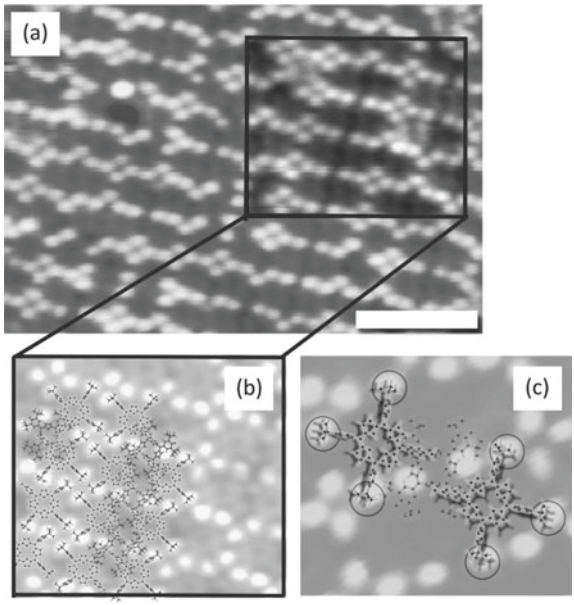

Fig. 4 On-surface STM images of N_{21},N_{23}-bis(porphyrinyl)-**OxP**, **4**. **a** Solution dropcast and annealed ($V_t = +2.5$ V; $I_s =$ 0.1 nA). **b** Model of the monolayer at the area indicated in **a**. **c** Bright spots are due to porphyrinyl 4-*t*-butylphenyl substituents. Surface-contacted **OxP** units (shown in the model in the background) are hidden by the porphyrin assembly. Scale bar: 5 nm

a variability in the angles of pyrrole groups composing the macrocycle (Fig. 5a). DFT calculations (Fig. 5b) subsequently revealed that the **OxP** macrocycle is stable even under severe distortions caused by applying stretching forces between the N-substituents being 'stretchable' by distances up to 1 nm.

The matters mentioned in this section illustrate some of the structural aspects relevant to **OxP**. However, **OxP** and its compounds possess substantial color, meaning that their chromophore properties should also be of interest. This is in addition to its electron deficiency relative to other molecules, which make it attractive as an electron acceptor with electron deficiency approaching that of fullerene C_{60} [10].

3 Controlling Charge Separation in OxP Oligochromophores

The strong visible absorption and electron deficiency of **OxP** make it a logical selection for incorporation into oligochromophoric systems, which have been extensively studied for their intramolecular electron and energy transfer processes analogous with the critical processes that occur in photosynthetic light-harvesting systems [23]. These processes are also of relevance to photochemical switching and molecular electronic systems and could be important in future molecule-level information processing. An important aspect of such systems are the relative redox potentials of the components. This factor governs how easy it will be for an electron (or hole) to move from one component to another and is affected by the stabilities of the different

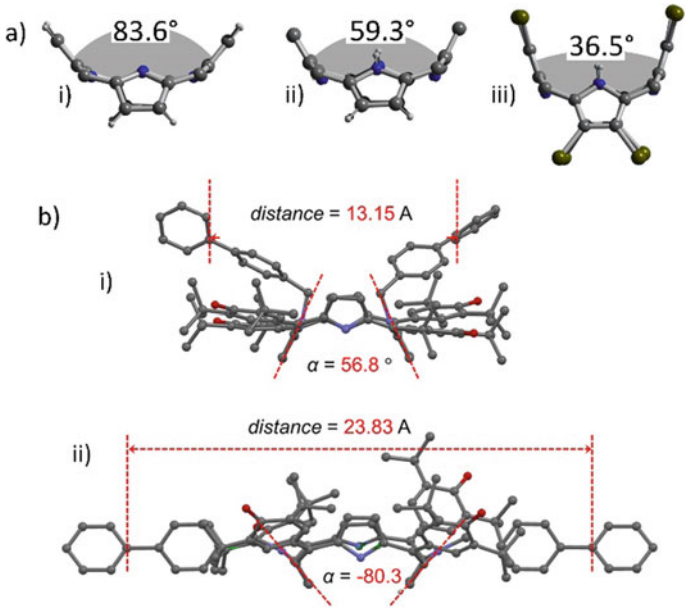

Fig. 5 **a** Calix[4]pyrrole macrocycle from the X-ray crystal structures of **OxP** derivatives: (i) **OxP** [16], (ii) N_{21},N_{23}-bis(4-bromobenzyl)-**OxP** [21], (iii) 2,3,7,8,12,13,16,17-octabromo-N_{21},N_{23}-bis(4-bromobenzyl)-**OxP** [22]. Angles are subtended between planes of opposing (N-alkylated) pyrrole groups. **b** Energy minimization for N_{21},N_{23}-disubstituted-**OxP** (i) while unconstrained and (ii) where N-substituents are constrained at fixed points. Reprinted from [20], Copyright 2018, with permission from John Wiley & Sons

oxidation states of molecules. For instance, removing 2-electrons from the porphyrin **TD*t*BHPP** makes the resulting **OxP** compound electron deficient relative to other porphyrins making it suitable as an electron acceptor in complement to an electron donor such as *meso*-tetraphenylporphyrinatozinc(II) (**ZnP**). An electron of **ZnP** in excited **ZnP*** would then be capable of transferring to **OxP** because of its electron deficiency and resulting lower reduction potential. Another electron acceptor, C_{60}, is even more electron deficient than **OxP** and electron transfer might occur from **OxP** to C_{60} by the same mechanism. By this means, sites of oxidation/reduction can be controlled but only if these molecules are predisposed to this behavior by their relative proximity and or geometry. Photo-induced electron and energy transfer is proposed as a means of light harvesting and is inspired by natural systems where the transport of energy (photons) and electrons are modulated in highly evolved aggregates and protein complexes where intermolecular energy and redox gradients have been established.

First [24], we investigated the effects of introducing porphyrin groups (**ZnP**) to the **OxP** molecule through substitution at the central N atoms. Initially, it was thought that this could be interesting from the viewpoint that intramolecular electron transfer processes, i.e., resulting in the transfer of an electron from **ZnP** to **OxP**,

lead to a state where the **ZnP** cation radical is linked to an **OxP** anion radical, which might also formally speaking be a porphyrin cation radical. However, the conjugation of the **OxP** meso-substituents with the macrocycle leads to a chromophore with considerably different properties that can no longer be considered a porphyrin. Regardless, the **OxP** chromophore has now been incorporated into a variety of multichromophore manifolds, even those containing C_{60} fullerene moieties as the terminal electron acceptor. A combination of covalent and supramolecular syntheses has been employed in this case, illustrating the utility of both methods. Examples of the compounds are shown in Fig. 6.

Compound **5** was the first porphyrin-quinonoid donor–acceptor triad containing tetraphenyl- porphyrinatozinc(II) moieties linked to an oxoporphyrinogen through its macrocyclic nitrogen atoms to be studied from the viewpoint of its photoinduced intramolecular energy and/or electron transfer properties. This arrangement of chromophores results in an interesting interplay between the electron-donating zinc porphyrin(s) and the electron/energy-accepting oxoporphyrinogen. Time-resolved fluorescence studies revealed that in *nonpolar* solvents, the excited-state energy transfer from zinc porphyrin to oxoporphyrinogen occurs. Data from nanosecond transient absorption studies and time-resolved fluorescence studies in *polar* solvents indicate photoinduced electron transfer from the singlet excited zinc porphyrin to the oxoporphyrinogen forming a radical ion-pair (RIP). We later built on this study by adding various aspects of supramolecular chemistry, i.e., by binding an additional electron acceptor (C_{60} derivatives: compounds **6** and **7**) or by investigating allosteric

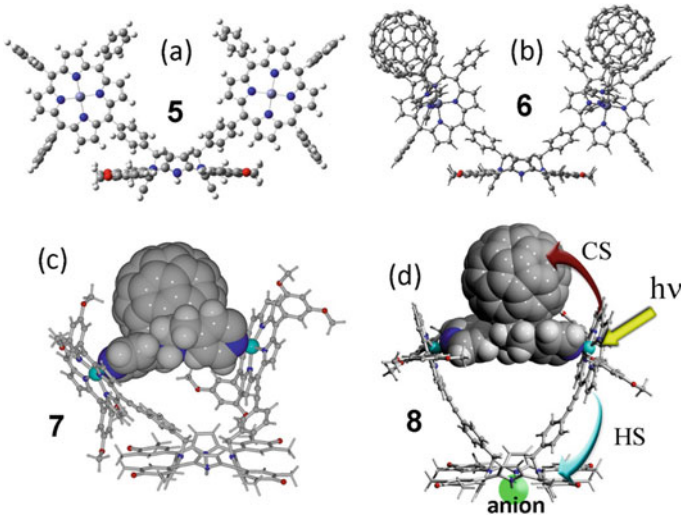

Fig. 6 Chemical structures of compounds and complexes used to study photoinduced processes in **OxP** conjugates: **5**: N_{21},N_{23}-bis(porphyrinyl-substituted)-**OxP** [24]; **6**: bis-C_{60}-fulleride complex of **5** [25]; **7**: bis(4-pyridyl)fulleride complex with N_{21},N_{23}-bis(porphyrinyl-substituted)-**OxP** [26]; **8**: anion-bound complex [26]. Panel (c) adapted with permission from D'Souza et al., J. Am. Chem. Soc. **131**, 16,138–16,146 (2009). Copyright (2009) American Chemical Society

effects involving the **OxP** (calix[4]pyrrole)-binding of anionic cofactors (compound **8**).

The 'covalent-coordinate' approach to the formation of oligochromophore systems involves the synthesis of molecules that can be organized according to coordinative binding of an incoming guest. In this case, we synthesized porphyrin-**OxP** conjugates containing zinc(II) porphyrin elements that can be used to bind nitrogen bases, such as imidazole, or pyridine derivatives. For **6**, we applied an imidazole-C_{60} fullerene derivative C_{60}Im, which can form a complex with porphyrin groups so that C_{60} is maintained in suitable proximity for intramolecular processes to occur. In **6**, it was found that the lifetimes of RIPs, determined using nanosecond transient absorption spectroscopy, are on the scale of hundreds of nanoseconds, strongly indicating charge stabilization in these more complex supramolecular complexes. We similarly studied compound **7**, where a bis-(4-pyridyl)-substituted fullerene was applied. In that case, the modulation of charge transfer occurred upon the introduction of the fullerene guests since electron transfer processes from the porphyrin **ZnP** to the **OxP** moiety switched in the presence of the guest ending with electron transfer processes involving **ZnP** and C_{60}. The identities of species found in **6** and **7** systems are shown in Fig. 7.

In an interesting further adaptation of these systems, the effect of fluoride binding as a cofactor was assessed in compound **8**. Thus, **8** is a supramolecular system containing exclusive binding sites for an incoming electron acceptor as well as an anionic cofactor species. As a result, the anion-binding-induced stabilization of a

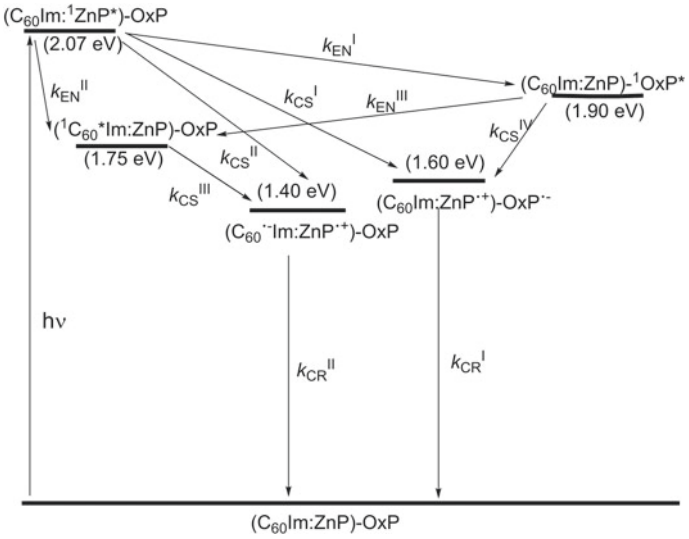

Fig. 7 Energy level diagram showing the different photochemical events of (C_{60}Im:ZnP)-**OxP** (**5**) in 1,2-dichlorobenzene. EN, CS and CR respectively denote energy transfer, charge separation and charge recombination processes. Reprinted from [25], Copyright 2007, with permission from John Wiley & Sons

charge-separated (CS) state was successfully demonstrated. The intramolecular and intermolecular photochemical processes of the **8** system were investigated by using femtosecond and nanosecond laser flash photolysis. Femtosecond laser flash photolysis was used to generate transient absorption spectra of the supramolecular complex, which revealed that there is efficient electron transfer from the porphyrin group to the fullerene with a subsequent more rapid back electron transfer returning to the ground state. The interaction of different anionic species at pyrrole NH groups of the **OxP** unit of the complex improved the rate of photoinduced electron transfer, probably owing to the structural change that favors this process. Anion binding improves the stability of the photoinduced CS state involving the anion-bound **OxP** and fullerene groups. The CS state is produced by electron transfer from the triplet excited state of porphyrins to free fullerene molecules, as indicated by nanosecond laser flash photolysis. For fluoride anion binding, the CS state is subject to anion-complexation-induced stabilization giving a 90-fold increase in the duration of the CS lifetime from 163 ns to 14 μs. The processes and various species involved in this system are shown in Fig. 8 alongside a model of the structure of the complex.

The presence of different anions (e.g., acetate, dihydrogenphosphate) also yields the stabilization of the CS state, although weakly bound perchlorate anions lead to no significant improvement. The complexation of anions to **OxP** reduces its oxidation potential by approximately 600 mV, introducing an intermediate energy level for charge migration from the $\mathbf{ZnP}^{\bullet+}$ cation radical to the **OxP** calix[4]pyrrole:anion complex. The resulting increase in the reorganizational energy for the transfer of electrons combines with a decrease in the charge recombination (CR) driving force due to anion binding, resulting in the observed increase in the lifetime of CS states in these complexes.

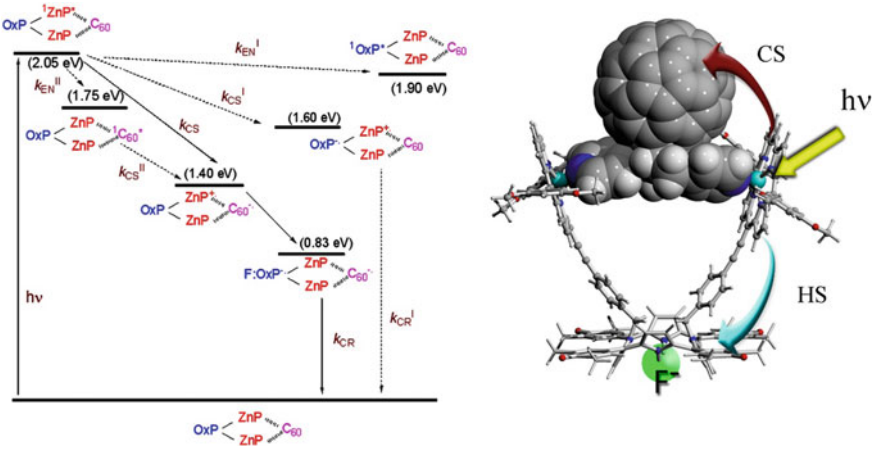

Fig. 8 Energy level diagram of species formed in the anion-bound supramolecular conjugate shown to the right. Anion binding promotes hole transfer from the porphyrin radical cation to the **OxP** macrocycle. EN, CS and CR respectively denote energy transfer, charge separation and charge recombination processes

To summarize this section, the **OxP** macrocycle provides an excellent chromophore for elaboration as a scaffold to create these complicated supramolecular manifolds that can act as models for the photosynthetic processes, which in turn give insight into how artificial light-harvesting systems might be constructed.

4 Diverse Molecular Sensing Using OxP Derivatives

The highly colored nature of **OxP** and its derivatives leads logically to their potential applications as optical sensors. Initially, we investigated the use of a simple **OxP** derivative for the detection of anionic species in organic solvents. For instance, anions such as fluoride and cyanide are important environmental pollutants whose detection and determination would be beneficial, and calixpyrroles are known to be excellent binders of anions. If we add to this the feature of strong optical absorption, then it is natural to assume that **OxP** derivatives that combine a calix[4]pyrrole binding unit might be excellent indicators for anions. This indeed proved to be the case [27], although a significant interfering factor is introduced by concurrent solvent binding through hydrogen bonding at the anion binding site, and selectivity was only found for fluoride anions, as is often the case for simple anion-interacting agents. While selective anion detection remains a subject of interest in our laboratories, our investigation of the sensing activity of **OxP** has now been extended to include other analytes. Perhaps, the simplest possible analyte or contaminating agent for which there is a detection requirement is water.

4.1 Water Sensing

The analysis of H_2O contained in organic solvents is important from both fundamental and industrial perspectives [28]. This is especially true for polar aprotic solvents where water is miscible since these are often used for the preparation and distribution of water-flammable reagents (e.g., organolithiums, alkali metals, Grignard reagents). Water can be detected using the Karl–Fischer method [29] at the ~1 ppm level but it is less convenient owing to its use of toxic reagents (i.e., methanol, I_2 and SO_2) and its special instrumental requirements. Alternative methods of analysis might make use of dyes as a "water indicator", thus facilitating H_2O detection in organic media. We have discovered that **OxP** dyes interact with water molecules through both pyrrolic NH and quinonoid carbonyl groups, leading to visible changes in color caused by the variation in the electronic structure of the **OxP** chromophore. The introduction of hydrophilic N-substituents at two of the **OxP** pyrrole NH groups also improves sensitivity to water, and **OxP** derivative **9** (Fig. 9a) can be considered a colorimetric indicator of minute traces of water in THF [30]. As illustrated in Fig. 9b, the presence of water above 50 ppm is denoted by a visible color variation. The related spectroscopic changes and the sensitivity of the method are described in

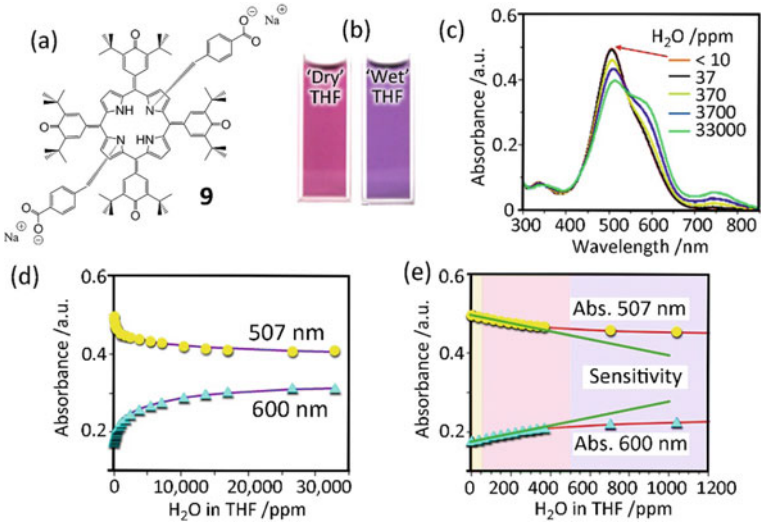

Fig. 9 **a** Chemical structure of **OxP** derivative **9**. **b** Variation in color of **9** in dry and wet tetrahydrofuran. **c** Changes in absorption spectra of **9** with H_2O concentration (THF, [9] = 3.5×10^{-6} M, 1 cm cell). **d**, **e** Changes in the intensity of absorbance at 507 nm and 600 nm for **9** with H_2O concentration in THF (a binding isotherm). In **e**, an expansion of the graph shown in **d** along the x-axis, water concentration is classed as three regions: yellow (anhyd.: [H_2O] <50 ppm), pink (moderate: 50 ppm < [H_2O] < 500 ppm), and mauve ('saturated': 500 ppm < [H_2O]) according to the level of water in commercially available THF. Adapted from [30]

Fig. 9c, d and e, respectively. At the outset of this work, we had assumed that color changes of the chromophore were due to binding of water at the central pyrrole NH groups. However, a computational analysis (density functional theory and molecular dynamics) revealed to our surprise that hydrogen bonding interactions of the hemquinonoid oxygen atoms are responsible for the change in shape and shift of the absorption bands of **OxP**.

4.2 Alcohol Sensing/Differentiation

Water detection could be extended to alcohol detection with the main finding in this case being that methanol can be differentiated from ethanol using the synergetic effect obtained by combining a carboxylated derivative of **OxP** (**9**, the same compound as that used for water sensing) with a layered double hydroxide (LDH, hydrotalcite-type $Mg_3Al(OH)_8(AcO)0.2H_2O$, where AcO = $CH_3CO_2^-$ = acetate). Carboxylate groups were introduced to **OxP** so that it could be exchanged with the LDH acetate counteranions contained at the layer interstitial spaces. This facilitates synthesis and stabilizes highly colored **OxP**-LDH composites, which could then be used to discriminate methanol from ethanol. This matter has become increasingly important

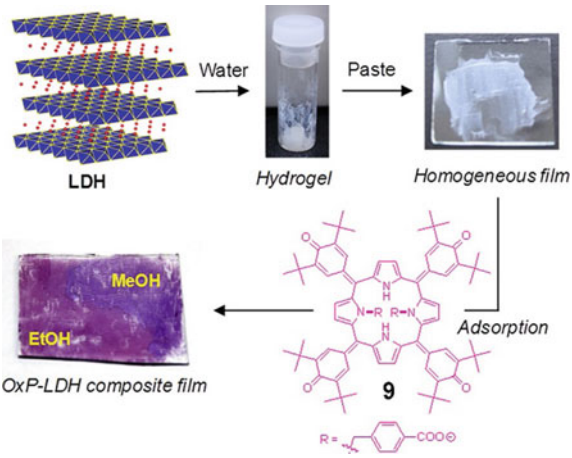

Fig. 10 Schematic illustration for the preparation of **OxP**-LDH composite film demonstrating visible color variation of compound **9** when exposed to methanol or ethanol**.** Reprinted with permission from reference [31] Ishihara et al., ACS Applied Materials and Interfaces **5**, 5927–5930 (2013). Copyright (2013), American Chemical Society

in the detection of contaminating methanol in ethanol-containing products such as alcoholic beverages and gasoline. Obviously, the former represents severe health risks while the latter can lead to egregious damage to automotive components. The selective sensing of methanol and ethanol is shown in Fig. 10 [31] although the physical basis for color-based differentiation in this case remains unknown.

4.3 Sensing in Chiral Systems

The saddle-shaped conformation of **OxP** results in the binding of guests through hydrogen bonding interactions at the macrocyclic pyrrole NH groups. We discovered that N_{21},N_{23}-substituted **OxP** derivatives can also be used as chiral solvating agents for the determination of the enantiomeric excess of chiral molecules. This is all the more remarkable because **OxP** itself lacks chirality.

Chirality is a critical feature of biochemical systems and is of substantial importance in the synthesis of ethical pharmaceuticals [32]. It affects organic reactions [33] such as those involved in asymmetric catalysis [34, 35], and is involved in aspects of supramolecular chemistry [36–38]. Therefore, the analysis of chirality, including enantiomeric purity and intermolecular chiral interactions, is a highly active research area. Nuclear magnetic resonance (NMR) analytical methods using chiral auxiliaries such as chiral derivatizing agents, [39, 40] chemical shift reagents [39, 41] and chiral solvating agents (CSA) [42, 43] have been investigated. The NMR method is intrinsically achiral and so cannot be used directly to sense chirality or related enantiomeric excess (*ee*) without using a chiral auxiliary or in the absence of intermolecular interactions having an equivalent or similar effect. In all cases, diastereomeric species are formed, and the application of NMR together with achiral shift reagents without the formation of diastereomers to probe enantiomeric excess was challenging prior to this work. However, chemical processes where achiral probes might sense chirality

could be important for investigations on enantioselective amplification including the origins of homochirality in living organisms. We have found [44] that simple symmetrical achiral N_{21},N_{23}-disubstituted **OxP** molecule **10** can be applied as a reporter of enantiomeric excess for a wide range of chiral guest molecules (Fig. 11). Enantiomeric excess detection is based on its proportionality to the splitting of ^{1}H-NMR resonances of the host molecule **10** (Fig. 11c, d). The physical reason for the observation of splitting is also described in Fig. 11e, which shows the asymmetrical profile of one enantiomer of a typical chiral guest (ibuprofen) during interaction with **OxP** derivative **10**.

In this work [44], we also demonstrated that there are no diastereomeric species present in solution during analysis because the complexes of **10** with each enantiomer or analyte have identical physical properties (actually, they are enantiomers

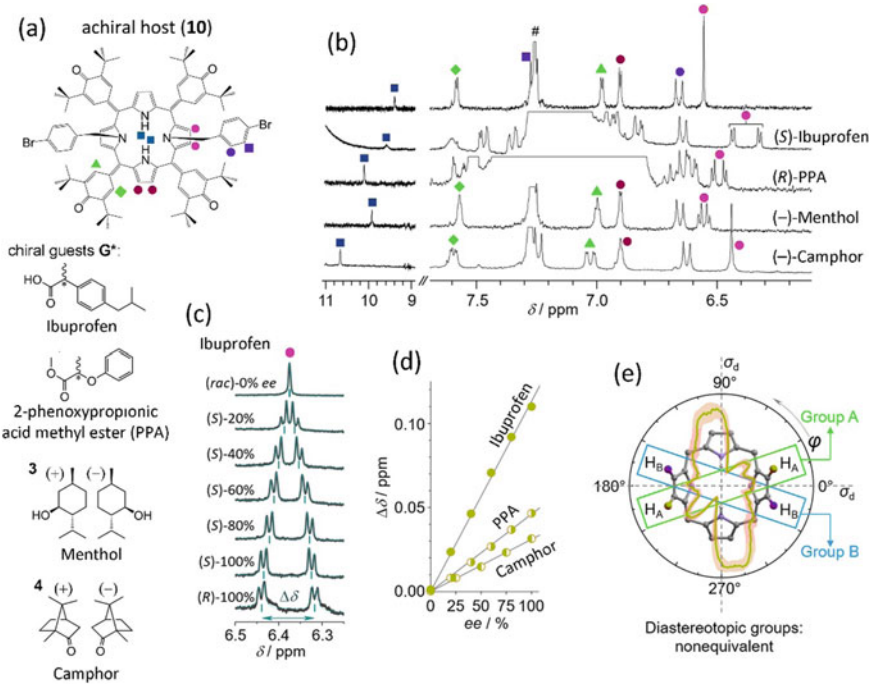

Fig. 11 **a** Structure of the achiral host molecule **10** and several guests (**G***). **b** Typical ^{1}H-NMR spectra of the host in the presence of large excesses of the chiral guests. **c** ^{1}H-NMR spectra in the pyrrolic resonance region of the host in the presence of ibuprofen with increasing *ee* (cyan curves are spectral fits; cyan bars under each spectrum denote the position of true resonances of the pyrrolic system). **d** Linear correlation between host resonance splitting and *ee* for ibuprofen, 2-phenoxypropionic acid methyl ester and camphor. **e** Origin of host resonance splitting. The pale pink region with the olive line denotes the average location of the guest (ibuprofen) with respect to the host leading to the shielding non-equivalence of protons H_A and H_B with the consequent J-coupled spectral pattern of their resonances

themselves). The chiral sensing mechanism was described in terms of the elimination of the host's symmetry during interactions with chiral guests undergoing fast exchange. Identification of the enantiomer can also be achieved through the addition of an aliquot of an enantiomer guest whose chirality is known. Symmetrical molecules used as *ee* sensors have certain advantages over traditional CSAs in that each enantiomer interacts with the same binding strength, leading to *ee* determination unaffected by kinetic resolution. These achiral sensing systems ought to add to our understanding of chirality features including majority rule, chiral transfer between molecules and asymmetric synthesis processes.

An additional outcome of this work on the sensitivity of **OxP** to chiral analytes was an in-depth investigation of macrocyclic dynamics of the **OxP** system, which could only be accomplished in the presence of a chiral guest as the probe species [45]. By using mandelic acid as a typical chiral guest molecule, it was possible to establish the behavior of different **OxP** species present in solutions. As a simplification, species found in solution could be described as shown in Fig. 12—neutral uncomplexed, deprotonated/H-bonded and a neutral flip-active form capable of undergoing macrocyclic inversion.

An important aspect of this work is that it illustrates the utility of chiral host–guest complexation for the analysis of effects beyond those related solely to the guest's chirality. Diprotonated **OxP** shows the dynamic interconversion (racemization) of its enantiomers by mechanisms involving tautomerism and ring-flipping. At low temperatures, this interconversion is halted with the ratio of enantiomers being affected by the protonating agent used (such as (*R*)-mandelic acid, (*S*)-(–)-2-phenoxypropionic acid, etc.). Importantly, these observations suggest that functional group reactivity in tautomeric or ring-flip-active molecules can be varied so that different yields of products might be obtained from (e.g., asymmetric) reactions depending on the solution characteristics such as reactant concentrations or the presence of any impurities, especially water.

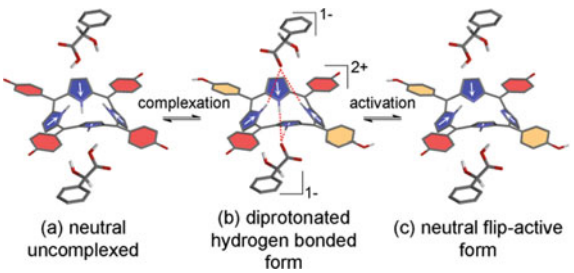

Fig. 12 Equilibrium of **OxP** in the presence of mandelic acid. **a** Neutral uncomplexed **OxP** form. **b** Hydrogen-bonded flip-non-active form. **c** Possible ring flip-active form. The *t*-butyl substituents of **OxP** have been omitted for clarity. In **b**, protonation occurs at two meso-substituent oxygen atoms. Reprinted with permission from [45], Labuta et al., J. Am. Chem. Soc. **136**, 2112–2118 (2014). Copyright (2014) American Chemical Society

4.4 Halochromism and Related Sensing in OxP Derivatives

Finally, **OxP** and N-substituted **OxP** derivatives have been developed as pH-sensing molecules [46, 47]. This is a result of different effects involving the protonation of the molecule at different sites and also involves some tautomeric processes. The first finding is that these dyes can be adapted to probe acidity in nonpolar solvents, a feat that has rarely been accomplished and is under development by us as a commercial indicator. Second, increasing N-substitution can tune the colorimetric response of **OxP** leading to an integrated multidye approach to acidity sensing perhaps similar to that already well established for universal indicator but which can be implemented in organic solvents or even as acidity probes of neat organic acids.

The colorimetric detection of acidity in an organic solvent (dichloromethane) using pure **OxP** is illustrated in Fig. 13, where structures of the chemical species responsible for the colorimetric variation are shown (Fig. 13a). These structures have been determined on the basis of physical measurements including ^{1}H NMR spectroscopy including titrations and infrared spectroscopy (generally to detect the

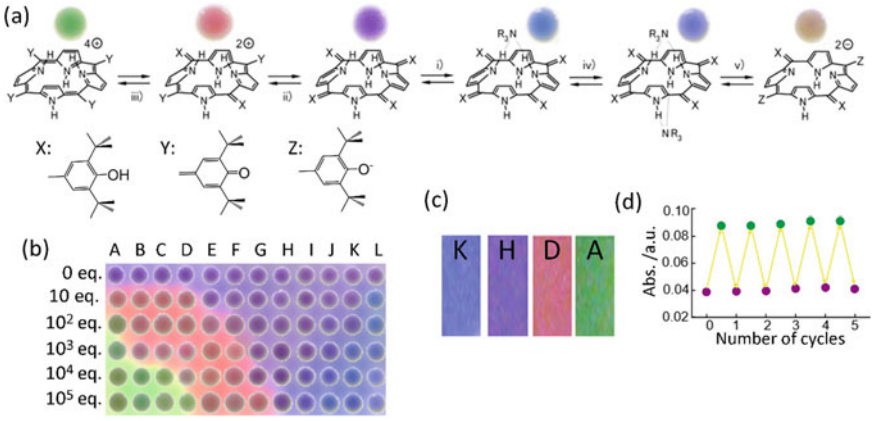

Fig. 13 **OxP** as a colorimetric detector of acidity. **a** Chemical species assigned to each color of **OxP** under different conditions, from left: double diprotonation (green), diprotonation (red, tautomer), neutral, 1:1 base complex, 1:2 base complex, deprotonation. Circles above each species are photographs taken of solutions of the species contained on a white ceramic well plate. Mauve color exists in the absence of reagents. **b** Color map of **OxP** color variation in the presence of different acids/bases from 0 to 10^5 equivalents (eq.) of each reagent against **OxP**. Circular parts are photographs taken of solutions in the presence (and absence: 0 eq) of the reagents noted contained on a white ceramic well plate. **c** Photographs of films of polymer-containing **OxP** treated with analyte vapors of increasing acidity (from left to right). **d** A variation at 780 nm during alternating exposure of **OxP** contained in a polymer film to TFA vapor followed by N_2 gas flow. Variation in absorbance in the UV–Vis spectrum is most significant at this wavelength. Reagent key: (A) methanesulfonic acid, (B) trifluoroacetic acid (TFA), (C) trichloroacetic acid, (D) dichloroacetic acid, (E) 2-nitrobenzoic acid, (F) chloroacetic acid, (G) 4-nitrobenzoic acid, (H) propionic acid, (I) pyridine, (J) 4-dimethylaminopyridine, (K) triethylamine, (L) 1,8-diazabicyclo[5.4.0]undec-7-ene (DBU)

existence of group X, see Fig. 13). There is a clear pattern in the development of color based on the prevailing acidity (or basicity) in solution (Fig. 13b) and, although it has proved difficult to construct a numerical scale to delineate this owing to the lack of known acidity parameters in organic solvents, it was possible to incorporate the **OxP** dye into polymer films, whose colors respond reversibly according to the prevailing acidity (Fig. 13c), and demonstrate the reversibility of the colorimetric response (Fig. 13d).

While **OxP** itself clearly exhibits a wide ranging color change depending on the prevailing acidity as shown in Fig. 13, **OxP** does have a propensity to undergo reductive processes especially in the presence of acid regenerating the porphyrin **TD*t*BHPP**. This system can be elaborated by the simple addition of N-substituents at the **OxP** core, which amounts to binding-site blocking of the analyte-sensitive calix[4]pyrrole core, and also prevents reduction of the **OxP** chromophore back to **TD*t*BHPP**. This was found to have a substantial effect on the response of **OxP** to acidity in organic solvents and was investigated using mixtures of organic acids in organic solvents. For this purpose, **OxP** and the N_{21},N_{23}-dibenzylated (**Bz_2OxP**) and N_{21},N_{22},N_{23},N_{24}-tetrabenzylated (**Bz_4OxP**) derivatives were studied (Fig. 14). The variable halochromic outputs of the compounds permitted us to construct a color scale for acidity in nonpolar solvents since the compounds **OxP**, **Bz_2OxP** and **Bz_4OxP** become increasingly resistant to protonation with increasing N-substitution but retain their property of color variation during interaction with acids (Fig. 15a for **Bz_2OxP**). The binding-site blocking and variation of sensitivity to acids on N-alkylation are important to establish the applications of these and other colorimetric indicators.

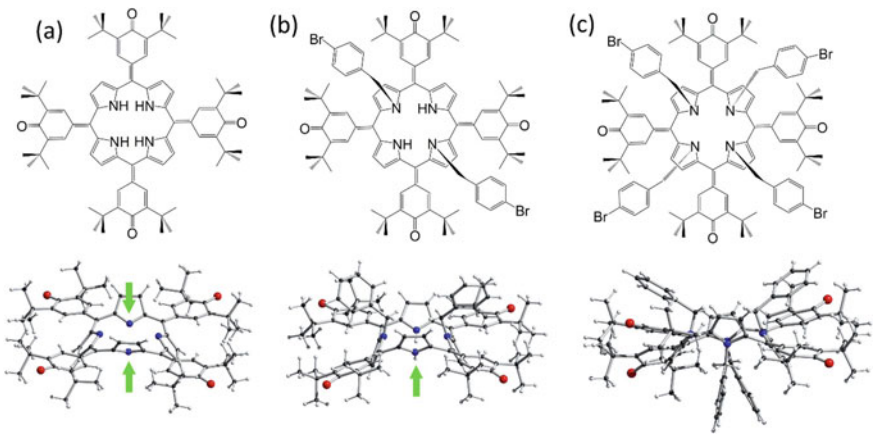

Fig. 14 Chemical structures (upper) and X-ray crystal structures (lower) of **a** oxoporphyrinogen (**OxP**), **b** N_{21},N_{23}-bis(4-bromobenzyl) oxoporphyrinogen (**Bz_2OxP**), **c** N_{21},N_{22},N_{23},N_{24}-tetrakis(4-bromobenzyl) oxoporphyrinogen, (**Bz_4OxP**), used in this work. The X-ray crystal structures in **b** and **c** are of the non-brominated derivatives. Accessible calix[4]pyrrole-type binding sites are denoted by green arrows

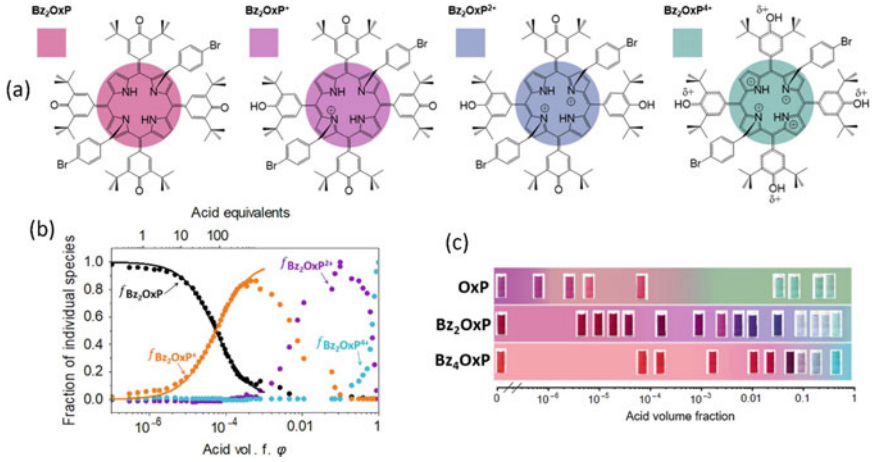

Fig. 15 **a** Chemical structures and colors of absorbing species. Note the increasing multiplicity of phenol meso-substituents passing from left to right yielding ultimately the tetraphenol/tetracation with positive charge effectively delocalized on the electronegative atoms. Colored squares and circles at each species represent RGB generated color from measured UV–Vis spectrum using Spectral Calculator [48]. **b** Dependency of fraction of each absorbing species on acid volume fraction. **c** Interleaved color scale constructed using the three dyes **OxP**, **Bz$_2$OxP** and **Bz$_4$OxP**. Rectangular parts are photographs taken of solutions in the presence (and absence: 0 volume fraction) of trifluoroacetic acid (for **OxP**) or difluoroacetic acid (for **Bz$_2$OxP** and **Bz$_4$OxP**) in 1 cm UV–Vis cuvettes. Note the match between calculated colors for **Bz$_2$OxP** in **a** and photographs of cuvettes in **c**

OxP, **Bz$_2$OxP** and **Bz$_4$OxP** make up a range of halochromic dyes (dyes sensitive to acids) that operate as indicators over a wide range of acid contents in nonpolar solvents. This is made possible by the up to quadruple protonation of **OxP** derivatives (Fig. 15a, b). Protonation is tuned by N-alkylation, which essentially shifts the sensitivity and colorimetric range as the protonation of **OxP** is made increasingly difficult. This causes a gradual color change over a wide range of acid compositions (from volume fractions of 10^{-7} up to 1, i.e., neat) with sensitivity decreasing in the order **OxP** > **Bz$_2$OxP** > **Bz$_4$OxP** (Fig. 15c). While the X-ray crystal structures of these compounds give general information about their neutral conformations, ^{1}H NMR spectroscopy and electronic absorption spectrophotometry have been used to establish the structures and prevalence of these compounds.

For the series **OxP**, **Bz$_2$OxP** and **Bz$_4$OxP**, the selection of the molecular structure was based initially on the blocking of the calix[4]pyrrole binding sites and how it affects the **OxP** colorimetric response. We expected that the removal of binding sites would result in the stepwise attenuation of colorimetric responses. However, to our surprise, acid responsivity was retained even in the fully N-substituted derivative **Bz$_4$OxP**. Another advantage of this **OxP** indicator is that the compounds are similar in structure and properties, which could facilitate application as mixtures of **OxP** derivatives. The effects of binding-site blocking, which effectively modulate acidity

sensitivity, present important new features for the preparation of chemical indicators for different applications.

5 Concluding Remarks

In this chapter, we have illustrated paths to molecular functionality using the **OxP** system as an example. These functions include photochemical reactivity, structural modulation and extremely wide-ranging sensing applications extending even to enantiomeric excess determination for chiral compounds. It is noteworthy that, although molecules based on **OxP** might ostensibly be considered rigid and nondynamic, we have found highly dynamic molecular actions (flipping, tautomerism, stretching) affecting their properties. The **OxP** molecule has physical dimensions on the nanometer scale and this, combined with its excellent diverse functionality, makes it an ideal organic component for preparing composite nanostructured materials and devices using the nanoarchitectonic principle. We have demonstrated this here by the incorporation of **OxP** into polymer composite films and organic–inorganic composites where, remarkably, **OxP** not only retains its properties but has also been subject to synergetic effects in a nanoarchitected system (i.e., **OxP**-LDH). We look forward to demonstrating the further utility of the **OxP** molecular system for the preparation of synthetic nanoarchitectures by combining organic synthesis procedures with nanoarchitectonics.

References

1. Rothemund P (1936) A new porphyrin synthesis. The synthesis of porphin. J Am Chem Soc 58:625–627
2. Milgrom LR (1997) The colors of life: an introduction to the chemistry of porphyrins and related compounds. Oxford University Press, Oxford
3. Ruckpaul K, Rein H (1984) Cytochrome P-450. Akademie-Verlag, Berlin
4. Kadish KM, Smith KM, Guilard R (eds) (2003) The porphyrin handbook volumes 1–10. Academic Press, San Diego
5. Milgrom LR (1983) The facile aerial oxidation of a porphyrin. Tetrahedron 39:3895–3898
6. Mulky MJ (1976) Butylated hydroxy anisole (BHA) and Butylated Hydroxy Toluene (BHT) as foods antioxidants. J Oil Technol Assoc India 8:134–139
7. Milgrom LR, Hill JP, Dempsey PJF (1994) Facile aerial oxidation of a porphyrin. Part 19. Alkylation of 5,10,17-Tris(3,5-di-t-butyl-4-hydroxyphenyl)-20-(4-pyridyl)porphyrin. Tetrahedron 50:13477–13484
8. Milgrom LR, Flitter WD (1991) Facile aerial oxidation of a porphyrin. Part 8. Decay of radical formed during the aerial oxidation of meso-tetrakis(3,5-di-t-butyl-4-hydroxyphenyl)porphyrin. Tetrahedron 47:7683–7688
9. Sessler JL, Anzenbacher P, Miyaji H, Jursíková K, Bleasdale ER, Gale PA (2000) Modified Calix[4]pyrroles. Ind Eng Chem Res 39:3471–3478
10. Hill JP, Hewitt IJ, Anson CE, Powell AK, McCarthy AL, Karr P, Zandler ML, D'Souza F (2004) Highly nonplanar, electron deficient, n-substituted tetra-oxocyclohexadienylidene

porphyrinogens: structural, cmputational, and electrochemical investigations. J Org Chem 69:5861–5869
11. Labuta J, Hill JP, Elsegood MRJ, Ariga K (2010) Stable pseudotetrahedral supermolecules based on an oxoporphyrinogen. Tetrahedron Lett 51:2935–2938
12. Hill JP, Schmitt W, McCarty AL, Ariga K, D'Souza F (2005) Structures, spectral and electrochemical properties of N-(Naphth-2-ylmethyl)-appended porphyrinogens. Eur J Org Chem 2005:2893–2902
13. Evans TA, Srivatsa GS, Sawyer DT, Traylor TG (1985) Redox chemistry of tetrakis(3,5-di-tert-butyl-4-hydroxyphenyl)porphine and its Zinc(II) complex in dimethylformamide. Inorg Chem 24:4733–4735
14. Milgrom LR, Yahioglu G, Jogiya NN (1996) Redox behaviour of phenolic porphyrins in basic solutions: a reappraisal. Free Radical Res 24:19–29
15. Hill JP, Wakayama Y, Schmitt W, Tsuruoka T, Nakanishi T, Karr PA, Zandler ML, McCarty AL, D'Souza F, Milgrom LR, Ariga K (2006) Regulating the stability of 2D crystal structures using an oxidation state dependent molecular conformation. Chem Commun 42:2320–2322
16. Golder AJ, Milgrom LR, Nolan KB, Povey DC (1989) 5,10,15,20-Mesotetrakis(3,5-di-t-butyl-4-hydroxyphenyl)porphyrinogen: a highly puckered tetrapyrrolic macrocycle from the facile aerial oxidation of a phenolic porphyrin. J Chem Soc, Chem Commun 22:1751–1753
17. Jung TA, Schittler RR, Gimzewski JK (1997) Conformational identification of individual adsorbed molecules with the STM. Nature 386:696–698
18. Geng F, Gao H, Meng Q, Dong Z, Wakayama Y, Akada M, Ariga K, Hill JP (2011) Anchoring of self-assembled monolayers of unsymmetrically-substituted chromophores with an oxoporphyrinogen surface clamp. Chem Commun 47:8533–8535
19. Sessler JL, Gross DE, Cho W-S, Lynch VM, Schmidtchen FP, Bates GW, Light ME, Gale PA (2006) Calix[4]pyrrole as a chloride anion receptor: solvent and countercation effects. J Am Chem Soc 128:12281–12288
20. Stefani D, Perrin M, Gutiérrez-Cerón C, Aragonès AC, Labra-Muñoz J, Carrasco RDC, Matsushita Y, Futera Z, Labuta J, Ngo TH, Ariga K, Díez-Pérez I, van der Zant H, Dulić D, Hill JP (2018) Mechanical tuning of through molecule conductance in a conjugated Calix[4]pyrrole. ChemistrySelect 3:6473–6478
21. Xie Y, Hill JP, Schumacher AL, Sandanayaka ASD, Araki Y, Karr PA, Labuta J, D'Souza F, Ito O, Anson CE, Powell AK, Ariga K (2008) Twisted, two-faced porphyrins as hosts for bispyridyl fullerenes: construction and photophysical properties. J Phys Chem C 112:10559–10572
22. Commins PJ, Hill JP, Matsushita Y, Webre WA, D'Souza F, Ariga K (2016) Selective octabromination of tetraarylporphyrins based on meso-substituent identity: structural and electrochemical studies. J Porphyrins Phthalocyanines 20:213–222
23. Noy D, Moser CC, Dutton PL (2006) Design and engineering of photosynthetic light-harvesting and electron transfer using length, time, and energy scales. Biochim Biophys Acta Bioenerg 1757:90–105
24. Hill JP, Sandanayaka ASD, McCarty AL, Karr PA, Zandler ME, Charvet R, Ariga K, Araki Y, Ito O, D'Souza F (2006) A novel Bis(Zinc-Porphyrin)-oxpophyrinogen donor-acceptor triad: synthesis, electrochemical, computational and photochemical studies. Eur J Org Chem 2006:595–603
25. Schumacher AL, Sandanayaka ASD, Hill JP, Ariga K, Karr PA, Araki Y, Ito O, D'Souza F (2007) Supramolecular triad and pentad composed of zinc-porphyrin(s), oxoporphyrinogen, and fullerene(s): design and electron-transfer studies. Chem Eur J 13:4628–4635
26. D'Souza F, Subbaiyan NK, Xie Y, Hill JP, Ariga K, Ohkubo K, Fukuzumi S (2009) Anion-complexation-induced stabilization of charge separation. J Am Chem Soc 131:16138–16146
27. Hill JP, Schumacher AL, D'Souza F, Labuta J, Redshaw C, Elsegood MJR, Aoyagi M, Nakanishi T, Ariga K (2006) Chromogenic indicator for anion reporting based on an n-substituted oxoporphyrinogen. Inorg Chem 45:8288–8296
28. Šedivec V, Flek J (1976) Handbook of analysis of organic solvents. John Wiley Inc., New York
29. Fischer K (1935) Neues Verfahren zur maßanalytischen Bestimmung des Wassergehaltes von Flüssigkeiten und festen Kőrpern. Angew Chem 48:394–396

30. Ishihara S, Labuta J, Šikorský T, Burda JV, Okamoto N, Abe H, Ariga K, Hill JP (2012) Colorimetric detection of trace water in tetrahydrofuran using *N,N'*-substituted oxoporphyrinogens. Chem Commun 48:3933–3935
31. Ishihara S, Iyi N, Labuta J, Deguchi K, Ohki S, Tansho M, Shimizu T, Yamauchi Y, Naito M, Abe H, Hill JP, Ariga K (2013) Naked-eye discrimination of methanol from ethanol using composite film of oxoporphyrinogen and layered double hydroxide. ACS Appl Mater Interfaces 5:5927–5930
32. Hutt AJ (2006) Drug chirality and its pharmacological consequences in introduction to the principles of drug design and action. CRC Press, Taylor & Francis, Boca Raton
33. Jacobsen EN, Pfaltz A, Yamamoto H (1999) Comprehensive organic catalysis, vols. I to III. Springer, New York
34. Heitbaum M, Glorius F, Escher I (2006) Asymmetric heterogeneous catalysis. Angew Chem Int Ed 45:4732–4762
35. Yoon TP, Jacobsen EN (2003) Privileged chiral catalysts. Science 299:1691–1693
36. Kondo T, Oyama K, Yoshida K (2001) Chiral molecular recognition on formation of a metalloanthocyanin: a supramolecular metal complex pigment from blue flowers of *salvia patens.* Angew Chem Int Ed 40:894–897
37. Ishi-i T, Crego-Calama M, Timmerman P, Reinhoudt DN, Shinkai S (2002) Enantioselective formation of a dynamic hydrogen-bonded assembly based on the chiral memory concept. J Am Chem Soc 124:14631–14641
38. Maeda K, Morino K, Okamoto Y, Sato T, Yashima E (2004) Mechanism of helix induction on a stereoregular Poly((4-carboxyphenyl)acetylene) with chiral amines and memory of the macromolecular helicity assisted by interaction with achiral amines. J Am Chem Soc 126:4329–4342
39. Dale JA, Dull DL, Mosher HS (1969) α-Methoxy-α-trifluromethylphenylacetic acid, a versatile reagent for the determination of enantiomeric composition of alcohols and amines. J Org Chem 34:2543−2549
40. Parker D (1991) NMR determination of enantiomeric impurity. Chem Rev 91:1441−1457
41. Duddeck H, Gómez ED (2009) Chiral recognition of ethers by NMR spectroscopy. Chirality 21:51–68
42. Wenzel TJ, Chisholm CD (2011) Assignment of absolute configuration using chiral reagents and NMR spectroscopy. Chirality 23:190−214
43. Schwenninger R, Schlögl J, Maynollo J, Gruber K, Ochsenbein P, Bürgi H-B, Konrat R, Kraütler B (2001) Metal complexes of a biconcave porphyrin with D_4-structure—versatile chiral shift agents. Chem Eur J 7:2676–2686
44. Labuta J, Ishihara S, Šikorský T, Futera Z, Shundo A, Hanyková L, Burda JV, Ariga K, Hill JP (2013) NMR spectroscopic detection of chirality and enantiopurity in referenced systems without formation of diastereomers. Nat Commun 4:2188
45. Labuta J, Futera Z, Ishihara S, Kourilova H, Tateyama Y, Ariga K, Hill JP (2014) J Chiral guest binding as a probe of macrocycle dynamics and tautomerism in a conjugated tetrapyrrole. Am Chem Soc 136:2112–2118
46. Shundo A, Ishihara S, Labuta J, Onuma Y, Sakai H, Abe M, Ariga K, Hill JP (2013) Colorimetric visualization of acid-base equilibria in non-polar solvent. Chem Commun 49:6870–6872
47. Březina V, Ishihara S, Lang J, Hanyková L, Ariga K, Hill JP, Labuta J (2018) Structural modulation of chromic response: effects of binding-site blocking in a conjugated Calix[4]pyrrole chromophore. ChemistryOpen 7:323–335
48. Lindbloom B, Spectral Calculator. http://www.brucelindbloom.com/. Accessed 20 May 2020

Growth and Electronic and Optoelectronic Applications of Surface Oxides on Atomically Thin WSe_2

Mahito Yamamoto and Kazuhito Tsukagoshi

1 Introduction

Atomically thin layered materials such as graphene, transition metal dichalcogenides (TMDCs), and phosphorene have emerged as a new class of materials with potential for a broad range of applications [1–4]. Among them, group VI TMDCs (MX_2, where M = Mo and W and X = S, Se, and Te) are of particular interest for applications in electronics and optoelectronics because of their semiconducting properties [5–7]. The bandgap of MX_2 is known to depend on the combination of M and X. For example, bulk MoS_2 has a bandgap of ~1.3 eV [8, 9], whereas the bandgap of $MoTe_2$ is 1.0 eV in the bulk form [10]. The bandgap of MX_2 increases with decreasing number of layers and, most notably, a transition from the indirect to direct bandgap is induced in the single-layer limit [8, 9]. Thanks to the sizable direct bandgap, single-layer MX_2 has attracted much attention for applications in electronic and optoelectronic devices, such as field-effect transistors (FETs) [11], photodetectors [12, 13], and light-emitting diodes (LEDs) [14–16].

Although atomically thin MX_2 shows great promise for electronic and optoelectronic devices, some technological hurdles still need to be addressed for practical use. One of the challenges is to create "good" electrical contacts to atomically thin MX_2 [17, 18]. Previous studies have shown that when MX_2 is placed in contact with a metal, the Fermi level is pinned inside the bandgap, independent of the metal work function, hence resulting in a large Schottky barrier at the interface [19–22]. The resulting Schottky contact severely limits the performance of MX_2-based devices, including the effective carrier mobility in the FET and the photoresponsivity in

M. Yamamoto · K. Tsukagoshi (✉)
International Center for Materials Nanoarchitectonics (WPI-MANA), National Institute for Materials Science (NIMS), 1-1 Namiki, Tsukuba 305-0044, Ibaraki, Japan
e-mail: TSUKAGOSHI.Kazuhito@nims.go.jp

M. Yamamoto
Institute of Scientific and Industrial Research, Osaka University, Ibaraki 567-0047, Osaka, Japan

Y. Wakayama and K. Ariga (eds.), *System-Materials Nanoarchitectonics*,
NIMS Monographs, https://doi.org/10.1007/978-4-431-56912-1_9

the photodetector. Therefore, contact engineering is necessary for the realization of high-performance atomically thin MX_2-based devices.

Various approaches have been employed to improve the electrical contacts of atomically thin MX_2-based devices. An effective approach is to dope MX_2. Doping of atomically thin MX_2 lead to the band bending at the interface and, as a result, carriers can be injected from the contacting metal into MX_2 by quantum tunneling, rather than by thermionic emission over the Schottky barrier. As a result, the contact resistance is significantly reduced and, consequently, the performance of the MX_2 device can be enhanced.

However, in contrast with bulk semiconductors, chemical doping approaches such as an ion implantation are challenging for atomically thin semiconductors because the doping process could readily destroy the crystal structure. Instead, the adsorption of charge transfer agents has been often employed to effectively dope atomically thin semiconductors. Such surface dopants were introduced in previous works. For example, potassium was used to degenerately n-dope few-layer MoS_2 and WSe_2 [23]. Then, potassium-treated MoS_2 and WSe_2 transistors were observed to show a much higher electron mobility than those without the treatment. Also, NO_2 was found to serve as a strong hole dopant for single-layer WSe_2 and, hence, can be used to enhance the hole mobility in transistors [24]. Also, molecules have been proposed for the n-type dopant of MoS_2. The adsorption of benzyl viologen leads to the n-doping of atomically thin MoS_2, and the improvement of the electrical contact was reported for the surface treated MoS_2 device [25]. Also, chloride molecules were used to n-dope few-layer MoS_2 and WS_2 to reduce the contact resistances [26].

In this review, we show that surface oxidation is a simple, effective, and controllable approach to the surface hole doping of atomically thin WSe_2. First, we show how to grow a uniform surface oxide on atomically thin WSe_2 [27]. Second, we show that the surface oxidation indeed leads to the enhanced p-type performance of atomically thin WSe_2 transistors [28]. Finally, we introduce another aspect of the surface oxide on atomically thin WSe_2. We show that the surface oxide is an effective electron trap and can be used to facilitate the photogating effect in atomically thin WSe_2-based photodetectors [29].

2 Growth of Surface Oxides on Atomically Thin WSe_2

First, we review the growth of a tungsten oxide (WO_x with $x < 3$) thin film on atomically thin WSe_2. Transition metal oxides (TMOs) such as MoO_3 and WO_3 are n-type semiconductors, with great attention as hole contacts and surface dopants for electronics, owing to their high work functions and electron affinity. Indeed, TMOs were initially introduced as effective hole injection layers for organic LEDs and photovoltaic devices [30]. Recently, thermally evaporated thin films of MoO_3 have been used as effective hole contacts for MoS_2 and WSe_2 transistors [31]. Since TMOs and TMDCs have the same cations, one may expect that TMO thin films can be directly grown on the surfaces of TMDCs simply by oxidation and, then, the

surface oxides can be used as hole dopants/contacts for the TMDC devices. In the following, we introduce our approach to growing a homogeneous surface oxide on atomically thin WSe_2.

TMDCs are relatively inert to oxidation because of the absence of dangling bonds on the basal plane surfaces, making it difficult to grow homogeneous oxides on the surfaces. However, TMDCs have been observed to show high oxidative reactivity at vacancy defects on their surfaces and edges [32–34]. Therefore, surface oxides can be nucleated from such structural disorders in a TMDC and expand laterally to form a uniform thin film. Figure 1a–c respectively show atomic force microscopy (AFM)

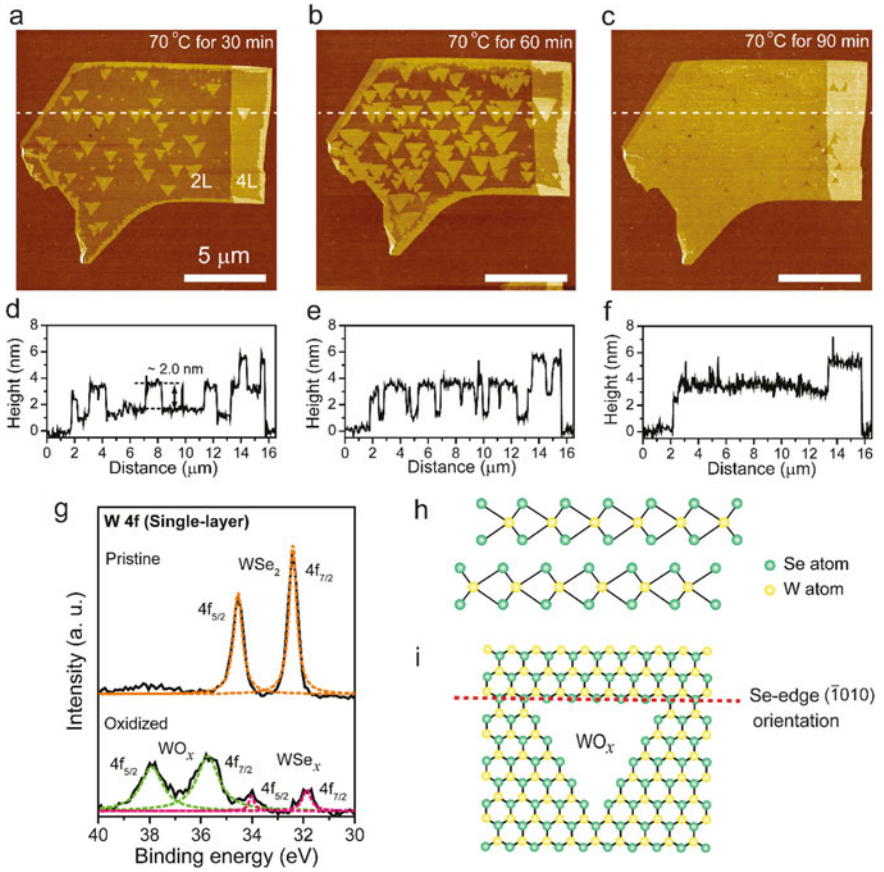

Fig. 1 AFM images of bilayer (2L) and four-layer (4L) WSe_2 after O_3 exposure at 70 ºC for **a** 30, **b** 60, and **c** 90 min. **d–f** The height profiles along the dashed lines in (**a–c**). **g** XPS spectra of a W 4f core level of pristine single-layer WSe_2 and oxidized single-layer WSe_2. The oxidized WSe_2 shows peaks from WO_x with $x < 3$, in addition to peaks from WSe_x with $x < 2$ **h** Crystal structure of bilayer WSe_2 in the side view. Each layer is weakly coupled by the van der Waals interaction. **i** Schematic of a WSe_2 surface with triangular oxide WO_x. The red dashed line indicates a Se zigzag edge $(\bar{1}\,010)$ orientation. Adapted with permission from Ref. 27. Copyright 2015. American Chemical Society

images of atomically thin WSe_2 on a Si/SiO_2 substrate after ozone (O_3) exposure at 70 ºC for 30, 60, and 90 min. The WSe_2 films were mechanically exfoliated from bulk single crystals synthesized by the chemical vapor transport method [28]. We found that O_3 exposure leads to the formation of triangular islands with a uniform thickness of ~2 nm on the surface of WSe_2 (Fig. 1d–f). The islands grow laterally with time (Fig. 1b) and coalesce with each other to form a uniform film (Fig. 1c). We do not observe the formation of such oxide films on the bottom surface of WSe_2 likely because the bottom layer adheres to the SiO_2 surface rigidly due to the van der Waals interaction and, therefore, is protected from oxidation. By X-ray photoemission spectroscopy (XPS), the resulting film was found to be substoichiometric tungsten oxide WO_x with $x < 3$ (Fig. 1g). Such a tungsten oxide film cannot be grown on atomically thin WSe_2 by oxygen (O_2) exposure because of the lower reactivity of O_2. The triangular shapes of the islands suggest that the oxidation of WSe_2 is induced along selenium zigzag $(\bar{1}\,010)$ orientations, as illustrated in Figs. 1h, i. The selenium atoms in WSe_2 may be sublimed after the O_3 treatment.

Interestingly and importantly, the low-temperature oxidation of atomically thin WSe_2 is terminated at the single-layer thickness. In Fig. 2a, b, we show optical images of atomically thin WSe_2 before and after O_3 exposure at 100 ºC for 1 h. The 1 h-O_3 treatment leads to a change in the optical contrast of WSe_2 owing to the surface oxidation of the layers. The contrast of single-layer WSe_2 coincides with that of SiO_2. However, the AFM measurements confirm that the WSe_2 layer is not etched out but oxidized to form a homogeneous WO_x film with a thickness of ~2 nm. By comparing the contrasts before and after oxidation, we estimated that only the top single layer is oxidized by the O_3 treatment. The top single-layer oxidation of WSe_2 is confirmed by Raman spectroscopy. Figure 2c shows the Raman spectra of single-layer and bilayer WSe_2 before and after oxidation. The Raman peak of the E^1_{2g} (or A_{1g}) mode of single-layer WSe_2 disappears after the surface oxidation, whereas the Raman peak of bilayer WSe_2 remains. Additionally, the Raman B^1_{2g} peak of bilayer WSe_2, which is absent in single-layer WSe_2, disappears after oxidation. We noted

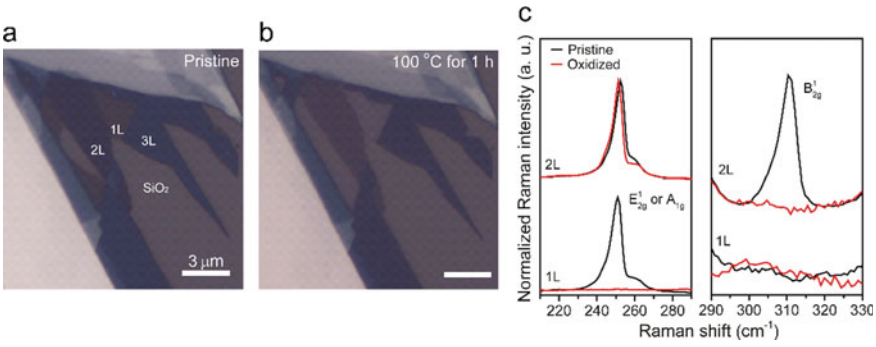

Fig. 2 Optical images of atomically thin WSe_2 **a** before and **b** after O_3 exposure at 100 ºC for 1 h. **c** Raman spectra of pristine and surface-oxidized single-layer (1L) and bilayer (2L) WSe_2. Adapted with permission from Ref. 27. Copyright 2015. American Chemical Society

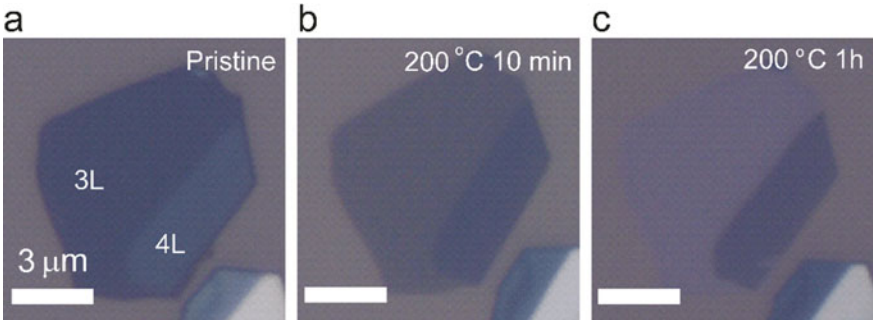

Fig. 3 Optical images of atomically thin WSe_2 **a** before and after O_3 exposure at 200 ºC for **b** 10 min and **c** 1 h. Adapted with permission from Ref. 27. Copyright 2015. American Chemical Society

that the surface oxidation does not proceed even after longer O_3 exposure. Namely, the surface oxidation of WSe_2 is limited to the single-layer thickness, and the surface oxide is isolated from the underlying WSe_2 and no chemical bonding is expected to exist between them. The self-limiting oxidation is most likely because the surface oxide protects the underlying WSe_2 from further oxidation (see Fig. 2h for the crystal structure of WSe_2). However, the oxidation can proceed to deeper WSe_2 layers with increasing temperature. Figure 3a–c show optical images of atomically thin WSe_2 before and after O_3 exposure at 200 ºC for 10 min and 1 h. The optical contrast of atomically thin WSe_2 changes with the oxidation time, suggesting that WSe_2 is oxidized in a layer-by-layer manner. Ultimately, the upper trilayer WSe_2 is oxidized in 1 h, with the lowermost layer decoupled from the covering oxide.

3 Electronic Applications of Surface Oxides

In the previous section, we showed that a homogeneous WO_x film can be grown on the surface of atomically thin WSe_2 simply by O_3 exposure. Furthermore, the surface oxide is isolated from the underlying WSe_2 and the van der Waals gap is expected to be present between them. These observations have important implications for applications of the surface oxide as hole injection layers for atomically thin WSe_2-based devices. In this section, we show that the surface oxide can indeed be used as hole contacts and surface dopants for atomically thin WSe_2 transistors.

Figure 4a, b show a schematic and optical images of atomically thin WSe_2 transistors, respectively. In this transistor configuration, the Si/SiO_2 substrate serves as the gate electrode and dielectric, whereas Ti/Au is used for the source and drain electrodes. In Fig. 4c, we show the transfer characteristics of a bilayer WSe_2 transistor before and after O_3 exposure for 1 h at 100 ºC. Before oxidation, the WSe_2 transistor shows ambipolar transport, with higher conductivity in the electron branch (see the black curve in Fig. 4c). The ambipolar behavior is due to the Fermi level pinning

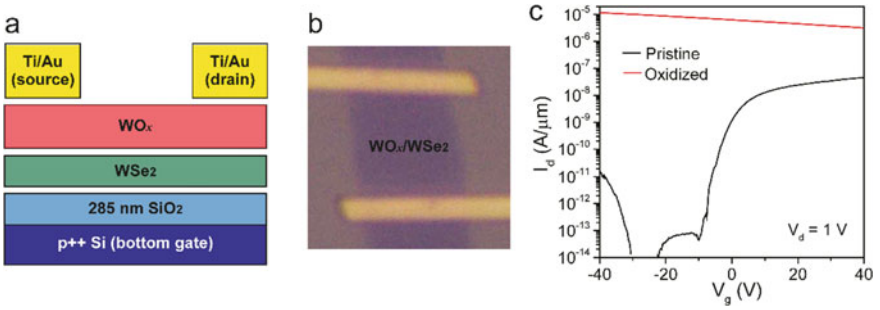

Fig. 4 **a** Schematic and **b** optical images of a surface-oxidized bilayer WSe_2 transistor. **c** Transfer characteristics of a pristine (black curve) and oxidized (red curve) bilayer WSe_2 transistor. The drain bias (V_d) is 1 V. Adapted with permission from Ref. 28. Copyright 2016. American Chemical Society

near the midgap of WSe_2 [35]. Owing to the large Schottky barrier at the contact, the WSe_2 transistor shows relatively poor performance; the on-current is ~10 nA and the electron mobility is >1 $cm^2/(Vs)$. However, the transistor performance can be improved significantly after O_3 exposure for 1 h at 100 ºC (the O_3 treatment leads to the oxidation of the topmost layer of WSe_2, as shown in Fig. 2). After the O_3 treatment, the WSe_2 transistor shows p-type transport with a high drain current of >1 μA and a carrier mobility of 57 $cm^2/(Vs)$. The p-type conductivity and hole mobility of the oxidized WSe_2 transistor are high one because the surface WO_x serves as effective hole contacts with low resistances. Additionally, WO_x leads to electron transfer from the underlying WSe_2 and, therefore, works as a surface hole dopant. We note that the lateral resistance of WO_x is extremely high and, thus, the current flows only in the WSe_2 channel in the transistor configuration shown in Fig. 4a [28].

To illustrate the effect of the surface oxidation on the performance of the atomically thin WSe_2 transistor, we show band diagrams of Ti-contacted WSe_2 and WO_x-contacted WSe_2 in Fig. 5. When WSe_2 is in contact with Ti, the Fermi level is pinned near the midgap, resulting in a large Schottky barrier for both holes and electrons. Namely, at the Ti/WSe_2 contact, the carriers are injected into WSe_2 by thermionic emission over the barrier (Fig. 5a). At the WO_x/WSe_2 contact, holes rather than electrons are injected into WSe_2 since WO_x has a high work function (Fig. 5b) [30]. Here, we draw the band of WO_x as a metal since the Fermi level is close to the conduction band edge. Although the Schottky barrier still exists at the WO_x/WSe_2 contact, the width of the Schottky barrier is thinned by the large band bending of the WSe_2 channel caused by hole doping. As a result of the thinning of the Schottky barrier width, the tunneling of holes through the barrier is facilitated. Consequently, the contact resistance is significantly reduced for holes and high p-type performance can be realized in the oxidized WSe_2 transistor.

The carrier density of the oxidized WSe_2 is estimated to be 2.6×10^{12} cm^{-2} at zero gate voltage, indicating that the underlying WSe_2 is degenerately hole-doped. Namely, the off-state is absent in the WSe_2 transistor. The absence of the off-state

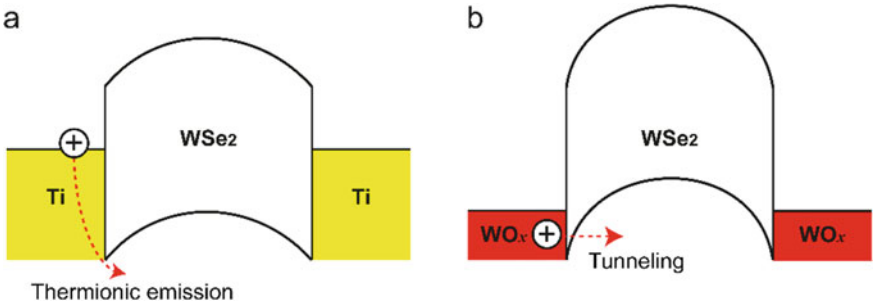

Fig. 5 Qualitative band diagrams for **a** Ti-WSe_2 contacts and **b** WO_x-WSe_2 contacts. At the Ti-WSe_2 contact, holes are injected into WSe_2 by thermionic emission. At the WO_x-WSe_2 contact, holes are injected by tunneling from WO_x to WSe_2 owing to the large band bending caused by hole doping

in the WSe_2 transistor is unfavorable for practical use. Thus, control of the hole dopant concentration is essential. Previous studies have shown that the hole injection properties of TMOs can be suppressed by air exposure [30]. Therefore, we employ air exposure to control the hole dopant concentration of oxidized WSe_2. Figure 6a shows the transfer characteristics of an oxidized bilayer WSe_2 transistor before and after air exposure at room temperature. In fact, the hole conductivity is reduced with time by air exposure and, ultimately, the off-state appears in the transfer curves. This is most likely because of the adsorption of carbon impurities on the surface of WO_x, as reported previously [30]. Importantly, the WSe_2 transistor still shows reasonable performance even after air exposure, suggesting the effectiveness of the treatment. Moreover, as shown in Fig. 6b, the hole conductivity can be recovered to the initial state by O_3 exposure at room temperature. The O_3 treatment is expected to lead to the removal of the carbon impurities from the WO_x surface. Namely, the

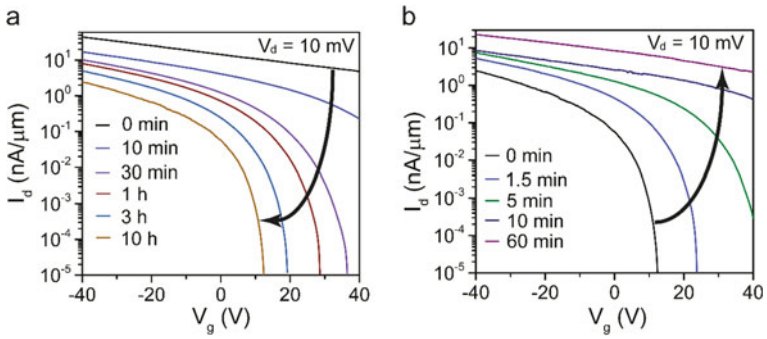

Fig. 6 **a** Transfer characteristics of a surface-oxidized bilayer WSe_2 transistor upon intermittent air exposure from 0 to 10 h at room temperature. **b** Transfer characteristics of the same transistor upon intermittent O_3 exposure from 0 to 60 min at room temperature. Adapted with permission from Ref. 28. Copyright 2016. American Chemical Society

oxidation-mediated hole doping of WSe_2 is controllable from the degenerate to the non-degenerate regime. These results suggest that surface oxidation is an effective and controllable approach to creating good p-type contacts and dopants for atomically thin WSe_2-based devices.

4 Optoelectronic Applications of Surface Oxides

In the previous section, we showed that oxidation results in the formation of effective p-type contacts and dopants on the surface of atomically thin WSe_2, which facilitates the p-type transistor performance. In this section, we show that surface oxidation can also be used to enhance the responsivity of atomically thin WSe_2-based phototransistors.

Before discussing the photoresponsivity of an oxidized WSe_2 phototransistor, we briefly review the photocurrent generation mechanisms in atomically thin MX_2-based phototransistors. There are two main photocurrent generation mechanisms, namely, the photoconductive and photogating effects [36, 37]. When atomically thin MX_2 is illuminated with light, electron–hole pairs are generated. In the photoconductive effect, the generated charges serve as carriers in MX_2 and, thus, directly contribute to the conductivity. In the photogating effect, alternatively, the generated charges are trapped on and/or in MX_2 and serve as effective gates. Compared with the photoconductive effect, the photogating effect produces high responsivity (although the response time is much slower) [12, 38]. Therefore, inducing the photogating effect is important for the realization of a highly responsive photodetector based on atomically thin MX_2.

Here, we show that surface oxides can serve as effective electron traps for atomically thin WSe_2 and, therefore, facilitate the photogating effect. First, we show the electron–trapping property of the surface WO_x grown on WSe_2. As shown in Fig. 7a, the p-type transistor consistently shows hysteresis in the transfer characteristic (this transistor was exposed to air after the formation of the surface WO_x layer in order to realize a reasonable off-state). The hysteresis is caused because the positive voltage gating leads to the increase in the electron density in the WSe_2 channel and the electrons are trapped in the surface WO_x, as observed in transistors based on MoS_2 on SiO_2 [39]. The hysteresis window, which is proportional to the trap density, is widened with increasing maximum gate voltage. Figure 7b shows the density of traps in the surface WO_x as a function of the maximum gate voltage. We see that the trap density can exceed 10^{12} cm^{-2} at a higher gate voltage, which is larger than the typical trap density in SiO_2 [40]. The large electron trap density suggests the potential use of WO_x to mediate the photogating effect in the underlying WSe_2.

Figure 8a shows the transfer characteristics of a surface-oxidized four-layer WSe_2 transistor measured under dark and white light illumination. White light illumination results in the generation of the photocurrent for all the gate voltages. The signature of the photogating effect can be identified in the slow photoresponse of the WSe_2 transistor. As shown in Fig. 8b, while the photocurrent initially increases rapidly due

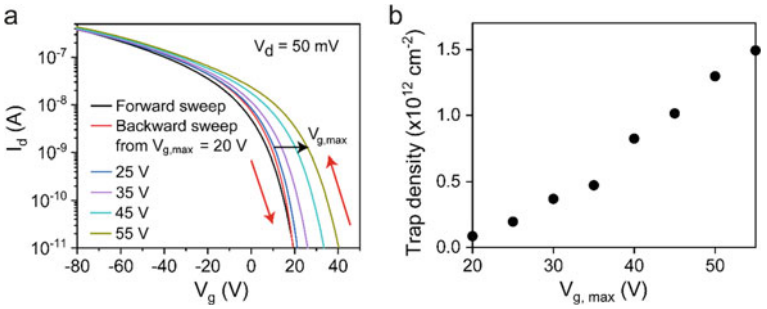

Fig. 7 **a** Transfer characteristics of a surface-oxidized bilayer WSe_2 transistor. The forward sweep is initiated from −80 V, whereas the backward sweep is initiated from the maximum gate voltage ($V_{g,max}$), which ranges from 20 to 55 V. The red arrows indicate the gate sweep directions. **b** Trap density in the surface WO_x as a function of the maximum gate voltage. Reproduced from Ref. 29 with the permission of AIP Publishing

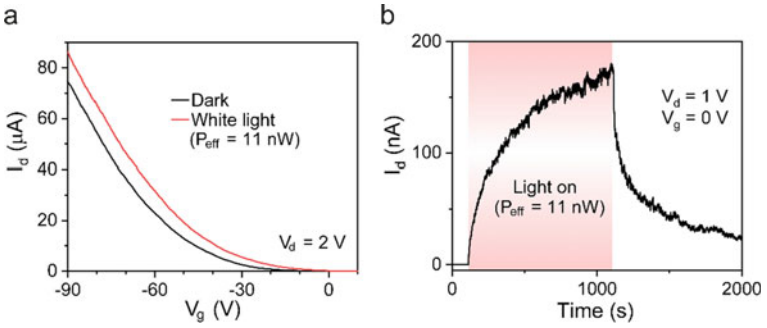

Fig. 8 **a** Transfer characteristics of a surface-oxidized four-layer WSe_2 transistor under dark (black curve) and white light illumination with an optical power of 11 nW (red curve). The drain bias voltage is 2 V. **b** Time evolution of the drain current under illumination with an incident power of 11 nW. The drain and gate bias voltages are 1 and 0 V, respectively. Reproduced from Ref. 29 with the permission of AIP Publishing

to the increase in the hole concentration, the rate of the current increase is reduced significantly to the time scale of seconds because more electrons are transferred and trapped in the surface WO_x with time. This behavior is in sharp contrast to the fast photoresponse observed in the pristine WSe_2 transistor, where the photoconductive effect is dominant [37].

Now, we discuss the responsivity of the surface-oxidized WSe_2 transistor. In the photogating effect, the responsivity increases with increasing carrier mobility as well as decreasing power of illumination. Since the p-type oxidized WSe_2 transistor has a larger carrier mobility at the negative gate voltage, we examine the responsivity at a gate voltage of −90 V and a power of 1.1 nW. Under these conditions, the responsivity of the oxidized WSe_2 transistor is found to exceed 3000 A/W. This value is comparable to the previous record performance under similar measurement

conditions [37], suggesting that the surface oxidation is an effective approach to enhancing the responsivity. The responsivity can be further improved by decreasing the optical power as well as increasing the illumination time. Such a highly responsive operation could be useful for image sensors and optical memory.

5 Conclusions

In this review, we showed that the surface oxide can be used to boost the performance of atomically thin WSe_2-based electronic and optoelectronic devices. The surface oxides serve as p-type contacts and surface dopants for atomically thin WSe_2 transistors. Thus, surface-oxidized WSe_2 transistors show high hole conductivity and mobility. Additionally, the surface oxides serve as effective electron traps to facilitate the photogating effect in atomically thin WSe_2-based photodetectors. Owing to the photogating effect, the WSe_2 photodetector has a large responsivity. Surface oxidation is a ubiquitous phenomenon in atomically thin semiconductors and, hence, this methodology is expected to be applied to other atomically thin semiconductor-based devices [41–43].

Acknowledgements We would like to thank K. Ueno, M. S. Fuhrer, K. Wakabayashi, S. Nakaharai, S. Aikawa, and S. Dutta for their substantial contributions to these work. This work was partly supported by JSPS KAKENHI (Grant Nos. 18K18868 and 17K14658).

References

1. Geim AK (2009) Graphene: status and prospects. Sci 324:1530–1534
2. Butler SZ et al (2013) Progress, challenges, and opportunities in two-dimensional materials beyond graphene. ACS Nano 7:2898–2926
3. Bhimanapati GR et al (2015) Recent advances in two-dimensional materials beyond graphene. ACS Nano 9:11509–11539
4. Kou L, Chen C, Smith SC (2015) Phosphorene: fabrication, properties, and applications. J Phys Chem Lett 6:2794–2805
5. Wang QH, Kalantar-Zadeh K, Kis A, Coleman JN, Strano MS (2012) Electronics and optoelectronics of two-dimensional transition metal dichalcogenides. Nat Nanotechnol 7:699–712
6. Chhowalla M et al (2013) The chemistry of two-dimensional layered transition metal dichalcogenide nanosheets. Nat Chem 5:263–275
7. Jariwala D, Sangwan VK, Lauhon LJ, Marks TJ, Hersam MC (2014) Emerging device applications for semiconducting two-dimensional transition metal dichalcogenides. ACS Nano 8:1102–1120
8. Mak KF, Lee C, Hone J, Shan J, Heinz TF (2010) Atomically thin MoS_2: a new direct-gap semiconductor. Phys Rev Lett 105:2–5
9. Splendiani A et al (2010) Emerging photoluminescence in monolayer MoS_2. Nano Lett 10:1271–1275
10. Ruppert C, Aslan OB, Heinz TF (2014) Optical properties and band gap of single- and few-layer $MoTe_2$ crystals. Nano Lett 14:6231–6236

11. Radisavljevic B, Radenovic A, Brivio J, Giacometti V, Kis A (2011) Single-layer MoS_2 transistors. Nat Nanotechnol 6:147–150
12. Lopez-Sanchez O, Lembke D, Kayci M, Radenovic A, Kis A (2013) Ultrasensitive photodetectors based on monolayer MoS_2. Nat Nanotechnol 8:497–501
13. Yin Z et al (2012) Single-layer MoS_2 phototransistors. ACS Nano 6:74–80
14. Baugher BWH, Churchill HOH, Yang Y, Jarillo-Herrero P (2014) Optoelectronic devices based on electrically tunable p-n diodes in a monolayer dichalcogenide. Nat Nanotechnol 9:262–267
15. Ross JS et al (2014) Electrically tunable excitonic light-emitting diodes based on monolayer WSe_2 p-n junctions. Nat Nanotechnol 9:268–272
16. Pospischil A, Furchi MM, Mueller T (2014) Solar-energy conversion and light emission in an atomic monolayer p-n diode. Nat Nanotechnol 9:257–261
17. Allain A, Kang J, Banerjee K, Kis A (2015) Electrical contacts to two-dimensional semiconductors. Nat Mater 14:1195–1205
18. Xu Y et al (2016) Contacts between two- and three-dimensional materials: ohmic, Schottky, and p-n heterojunctions. ACS Nano 10:4895–4919
19. Das S, Chen HY, Penumatcha AV, Appenzeller J (2013) High performance multilayer MoS_2 transistors with scandium contacts. Nano Lett 13:100–105
20. Liu W et al (2013) Role of metal contacts in designing high-performance monolayer n-type WSe_2 field effect transistors. Nano Lett 13:1983–1990
21. Gong C, Colombo L, Wallace RM, Cho K (2014) The unusual mechanism of partial fermi level pinning at metal-MoS_2 interfaces. Nano Lett 14:1714–1720
22. Kang J, Liu W, Sarkar D, Jena D, Banerjee K (2014) Computational study of metal contacts to monolayer transition-metal dichalcogenide semiconductors. Phys Rev X 4:031005
23. Fang H et al (2013) Degenerate n-doping of few-layer transition metal dichalcogenides by potassium. Nano Lett 13:1991–1995
24. Fang H et al (2012) High-performance single layered WSe_2 p-FETs with chemically doped contacts. Nano Lett 12:3788–3792
25. Kiriya D, Tosun M, Zhao P, Kang JS, Javey A (2014) Air-stable surface charge transfer doping of MoS_2 by benzyl viologen. J Am Chem Soc 136:7853–7856
26. Yang L et al (2014) Chloride molecular doping technique on 2D materials: WS_2 and MoS_2. Nano Lett 14:6275–6280
27. Yamamoto M et al (2015) Self-limiting layer-by-layer oxidation of atomically thin WSe_2. Nano Lett 15:2067–2073
28. Yamamoto M, Nakaharai S, Ueno K, Tsukagoshi K (2016) Self-limiting oxides on WSe_2 as controlled surface acceptors and low-resistance hole contacts. Nano Lett 16:2720–2727
29. Yamamoto M, Ueno K, Tsukagoshi K (2018) Pronounced photogating effect in atomically thin WSe_2 with a self-limiting surface oxide layer. Appl Phys Lett 112:181902
30. Meyer J et al (2012) Transition metal oxides for organic electronics: energetics, device physics and applications. Adv Mater 24:5408–5427
31. Chuang S et al (2014) MoS_2 p-type transistors and diodes enabled by high work function MoO_x contacts. Nano Lett 14:1337–1342
32. Yamamoto M, Einstein TL, Fuhrer MS, Cullen WG (2013) Anisotropic etching of atomically thin MoS_2. J Phys Chem C 117:25643–25649
33. Wu J et al (2013) Layer thinning and etching of mechanically exfoliated MoS_2 nanosheets by thermal annealing in air. Small 9:3314–3319
34. Zhou H et al (2013) Thickness-dependent patterning of MoS_2 sheets with well-oriented triangular pits by heating in air. Nano Res 6:703–711
35. Das S, Appenzeller J (2013) WSe_2 field effect transistors with enhanced ambipolar characteristics. Appl Phys Lett 103:103501
36. Furchi MM, Polyushkin DK, Pospischil A, Mueller T (2014) Mechanisms of photoconductivity in atomically thin MoS_2. Nano Lett 14:6165–6170
37. Buscema M et al (2015) Photocurrent generation with two-dimensional van der Waals semiconductors. Chem Soc Rev 44:3691–3718

38. Zhang W et al (2013) High-gain phototransistors based on a CVD MoS_2 monolayer. Adv Mater 25:3456–3461
39. Late DJ, Liu B, Matte HSSR, Dravid VP, Rao CNR (2012) Hysteresis in single-layer MoS_2 field effect transistors. ACS Nano 6:5635–5641
40. Watanabe K (1996) Dependence of effective carrier lifetime in iron-doped silicon crystals on the carrier injection level. Semicond Sci Technol 11:1713–1717
41. Mleczko MJ et al (2017) $HfSe_2$ and $ZrSe_2$: two-dimensional semiconductors with native high-κ oxides. Sci Adv 3:e1700481
42. Shim J et al (2016) High-performance 2D rhenium disulfide (ReS_2) transistors and photodetectors by oxygen plasma treatment. Adv Mater 28:6985–6992
43. Ho PH et al (2017) High-mobility InSe transistors: the role of surface oxides. ACS Nano 11:7362–7370

Portable Toxic Gas Sensors Based on Functionalized Carbon Nanotubes

Shinsuke Ishihara

1 Introduction

Toxic chemicals, particularly in the gaseous phase, can spread to large areas and cause serious harm to many people. Toxic gas sensors can recognize the presence of toxic gases at an early stage (even if the gas is odorless), which can improve public safety, security, and health. The broad adoption of toxic gas sensors can be achieved by developing sensitive, selective, and low-cost sensors that can be interfaced with portable electronic devices, and material design is the key factor for the development of such advanced life-saving sensors. Among various types of detection mechanisms (e.g., optical, electronic, spectroscopic), chemiresistive sensors, which monitor the variation of electric conductivity in semiconducting materials (e.g., metal-oxides, π-conjugate polymers, carbon materials) in response to chemical substances, have attracted great interest due to the capability of preparing low cost and portable sensing devices [1]. Chemiresistive materials based on metal-oxides (e.g., SnO_2) are practically utilized in gas sensors over decades, however, such conventional gas sensors consume a lot of energy for heating of metal-oxides around 200–400 ℃ (metal-oxides are insulating at room temperature). Recently, nanostructured carbon materials, particularly single-walled carbon nanotubes (SWCNTs) [2], attract great interests as a chemiresistive material since SWCNTs are conducting at room temperature. SWCNT can be formed by rolling one graphene sheet, and depending on the way of rolling, a varieties of SWCNTs with different diameter and chirality can be generated. Electric properties of SWCNTs depend on the their chirality (i.e., how graphene sheet was rolled-up), and demonstrate either metallic or semiconducting behaviors. Since as-prepared SWCNTs are mixture of metallic (1/3) and semiconducting (2/3)

S. Ishihara (✉)
Frontier Molecules Group, International Center for Materials Nanoarchitectonics (WPI-MANA), National Institute for Materials Science (NIMS), 1-1 Namiki, Tsukuba 305-0044, Ibaraki, Japan
e-mail: ISHIHARA.Shinsuke@nims.go.jp

Y. Wakayama and K. Ariga (eds.), *System-Materials Nanoarchitectonics*, NIMS Monographs, https://doi.org/10.1007/978-4-431-56912-1_10

ones, isolation of semiconducting SWCNTs is also an important research topic for development of high performance electric devices (sensors, transistors, etc.) [2].

In this chapter, some recent examples of single-walled carbon nanotube (SWCNT)-based toxic gas sensors by the author and coworkers are briefly introduced (see other literatures [3–6] for comprehensive review of SWCNT-based chemical sensors). As mentioned above, SWCNTs are ideal chemiresistive materials that perform at room temperature, in contrast to metal oxide-based semiconducting materials, which require heating at a temperature above 200 °C [2]. Moreover, high chemical stability of SWCNTs is advantageous for operation under harsh environments. In general, toxic gases can be classified into two categories based on their effects, namely, acute toxicity and chronic toxicity. For toxic gases with acute toxicity, sensors should have a prompt response so that the health hazard can be avoided and/or minimized as soon as possible. For toxic gases with chronic toxicity, a prompt response may not be so important, but sensors must be highly sensitive so that trace amounts (usually, sub-ppm or lower) of toxic gases can be detected. A key in research is the design of an SWCNT-based chemiresistor for the sensitive and selective detection of the target analyte, through decoration of SWCNTs with other materials (e.g., molecules, polymers, metals, metal oxides) either by covalent or non-covalent ways.

As a typical example of a sensor for detecting gases with acute toxicity, a nerve agent sensor based on metallo-supramolecular polymer (MSP)-wrapped SWCNTs is discussed. The cooperative π-π interaction between the MSP and the SWCNT surface is effectively utilized to amplify and transduce molecular-scale chemical events (depolymerization of the MSP by the nerve agent) to a macroscopic electric response (change in the electric conductivity of the SWCNT network). Then, an SWCNT-based formaldehyde sensor is reviewed as an example of a sensor for detecting gases with chronic toxicity (e.g., allergens and carcinogens). Chemical compounds that selectively react with formaldehyde are combined with this SWCNT-based detector. Finally, the combination of SWCNT-based toxic gas sensors with near-field communication (NFC) technology is discussed regarding the broad adoption of toxic gas sensors in public. A wireless sensing system will enable the detection of toxic gases using commercially available smartphones.

2 SWCNT-Based Chemical Sensor

2.1 Detection of Nerve Agent

Nerve agents have fatal acute toxicity and could be used in a terrorist attack and/or civil war. However, they are basically slow-acting, and their detection at an early stage of exposure enables the use of antidotes (e.g., pralidoxime methiodide, atropine). In addition, most nerve agents can be deactivated through hydrolysis. Regardless of the gas, detection is the first step. Our strategy for the sensitive and selective detection of nerve agents (e.g., sarin) is to wrap SWCNTs with an insulating polymer that

can be selectively disassembled (in other words, depolymerized) in response to the target analyte gases (Fig. 1a) [7]. Thus, we have designed an MSP that is connected through square planar metal–ligand complexes, enabling the alignment of anthracene π-aromatic units in the same plane (Fig. 1b). Aligned anthracenes can be adhered on the surface of SWCNTs through cooperative π-π interactions, while in turn, the individual ligand monomers do not effectively interact with the SWCNTs owing to the weakness of the individual π-π interactions (compared with the π-π interactions between SWCNTs). The SWCNT network wrapped by the MSP is electronically insulated because the MSP wrappers are located at the junctions of the SWCNT network. Connections in MSPs can be cleaved by strong acids. In addition, we have introduced oxime units (which are strong nucleophiles due to the α-effect) in the ligands, so that the polymers can also be sensitively cleaved by electrophiles (note that a nerve agent has a leaving group for binding with the serine moiety (OH group)

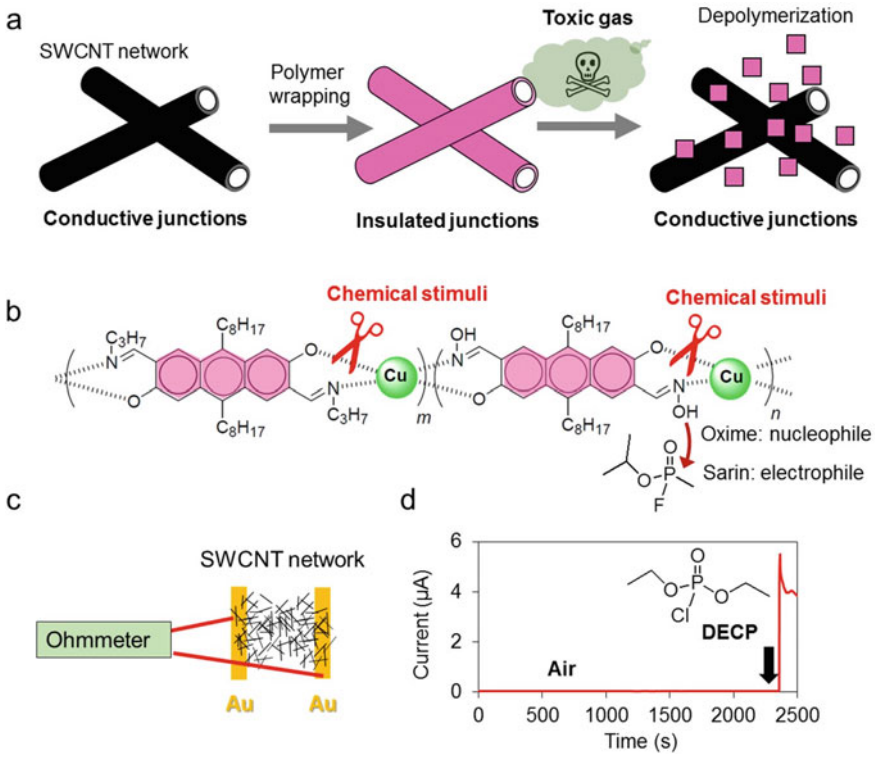

Fig. 1 **a** Triggered disassembly of MSP-based SWCNT wrapper for amplifying and transducing molecular-scale chemical reactions to electric response. **b** Design of MSP connected through noncovalent interactions that can be cleaved by chemical stimuli including strong acids and/or electrophiles. **c** Monitoring of electric response in SWCNT-based chemical sensor using simple and low-cost device. **d** Strong electric response of MSP-wrapped s-SWCNTs for DECP vapor. Data *Source* Reference [7, 8]

in acetylcholinesterase). As a result of the depolymerization of the MSP by the nerve agent, the electric conductivity of the SWCNT network is markedly increased through better electric contact at the SWCNT junctions. This electric transition in the SWCNT network can be easily monitored by low-cost devices such as ohmmeters (Fig. 1c). MSP-wrapped SWCNTs show an amplified and time-accumulated increase in electrical conductivity (up to 30-fold increase in conductivity) when exposed to a ppm-level nerve agent simulant (diethylechlorophosphate, DECP). The response is basically irreversible, so the dose (i.e., concentration × time) of DECP can be evaluated from the response, which is beneficial for discriminating heavily exposed patients.

It is known that as-prepared SWCNTs are a mixture of semiconducting and metallic tubes, and the use of separated SWCNTs could improve sensing performance. We used purified semiconducting-SWCNTs (s-SWCNTs) to create an MSP-wrapped s-SWCNT sensor [8]. Purified s-SWCNTs can be isolated from as-prepared SWCNTs at the gram scale using chromatography [9]. As expected, the MSP-wrapped s-SWCNT sensor demonstrated a higher sensitivity (up to 100-fold higher in conductivity) in response to DECP (Fig. 1d), and ppm-level DECP could be discriminated in 5 s. This sensor also showed excellent selectivity, and its response to other volatile organic compounds (VOCs) and changes in temperature were much smaller than that to DECP.

2.2 Detection of Formaldehyde

Formaldehyde (HCHO) is a common indoor air pollutant that potentially causes asthma, dermatitis, and cancer. There are established methodologies to monitor formaldehyde in air, such as colorimetric methods (e.g., detection tubes) and high-pressure liquid chromatography (HPLC). However, these methods require expensive instruments or manual sampling. Such formaldehyde sensors can therefore be regarded as "detect to treat" sensors. Usually, these sensors are employed after symptoms of sickness have already appeared. In contrast, "detect to warn" sensors continuously monitor toxic chemicals and can provide an alert before symptoms of sickness appear. Thus, these chemical sensors are highly in demand for improving safety, security, and health in public. The World Health Organization (WHO) recommends an indoor concentration of formaldehyde of less than 0.08 ppm, and the detection of such a trace amount of a chemical using a small and low-cost sensor is challenging.

We developed a "detect to warn" formaldehyde sensor in combination with a formaldehyde selector (hydroxylamine hydrochloride) and an s-SWCNT-based detector (Fig. 2a) [10]. Hydroxylamine hydrochloride undergoes a condensation reaction with formaldehyde, leading to the emission of trace HCl vapor. HCl vapor can be detected by a chemiresistor based on an s-SWCNT network since the conductivity of s-SWCNTs is very sensitive to hole dopants such as HCl. The sensing response is easily read out as an increase in the conductivity of the SWCNT network. The limit of detection (LoD) of the sensor was estimated to be 0.016 ppm, which

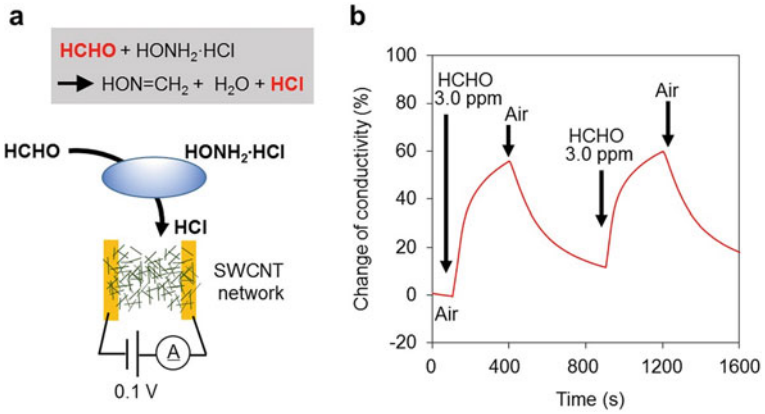

Fig. 2 **a** Formaldehyde sensor based on hydroxylamine hydrochloride and s-SWCNT-based electrodes. **b** Reversible response to 3.0 ppm formaldehyde (HCHO) in air (relative humidity = 37%). Data *Source* Ref. [10]

is sufficient for detecting the WHO-recommended concentration (0.08 ppm). The condensation reaction between formaldehyde and hydroxylamine hydrochloride is irreversible. However, because the amount of hydroxylamine hydrochloride loaded in the sensory system is much larger than the ppm-order amount of formaldehyde, the sensor practically shows a reversible response (Fig. 2b). The selectivity to formaldehyde is $5-6$ orders of magnitude higher than that to other VOCs such as methanol, ethanol, and toluene.

2.3 Detection of Toxic Gases Using Smartphone and NFC Tags

One advantage of SWCNT-based toxic gas sensors is that the sensing response can be easily read out as an electric signal using low-cost electric devices (such as an ohmmeter) without complicated signal transduction. Toward the broad adoption of toxic gas sensors in society, we demonstrate the utility of an SWCNT-based toxic gas sensor in a wirelessly powered sensing system based on a near-field communication (NFC) tag (Fig. 3a) [7, 11, 12] An SWCNT-based chemiresistor is inserted within the electric circuit of a commercially available NFC tag. First, we created a turn-on sensor, in which an unreadable tag became readable with an NFC tag reader after the exposure to a toxic gas reached a certain dose (Fig. 3b). Specifically, a commercially available smartphone was utilized as the NFC reader, and a ppm level of a toxic gas could be detected by the smartphone with an attached SWCNT-modified NFC tag. Alternatively, we created a turn-off sensor by changing the location where the SWCNT sensor was inserted (Fig. 3c). In this case, the readable NFC tag became unreadable after exposure to a toxic gas. The cost of an NFC tag is quite low (less

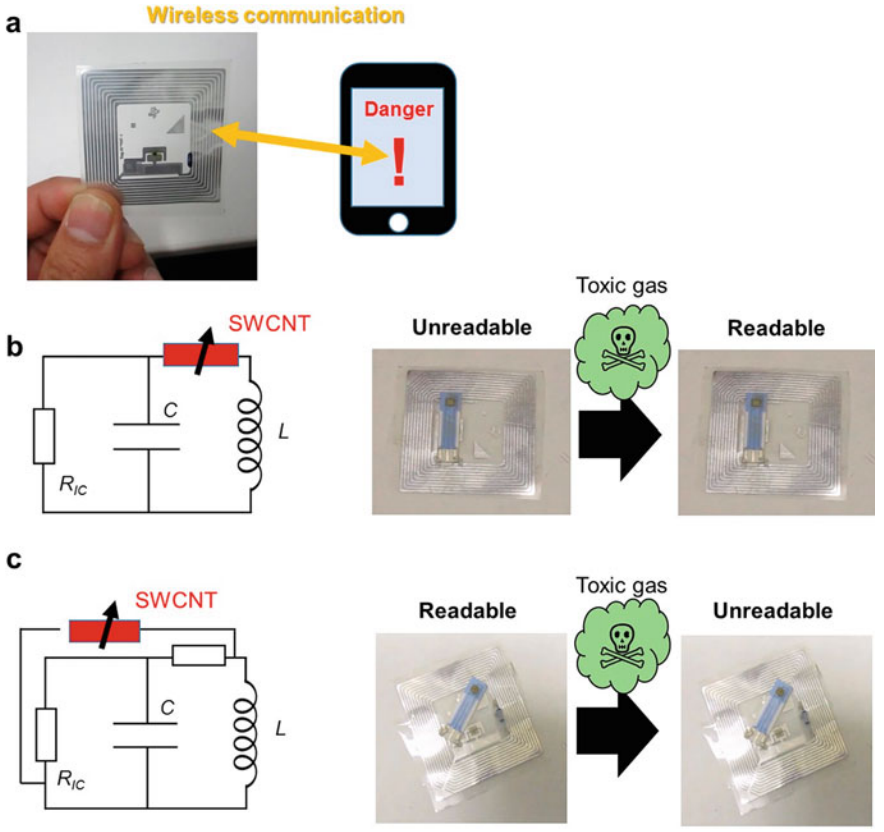

Fig. 3 **a** Photograph and circuit of NFC tag. The NFC tag interacts with a commercially available smartphone using inductively powered wireless communication. **b** Turn-on sensor using NFC tag and SWCNT sensor. **c** Turn-off sensor using NFC tag and SWCNT sensor. Data *Source* Ref. [7]

than 0.5 USD) and only a trace amount of SWCNTs (ca. 1 μg) is used in each sensor. Moreover, users do not need to purchase a costly device for the detection of toxic gases.

3 Summary

Low-cost, portable, and internet-connected chemical sensors based on modified SWCNTs and NFC tags have been created. Once chemical information is converted to an electrical response (e.g., resistance change), a broad range of toxic gases can be detected by low-cost electric devices such as NFC tags and smartphones. For this purpose, a key factor is the design of an SWCNT-based chemiresistor for the sensitive and selective detection of the target analyte. Big data obtained from many

different types of sensors can be monitored, accumulated, and analyzed in real time, and such sensor network technology should improve public safety and security. We expect to create broad families of highly sensitive and selective toxic gas sensors towards this goal.

Acknowledgements These works were partly supported by World Premier International (WPI) Research Center Initiative on Materials Nanoarchitectonics (MANA) from Japan Society for the Promotion of Science (JSPS), National Science Foundation (DMR-1410718), JSPS KAKENHI (grant no. 18H02016, 25220602), and a JSPS Fellowship for Research Abroad. The author would like to thank all collaborators involved in the study.

References

1. Neri G (2015) First fifty years of chemoresistive gas sensors. Chemosensors 3:1–20
2. Samanta SK, Fritsch M, Scherf U, Gomulya W, Bisri SZ, Loi MA (2014) Conjugated polymer-assisted dispersion of single-wall carbo nanotubes: the power of polymer wrapping. Acc Chem Res 47:2446–2456
3. Snow ES, Perkins FK, Robinson JA (2006) Chemical vapor detection using single-walled carbon nanotubes. Chem Soc Rev 35:790–798
4. Kauffman DR, Star A (2008) Carbon nanotube gas and vapor sensors. Angew Chem Int Ed 47:6550–6570
5. Fennell JF, Liu SF, Azzarelli JM, Weis JG, Rochat S, Mirica KA, Ravnsbæk JB, Swager TM (2016) Nanowire chemical/biological sensors: status and a roadmap for the future. Angew Chem Int Ed 55:1266–1281
6. Schroeder V, Savagatrup S, He M, Lin S, Swager TM (2019) Carbon nanotube chemical sensors. Chem Rev 119:599–663
7. Ishihara S, Azzarelli JM, Krikorian M, Swager TM (2016) Ultratrace detection of toxic chemicals: triggered disassembly of supramolecular nanotube wrappers. J Am Chem Soc 138:8221–8227
8. Ishihara S, O'Kelly CJ, Tanaka T, Kataura H, Labuta J, Shingaya Y, Nakayama T, Ohsawa T, Nakanishi T, Swager TM (2017) Metallic versus semiconducting SWCNT chemiresistors: a case for separated SWCNTs wrapped by metallo-supramolecular polymer. ACS Appl Mater Interfaces 9:38062–38067
9. Yomogida Y, Tanaka T, Zhang M, Yudasaka M, Wei X, Kataura H (2016) Industrial-scale separation of high-purity single-chirality single-wall carbon nanotubes for biological imaging. Nat Commun 7:12056
10. Ishihara S, Labuta J, Nakanishi T, Tanaka T, Kataura H (2017) Amperometric detection of sub-ppm formaldehyde using SWCNTs and hydroxylamines: a referenced chemiresistive system. ACS Sensors 2:1405–1409
11. Azzarelli JM, Mirica KA, Ravnsbæk JB, Swager TM (2014) Wireless gas detection with a smartphone via rf communication. Proc Natl Acad Sci U. S. A. 111:18162–18166
12. Swager TM, Azzarelli JM, Ishihara S, Dynamic resonant circuits for chemical and physical sensing with a reader and RFID tags. US Patent Application No. US20180224443A1

Advanced Nanomechanical Sensor for Artificial Olfactory System: Membrane-Type Surface Stress Sensor (MSS)

Huynh Thien Ngo, Kosuke Minami, Kota Shiba, and Genki Yoshikawa

1 Introduction

The smells/odors that we experience daily are known to be constituted by over 400,000 types of molecules [1]. In most cases, we experience the sensation of a single smell/odor as a simultaneous interaction of hundreds to thousands of different types of molecules with our olfactory receptors. Such complexity of smells/odors inhibits the efficient development of artificial olfactory sensors. In contrast to other sensors that perceive physical stimuli (e.g., sound (ear), light (eye), and pressure (skin)) and have been comprehensively investigated and developed, olfactory sensors have not been practically commercialized because of the complex perception mechanism of olfaction and the lack of a comprehensive understanding of the chemical interactions between the receptors and the analytes.

H. T. Ngo · K. Minami · K. Shiba · G. Yoshikawa (✉)
Center for Functional Sensor and Actuator, Research Center for Functional Materials, National Institute for Materials Science (NIMS), 1-1 Namiki, Tsukuba 305-0044, Ibaraki, Japan
e-mail: YOSHIKAWA.Genki@nims.go.jp

International Center for Materials Nanoarchitectonics (WPI-MANA), National Institute for Materials Science (NIMS), 1-1 Namiki, Tsukuba 305-0044, Ibaraki, Japan

K. Minami
e-mail: MINAMI.Kosuke@nims.go.jp

K. Shiba
e-mail: SHIBA.Kota@nims.go.jp

K. Minami
International Center for Young Scientists (ICYS), National Institute for Materials Science (NIMS), 1-1 Namiki, Tsukuba 305-0044, Ibaraki, Japan

G. Yoshikawa
Materials Science and Engineering, Graduate School of Pure and Applied Science, University of Tsukuba, 1-1-1 Tennodai, Tsukuba 305-8571, Ibaraki, Japan

Y. Wakayama and K. Ariga (eds.), *System-Materials Nanoarchitectonics*,
NIMS Monographs, https://doi.org/10.1007/978-4-431-56912-1_11

Gas chromatography combined with mass spectrometry (GC/MS) is one of the standard techniques to analyze smells/odors. It allows the isolation and quantification of most compounds making up smells/odors. This approach can provide molecular information, but the obtained data require specific handling by experts, and the expensive/large instruments prevent this approach from being applied to everyday use. Moreover, without careful condensation/extraction processes, GC/MS could miss some odorous molecules with concentrations below ppm level. Hence, it is still challenging to achieve cost efficiency and compactness together with high sensitivity and selectivity at the same time in a single device for the detection of an odor composed of various types of molecules.

Olfactory sensors could be an effective approach to tackle this problem. They measure each smell as a single sample without the separation of its components. In the last few decades, significant attention was directed to sensor arrays comprising multiple sensing elements with diverse chemical selectivity. Such arrays are called an "electronic nose" or "artificial olfaction" as they mimic the mammalian smelling process. The recent achievements in the size reduction of sensor elements and outer electronic components have advanced the olfactory sensor technology towards mobile and Internet of Things (IoT)-type applications.

Nanomechanical sensors are one of the promising technologies for olfactory sensors. They detect volume- and/or mass-induced mechanical changes of a sensing unit. Such mechanical changes caused by the adsorption/desorption of target analytes are transduced into electric signals. Therefore, a nanomechanical sensor can be considered as a mechanical transducer with nanometer precision. In 1994, Gimzewski and coworkers reported the first chemical sensing application using a nanomechanical cantilever sensor [2]. They employed the static bending of a cantilever to monitor the catalytic reaction taking place on the surface of the cantilever. Many research groups have demonstrated that nanomechanical sensors can be used to detect a variety of targets and phenomena, i.e., mercury vapor [3], formation of self-assembled monolayers [4], and hybridization of DNA [5]. Here, we focus on a specific nanomechanical sensor with superior performance: a Membrane-type Surface stress Sensor (MSS).

2 Membrane-Type Surface Stress Sensor (MSS)

The MSS is an optimized nanomechanical sensor technology operated in a so-called static mode [6–9]. It is constructed as a thin silicon membrane suspended by four sensing bridges, in which piezoresistors are embedded. The receptor layer coated on the membrane interacts with analytes, causing a deformation of the receptor layer. This deformation generates surface stress on the membrane. The piezoresistors allow highly sensitive electric readouts of stress/strain induced by the sorption of gas molecules in the receptor layer. The piezoresistors efficiently transduce these stresses into electric signals.

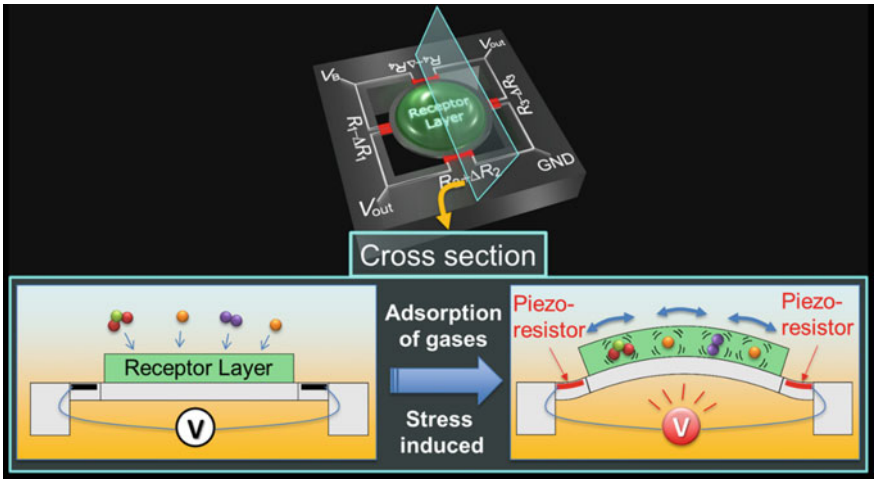

Fig. 1 Schematic illustration of MSS (top). Working principle of MSS (bottom). The sorption of gaseous molecules on a receptor layer coated on the center membrane of the MSS induces surface stress, which is electrically detected by the piezoresistors (resistances change with mechanical stress) embedded on the narrow supporting beams

Originally, the low sensitivity of the piezoresistor-based electric readout was a huge disadvantage, but the small size of the device is an attractive feature over the more sensitive conventional optical readout cantilever sensors that require larger equipment. After the comprehensive optimization in collaboration with Dr. Heinrich Rohrer and with Dr. Terunobu Akiyama [10], Dr. Peter Vettiger, and their colleagues in the MEMS team at École Polytechnique Fédérale de Lausanne (EPFL), Yoshikawa developed an MSS that realizes both high sensitivity and miniaturization at the same time (Fig. 1) [6]. This optimized structure permits the highly sensitive electric readouts of stress/strain of the receptor layer induced by the sorption of gaseous molecules. In addition to the high sensitivity (with the detection limit reaching 0.1 mN/m), the MSS also has high electric/mechanical stability (with self-compensation by a full Wheatstone bridge), a simple coating procedure of the various receptor materials, low cost, a compact system, fast response, and the capability of mass production. Therefore, the MSS is a prime candidate for an olfactory sensing system for daily use.

3 Receptor Materials

The potential applications of gas sensors cover a wide range of industries: food, agriculture, cosmetics, medicine, and so forth. This also requires high versatility of the sensors because the sensors must exhibit different selectivity and sensitivity to

distinctive gases for each application. It has been observed that almost all solid materials show mechanical deformation upon gas sorption. Therefore, the MSS can detect diverse analytes when various types of materials are used as a receptor layer: polymers, inorganic and organic materials, or their hybrids. The selection of the receptor materials is based on the selectivity and sensitivity of the materials toward the target analytes. Such sensitivity and selectivity depend on the physical and chemical interactions between the receptor materials and the analytes: i.e. van der Waals interactions, π-π stacking, hydrogen bonds, etc. Moreover, the interactions at the interface between the receptor materials and the silicon membrane also play a significant role. Depending on the interface interactions and membrane area coverage, sensitivity can be varied. Minami and coworkers investigated this tendency by numerical calculations of the various interfacial attachment models through FEA using COMSOL Multiphysics® 5.4 with the Structural Mechanics module [11].

The receptor material properties, particularly Young's modulus and thickness, will determine the sensitivity of nanomechanical sensors as formulated by Yoshikawa [12]. To optimize the thickness and Young's modulus of a receptor layer, we need an analytical model that describes the relationship between the deflection of a cantilever and the various physical parameters of the cantilever itself and the receptor layer on it. Timoshenko's beam theory [13] was originally developed to analyze a bimetal strip but can be utilized as an analytical model for the static deflection of a cantilever-type sensor coated with a solid layer. For a simple cantilever coated with a solid receptor layer, the deflection of the cantilever (Δz) is described as follows [12]:

$\Delta z = \frac{3l^2(t_f+t_c)}{(A+4)t_f^2+(A^{-1}+4)t_c^2+6t_f t_c}\varepsilon_f$, $A = \frac{E_f w_f t_f(1-\nu_c)}{E_c w_c t_c(1-\nu_f)}$	E_f = Young's modulus of receptor layer ν_f = Poisson's ratio of receptor layer t_f = thickness of receptor layer w_f = width of receptor layer E_c = Young's modulus of cantilever ν_c = Poisson's ratio of cantilever t_c = thickness of cantilever w_c = width of cantilever

This model tells us that the optimum thickness of a receptor layer depends on its Young's modulus. This optimum coating thickness is a specific value where the additional stiffness due to the additional thickness of the coating film becomes dominant over the effective force induced in the entire coating film.

As shown in Fig. 2, there is a general trend of higher sensitivity with stiffer materials having an appropriate thickness. Inorganic nanoparticles are one of the most promising candidates as stiff materials because of their stability and easy functionalization. As a proof of concept, various nanoparticles with different surface functionalities were synthesized (Fig. 3, left) and used for the MSS. The discrimination of various vapors from 23 different chemicals (Fig. 3, right) was demonstrated. Principal component analysis (PCA) displayed well-separated clusters of different species according to their chemical functional groups: alcohols, ketones, alkanes, aromatic compounds, and so forth. This shows the superior performance of the inorganic nanoparticles as nanomechanical sensing materials.

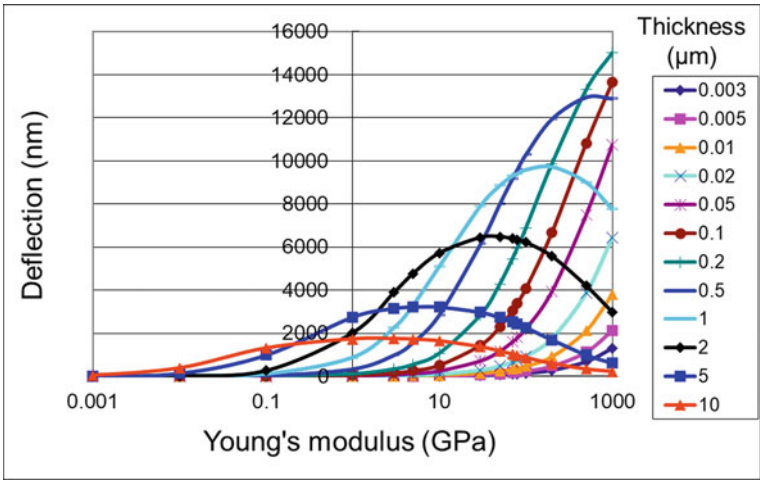

Fig. 2 Deflection of a cantilever operated in static mode as a function of Young's modulus and thickness of receptor layer

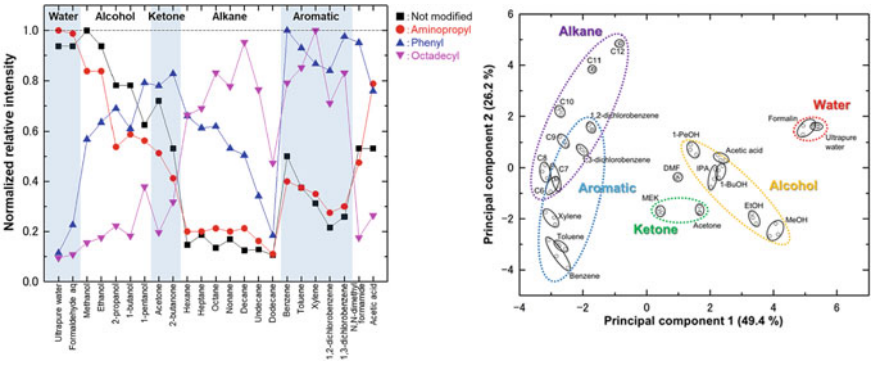

Fig. 3 Sensitivity to different gases of the nanoparticles containing different surface modifications (left). PCA of the 23 different gases categorized with their functional groups (right)

In addition to the characteristic stiffness, another important property that affects sensitivity is the nanostructural morphology of the receptor material. High surface area and porosity can be effective to enhance the controlled adsorption/desorption process of gas molecules. Shiba and coworkers established a synthetic procedure to prepare metal-oxide-based porous nanoparticles with extremely high monodispersity [14]. To enhance the versatility of the nanoparticles, one can combine inorganic nanoparticles with an organic material. The latter lacks chemical stability but offers a rich chemistry to a specific analyte and easy modification of the molecular functionality. To combine the advantage of both systems, porous inorganic nanoparticles

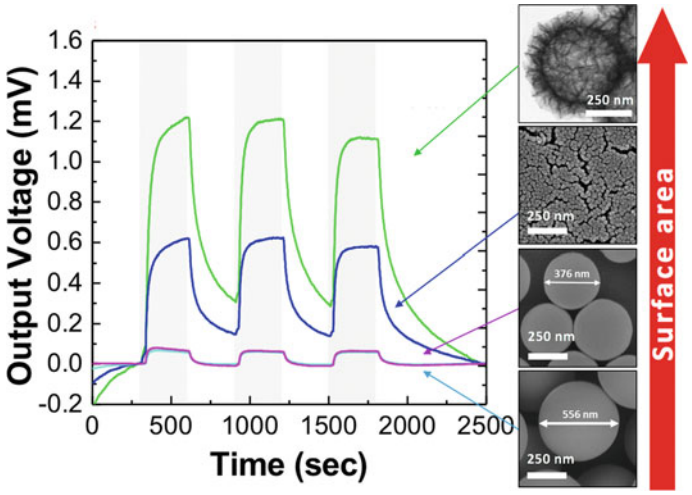

Fig. 4 Sensing signal intensity of the nanoparticles functionalized with a metalloporphyrin. Sensitivity increases with higher porosity and surface area

were decorated with organic functionalities on the surface as a useful receptor material platform. One example is a silica flake shell with a metalloporphyrin on its surface (Fig. 4) [15]. This receptor material detects acetone at a low concentration of 50 ppm with a high signal-to-noise ratio. Figure 4 shows the general tendency of the enhancement of sensitivity to acetone owing to the large surface area of the receptor materials.

Porosity and surface area provide a physical approach to enhance the sensitivity of sensor materials. To investigate the chemical aspect, we have recently focused on single complex molecular systems such as porphyrinoids. Ngo et al. reported metalloporphines as receptor materials for the MSS with selectivity and high robustness to humidity (Fig. 5) [16]. Porphine is the central molecular structure of porphyrins—a porphyrin without substituents. By employing a porphine and metalloporphines, they can omit the effects of peripheral substituents and concentrate on the individual effect of the center metal ions and the central polypyrrole macrocycle on gas uptake. The sensitivity can be adjusted at the atomic scale by changing a single central metal atom. The insertion of a metal into the porphine core leads to substantial changes in sensitivity, following the different coordination preferences of the axial guest molecules to the center metal ions in the porphine. The gas-sensing properties of four porphine derivatives, i.e., free-base porphine, nickel porphine, zinc porphine, and iron porphine, were measured. Nickel and zinc insertion into porphines gave rise to equivalent or less sensitivity than that of the free-base porphine, whereas iron porphine exhibited enhanced sensitivity because of its strong capability to bind ligands. Interestingly, in this study, they also demonstrated the high-humidity-resistant sensing capability of iron porphine. Even under a highly humidified condition (70% relative

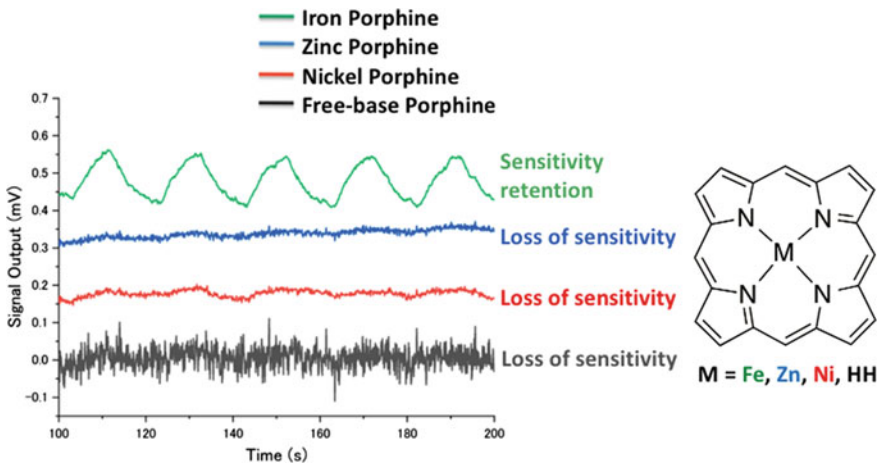

Fig. 5 Structure of metalloporphine derivatives (right). Sensing signals of metalloporphine derivatives to propionic acid gas (19 ppm) at 70% RH (left)

humidity (RH)), iron porphine could clearly detect propionic acid vapor at a concentration of as low as 19 ppm. This study can serve as a reference for future studies where the effect of metals on the materials properties in porphyrinoids plays a vital role in sensing performance, leading to advanced sensing applications, including receptor materials for an artificial olfactory sensor system in ambient environment.

The two above mentioned examples demonstrate that the surface area of the receptor materials and the relative humidity strongly affect the sensitivity. By detailed modification of the material morphology and molecular structure, the sensitivity can be controlled. Another parameter that plays an important role to determine the sensitivity is partial vapor pressure of the analytes. For gas–solid equilibrium-based gas sensors including MSS, it was confirmed that the signal intensity at the equilibrium state depends not on the volume concentration but on the partial pressure of the analytes. Thus, a decreasing partial vapor pressure of the analyte suppresses the signal intensity and induces the delay in the starting point of a signal response. This phenomenon influences the baseline of the signals. Using MSS, Minami and coworkers demonstrated that the limit of detection of ppt level could be reached when taking into account the signal to noise ratio [17].

4 Machine-Learning-Based Analysis

The extraction of specific information from smells/odors is extremely challenging because of their complex composition of thousands of chemicals with various concentrations. However, recent advancements in machine learning can be useful to unravel hidden patterns from the complexity of the obtained sensing data. Shiba and

coworkers applied machine learning to the MSS technology to predict the alcohol content of liquors based on their smells [18]. In this study, the MSS sensor array has four channels, each of which was coated with silica/titania hybrid nanoparticles with various surface functionalities. Because of the different chemical interactions of each sensor element in the sensor array to a smell, the signal output forms a unique pattern. On the basis of this pattern, they demonstrated that such a sensor array system combined with a machine learning technique can be utilized to derive quantitative information, such as alcohol content from smell. In this case, they used kernel ridge regression, which can be applied to a nonlinear problem while avoiding overfitting. This strategy led to the successful extraction of specific information. In Fig. 6, one can see that the model can predict the alcohol content of unknown samples with high accuracy on the basis of their smells. The accuracy can be further improved with increasing training data. Such an approach can be extended to a more detailed investigation of complex liquid samples, such as blood, coffee, and environmental water. Recently, the quantitative prediction of the concentration of each component in a ternary mixture has also been achieved through systematic material-design-based nanomechanical sensing combined with machine learning [19]. Ternary mixtures containing water, ethanol, and methanol with various concentrations were selected as a model system, where a target molecule coexists with structurally similar species

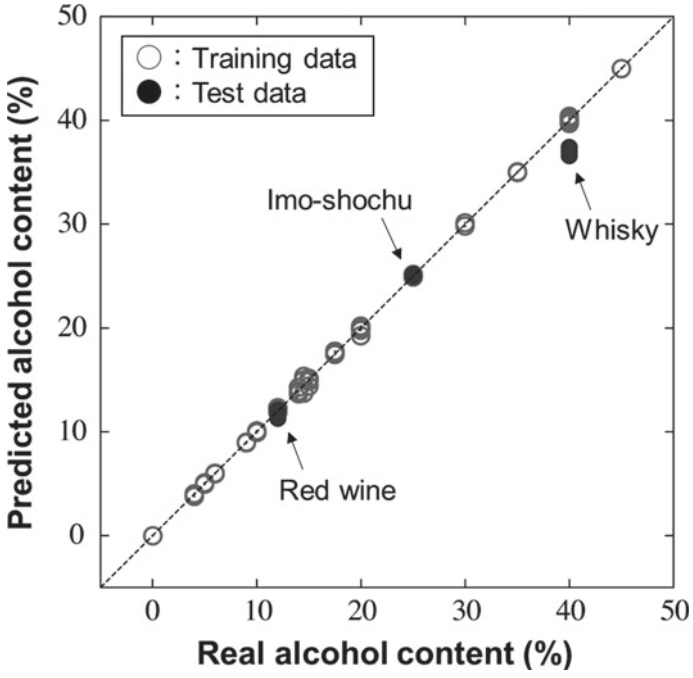

Fig. 6 Alcohol content prediction of liquors based on their smells: open and closed circles correspond to training and test data, respectively

under a humidified condition. The fine-tuning of the receptor materials based on the feedback obtained by the machine learning achieved higher prediction accuracy for each species [19].

5 Applications of Artificial Olfaction

MSS can detect almost all kinds of gaseous molecules because of its simple mechanism; the stress or deformation of the receptor layer induced by gas absorption is transduced into a measurable signal. The interpretation of the observed signal is a key to understanding the gas composition of the analytes. Imamura and coworkers have developed a parameter estimation protocol from sensing signals of a nanomechanical sensor coated with a viscoelastic material [20]. This study provides a method for MSS to differentiate similar gas mixtures. Moreover, the versatility of receptor materials that can be employed in the MSS system offers a diverse sensing platform that finds many applications in different industries, such as cosmetics, healthcare, medicine, food, agriculture, and environment.

One of the most advanced and challenging applications of artificial olfactory sensors is the monitoring of health conditions and medical diagnosis. Nowadays, healthcare strategies strongly emphasize noninvasive techniques for early diagnosis. For example, cancer is one of the most severe diseases in the world today with the highest mortality. Early diagnosis of cancer is vital to successful treatment, improving the survival rate of patients. Almost all of the current diagnoses rely on invasive methods for the detection of specific biomarkers in blood or endoscopy. It is known that some of the smells, including breath, sweat, and gases in urine and blood, change depending on patients' health conditions as well as their diseases. Hence, artificial olfaction may have the potential to contribute to the early diagnosis and detection of certain diseases as a noninvasive method based on the smell of patients' breath. Disease-related volatile organic compounds (VOCs) in patients' breath would exhibit only a slight difference, especially in the early stages of diseases. The MSS, with its high sensitivity, can be one of the candidates for detecting such traces. To demonstrate this concept, Loizeau and coworkers utilized an array of 16 MSS channels coated with 16 different polymers, which have various chemical/physical properties [21]. Each MSS sensing unit responds differently to the same analyte, creating a unique "pattern". Breath samples of both healthy people and head and neck cancer patients were analyzed in a double-blind trial. Tedlar bags were employed to transport the breath samples and were stored at a temperature of 4 °C for 5 h before analysis. Each sample was pumped into a gas chamber containing the functionalized MSS array. The sensors' responses were recorded six times and analyzed by PCA to reveal the differences between samples. The data showed clear differentiation between the breath samples of healthy persons and those of patients suffering from head and neck cancer (Fig. 7). In addition, when the cancer patients underwent surgery to remove the tumors, their breath after surgery was categorized as that of healthy persons. Although the number of samples examined in this investigation was still limited,

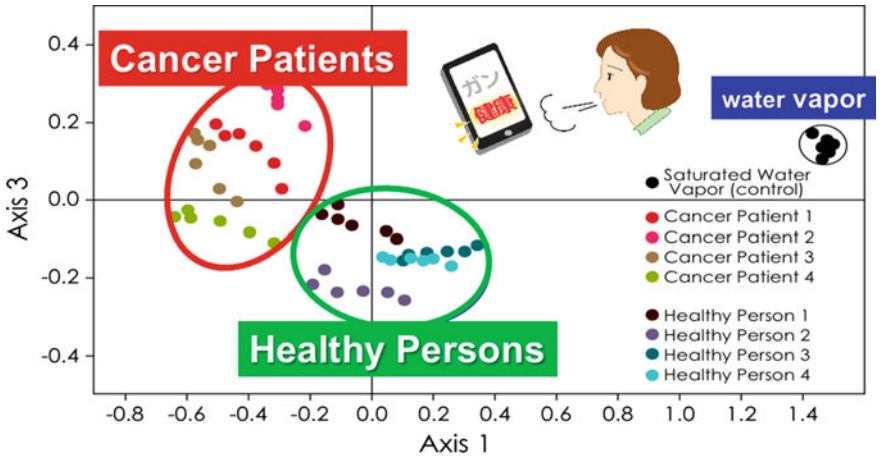

Fig. 7 Breath analysis using MSS showing a differentiation between healthy persons' and neck cancer patients' breath

the differentiation accuracy is expected to be improved by increasing the number of samples in combination with the machine learning technique.

Recently, Minami et al. have developed a new method for the pattern recognition of solid materials by using nanomechanical sensors, e.g., an MSS [22]. Since the gas-sensing signals measured by nanomechanical sensors are based on the gas–solid interactions, either a gas or a solid can be a probe or a target. While known solid receptors are used as probes to identify unknown target gases in common gas sensing, known gases can be utilized as probes to identify unknown solid materials. This *reverse* approach was demonstrated by identifying the molecular weights of the same type of polymer as well as the different types of polymers. Machine learning analysis can provide the best combination of probe gases for highly accurate identification. Since the probe gases can be prepared with arbitrary components with various concentrations, the resolution of identification can be set at virtually any level by choosing appropriate gas combinations. This approach will also be useful for identifying natural products, which are usually difficult to analyze by conventional approaches using specific parameters.

6 MSS Alliance/Forum and Internet of Things

Sensors in general are considered one of the core devices in the IoT model. The MSS sensing technology in combination with information and communication technology (ICT) is expected to make important contributions to realizing this concept in our daily life. However, real practical olfaction devices are not ready yet as several challenging issues need to be overcome: optimization of the receptor layer coating,

precise calibration with standard gases, mass production of sensor chips and devices, efficient connections with edge computing and cloud systems, and so forth. These challenges require the integration of science and technologies in collaboration with academia and industry. To integrate all the required cutting-edge technologies, the MSS Alliance was launched by NIMS, Kyocera, Osaka University, NEC, Sumitomo Seika, Asahi Kasei (joined in April 2017), and NanoWorld in 2015 [23]. Each member of the MSS Alliance, with its own expertise, has been contributing to the development of various technologies required for practical artificial olfaction. To encourage interested companies and institutes to perform demonstration experiments, the MSS Forum was launched in November 2017 [24, 25]. Then, from April 2020, the MSS Forum became an open platform to share the most up-to-date information regarding the MSS and related technologies towards practical implementation of artificial olfaction into society.

7 Conclusion

Compared with the conventional cantilever-type nanomechanical sensors with piezoresistive readout, the MSS has achieved high sensitivity in addition to various practical requirements. The MSS is an effective platform for artificial olfactory sensing because of its versatility with diverse types of receptor materials for gas sensing. The demonstrations in food and biomedical applications showed the high potential of the MSS as a practical technology in various real-life applications. The MSS integrated with related cutting-edge hardware/software technologies will soon become a standard platform for olfactory sensing systems.

References

1. Gottfried JA (2009) Function follows form: ecological constraints on odor codes and olfactory percepts. Curr Opin Neurobiol 19:422–429
2. Gimzewski JK, Gerber C, Meyer E, Schlittler RR (1994) Observation of a chemical reaction using a micromechanical sensor. Chem Phys Lett 217:589–594
3. Thundat T, Warmack RJ, Chen GY, Allison DP (1994) Thermal and ambient-induced deflections of scanning force microscope cantilevers. Appl Phys Lett 64:2894–2896
4. Berger R, Delamarche E, Lang HP, Gerber C, Gimzewski JK, Meyer E, Guntherodt HJ (1997) Surface stress in the self-assembly of alkanethiols on gold. Science 276:2021–2024
5. Fritz J, Baller MK, Lang HP, Rothuizen H, Vettiger P, Meyer E, Guntherodt HJ, Gerber C, Gimzewski JK (2000) Translating biomolecular recognition into nanomechanics. Science 288:316–318
6. Yoshikawa G, Akiyama T, Gautsch S, Vettiger P, Rohrer H (2011) Nanomechanical membrane-type surface stress sensor. Nano Lett 11:1044–1048
7. Yoshikawa G, Akiyama T, Loizeau F, Shiba K, Gautsch S, Nakayama T, Vettiger P, Rooij FN, Aono M (2012) Two dimensional array of piezoresistive nanomechanical membrane-type surface stress sensor (MSS) with improved sensitivity. Sensors 12:15873–15887

8. Yoshikawa G, Loizeau F, Lee CJY, Akiyama T, Shiba K, Gautsch S, Nakayama T, Vettiger P, de Rooij NF, Aono M (2013) Double-side-coated nanomechanical membrane-type surface stress sensor (MSS) for one-chip–one-channel setup. Langmuir 29:7551–7556
9. Guerrero RJ, Nguyen F, Yoshikawa G (2014) Real-time gas identification on mobile platforms using a nanomechanical membrane-type surface stress sensor. EPJ Tech Instrum 1:9
10. Present affiliation of Dr. Terunobu Akiyama: NanoWorld AG
11. Minami K, Yoshikawa G (2020) Finite element analysis of interface dependence on nanomechanical sensing. Sensors 20:1518
12. Yoshikawa G, Mechanical analysis and optimization of a microcantilever sensor coated with a solid receptor film. Appl Phys Lett 98:173502 (2011)
13. Timoshenko T (1925) Analysis of bi-metal thermostats. J Opt Soc Am 11:233–255
14. Shiba K, Ogawa M (2009) Microfluidic syntheses of well-defined sub-micron nanoporous titania spherical particles. Chem Commun 6851−6853
15. Osica I, Imamura G, Shiba K, Ji Q, Shrestha LK, Hill JP, Kurzydłowski KJ, Yoshikawa G, Ariga K (2017) Highly networked capsular silica-porphyrin hybrid nanostructures as efficient materials for acetone vapor sensing. ACS Appl Mater Interfaces 9:9945–9954
16. Ngo HT, Minami K, Imamura G, Shiba K, Yoshikawa G (2018) Effects of center metals in porphines on nanomechanical gas sensing. Sensors 18:1640
17. Minami K, Shiba K, Yoshikawa G (2018) Discrimination of structurally similar odorous molecules with various concentrations by using a nanomechanical sensor. Anal Methods 10:3720–3726
18. Shiba K, Tamura R, Imamura G, Yoshikawa G (2017) Data-driven nanomechanical sensing: specific information extraction from a complex system. Sci Rep 7:3661
19. Shiba K, Tamura R, Sugiyama T, Kameyama Y, Koda K, Sakon E, Minami K, Ngo HT, Imamura G, Tsuda K, Yoshikawa G (2018) Functional nanoparticles-coated nanomechanical sensor arrays for machine learning-based quantitative odor analysis. ACS Sens 3:1592–1600
20. Imamura G, Shiba K, Yoshikawa G, Washio T (2018) Analysis of nanomechanical sensing signals; physical parameter estimation for gas identification. AIP Adv 8:075007
21. Loizeau F, Lang HP, Akiyama T, Gautsch S, Vettiger P, Tonin A, Yoshikawa G, Gerber C, de Rooij N (2013) Piezoresistive membrane-type surface stress sensor arranged in arrays for cancer diagnosis through breath analysis. In: 2013 IEEE 26th international conference on micro electro mechanical systems (MEMS), pp 621–624
22. Minami K, Imamura G, Nemoto T, Shiba K, Yoshikawa G (2019) Pattern recognition of solid materials by multiple probe gases. Mater Horiz 6:580–586
23. MSS Alliance (Press release: http://www.nims.go.jp/eng/news/press/2015/10/201510130.html)
24. MSS Forum (Press release: http://www.nims.go.jp/eng/news/press/2017/201710160.html)
25. MSS Forum (Web page: http://mss-forum.com/en/)

Quantum Molecular Devices Toward Large-Scale Integration

Ryoma Hayakawa, Toyohiro Chikyow, and Yutaka Wakayama

1 Introduction

The evolution of current complementary metal–oxide–semiconductor (CMOS) devices is now facing a major turning point owing to the critical limit imposed by the increases in large-scale integration and power consumption. These serious obstacles are highlighted by the terms "More than Moore" and "Beyond CMOS". The development of new nanoelectronic devices, with the integration of new operating principles and attractive materials, is therefore an urgent issue for future CMOS technology. Various types of state-of-the-art devices have been proposed, including Ge/III-V channel transistors, nanowire transistors, and two-dimensional transistors such as graphene and transition metal dichalcogenides [1–5]. Among these devices, tunneling transistors hold considerable promise for future CMOS devices [6–9]. The key technique is the use of the tunneling current that flows between source and drain electrodes. Carrier tunneling achieves the sharp switching of the drain current beyond the theoretical limitation in current Si transistors, leading to extremely low power consumption. However, the basic device operation is the same as that of conventional Si transistors, namely a binary operation of "0" or "1". A multilevel transistor operation is thus required for the further enhancement of operation capabilities and for large-scale integration.

Meanwhile, the realization of quantum molecular devices, where single molecules are employed as electronic components in transistors and memories, has been long awaited since the proposal made by Aviram and Ratner in 1974 [10–14]. This is because organic molecules have many advantages over inorganic materials. First, molecules have ultimately small and regulated sizes on a nanometer scale.

R. Hayakawa (✉) · T. Chikyow · Y. Wakayama
International Center for Materials Nanoarchitectonics (WPI-MANA), National Institute for Materials Science (NIMS), 1-1 Namiki, Tsukuba 305-0044, Ibaraki, Japan
e-mail: HAYAKAWA.Ryoma@nims.go.jp

Y. Wakayama and K. Ariga (eds.), *System-Materials Nanoarchitectonics*,
NIMS Monographs, https://doi.org/10.1007/978-4-431-56912-1_12

This feature of the molecules has generated interest in inducing quantum transport phenomena such as Coulomb blockades and resonant tunneling. The effective gate modulation of such quantum transport has the potential to allow multilevel operations and a further reduction in power consumption, which are necessary for future nanoelectronics [11, 13, 14]. In contrast, inorganic materials such as Si, Ge, and GaAs suffer from irreproducible device operations, which are caused by the difficulty in controlling the size of quantum dots [15–18]. Therefore, the adoption of organic molecules is expected to overcome this crucial issue with inorganic quantum dots. In addition, the energy levels of molecules can be tuned by attaching substituents, including electron-withdrawing (or electron-donating) groups [19, 20]. Moreover, the adoption of photochromic molecules, such as diarylethene and azobenzene molecules, would allow quantum transport control by external triggers, namely light irradiation and electric field [21–25]. These features are unique to organic molecules and are not obtainable with inorganic quantum dots.

Quantum transport driven by single molecules is currently evaluated by scanning tunneling microscopy (STM) and nanogap electrode techniques. Many attractive behaviors, including single-electron transport, photoswitching, and negative differential resistance, have been reported in these single-molecular junctions [26–32]. However, practical applications remain a long way off, even though more than 40 years have been passed since molecular devices were first proposed. The main obstacle is the lack of effective device structures for the large-scale integration of molecular devices. These methodologies with STM and nanogap electrodes are incompatible with current CMOS applications.

In this chapter, we demonstrate a new strategy for developing practical molecular devices for large-scale integration (Fig. 1) [33–36]. The basic idea is to integrate attractive molecular functions into a Si-based tunnel transistor, which is a promising candidate for future CMOS devices. For this purpose, organic molecules, which are isolated from each other, are embedded as quantum dots in an insulating layer of a MOS structure, which is a fundamental component of current Si transistors. Therefore, the structure satisfies both the above requirements, namely,

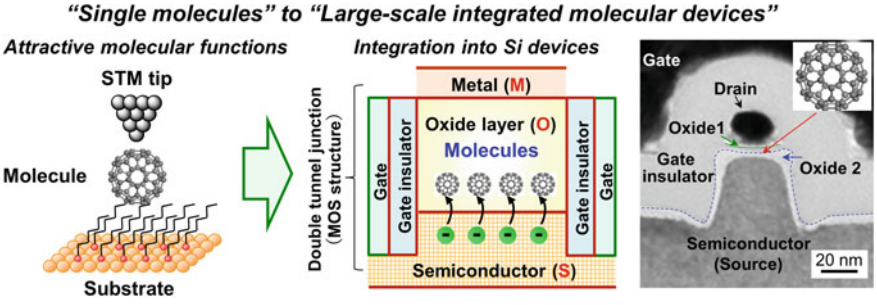

Fig. 1 Our strategy for developing new CMOS devices by integrating molecular functions into Si devices. The transmission electron microscopy image is reprinted from [36] with certain modifications; copyright 2017, Royal Society of Chemistry

the integration of molecular functions and close compatibility with current CMOS devices. First, we demonstrated resonant tunneling induced by the discrete molecular orbitals in our devices [33]. This finding gave rise to the attractive manipulations of the tunneling current described below. The use of the binary molecules copper phthalocyanine (CuPc) and copper hexadecafluorophthalocyanine (F_{16}CuPc) enabled multilevel control of the resonant tunneling [34]. Furthermore, the introduction of diarylethene photochromic molecules enabled the optical control of the tunneling current [35]. Consequently, we achieved a vertical resonant tunneling transistor for the large-scale integration of molecular devices to accompany the abovementioned achievements [36]. Our proposed device therefore has the potential to break through the limit faced by conventional Si technology and to integrate attractive molecular functionalities into Si devices, which is the true meaning of "beyond the present CMOS".

2 Quantum Transport Induced by Organic Molecules in a Double-Tunnel Junction

In this section, we discuss the fundamental carrier transport through organic molecules in our proposed devices. The device structure is illustrated in Fig. 2a. Here, C_{60} molecules were used as quantum dots because the electronic structure and transport property of the molecules have been well examined, and thus the molecules are suitable for use in understanding the carrier transport in our devices [37–39]. The Au/aluminum oxide (Al_2O_3)/molecules/silicon oxide (SiO_2) structure was prepared on highly doped p-type Si (100) substrates (<0.01 Ωcm) using a system that combines an organic vacuum deposition chamber and an atomic layer deposition (ALD) system [33]. Here, the Al_2O_3 and SiO_2 thin films served as the top and bottom tunneling barrier layers, respectively. The layer thicknesses were estimated to be 1.2 nm for the

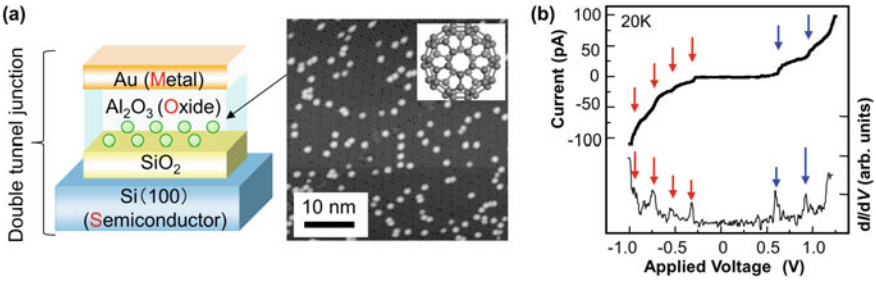

Fig. 2 **a** Schematic illustration of a MOS structure with C_{60} molecules embedded in an insulating layer and STM image of C_{60} molecules on a Si (111) 7 × 7 surface. **b** *I*–*V* and d*I*/d*V* curves of a sample with C_{60} molecules. The STM image and *I*–*V* and d*I*/d*V* curves are reprinted from [33] with certain modifications; copyright 2011, Wiley–VCH, Weinheim, Germany

SiO_2 film and 3.4 nm for the Al_2O_3 film by X-ray reflection spectroscopy measurements. In addition, the number density of the molecules was calculated from the STM images of C_{60} molecules distributed on a Si (111) 7 × 7 surface (Fig. 2a). Note that, in the calculation, the molecules were assumed to be distributed in a similar manner on the SiO_2 surface, because they were considered to be immobile on both the Si (111) 7 × 7 and SiO_2 surfaces. The estimated number density of the molecules was 7×10^{12} cm^{-2}. Of significance is that the molecules were completely isolated from each other on the surface, and so each molecule is expected to act as a quantum dot.

Figure 2b shows the current–voltage (I–V) and differential conductance (dI/dV) curves of a sample with C_{60} molecules as quantum dots. Staircases can be clearly seen in the I–V curve obtained at 20 K. The dI/dV curve in Fig. 2b exhibits two sharp peaks at 0.62 and 0.95 V with a positive voltage (given by blue arrows); on the other hand, there are four peaks at −0.30, −0.54, −0.70, and −0.96 V (depicted by red arrows). These results indicate that the C_{60} molecules were not destroyed and acted as quantum dots in the MOS-structure-based double-tunnel junction. The staircases remained even at room temperature [33, 36], which is expected to lead to the realization of quantum molecular devices driven at room temperature.

We then considered the origin of the staircases in the samples with C_{60} molecules. It is noteworthy that the intervals between neighboring staircases were nonuniform, in contrast to those obtained with conventional single-electron tunneling for inorganic quantum dots [40]. The electrochemical potential $U(N)$ of a quantum dot is described in Eq. (1) in terms of the discrete energy level and electrostatic potential as parameters [41, 42].

$$U(N) = \varepsilon_N + \frac{e^2}{C}\left(N - \frac{1}{2}\right) \tag{1}$$

Here, ε_N and N are the energy level of the nth electron and the number of electrons in a quantum dot, respectively. C is the capacitance of a double-tunnel junction. The energy $\mu(N)$ required to transport a single electron via a quantum dot is given as [41, 42]

$$\mu(N) = U(N+1) - U(N) = (\varepsilon_{N+1} - \varepsilon_N) + \frac{e^2}{C} \tag{2}$$

where e^2/C is the charging energy of a quantum dot. $\Delta\varepsilon = \varepsilon_{N+1} - \varepsilon_N$ represents the energy splitting in a dot and thereby corresponds to the gap between the highest occupied molecular orbital (HOMO) and the lowest unoccupied molecular orbital (LUMO) for organic molecules [43]. Quantum transport thus occurs when the charging energy (e^2/C) or the interval between the discrete energy levels ($\Delta\varepsilon = \varepsilon_{N+1} - \varepsilon_N$) in a dot is larger than the ambient thermal energy.

In addition, in our devices, the ratio of the capacitances of the Al_2O_3 and SiO_2 layers was calculated to be 2:1. Namely, two-thirds of the total voltage was applied

to the SiO_2 layer, resulting in the carrier injection of both holes and electrons from the Si substrate to the molecules through the SiO_2 layer. The electrons tunnel into the molecules from the Si substrate with a positive voltage. Accordingly, the dI/dV peaks with a positive voltage can be assigned to unoccupied molecular orbitals. Meanwhile, hole injection occurs from the Si substrate into the molecules at a negative voltage, and thus the dI/dV peaks at a negative voltage can be attributed to occupied molecular orbitals.

The molecular orbitals of single C_{60} molecules have been evaluated by scanning tunneling spectroscopy (STS) measurements. Although the HOMO level consists of fivefold-degenerate h_{1u} and the LUMO level is composed of threefold-degenerate t_{1u}, these degenerate levels are reportedly resolved by the distortion of the molecules and carrier injection into the degenerate levels [44–46]. Comparison with the reported molecular orbitals shows that the two peaks observed at 0.62 and 0.95 V in the dI/dV curve can be attributed to the split LUMO levels (blue arrows in Fig. 2b). Meanwhile, the four peaks visible at −0.30, −0.54, −0.70, and −0.96 V can be assigned to the split HOMO levels (red arrows in Fig. 2b). The estimated energy levels are illustrated in Fig. 3a, b. The HOMO–LUMO gap was found to be 0.92 eV, in good agreement with the values obtained from STS measurements of single C_{60} molecules (0.75–0.95 eV) [39, 44].

On the basis of the above arguments, we ascribed the nonuniform staircases to resonant tunneling induced by the embedded molecules. We place particular emphasis on the fact that the quantum transport via single molecules can be evaluated in our devices, by analogy with STS measurements. This fact further implies that the threshold voltage (V_{th}) of the resonant tunneling current can be tuned by controlling the energy levels of the embedded molecules. In the next section, we describe two unique approaches to controlling the resonant tunneling. First, the adaption of

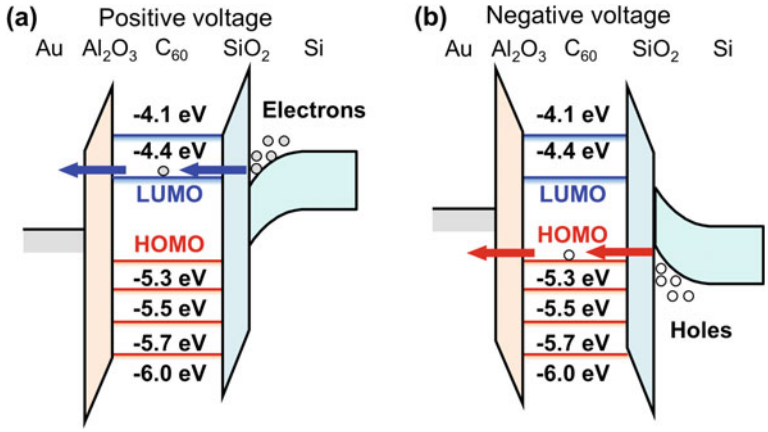

Fig. 3 Energy diagram of the Au/Al_2O_3/C_{60}/SiO_2/p-type Si substrate at **a** positive and **b** negative voltages. Here, the molecular orbitals were calculated from the peak positions in the dI/dV curve in Fig. 2b

the heterogeneous binary molecules CuPc and F_{16}CuPc provided multilevel control of the resonant tunneling. Second, the use of diarylethene photochromic molecules allowed the tunneling to be optically manipulated. These are the unique features observed when using organic molecules for quantum dots.

3 Unique Device Operations Controllable by Molecular Orbitals

3.1 Multilevel Control of Resonant Tunneling by Using Binary Molecules

In this study, the binary molecules CuPc and F_{16}CuPc were utilized to achieve multilevel control of the tunneling current (Fig. 4a). The reason for this is that the molecular orbitals of these molecules can be varied simply by fluoridation, without changing the molecular frame. The reported HOMO and LUMO levels are respectively −5.2 and −3.5 eV for CuPc and −6.3 and −4.8 eV for F_{16}CuPc (Fig. 4b) [19, 20]. This means that, overall, the molecular orbitals of F_{16}CuPc molecules are 1 eV lower than those of CuPc molecules owing to the strong electron affinity of the fluorine atoms. It is very difficult to control the discrete energy levels in inorganic quantum dots because the energy level intervals are determined by the charging energy, that is, they are dependent on the size of the quantum dots. Hence, the variation in the dot sizes leads to an unstable operation temperature, which is a serious problem with inorganic materials. Thus, the fine controllability of molecular orbitals achieved by attaching the substituents is advantageous with regard to the utilization of organic molecules.

Figure 5a, b show I–V and dI/dV curves of a sample, where both the CuPc and F_{16}CuPc are spontaneously embedded in the same insulating layer and an n-type Si substrate was used as the bottom electrode. The measurements were conducted at 60 K. The I–V curve of the sample with both molecules exhibited nonuniform steps as observed for the sample with C_{60} molecules (Fig. 5a). The dI/dV curve exhibited

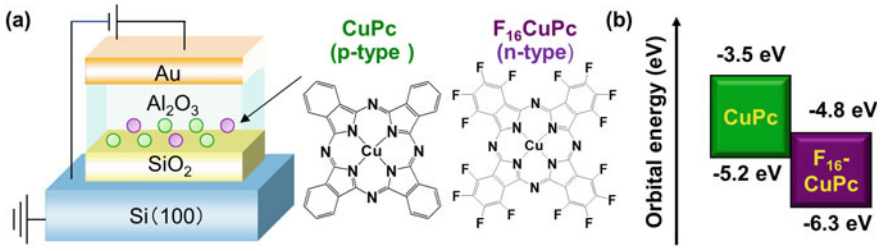

Fig. 4 **a** Schematic illustration of the MOS structure with CuPc and F_{16}CuPc molecules. **b** Energy levels of CuPc and F_{16}CuPc molecules [34]

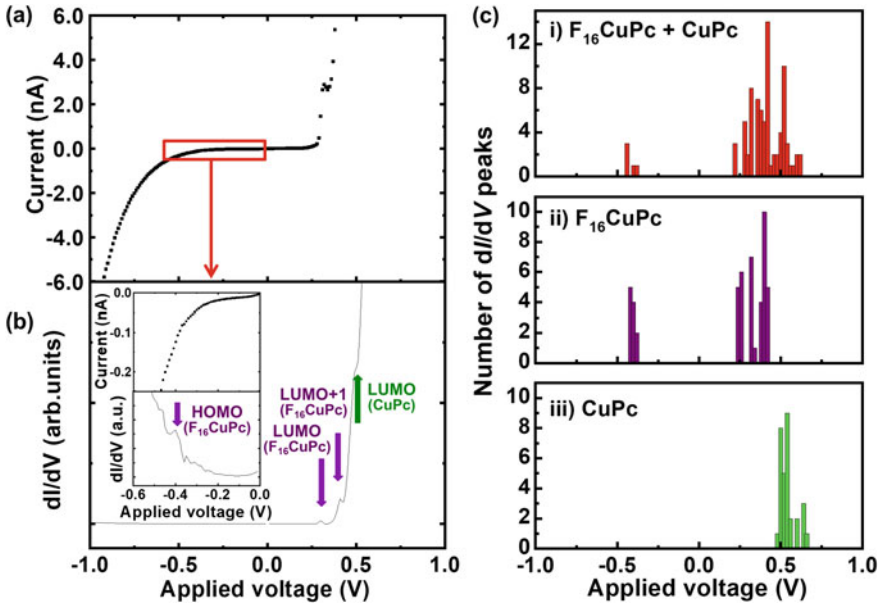

Fig. 5 **a** *I*–*V* and **b** d*I*/d*V* curves of a sample with F_{16}CuPc and CuPc. The inset in (b) shows enlarged *I*–*V* and d*I*/d*V* curves in the 0 to −0.6 V range. **c** Histograms of peak positions in d*I*/d*V* curves of samples with (i) F_{16}CuPc + CuPc, (ii) F_{16}CuPc, and (iii) CuPc. Reprinted from [34] with certain modifications; copyright 2011, American Chemical Society

three peaks observed at positive voltages of 0.30, 0.41 and 0.52 V (Fig. 5b), whereas a single peak appeared at a negative voltage of –0.40 V (inset of Fig. 5b). Considering the d*I*/d*V* curves of the molecules, the peaks seen at 0.30 and 0.41 V can be assigned to the LUMO and LUMO + 1 of F_{16}CuPc, respectively. On the other hand, the peak observed at 0.52 V can be attributed to the LUMO of CuPc. As shown above, the multiple staircases obtained in the sample with the binary molecules can be explained as a superposition of resonant tunneling through the CuPc and F_{16}CuPc.

To provide clear evidence that the observed current is the summation of the tunneling currents via the CuPc and F_{16}CuPc molecules, we constructed histograms of the peak positions in d*I*/d*V* curves obtained from the samples with CuPc, F_{16}CuPc, and both (Fig. 5c). The histogram of the sample with CuPc and F_{16}CuPc can be divided into histograms of the individual components (Fig. 5c(i)), i.e., the peak at 0.36 V coincided with the unoccupied molecular orbitals (LUMO and LUMO + 1) of F_{16}CuPc, and that observed at 0.53 V corresponded to the LUMO of CuPc. Furthermore, the peak at −0.40 V visible in Fig. 5c(i) agreed with the HOMO of F_{16}CuPc (Fig. 5c(ii)). Note that no peak from the HOMO was observed in the histogram of the sample with CuPc (Fig. 5c(iii)). This is because the tunneling current was suppressed to a negative voltage owing to a depletion layer that formed in the n-type Si substrate [34].

On the basis of the above arguments, we conclude that the tunneling current in the sample with both CuPc and F_{16}CuPc was a superposition of tunneling currents through respective molecular components, and therefore the combination of the binary molecules enabled the multilevel control of the resonant tunneling in the double-tunnel junction.

3.2 *Optical Control of Resonant Tunneling with Photochromic Molecules*

A sample structure of resonant tunneling devices with photochromic molecules is shown in Fig. 6a. Here, we used a transparent indium tin oxide (ITO) film instead of a Au film as a top electrode to provide UV and VIS light irradiation. Of importance is that a diarylethene (DAE) derivative, 1,2-bis(2-methyl-5-(4-biphenyl)-3-thienyl)hexafluorocyclopentene, was used for the form of optically controllable quantum dots in the devices. This was because the photoisomerization between the open- and closed-ring isomers of the molecules induces a considerable change in the molecular orbitals (Fig. 6b) [47, 48]. Moreover, the photoisomerization is accompanied by a minimal change in the molecular structure, and thus we expect structural changes to occur even in the insulating layer.

Figure 7a, b show I–V and dI/dV curves of a sample with DAE molecules after UV or VIS light irradiation. The irradiated UV and VIS lights include wavelengths in the 300 to 400 nm and 400 to 700 nm ranges, respectively. The powers of the irradiated lights were estimated to be 11 mW/cm^2 for the UV light and 72 mW/cm^2 for the VIS light. The measurements were carried out at 20 K. Before the measurements, the sample was irradiated with VIS light for 10 min to increase the open-ring to closed-ring isomer ratio. This ratio was calculated to be 84%, which shows that the

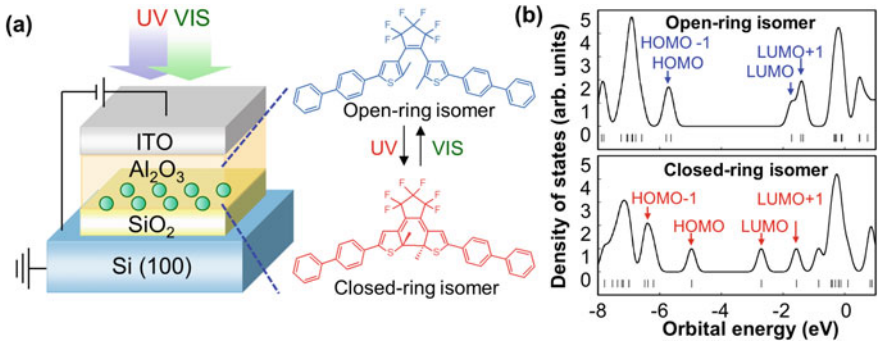

Fig. 6 **a** Schematic illustration of a MOS structure with DAE molecules. **b** Density of states of DAE molecules with open- and closed-ring configurations. Here, the densities of states of the respective isomers were calculated with DFT B3LYP/6-31G(d) using a Gaussian 09 program package. Reprinted from [35] with certain modifications; copyright 2013, American Chemical Society

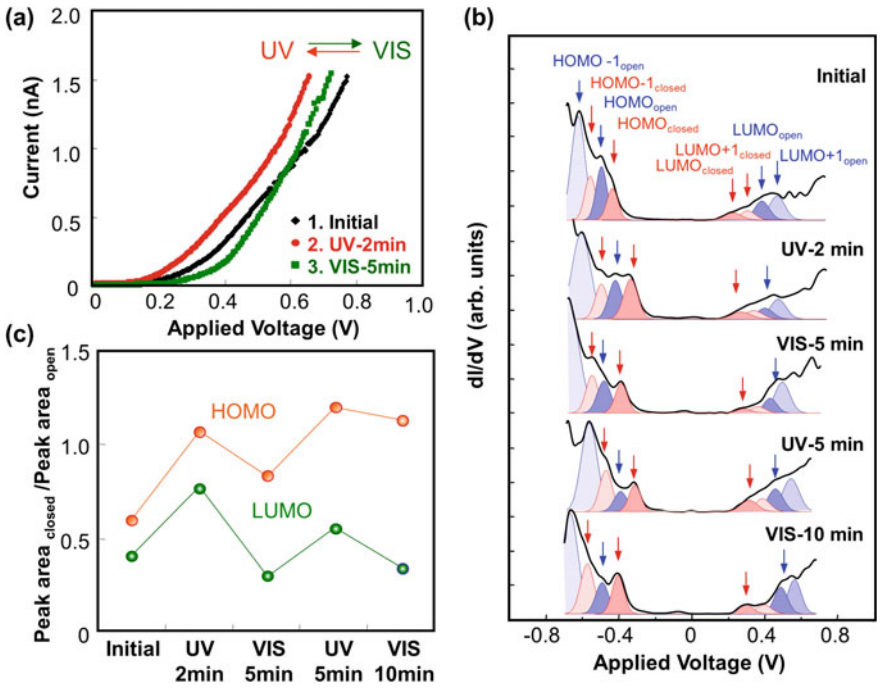

Fig. 7 **a** Optical switching of I–V curves and **b** change in the dI/dV curves induced by the irradiation of UV and VIS lights. Here, the dI/dV curves were deconvoluted by the peaks assigned in (**b**) using a Gaussian function. **c** Optical switching of the peak ratios between the open- and closed-ring isomers induced by alternating UV and VIS light irradiation. In this calculation, we used the peak areas of the HOMO and LUMO of the respective isomers in the dI/dV curve in (**b**). Reprinted from [35] with permission; copyright 2013, American Chemical Society

open-ring isomer is predominant after the initial VIS light irradiation [35]. Multiple staircases were seen in the I–V curve (Fig. 7a) and sharp peaks were also visible in the dI/dV curve, which indicates that the DAE molecules acted as quantum dots for resonant tunneling in the double-tunnel junction (Fig. 7b).

Subsequent UV light irradiation for 2 min induced a structural change from open- to closed-ring isomers, where the closed-ring isomer ratio was calculated to be 75% [35]. As a result, the V_{th} value of the tunneling current was reduced owing to the photoisomerization of the DAE molecules (Fig. 7a). After that, VIS light irradiation for 5 min induced a reversible change from closed- to open-ring isomers so that V_{th} was restored to its original value. In this manner, the variation in V_{th} was observed repeatedly by alternating UV and VIS light irradiation. Another essential point is that even a day later, no change was observed in the V_{th} value under a dark condition without any light irradiation.

To provide further evidence that the change in the tunneling current was invoked by the photoisomerization of the DAE molecules, we analyzed the dI/dV curves in the sample after UV or VIS light irradiation (Fig. 7b) based on a theoretical calculation

of the molecular orbitals. The B3LYP/6-31G(d) level of density functional theory was used to calculate the density of states of the open- and closed-ring isomers of the DAE molecules (Fig. 6b). Then, all the dI/dV curves shown in Fig. 7b were deconvoluted into at least eight peaks by Gaussian fitting, as indicated by the arrows in the figure. The peaks were assigned to the molecular orbitals of the open- and closed-ring isomers.

Figure 7c shows the light-induced change in the ratios of the peak areas between the HOMO and LUMO of the respective isomers. The closed- to open-ring isomer ratio was increased by UV light irradiation. The value was in turn reduced by VIS light irradiation, that is, the open-ring isomers were predominant. In all events, the reversible change in the resonant tunneling originated from the photoisomerization of the DAE molecules.

The abovementioned results clarify that the DAE molecules can behave as optically controllable quantum dots in our device configuration. Our proposed device has the potential to allow us to integrate photonic functionalities in Si-based devices.

4 Vertical Resonant Tunneling Transistor with Molecular Quantum Dots

Consequently, we realized a novel vertical resonant tunneling transistor for the large-scale integration of molecular devices based on the abovementioned achievements.

The device configuration of a vertical resonant tunneling transistor is shown in Fig. 8a, where a MOS-structure-based double-tunnel junction with C_{60} molecules is used as the transistor channel [36]. In the transistor, the width of the channel was scaled down to 50 ± 10 nm for the effective application of gate voltages (Fig. 8b), and the lengths were in the 50 to 150 μm range (Fig. 8c) to increase the drain current. A key feature of the device is that the one-dimensional transistor channel was formed by standard electron-beam lithography. Designing effective microfabrication processes is a challenging requirement in the organic electronics field. However, there are still only few examples of the formation of nanostructures by lithography techniques

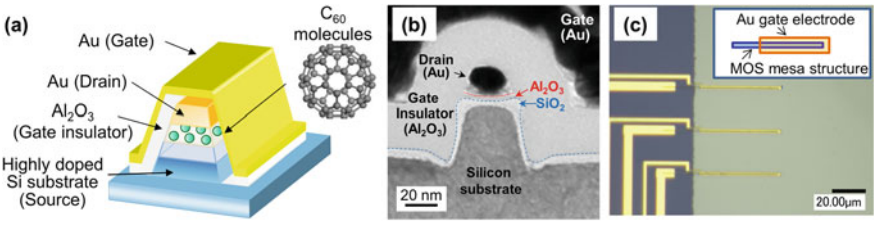

Fig. 8 **a** Schematic illustration of a vertical resonant tunneling transistor with C_{60} molecules as quantum dots. **b** Transmission electron microscopy image and **c** optical microscope image of the transistors. Reprinted from [36] with permission; copyright 2017, Royal Society of Chemistry

because of the complicated processes required to take into account the solubility and reactivity between organic materials and photoresists [49, 50]. However, in our proposed transistor, the molecules are protected by the surrounding insulating layers, which allows the well-defined nanoscale patterning of the structure by standard lithographic techniques without destroying molecules.

Figure 9a, b show typical transistor properties, namely, the drain current—drain voltage (I_d–V_d) and drain current—gate voltage (I_d–V_g) characteristics, respectively, in a sample with an n-type Si substrate. The measurements were performed at 20 K. Multiple staircases were visible at 0.5, 0.8, and 1.0 V in the I_d–V_d curve without a gate voltage (Fig. 9a), which coincided with the unoccupied molecular orbitals (LUMO, LUMO + 1, and LUMO + 2) of C_{60} molecules as well as those seen in the two-terminal device (Fig. 2b) [33]. The result proves that the molecules were not destroyed during any of the lithographic processes. Then, the drain current was effectively reduced by increasing V_g from 0 to −15 V as shown in the I_d–V_d curve (Fig. 9a). The same reduction in drain current was confirmed in the I_d–V_g curve (see Fig. 9b), where the drain voltage was fixed at 1 V. A steep drop appeared at gate

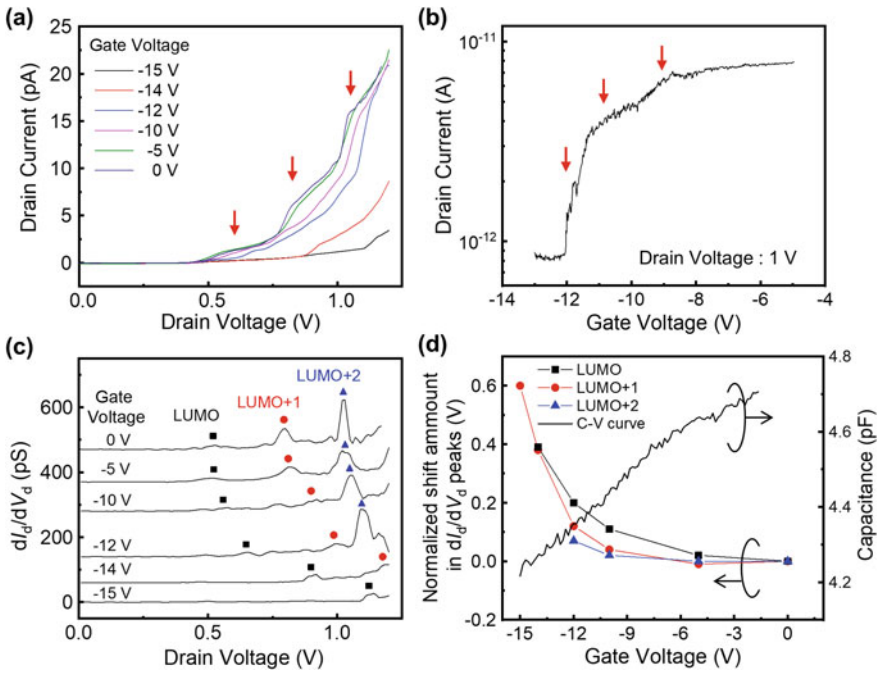

Fig. 9 **a** I_d–V_d and **b** I_d–V_g curves for a vertical transistor with an n-type Si substrate. **c** dI_d/dV_d curves for different gate voltages in the n-type Si substrate, where the curves were obtained by the numerical derivation of (**a**). The curves are shifted vertically for better visibility. **d** Gate voltage dependence of the capacitance between gate and [36] source electrodes and the normalized peak shifts on unoccupied molecular orbitals. Reprinted from with permission; copyright 2017, Royal Society of Chemistry

voltages of less than −10 V. Particular emphasis should be placed on the fact that distinct multiple steps, reflecting the molecular orbitals, were visible in both the I_d–V_g and I_d–V_g curves. Namely, an operation analogous with that of single-molecule transistors ([51, 52]) occurred in the device configuration, which enabled large-scale integration. The finding has the potential to realize multilevel transistor operation, which can be tuned by molecules embedded in vertical transistors.

We now discuss the operating principle of the vertical transistor. Transistor operations are generally explained by the shift in molecular energy levels and/or the variation in the charging energies in accordance with the gate voltage [14, 51, 52]. Another possible reason is the impact of a depletion layer in the Si substrate. This impact is not usually felt in conventional single-molecule transistors because the molecules are directly connected to metallic source and drain electrodes. However, when a Si substrate functions as a source electrode in our transistors, the change in the depletion layer with the gate voltage plays an essential role in the transistor operation.

To investigate these possible mechanisms in our transistor, we evaluated the gate voltage dependence of the peak positions in the dI_d/dV_d curves under distinct gate voltages in a transistor with an n-type Si substrate (Fig. 9c). First, three peaks were seen at 0.5, 0.8, and 1.0 V in the V_g range of 0 to –5 V in the dI_d/dV_d curves. The peak locations agreed with those of unoccupied molecular orbitals, which are denoted as LUMO, LUMO + 1, and LUMO + 2. The dI_d/dV_d peaks were shifted toward the positive drain voltage as V_g decreased from –10 to –15 V. Significantly, the shifts in the dI_d/dV_d peaks occurred at $V_g < -10$ V, which corresponded to the drain current suppression region (see Fig. 9b). In addition, the peak shift amplitude was closely related to the reduction in the capacitance between the source and gate electrodes (Fig. 9d). These results reveal that the formation of the depletion layer in the Si substrate is responsible for the variation in the dI_d/dV_d peaks, which is a benefit brought about by the integration of molecules into Si devices.

5 Conclusions

We realized resonant tunneling devices in which organic molecules are embedded as quantum dots in MOS-structure-based double-tunnel junctions. The tunneling currents were controlled by the molecular orbitals, leading to multilevel control by binary molecules and optical manipulation with photochromic molecules. These are unique features that allow organic molecules to be employed as quantum dots and are not obtained using inorganic molecules. Moreover, we formed a vertical tunneling transistor using conventional lithographic techniques. The transistor attained the multilevel control of the stepwise drain currents, which can be manipulated by controlling the energy levels of the embedded molecules. This feature is expected to realize attractive molecular functions, such as multilevel transistor operation with the rational design of molecules, and optical memory functions provided by photochromic molecules based on our achievements. Furthermore, the depletion

layer generated in the Si substrate provided effective modulation of the drain current. As a result, an operation analogous to that of single-molecule transistors was demonstrated in a device configuration with close affinity to current CMOS devices. Our proposed devices therefore have the potential to integrate molecular functions into future nanoelectronic devices and to deliver unique device operations unobtainable with inorganic quantum dots.

References

1. Takagi S, Takenaka M (2011) Prospective and critical issues of III-V/Ge CMOS on Si platform. ECS Trans 35:279–298
2. Heinzig A, Slesazeck S, Kreupl F, Mikolajick T, Weber WM (2012) Reconfigurable silicon nanowire transistors. Nano Lett **12**:119–124
3. Fang WW, Singh N, Bera LK, Nguyen HS, Rustagi SC, Lo GQ, Balasubramanian N, Kwong D-L (2007) Vertically stacked SiGe nanowire array channel CMOS transistors. IEEE Electron Device Lett 28:211–213
4. Geim AK (2009) Graphene: status and prospects. Science 324:1530–1534
5. Wang QH, Kalantar-Zadeh K, Kis A, Coleman JN, Strano MS (2012) Electronics and optoelectronics of two-dimensional transition metal dichalcogenides. Nat Nanotechnol 7:699–712
6. Tomioka K, Yoshimura M, Fukui T (2012) A III-V nanowire channel on silicon for high-performance vertical transistors. Nature 488:189–192
7. Ionescu AM, Riel H (2011) Tunnel field-effect transistors as energy-efficient electronic switches. Nature 479:329–337
8. Sarkar D, Xie X, Liu W, Cao W, Kang J, Gong Y, Kraemer S, Ajayan PM, Banerjee K (2015) A subthermionic tunnel field-effect transistor with an atomically thin channel. Nature 526:91–95
9. Lin Y-C, Ghosh RK, Addou R, Lu N, Eichfeld SM, Zhu H, Li M-Y, Peng X, Kim MJ, Li L-J, Wallace RM, Datta S, Robinson JA (2015) Atomically thin resonant tunnel diodes built from synthetic van der Waals heterostructures. Nat Commun 6:7311–1–6
10. Aviram A, Ratner MA (1974) Molecular rectifiers. Chem Phys Lett 29:277–283
11. Joachim C, Gimzewski JK, Aviram A (2000) Electronics using hybrid-molecular and mono-molecular devices. Nature 408:541–548
12. Akkerman HB, Blom PWM, de Leeuw DM, de Boer B (2006) Towards molecular electronics with large-area molecular junctions. Nature 441:69–72
13. Collier CP, Wong EW, Belohradsky M, Raymo FM, Atoddart JF, Kuekes PJ, Williams RS, Heath JR (1999) Electronically configurable molecular-based logic gates. Science 285:391–394
14. Martínez-Blanco J, Nacci C, Erwin SC, Kanisawa K, Locane E, Thomas M, von Oppen F, Brouwer PW, Fölsch S (2015) Gating a single-molecule transistor with individual atoms. Nat Phys 11:640–644
15. Angus SJ, Ferguson AJ, Dzurak AS, Clark RG (2007) Gate-defined quantum dots in intrinsic silicon. Nano Lett **7**, 2051–2055
16. Kwon YH, Park CJ, Lee WC, Fu DJ, Shon Y, Kang TW, Hong CY, Cho HY, Wang KL (2002) Memory effects related to deep levels in metal-oxide-semiconductor structure with nanocrystalline Si. Appl Phys Lett 80:2502–2504
17. Chen K-H, Chien C-Y, Li P-W (2010) Precise Ge quantum dot placement for quantum tunneling devices. Nanotechnology 21:055302–1–55309
18. Kang K, Min BI (1997) Effect of quantum confinement on electron tunneling through a quantum dot. Phys Rev B 55:15412–15415
19. Lei S-B, Deng K, Yang D-L, Zeng Q-D, Wang C (2006) Charge-transfer effect at the interface of phthalocyanine—electrode contact studied by scanning tunneling spectroscopy. J Phys Chem B 110:1256–1260

20. Peisert H, Knupfer M, Schwieger T, Fuentes GG, Olligs D, Fink J, Schmidt T (2003) Fluorination of copper phthalocyanines: electronic structure and interface properties. J Appl Phys 93:9683–9692
21. Irie M, Fukaminato T, Matsuda M, Kobatake S (2014) Photochromism of diarylethene molecules and crystals: memories, switches, and actuators. Chem Rev 114:12174–12277
22. Crivillers N, Orgiu E, Reinders F, Mayer M, Samorì P (2011) Optical modulation of the charge injection in an organic field-effect transistor based on photochromic self-assembled-monolayer-functionalized electrodes. Adv Mater 23:1447–1452
23. MativetskyJM, Pace G, Elbing M, Rampi MA, Mayor M, Samorì P (2008) Azobenzenes as light-controlled molecular electronic switches in nanoscale metal—molecule—metal junctions. J Am Chem Soc 130:9192–9193
24. Zhang H, Guo X, Hui J, Hu S, Xu W, Zhu D (2011) Interface engineering of semiconductor/dielectric heterojunctions toward functional organic thin-film transistors. Nano Lett 11:4939–4946
25. Irie M (2000) Diarylethenes for memories and switches. Chem Rev 100:1685–1716
26. Kim Y, Hellmuth TJ, Sysoiev D, Pauly F, Pietsch T, Wolf J, Erbe A, Huhn T, Groth U, Steiner UE, Scheer E (2012) Nano Lett 12:3736–3742
27. Perrin ML, Frisenda R, Koole M, Seldenthuis JS, Gil JAC, Valkenier H, Hummelen JC, Renaud N, Grozema FC, Thijssen JM, Dulić D, van der Zant HSJ (2014) Large negative differential conductance in single-molecule break junctions. Nat Nanotechnol 9:830–834
28. Majima Y, Ogawa D, Iwamoto M, Azuma Y, Tsurumaki E, Osuka A (2013) Negative differential resistance by molecular resonant tunneling between neutral tribenzosubporphine anchored to a Au(111) surface and tribenzosubporphine cation adsorbed on to a tungsten tip. J Am Chem Soc 135:14159–14166
29. Burzurí E, Yamamoto Y, Warnock M, Zhong X, Park K, Cornia A, van der Zant HSJ (2014) Franck-Condon blockade in a single-molecule transistor. Nano Lett 14:3191–3196
30. Vincent R, Klyatskaya S, Ruben M, Wernsdorfer W, Balestro F (2012) Electronic read-out of a single nuclear spin using a molecular spin transistor. Nature 488:357–360
31. Warner B, Hallak FE, Prüser H, Sharp J, Persson M, Fisher AJ, Hirjibehedin CF (2015) Tunable magnetoresistance in an asymmetrically coupled single-molecule junction. Nat Nanotechnol 10:259–263
32. Schwarz F, Kastlunger G, Lissel F, Egler-Lucas C, Semenov SN, Venkatesan K, Berke H, Stadler R, Lörtscher E (2015) Field-induced conductance switching by charge-state alternation in organometallic single-molecule junctions. Nat Nanotechnol 11:170–177
33. Hayakawa R, Hiroshiba N, Chikyow T, Wakayama Y (2011) Single-electron tunneling through molecular quantum dots in a metal-insulator-semiconductor structure. Adv Funct Mater 21:2933–2937
34. Seo H-S, Hayakawa R, Chikyow T, Wakayama Y (2014) Multilevel operation of resonant tunneling with binary molecules in a metal–insulator–semiconductor configuration. J Phys Chem C 118:6467–6472
35. Hayakawa R, Higashiguchi K, Matsuda K, Chikyow T, Wakayama Y (2013) Photoisomerization-induced manipulation of single-electron tunneling for novel Si-based optical memory. ACS Appl Mater Interfaces 5:11371–11376
36. Hayakawa R, Chikyow T, Wakayama Y (2017) Vertical resonant tunneling transistors with molecular quantum dots for large-scale integration. Nanoscale 9:11297–11302
37. Golden MS, Knupfer M, Fink J, Armbruster JF, Cummins TR, Romberg HA, Roth M, Sing M, Schmidt M, Sohmen E (1995) The electronic structure of fullerenes and fullerene compounds from high-energy spectroscopy. J Phys: Condens Matter 7:8219–8247
38. Joachim C, Gimzewski JK, Schlittler RR, Chavy C (1995) Electronic transparence of a single C_{60} molecule. Phys Rev Lett 74:2102–2105
39. Porath D, Millo O (1997) Single electron tunneling and level spectroscopy of isolated C_{60} molecules. J Appl Phys 81:2241–2244
40. Zhang H, Yasutake Y, Shichibu Y, Teranishi T, Majima Y (2005) Tunneling resistance of double-barrier tunneling structures with an alkanethiol-protected Au nanoparticle. Phys Rev B 72:205441–1–205447

41. Kouwenhoven LP, Marcus CM, McEuen PL, Tarucha S, Westervelt RM, Wingreen NS (1997) Electron transport in quantum dots. In: Sohn LL, Kouwenhoven LP, Schon G (ed) Mesoscopic electron transport, vol 345. Kluwer, NATO Science Series E, pp 105–214
42. van Houten H, Beenakker CWJ, Staring AAM (1992) Coulomb-blockade oscillations in semiconductor nanostructures. In: Grabert H, Devoret MH (eds) Single charge tunneling coulomb blockade phenomena in nanostructures. Plenum Press, New York, pp 167–216
43. Perrin ML, Burzurí E, van der Zant HSJ (2015) Single-molecule transistors. Chem Soc Rev 44:902–919
44. Porath D, Levi Y, Tarabiah M, Millo O (1997) Tunneling spectroscopy of isolated C_{60} molecules in the presence of charging effects. Phys Rev B 56:9829–9833
45. Negri F, Orlandi G, Zerbetto F (1988) Quantum-chemical investigation of Franck-Condon and Jahn-Teller activity in the electronic spectra of Buckminsterfullerene. Chem Phys Lett 144:31–37
46. Joachim C, Gimzewski JK, Tang H (1998) Physical principles of the single C_{60} transistor effect. Phys Rev B 58:16407–16417
47. Hayakawa R, Higashiguchi K, Matsuda K, Chikyow T, Wakayama Y (2013) Optically and electrically driven organic thin film transistors with diarylethene photochromic channel layers. ACS Appl Mater Interfaces 5:3625–3630
48. Hayakawa R, Petit M, Higashiguchi K, Matsuda K, Chikyow T, Wakayama Y (2015) Interface engineering for improving optical switching in a diarylethene-channel transistor. Org Electron 21:149–154
49. Kleemann H, Günther AA, Leo K, Lüssem B (2013) High-performance vertical organic transistors. Small 9:3670–3677
50. Kymissis I, Akinwande AI, Bulović V (2005) A lithographic process for integrated organic field-effect transistors. J Disp Technol 1:289–294
51. Park H, Park J, Lim AKL, Anderson EH, Alivisatos AP, McEuen PL (2000) Nanomechanical oscillations in a single-C_{60} transistor. Nature 407:57–60
52. Song H, Kim Y, Jang YH, Jeong H, Reed MA, Lee T (2009) Observation of molecular orbital gating. Nature 2009(462):1039–1043

Energy and Life with Nanoarchiteconics

Nanostructured Bulk Thermoelectric Materials for Energy Harvesting

Zihang Liu and Takao Mori

1 Introduction

Thermoelectric devices, having unique advantages of no moving parts, no pollutants, high reliability, and simplicity, can directly convert heat energy into electrical energy and vice versa [1]. They have long been used in NASA deep-space missions for supplying the electric power of space crafts or for various cooling applications [2]. In the context of the increased world energy consumption and concerns about human-induced global warming, developing clean and renewable energy conversion technologies have received intensive interests during the last decade [3]. Namely, according to Lawrence Livermore's U.S. Energy Flow Chart, in 2017 two thirds of the primary energy consumed in the United States, for example, is ultimately wasted [4]. The potential various heat resources provide great opportunities for utilizing thermoelectric power generation for waste heat harvesting. And not just in terms of energy saving, thermoelectrics is also a promising energy harvesting technology to dynamically power Internet of Things (IoT) sensors and devices [5–8]. Ideally, the conversion efficiency η is dominated by the dimensionless thermoelectric figure of merit $ZT = (S^2\sigma/(\kappa_{lat} + \kappa_{ele}))T$ while the maximum output power density ω_{max} is decided by the power factor $PF = S^2\sigma$, as shown in the following equations:

$$\eta = \frac{T_h - T_c}{T_h}\left[\frac{\sqrt{1+ZT}-1}{\sqrt{1+ZT}+T_c/T_h}\right] \tag{1}$$

$$\omega_{\max} = \frac{1}{4}\frac{(T_h - T_c)^2}{L}PF \tag{2}$$

Z. Liu · T. Mori (✉)
International Center for Materials Nanoarchitectonics (WPI-MANA), National Institute for Materials Science (NIMS), 1-1 Namiki, Tsukuba 305-0047, Ibaraki, Japan
e-mail: MORI.Takao@nims.go.jp

Y. Wakayama and K. Ariga (eds.), *System-Materials Nanoarchitectonics*,
NIMS Monographs, https://doi.org/10.1007/978-4-431-56912-1_13

where S, σ, κ_{lat}, κ_{ele}, T_H, T_C, and L are the Seebeck coefficient, electrical conductivity, lattice thermal conductivity, electronic thermal conductivity, the hot side and cold side temperature, and leg length, respectively. Therefore, in regard to the material level considerations, developing high-performance thermoelectric devices with high efficiency relies on pursing a high ZT.

Since these fundamental thermoelectric parameters are mutually cross-correlated or even contradicted [9, 10], ZT above unity has long been regarded as a benchmark for bulk thermoelectric materials from the 1950s to 1990s. In 1993, two seminal papers by L. D. Hicks and M. S. Dresselhaus proposed a new and creative concept of quantum effect in thermoelectric [11, 12], which provides the possibility of increasing power factor ($PF = S^2\sigma$) and simultaneously reducing lattice thermal conductivity through controlling the reduced dimensionality. While thermoelectric enhancement through the quantum confinement effect has not been widely observed experimentally, the focus on utilizing nanotechnology has led to the "renaissance of the thermoelectric field" to date [13–16], where most of the significant advances in the bulk thermoelectric area come from designing nanostructured materials to further enhance ZT [17–19]. Here it should be addressed that bulk nanostructured thermoelectric materials in principle mean that the three-dimensional solid contains intriguing microstructural features on the nanoscale, including linear defects, interfacial defects, and volume defects. Another popular route involves discovering new materials with an intrinsically low thermal conductivity due to the unique bonding environment and lattice dynamics [20–23], which may provide an opportunity for achieving high ZT after fully optimizing electrical transport properties by extrinsic doping.

During the last decade, we have deepened the fundamental understanding of mesoscopic and nanoscale transport theory [24, 25], witnessed high ZT close or above 2 for the state-of-the-art nanostructured thermoelectric materials [26], and achieved high conversion efficiency around 10% for single leg, unicouple, or module based on the nanostructured materials [27, 28]. To review these big developments in the nanostructured thermoelectric materials and devices, in this chapter we discussed the influence of nano-microstructural defects on phonon and electron transport behavior in bulk nanostructured thermoelectric materials, summarized the cutting-edge achievements in the high-performance nanostructured thermoelectric devices, and finally present some critical issues in these areas.

2 The Influence of Nano-Microstructural Defects on Electron and Phonon Transport Behavior

Electrons and phonons are fundamentally basic particles (or quasiparticles) in condensed matter, which crucially affect the material's electrical conductivity, magnetic properties, thermal conductivity, etc. For semiconductors, phonons typically have a broad mean free path (MFP) range, spanning from several nanometers

to micrometers [29]. In contrast, the MFP range of electrons is typically sharp, just around the nanometer scale [29]. Figure 1 compares the phonon and electron MFP distributions in several representative materials, including SnTe [30], GaAs [31, 32], Si [31, 33], and PbTe [34, 35],. Taking bulk crystalline silicon as a representative example, its room-temperature phonon MFP spectrum spans over 5 orders of magnitude from several nanometers to 100 μm while the electron MFP spectrum is located around dozens of nanometers [31, 33]. This critical difference enables realizing the relatively independent manipulation of electron and phonon transport behavior through designing nano-microstructural defects.

The formation of point defects is a common phenomenon in thermoelectric materials due to intrinsic reasons or intentional doping. For instance, GeTe possesses a high concentration of intrinsic Ge vacancies that critically depends on the crystal symmetry, which significantly affects the electrical and thermal transport behavior [36, 37]. Here we only focus on the effect of linear defects (dislocations), interfacial defects (grain boundaries, stacking faults, and twin boundaries), and volume defects (precipitates, secondary phases, and voids) in the context of bulk nanostructured thermoelectric materials. Figure 2 shows the schematic diagram and corresponding transmission electron microscopy (TEM) or scanning electron microscope (SEM) image of common defects in solid except for point defects [38–42], which will be discussed individually in the following.

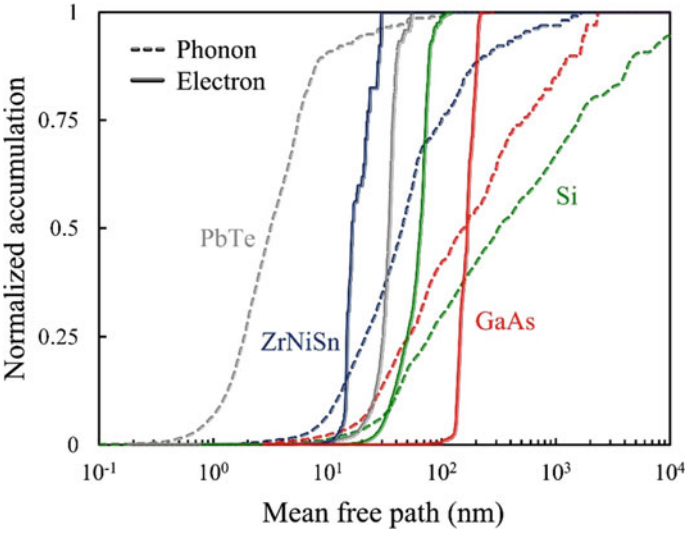

Fig. 1 Normalized accumulation of thermal (dashed) and electrical conductivity (solid lines) for four representative materials. The blue, red, green, and gray lines represent the MFP spectra of SnTe [30], GaAs [31, 32], Si [31, 33], and PbTe [34, 35], respectively. The electrical conductivities are calculated at *n*-type carrier concentration of 1×10^{20}, 1×10^{13}, 1×10^{14}, and 1×10^{17} cm^{-3} for SnTe, GaAs, Si, and PbTe, respectively [29]. Reprinted with permission from Ref. [29]. © 2018 Cambridge University Press

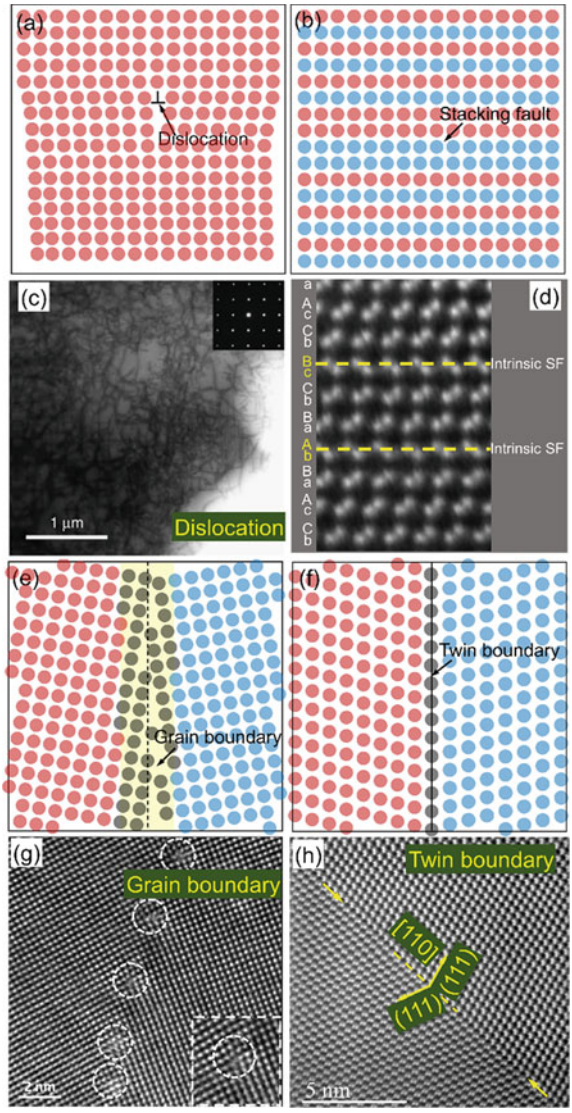

Fig. 2 The schematic diagram and corresponding TEM or SEM image of common defects in solid except for point defects. **a** and **c** dislocations [38], reprinted with permission from Ref. [38]. © 2017, Nature Publishing Group. **b** and **d** stacking fault [39], reprinted with permission from Ref. [39]. © 2017, Elsevier. **e** and **g** grain boundaries [40], reprinted with permission from Ref. [40]. © 2014, Wiley. **f** and **h** twin boundaries [39], reprinted with permission from Ref. [39]. © 2017, Elsevier. **i** and **k** nanoprecipitates [41], reprinted with permission from Ref. [41]. © 2012, Nature Publishing Group. **j** and **l** nanopores [42], reprinted with permission from Ref. [42]. © 2017, Elsevier [29]. Reprinted with permission from Ref. [29]. © 2018 Cambridge University Press

2.1 Linear Defects

Dislocations, including edge dislocations and screw dislocations, were first introduced to explain the plastic deformation properties of metal in the 1930s. For semiconductors, dislocations significantly affect the electron mobility [43], electron concentration [44], thermal conductivity [45], etc. The most investigated example is GaN film that is commonly used in light-emitting diodes and field-effect transistors. Hansen et al. employed the combination of atomic force microscopy and scanning

capacitance microscopy to first show the negative charge in the vicinity of dislocations [44], which clearly demonstrated the acceptor-like traps of threading dislocations. Weimann et al. first proposed a charged-dislocation-line scattering model for electrons when the dislocation density is higher than 10^8 cm^{-2}, where filled traps along threading dislocation lines acted as Coulomb scattering centers [43]. They first theoretically explained the reduction of carrier mobility at high dislocation densities range. For thermal properties, Klemens applied the second-order perturbation theory to treat the phonon scattering by static imperfections, including the effect of both dislocations cores and the corresponding elastic stress field [46, 47]. The phonon scattering rates from the dislocation core and strain field are described by $\tau_{DC}^{-1} \sim \omega^3$ and $\tau_{DS}^{-1} \sim \omega$, respectively. Scattering via dislocation cores can be considered in a short-range-interaction model similar to mass-difference scattering on point defects, whereas phonon scattering via the elastic field shows the long-range characteristics that depend on the type of dislocations [48]. Very recently, Li et al. utilized a fully quantized dislocation field, called as a "dislon", demonstrating that dislocation-phonon interaction possesses the nature of phonon renormalization, shown in Fig. 3 [45]. It provides new insights to study the influence of dislocation on the thermal properties from nanomaterials to bulk materials.

Traditionally, plastic deformation can increase the dislocation density in metals [49]. The dislocation formation mechanism is due to homogeneous nucleation, grain boundary initiation, or interfaces and surfaces between lattices and surfaces, precipitates, dispersed phases, or reinforcing fibers [50]. For example, He et al. found the large strain and misfit dislocations at the Sb nanoprecipitate/PbTe interfaces, which strengthened the phonon scattering [51]. Shen et al. applied the simple hot forging process to the coarse-grained $Bi_{0.5}Sb_{1.5}Te_3$ alloy [52], where in situ nanostructures and high density of dislocations can be observed. Since bulk semiconductors typically have a low density of dislocations at equilibrium, the critical role of dislocation scattering in thermoelectric materials has long been underestimated or neglected. In 2015, Kim et al. introduced the high-density dislocation arrays (~2×10^{11} cm^{-2}) at grain boundaries using the liquid-phase sintering technique in $Bi_{0.5}Sb_{1.5}Te_3$ alloy [53], which effectively scattered midfrequency phonons. Since grain boundaries and point defect scattering target the low- and high- frequency ends, thereby we can realize full-spectrum phonon scattering, and therefore, significantly reduce thermal conductivity (Fig. 4a). This achieved ultralow lattice thermal conductivity, *e.g.* 0.33 W m^{-1} K^{-1} at 320 K, leading to a record-high $ZT \sim 1.86 \pm 0.15$ (Fig. 4b).

Very recently, they claimed that dislocation arrays also enabled the suppression of minority carriers, resulting in an increase of the Seebeck coefficient and the carrier mobility [54]. Subsequently, Meng and Liu et al. used the same synthesis method for fabricating Yb-filled $CoSb_3$ with excess Sb content [55, 56]. Except for the dislocation-phonon scattering, it is the first experimental observation that dislocations arrays resulted in the energy filtering effect with little deterioration on the carrier mobility, as shown in Fig. 5. Because dislocation cores and corresponding strain fields are comparable with the mean free paths of electrons, they acted as the headstreams of the energy filtering effect and thus screened the lower-energy carriers. Low-temperature range Seebeck coefficients were thus largely enhanced, which led

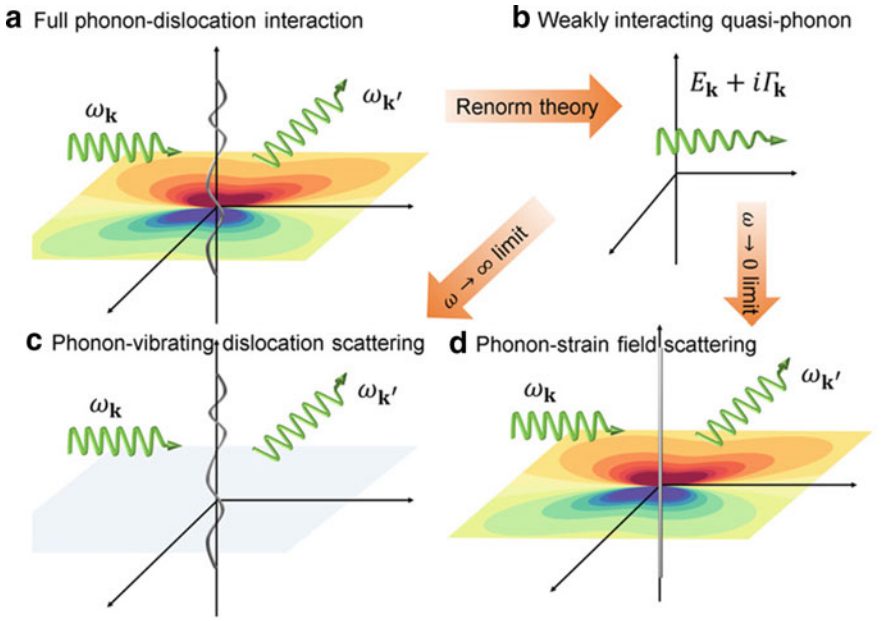

Fig. 3 **a** Schematics of classical dynamic dislocation-phonon scattering, where scattering is accomplished when the dislocation absorbs an incoming phonon ω_k and re-emits another phonon $\omega_{k'}$. **b** Due to the electron–ion drag force, an electron is renormalized to a quasi-particle called a "polaron". **c** The quantum picture of the dislocation—phonon interaction (DPI). Due to the long-range field of the dislocation, a phonon ω_k starts to interact with the dislocation even far away from the core region, making renormalization a more suitable picture than scattering. After renormalization, the strong DPI disappears. We are left with the weakly interacting quasi-phonons with a renormalized energy E_k and a finite lifetime Γ_k [45]. Reprinted with permission from Ref. [45] © 2017, American Chemical Society

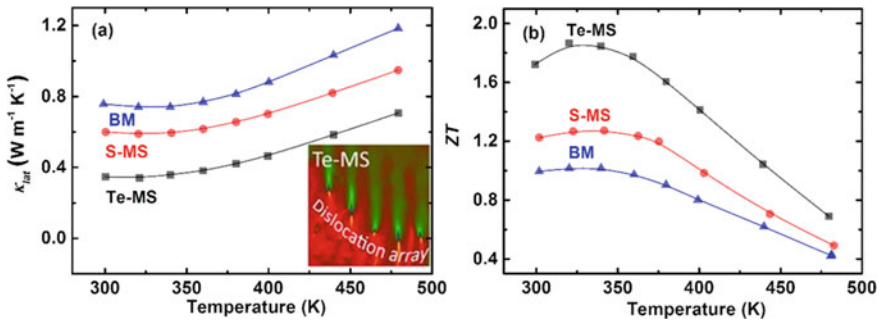

Fig. 4 Full-spectrum phonon scattering in high-performance bulk thermoelectrics. **a** Lattice thermal conductivity (κ_{lat}) for $Bi_{0.5}Sb_{1.5}Te_3$ alloys produced solid-phase compaction (BM and S-MS) and liquid-phase compaction (Te-MS). **b** The figure of merit (ZT) as a function of temperature for $Bi_{0.5}Sb_{1.5}Te_3$ alloys [53]. Reprinted with permission from Ref. [53]. © 2015, American Association for the Advancement of Science

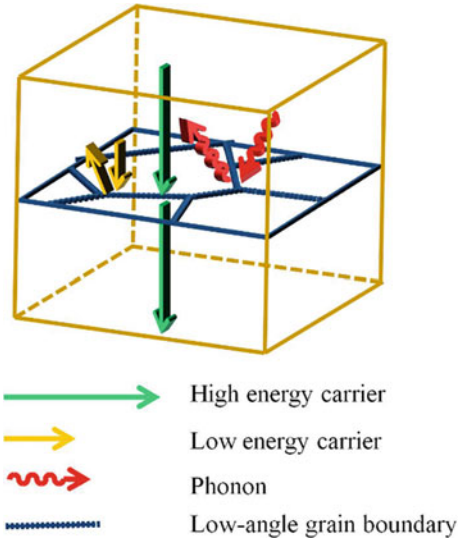

Fig. 5 Schematic diagram of carrier and phonon scattering mechanism by low-angle grain boundaries for the Yb filled $CoSb_3$ with excess Sb content prepared by liquid phase compaction [55]. Reprinted with permission from Ref. [55]. © 2017, Wiley

to a high room-temperature power factor value around 47 μW cm^{-2} K^{-1} and a high average ZT ~ 1.08 from 300 to 850 K. Introducing dense dislocations using the liquid phase compaction method were also observed in n-type Bi_2Te_3 and p-type cerium filled $CoSb_3$ [57, 58]. Pei et al. used a different approach whereby dislocation loops were generated by the collapse of vacancies discs in lead chalcogenides [38, 59]. The observed high ZT was mainly attributed to the significant reduction of the lattice thermal conductivity through the scattering of mid-frequency phonons by dense dislocations. Zhao et al. proposed a bottom-up nanostructure synthesis approach for half-Heusler alloys, namely n-type $Hf_{0.25}Zr_{0.75}NiSn_{0.97}Sb_{0.03}$ and p-type $Nb_{0.8}Ti_{0.2}FeSb$, with dense dislocation arrays at the grain boundaries based on the displacement reaction between metal chlorides/bromides and magnesium (or lithium), followed by vacuum-assisted spark plasma sintering (SPS) process [60]. The measured lowest lattice thermal conductivity κ_{lat} was about 1 W m^{-1} K^{-1} at 900 K, leading to the relatively high ZT ~ 1.

2.2 *Interfacial Defects*

Interfacial defects, including grain boundaries, stacking faults, and twin boundaries, are usually observed in thermoelectric materials, where grain boundaries, dominating the grain size, play a more pronounced role in the thermoelectric properties. For achieving nanostructured materials with grain size below or around several hundreds of nanometers, the fabrication method can be simply divided into two main categories: top-down and bottom-up approaches. The top-down approach means from the top (larger) to bottom (smaller) whereas the bottom-up approach means from the

bottom (smaller) to top or up (larger). In the following, we just briefly talk about these two common approaches for the preparation of nanostructured thermoelectric materials.

The most conventional top-down approach in thermoelectric science is ball milling method for directly and efficiently reducing the grain size. Ball milling enables producing fine powder around microsize, sometimes even down to the nanoscale, where raw materials can be synthesized by quartz tube melting or arc melting, or any method which produces the required elements and compounds with large grain size. According to the main motion of the jar, there are three common ball milling machines, including rotary, planetary, and shaker (Fig. 6), where planetary and shaker ball milling are more efficient to grind materials, especially for the purpose of mechanical alloying, due to the inputted high dynamic energy resulted from the difference in speeds between the balls and grinding jaws. For example, Umemoto et al. used mechanical alloying to prepare β-$FeSi_2$ doped with Al and Mn by the conventional rotary ball milling around 300 h with a milling speed of 95 rpm [61]. For planetary ball milling, the maximum milling speed is around 400–500 rpm which can easily grind the raw materials down to micro range ~0.1–1 μm with a long ball milling time. This fabrication method is widely used in academic research institutes related to material science, even for some industrial productions. For example, Schilz et al. systematically studied the influence of the planetary ball mill setting parameters on the evolution of alloy formation on the thermoelectric semiconductor systems [62], Si-Ge, Mg_2Si, and Mg_2(Si, Sn), demonstrating that the geometry of the mill and the ratio of the angular velocities of the planetary and the system wheel played a crucial role in milling performance. Shaker ball milling, or so-called high energy ball milling, has a higher milling speed around 1000 rpm through shaking in a complex motion that combines back-and-forth swings lateral movements. Therefore, the related ball milling time can be sharply reduced and the powder size can even be decreased to several nanometers, depending on the material's properties. For example, Cook et al. tried to prepare SiGe based thermoelectric materials by planetary ball milling [63], but X-ray diffraction measurements taken of the ball-milled powder after 72 h of processing showed that the Si and Ge lines had not changed,

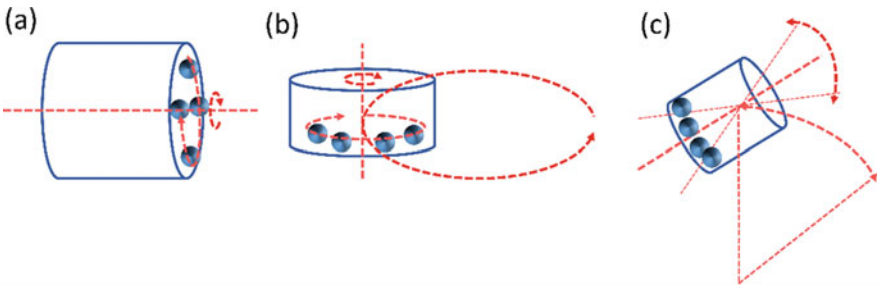

Fig. 6 Schematic pictures of ball milling motions. **a** 1-dimensional rotary ball mill, **b** 2-dimensional planetary ball mill, and **c** 3-dimensional shaker ball mill [64]. Reprinted with permission from Ref. [64]. © 2013, Springer

indicating alloying had not occurred. Instead, using high energy ball milling for 6 h, the powder X-ray diffraction measurement indicated that an alloy had formed, having a lattice parameter corresponding to the relative amounts of starting materials.

Another popular top-down approach is the melting spinning technique used for the rapid cooling of liquids (Fig. 7a), which has gained wide acceptance as a means of producing amorphous or ultrathin ribbons. Due to the different cooling rate during the melt spin process, a gradient of multiscale microstructures is observed along the thickness direction of the ribbon, from the amorphous phase near the contact surface to the randomly oriented nanocrystalline domains in the midpart of the ribbon, and finally to the microsize crystals near the free surface (Fig. 7b) [65]. More importantly, the preparation time for certain compounds can be greatly shortened by using the melting spinning process because of the much shorter atom diffusion distances in nanoscale grains. For example, the formation of the skutterudite phase usually needs an additional long-time annealing process around 7 days, but melting spinning technique can reduce the preparation time to less than 24 h [66, 67].

The bottom-up approach usually means the solution chemistry approach for the preparation of nanostructured thermoelectric materials [68, 69]. The most widely used solution chemistry approaches generally include hydro/solvo-thermal [70, 71], microwave-assisted synthesis [72, 73], sonochemical and ligand-based synthesis [74, 75], where simple chalcogenides compounds, like Bi_2Te_3 [70, 71, 74–76], PbTe [70, 77], SnSe [78, 79], Bi_2S_3, [80, 81], etc., are the most commonly investigated system. Using the solution chemistry approaches enables the precise control of the composition, size, shape, boundary roughness, and crystallinity of produced nanoparticles. One example carried out in our lab, is the solvothermal fabrication of $Cu_{1.75}Te$ nanosheets with a few nanometers in thickness and lateral dimensions in the order of micrometers, leading to a dramatic reduction in thermal conductivity [82].

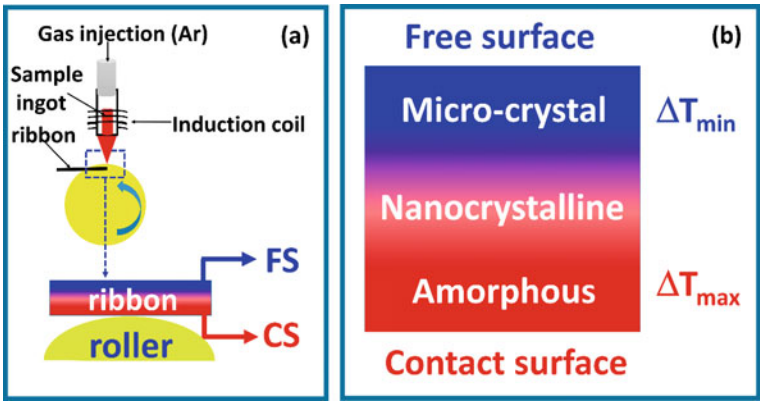

Fig. 7 **a** Diagram of the melting spinning process denoting the free surface (FS) and contact surface (CS), **b** schematic structure distribution in the ribbon from the contact surface to free surface [65]. Reprinted with permission from Ref. [65] © 2010, American Chemical Society

Actually, research about the effect of grain size on thermoelectric properties has been carried out from around the 1970s [83–86], especially for SiGe alloys [85]. However, due to the contamination of fine powders and also still large grain size after hot press [84, 85], the corresponding thermoelectric performance did not show observable enhancement. Until the broad spreading of the spark plasma sintering (SPS) technique in the 1990s [87], nanostructured thermoelectric materials with fine grains showed much higher performance than its counterpart with coarse grains. For example, Li group at Tsinghua University, China used mechanical alloying (planetary ball milling) coupled with SPS to enhance the thermoelectric performance in various systems, including Bi_2Te_3 [88], $CoSb_3$ [89], $AgPb_mSbTe_{2+m}$ [90], and sulfide compounds [91]. For the $AgPb_mSbTe_{2+m}$ compound, single-phase can be obtained by mechanical alloying in a relatively short time 3 h, where the average grain size after SPS was about 1 μm and the highest *ZT* was about 1.37 at 673 K [92]. Ren group in Boston College (now moving to the University of Houston) employed the high energy ball milling and quick hot process to successfully fabricated high-performance nanostructured thermoelectric materials, like Bi_2Te_3 [93, 94], $CoSb_3$ [95, 96], Mg_2Si [97, 98], SiGe [99, 100], and half-Heusler alloys [101, 102], and, more importantly, synthesize some new compounds, like α-MgAgSb [103–106] and Zintl phase [107–109]. For the nanostructured α-MgAgSb, two-step ball-milling method in combination with quick hot press process can obtain nanostructured materials with all-scale hierarchical architectures, including nano-micro scale grains, nanoinclusions, stacking faults, nanotwins, and high density of dislocations (Fig. 8).

Benefitting from hierarchical microstructure for phonon scattering and getting rid of impurity phases, the corresponding maximum *ZT* was around 1.2 at 548 K, much higher than α-MgAgSb with coarse grains by Ying et al. [111] and Kirkham et al. [112] (Fig. 9), making it very promising for power generation for room to mid-temperature applications [94]. Tang group in the Wuhan University of Technology, China synthesized nanostructured Bi_2Te_3 [65], $CoSb_3$ [67], Zn_4Sb_3 [113], and $MnSi_{1.8}$ [114] with high performance using the rapid melting spinning followed by an SPS process. For the nanostructured p-type $(Bi, Sb)_2Te_3$, the grain size was around several hundreds of nanometers with 10–20 nm nanocrystals embedded in the bulk matrix. Compared to the commercial zone melting material, a 50% enhancement in the *ZT* over a wide temperature range can be obtained for nanostructured p-type $(Bi, Sb)_2Te_3$, which was attributed to the sharp reduction of lattice thermal conductivity [65]. Cabot group in Catalonia Institute for Energy Research, Spain, used the colloidal synthetic route to prepare nanoparticles for binary, ternary, and quaternary chalcogenides compounds, like PbS [115], Cu_2SnSe_3 [116], $Cu_2ZnGeSe_4$ [117], respectively, which served as building blocks for fabricating bulk nanostructured high-performance thermoelectric materials.

The origin of high performance of nanostructured thermoelectric materials with fine grains is mainly attributed to the sharp reduction of lattice thermal conductivity through the strong phonon-boundary scattering. The grain boundary scattering rate shows independence from phonon frequency, $\tau_{GB}^{-1} \sim \omega^0$, when the misfit angle is small (less than 15°), which means stronger interaction with low-frequency phonons because of their long wavelength [118]. However, grain boundaries also

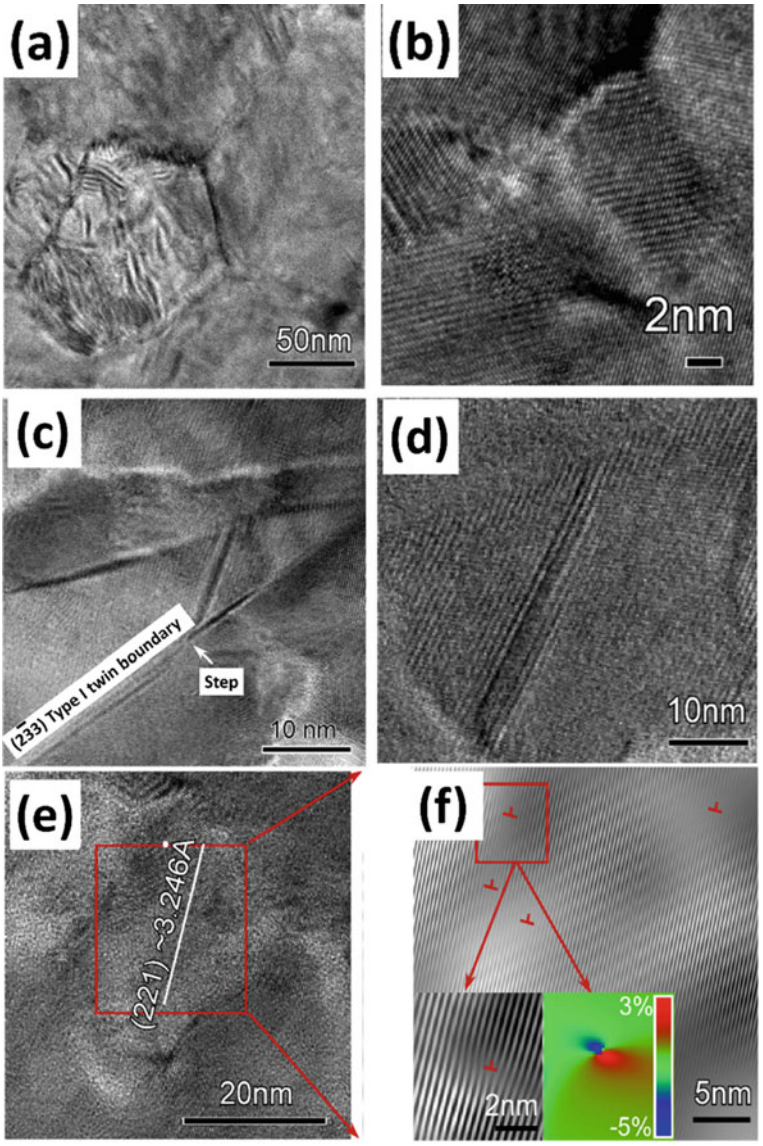

Fig. 8 Typical microstructures for nanostructured α-MgAgSb. **a** nano-micro scale grains, **b** nanoinclusions, **c** spearhead shaped type-I nanotwins, **d** stacking faults, **e** high density of dislocations inside the grain, and **f** corresponding inverse FFT (IFFT) images with the enlarged dislocations and GPA analysis images as insets [105, 110] Reprinted with permission from Ref. [105]. © 2016, WILEY and [110] 2017, Elsevier

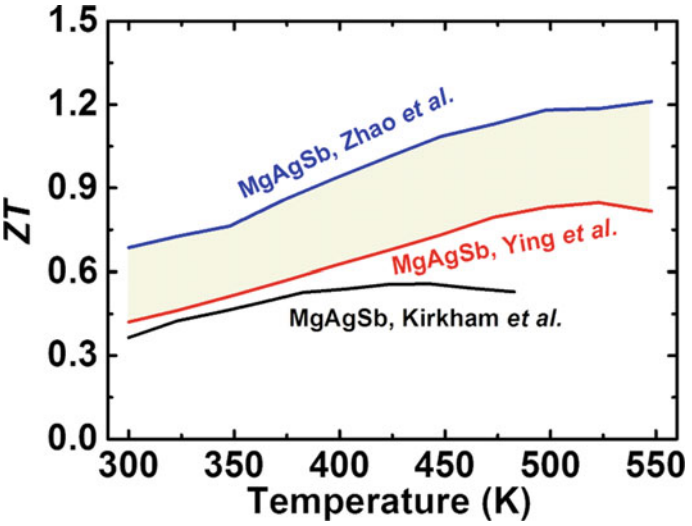

Fig. 9 Comparison of temperature-dependent *ZT* among nanostructured α-MgAgSb [106], α-MgAgSb with coarse grains by Ying et al. [111] and Kirkham et al. [106, 112] Reprinted with permission from Ref. [106]. © 2018, The Royal Society of Chemistry

inevitably scatter electrons, resulting in decreased carrier mobilities. Therefore, the final enhancement of *ZT* depends on the balance between phonon-boundary scattering and electron-boundary scattering. It should be mentioned that the energy filtering effect in thermoelectrics was first proposed by Mahan and Woods [119], and also Shakouri et al. [120], for superlattice structures. Energy filtering enhancement was demonstrated in nanostructured PbTe by Heremans et al. [121], where an enhancement in the Seebeck coefficient of PbTe nanostructures with grain sizes on the order of 30–50 nm was observed, relative to the bulk. Enhancement of power factor can usually only be achieved by band engineering [122], which is not trivial to implement. Therefore, more readily introduced nanostructuring methods are attractive. Incidentally, power factor enhancement has also recently been demonstrated by utilizing magnetism, i.e. magnetic interactions [123–128]. Spin fluctuation has also recently been demonstrated to lead to significant enhancement of high power factors [129].

Other interfacial defects, including stacking faults and twin boundaries, also affect the phonon and electron transport behavior. Stacking faults and twin boundaries are usually observed in close-packed crystal structures that have a low defect formation energy or are related to the solid-state phase transformations [130, 131]. For example, GeTe compound exhibits a ferroelectric phase transition from the low-temperature rhombohedral structure to high-temperature cubic structure [132, 133], so twin boundaries are easily observed for GeTe based materials [131, 134]. Due to the lower formation energies of stacking faults or twin boundaries in comparison

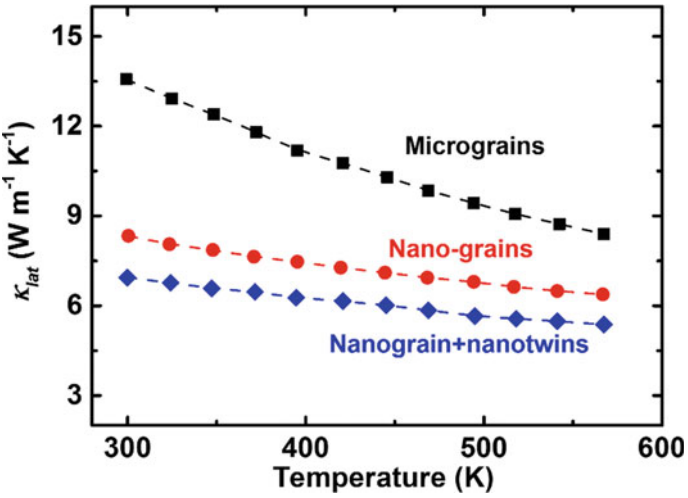

Fig. 10 Comparison of lattice thermal conductivity between different InSb samples [39]. Reprinted with permission from Ref. [39]. 2017, Elsevier

with high-angle grain boundaries, the presence of stacking faults and twin boundaries would thus decrease the total interfacial energy from a thermodynamic viewpoint [135]. Therefore, sometimes the strong plastic deformation can also increase the density of stacking faults or twin boundaries [39, 110, 136]. Here, it should be highlighted that nanoscale stacking faults can be also frequently observed in some compounds having natural superlattice structures, like $(MX)_{1+x}(TX_2)_n$ (M = Pb, Bi, Sn, Sb, rare earth elements; T = Ti, V, Cr, Nb, Ta, X = S, Se; n = 1, 2, 3) owing to the disordered stacking sequence along the c-axis [137]. Generally, stacking faults and twin boundaries have a weak scattering process for phonons and electrons compared with normal high-angle grain boundaries due to the semi-coherent or coherent boundary characteristics. For example, Mao et al. experimentally demonstrated that nanotwin boundaries in the InSb compound slightly suppressed the lattice thermal conductivity, around 17% at 300 K, whereas these normal grain boundaries led to a 40% reduction of lattice thermal conductivity [39], as shown in Fig. 10. Besides, it is also reported that nanotwin boundaries in Cu-Ni alloy selectively screen low-energy carriers by potential barrier scattering, which resulted in enhancement of the Seebeck coefficient by increasing the density-of-states (DOS) effective mass [138].

2.3 Volume Defects

Volume defects in crystals are three-dimensional aggregates of atoms or vacancies. In thermoelectrics, it is usual to divide them into three classes based on a combination

of the size and effect of the particle, including precipitates, secondary phases, and voids.

Precipitates refer to small particles that are introduced into the matrix by solid-state reactions. Generally, the purpose of precipitates in the solid matrix is to increase the material's mechanical strength by acting as obstacles to the motion of dislocations. In thermoelectrics, since the interface between precipitates and matrix is semi-coherent or coherent, it is generally assumed that nanoprecipitates can scatter phonons with little or no deterioration of carrier mobility [139]. Nucleation and growth process is the common approach to introduce precipitates in the matrix. It requires that precipitates have low or no solubility in the solid state, but complete solubility in the liquid state, as shown in Fig. 11a [140]. Due to the final increased system free energy, interfacial energy and strain energy codetermine the final morphology of precipitates. Kanatzidis group in the Northwestern University developed nanostructured $AgPb_mSbTe_{2+m}$ with ultrahigh ZT of ~2.2 at 800 K, in which the endotaxially embedded Ag-Sb–rich nanoprecipitates in the matrix were assumed to play a profound role [139]. This strategy of forming in-situ nanoprecipitates in the matrix strongly stimulates the development of nanostructured thermoelectric materials in other chalcogenides systems [141–145]. It should be mentioned that the appearance of elemental Ge precipitates is the normal phenomenon in GeTe based materials owing to the low defect formation energy of Ge vacancy. This provides a feasible method to manipulate the precipitate concentration by doping or alloying for reducing the thermal conductivity and enhancing ZT [146].

Another approach is to use Spinodal decomposition to realize a uniform-sized and periodic fine microstructure. In contrast with the nucleation and growth process, Spinodal decomposition is a typical "uphill" diffusion process without the requirement

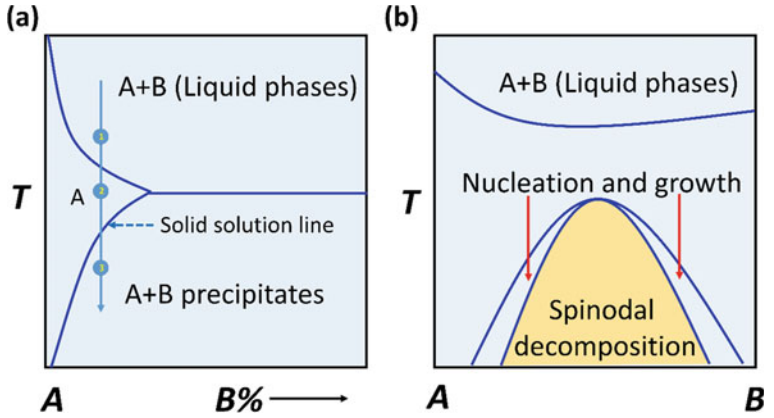

Fig. 11 Schematic diagram of nanoprecipitates formation approach: **a** a strongly temperature-dependent solubility of the secondary phase of B in the A matrix, **b** a complete solid solution exists between the two end-members A and B, including Spinodal decomposition and typical nucleation and growth [147]. Reprinted with permission from Ref. [147] © 2014, The Royal Society of Chemistry

to overcome the thermodynamic barrier [140], where Fig. 11b shows the schematic diagram of Spinodal decomposition formation mechanism between the two end-members A and B [147]. Therefore, the phase interfaces generally keep coherent or semicoherent and, more importantly, the separate regions with different chemical compositions hold the same crystal structure, which situation is believed to have little detrimental influence on the electron transport process. However, there are only a few concrete examples showing the typical morphology of Spinodal decomposition, including PbTe/GeTe [148], PbTe/PbS [149], (Ti, Zr, Hf) NiSn alloys [150], and p-type filled skutterudite [151].

In certain circumstances, some nanoscale secondary phases are also intentionally incorporated into the thermoelectric parent phase to form nanocomposites, including SiC [152], B_4C [153], carbon nanotube [154], reduced graphene oxide [155], etc. Due to the different structure and properties between the secondary phase and matrix, the introduction of nanoscale secondary phases sharply suppresses the lattice thermal conductivity. Meanwhile, the mechanical properties can be also improved due to the particle hardening [88, 152, 156], which is beneficial for real applications. For example, these homogeneously dispersed CoSi nanoprecipitates in the matrix of $Yb_{0.3}Co_4Sb_{12}$ not only enhance the average *ZT* but also increase the hardness and indentation fracture toughness [156]. Figure 12 showed the microscopy images of indentation microstructural of p-type $Bi_{0.3}Sb_{1.7}Te_3$ without and with different nano-SiC content, in which the morphology evolution under indentation clearly revealed that the resistance against cracking and fracture was increased by the dispersion

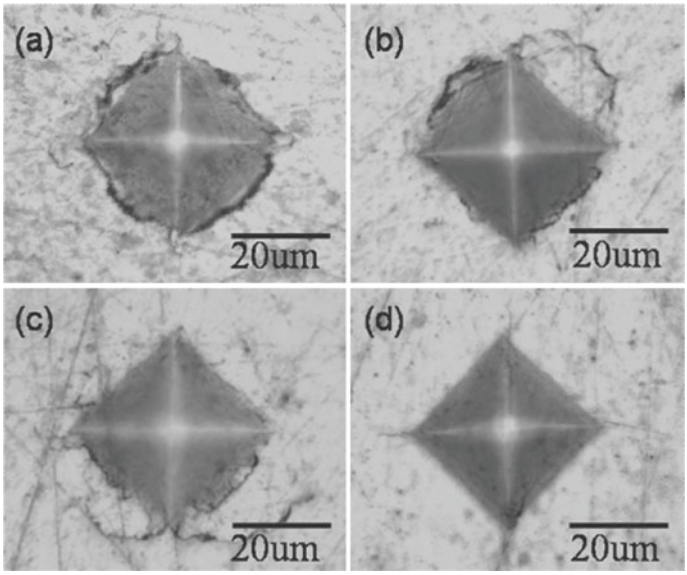

Fig. 12 Microscopy images of indentation of $Bi_{0.3}Sb_{1.7}Te_3$ without and with different nano-SiC content: **a** 0 vol% SiC, **b** 0.1 vol% SiC, **c** 0.4 vol% SiC, and **d** 0.6 vol% SiC [152]. Reprinted with permission from Ref. [152] © 2013, WILEY

of SiC nanoparticles. However, special attention should be placed on the drop of carrier mobility owing to the strong scattering from incoherent interfaces, which may eventually reduce *ZT*.

As another beneficial nanocomposite effect, for some compounds with relatively low electrical conductivity and large Seebeck coefficients, the introduction of nanoscale metallic secondary phases with partial connecting networks has resulted in the large increase of electrical conductivity and the overall increase in power factor [157–160]. While very high $ZT > 1$ has not been observed yet, this is another interesting strategy.

To simply analyze the contribution of phonon-scattering from nanoparticles or nanoprecipitates, their morphologies are generally assumed as the polydispersed spherical type with one single size. Based on two limiting cases, where the particle size parameter approaches zero and the size parameter approaches infinity, the relaxation time of phonon scattering due to the nanometer-scale precipitates can be estimated by $\tau_{NP}^{-1} \sim \omega^0 + \omega^4$. Therefore, its relaxation time interpolates between the long (geometrical scattering) and short (Rayleigh limit) wavelength scattering regimes. This indicates that nanoparticles or nanoprecipitates can scatter the phonon in a wider range of frequencies [161]. Zhang et al. reported that a broad spectrum of thermal phonons can be most effectively scattered not by a similarly broad distribution of nanoparticle or nanoprecipitate size, but by one with a few discrete peaks at well-chosen radii based on the results of theoretical calculations [162]. However, for the model of carrier-scattering by nanoparticles or nanoprecipitates, there is no elegant model or formula to describe it. However, in addition to the normal carrier-scattering process by nanoparticles or nanoprecipitates, an induced carrier filtering effect can result in an increase in the energy dependence of the relaxation time, thereby enhancing the Seebeck coefficient. For example, as mentioned before, Heremans et al. experimentally demonstrated that PbTe sample containing Pb precipitates with sizes on the order of 30–40 nm showed enhanced Seebeck coefficients, which was related with the carrier filter effect as revealed by the measurements of thermoelectric and thermomagnetic transport coefficients [163]. One interesting study was done checking the long term stability of the thermoelectric performance of nanocomposites. Oxide nanoparticles in $Bi_{0.5}Sb_{1.5}Te_3$ led to the enhancement of Seebeck and maximum of $ZT \sim 1.5$ at 350 K, with $ZT > 1.0$ for a wide temperature range up to 450 K. A study over two years revealed that *ZT* shows a slight but not large degradation in this case, at least [164].

Fabricating bulk sample with porous structure is challenging, especially for making nanopores. Generally, lowering the hot press temperature or pressure [165], or the introduction of low volatile phases or hollow precursor [166] can help the formation of the porous bulk thermoelectric materials. For bulk sample with a porous structure, the effective medium model is normally used to explore the effect of porosity on the thermoelectric properties [167]. In this case, the porosity is the only dominating factor. However, Song et al. observed a significant phonon size effect by measuring the thermal conductivity of single-crystalline silicon membranes with periodic through-membrane pores of nominal pore diameters of 2 and 10 μm [168], where small-pore membranes have smaller thermal conductivity compared

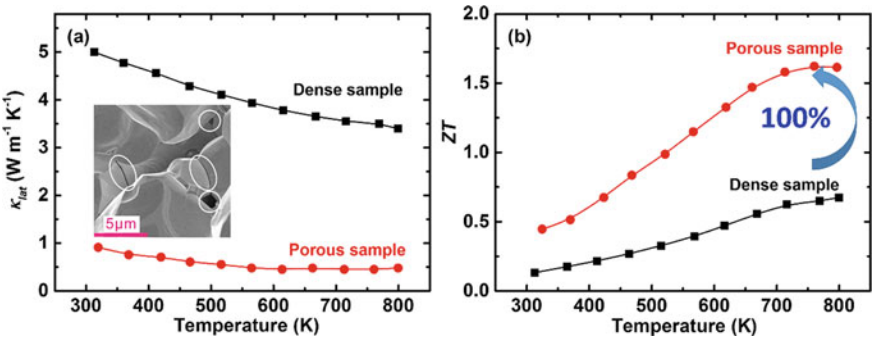

Fig. 13 **a** and **b** Temperature-dependent lattice thermal conductivity and *ZT* for pristine and porous $Co_{23.4}Sb_{69.1}Si_{1.5}Te_{6.0}$ sample, respectively, where the inset as the typical SEM micrograph of porous microstructure

with the large-pore ones despite the comparable porosity. Lee et al. pointed out that the alignment of nanometer-sized pores is important to preserve power factor values comparable with those of bulk Si by molecular dynamics calculations and ab initio density functional theory [169]. Besides, it is assumed that the majority of reduced thermal conductivity is due to the low-frequency phonon scattering of the pore boundaries [170]. Nanoscale pore also induces the energy filtering effect, contributing to increasing the Seebeck coefficient [171]. However, the validity of enhancing *ZT* via porous structure significantly depends on the competition and offset between the decreased thermal conductivity, the increased Seebeck coefficient, and the sharply decreased carrier mobility. In reality, there are already some experimental reports about the beneficial role of designing a porous structure to enhance bulk thermoelectric performance for some systems, like Si [172], $CoSb_3$ [42], Bi_2Te_3 [173], Cu_2Se [174], etc. Among them, our group designed a porous bulk architecture contains nano- to micrometer size and randomly-oriented pores in rare-earth–free un-filled skutterudites $Co_{23.4}Sb_{69.1}Si_{1.5}Te_{6.0}$ by high-temperature annealing, shown in the inset of Fig. 13a. This nano-micro porous structure effectively scattered a wide spectrum of phonon and therefore lattice thermal conductivity reached the phonon glass limit (Fig. 13a), which led to an unprecedented and very promising *ZT* of 1.6, around 100% enhancement in comparison with dense samples (Fig. 13b) [42].

3 Nanostructured Thermoelectric Devices for Energy Harvesting

Nanostructuring method has, no doubt, advanced the rapid development of efficient high-performance thermoelectric materials. However, in terms of nanostructured thermoelectric devices, in fact, there are few remarkable achievements because of

the complex and difficult device-fabricating and properties-measuring process. Thermoelectric modules consist of an array of p- and n-type thermoelectric legs, which are connected electrically and thermally in parallel between two ceramic substrates. Figure 14 shows the schematic diagram of a practical thermoelectric module configuration and the stacking layers between the thermoelectric leg and the conducting strip, where a metalized contact layer is needed between thermoelectric elements

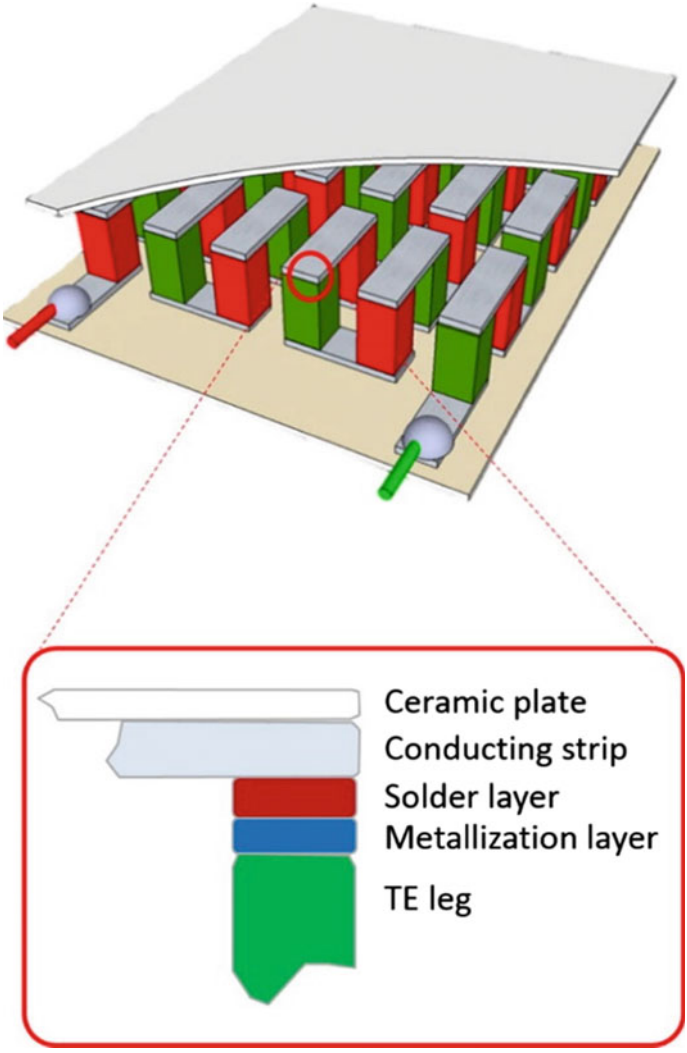

Fig. 14 Schematic diagram of a practical thermoelectric module configuration and the stacking layers between the thermoelectric leg and the conducting strip [175]. Reprinted with permission from Ref. [175], 2015, Elsevier

and solder for most good thermoelectric materials [175]. Since the module assembling process involves great mechanical engineering efforts, reports about fabrication method and properties measurement of single leg or unicouple are more common in thermoelectric community where the process is more simple. In the following, we just briefly summarized the fabrication method and measurement results of some typical high-performance nanostructured thermoelectric single leg, unicouple, and modules.

3.1 Thermoelectric Single Leg

To validate the high *ZT* of the thermoelectric material or test if the contact layer is suitable or not, thermoelectric single-leg measurement is the most reliable and recommended way. Figure 15 shows the **e**xperimental setup to measure single thermoelectric leg efficiency under a large temperature difference in a home-made measurement facility [176]. The measurement principle has also been detailed [176, 177]. Single-leg of p-type nanostructured MgAgSb thermoelectric materials with Ag contact pads fabricated by the one-step hot-press technique demonstrated a record high thermoelectric conversion efficiency of 8.5% at a relatively low-temperature difference of 225 K between 293 and 518 K [106, 177]. Single-leg of n-type nanostructured Mg_3Sb_2-based thermoelectric materials showed a high conversion efficiency ~10.6% at a temperature difference of 400 K from 373 to 773 K using the Fe contact layer [176]. Further optimization via reducing the contact resistance by using 304 stainless steel power as the contact layer contributed to the suppressed interfacial reaction, ideal electrical properties, and robust mechanical properties, lead to the increased efficiency [178]. Nanostructured NbFeSb half-Heusler alloy, which is famous for its high power factor over 100 $\mu W \cdot cm^{-1} \cdot K^{-2}$, demonstrated a record output power density around 22 $W \cdot cm^{-2}$ based on a single-leg device using Ti or Hf doping [179, 180]. Very recently, p-type ZrCoBi-based nanostructured half-Heusler alloy, with a high *ZT* ~ 1.4 at 973 K, showed a high output power density and conversion efficiency of ~9.3 W cm^{-2} and ~9% with cold-side and hot-side temperature being 323 and 823 K for the single leg [181]. P-type TaFeSb-based nanostructured half-Heusler alloy had a record-high *ZT* of ~ 1.5 at 973 K, which demonstrated a high conversion efficiency ~11.4% at the cold-side temperature of 317 K and hot-side temperature of 973 K for the single leg [182].

3.2 Thermoelectric Unicouple

Taking the nanostructured half-Heusler materials as a representative sample, Fig. 16 shows the flow diagram illustrating the fabrication processes of the high-performance thermoelectric generators, where the thermoelectric unicouple is the smallest constitutional unit. Using nanostructured BiSbTe and commercial n-type Bi_2Te_3 material,

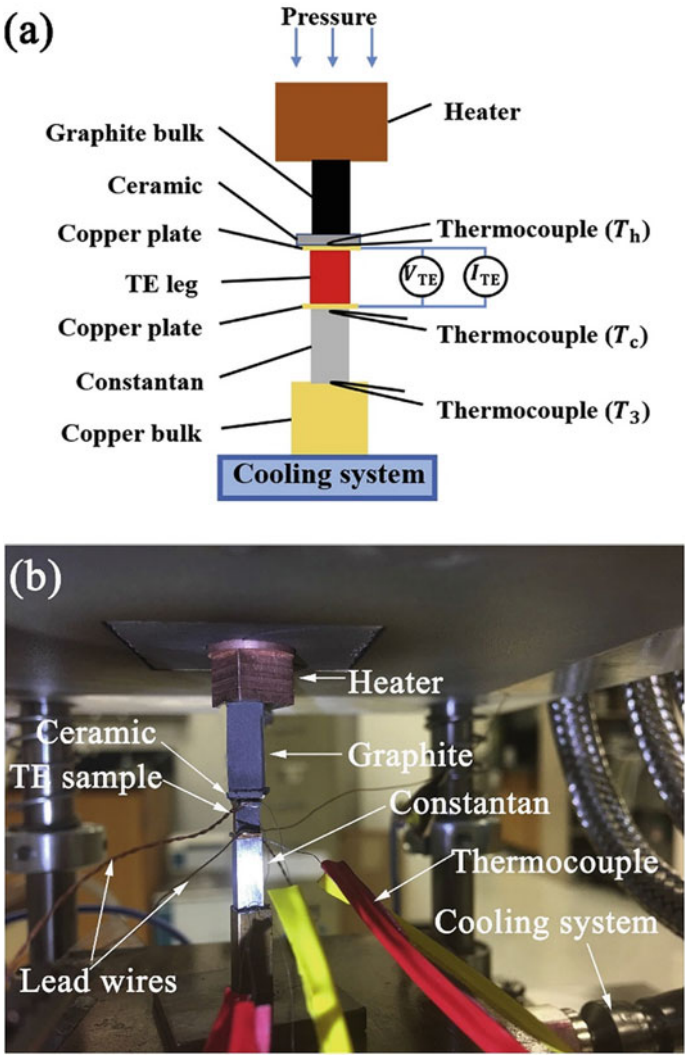

Fig. 15 Experimental setup to measure single thermoelectric leg efficiency under a large temperature difference: **a** schematic and **b** real image of the setup [176]. Reprinted with permission from Ref. [176], 2019, Elsevier

unicouple cooling devices were fabricated, which produced high-temperature differences of 86, 106, and 119 K with hot-side temperatures set at 323 K, 373 K, and 423 K, respectively [94]. Nanostructured skutterudite unicouple, where $CoSi_2$ is used as the electrode for the n-type skutterudite ($Yb_{0.35}Co_4Sb_{12}$) and Co_2Si for the p-type skutterudite ($NdFe_{3.5}Co_{0.5}Sb_{12}$), showed a maximum efficiency of 9.1% operating between 373 and 823 K [183]. Based on the nanostructured half-Heusler alloys, where TiCoSb and ZrNiSn based materials as the p-type and n-type, respectively,

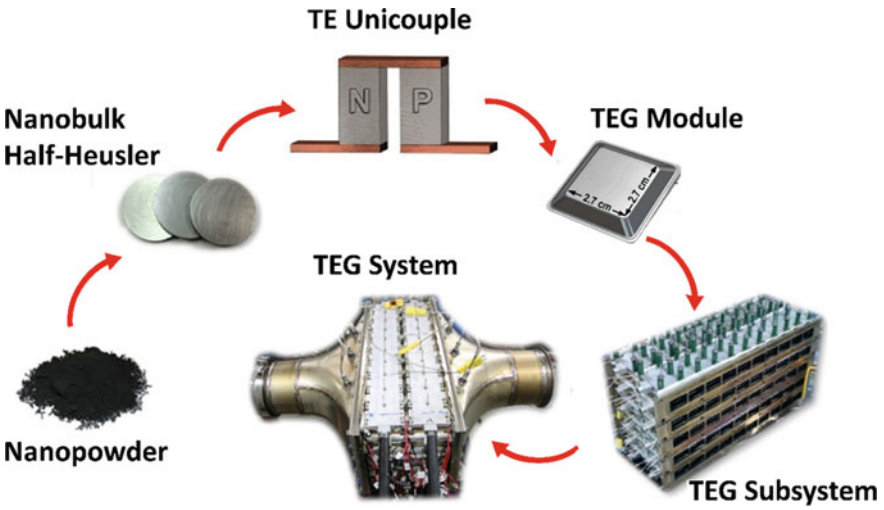

Fig. 16 Pictures illustrating the fabrication processes of the high-performance thermoelectric generators [184]. Reprinted with permission from Ref. [184], 2015, Elsevier

a unicouple device generated a high power density of 5.26 W cm^{-2} between hot and cold sides as 373 K and 873 K, respectively. This unicouple power density demonstrated negligible degradation after 200 thermal cycles, indicating excellent reliability despite high thermal stresses under large differences [184].

3.3 Thermoelectric Module

The majority of commercial companies focus on the Bi_2Te_3 thermoelectric modules for low-temperature applications whereas these academic institutes or universities also investigate the fabrication and optimization of medium and high-temperature thermoelectric modules, such as skutterudite, PbTe, half-Heusler alloys, etc. A typical photo of the thermoelectric module is shown in Fig. 17a that is Skutterudite-based thermoelectric modules manufactured by the Shanghai Institute of Ceramics, Chinese Academy of Sciences [185]. In the following, some representative work related to the design and optimization of thermoelectric modules is highlighted. A 16 leg thermoelectric module was made by using n- and p-type skutterudite-graphene nanocomposites, where the introduced reduced graphene oxide (rGO) largely increased the grain boundary thermal resistivity with no deterioration of electrical transport properties. The measured maximum power output ~3.8 W and conversion efficiency ~8.4% can be achieved under hot/cold-side temperature 873 K/296 K, respectively (Fig. 17b). The conversion efficiency of skutterudite–graphene nanocomposites was 24% higher compared to 6.8% for a module made of n- and p-type skutterudite without rGO [186]. P-type sample of PbTe–2% MgTe doped with 4% Na with a

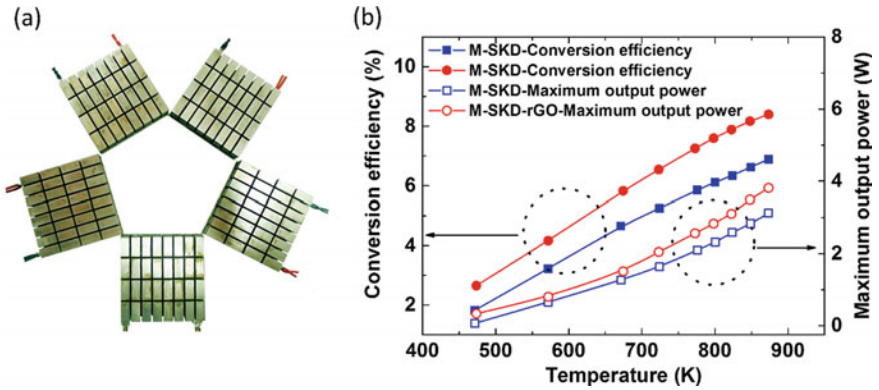

Fig. 17 **a** A photo of Skutterudite-based thermoelectric modules (50 × 50 mm) manufactured by the Shanghai Institute of Ceramics, Chinese Academy of Sciences [185]. reprinted with permission from Ref. [185]. © 2016, Nature Publishing Group. **b** The maximum conversion efficiency and power output as a function of hot side temperature T_h for the skutterudite/rGO based modules (M-SKD/rGO) and the reference device made of pure SKD (M-SKD) [155]. Reprinted with permission from Ref. [155]. © 2017, The Royal Society of Chemistry

high ZT ~ 1.8 at 810 K due to the largely suppressed lattice thermal conductivity from nanoprecipitates scattering and n-type sample of PbTe doped with 0.2% PbI_2 with high ZT ~ 1.4 at 750 K were used as p- and n-type thermoelectric legs, where $Co_{0.8}Fe_{0.2}$ alloy was chosen as diffusion barriers. The eight-couple (sixteen-leg) PbTe-based module was fabricated, which exhibited the maximum conversion efficiency of 8.8% under hot/cold-side temperature of 873 K/303 K [187]. Similarly, using p-type nanostructured $Pb_{0.953}Na_{0.040}Ge_{0.007}Te$ with nanoprecipitates as a p-type leg and $PbTe_{0.9964}I_{0.0036}$ as an n-type leg, the fabricated eight-pair module had a high efficiency of 8.5% under hot/cold-side temperature 873 K/283 K [188]. In addition, 1 kW thermoelectric generators system based on the nanostructured half-Heusler alloys was experimentally demonstrated by recovering the exhaust waste heat from an automotive diesel engine, with a maximum conversion efficiency around 2.1% [184].

In regards to industrial compatible fabrication processes, our lab has previously utilized a semiconductor fabrication process, i.e. photolithography, to fabricate an organic π-type thermoelectric module outputting over 250 mV with 80 °C [189]. The high contact resistance and relatively low thermoelectric performance of the organic materials used remains a large issue to solve.

4 Conclusion and Outlook

In summary, significant breakthroughs in nanostructured thermoelectric materials have been witnessed in the past decade and some of them also demonstrated high

output power density or high conversion efficiency, or both, when fabricated as the single leg, unicouple, or module. However, to compete with the traditional heat engines for power generation, nanostructured thermoelectric materials and devices still need to be more efficient and cost-effective. Currently, the maximum conversion efficiency of single-stage thermoelectric devices is still below 10% [190], far lower than heat engines (20–50%). In addition, in regards to the cost-performance analyses, the $ per W value of thermoelectric modules (at least above $5/W) is more costly than primary power generation sources, such as coal and natural gas power plants which have less than $3/W [191]. This situation requires further great efforts coming from physicists, chemists, material scientists, and mechanical engineers to address these two aspects; striving for higher efficiency, i.e. higher ZT, and higher cost efficiency, i.e. being compatible with industry fabrication processes. What is necessary is to further understand underlying physical property mechanisms and introduce emerging concepts for higher ZT, identify new higher ZT compounds, develop advanced fabrication methods and design new device structures compatible with industry, etc. In the following, several critical issues are discussed regarding the nanostructured thermoelectric materials and devices, in particular, ranging from fundamental understanding to real applications.

1. Some of the phonon-defect scattering analysis in thermoelectric is based on the classical models proposed by Klemens and Callaway [46, 192]. Due to the employed fitting parameters, this model only provides qualitative conclusions for low-temperature thermal transport data. Therefore, first-principles based phonon simulation tools or molecular dynamics analysis for understanding phonon-defect scattering should be highly considered. For the high-temperature carrier scattering of semiconductors, the dominant source is normally phonon scattering, including acoustic phonons and optical phonons. Therefore, there are few available carrier-defect scattering models at present, let alone gaining insight into realistic materials with hierarchical defects. In addition, fully first-principles simulations are also based on the constant relaxation time approximation to realize electron thermoelectric transport properties, which further makes the detailed understanding of defect-carrier mechanisms difficult.
2. Recently, Deng et al. observed that liquid phase sintering in the BiSbTe system reported by Kim et al. [53] resulted in grain alignment and therefore obvious anisotropy of microstructure and thermoelectric properties [193], which indicated that grain boundary dislocation networks are not the primary cause of enhanced *ZT* through the reduction in thermal conductivity. This critical work specifically pointed out that the formation process of microstructural defect may be related with some unusual consequences, like anisotropic properties, which may seriously overestimate the role of microstructure defects on enhancing performance. Therefore, measuring the output power and conversion efficiency of the single leg with claimed high performance can definitely confirm the

accuracy and reliability of reported ultrahigh *ZT* as calculated by conventional measurements. In addition, the long-term thermal stability of nanostructured thermoelectric materials during thermal cycling process is another critical challenge [17].

3. Thermoelectric materials research is an application-driven fundamental research field, which should truly have the potential for the efficient energy harvesting or cooling applications not confined to a niche market. However, nowadays few achievements in designing and fabricating high-performance thermoelectric devices have been reported yet, which may seriously affect the confidence and prospects of investment. Therefore, bridging the gap between thermoelectric materials and devices is critical for further research, and tangible steps and strategies need to be towards the realization of high-performance thermoelectric devices.

Acknowledgements This work was supported by NIMS, WPI-MANA and JST Mirai Grant Number JPMJMI19A1 and JSPS KAKENHI Grant Numbers JP16H06441, JP17H02749, and JP19H00833.

References

1. Zhang QH, Huang XY, Bai SQ, Shi X, Uher C, Chen LD (2016) Thermoelectric devices for power generation: recent progress and future challenges . Adv Eng Mater 18(2):194–213
2. DiSalvo FJ (1999) Thermoelectric cooling and power generation. Science 285(5428):703–706
3. Dresselhaus M, Thomas I (2001) Alternative energy technologies. Nature 414(6861):332–337
4. Energy Flow Charts (2017). https://flowcharts.llnl.gov/commodities/energy
5. Mori T, Priya S (2018) Materials for energy harvesting: At the forefront of a new wave. MRS Bull 43(3):176–180
6. Akinaga H, Fujita H, Mizuguchi M, Mori T (2018) Focus on advanced materials for energy harvesting: prospects and approaches of energy harvesting technologies. Sci Technol Adv Mater 19(1):543
7. Soleimani Z, Zoras S, Ceranic B, Shahzad S, Cui Y (2020) A review on recent developments of thermoelectric materials for room-temperature applications, Sustain Energy Technol Assessments 37:100604
8. Nandihalli N, Liu C-J, Mori T (2020) Polymer based thermoelectric nanocomposite materials and devices: fabrication and characteristics. Nano Energy 78:105186
9. Snyder GJ, Toberer ES (2008) Complex thermoelectric materials. Nat Mater 7(2):105–114
10. Zhu TJ, Liu YT, Fu CG, Heremans JP, Snyder JG, Zhao XB (2017) Compromise and synergy in high-efficiency thermoelectric materials. Adv Mater 29:1605884
11. Hicks LD, Dresselhaus MS (1993) Effect of quantum-well structures on the thermoelectric figure of merit. Phys Rev B 47(19):12727
12. Hicks LD, Dresselhaus MS (1993) Thermoelectric figure of merit of a one-dimensional conductor. Phys Rev B 47(24):16631
13. Dresselhaus MS, Chen G, Tang MY, Yang RG, Lee H, Wang DZ, Ren ZF, Fleurial JP, Gogna P (2007) New directions for low-dimensional thermoelectric materials. Adv Mater 19(8):1043–1053

14. Mori T (2017) Novel principles and nanostructuring methods for enhanced thermoelectrics. Small 13(45):1702013-n/a
15. Mao J, Liu ZH, Zhou JW, Zhu HT, Zhang Q, Chen G, Ren ZF (2018) Advances in thermoelectrics. Adv Phys 67(2):69–147
16. Xiao Y, Zhao L-D (2020) Seeking new, highly effective thermoelectrics. Science 367(6483):1196–1197
17. Minnich AJ, Dresselhaus MS, Ren ZF, Chen G (2009) Bulk nanostructured thermoelectric materials: current research and future prospects. Energy Environ Sci 2(5):466–479
18. Kanatzidis MG (2009) Nanostructured thermoelectrics: the new paradigm? Chem Mater 22(3):648–659
19. Liu WS, Yan X, Chen G, Ren ZF (2012) Recent advances in thermoelectric nanocomposites. Nano Energy 1(1):42–56
20. Morelli D, Jovovic V, Heremans J (2008) Intrinsically minimal thermal conductivity in cubic I− V− VI 2 semiconductors. Phys Rev Lett 101(3):035901
21. Lee S, Esfarjani K, Luo TF, Zhou JW, Tian ZT, Chen G (2014) Resonant bonding leads to low lattice thermal conductivity. Nat Commun 5:3525
22. Zhao L-D, Lo S-H, Zhang YS, Sun H, Tan GJ, Uher C, Wolverton C, Dravid VP, Kanatzidis MG (2014) Ultralow thermal conductivity and high thermoelectric figure of merit in SnSe crystals. Nature 508(7496):373–377
23. Zhang WH, Sato N, Tobita K, Kimura K, Mori T (2020) Unusual lattice dynamics and anisotropic thermal conductivity in In2Te5 due to a layered structure and planar-coordinated te-chains. Chem Mater 32(12):5335–5342
24. Sohn LL, Kouwenhoven LP, Schön G (2013) Mesoscopic electron transport. Springer Science & Business Media
25. Cahill DG, Braun PV, Chen G, Clarke DR, Fan S, Goodson KE, Keblinski P, King WP, Mahan GD, Majumdar A, Maris HJ, Phillpot SR, Pop E, Shi L (2014) Nanoscale thermal transport. II. 2003–2012, Appl Phys Rev 1(1):011305
26. Tan GJ, Zhao LD, Kanatzidis MG (2016) Rationally designing high-performance bulk thermoelectric materials. Chem Rev 116(19):12123–12149
27. He R, Schierning G, Nielsch K (2018) Thermoelectric devices: a review of devices, architectures, and contact optimization. Adv Mater Technol 3(4):1700256
28. Petsagkourakis I, Tybrandt K, Crispin X, Ohkubo I, Satoh N, Mori T (2018) Thermoelectric materials and applications for energy harvesting power generation. Sci Technol Adv Mater 19(1):836–862
29. Liu ZH, Mao J, Liu T-H, Chen G, Ren ZF (2018) Nano-microstructural control of phonon engineering for thermoelectric energy harvesting. MRS Bull 43(3):181–186
30. Liu T-H, Zhou JW, Li MD, Ding ZW, Song QC, Liao BL, Fu L, Chen G (2018) Electron mean-free-path filtering in Dirac material for improved thermoelectric performance. Proc Natl Acad Sci U.S.A. 115(5):879–884
31. Qiu B, Tian ZT, Vallabhaneni A, Liao BL, Mendoza JM, Restrepo OD, Ruan XL, Chen G (2015) First-principles simulation of electron mean-free-path spectra and thermoelectric properties in silicon. EPL (Europhys Lett) 109(5):57006
32. Luo T, Garg J, Shiomi J, Esfarjani K, Chen G (2013) Gallium arsenide thermal conductivity and optical phonon relaxation times from first-principles calculations. EPL (Europhys Lett) 101(1):16001
33. Esfarjani K, Chen G, Stokes HT (2011) Heat transport in silicon from first-principles calculations. Phys Rev B 84(8):085204
34. Tian ZT, Garg J, Esfarjani K, Shiga T, Shiomi J, Chen G (2012) Phonon conduction in PbSe, PbTe, and PbTe 1−xSex from first-principles calculations. Phys Rev B 85(18):184303
35. Song QC, Liu T-H, Zhou JW, Ding ZW, Chen G (2017) Ab initio study of electron mean free paths and thermoelectric properties of lead telluride. Mater Today Phys 2:69–77
36. Liu WD, Wang DZ, Liu Q, Zhou W, Shao Z, Chen ZG (2020) High-performance gete-based thermoelectrics: from materials to devices. Adv Energy Mater 10(19):2000367

37. Liu ZH, Sato N, Guo QS, Gao WH, Mori T (2020) Shaping the role of germanium vacancies in germanium telluride: metastable cubic structure stabilization, band structure modification, and stable N-type conduction. NPG Asia Mater 12(1):66
38. Chen ZW, Ge BH, Li W, Lin SQ, Shen JW, Chang YJ, Hanus R, Snyder GJ, Pei YZ (2017) Vacancy-induced dislocations within grains for high-performance PbSe thermoelectrics. Nat Commun 8:13828
39. Mao J, Wang YM, Liu ZH, Ge BH, Ren ZF (2017) Phonon scattering by nanoscale twin boundaries. Nano Energy 32:174–179
40. Wu D, Pei YL, Wang Z, Wu HJ, Huang L, Zhao LD, He JQ (2014) Significantly enhanced thermoelectric performance in n-type heterogeneous BiAgSeS composites. Adv Funct Mater 24(48):7763–7771
41. Biswas K, He JQ, Blum ID, Wu C-I, Hogan TP, Seidman DN, Dravid VP, Kanatzidis MG (2012) High-performance bulk thermoelectrics with all-scale hierarchical architectures. Nature 489(7416):414–418
42. Khan AU, Kobayashi K, Tang D-M, Yamauchi Y, Hasegawa K, Mitome M, Xue YM, Jiang BZ, Tsuchiya K, Golberg D, Bando Y, Mori T (2017) Nano-micro-porous skutterudites with 100% enhancement in ZT for high performance thermoelectricity. Nano Energy 31:152–159
43. Weimann NG, Eastman LF, Doppalapudi D, Ng HM, Moustakas TD (1998) Scattering of electrons at threading dislocations in GaN. J Appl Phys 83(7):3656–3659
44. Hansen P, Strausser Y, Erickson A, Tarsa E, Kozodoy P, Brazel E, Ibbetson J, Mishra U, Narayanamurti V, DenBaars S (1998) Scanning capacitance microscopy imaging of threading dislocations in GaN films grown on (0001) sapphire by metalorganic chemical vapor deposition. Appl Phys Lett 72(18):2247–2249
45. Li MD, Ding ZW, Meng QP, Zhou JW, Zhu YM, Liu H, Dresselhaus MS, Chen G (2017) Nonperturbative quantum nature of the dislocation-phonon interaction. Nano Lett 17(3):1587–1594
46. Klemens PG (1955) The scattering of low-frequency lattice waves by static imperfections. Proc Phys Soc Sec A 68(12):1113
47. Klemens PG (1958) Thermal conductivity and lattice vibrational modes. Solid State Phys 7:1–98
48. Carruthers P (1961) Theory of thermal conductivity of solids at low temperatures. Rev Mod Phys 33(1):92
49. Kuhlmann-Wilsdorf D (1989) Theory of plastic deformation:-properties of low energy dislocation structures. Mater Sci Eng, A 113:1–41
50. Hull D, Bacon DJ (2001) Introduction to dislocations. Butterworth-Heinemann, Oxford
51. He JQ, Sootsman JR, Girard SN, Zheng JC, Wen JG, Zhu YM, Kanatzidis MG, Dravid VP (2010) On the origin of increased phonon scattering in nanostructured PbTe based thermoelectric materials. J Am Chem Soc 132(25):8669–8675
52. Shen J-J, Zhu T-J, Zhao X-B, Zhang S-N, Yang S-H, Yin Z-Z (2010) Recrystallization induced in situ nanostructures in bulk bismuth antimony tellurides: a simple top down route and improved thermoelectric properties. Energy Environ Sci 3(10):1519–1523
53. Kim SI, Lee KH, Mun HA, Kim HS, Hwang SW, Roh JW, Yang DJ, Shin WH, Li XS, Lee YH, Snyder GJ, Kim SW (2015) Dense dislocation arrays embedded in grain boundaries for high-performance bulk thermoelectrics. Science 348(6230):109–114
54. Hwang JY, Kim J, Kim HS, Kim SI, Lee KH, Kim SW (2018) Effect of dislocation arrays at grain boundaries on electronic transport properties of bismuth antimony telluride: unified strategy for high thermoelectric performance. Adv Energy Mater 1800065
55. Meng XF, Liu ZH, Cui B, Qin DD, Geng HY, Cai W, Fu LW, He JQ, Ren ZF, Sui JH (2017) Grain boundary engineering for achieving high thermoelectric performance in n-type skutterudites. Adv Energy Mater 7:1602582
56. Liu ZH, Meng XF, Qin DD, Cui B, Wu HJ, Zhang Y, Pennycook SJ, Cai W, Sui JH (2019) New insights into the role of dislocation engineering in N-type filled skutterudite CoSb3. J Mater Chem C 7(43):13622–13631

57. Zhu B, Huang Z-Y, Wang X-Y, Yu Y, Yang L, Gao N, Chen Z-G, Zu F-Q (2017) Attaining ultrahigh thermoelectric performance of direction-solidified bulk n-type Bi2Te2.4Se0.6 via its liquid state treatment. Nano Energy 42:8–16
58. Meng XF, Liu Y, Cui B, Qin DD, Cao J, Liu WS, Liu ZH, Cai W, Sui JH (2018) High thermoelectric performance of single phase p-type cerium-filled skutterudites by dislocation engineering. J Mater Chem A 6(41):20128–20137
59. Chen ZW, Jian ZZ, Li W, Chang YJ, Ge BH, Hanus R, Yang J, Chen Y, Huang MX, Snyder GJ, Pei YZ (2017) Lattice dislocations enhancing thermoelectric PbTe in addition to band convergence. Adv Mater 29(23):1606768-n/a
60. Zhao HZ, Cao BL, Li S, Liu N, Shen JW, Li S, Jian JK, Gu L, Pei YZ, Snyder GJ, Ren ZF, Chen XL (2017) Engineering the thermoelectric transport in half-heusler materials through a bottom-up nanostructure synthesis. Adv Energy Mater 7(18):1700446
61. Umemoto M (1995) Preparation of thermoelectric β-FeSi2 doped with Al and Mn by mechanical alloying (Overview). Mater Trans, JIM 36(2):373–383
62. Schilz J, Riffel M, Pixius K, Meyer H-J (1999) Synthesis of thermoelectric materials by mechanical alloying in planetary ball mills. Powder Technol 105(1–3):149–154
63. Cook B, Beaudry B, Harringa J, Barnett W (1989) The preparation of SiGe thermoelectric materials by mechanical alloying. In: Proceedings of the 24th intersociety energy conversion engineering conference. IEEE, pp 693–700
64. Liu WS, Ren ZF, Chen G (2013) Nanostructured thermoelectric materials. Springer, Thermoelectric Nanomaterials, pp 255–285
65. Xie WJ, He J, Kang HJ, Tang XF, Zhu S, Laver M, Wang SY, Copley JR, Brown CM, Zhang QJ (2010) Identifying the specific nanostructures responsible for the high thermoelectric performance of (Bi, Sb) 2Te3 nanocomposites. Nano Lett 10(9):3283–3289
66. Tan GJ, Liu W, Wang SY, Yan YG, Li H, Tang XF, Uher C (2013) Rapid preparation of CeFe 4 Sb 12 skutterudite by melt spinning: rich nanostructures and high thermoelectric performance. J Mater Chem A 1(40):12657–12668
67. Li H, Tang X, Zhang Q, Uher C (2008) Rapid preparation method of bulk nanostructured Yb0.3Co4Sb12+y compounds and their improved thermoelectric performance. Appl Phys Lett 93(25):252109
68. Zhao YX, Dyck JS, Burda C (2011) Toward high-performance nanostructured thermoelectric materials: the progress of bottom-up solution chemistry approaches. J Mater Chem 21(43):17049–17058
69. Ortega S, Ibáñez M, Liu Y, Zhang Y, Kovalenko MV, Cadavid D, Cabot A (2017) Bottom-up engineering of thermoelectric nanomaterials and devices from solution-processed nanoparticle building blocks. Chem Soc Rev 46(12):3510–3528
70. Ji X, Zhang B, Tritt T, Kolis J, Kumbhar A (2007) Solution-chemical syntheses of nanostructured Bi 2 Te 3 and PbTe thermoelectric materials. J Electron Mater 36(7):721–726
71. Cao Y, Zhu T, Zhao X (2008) Thermoelectric Bi2Te3 nanotubes synthesized by low-temperature aqueous chemical method. J Alloys Compd 449(1–2):109–112
72. Biswas K, Muir S, Subramanian M (2011) Rapid microwave synthesis of indium filled skutterudites: an energy efficient route to high performance thermoelectric materials. Mater Res Bull 46(12):2288–2290
73. Mehta RJ, Zhang Y, Karthik C, Singh B, Siegel RW, Borca-Tasciuc T, Ramanath G (2012) A new class of doped nanobulk high-figure-of-merit thermoelectrics by scalable bottom-up assembly. Nat Mater 11(3):233
74. Zheng Y, Zhu T, Zhao X, Tu J, Cao G (2005) Sonochemical synthesis of nanocrystalline Bi2Te3 thermoelectric compounds. Mater Lett 59(23):2886–2888
75. Zhao YX, Dyck JS, Hernandez BM, Burda C (2010) Improving thermoelectric properties of chemically synthesized Bi2Te3-based nanocrystals by annealing. J Phys Chem C 114(26):11607–11613
76. Zhou B, Zhao Y, Pu L, Zhu J-J (2006) Microwave-assisted synthesis of nanocrystalline Bi2Te3. Mater Chem Phys 96(2–3):192–196

77. Zhu T, Liu Y, Zhao X (2008) Synthesis of PbTe thermoelectric materials by alkaline reducing chemical routes. Mater Res Bull 43(11):2850–2854
78. Han G, Popuri SR, Greer HF, Llin LF, Bos JWG, Zhou W, Paul DJ, Ménard H, Knox AR, Montecucco A (2017) Chlorine-enabled electron doping in solution-synthesized SnSe thermoelectric nanomaterials. Adv Energy Mater 7(13):1602328
79. Li X, Chen C, Xue W, Li S, Cao F, Chen Y, He J, Sui J, Liu X, Wang Y (2018) N-type bi-doped snse thermoelectric nanomaterials synthesized by a facile solution method. Inorg Chem 57(21):13800–13808
80. Liu W, Guo CF, Yao M, Lan Y, Zhang H, Zhang Q, Chen S, Opeil CP, Ren Z (2014) Bi2S3 nanonetwork as precursor for improved thermoelectric performance. Nano Energy 4:113–122
81. Ge Z-H, Qin P, He D, Chong X, Feng D, Ji Y-H, Feng J, He J (2017) Highly enhanced thermoelectric properties of Bi/Bi2S3 nanocomposites. ACS Appl Mater Interfaces 9(5):4828–4834
82. Nethravathi C, Rajamathi CR, Rajamathi M, Maki R, Mori T, Golberg D, Bando Y (2014) Synthesis and thermoelectric behaviour of copper telluride nanosheets. J Mater Chem A 2(4):985–990
83. Jaklovszky J, Ionescu R, Nistor N, Chiculiţa A (1975) Grain size effect on the figure of merit of sintered solid solutions based on Bi2Te3. Phys Status Solidi (a) 27(2):329–332
84. Cope R, Penn A (1968) The powder metallurgy of n-type Bi 2 Te 2.55 Se 0.45 thermoelectric material. J Mater Sci 3(2):103–109
85. Bhandari CM, Rowe DM (1980) Silicon–germanium alloys as high-temperature thermoelectric materials. Contemp Phys 21(3):219–242
86. Wood C (1988) Materials for thermoelectric energy conversion. Rep Prog Phys 51(4):459
87. Omori M (2000) Sintering, consolidation, reaction and crystal growth by the spark plasma system (SPS). Mater Sci Eng, A 287(2):183–188
88. Zhao L-D, Zhang B-P, Li J-F, Zhou M, Liu W-S, Liu J (2008) Thermoelectric and mechanical properties of nano-SiC-dispersed Bi 2 Te 3 fabricated by mechanical alloying and spark plasma sintering. J Alloys Compd 455(1):259–264
89. Liu W-S, Zhang B-P, Li J-F, Zhao L-D (2007) Thermoelectric property of fine-grained CoSb3 skutterudite compound fabricated by mechanical alloying and spark plasma sintering. J Phys D Appl Phys 40(2):566
90. Zhou M, Li JF, Kita T (2008) Nanostructured AgPb(m)SbTe(m+2) system bulk materials with enhanced thermoelectric performance. J Am Chem Soc 130(13):4527–4532
91. Zhao L-D, Zhang B-P, Liu W-S, Zhang H-L, Li J-F (2008) Enhanced thermoelectric properties of bismuth sulfide polycrystals prepared by mechanical alloying and spark plasma sintering. J Solid State Chem 181(12):3278–3282
92. Wang H, Li J-F, Nan C-W, Zhou M, Liu WS, Zhang B-P, Kita T (2006) High-performance Ag 0.8 Pb 18+ x SbTe 20 thermoelectric bulk materials fabricated by mechanical alloying and spark plasma sintering. Appl Phys Lett 88(9):092104
93. Liu WS, Zhang QY, Lan YC, Chen S, Yan X, Zhang Q, Wang H, Wang DZ, Chen G, Ren ZF (2011) Thermoelectric property studies on Cu-doped n-type CuxBi2Te2. 7Se0. 3 nanocomposites. Adv Energy Mater 1(4):577–587
94. Poudel B, Hao Q, Ma Y, Lan YC, Minnich A, Yu B, Yan X, Wang DZ, Muto A, Vashaee D, Chen XY, Liu JM, Dresselhaus MS, Chen G, Ren ZF (2008) High-thermoelectric performance of nanostructured bismuth antimony telluride bulk alloys. Science 320(5876):634–638
95. Jie Q, Wang HZ, Liu WS, Wang H, Chen G, Ren ZF (2013) Fast phase formation of double-filled p-type skutterudites by ball-milling and hot-pressing. Phys Chem Chem Phys 15(18):6809–6816
96. Dahal T, Jie Q, Joshi G, Chen S, Guo CF, Lan YC, Ren ZF (2014) Thermoelectric property enhancement in Yb-doped n-type skutterudites YbxCo4Sb12. Acta Mater 75:316–321
97. Liu WS, Kim HS, Chen S, Jie Q, Lv B, Yao ML, Ren ZS, Opeil CP, Wilson S, Chu C-W, Ren ZF (2015) n-type thermoelectric material Mg2Sn0.75Ge0. 25 for high power generation. Proc Natl Acad Sci U.S.A. 112(11):3269–3274
98. Mao J, Kim HS, Shuai J, Liu ZH, He R, Saparamadu U, Tian F, Liu WS, Ren ZF (2016) Thermoelectric properties of materials near the band crossing line in Mg2Sn–Mg2Ge–Mg2Si system. Acta Mater 103:633–642

99. Wang XW, Lee H, Lan YC, Zhu GH, Joshi G, Wang DZ, Yang J, Muto AJ, Tang MY, Klatsky J, Song S, Dresselhaus MS, Chen G, Ren ZF (2008) Enhanced thermoelectric figure of merit in nanostructured n-type silicon germanium bulk alloy. Appl Phys Lett 93(19):193121
100. Joshi G, Lee H, Lan YC, Wang XW, Zhu GH, Wang DZ, Gould RW, Cuff DC, Tang MY, Dresselhaus MS (2008) Enhanced thermoelectric figure-of-merit in nanostructured p-type silicon germanium bulk alloys. Nano Lett 8(12):4670–4674
101. Chen S, Lukas KC, Liu WS, Opeil CP, Chen G, Ren ZF (2013) Effect of Hf concentration on thermoelectric properties of nanostructured n-type half-heusler materials HfxZr1–xNiSn0.99Sb0.01. Adv Energy Mater 3(9):1210–1214
102. Chen S, Ren ZF (2013) Recent progress of half-Heusler for moderate temperature thermoelectric applications. Mater Today 16(10):387–395
103. Zhao HZ, Sui JH, Tang ZJ, Lan YC, Jie Q, Kraemer D, McEnaney K, Guloy A, Chen G, Ren ZF (2014) High thermoelectric performance of MgAgSb-based materials. Nano Energy 7:97–103
104. Liu W, Tan XJ, Yin K, Liu HJ, Tang XF, Shi J, Zhang QJ, Uher C (2012) Convergence of conduction bands as a means of enhancing thermoelectric performance of n-type Mg2Si1−xSnx solid solutions. Phys Rev Lett 108(16):166601
105. Liu ZH, Wang YM, Mao J, Geng HY, Shuai J, Wang YX, He R, Cai W, Sui JH, Ren ZF (2016) Lithium doping to enhance thermoelectric performance of MgAgSb with weak electron-phonon coupling. Adv Energy Mater 6(7):1502269
106. Liu ZH, Mao J, Sui JH, Ren ZF (2018) High thermoelectric performance of [small alpha]-MgAgSb for power generation. Energy Environ Sci 11(1):23–44
107. Shuai J, Geng HY, Lan YC, Zhu Z, Wang C, Liu ZH, Bao JM, Chu C-W, Sui JH, Ren ZF (2016) Higher thermoelectric performance of Zintl phases (Eu0. 5Yb0. 5) 1− xCaxMg2Bi2 by band engineering and strain fluctuation. Proc Natl Acad Sci U.S.A. 201608794
108. Shuai J, Mao J, Song SW, Zhu Q, Sun JF, Wang YM, He R, Zhou JW, Chen G, Singh DJ, Ren ZF (2017) Tuning the carrier scattering mechanism to effectively improve the thermoelectric properties. Energy Environ Sci 10(3):799–807
109. Mao J, Shuai J, Song SW, Wu Y, Dally R, Zhou JW, Liu ZH, Sun JF, Zhang QY, dela Cruz C, Wilson S, Pei YZ, Singh DJ, Chen G, Chu C-W, Ren ZF (2017) Manipulation of ionized impurity scattering for achieving high thermoelectric performance in n-type Mg3Sb2-based materials. Proc Natl Acad Sci U.S.A. 114(40):10548–10553
110. Liu ZH, Wang YM, Gao WH, Mao J, Geng HY, Shuai J, Cai W, Sui JH, Ren ZF (2017) The influence of doping sites on achieving higher thermoelectric performance for nanostructured α-MgAgSb. Nano Energy 31:194–200
111. Ying PJ, Liu XH, Fu CG, Yue XQ, Xie HH, Zhao XB, Zhang WQ, Zhu TJ (2015) High performance α-MgAgSb thermoelectric materials for low temperature power generation. Chem Mater 27(3):909–913
112. Kirkham MJ, dos Santos AM, Rawn CJ, Lara-Curzio E, Sharp JW, Thompson AJ (2012) Abinitio determination of crystal structures of the thermoelectric material MgAgSb. Phys Rev B 85(14):144120
113. Wang S, Li H, Qi D, Xie W, Tang X (2011) Enhancement of the thermoelectric performance of β-Zn4Sb3 by in situ nanostructures and minute Cd-doping. Acta Mater 59(12):4805–4817
114. Luo WH, Li H, Fu F, Hao W, Tang XF (2011) Improved thermoelectric properties of Al-doped higher manganese silicide prepared by a rapid solidification method. J Electron Mater 40(5):1233
115. Ibáñez M, Zamani R, Gorsse S, Fan J, Ortega S, Cadavid D, Morante JR, Arbiol J, Cabot A (2013) Core–shell nanoparticles as building blocks for the bottom-up production of functional nanocomposites: PbTe–PbS thermoelectric properties. ACS Nano 7(3):2573–2586
116. Ibáñez M, Cadavid D, Anselmi-Tamburini U, Zamani R, Gorsse S, Li W, López AM, Morante JR, Arbiol J, Cabot A (2013) Colloidal synthesis and thermoelectric properties of Cu 2 SnSe 3 nanocrystals. J Mater Chem A 1(4):1421–1426
117. Ibáñez M, Zamani R, LaLonde A, Cadavid D, Li W, Shavel A, Arbiol J, Morante JR, Gorsse S, Snyder GJ (2012) Cu2ZnGeSe4 nanocrystals: synthesis and thermoelectric properties. J Am Chem Soc 134(9):4060–4063

118. Klemens PG (1994) Phonon scattering and thermal resistance due to grain boundaries. Int J Thermophys 15(6):1345–1351
119. Mahan GD, Woods LM (1998) Multilayer thermionic refrigeration. Phys Rev Lett 80(18):4016–4019
120. Shakouri A, LaBounty C, Abraham P, Piprek J, Bowers JE (1998) Enhanced thermionic emission cooling in high barrier superlattice heterostructures. MRS Online Proceedings Library Archive 545
121. Heremans JP, Thrush CM, Morelli DT (2004) Thermopower enhancement in lead telluride nanostructures. Phys Rev B 70(11):2516–2528
122. Koumoto K, Mori T (2015) Thermoelectric nanomaterials. Springer
123. Tsujii N, Mori T (2013) High thermoelectric power factor in a carrier-doped magnetic semiconductor CuFeS2. Appl Phys Express 6(4):043001
124. Ang R, Khan AU, Tsujii N, Takai K, Nakamura R, Mori T (2015) Thermoelectricity generation and electron-magnon scattering in a natural chalcopyrite mineral from a deep-sea hydrothermal vent. Angew Chem Int Ed 54(44):12909–12913
125. Ahmed F, Tsujii N, Mori T (2017) Thermoelectric properties of CuGa 1–x Mn x Te 2: power factor enhancement by incorporation of magnetic ions. J Mater Chem A 5(16):7545–7554
126. Takaki H, Kobayashi K, Shimono M, Kobayashi N, Hirose K, Tsujii N, Mori T (2017) Thermoelectric properties of a magnetic semiconductor CuFeS2. Mater Today Phys 3:85–92
127. Acharya S, Anwar S, Mori T, Soni A (2018) Coupling of charge carriers with magnetic entropy for power factor enhancement in Mn doped Sn 1.03 Te for thermoelectric applications. J Mater Chem C 6(24):6489–6493
128. Vaney J-B, Yamini SA, Takaki H, Kobayashi K, Kobayashi N, Mori T (2019) Magnetism-mediated thermoelectric performance of the Cr-doped bismuth telluride tetradymite. Mater Today Phys 9:100090
129. Tsujii N, Nishide A, Hayakawa J, Mori T (2019) Observation of enhanced thermopower due to spin fluctuation in weak itinerant ferromagnet. Sci Adv 5(2):eaat5935
130. Gao WH, Yi XY, Sun B, Meng XL, Cai W, Zhao LC (2017) Microstructural evolution of martensite during deformation in Zr50Cu50 shape memory alloy. Acta Mater 132(Supplement C):405–415
131. Cook BA, Kramer MJ, Wei X, Harringa JL, Levin EM (2007) Nature of the cubic to rhombohedral structural transformation in (AgSbTe2) 15 (GeTe) 85 thermoelectric material. J Appl Phys 101(5):053715
132. Chattopadhyay T, Boucherle J (1987) Neutron diffraction study on the structural phase transition in GeTe. J Phys C: Solid State Phys 20(10):1431
133. Liu ZH, Sun JF, Mao J, Zhu HT, Ren WY, Zhou JC, Wang ZM, Singh DJ, Sui JH, Chu C-W, Ren ZF (2018) Phase-transition temperature suppression to achieve cubic GeTe and high thermoelectric performance by Bi and Mn codoping. Proc Natl Acad Sci U.S.A. 115(21):5332–5337
134. Snykers M, Delavignette P, Amelinckx S (1972) The domain structure of GeTe as observed by electron microscopy. Mater Res Bull 7(8):831–839
135. Lu K (2016) Stabilizing nanostructures in metals using grain and twin boundary architectures. Nat Rev Mater 1:16019
136. Lu L, Shen YF, Chen XH, Qian LH, Lu K (2004) Ultrahigh strength and high electrical conductivity in copper. Science 304(5669):422–426
137. Wan C, Wang Y, Norimatsu W, Kusunoki M, Koumoto K (2012) Nanoscale stacking faults induced low thermal conductivity in thermoelectric layered metal sulfides. Appl Phys Lett 100(10):101913
138. Mao J, Wang YM, Kim HS, Liu ZH, Saparamadu U, Tian F, Dahal K, Sun JY, Chen S, Liu WS, Ren ZF (2015) High thermoelectric power factor in Cu–Ni alloy originate from potential barrier scattering of twin boundaries. Nano Energy 17:279–289
139. Hsu KF, Loo S, Guo F, Chen W, Dyck JS, Uher C, Hogan T, Polychroniadis EK, Kanatzidis MG (2004) Cubic AgPbmSbTe2+ m: bulk thermoelectric materials with high figure of merit. Science 303(5659):818–821

140. Callister WD, Rethwisch DG (2011) Materials science and engineering. Wiley NY, New York
141. Pei Y, Lensch-Falk J, Toberer ES, Medlin DL, Snyder GJ (2011) High thermoelectric performance in PbTe due to large nanoscale Ag2Te precipitates and La doping. Adv Funct Mater 21(2):241–249
142. Zhao L-D, He J, Wu C-I, Hogan TP, Zhou X, Uher C, Dravid VP, Kanatzidis MG (2012) Thermoelectrics with earth abundant elements: high performance p-type PbS nanostructured with SrS and CaS. J Am Chem Soc 134(18):7902–7912
143. Liu ZH, Pei YL, Geng HY, Zhou JC, Meng XF, Cai W, Liu WS, Sui JH (2015) Enhanced thermoelectric performance of Bi 2 S 3 by synergistical action of bromine substitution and copper nanoparticles. Nano Energy 13:554–562
144. Tan GJ, Zhao LD, Shi FY, Doak JW, Lo S-H, Sun H, Wolverton C, Dravid VP, Uher C, Kanatzidis MG (2014) High thermoelectric performance of p-type SnTe via a synergistic band engineering and nanostructuring approach. J Am Chem Soc 136(19):7006–7017
145. Ahmed F, Tsujii N, Mori T (2018) Microstructure analysis and thermoelectric properties of iron doped CuGaTe2. J Materiomics 4(3):221–227
146. Shuai J, Sun Y, Tan X, Mori T (2020) Manipulating the Ge vacancies and Ge precipitates through Cr doping for realizing the high-performance GeTe thermoelectric material. Small 1906921
147. Zhao L-D, Dravid VP, Kanatzidis MG (2014) The panoscopic approach to high performance thermoelectrics. Energy Environ Sci 7(1):251–268
148. Gelbstein Y, Dado B, Ben-Yehuda O, Sadia Y, Dashevsky Z, Dariel MP (2009) High thermoelectric figure of merit and nanostructuring in bulk p-type Ge x (Sn y Pb1− y) 1–x Te alloys following a spinodal decomposition reaction. Chem Mater 22(3):1054–1058
149. He JQ, Girard SN, Kanatzidis MG, Dravid VP (2010) Microstructure-lattice thermal conductivity correlation in nanostructured PbTe0. 7S0. 3 thermoelectric materials. Adv Funct Mater 20(5):764–772
150. Kirievsky K, Gelbstein Y, Fuks D (2013) Phase separation and antisite defects in the thermoelectric TiNiSn half-Heusler alloys. J Solid State Chem 203:247–254
151. Wei R, Hui Yuan G, Zi Hao Z, Li Xia Z (2017) Filling-fraction fluctuation leading to glasslike ultralow thermal conductivity in caged skutterudites. Phys Rev Lett 118(24):245901
152. Li JH, Tan Q, Li JF, Liu DW, Li F, Li ZY, Zou M, Wang K (2013) BiSbTe-based nanocomposites with high ZT: the effect of SiC nanodispersion on thermoelectric properties. Adv Funct Mater 23(35):4317–4323
153. Jung S-J, Park S-Y, Kim BK, Kwon B, Kim SK, Park H-H, Kim D-I, Kim J-Y, Hyun D-B, Kim J-S (2015) Hardening of Bi–Te based alloys by dispersing B4C nanoparticles. Acta Mater 97:68–74
154. Kim KT, Choi SY, Shin EH, Moon KS, Koo HY, Lee G-G, Ha GH (2013) The influence of CNTs on the thermoelectric properties of a CNT/Bi 2 Te 3 composite. Carbon 52:541–549
155. Zong PA, Hanus R, Dylla M, Tang YS, Liao JC, Zhang QH, Snyder GJ, Chen LD (2017) Skutterudite with graphene-modified grain-boundary complexion enhances zT enabling high-efficiency thermoelectric device. Energy Environ Sci 10(1):183–191
156. Qin D, Wu H, Cai S, Zhu J, Cui B, Yin L, Qin H, Shi W, Zhang Y, Zhang Q, Liu W, Cao J, Pennycook SJ, Cai W, Sui J (2019) Enhanced thermoelectric and mechanical properties in Yb0.3Co4Sb12 with in situ formed CoSi nanoprecipitates. Adv Energy Mater 9(42):1902435
157. Prytuliak A, Maruyama S, Mori T (2013) Anomalous effect of vanadium boride seeding on thermoelectric properties of YB22C2N. Mater Res Bull 48(5):1972–1977
158. Mori T, Hara T (2016) Hybrid effect to possibly overcome the trade-off between Seebeck coefficient and electrical conductivity. Scr Mater 111:44–48
159. Feng B, Martin H-P, Michaelis A (2013) In situ preparation and thermoelectric properties of B 4 C 1–x–TiB 2 composites. J Electron Mater 42(7):2314–2319
160. Guo J, Qin P, Ma Z, Yang Q-L, Feng J, Ge Z-H (2019) Ni metal coating boosting the thermoelectric performance of In_2O_3 (ZnO) 5 ceramics. Scr Mater 164:71–75
161. Kim W, Majumdar A (2006) Phonon scattering cross section of polydispersed spherical nanoparticles. J Appl Phys 99(8):084306

162. Pakdel Zhang H, Minnich AJ (2015) The best nanoparticle size distribution for minimum thermal conductivity. Sci Rep 5
163. J.P. Heremans, C.M. Thrush, D.T. Morelli (2005) Thermopower enhancement in PbTe with Pb precipitates. J. Appl. Phys. 98(6)
164. Pakdel A, Guo Q, Nicolosi V, Mori T (2018) Enhanced thermoelectric performance of Bi–Sb–Te/Sb 2 O 3 nanocomposites by energy filtering effect. J Mater Chem A 6(43):21341–21349
165. Ning HP, Mastrorillo GD, Grasso S, Du B, Mori T, Hu C, Xu Y, Simpson K, Maizza G, Reece MJ (2015) Enhanced thermoelectric performance of porous magnesium tin silicide prepared using pressure-less spark plasma sintering. J Mater Chem A 3(33):17426–17432
166. Fujisawa M, Hata T, Kitagawa H, Bronsveld P, Suzuki Y, Hasezaki K, Noda Y, Imamura Y (2008) Thermoelectric properties of porous SiC/C composites. Renew Energy 33(2):309–313
167. Choy TC (2015) Effective medium theory: principles and applications. Oxford University Press
168. Song D, Chen G (2004) Thermal conductivity of periodic microporous silicon films. Appl Phys Lett 84(5):687–689
169. Lee J-H, Grossman J, Reed J, Galli G (2007) Lattice thermal conductivity of nanoporous Si: Molecular dynamics study. Appl Phys Lett 91(22):223110
170. Hopkins PE, Rakich PT, Olsson RH, El-Kady IF, Phinney LM (2009) Origin of reduction in phonon thermal conductivity of microporous solids. Appl Phys Lett 95(16):161902
171. Valalaki K, Benech P, Nassiopoulou AG (2016) High seebeck coefficient of porous silicon: study of the porosity dependence. Nanoscale Res Lett 11(1):201
172. De Boor J, Kim D, Ao X, Becker M, Hinsche N, Mertig I, Zahn P, Schmidt V (2012) Thermoelectric properties of porous silicon. Appl Phys A 107(4):789–794
173. Zhang Y, Day T, Snedaker ML, Wang H, Krämer S, Birkel CS, Ji X, Liu D, Snyder GJ, Stucky GD (2012) A mesoporous anisotropic n-type Bi2Te3 monolith with low thermal conductivity as an efficient thermoelectric material. Adv Mater 24(37):5065–5070
174. Zhao KP, Duan HZ, Raghavendra N, Qiu PF, Zeng Y, Zhang WQ, Yang JH, Shi X, Chen LD (2017) Solid-state explosive reaction for nanoporous bulk thermoelectric materials. Adv Mater 29(42):1701148
175. Liu WS, Jie Q, Kim HS, Ren ZF (2015) Current progress and future challenges in thermoelectric power generation: from materials to devices. Acta Mater 87:357–376
176. Zhu Q, Song SW, Zhu HT, Ren ZF (2019) Realizing high conversion efficiency of Mg3Sb2-based thermoelectric materials. J Power Sources 414:393–400
177. Kraemer D, Sui JH, McEnaney K, Zhao HZ, Jie Q, Ren ZF, Chen G (2015) High thermoelectric conversion efficiency of MgAgSb-based material with hot-pressed contacts. Energy Environ Sci 8(4):1299–1308
178. Yin L, Chen C, Zhang F, Li X, Bai F, Zhang Z, Wang X, Mao J, Cao F, Chen X, Sui J, Liu X, Zhang Q (2020) Reliable N-type Mg3.2Sb1.5Bi0.49Te0.01/304 stainless steel junction for thermoelectric applications. Acta Mater 198:25–34
179. He R, Kraemer D, Mao J, Zeng LP, Jie Q, Lan YC, Li CH, Shuai J, Kim HS, Liu Y, Broido D, Chu C-W, Chen G, Ren ZF (2016) Achieving high power factor and output power density in p-type half-Heuslers Nb1-xTixFeSb. Proc Natl Acad Sci U.S.A. 113(48):13576–13581
180. Ren WY, Zhu HT, Zhu Q, Saparamadu U, He R, Liu ZH, Mao J, Wang C, Nielsch K, Wang ZM, Ren ZF (2018) Ultrahigh power factor in thermoelectric system Nb0. 95M0. 05FeSb (M= Hf, Zr, and Ti). Adv Sci 5:1800278
181. Zhu HT, He R, Mao J, Zhu Q, Li CH, Sun JF, Ren WY, Wang YM, Liu ZH, Tang ZJ, Sotnikov A, Wang ZM, Broido D, Singh DJ, Chen G, Nielsch K, Ren ZF (2018) Discovery of ZrCoBi based half Heuslers with high thermoelectric conversion efficiency. Nat Commun 9(1):2497
182. Zhu HT, Mao J, Li YW, Sun JF, Wang YM, Zhu Q, Li GN, Song QC, Zhou JW, Fu YH, He R, Tong T, Liu ZH, Ren WY, You L, Wang ZM, Luo J, Sotnikov A, Bao JM, Nielsch K, Chen G, Singh DJ, Ren ZF (2019) Discovery of TaFeSb-based half-Heuslers with high thermoelectric performance. Nat Commun 10(1):270
183. Muto A, Yang J, Poudel B, Ren ZF, Chen G (2012) Skutterudite unicouple characterization for energy harvesting applications. Adv Energy Mater 3(2):245–251

184. Zhang YL, Cleary M, Wang XW, Kempf N, Schoensee L, Yang J, Joshi G, Meda L (2015) High-temperature and high-power-density nanostructured thermoelectric generator for automotive waste heat recovery. Energy Convers Manage 105:946–950
185. Shi X, Chen L (2016) Thermoelectric materials step up. Nat Mater 15(7):691–692
186. Zhang QH, Zhou ZX, Dylla M, Agne MT, Pei YZ, Wang LJ, Tang YS, Liao JC, Li J, Bai SQ, Jiang W, Chen LD, Jeffrey Snyder G (2017) Realizing high-performance thermoelectric power generation through grain boundary engineering of skutterudite-based nanocomposites. Nano Energy 41:501–510
187. Hu X, Jood P, Ohta M, Kunii M, Nagase K, Nishiate H, Kanatzidis MG, Yamamoto A (2016) Power generation from nanostructured PbTe-based thermoelectrics: comprehensive development from materials to modules. Energy Environ Sci 9(2):517–529
188. Jood P, Ohta M, Yamamoto A, Kanatzidis MG (2018) Excessively doped PbTe with Ge-induced nanostructures enables high-efficiency thermoelectric modules. Joule 2(7):1339–1355
189. Satoh N, Otsuka M, Ohki T, Ohi A, Sakurai Y, Yamashita Y, Mori T (2018) Organic π-type thermoelectric module supported by photolithographic mold: a working hypothesis of sticky thermoelectric materials. Sci Technol Adv Mater 19(1):517–525
190. Tan G, Ohta M, Kanatzidis MG (2019) Thermoelectric power generation: from new materials to devices. Philos Trans Roy Soc A 377(2152):20180450
191. LeBlanc S, Yee SK, Scullin ML, Dames C, Goodson KE (2014) Material and manufacturing cost considerations for thermoelectrics. Renew Sustain Energy Rev 32:313–327
192. Callaway J (1959) Model for lattice thermal conductivity at low temperatures. Phys Rev 113(4):1046
193. Deng RG, Su XL, Zheng Z, Liu W, Yan YG, Zhang QJ, Dravid VP, Uher C, Kanatzidis MG, Tang XF (2018) Thermal conductivity in Bi0. 5Sb1. 5Te3+ x and the role of dense dislocation arrays at grain boundaries. Sci Adv 4(6):eaar5606

Artificial Photosynthesis: Fundamentals, Challenges, and Strategies

Davin Philo, Hamza El-Hosainy, Shunqin Luo, Hao Huang, Fumihiko Ichihara, and Jinhua Ye

1 Introduction

Natural photosynthesis (NPS) is a chemical process conducted by green plants, photosynthetic bacteria, and all other photosynthetic organisms, where CO_2 and water are transformed into carbohydrates and molecular oxygen, respectively [1, 2]. This process can be considered as the most efficient and effective method of converting light energy into chemical energy. Over billions of years, NPS has provided an overwhelming amount of energy stock, mostly in the form of fossil fuels, for the world [3]. However, as is widely known, the rate of depletion of this energy stock is much higher than the rate at which nature can replenish it [2, 4]. Consequently, it is only a matter of time before fossil fuels finally run out. With this looming energy crisis, many approaches have been made to imitate NPS by artificially utilizing light energy to drive the thermodynamically uphill reactions of abundant substances to produce energy-containing chemicals, such as hydrogen, hydrocarbons, and ammonia [1, 3]. At present, this method is known as artificial photosynthesis (APS) or the so-called photocatalytic process [5].

As is widely known, the green chlorophyll pigment plays a major role in the NPS reaction. Generally, light energy or photons are absorbed by chlorophyll and used to remove electrons from water molecules to produce oxygen gas as follows:

$$2H_2O \xrightarrow{light} O_2 + 4H^+ + 4e^-. \quad (1)$$

This oxidation reaction occurs in the reaction center of photosystem II. Afterwards, the freed hydrogen and electrons are transferred to photosystem I and trigger the reduction of carbon dioxide (CO_2) to produce sugar ($C_6H_{12}O_6$) through the Calvin

D. Philo · H. El-Hosainy · S. Luo · H. Huang · F. Ichihara · J. Ye (✉)
International Center for Materials Nanoarchitectonics (WPI-MANA), National Institute for Materials Science (NIMS), 1-1 Namiki, Tsukuba 305-0044, Ibaraki, Japan
e-mail: Jinhua.YE@nims.go.jp

Y. Wakayama and K. Ariga (eds.), *System-Materials Nanoarchitectonics*,
NIMS Monographs, https://doi.org/10.1007/978-4-431-56912-1_14

cycle:

$$CO_2 + 4H^+ + 4e^- \xrightarrow{light} \frac{1}{6}C_6H_{12}O_6 + H_2O. \tag{2}$$

The overall reaction of NPS is written as

$$CO_2 + H_2O \xrightarrow{light} \frac{1}{6}C_6H_{12}O_6 + O_2. \tag{3}$$

Meanwhile, in APS, a material called a photocatalyst (mostly a semiconductor) is usually employed to harvest light energy [5]. Similar to NPS, this photon energy is used by the photocatalyst to generate charge carriers or excitons, i.e., electrons (e^-) and holes (h^+). In detail, upon light illumination, e^- is excited from the valence band (VB) to the conduction band (CB) of the photocatalyst, leaving behind the h^+ in the valence band region [6]. These charge carriers are transferred separately to different reaction centers, where they trigger some endothermic redox reactions; electrons drive the reduction reaction while holes drive the oxidation reaction as follows:

$$A + e^- \xrightarrow{light} A^-, \tag{4}$$

$$D + h^+ \xrightarrow{light} D^+. \tag{5}$$

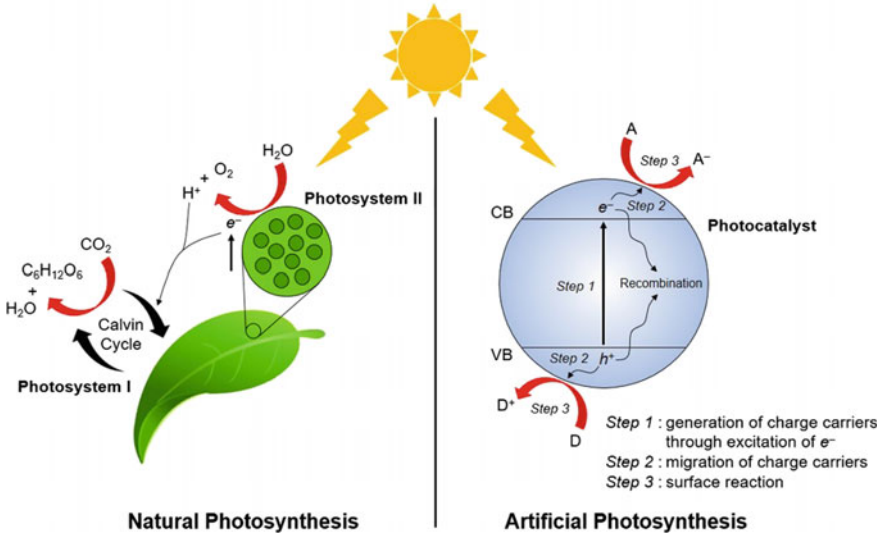

Fig. 1 Comparison between natural and artificial photosynthesis

A and D represent an electron acceptor and electron donor, respectively. Figure 1 illustrates a comparison between NPS and APS.

In the past few decades, many studies have been carried out to obtain a full understanding of the reaction mechanisms, kinetics, substances involved, and other important properties of NPS [5]. Even though we do not yet have sufficient understanding to further proceed to the industrial stage, much progress has been made toward applying the key features of NPS to APS [7]. To date, there are three very well known APS reactions that have attracted considerable attention from scientists and researchers worldwide, i.e., water (H_2O) splitting, carbon dioxide (CO_2) reduction, and nitrogen (N_2) fixation; water, CO_2, and N_2 are very suitable raw materials for APS applications because they are abundant and easily obtained from the natural environment. In this chapter, we provide a summary of the principles, requirements, and latest developments of APS-based reactions.

Before proceeding with the above-mentioned discussion, it is necessary to define a general term that is often used to evaluate photocatalytic efficiency for any APS reaction, i.e., apparent quantum yield (AQY). The concept of AQY has been widely used to make valid comparisons between different experimental and illumination conditions [6]. AQY is evaluated for a certain photon wavelength (monochromatic) and calculated as

$$\mathrm{AQY} = \mathrm{nr}/\mathrm{I}, \tag{6}$$

where n, r, and I represent the number of e^- involved in the photocatalytic reaction, the corresponding production rate, and the rate of incident photons, respectively. Typically, the wavelength-dependent AQY follows the optical absorbance pattern of the semiconductor, which decreases as the irradiation wavelength approaches the absorption edge because of the lower absorption coefficients and larger migration distances for photogenerated carriers [6].

2 Requirements for Artificial Photosynthesis

Since the purpose of APS is to drive some thermodynamically uphill reactions, there are some principal conditions that must be fulfilled so that the reaction may occur effectively and efficiently. These requirements apply to all APS reactions, and therefore, it is important to identify them as the very first stepping stones toward designing any photocatalytic system.

2.1 Thermodynamic Boundaries and Photon Absorption

To successfully perform any redox reaction, one needs to pay careful attention to the thermodynamic constraints of the reaction. In this case, we mostly use the term reduction potential to quantify the thermodynamic state of a certain reaction. The reduction potential or electrode potential is usually defined as a value for measuring the tendency of some substances to receive electrons, and thus be reduced. It is measured as the energy level, with volt (V) as the unit, with respect to a certain standard potential, such as the standard hydrogen electrode (SHE).[1] The higher (more negative) the value of this potential, the greater the likelihood of the species acquiring electrons and being reduced. In contrast, the lower (more positive) this value, the greater the tendency for the backward reaction (oxidation) of the species to occur. For a redox photon-induced reaction to occur, the CB energy level of the photocatalyst must be higher than the potential of the reduction reaction, while the VB must be located at a more positive potential than the oxidation reaction. Since different reactions require different thermodynamic boundaries, some photocatalysts will be suitable for a certain reaction but might not be suitable for other reactions. However, it is also possible to shift the position of the energy band by introducing some impurities, known as dopants, to meet different thermodynamic requirements [8]. More details of the thermodynamic constraints of each APS reaction and the corresponding implications will be presented in later sections.

Furthermore, since the ultimate aim of APS is to utilize the energy emitted by the sun, we also need to consider the characteristics of sunlight itself. The sun emits a spectrum of electromagnetic waves with a relatively broad wavelength, which comprises 3–5% UV (<400 nm), 42–43% visible light (400–700 nm), and 52–55% infrared (>700 nm) [9]. Thus, the utilization of visible light, near infrared (NIR), and infrared is essential to achieving substantial solar energy conversion, although this is more challenging. We often use the term band gap (E_g) to evaluate the light-harvesting ability of a semiconductor photocatalytic material. In the electronic structure of solid materials, including semiconductors, the band gap is usually defined as the energy difference between the top of the valence band (valence band maximum, VBM) and the bottom of the conduction band (conduction band minimum, CBM). The value of E_g is usually obtained by applying the Kubelka–Munk transformation and can be used to determine the maximum wavelength of light (λ_{max}) that the photocatalyst can absorb using the following equation:

$$\lambda_{\max} = hc/E_g, \tag{7}$$

where h is Planck's constant (6.626×10^{-34} m^2 kg/s) and c is the speed of light (3×10^8 m/s). Generally, a photocatalyst can absorb light with a higher energy than its band gap, or in other words, a wavelength less than the value of λ_{max} calculated as

[1] In SHE, the standard electrode potential (E°) of H^+/H_2 is assumed to be 0, where the pressure of hydrogen gas is 1 bar and the activity of H^+ in the solution is equal to 1 (in short, pH 0).

Table 1 List of popular and potential semiconductors that have been applied in APS

Semiconductor	Band gap (eV)	Photocatalytic applications
TiO_2	3.2	Water splitting [12–15], CO_2 reduction [16–18], N_2 fixation [19–21]
$SrTiO_3$	3.2	Water splitting [22–24], CO_2 reduction [25], N_2 fixation [26, 27]
ZnO	3.4	Water splitting [28, 29], CO_2 reduction [30, 31]
$BiVO_4$	2.4	Water splitting[a] [32, 33], CO_2 reduction [34]
WO_3	2.8	Water splitting[a] [32, 35], CO_2 reduction [36, 37]
GaN	3.5	Water splitting [28, 38], CO_2 reduction [39]
GaP	2.2	Water splitting[b] [40, 41], CO_2 reduction [42, 43]
TaON	2.5	Water splitting [44, 45]
Cu_2O	2.0–2.2	Water splitting [46, 47]
CdS	2.4	Water splitting[c] [48–50], CO_2 reduction [51, 52], N_2 fixation [53, 54]
ZnS	3.7	Water splitting[c] [55, 56], CO_2 reduction [57–59]
CoO	2.6	Water splitting [60, 61]
g-C_3N_4	2.7	Water splitting [62–65], CO_2 reduction [66–68], N_2 fixation [69]
Black Phosphorus	0.45–0.76	Water splitting[b] [70]
BiOCl	3.3	N_2 fixation [71, 72]
BiOBr	2.8–2.9	N_2 fixation [73, 74]

[a]only for water oxidation (O_2 production); [b]only for water reduction (H_2 production); [c]mostly for H_2 production owing to the instability of the material

above. Hence, to enable the absorption of a larger proportion of the solar spectrum, a semiconductor with a smaller band gap is preferred. Table 1 shows a list of some semiconductors that have been applied in APS and their corresponding band gaps.

Given that some semiconductors have relatively large band gaps, some approaches to band-gap narrowing have involved inserting some dopant(s) into the molecular arrangement of a semiconductor, thus modifying its electronic structure. The basic concept of this method is to introduce a new energy level below or above the constituent orbital state [10], so that it may change the position of the CBM or VBM, which is also beneficial for meeting different thermodynamic requirements of different reactions as mentioned earlier [8]. For example, one can shift the VBM level of some oxide materials (usually consisting of the O_{2p} state) upwards by adding nitrogen as a dopant, thus introducing the new N_{2p} state, which lies above the O_{2p} state, and generating a higher VBM position [11]. On the other hand, this doping method also has the drawback that the doping sites can act as recombination centers for charge carriers [11]. Therefore, in the design of photocatalytic materials, one must strive to achieve a balance between the modulation of light absorption and the recombination probability [10].

2.2 Charge Carrier Dynamics in Light-Harvesting Material

Following the generation of charge carriers due to photon absorption, the electron–hole pairs need to be separated immediately and transported into different zones; otherwise, they will recombine with each other within the photocatalyst [75, 76]. This electron–hole recombination usually results in a significant loss of energy, thus limiting the quantum efficiency of the photocatalytic system [5]. Consequently, the migration step, which is strongly correlated with the charge carrier dynamics, plays an essential role in an effective photocatalytic system. There are two parameters that are usually used to characterize the charge carrier dynamics of a semiconductor: carrier lifetime and diffusion length [76]. The carrier lifetime can be described as the average time taken for the charge carriers to recombine, whereas the diffusion length is defined as the distance that the carriers can travel before they recombine. From these definitions, it can be easily understood that the higher their values, the higher the probability that the charge carriers reach the surface of the photocatalyst and subsequently participate in the surface reactions. Hence, extensive effort has been made to improve these values, i.e., (1) controlling the shape, structure, and size of the photocatalysts to reduce the distance that the charge carriers must travel before reaching the surface of the photocatalyst; (2) formation of a homojunction and heterojunction to promote the spatial separation of electrons and holes; (3) utilization of a sacrificial agent as a scavenger of particular charge carriers, thus increasing the proportion of oppositely charged carriers in the photocatalyst; and (4) introduction of a cocatalyst on the surface of a photocatalyst that can provide charge accumulation centers and also accelerate interfacial reaction kinetics [5, 75, 77].

2.3 Existence of Reactive Sites

Last but not least, a photocatalyst material should have active catalytic sites on its surface for the APS reaction to occur. However, most photocatalyst surfaces are not typically designed to catalyze redox reactions [76]. To address this problem, a cocatalyst that can provide reactive sites for a certain APS reaction is frequently loaded and dispersed on the surface of the photocatalyst [78]. For this purpose, cocatalyst components are often adapted from the components of electrocatalysts applied for the same reactions [10]. In other cases, some surface defects are introduced on the surface of the photocatalyst, which can unexpectedly provide reactive sites for APS reactions, especially CO_2 reduction [59, 79, 80] and N_2 fixation reactions [69, 71, 73].

To establish effective surface reactions, the reactive sites must be designed according to the Sabatier principle,[2] which states that the catalytic surface must have a trade-off between being reactive and not being poisoned by the reaction intermediates [81]. Hence, the interactions between the sites and the substances (either

[2] This is often associated with the activity volcano plots used to evaluate the adsorption–desorption property of any metal (since most of the active sites for the APS reaction are metal atoms) [78].

the reactant or the product) should be modest: neither too weak so that the sites can adequately bind the reactant and the surface reaction (through the electron transfer process) may take place, nor too strong so that the product can easily desorb from the catalytic surface [82–84]. Secondly, if a cocatalyst is employed, it should form a good coordination with the semiconductor to ensure smooth charge migration into and from the reactive sites [10, 50]. This is because, for any catalytic reaction, a sustained charge carrier supply is the key to a continuous and effective surface reaction [85]. Accordingly, a suitable loading method and a precursor of the cocatalyst are crucial. Finally, increasing the number of reactive sites by either altering the morphology of the material to a low-dimensional structure [48, 86, 87], exposing more active edges of the cocatalyst [88, 89], or reducing the size of the cocatalyst into clusters [90–92] or single atoms [64, 93–95] is also an effective way of enhancing the photocatalytic activity.

Recently, an advanced strategy to satisfy such requirements has been demonstrated by downsizing transition-metal-based cocatalysts to the molecular scale, thus maximizing the catalytic activity [50]. By anchoring well-dispersed single-site Co/Ni species on a sulfide semiconductor, excellent photocatalytic H_2 production was achieved, with AQY as high as 56.2 and 67.5% at 420 nm for Co and Ni species, respectively. These outcomes indicate the importance of the good dispersion of cocatalyst species as well as good coordination between the cocatalyst and the semiconductor, which will result in the full utilization of reactive sites, efficient charge transfer, and favorable kinetics for better catalytic performance [50].

3 Water Splitting

Following the pioneering work of photo-electrochemical water splitting by Fujishima and Honda in the early 1970s [12], much effort has been made toward developing an effective and efficient water-splitting photocatalytic system. Water splitting itself is an uphill redox reaction with an increase in Gibbs free energy (ΔG°) of about 237.13 kJ/mol [78], which can be written as

$$2H_2O \xrightarrow{light} 2H_2 + O_2 \tag{8}$$

The water splitting reaction can be divided into two half reactions, i.e., a hydrogen evolution reaction (HER) and an oxygen evolution reaction (OER):

$$2H^+ + 2e^- \rightarrow H_2, \tag{9}$$

$$2H_2O + 4h^+ \rightarrow O_2 + 4H^+. \tag{10}$$

As already explained for the thermodynamic constraints, the CBM of the semiconductor must be located at a more negative level than the H^+/H_2 reduction potential

(0 V vs. SHE at pH 0), while the VBM should be more positive than the O_2/H_2O energy level (1.23 V vs. SHE at pH 0). Consequently, the theoretical minimum band gap energy required to drive water splitting is 1.23 eV. Nevertheless, considering the possible thermodynamic losses (0.4 eV) and overpotentials (0.3–0.4 eV), the practical minimum band gap energy of the semiconductor for this reaction should be around 1.9 eV [5, 61]. Generally, if one of these thermodynamic requirements is not fulfilled, no water splitting will take place. Therefore, using a semiconductor with suitable band positions is indispensable in this case.

To assess the water splitting performance of any photocatalytic system, the concept of solar to hydrogen efficiency (STH) is also often used together with the AQY evaluation. STH is defined as the product of the hydrogen production rate and the increase in Gibbs free energy (ΔG°) for the water splitting reaction divided by the total energy of incident solar irradiation:

$$\mathrm{STH} = \frac{\text{output energy}}{\text{incident solar light energy}} = \frac{r_{H_2} \times \Delta G^\circ}{P_{\text{sun}} \times S}, \tag{11}$$

where P_{sun} and S represent the flux energy of solar irradiation and the surface area of the system available for incident light, respectively. STH is considered as an absolute and practical standard to evaluate the water splitting performance of any photocatalyst under solar light irradiation [6]. An AM 1.5 G solar simulator (100 mW/cm^2) is commonly used as the source of solar light to evaluate STH.

In a recent review, it was estimated that for any photocatalytic water splitting system to compete with the conventional methane steam reforming process, it must attain STH of 10% and a lifetime exceeding 10 years [6, 10, 96]. Figure 2 shows the relationship between STH and available photon wavelength in an AM 1.5 G simulator at different AQYs [6]. For example, to achieve an STH of 10% when using solar irradiation with a wavelength of less than 600 nm, an AQY of 60% is needed. For UV utilization (<400 nm), the maximum possible STH is 1.7% even at an AQY of 100%. These calculations once again show the need to develop a photocatalytic system that can operate using a wider range of wavelengths of the solar spectrum.

3.1 Overall Water Splitting

To perform successful overall water splitting (OWS), there is a critical issue related to the rapid backward reaction (reformation of H_2O), which is thermodynamically predominant over the forward reaction. Consequently, deactivating the reverse reaction must be the top priority in designing any photocatalytic system for OWS [97]. One of the most popular methods of dealing with this problem is to apply a surface nanolayer coating [10]. This layer should be able to function as a molecular sieve, selectively allowing H_2 and water molecules to permeate through the layer while preventing O_2 molecules from diffusing and reaching the surface of the cocatalyst

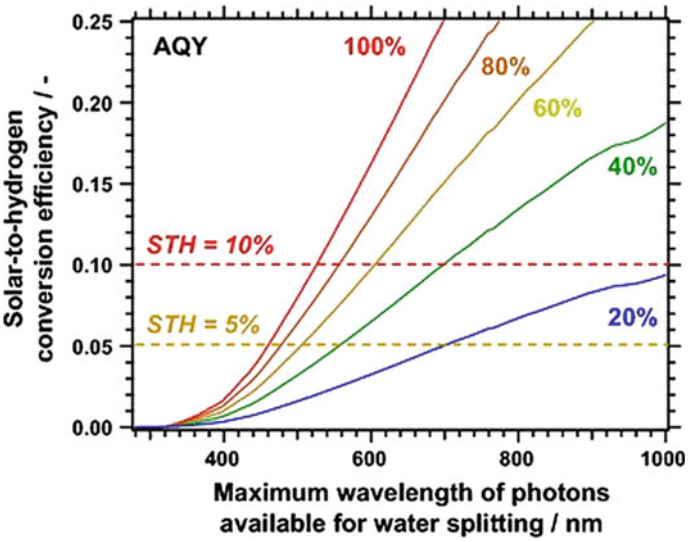

Fig. 2 Relationship between STH conversion efficiency and photon wavelength at different AQYs for photocatalytic water splitting. Reprinted with permission from Springer Science + Business Media New York: Springer US [6], Copyright (2014)

[98]. Since the reactive sites for backward and forward reactions are typically the same, this method effectively hinders the backward reaction. For example, a Cr_2O_3 nanolayer has been applied in many studies and found to be effective for inhibiting the reverse reaction, thus improving the photocatalytic OWS performance [22, 99]. The Cr_2O_3 nanolayer can be photodeposited on the surface of a cocatalyst by reducing the CrO_4^{2-} ions where it encapsulates the cocatalyst, thus producing a core–shell structure [99]. Figure 3 illustrates the mechanism by which the Cr_2O_3 nanolayer coating suppresses the backward reaction in photocatalytic OWS [100]. The Ni/NiO core/shell cocatalyst and hydrophilic nanolayers of amorphous oxyhydroxides of group IV and V transition metals (Ti, Nb, Zr, and Ta) are other successful examples of this technique [101, 102].

As mentioned earlier, a photocatalyst with suitable band positions is necessary to fulfill the thermodynamic requirement of any APS reaction. However, it is quite difficult to find a suitable semiconductor with CBM and VBM levels straddling the redox potentials of H^+/H_2 and O_2/H_2O. An appealing solution to this problem was demonstrated by Domen and his group, who used two semiconductors to form a two-step photoexcitation system, so-called Z-scheme water splitting (see Fig. 4), achieving STH exceeding 1% [22]. This method is inspired by natural photosynthesis, which also involves two photosystems where two different reactions occur separately as previously explained. Similarly, in the Z-scheme system, one semiconductor acts as a hydrogen evolution photocatalyst (HEP), while the other acts as an oxygen evolution photocatalyst (OEP). The remaining holes and electrons in the HEP and OEP respectively recombine through a solid-state electron mediator (e.g., Au, Rh, Ni,

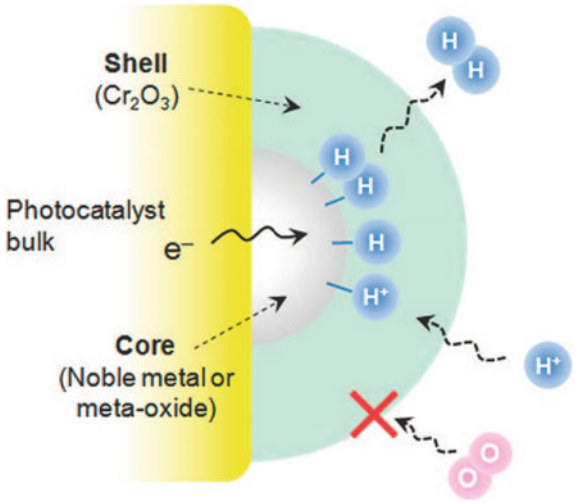

Fig. 3 Schematic illustration of the cocatalyst-Cr_2O_3 core–shell for suppressing the backward reaction in photocatalytic OWS. Reprinted with permission from Maeda and Domen, J. Phys. Chem. Lett., 1, 2,655–2,661 (2010) [100]. Copyright (2010) American Chemical Society

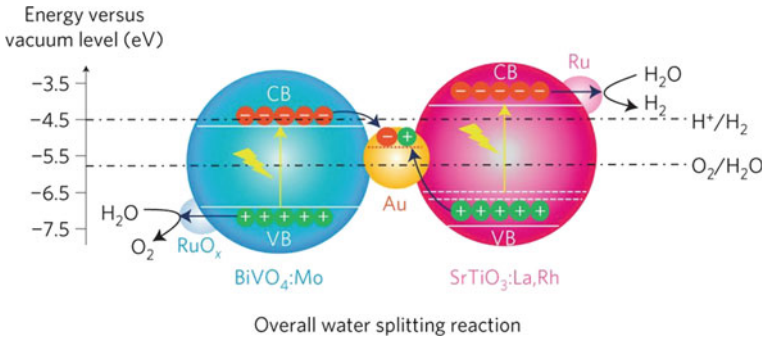

Fig. 4 Schematic of Z-scheme OWS on Ru-modified $SrTiO_3$:La,Rh/Au/$BiVO_4$:Mo particulate photocatalyst sheets. Reprinted with permission from Springer Nature [22], Copyright (2016)

Ag, Ir, and RGO) [22, 24, 103–105] or an aqueous redox mediator (e.g., Fe^{3+}/Fe^{2+} and IO_3^-/I^- solutions) [23, 106]. With this technique, semiconductors with unsuitable band positions (CBM lower than the H^+/H_2 redox potential or VBM higher than the O_2/H_2O potential) and a relatively small band gap can be utilized, thus expanding the choice of semiconductors [5, 9]. Furthermore, this system also provides a larger driving force for water splitting than the conventional photocatalytic system (one semiconductor) [10]. However, the major drawback of Z-scheme water splitting is the reduced amount of H_2 and O_2 produced, since half of the charge carriers recombine within the mediator [77].

3.2 Hydrogen Production from Sacrificial Water Splitting

Achieving OWS using a simple photocatalytic system is difficult in practice owing to many strict requirements that must be simultaneously satisfied [75]. Therefore, some researchers have attempted to apply a sacrificial agent as an irreversible electron donor or acceptor to perform an HER or OER separately, thus greatly reducing the complexity of the reaction. This sacrificial water splitting (SWS) method is relatively effective and efficient for assessing the suitability of a certain photocatalytic system for performing water splitting in terms of band positions, photogenerated charge dynamics, compatibility of the cocatalyst, and other properties [75]. Furthermore, since the reverse reaction (water formation) can be annulled in SWS, it is common to obtain a higher apparent production rate and quantum yield than in the case of OWS.

For HER, different semiconductors require different sacrificial agents (as an electron donor or hole scavenger) to obtain good performance. This phenomenon is due to the wide range of ability of semiconductors to oxidize a sacrificial agent [107]. For example, the semiconductor graphitic carbon nitride (g-C_3N_4) can exhibit superior performance when triethanolamine (TEOA) is used as a hole scavenger but has a rather poor performance when a different sacrificial agent is applied. Considering the cost and efficiency, the realization of this sacrificial photocatalytic hydrogen production strategy by utilizing biomass and abundant compounds in nature or industrial waste as the sacrificial agent will be of great significance [75].

CdS is an important and popular semiconductor which is often used in sacrificial HER. Although CdS has a very suitable band position for water splitting with a visible-light-responsive band gap (2.4 eV), it is ineffective for OWS owing to the self-photocorrosion phenomenon, which is often encountered with the use of sulfide materials [97]. The sulfur (S^{2-}) in CdS, instead of H_2O, is very susceptible to oxidation by photogenerated holes accompanied by the elution of the Cd^{2+} cation, as shown by the following equation [75]:

$$\mathrm{CdS} + 2h^+ \rightarrow \mathrm{Cd}^{2+} + \mathrm{S}. \tag{12}$$

Owing to this problem, a mixture of Na_2S and Na_2SO_3 is often utilized as a sacrificial agent, which not only protects the sulfide semiconductor from photocorrosion, thus producing a stable photocatalyst, but also greatly boosts its photocatalytic HER performance [48].

An interesting study about nature-inspired environmental phosphorylation to boost the sacrificial hydrogen production of g-C_3N_4 and several other semiconductors has been reported [62]. In NPS, phosphates play vital roles in establishing the Calvin cycle, acting as the transporter and pump for charge carrier transfer during light-dependent reactions and as mediators in carbon fixation during the dark reactions of photosynthesis. In this study, it was found that the addition of a phosphate component (KH_2PO_4) markedly boosted the H_2 generation of Pt/g-C_3N_4 by establishing a similar proton reduction mechanism to the one found in NPS (see Fig. 5),

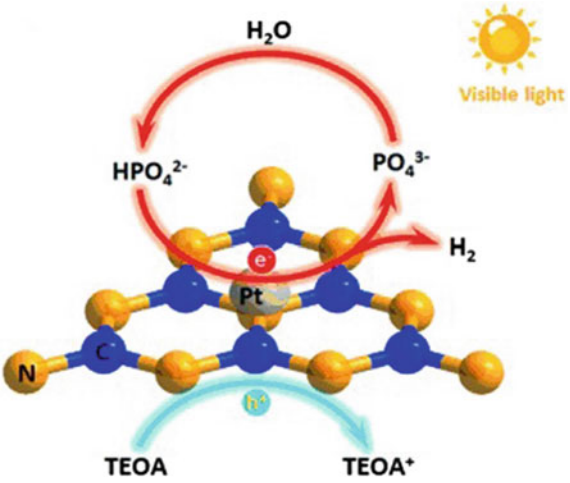

Fig. 5 Schematic illustration of photocatalytic H_2 evolution via the proton reduction mechanism involving HPO_4^{2-}. From Liu et al., Angew. Chem. Int. Ed., 54, 13,561–13,565 (2015) [62]. Copyright Wiley–VCH Verlag GmbH & Co. KGaA. Reproduced with permission

achieving a very high AQY of 26.1% at a wavelength of 420 nm for a g-C_3N_4-based photocatalyst. This finding may provide a promising and facile approach to highly efficient photocatalysis for both SWS and OWS in the future.

4 CO_2 Reduction

In modern society, owing to the rapidly increasing demand for energy, CO_2 emissions have escalated, resulting in a very serious state with NPS no longer compensating for CO_2 emission [108]. CO_2 is generally regarded as the main greenhouse gas, with excess CO_2 causing environmental problems, such as global warming, melting of the polar ice caps, sea level rises, and worsening droughts [108, 109]. These concerns have led to attempts to control the amount of CO_2 by converting CO_2 into harmless and useful chemical feedstocks [110]. Regarding this approach, solar-driven CO_2 conversion through APS is considered as one of the most reasonable and ideal approaches not only to reduce the imbalance between NPS and CO_2 emission, but also to provide a new type of energy feedstock, thus increasing the capacity of the global energy storage system [83, 111].

Since the carbon atom in CO_2 molecules possesses the highest valence, the photoreduction of CO_2 may result in a wide variety of carbon products with different oxidation states, ranging from gaseous CO and CH_4 to higher hydrocarbon species (e.g., C_2H_4, C_3H_8), as well as liquid-phase oxygenated hydrocarbons, such as CH_3OH and HCOOH (but not complex products such as carbohydrates) [112]. Table 2 shows the standard electrode potentials ($E°$) for the transformation of CO_2 into various products in aqueous media at pH 7 with respect to SHE. Unfortunately, CO_2 photoreduction is difficult to realize owing to the extreme stability of the CO_2

Table 2 Standard reduction potentials (pH 7) for the reactions of CO_2 reduction to different products in aqueous media

Reaction	E° versus SHE (V)
$CO_{2(g)} + e^- \rightarrow CO_2^-$	−1.90
$CO2_{(g)} + 2\ H^+_{(aq)} + 2\ e^- \rightarrow HCOOH_{(aq)}$	−0.61
$CO2_{(g)} + 2\ H^+_{(aq)} + 2\ e^- \rightarrow CO_{(g)} + H_2O_{(l)}$	−0.52
$CO2_{(g)} + 4\ H^+_{(aq)} + 4\ e^- \rightarrow HCHO_{(l)} + H_2O_{(l)}$	−0.48
$CO2_{(g)} + 6\ H^+_{(aq)} + 6\ e^- \rightarrow CH_3OH_{(l)} + H_2O_{(l)}$	−0.38
$CO2_{(g)} + 8\ H^+_{(aq)} + 8\ e^- \rightarrow CH_{4(g)} + H_2O_{(l)}$	−0.24
$2\ H^+_{(aq)} + 2\ e^- \rightarrow H_{2(g)}$	−0.41
$2\ H_2O_{(l)} \rightarrow O_{2(g)} + 4\ H^+_{(aq)} + 4\ e^-$	0.82

Source [83, 113]

molecule, ascribed to its two symmetric C = O bonds, which possess a high dissociation energy of about 750 kJ/mol [83]. In this case, the activation of CO_2 molecules very likely becomes the rate-determining step for the CO_2 reduction reaction [112]. Moreover, in the presence of water, CO_2 reduction must compete with proton reduction owing to the similar reduction potential and also the preferential adsorption of water compared with CO_2, thus resulting in the low selectivity and efficiency of the desired reaction [83].

From the kinetic perspective, the CO_2 reduction reaction is also challenging. The first step in CO_2 reduction is generally considered to be the formation of an intermediate CO_2^- (through a single electron transfer (ET) to a CO_2 molecule), whose reduction potential is very high (about −1.9 V) [112], as shown in Table 2. Consequently, a high overpotential is necessary[3] for the CO_2 reduction reaction to further proceed. Given this, an alternative reaction route involving a series of multiple proton-coupled electron transfer (PCET)[4] processes can be employed to bypass the formation of CO_2^-, thus avoiding the large activation barrier and the formation of unstable and high-energy intermediates [4, 83] (see Table 2). However, the PCET process is kinetically dependent on both the concentration of protons in the solution and the surface electron density at the reactive sites [112]. Moreover, since most of the CO_2 reduction products require multielectron transfer, the corresponding CO_2 reduction reactions are less kinetically favorable than the reduction of water, which only involves two electrons [112].

[3] Very few semiconductors have a CB level exceeding the $CO_2/\ CO_2^-$ reduction potential.

[4] In PCET, electron transfer is associated with proton (H^+) transfer. For the case of CO_2 reduction, the number of protons and electrons involved will also determine the products and reduction potential of the correponding reaction, as listed in Table 2.

In the following sections, we will briefly discuss the strategies for addressing some challenges in CO_2 reduction reactions: the activation of CO_2 molecules and controlling the selectivity of CO_2 reduction.

4.1 Activation of CO_2 Molecules

The activation of a CO_2 molecule is closely related to its adsorption by the surface atoms of a photocatalyst. The chemisorption of a CO_2 molecule induces the formation of a partially charged $CO_2^{\delta\bullet-}$ adsorbate, which no longer possesses a linear symmetrical structure [114]. The bending of CO_2 molecules is beneficial for lowering the barrier for electron transfer into CO_2 owing to the decrease in the lowest unoccupied molecular orbital (LUMO) level [114]. Hence, the basic strategy for driving the activation of CO_2 molecules is to promote the chemisorption of CO_2. Figure 6 shows some possible binding modes for the adsorption of a CO_2 molecule on the surface of a metal oxide (such as TiO_2), a popular photocatalyst for the photoreduction of CO_2 [115].

As approaches to activating CO_2 molecules, several practical strategies have been experimentally demonstrated, i.e., increasing the available surface area for adsorption, establishing surface defects, introducing surface basic sites, and employing a cocatalyst on the photocatalyst surface. In general, increasing the surface area of the photocatalyst, either by modifying the structure and morphology of the photocatalyst or by using a porous material, will provide more reactive sites for CO_2 adsorption [116–119]. Surface defects, such as oxygen vacancies [25, 79, 80] and sulfur vacancies [57–59], have attracted considerable attention in the last decade owing to their potential for generating an active trapping surface for CO_2 molecules. The challenge in this strategy is to prevent the formation of bulk defects, which usually occurs alongside the formation of surface defects, because bulk defects can act as recombination centers, which adversely affect the photocatalytic performance [75]. The formation of surface basic sites is also beneficial for CO_2 chemisorption owing to the Lewis acidity of the C atom, which enables CO_2 molecules to interact with the alkaline surface, thus leading to the formation of carbonate or bicarbonate intermediates [120–122]. Finally, a cocatalyst with a large work function, such as a noble metal, can also be employed, which may induce electron backdonation from metal d-orbitals into the (C–O) π^* orbital of CO_2, causing the formation of a $CO_2^{\delta\bullet-}$ adsorbate [109, 112].

It has also been reported that CO_2 molecules can be polarized and subsequently activated by utilizing highly energetic electrons excited by the localized surface plasmon resonance (LSPR) of some plasmonic nanometals (e.g., Au, Pt, Pd, etc.), assisted by thermal energy [123–127]. The LSPR effect is defined as the resonant photon-induced collective oscillation of valence electrons, established when the frequency of the photons matches the natural frequency of the surface electrons oscillating against the restoring force of positive nuclei [128]. This phenomenon generates hot electrons with very high energy, which are very effective for disrupting

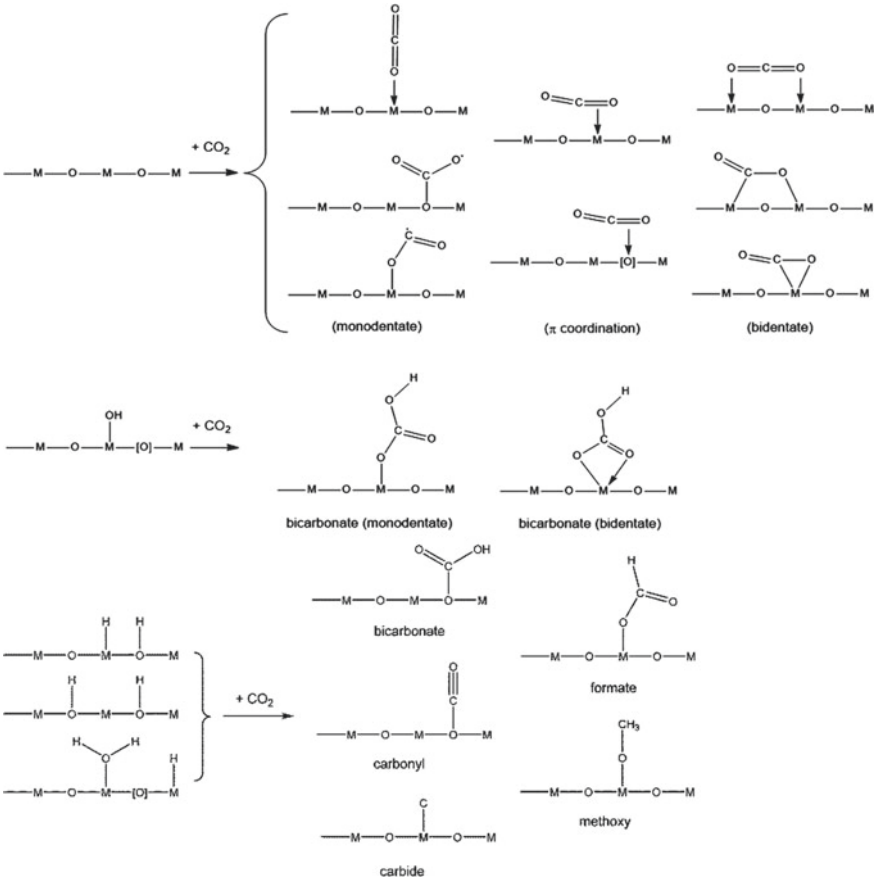

Fig. 6 Modes of adsorption for CO_2 on the surfaces of regular and modified metal oxides. Reproduced from Ref. [115] with permission from The Royal Society of Chemistry

the stability of CO_2 molecules [129]. Figure 7 illustrates a schematic and the reaction mechanism of the LSPR effect over a Pt-Au/SiO_2 catalyst for the photoreduction of CO_2 [127]. Following these studies, the photothermal effect through the self-heating process was observed on an illuminated boron catalyst[5] [130]. It is well known that CO_2 molecules are more reactive at high temperatures. In this case, the photothermal effect of boron can induce a high local temperature, which facilitates CO_2 activation. It also triggers the self-hydrolysis of boron particles, which in situ produces H_2 as the active proton source and electron donor for CO_2 reduction, as well as boron oxides that function as promoters of CO_2 adsorption onto the surface of boron catalysts. All these effects synergistically promote the CO_2 reduction reaction.

[5] The corresponding photothermal process is actually considerably different from the conventional APS process, which involves the generation of charge carriers. However, since this effect is entirely driven by the illumination of light, we decided to include this study in the discussion.

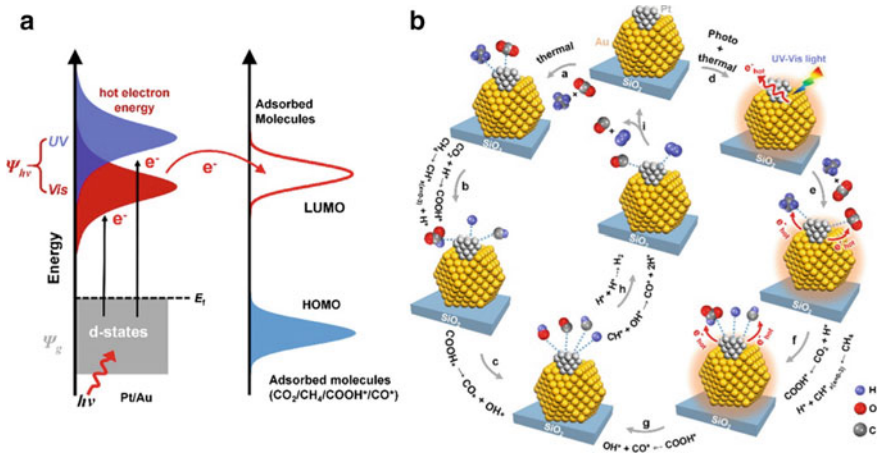

Fig. 7 **a** Schematic of LSPR effect generating light-excited hot electrons for the activation of stable compounds, such as CO_2 and CH_4. **b** Proposed reaction mechanism for photocatalytic CO_2 reduction over Pt-Au/SiO_2 by utilizing the dry reforming of methane (DRM) reaction. Reprinted with permission from Song et al., ACS Appl. Mater. Interfaces, 10, 408–416 (2018) [127]. Copyright (2018) American Chemical Society

4.2 Controlling the Selectivity of CO_2 Reduction

As mentioned earlier, CO_2 reduction has several possible reaction pathways, depending on the number of electrons involved in the reactions, leading to various carbon products. Therefore, in addition to the competition with proton reduction, it is also important to ensure that the CO_2 reduction selectively proceeds through the desired reaction. In short, the binding mode of CO_2 during the adsorption state (see Fig. 6) determines the route that the reaction takes [112, 115]. Accordingly, tuning the surface features of the photocatalyst to favor the formation of a particular adsorbate intermediate, which in turn will be converted into the desired carbon product, is the key to controlling the selectivity of CO_2 reduction.

The cocatalyst is also important for not only kinetically driving the multielectron reaction of CO_2 reduction (since it may serve as an electron-trapping center), but also tuning the selectivity of the reaction [109]. The final product of the reaction may vary with the adsorption properties of the intermediate, electron transfer (for proton reduction and CO_2 activation) overpotentials, loading method, elemental composition, dispersion, particle size, structure, and exposed sites of the cocatalyst [109, 112, 131]. Therefore, the careful selection and design of the cocatalyst are indispensable for regulating the reaction mechanism [109]. Figure 8 summarizes the general selectivity trends of CO_2 reduction over various metal-based cathodes [132]. In addition, it is also necessary to tune the experimental conditions. Among the many experimental parameters, the pH of the solution can considerably affect the CO_2 reduction reaction mechanism [131]. pH not only determines the concentration

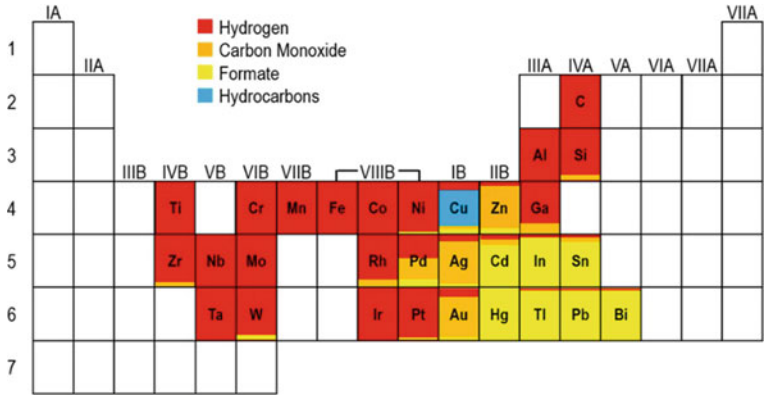

Fig. 8 Section of the periodic table depicting the primary products in CO_2 reduction over some metal-based electrodes. Reprinted with permission from White et al., Chem. Rev., 115, 12,888–12,935 (2015) [132]. Copyright (2015) American Chemical Society

of H^+ ions in the solution (which is related to the rate of H_2 evolution), but also affects the solubility of CO_2 and the relative concentrations of CO_3^{2-} and HCO_3^-, which are strongly correlated with the modes of CO_2 adsorption [112, 131].

5 N_2 Fixation

The N_2 fixation reaction can be regarded as one of the most crucial chemical processes in nature, considering the importance of fixed nitrogen compounds[6] for living organisms on this planet, owing to its integral role in producing basic biological building blocks [85, 133, 134]. In particular, ammonia (NH_3), the main product of N_2 fixation, is a very important raw material for the production of fertilizers and also as a promising carbon-free energy carrier [135–137]. The first work on photocatalytic nitrogen fixation in sterile soils containing natural abundant oxides was performed by Dhar and Pant in the early 1940s [138]. Subsequently, around 30–40 years later, Schrauzer and Guth provided more thorough reports of photon-driven nitrogen fixation over natural materials and as-synthesized TiO_2 [19, 139]. These early studies triggered numerous extensive works to investigate nitrogen fixation over some well-designed synthetic photocatalysts [133]. Unfortunately, in the following decades, the studies on semiconductor-based photocatalytic nitrogen fixation were considerably hindered (as indicated by the substantially fewer reported studies) by the difficulties in N_2 adsorption and activation over the catalytic surface, which were a stumbling block to further development and achieving competitive performance with other methods [133, 136, 137]. Nevertheless, owing to the recent advancement

[6] They are identified by their lack of N–N bonds and can take both the oxidized and reduced forms of N_2, such as NH_3, nitrogen oxides, nitrates, and urea [133].

of nanotechnologies and nanomaterials, which can provide solutions to such kinetic limitations, photocatalytic N_2 fixation has returned to the main stage in the field of APS in the past few years [85].

Being the 'youngest' of the APS applications, photon-driven N_2 fixation still has a long way to go before an ideal catalytic N_2 photofixation system can be devised, inasmuch as the comprehensive knowledge and understanding of the mechanistic principles of the reaction and also suitable materials are still lacking [85]. In this section, we briefly discuss the basic mechanism of N_2 photofixation (especially to NH_3), the requirements and challenges in achieving effective reaction processes, and the possible approaches to deal with them. The discussion herein is expected to contribute to filling the knowledge gap in the study of APS-based N_2 fixation.

5.1 Fundamentals of Photon-Driven N_2 Fixation

The N_2 fixation and CO_2 reduction reactions actually have many things in common. Similar to the CO_2 molecule, the N_2 molecule is also very stable owing to its extremely strong N≡N bond, with a dissociation energy of 945 kJ/mol for the direct cleavage of the triple bond [85]. As a result, a single ET (−4.16 V vs. SHE) and PCET (−3.20 V vs. SHE) to the N_2 molecule (for its activation) are almost thermodynamically imposible with currently available semiconductors owing to their very high reduction potentials. Therefore, in a similar way to the CO_2 reduction reaction mechanism, multiple PCET processes can also be applied in the N_2 reduction reaction to avoid the principal energy barrier while bypassing the formation of high-energy intermediates [140, 141]. Multiple PCET, depending on the number of protons and electrons involved, may lead to various partially reduced and stable intermediate species (e.g., N_2H_2 and N_2H_4) other than NH_3, thus resulting in competition between them and also with the water reduction reaction [140]. Table 3 provides

Table 3 Standard reduction potentials (pH 0) for the reactions of N_2 reduction to NH_3 in aqueous media

Reaction	$E°$ versus SHE (V)
$N_{2(g)} + e^- \rightarrow {N_2}^-{}_{(aq)}$	−4.16
$N_{2(g)} + {H^+}_{(aq)} + e^- \rightarrow N_2H_{(g)}$	−3.20
$N_{2(g)} + 2\ {H^+}_{(aq)} + 2\ e^- \rightarrow N_2H_{2(g)}$	−1.20
$N_{2(g)} + 4\ {H^+}_{(aq)} + 4\ e^- \rightarrow N_2H_{4(g)}$	−0.33
$N_{2(g)} + 5\ {H^+}_{(aq)} + 4\ e^- \rightarrow {N_2H_5}^+{}_{(aq)}$	−0.23
$N2_{(g)} + 6\ {H^+}_{(aq)} + 6\ e^- \rightarrow 2\ NH_{3(g)}$	0.09
$N2_{(g)} + 8\ {H^+}_{(aq)} + 6\ e^- \rightarrow 2\ {NH_4}^+{}_{(aq)}$	0.27
$2\ {H^+}_{(aq)} + 2\ e^- \rightarrow H_{2(g)}$	0.00
$2\ H_2O_{(l)} \rightarrow O_{2(g)} + 4\ {H^+}_{(aq)} + 4\ e^-$	1.23

Source [140, 141, 143]

a list of possible N_2 reduction reactions in aqueous media and their corresponding standard reduction potentials.

The extremely high stability of the N_2 molecule is also a major disadvantage regarding the kinetic feasibility of the N_2 fixation reaction. Because of the high stability, the adsorption and activation of the N_2 molecule can be considered as the rate-limiting steps of the overall reaction [142]. For the same reason, it still remains a major challenge to enhance the kinetic feasibility of the N_2 photofixation reaction. Therefore, even though there are other concerns that must be looked into and dealt with carefully, in the next section, we will only discuss the adsorption and activation of N_2, the most crucial yet challenging steps in the N_2 fixation reaction.

5.2 Adsorption and Activation of N_2 Molecules

Similar to the CO_2 molecule, the activation of the N_2 molecule is also strongly associated with the adsorption of the species on the catalytic surface, since electron transfer can only occur when there is an intimate interaction between the chemical species and the catalyst [142]. Generally, a photocatalyst with a high surface area is favorable for heterogeneous catalytic reactions, including N_2 fixation, owing to its capability of adsorbing more reactants [144]. Some other potential approaches for promoting the adsorption of N_2 molecules by employing surface defects, such as nitrogen vacancies [69, 145] and oxygen vacancies [74, 146], have been succesfully demonstrated for various nitride and oxide semiconductors, respectively. The vacancy species on the surface of a semiconductor can be occupied by N atoms, thus enabling swift electron donation to the adsorbed N_2 owing to the direct contact between the photocatalyst and the N_2 molecules. Such a phenomenon is essential for the N_2 activation step and will be discussed later. To suppress the faster H_2 reduction reaction, employing a metal-based catalyst with stronger adsorption of N atoms than that of H atoms might be a promising strategy worth investigating and exploring more thoroughly [147, 148].

Regarding N_2 activation, it is beneficial for the adsorbing sites to be able to synergically accept electrons from and backdonate to N_2, which simultaneously weakens the N_2 bond[7] and strengthens the bond between the sites and N_2, as illustrated in Fig. 9 [135]. As a result, the adsorbed N_2 is more susceptible to electron donation owing to the reduced resistance and activation energy barrier of the attenuated N_2 bond. Subsequently promoting charge exchange between the catalyst and N_2 is essential to provide an accessible kinetic pathway towards the activation step and later stages of the reaction [85]. Interestingly, the above-mentioned strategies can be simultaneously employed by generating vacancy species on the surface of a semiconductor, which is a powerful method of promoting the photocatalytic N_2 fixation reaction, as mentioned earlier, owing to the N_2-capturing ability and nature of the vacancy as an

[7] The weakening of the N_2 bond is usually associated with an increase in its bond length, indicating a lower bond energy.

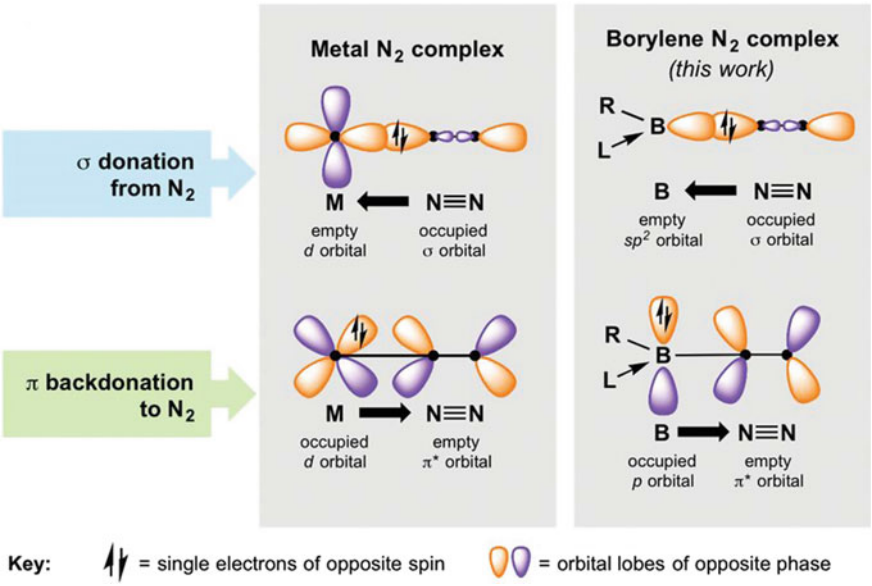

Fig. 9 Simplified schematic of bonding in well-known end-on bound transition metal N_2 complexes (left) and monovalent boron species (right). From Légaré et al., Science, 359, 896–900 (2018) [135]. Reprinted with permission from AAAS

electron localization center [74]. When the surface vacancy successfully binds a N_2 molecule, the backtransfer of charges from the vacancy to the adsorbed N_2 occurs, rendering electron depletion on the vacancy and electron accumulation on the N_2 molecule [71].

Even though a vacancy possesses great potential for N_2 adsorption and activation, a surface vacancy can be easily consumed through oxidation or a similar phenomenon, leading to the deactivation of the photocatalyst [149]. Vacancy stabilization through the self-regeneration of the vacancy under light irradiation is therefore an ideal solution to this problem [74, 149]. Very recently, an excellent example of light-switchable oxygen vacancy circulation for sustainable N_2 fixation on an ultrafine Bi_5O_7Br nanotube has been reported, the scheme of which is shown in Fig. 10 [74]. In addition, similar to the CO_2 molecule, the N_2 molecule can also be activated by utilizing hot electrons produced through the LSPR effect [26, 27, 150].

6 Summary and Outlook

Owing to the rapid advancement of human civilization, both global energy consumption and environmental pollution have increased significantly and almost uncontrollably. To make matters worse, the regeneration of fossil fuels, our current primary

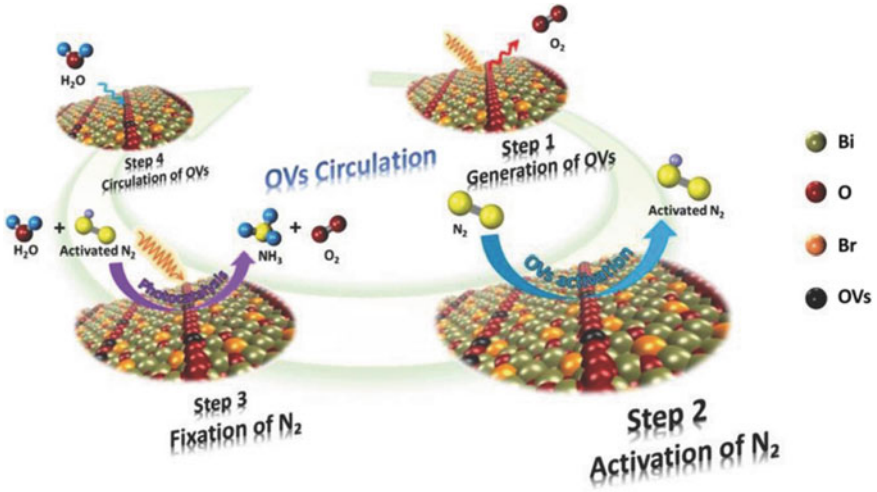

Fig. 10 Schematic illustration of photoinduced oxygen vacancy (OV) circulation for N_2 fixation on Bi_5O_7Br. From Wang et al., Adv. Mater. 29, 1,701,774 (2017) [74]. Copyright Wiley–VCH Verlag GmbH & Co. KGaA. Reproduced with permission

energy resource, is extremely slow. Thus, the realization of artifical photosynthesis (APS) technology to exploit and convert the limitless solar energy into renewable, clean, and sustainable energy feedstocks has become an urgent task requiring intensive and extensive effort and study. For this reason, many APS-based scientists and researchers have attempted to acquire in-depth and comprehensive knowledge on the APS reaction mechanism as well as practical and efficient approaches to devise an ideal photocatalytic system.

In this chapter, we have summarized the basic concepts in designing an effective photocatalytic system by examining the general steps in the APS process, i.e., photon absorption, charge carrier migration, and the surface reaction. Furthermore, the fundamentals of three important APS reactions (water splitting, CO_2 reduction, and N_2 fixation) as well as the specific challenges of each reaction and some possible strategies to address them were briefly introduced. We also discussed several effective strategies for improving the performance of some photocatalytic materials in diverse applications, such as a surface nanolayer coating, the Z-scheme system, the sacrificial photocatalytic reaction, the localized surface plasmon resonance (LSPR) phenomenon, and surface defects (self-regeneration).

While considerable advances in APS research have recently been accomplished, efficiency, stability, and cost are still the main issues that must be simultaneously overcome to enable APS technology to enter industrial use. The development of novel photocatalytic materials, either by modifying currently available materials or by discovering completely new materials, may lead to a significant breakthrough in these problems. Correspondingly, surface and interface engineering are indispensable for the fabrication of outstanding materials with distinctive and useful features, and

thus should be considered and further extended. Last but not least, it is also important to carry out an in-depth study of the mechanism through the combination of in situ observation and a theoretical approach (commonly by computational methods) to obtain a full, accurate, and detailed understanding of the mechanism behind all APS processes.

References

1. Bard AJ, Fox MA (1995) Artificial photosynthesis: solar splitting of water to hydrogen and oxygen. Acc Chem Res 28(3):141–145. https://doi.org/10.1021/ar00051a007
2. Benniston AC, Harriman A (2008) Artificial Photosynthesis. Mater Today 11(12):26–34. https://doi.org/10.1016/S1369-7021(08)70250-5
3. Balzani V, Credi A, Venturi M (2008) Photochemical conversion of solar energy. Chemsuschem 1(1–2):26–58. https://doi.org/10.1002/cssc.200700087
4. Lewis NS, Nocera DG (2006) Powering the planet: chemical challenges in solar energy utilization. Proc Natl Acad Sci U.S.A. 103(43):15729–15735. https://doi.org/10.1073/pnas.0603395103
5. Tachibana Y, Vayssieres L, Durrant JR (2012) Artificial photosynthesis for solar water-splitting. Nat. Photonics 6:511–518. https://doi.org/10.1038/nphoton.2012.175
6. Hisatomi T, Takanabe K, Domen K (2015) Photocatalytic water-splitting reaction from catalytic and kinetic perspectives. Catal Lett 145(1):95–108. https://doi.org/10.1007/s10562-014-1397-z
7. Zhu S, Wang D (2017) Photocatalysis: basic principles, diverse forms of implementations and emerging scientific opportunities. Adv Energy Mater 7(23):1700841. https://doi.org/10.1002/aenm.201700841
8. Zhang J, Hu S, Wang Y (2014) A convenient method to prepare a novel alkali metal sodium doped carbon nitride photocatalyst with a tunable band structure. RSC Adv 4(108):62912–62919. https://doi.org/10.1039/C4RA11377B
9. Wang Y, Suzuki H, Xie J, Tomita O, Martin DJ, Higashi M, Kong D, Abe R, Tang J (2018) Mimicking natural photosynthesis: solar to renewable H_2 fuel synthesis by Z-scheme water splitting systems. Chem Rev 118(10):5201–5241. https://doi.org/10.1021/acs.chemrev.7b00286
10. Chen S, Takata T, Domen K (2017) Particulate photocatalysts for overall water splitting. Nat Rev Mater 2:17050. https://doi.org/10.1038/natrevmats.2017.50
11. Maeda K, Domen K (2007) New non-oxide photocatalysts designed for overall water splitting under visible light. J Phys Chem C 111(22):7851–7861. https://doi.org/10.1021/jp070911w
12. Fujishima A, Honda K (1972) Electrochemical photolysis of water at a semiconductor electrode. Nature 238:37–38. https://doi.org/10.1038/238037a0
13. Slamet R, Gunlazuardi J, Dewi EL (2017) Enhanced photocatalytic activity of Pt deposited on titania nanotube arrays for the hydrogen production with glycerol as a sacrificial agent. Int J Hydrogen Energy 42(38):24014–24025. https://doi.org/10.1016/j.ijhydene.2017.07.208
14. Slamet TD, Valentina IM (2013) Photocatalytic hydrogen production from glycerol-water mixture over Pt-N-TiO_2 nanotube photocatalyst. Int J Energy Res 37(11):1372–1381. https://doi.org/10.1002/er.2939
15. de Brito JF, Tavella F, Genovese C, Ampelli C, Zanoni MVB, Centi G, Perathoner S (2018) Role of CuO in the modification of the photocatalytic water splitting behavior of TiO_2 nanotube thin films. Appl Catal B: Environ 224:136–145. https://doi.org/10.1016/j.apcatb.2017.09.071

16. Tan L-L, Ong W-J, Chai S-P, Mohamed AR (2015) Noble metal modified reduced graphene Oxide/TiO_2 ternary nanostructures for efficient visible-light-driven photoreduction of carbon dioxide into methane. Appl Catal B: Environ 166–167:251–259. https://doi.org/10.1016/j.apcatb.2014.11.035
17. Varghese OK, Paulose M, LaTempa TJ, Grimes CA (2009) High-rate solar photocatalytic conversion of CO_2 and water vapor to hydrocarbon fuels. Nano Lett 9(2):731–737. https://doi.org/10.1021/nl803258p
18. Ye M, Wang X, Liu E, Ye J, Wang D (2018) Boosting the photocatalytic activity of P25 for carbon dioxide reduction by using a surface-alkalinized titanium carbide MXene as cocatalyst. Chemsuschem 11(10):1606–1611. https://doi.org/10.1002/cssc.201800083
19. Schrauzer GN, Guth TD (1977) Photolysis of water and photoreduction of nitrogen on titanium dioxide. J Am Chem Soc 99(22):7189–7193. https://doi.org/10.1021/ja00464a015
20. Hirakawa H, Hashimoto M, Shiraishi Y, Hirai T (2017) Photocatalytic conversion of nitrogen to ammonia with water on surface oxygen vacancies of titanium dioxide. J Am Chem Soc 139(31):10929–10936. https://doi.org/10.1021/jacs.7b06634
21. Zhao W, Zhang J, Zhu X, Zhang M, Tang J, Tan M, Wang Y (2014) Enhanced nitrogen photofixation on Fe-doped TiO_2 with highly exposed (101) facets in the presence of ethanol as scavenger. Appl Catal B: Environ 144:468–477. https://doi.org/10.1016/j.apcatb.2013.07.047
22. Wang Q, Hisatomi T, Jia Q, Tokudome H, Zhong M, Wang C, Pan Z, Takata T, Nakabayashi M, Shibata N, Li Y, Sharp ID, Kudo A, Yamada T, Domen K (2016) Scalable water splitting on particulate photocatalyst sheets with a solar-to-hydrogen energy conversion efficiency exceeding 1%. Nat Mater 15:611–615. https://doi.org/10.1038/nmat4589
23. Kato H, Sasaki Y, Shirakura N, Kudo A (2013) Synthesis of highly active rhodium-doped $SrTiO_3$ powders in Z-scheme systems for visible-light-driven photocatalytic overall water splitting. J Mater Chem A 1(39):12327–12333. https://doi.org/10.1039/C3TA12803B
24. Wang Q, Li Y, Hisatomi T, Nakabayashi M, Shibata N, Kubota J, Domen K (2015) Z-scheme water splitting using particulate semiconductors immobilized onto metal layers for efficient electron relay. J Catal 328:308–315. https://doi.org/10.1016/j.jcat.2014.12.006
25. Xie K, Umezawa N, Zhang N, Reunchan P, Zhang Y, Ye J (2011) Self-doped $SrTiO_{3-\delta}$ photocatalyst with enhanced activity for artificial photosynthesis under visible light. Energy Environ Sci 4(10):4211–4219. https://doi.org/10.1039/C1EE01594J
26. Oshikiri T, Ueno K, Misawa H (2014) Plasmon-induced ammonia synthesis through nitrogen photofixation with visible light irradiation. Angew Chem Int Ed 53(37):9802–9805. https://doi.org/10.1002/anie.201404748
27. Oshikiri T, Ueno K, Misawa H (2016) Selective dinitrogen conversion to ammonia using water and visible light through plasmon-induced charge separation. Angew Chem Int Ed 55(12):3942–3946. https://doi.org/10.1002/anie.201511189
28. Ohno T, Bai L, Hisatomi T, Maeda K, Domen K (2012) Photocatalytic water splitting using modified GaN:ZnO solid solution under visible light: long-time operation and regeneration of activity. J Am Chem Soc 134(19):8254–8259. https://doi.org/10.1021/ja302479f
29. Yang X, Wolcott A, Wang G, Sobo A, Fitzmorris RC, Qian F, Zhang JZ, Li Y (2009) Nitrogen-doped ZnO nanowire arrays for photoelectrochemical water splitting. Nano Lett 9(6):2331–2336. https://doi.org/10.1021/nl900772q
30. Xin C, Hu M, Wang K, Wang X (2017) Significant enhancement of photocatalytic reduction of CO_2 with H_2O over ZnO by the formation of basic zinc carbonate. Langmuir 33(27):6667–6676. https://doi.org/10.1021/acs.langmuir.7b00620
31. Zhang S, Yin X, Zheng Y (2018) Enhanced photocatalytic reduction of CO_2 to methanol by ZnO nanoparticles deposited on ZnSe nanosheet. Chem Phys Lett 693:170–175. https://doi.org/10.1016/j.cplett.2018.01.018

32. Zhang X, Wang X, Wang D, Ye J (2019) Conformal $BiVO_4$-layer/WO_3-nanoplate-array heterojunction photoanode modified with cobalt phosphate cocatalyst for significantly enhanced photoelectrochemical performances. ACS Appl Mater Interfaces 11(6):5623–5631. https://doi.org/10.1021/acsami.8b05477
33. Pihosh Y, Turkevych I, Mawatari K, Asai T, Hisatomi T, Uemura J, Tosa M, Shimamura K, Kubota J, Domen K, Kitamori T (2014) Nanostructured WO_3/$BiVO_4$ photoanodes for efficient photoelectrochemical water splitting. Small 10(18):3692–3699. https://doi.org/10.1002/smll.201400276
34. Gao S, Gu B, Jiao X, Sun Y, Zu X, Yang F, Zhu W, Wang C, Feng Z, Ye B, Xie Y (2017) Highly efficient and exceptionally durable CO_2 photoreduction to methanol over freestanding defective single-unit-cell bismuth vanadate layers. J Am Chem Soc 139(9):3438–3445. https://doi.org/10.1021/jacs.6b11263
35. Dias P, Lopes T, Meda L, Andrade L, Mendes A (2016) Photoelectrochemical water splitting using WO_3 photoanodes: the substrate and temperature roles. PCCP 18(7):5232–5243. https://doi.org/10.1039/C5CP06851G
36. Chen X, Zhou Y, Liu Q, Li Z, Liu J, Zou Z (2012) Ultrathin, single-crystal WO_3 nanosheets by two-dimensional oriented attachment toward enhanced photocatalystic reduction of CO_2 into hydrocarbon fuels under visible light. ACS Appl Mater Interfaces 4(7):3372–3377. https://doi.org/10.1021/am300661s
37. Wang P-Q, Bai Y, Luo P-Y, Liu J-Y (2013) Graphene–WO_3 nanobelt composite: elevated conduction band toward photocatalytic reduction of CO_2 into hydrocarbon fuels. Catal Commun 38:82–85. https://doi.org/10.1016/j.catcom.2013.04.020
38. Wang D, Pierre A, Kibria MG, Cui K, Han X, Bevan KH, Guo H, Paradis S, Hakima A-R, Mi Z (2011) Wafer-level photocatalytic water splitting on GaN nanowire arrays grown by molecular beam epitaxy. Nano Lett 11(6):2353–2357. https://doi.org/10.1021/nl2006802
39. AlOtaibi B, Fan S, Wang D, Ye J, Mi Z (2015) Wafer-level artificial photosynthesis for CO_2 reduction into CH_4 and CO using GaN nanowires. ACS Catal 5(9):5342–5348. https://doi.org/10.1021/acscatal.5b00776
40. Standing A, Assali S, Gao L, Verheijen MA, van Dam D, Cui Y, Notten PHL, Haverkort JEM, Bakkers EPAM (2015) Efficient water reduction with gallium phosphide nanowires. Nat Commun 6:7824. https://doi.org/10.1038/ncomms8824
41. Sun J, Liu C, Yang P (2011) Surfactant-free, large-scale, solution–liquid–solid growth of gallium phosphide nanowires and their use for visible-light-driven hydrogen production from water reduction. J Am Chem Soc 133(48):19306–19309. https://doi.org/10.1021/ja2083398
42. Barton EE, Rampulla DM, Bocarsly AB (2008) Selective solar-driven reduction of CO_2 to methanol using a catalyzed p-GaP based photoelectrochemical Cell. J Am Chem Soc 130(20):6342–6344. https://doi.org/10.1021/ja0776327
43. Zeng G, Qiu J, Li Z, Pavaskar P, Cronin SB (2014) CO_2 reduction to methanol on TiO_2-passivated GaP photocatalysts. ACS Catal 4(10):3512–3516. https://doi.org/10.1021/cs500697w
44. Maeda K, Lu D, Domen K (2013) Direct water splitting into hydrogen and oxygen under visible light by using modified TaON photocatalysts with d^0 electronic configuration. Chem Eur J 19(16):4986–4991. https://doi.org/10.1002/chem.201300158
45. Ma SSK, Maeda K, Domen K (2012) Modification of TaON with ZrO_2 to improve photocatalytic hydrogen evolution activity under visible light: influence of preparation conditions on activity. Catal Sci Technol 2(4):818–823. https://doi.org/10.1039/C2CY00499B
46. Hara M, Kondo T, Komoda M, Ikeda S, Kondo JN, Domen K, Hara M, Shinohara K, Tanaka A (1998) Cu_2O as a photocatalyst for overall water splitting under visible light irradiation. Chem Commun 3:357–358. https://doi.org/10.1039/A707440I
47. Zhao Y, Wang W, Li Y, Zhang Y, Yan Z, Huo Z (2014) Hierarchical branched Cu_2O nanowires with enhanced photocatalytic activity and stability for H_2 production. Nanoscale 6(1):195–198. https://doi.org/10.1039/C3NR04280D

48. Chang K, Li M, Wang T, Ouyang S, Li P, Liu L, Ye J (2015) Drastic layer-number-dependent activity enhancement in photocatalytic H_2 evolution over $nMoS_2/CdS$ ($n \geq 1$) under visible light. Adv Energy Mater 5(10):1402279. https://doi.org/10.1002/aenm.201402279
49. Hai X, Zhou W, Wang S, Pang H, Chang K, Ichihara F, Ye J (2017) Rational design of freestanding MoS_2 monolayers for hydrogen evolution reaction. Nano Energy 39:409–417. https://doi.org/10.1016/j.nanoen.2017.07.021
50. Zhao G, Sun Y, Zhou W, Wang X, Chang K, Liu G, Liu H, Kako T, Ye J (2017) Superior photocatalytic H_2 production with cocatalytic Co/Ni species anchored on sulfide semiconductor. Adv Mater 29(40):1703258. https://doi.org/10.1002/adma.201703258
51. Zhao G, Zhou W, Sun Y, Wang X, Liu H, Meng X, Chang K, Ye J (2018) Efficient photocatalytic CO_2 reduction over Co(II) species modified CdS in aqueous solution. Appl Catal B: Environ 226:252–257. https://doi.org/10.1016/j.apcatb.2017.12.054
52. Jin J, Yu J, Guo D, Cui C, Ho W (2015) A hierarchical Z-scheme CdS–WO_3 photocatalyst with enhanced CO_2 reduction activity. Small 11(39):5262–5271. https://doi.org/10.1002/smll.201500926
53. Khan MMT, Bhardwaj RC, Bhardwaj C (1988) Catalytic fixation of nitrogen by the photocatalytic CdS/Pt/RuO_2 particulate system in the presence of aqueous $[Ru(Hedta)N_2]^{\ominus}$ complex. Angew Chem Int Ed Engl 27(7):923–925. https://doi.org/10.1002/anie.198809231
54. Brown KA, Harris DF, Wilker MB, Rasmussen A, Khadka N, Hamby H, Keable S, Dukovic G, Peters JW, Seefeldt LC, King PW (2016) Light-driven dinitrogen reduction catalyzed by a CdS: nitrogenase MoFe protein biohybrid. Science 352(6284):448–450. https://doi.org/10.1126/science.aaf2091
55. Zhang J, Yu J, Zhang Y, Li Q, Gong JR (2011) Visible light photocatalytic H_2-production activity of CuS/ZnS porous nanosheets based on photoinduced interfacial charge transfer. Nano Lett 11(11):4774–4779. https://doi.org/10.1021/nl202587b
56. Tsuji I, Kudo A (2003) H_2 evolution from aqueous sulfite solutions under visible-light irradiation over Pb and halogen-codoped ZnS photocatalysts. J Photochem Photobiol A 156(1):249–252. https://doi.org/10.1016/S1010-6030(02)00433-1
57. Meng X, Yu Q, Liu G, Shi L, Zhao G, Liu H, Li P, Chang K, Kako T, Ye J (2017) Efficient photocatalytic CO_2 reduction in all-inorganic aqueous environment: cooperation between reaction medium and Cd(II) modified colloidal ZnS. Nano Energy 34:524–532. https://doi.org/10.1016/j.nanoen.2017.03.021
58. Meng X, Zuo G, Zong P, Pang H, Ren J, Zeng X, Liu S, Shen Y, Zhou W, Ye J (2018) A rapidly room-temperature-synthesized Cd/ZnS: Cu nanocrystal photocatalyst for highly efficient solar-light-powered C_O2 reduction. Appl Catal B: Environ 237:68–73. https://doi.org/10.1016/j.apcatb.2018.05.066
59. Pang H, Meng X, Song H, Zhou W, Yang G, Zhang H, Izumi Y, Takei T, Jewasuwan W, Fukata N, Ye J (2019) Probing the role of nickel dopant in aqueous colloidal ZnS nanocrystals for efficient solar-driven CO_2 reduction. Appl Catal B: Environ 244:1013–1020. https://doi.org/10.1016/j.apcatb.2018.12.010
60. Liao L, Zhang Q, Su Z, Zhao Z, Wang Y, Li Y, Lu X, Wei D, Feng G, Yu Q, Cai X, Zhao J, Ren Z, Fang H, Robles-Hernandez F, Baldelli S, Bao J (2014) Efficient solar water-splitting using a nanocrystalline CoO photocatalyst. Nat Nanotechnol 9:69–73. https://doi.org/10.1038/nnano.2013.272
61. Liu Z, Ma C, Cai Q, Hong T, Guo K, Yan L (2017) Promising cobalt oxide and cobalt oxide/silver photocathodes for photoelectrochemical water splitting. Sol Energy Mater Sol Cells 161:46–51. https://doi.org/10.1016/j.solmat.2016.11.026
62. Liu G, Wang T, Zhang H, Meng X, Hao D, Chang K, Li P, Kako T, Ye J (2015) Nature-inspired environmental "Phosphorylation" boosts photocatalytic H_2 production over carbon nitride nanosheets under visible-light irradiation. Angew Chem Int Ed 54(46):13561–13565. https://doi.org/10.1002/anie.201505802

63. Liu G, Zhao G, Zhou W, Liu Y, Pang H, Zhang H, Hao D, Meng X, Li P, Kako T, Ye J (2016) In Situ bond modulation of graphitic carbon nitride to construct p–n homojunctions for enhanced photocatalytic hydrogen production. Adv Funct Mater 26(37):6822–6829. https://doi.org/10.1002/adfm.201602779
64. Liu W, Cao L, Cheng W, Cao Y, Liu X, Zhang W, Mou X, Jin L, Zheng X, Che W, Liu Q, Yao T, Wei S (2017) Single-site active cobalt-based photocatalyst with a long carrier lifetime for spontaneous overall water splitting. Angew Chem Int Ed 56(32):9312–9317. https://doi.org/10.1002/anie.201704358
65. Liu J, Liu Y, Liu N, Han Y, Zhang X, Huang H, Lifshitz Y, Lee S-T, Zhong J, Kang Z (2015) Metal-free efficient photocatalyst for stable visible water splitting via a two-electron pathway. Science 347(6225):970–974. https://doi.org/10.1126/science.aaa3145
66. Xu G, Zhang H, Wei J, Zhang H-X, Wu X, Li Y, Li C, Zhang J, Ye J (2018) Integrating the g-C_3N_4 nanosheet with B-H bonding decorated metal-organic framework for CO_2 activation and photoreduction. ACS Nano 12(6):5333–5340. https://doi.org/10.1021/acsnano.8b00110
67. Fang Y, Wang X (2018) Photocatalytic CO_2 conversion by polymeric carbon nitrides. Chem Commun 54(45):5674–5687. https://doi.org/10.1039/C8CC02046A
68. Ohno T, Murakami N, Koyanagi T, Yang Y (2014) Photocatalytic reduction of CO_2 over a hybrid photocatalyst composed of WO_3 and graphitic carbon nitride (g-C_3N_4) under visible light. J CO_2 Util 6:17–25. https://doi.org/10.1016/j.jcou.2014.02.002
69. Dong G, Ho W, Wang C (2015) Selective Photocatalytic N_2 fixation dependent on g-C_3N_4 Induced by nitrogen vacancies. J Mater Chem A 3(46):23435–23441. https://doi.org/10.1039/C5TA06540B
70. Zhu M, Kim S, Mao L, Fujitsuka M, Zhang J, Wang X, Majima T (2017) Metal-free photocatalyst for H_2 evolution in visible to near-infrared region: black phosphorus/graphitic carbon nitride. J Am Chem Soc 139(37):13234–13242. https://doi.org/10.1021/jacs.7b08416
71. Li H, Li J, Ai Z, Jia F, Zhang L (2018) Oxygen vacancy-mediated photocatalysis of BiOCl: reactivity, selectivity, and perspectives. Angew Chem Int Ed 57(1):122–138. https://doi.org/10.1002/anie.201705628
72. Li H, Shang J, Shi J, Zhao K, Zhang L (2016) Facet-dependent solar ammonia synthesis of BiOCl nanosheets via a proton-assisted electron transfer pathway. Nanoscale 8(4):1986–1993. https://doi.org/10.1039/C5NR07380D
73. Li H, Shang J, Ai Z, Zhang L (2015) Efficient visible light nitrogen fixation with BiOBr nanosheets of oxygen vacancies on the exposed 001 facets. J Am Chem Soc 137(19):6393–6399. https://doi.org/10.1021/jacs.5b03105
74. Wang S, Hai X, Ding X, Chang K, Xiang Y, Meng X, Yang Z, Chen H, Ye J (2017) Light-switchable oxygen vacancies in ultrafine Bi_5O_7Br nanotubes for boosting solar-driven nitrogen fixation in pure water. Adv Mater 29(31):1701774. https://doi.org/10.1002/adma.201701774
75. Kudo A, Miseki Y (2009) Heterogeneous photocatalyst materials for water splitting. Chem Soc Rev 38(1):253–278. https://doi.org/10.1039/B800489G
76. Takanabe K (2017) Photocatalytic water splitting: quantitative approaches toward photocatalyst by design. ACS Catal 7(11):8006–8022. https://doi.org/10.1021/acscatal.7b02662
77. Zhang L, Jaroniec M (2018) Toward designing semiconductor-semiconductor heterojunctions for photocatalytic applications. Appl Surf Sci 430:2–17. https://doi.org/10.1016/j.apsusc.2017.07.192
78. Yang J, Wang D, Han H, Li C (2013) Roles of cocatalysts in photocatalysis and photoelectrocatalysis. Acc Chem Res 46(8):1900–1909. https://doi.org/10.1021/ar300227e
79. Indrakanti VP, Kubicki JD, Schobert HH (2009) Photoinduced activation of CO_2 on Ti-based heterogeneous catalysts: current state, chemical physics-based insights and outlook. Energy Environ Sci 2(7):745–758. https://doi.org/10.1039/B822176F

80. Liu L, Zhao C, Li Y (2012) Spontaneous dissociation of CO_2 to CO on defective surface of Cu(I)/TiO_{2-x} nanoparticles at room temperature. J Phys Chem C 116(14):7904–7912. https://doi.org/10.1021/jp300932b
81. Rossmeisl J, Bessler WG (2008) Trends in catalytic activity for SOFC anode materials. Solid State Ionics 178(31):1694–1700. https://doi.org/10.1016/j.ssi.2007.10.016
82. Laursen AB, Varela AS, Dionigi F, Fanchiu H, Miller C, Trinhammer OL, Rossmeisl J, Dahl S (2012) Electrochemical hydrogen evolution: Sabatier's principle and the volcano plot. J Chem Educ 89(12):1595–1599. https://doi.org/10.1021/ed200818t
83. Pang H, Masuda T, Ye J (2018) Semiconductor-based photoelectrochemical conversion of carbon dioxide: stepping towards artificial photosynthesis. Chem Asian J 13(2):127–142. https://doi.org/10.1002/asia.201701596
84. Medford AJ, Vojvodic A, Hummelshøj JS, Voss J, Abild-Pedersen F, Studt F, Bligaard T, Nilsson A, Nørskov JK (2015) From the Sabatier principle to a predictive theory of transition-metal heterogeneous catalysis. J Catal 328:36–42. https://doi.org/10.1016/j.jcat.2014.12.033
85. Wang S, Ichihara F, Pang H, Chen H, Ye J (2018) Nitrogen fixation reaction derived from nanostructured catalytic materials. Adv Funct Mater 28(50):1803309. https://doi.org/10.1002/adfm.201803309
86. Hai X, Chang K, Pang H, Li M, Li P, Liu H, Shi L, Ye J (2016) Engineering the edges of MoS_2 (WS_2) crystals for direct exfoliation into monolayers in polar micromolecular solvents. J Am Chem Soc 138(45):14962–14969. https://doi.org/10.1021/jacs.6b08096
87. Wang P, Zhan S, Wang H, Xia Y, Hou Q, Zhou Q, Li Y, Kumar RR (2018) Cobalt phosphide nanowires as efficient Co-catalyst for photocatalytic hydrogen evolution over $Zn_{0.5}Cd_{0.5}S$. Appl Catal B: Environ 230:210–219. https://doi.org/10.1016/j.apcatb.2018.02.043
88. Chang K, Hai X, Pang H, Zhang H, Shi L, Liu G, Liu H, Zhao G, Li M, Ye J (2016) Targeted synthesis of 2H- and 1T-phase MoS_2 monolayers for catalytic hydrogen evolution. Adv Mater 28(45):10033–10041. https://doi.org/10.1002/adma.201603765
89. Fu J, Bie C, Cheng B, Jiang C, Yu J (2018) Hollow CoS_x polyhedrons act as high-efficiency cocatalyst for enhancing the photocatalytic hydrogen generation of g-C_3N_4. ACS Sustainable Chem Eng 6(2):2767–2779. https://doi.org/10.1021/acssuschemeng.7b04461
90. Attia Y, Samer M (2017) Metal clusters: new era of hydrogen production. Renew Sustain Energy Rev 79:878–892. https://doi.org/10.1016/j.rser.2017.05.113
91. Zhen W, Gao H, Tian B, Ma J, Lu G (2016) Fabrication of low adsorption energy Ni–Mo cluster cocatalyst in metal-organic frameworks for visible photocatalytic hydrogen evolution. ACS Appl Mater Interfaces 8(17):10808–10819. https://doi.org/10.1021/acsami.5b12524
92. Yamamoto M, Yoshida T, Yamamoto N, Nomoto T, Yamamoto Y, Yagi S, Yoshida H (2015) Photocatalytic reduction of CO_2 with water promoted By Ag clusters in Ag/Ga_2O_3 photocatalysts. J Mater Chem A 3(32):16810–16816. https://doi.org/10.1039/C5TA04815J
93. Cao Y, Chen S, Luo Q, Yan H, Lin Y, Liu W, Cao L, Lu J, Yang J, Yao T, Wei S (2017) Atomic-level insight into optimizing the hydrogen evolution pathway over a Co_1-N_4 single-site photocatalyst. Angew Chem Int Ed 56(40):12191–12196. https://doi.org/10.1002/anie.201706467
94. Zhao G, Liu H, Ye J (2018) Constructing and controlling of highly dispersed metallic sites for catalysis. Nano Today 19:108–125. https://doi.org/10.1016/j.nantod.2018.02.013
95. Zhang H, Wei J, Dong J, Liu G, Shi L, An P, Zhao G, Kong J, Wang X, Meng X, Zhang J, Ye J (2016) Efficient visible-light-driven carbon dioxide reduction by a single-atom implanted metal-organic framework. Angew Chem Int Ed 55(46):14310–14314. https://doi.org/10.1002/anie.201608597
96. Pinaud BA, Benck JD, Seitz LC, Forman AJ, Chen Z, Deutsch TG, James BD, Baum KN, Baum GN, Ardo S, Wang H, Miller E, Jaramillo TF (2013) Technical and economic feasibility of centralized facilities for solar hydrogen production via photocatalysis and photoelectrochemistry. Energy Environ Sci 6(7):1983–2002. https://doi.org/10.1039/C3EE40831K

97. Ryu A (2011) Development of a new system for photocatalytic water splitting into H_2 and O_2 under visible light irradiation. Bull Chem Soc Jpn 84(10):1000–1030. https://doi.org/10.1246/bcsj.20110132
98. Yoshida M, Takanabe K, Maeda K, Ishikawa A, Kubota J, Sakata Y, Ikezawa Y, Domen K (2009) Role and function of noble-metal/Cr-layer core/shell structure cocatalysts for photocatalytic overall water splitting studied by model electrodes. J Phys Chem C 113(23):10151–10157. https://doi.org/10.1021/jp901418u
99. Maeda K, Teramura K, Lu D, Saito N, Inoue Y, Domen K (2007) Roles of Rh/Cr_2O_3 (Core/Shell) nanoparticles photodeposited on visible-light-responsive $(Ga_{1-x}Zn_x)(N_{1-x}O_x)$ solid solutions in photocatalytic overall water splitting. J Phys Chem C 111(20):7554–7560. https://doi.org/10.1021/jp071056j
100. Maeda K, Domen K (2010) Photocatalytic water splitting: recent progress and future challenges. J Phys Chem Lett 1(18):2655–2661. https://doi.org/10.1021/jz1007966
101. Kato H, Kudo A (2003) Photocatalytic water splitting into H_2 and O_2 over various tantalate photocatalysts. Catal Today 78(1):561–569. https://doi.org/10.1016/S0920-5861(02)00355-3
102. Pan C, Takata T, Domen K (2016) Overall water splitting on the transition-metal oxynitride photocatalyst $LaMg_{1/3}Ta_{2/3}O_2N$ over a large portion of the visible-light spectrum. Chem Eur J 22(5):1854–1862. https://doi.org/10.1002/chem.201504376
103. Kobayashi R, Takashima T, Tanigawa S, Takeuchi S, Ohtani B, Irie H (2016) A heterojunction photocatalyst composed of zinc rhodium oxide, single crystal-derived bismuth vanadium oxide, and silver for overall pure-water splitting under visible light up to 740 nm. PCCP 18(40):27754–27760. https://doi.org/10.1039/C6CP02903E
104. Wang Q, Hisatomi T, Ma SSK, Li Y, Domen K (2014) Core/shell structured La- and Rh-codoped $SrTiO_3$ as a hydrogen evolution photocatalyst in Z-scheme overall water splitting under visible light irradiation. Chem Mater 26(14):4144–4150. https://doi.org/10.1021/cm5011983
105. Iwase A, Ng YH, Ishiguro Y, Kudo A, Amal R (2011) Reduced graphene oxide as a solid-state electron mediator in Z-scheme photocatalytic water splitting under visible light. J Am Chem Soc 133(29):11054–11057. https://doi.org/10.1021/ja203296z
106. Chen S, Qi Y, Hisatomi T, Ding Q, Asai T, Li Z, Ma SSK, Zhang F, Domen K, Li C (2015) Efficient visible-light-driven Z-scheme overall water splitting using a $MgTa_2O_{6-x}N_y$/TaON heterostructure photocatalyst for H_2 evolution. Angew Chem Int Ed 54(29):8498–8501. https://doi.org/10.1002/anie.201502686
107. Zong X, Wu G, Yan H, Ma G, Shi J, Wen F, Wang L, Li C (2010) Photocatalytic H_2 evolution on MoS_2/CdS catalysts under visible light irradiation. J Phys Chem C 114(4):1963–1968. https://doi.org/10.1021/jp904350e
108. Mikkelsen M, Jørgensen M, Krebs FC (2010) The teraton challenge. A review of fixation and transformation of carbon dioxide. Energy Environ Sci 3(1):43–81. https://doi.org/10.1039/B912904A
109. Ran J, Jaroniec M, Qiao S-Z (2018) Cocatalysts in semiconductor-based photocatalytic CO_2 reduction: achievements, challenges, and opportunities. Adv Mater 30(7):1704649. https://doi.org/10.1002/adma.201704649
110. Álvarez A, Borges M, Corral-Pérez JJ, Olcina JG, Hu L, Cornu D, Huang R, Stoian D, Urakawa A (2017) CO_2 activation over catalytic surfaces. ChemPhysChem 18(22):3135–3141. https://doi.org/10.1002/cphc.201700782
111. Olah GA, Prakash GKS, Goeppert A (2011) Anthropogenic chemical carbon cycle for a sustainable future. J Am Chem Soc 133(33):12881–12898. https://doi.org/10.1021/ja202642y
112. Chang X, Wang T, Gong J (2016) CO_2 photo-reduction: insights into CO_2 activation and reaction on surfaces of photocatalysts. Energy Environ Sci 9(7):2177–2196. https://doi.org/10.1039/C6EE00383D

113. Guo L-J, Wang Y-J, He T (2016) Photocatalytic reduction of CO_2 over heterostructure semiconductors into value-added chemicals. Chem Rec 16(4):1918–1933. https://doi.org/10.1002/tcr.201600008
114. Habisreutinger SN, Schmidt-Mende L, Stolarczyk JK (2013) Photocatalytic reduction of CO_2 on TiO_2 and other semiconductors. Angew Chem Int Ed 52(29):7372–7408. https://doi.org/10.1002/anie.201207199
115. Jia J, Qian C, Dong Y, Li YF, Wang H, Ghoussoub M, Butler KT, Walsh A, Ozin GA (2017) Heterogeneous catalytic hydrogenation of CO_2 by metal oxides: defect engineering—perfecting imperfection. Chem Soc Rev 46(15):4631–4644. https://doi.org/10.1039/C7CS00026J
116. Michalkiewicz B, Majewska J, Kądziołka G, Bubacz K, Mozia S, Morawski AW (2014) Reduction of CO_2 by adsorption and reaction on surface of TiO_2-nitrogen modified photocatalyst. J CO_2 Util 5:47–52. https://doi.org/10.1016/j.jcou.2013.12.004
117. Mao J, Peng T, Zhang X, Li K, Ye L, Zan L (2013) Effect of graphitic carbon nitride microstructures on the activity and selectivity of photocatalytic CO_2 reduction under visible light. Catal Sci Technol 3(5):1253–1260. https://doi.org/10.1039/C3CY20822B
118. Liu Q, Wu D, Zhou Y, Su H, Wang R, Zhang C, Yan S, Xiao M, Zou Z (2014) Single-crystalline, Ultrathin $ZnGa_2O_4$ nanosheet scaffolds to promote photocatalytic activity in CO_2 reduction into methane. ACS Appl Mater Interfaces 6(4):2356–2361. https://doi.org/10.1021/am404572g
119. Wang C, Xie Z, deKrafft KE, Lin W (2011) Doping metal-organic frameworks for water oxidation, carbon dioxide reduction, and organic photocatalysis. J Am Chem Soc 133(34):13445–13454. https://doi.org/10.1021/ja203564w
120. Liao Y, Cao S-W, Yuan Y, Gu Q, Zhang Z, Xue C (2014) Efficient CO_2 capture and photoreduction by amine-functionalized TiO_2. Chem Eur J 20(33):10220–10222. https://doi.org/10.1002/chem.201403321
121. Meng X, Ouyang S, Kako T, Li P, Yu Q, Wang T, Ye J (2014) Photocatalytic CO_2 conversion over alkali modified TiO_2 without loading noble metal cocatalyst. Chem Commun 50(78):11517–11519. https://doi.org/10.1039/C4CC04848B
122. Xie S, Wang Y, Zhang Q, Deng W, Wang Y (2014) MgO- and Pt-promoted TiO_2 as an efficient photocatalyst for the preferential reduction of carbon dioxide in the presence of water. ACS Catal 4(10):3644–3653. https://doi.org/10.1021/cs500648p
123. Liu H, Meng X, Dao TD, Zhang H, Li P, Chang K, Wang T, Li M, Nagao T, Ye J (2015) Conversion of carbon dioxide by methane reforming under visible-light irradiation: surface-plasmon-mediated nonpolar molecule activation. Angew Chem Int Ed 54(39):11545–11549. https://doi.org/10.1002/anie.201504933
124. Liu H, Li M, Dao TD, Liu Y, Zhou W, Liu L, Meng X, Nagao T, Ye J (2016) Design of PdAu alloy plasmonic nanoparticles for improved catalytic performance in CO_2 reduction with visible light irradiation. Nano Energy 26:398–404. https://doi.org/10.1016/j.nanoen.2016.05.045
125. Yu S, Wilson AJ, Heo J, Jain PK (2018) Plasmonic control of multi-electron transfer and C-C coupling in visible-light-driven CO_2 reduction on Au nanoparticles. Nano Lett 18(4):2189–2194. https://doi.org/10.1021/acs.nanolett.7b05410
126. Collado L, Reynal A, Coronado JM, Serrano DP, Durrant JR, de la Peña O'Shea VA (2015) Effect of Au surface plasmon nanoparticles on the selective CO_2 photoreduction to CH_4. Appl Catal B: Environ 178:177–185. https://doi.org/10.1016/j.apcatb.2014.09.032
127. Song H, Meng X, Dao TD, Zhou W, Liu H, Shi L, Zhang H, Nagao T, Kako T, Ye J (2018) Light-enhanced carbon dioxide activation and conversion by effective plasmonic coupling effect of Pt and Au nanoparticles. ACS Appl Mater Interfaces 10(1):408–416. https://doi.org/10.1021/acsami.7b13043
128. Linic S, Christopher P, Ingram DB (2011) Plasmonic-metal nanostructures for efficient conversion of solar to chemical energy. Nat Mater 10:911–921. https://doi.org/10.1038/nmat3151

129. Meng X, Liu L, Ouyang S, Xu H, Wang D, Zhao N, Ye J (2016) Nanometals for solar-to-chemical energy conversion: from semiconductor-based photocatalysis to plasmon-mediated photocatalysis and photo-thermocatalysis. Adv Mater 28(32):6781–6803. https://doi.org/10.1002/adma.201600305
130. Liu G, Meng X, Zhang H, Zhao G, Pang H, Wang T, Li P, Kako T, Ye J (2017) Elemental boron for efficient carbon dioxide reduction under light irradiation. Angew Chem Int Ed 56(20):5570–5574. https://doi.org/10.1002/anie.201701370
131. Lais A, Gondal MA, Dastageer MA, Al-Adel FF (2018) Experimental parameters affecting the photocatalytic reduction performance of CO_2 to methanol: a review. Int J Energy Res 42(6):2031–2049. https://doi.org/10.1002/er.3965
132. White JL, Baruch MF, Pander JE, Hu Y, Fortmeyer IC, Park JE, Zhang T, Liao K, Gu J, Yan Y, Shaw TW, Abelev E, Bocarsly AB (2015) Light-driven heterogeneous reduction of carbon dioxide: photocatalysts and photoelectrodes. Chem Rev 115(23):12888–12935. https://doi.org/10.1021/acs.chemrev.5b00370
133. Medford AJ, Hatzell MC (2017) Photon-driven nitrogen fixation: current progress, thermodynamic considerations, and future outlook. ACS Catal 7(4):2624–2643. https://doi.org/10.1021/acscatal.7b00439
134. Jia H-P, Quadrelli EA (2014) Mechanistic aspects of dinitrogen cleavage and hydrogenation to produce ammonia in catalysis and organometallic chemistry: relevance of metal hydride bonds and dihydrogen. Chem Soc Rev 43(2):547–564. https://doi.org/10.1039/C3CS60206K
135. Légaré M-A, Bélanger-Chabot G, Dewhurst RD, Welz E, Krummenacher I, Engels B, Braunschweig H (2018) Nitrogen fixation and reduction at boron. Science 359(6378):896–900. https://doi.org/10.1126/science.aaq1684
136. Chen X, Li N, Kong Z, Ong W-J, Zhao X (2018) Photocatalytic fixation of nitrogen to ammonia: state-of-the-art advancements and future prospects. Mater Horizons 5(1):9–27. https://doi.org/10.1039/C7MH00557A
137. Li J, Li H, Zhan G, Zhang L (2017) Solar water splitting and nitrogen fixation with layered bismuth oxyhalides. Acc Chem Res 50(1):112–121. https://doi.org/10.1021/acs.accounts.6b00523
138. Dhar NR, Pant NN (1944) Nitrogen loss from soils and oxide surfaces. Nature 153:115–116. https://doi.org/10.1038/153115a0
139. Schrauzer GN, Strampach N, Hui LN, Palmer MR, Salehi J (1983) Nitrogen photoreduction on desert sands under sterile conditions. Proc Natl Acad Sci U.S.A. 80(12):3873–3876. https://doi.org/10.1073/pnas.80.12.3873
140. Lindley BM, Appel AM, Krogh-Jespersen K, Mayer JM, Miller AJM (2016) Evaluating the thermodynamics of electrocatalytic N_2 reduction in acetonitrile. ACS Energy Lett 1(4):698–704. https://doi.org/10.1021/acsenergylett.6b00319
141. van der Ham CJM, Koper MTM, Hetterscheid DGH (2014) Challenges in reduction of dinitrogen by proton and electron transfer. Chem Soc Rev 43(15):5183–5191. https://doi.org/10.1039/C4CS00085D
142. Jacobsen CJH, Dahl S, Clausen BS, Bahn S, Logadottir A, Nørskov JK (2001) Catalyst design by interpolation in the periodic table: bimetallic ammonia synthesis catalysts. J Am Chem Soc 123(34):8404–8405. https://doi.org/10.1021/ja010963d
143. Zhu D, Zhang L, Ruther RE, Hamers RJ (2013) Photo-illuminated diamond as a solid-state source of solvated electrons in water for nitrogen reduction. Nat Mater 12:836–841. https://doi.org/10.1038/nmat3696
144. Bell AT (2003) The impact of nanoscience on heterogeneous catalysis. Science 299(5613):1688–1691. https://doi.org/10.1126/science.1083671
145. Matanović I, Garzon FH, Henson NJ (2014) Electro-reduction of nitrogen on molybdenum nitride: structure, energetics, and vibrational spectra from DFT. PCCP 16(7):3014–3026. https://doi.org/10.1039/C3CP54559H

146. Zhao Y, Zhao Y, Waterhouse GIN, Zheng L, Cao X, Teng F, Wu L-Z, Tung C-H, O'Hare D, Zhang T (2017) Layered-double-hydroxide nanosheets as efficient visible-light-driven photocatalysts for dinitrogen fixation. Adv Mater 29(42):1703828. https://doi.org/10.1002/adma.201703828
147. Skúlason E, Bligaard T, Gudmundsdóttir S, Studt F, Rossmeisl J, Abild-Pedersen F, Vegge T, Jónsson H, Nørskov JK (2012) A theoretical evaluation of possible transition metal electrocatalysts for N_2 reduction. PCCP 14(3):1235–1245. https://doi.org/10.1039/C1CP22271F
148. Abghoui Y, Garden AL, Hlynsson VF, Björgvinsdóttir S, Ólafsdóttir H, Skúlason E (2015) Enabling electrochemical reduction of nitrogen to ammonia at ambient conditions through rational catalyst design. PCCP 17(7):4909–4918. https://doi.org/10.1039/C4CP04838E
149. Li H, Shi J, Zhao K, Zhang L (2014) Sustainable molecular oxygen activation with oxygen vacancies on the 001 facets of BiOCl nanosheets under solar light. Nanoscale 6(23):14168–14173. https://doi.org/10.1039/C4NR04810E
150. Ali M, Zhou F, Chen K, Kotzur C, Xiao C, Bourgeois L, Zhang X, MacFarlane DR (2016) Nanostructured photoelectrochemical solar cell for nitrogen reduction using plasmon-enhanced black silicon. Nat Commun 7:11335. https://doi.org/10.1038/ncomms11335

Smart Polymers for Biomedical Applications

Mitsuhiro Ebara

1 Introduction of Biomaterials

Looking back at the last 50 years of biomaterials research, in earlier stages, the research was generally characterized by trial and error. However, with vigorous and steady research, our understanding of the biological events at the interface between materials and the human body has accelerated, leading to the development of immune-inert, immune-active, and immune-tolerant materials and devices. The word "biomaterials" was not used 50 years ago, but they are now widely used in medicine, dentistry and biotechnology. Interestingly, the introduction of tolerated foreign-material implants into the human body was noted far back in prehistory about 9000 years ago [1]. The remains of a human being were found near Kennewick, Washington, USA in 1996 (referred to as "Kennewick Man"), and a spear tip was found embedded in his hip. The wound caused by this tip had apparently healed and the embedded tip did not significantly impede his activity. This unintended implant illustrates the body's capacity to deal with implanted foreign materials.

Because foreign materials can elicit immune responses, grand challenges in biomaterials are how to control the recognition by immune system in the body. Thus, gaining control of "nano-" structures and properties of materials is a matter of great interest in biomedicine and healthcare. That is, controlling the behavior of water near surfaces is a very important challenge in bio-/nanomaterials sciences because water is the first molecule to come in contact with biomaterials in any clinical applications and is an active participant in biological processes, which simply could not proceed the way they do without the unique mediating properties of water [2, 3]. Indeed, water suspends living cells and is the principal constituent of the interstitial fluid

M. Ebara (✉)
International Center for Materials Nanoarchitectonics (WPI-MANA), National Institute for Materials Science (NIMS), 1-1 Namiki, Tsukuba 305-0044, Ibaraki, Japan
e-mail: EBARA.Mitsuhiro@nims.go.jp

Y. Wakayama and K. Ariga (eds.), *System-Materials Nanoarchitectonics*,
NIMS Monographs, https://doi.org/10.1007/978-4-431-56912-1_15

that bathes tissues. How can the role of water in biology be controlled, then? In the following sections, we present answers to this question from various viewpoints.

2 Classification of Smart Polymers

There has been renewed interest in controlling nanointerfaces, as mentioned above, and a considerable number of studies have been conducted on the design of novel materials to realize their applications [4–6]. For example, some polymers have emerged as a very useful class of polymers with their own unique chemical properties and applications in various areas [7–9]. These polymers are named on the basis of their physical or chemical properties, such as "stimuli-responsive", "environment-sensitive", "smart", or "intelligent" polymers. Hereafter, we shall use the name smart polymers for such polymer systems in this chapter, because "smart" means "able to adapt to one's environment, whereas "intelligent" comes from the Latin verb intellegere, which means "to understand" [10]. Indeed, smart polymers can adapt to changes in their environment by changing their interactions with water (Fig. 1). The characteristic feature that actually makes them smart is their capability to respond to very slight changes in the surrounding environment. The uniqueness of these materials lies in not only the fast macroscopic changes occurring in their structure but

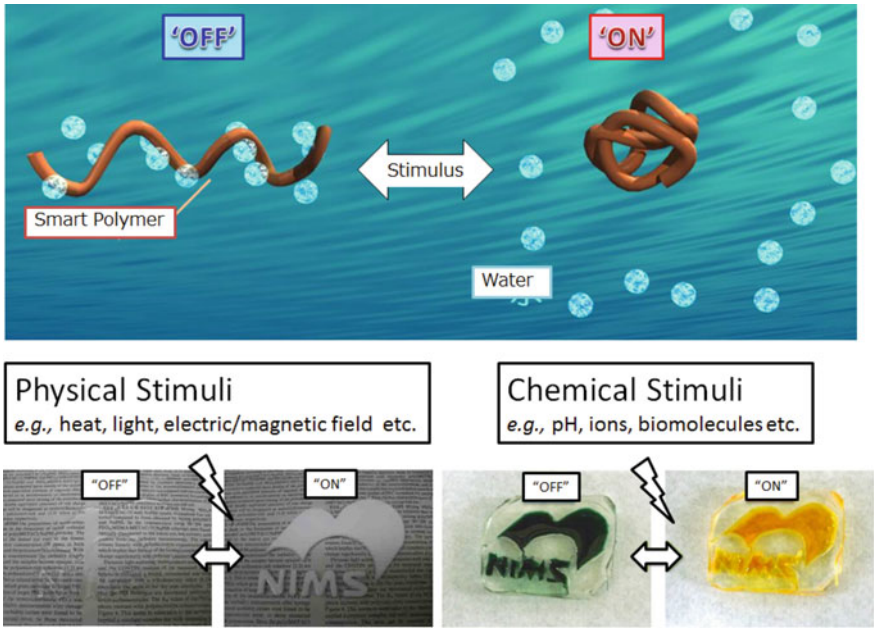

Fig. 1 Classification of stimuli-responsive polymers on the basis of stimuli (Physical stimuli; heat, light, and electric/magnetic field. Chemical stimuli; pH, ions, and biomolecules)

also the reversibility of such changes. The responses are manifested as, for example, changes in shape, surface characteristics, and/or solubility, the formation of an intricate molecular assembly, and a sol-to-gel transition [11]. The environmental trigger behind these transitions can include either a change in temperature or pH, an increase in ionic strength, or the presence of certain chemicals. More recently, changes in electric and magnetic fields, light intensity, or radiation forces have also been reported as stimuli for these polymers.

There are many polymers that exhibit thermally induced precipitation, and the polymer that has been studied most extensively is poly(*N*-isopropylacrylamide) (PNIPAAm) [12, 13]. This polymer is soluble in water below 32 °C, and it precipitates rapidly when the temperature is raised above 32 °C. The temperature at which a polymer precipitates is called the lower critical solution temperature (LCST). A critical insight into the precipitation mechanism was gained by Hoffman's group with their seminal work on PNIPAAm [14–16]. PNIPAAm can take many forms: dissolved in aqueous solution, adsorbed or grafted on aqueous-solid interfaces, or cross-linked in the form of hydrogels. Grafting of PNIPAAm onto solid surfaces makes the surfaces smart, where the surface energy can be controlled via the temperature [17–19]. PNIPAAm can also be functionalized by chemical conjugation to biomolecules such as a targeting ligand to yield a large and diverse family of polymer–biomolecule hybrid systems that can respond to biological as well as physical and chemical stimuli [20, 21]. Although these grafting and conjugation processes can produce smart surfaces or smart conjugations, derivatization of PNIPAAm side chains or end groups to form reactive groups have resulted in the disappearance of "smartness" from PNIPAAm. For example, if the NIPAAm monomer is copolymerized with a reactive monomer such as acrylic acid, the LCST increases and the NIPAAm monomer may even disappear [16, 22]. On basis of the hypothesis that appropriate proportions of hydrophobicity and hydrophilicity in the molecular structure of PNIPAAm are required for a sharp phase transition to occur, we have newly designed a series of monomers that have a parallel structure to the NIPAAm monomer to induce water molecules into behaving like those around PNIPAAm chains even though they have very hydrophilic reactive groups. For example, the hydrophilic reactive carboxyl, amino, and hydroxyl groups form carboxy-NIPAAm (CIPAAm) [22–24], amino-NIPAAm (AIPAAm) [25], and hydroxyl-NIPAAm (HIPAAm) [26], respectively (Fig. 2). The use of these monomers for copolymerization with NIPAAm can synergistically combine the individual properties of two or more components to yield new and desirable properties. One could say that these polymers are "double- or multismart".

3 Smart Hydrogels

Hydrogels are three-dimensional (3D) materials with the capability to absorb large amounts of water while maintaining their dimensional stability. Hydrogels with

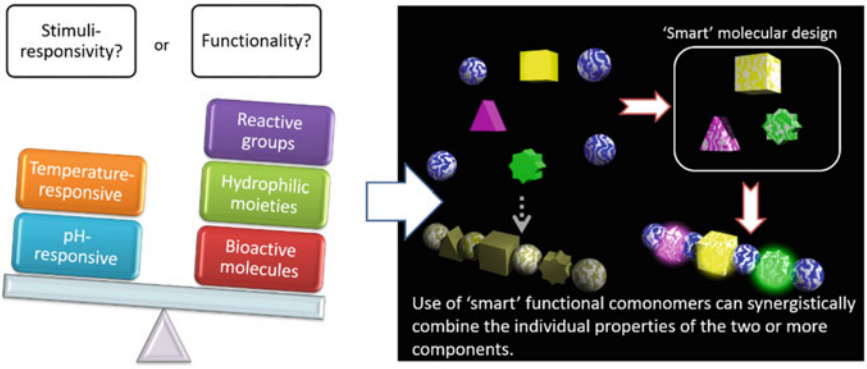

Fig. 2 Smart molecular design makes it possible to produce a series of comonomers which have a parallel structure with NIPAAm monomer to deceive water molecules into behaving like those around PNIPAAm chains even though they have hydrophilic groups such as carboxyl, amino and hydroxyl group. Use of these NIPAAm-like comonomers for copolymerization with NIPAAm can synergistically combine the individual properties of the two or more components to yield new and desirable properties

stimuli-responsive properties can undergo reversible volume phase transitions or gel–sol phase transitions upon minute changes in environmental conditions. These types of stimuli-responsive hydrogels are also called smart hydrogels. Smart hydrogels are promising materials for controlling drug delivery, since they change their properties in response to specific stimuli in our body. Temperature-responsive hydrogels have been studied most extensively to obtain an 'on–off' drug release profile in response to a stepwise temperature change [27–29]. Many researchers have also investigated the use of pH as a stimulus because pH-sensitive systems could facilitate drug delivery to regions of local acidosis, including sites of infection, neoplasia, or ischemia [30–32]. The incorporation of carboxylic acid-derived monomers has been carried out to impart pH sensitivity in a variety of copolymers. We demonstrated a timed explosive drug release from smart pH-responsive hydrogels by utilizing a photo-triggered spatial pH-jump reaction [33]. A photoinitiated proton-releasing reaction of *o*-nitrobenzaldehyde (*o*-NBA) was integrated into P(NIPAAm-*co*-CIPAAm) hydrogels. The *o*-NBA-incorporated hydrogels demonstrated the rapid release of protons upon UV irradiation, allowing the pH inside the gel to decrease to below the pKa value of P(NIPAAm-*co*-CIPAAm). After irradiation, the enhanced release of entrapped L-3,4-dihydroxyphenylalanine (DOPA) from the gels was observed, which was driven by the dissociation of DOPA from CIPAAm (Fig. 3). The proposed pH-jump system may be beneficial for the design of predictive and programmable devices for drug delivery because conventional systems can activate only the illuminated region, and their response is discontinuous when the light is turned off.

Another example of on–off drug release control is achieved by using sugar-responsive gels for the possible treatment of diabetes mellitus. Pancreatic islets release insulin to lower the blood glucose level and regulate the glucose level within

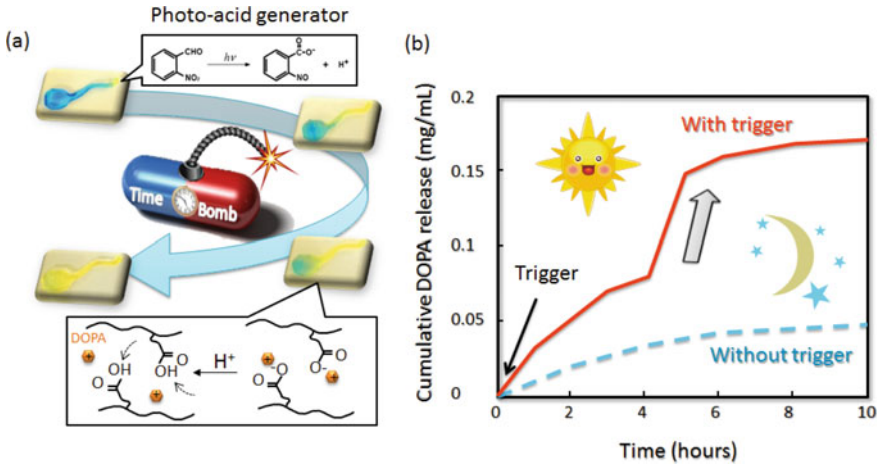

Fig. 3 **a** Schematic of timed explosive drug release from pH-responsive hydrogels utilizing a phototriggered spatial pH-jump reaction. **b** Drug release profiles of DOPA from gels with and without UV irradiation

the range from 70 to 110 mg/dl by an autofeedback mechanism under healthy physiological conditions. It is necessary to externally administer exogenous insulin to diabetic patients (type I IDDM) who cannot control their blood glucose level. However, an overdose of exogenous insulin may result in hypoglycemia and coma, which is a life-threatening state for these patients. Therefore, insulin must be carefully administered to avoid hypoglycemia in diabetic patients. Matsumoto and coworkers have developed a glucose-responsive hydrogel system using phenylboronic acid, a synthetic molecule capable of reversibly binding with 1, 2- or 1, 3-*cis*-diols including glucose [34, 35]. The release of insulin from the gel was continuously controlled by the skin layer with close correspondence to each addition of glucose. This system can be used in a self-regulated insulin delivery system to treat diabetes mellitus.

4 Smart Nanofibers

Polymeric nanofibers are an exciting new class of biomaterial and have attracted great attention because of their remarkable properties, such as high specific surface area, high porosity, high molecular alignment, or nanosize effects. The incorporation of stimuli-responsive polymers into nanofibers takes advantage of the extremely large surface area and porosity of nanofibers to generate a precision "on–off" switch to control the morphology and function of the nanofiber. We have been fabricating various temperature-responsive nanofibers using NIPAAm [36, 37]. For example, cryopreservation of mammalian cells was demonstrated without loss of viability during freezing process by using a PNIPAAm mesh because dehydrated

PNIPAAm chains suppressed the formation of large extracellular ice crystals during the freeze/thaw process [38]. A temperature-responsive fibrous hydrogel was also used as a cell capture and release membrane [39]. The fibrous hydrogel captured and released cells by self-wrapping, encapsulation, and shrinking in response to temperature changes.

We have also synthesized the nanofibers using a temperature-responsive polymer, P(NIPAAm-co–*N*-hydroxylmethylacrylamide(HMAAm)) for drug release control applications. Fluorescein isothiocyanate (FITC)-dextran was directly embedded into these nanofibers as the drug model. The prepared nanofibers showed on–off switchable swelling–shrinking behavior in response to temperature alternation cycles upon crossing the LCST; correspondingly, the dextran release profile also showed the on–off switchable behavior. After the first heating, approximately 30% of the loaded dextran was released from the nanofibers. The release stopped after cooling below the LCST, but the release restarted upon the second heating cycle. We also showed temperature- and magnetic-field-responsive electrospun nanofibers containing an anticancer drug and magnetic nanoparticles (MNPs). Upon applying an alternating magnetic field, the temperature-responsive nanofibers shrank in response to the increased temperature triggered by MNPs [40]. The incorporated drug was released from nanofibers owing to the hyperthermic effect. These nanofibers demonstrated the synergic effect of hyperthermia and chemotherapy for cancer cell therapy with the hyperthermic treatment, which can reduce the side effects on normal tissues or cells.

5 Smart Surfaces

Smart polymers also show considerable promise in designing smart switchable surface trap systems. For example, a reversible microchannel surface capture system was developed to capture/release bioanalytical beads (Fig. 4a) [41]. PNIPAAm was grafted onto polydimethylsiloxane (PDMS) surfaces by a UV-mediated graft polymerization from a photoinitiator that was preadsorbed in the channel wall. The surface traps captured PNIPAAm-grafted nanobeads uniformly above the LCST and facilitated their rapid release as the temperature was reversed to below the LCST. Lai and co-workers have developed magnetic nanoparticles for diagnostic target isolation because smaller particles display better association and binding properties to the target analytes [42, 43]. The pH-sensitive magnetic particles showed the sharply reversible change in size and magnetophoretic mobility to perform separation of particles under continuous flow processing conditions. This system had been shown to transfer more than 80% of a target protein from an input flow stream to a second flow stream in a continuous flow H-filter device.

We have developed a novel approach to observe dynamic affinity changes in RGD-integrin biding using RGD-immobilized temperature-responsive nano layer surfaces (Fig. 4b). RGD was successfully immobilized on PNIPAAm copolymer's side chains via reactive groups of comonomer, CIPAAm [44]. The nano designed

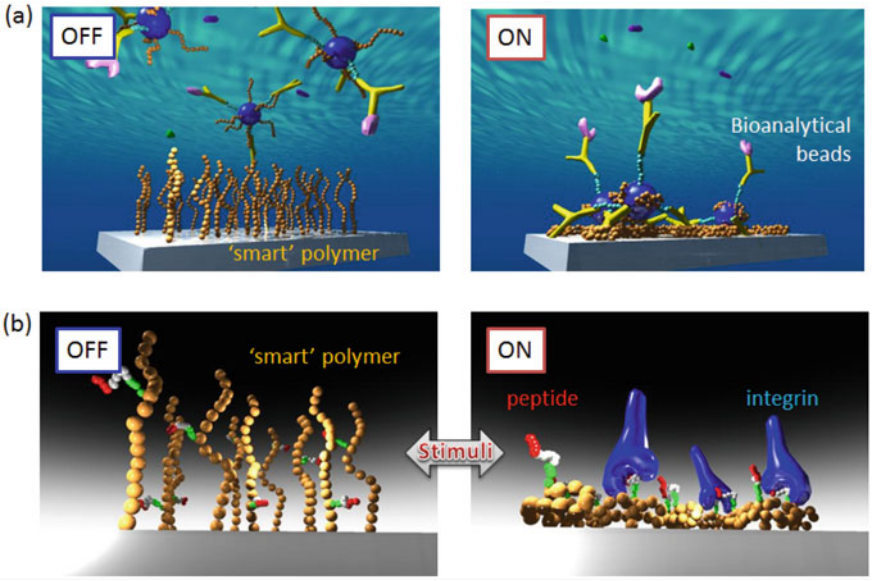

Fig. 4 **a** Smart separation and enrichment of dilute bioanalytical samples with simple 'on–off' switch control of the external stimuli. The microchannel walls are modified with the smart polymers to minimize non-specific adsorption of serum components at ambient temperature while allowing the trapping of the beads at selected positions in the channel at higher temperature. **b** Design concept for an 'on–off' affinity switch to measure integrin–peptide binding utilizing smart surfaces. At temperatures above the LCST, the grafted layer dehydrates and shrinks, thus exposing the immobilized peptides to integrins under cell culture conditions. Upon lowering the temperature, the grafted polymer is suddenly hydrated and extends outwards to shield the peptides from integrin access, resulting in decreased binding affinity between integrins and peptides, followed by cell detachment from the surface

surface can bind cells at 37 °C and spontaneously cause the detachment of cells at 20 °C. This phenomenon arises from the specific design of the grafted polymer, which protects peptides from integrin access below the LCST of PNIPAAm. The tight coupling between cells and peptides on the surfaces produces a delay in the detachment of cells from the surfaces. Indeed, the time required for cell detachment is strongly related to the cell adhesion strength according to the trend: RGD < RGDS < GRGD < GRGDS (R:Arg, G:Gly, D: Asp, S: Ser). This approach provides a quick and simple method for examining time-dependent affinity changes between cells and peptides. Also, we have successfully investigated the synergistic effect of PHSRN on integrin-mediated cell binding using the same technique [45]. The PHSRN and RGD co-immobilized NIPAAm surfaces dramatically retards cell detachment below the LCST only when the peptide sequences were specifically designed with the optimal distance between PHSRN and RGD, as observed in native fibronectin.

6 Conclusions

Although this chapter focuses solely on the roles of smart polymer-based nanotechnologies within the fields of medicine, they have an extensive range of applications. They are expected to help address many problems facing today's society. These technologies, for example, may make it possible to manufacture programmable materials that require less energy to produce less waste than conventional materials. Recent progress in polymeric synthesis has led to intriguing new "smart" polymer systems, resulting from novel approaches for synthesizing random, block, or graft copolymers as well as efficient control of molecular weight and its distributions. Furthermore, smart materials focus on many types of novel materials, including not only polymers, but also ceramics, hybrid composites, shape memory alloys, magnetorheological fluids, electrorheological materials, and nanotubes etc. These materials will enable us to develop better, faster, cheaper and more powerful "smart" technology that has the potential for improvements in health, safety, quality of life, particularly for wearable healthcare devices in the resource-limited environments such as aerospace, or low-infrastructure sites such as developing world.

References

1. Ratner BD (2004) A history of biomaterials. In: Ratner BD, Hoffman AS, Schoen FJ, Lemons JE (eds) Biomaterials Science: An Introduction to Materials in Medicine, 2nd edn, Elsevier, pp 10–19
2. Baier RE, Dutton RC (1969) Initial events in interactions of blood with a foreign surface. J Biomed Mater Res 3:191–206
3. Vogler EA (2004) Role of water in biomaterials. In: Ratner BD, Hoffman AS, Schoen FJ, Lemons JE (eds) Biomaterials Science: An Introduction to Materials in Medicine, 2nd edn, Elsevier, pp 59–65
4. Pancrazio JJ (2008) Neural interfaces at the nanoscale. Nanomed 3:823–830
5. Lafuma A, Quere D (2003) Superhydrophobic states. Nat Mater 2:457–460
6. Zheng Y, Gao X (2007) Directional adhesion of superhydrophobic butterfly wings. Soft Matter 3:178–182
7. Hoffman AS (2004) Applications of "smart polymers" as biomaterials. In: Ratner BD, Hoffman AS, Schoen FJ, Lemons JE (eds) Biomaterials science: An Introduction to Materials in Medicine, 2nd edn, Elsevier, pp 107–115
8. Jilie K, Li M (2008) Smart hydrogels. In: Galaev I, B Mattiasson B (eds) Smart Polymers: Applications in Biotechnology and Biomedicine, 2nd edn, CRC Press, pp 247–268
9. Lowe AB, McCormick CL (2001) Stimuli responsive water-soluble and amphiphilic (co)polymers. In: McCormick CL (ed) Stimuli-Responsive Water Soluble and Amphiphilic Polymers, vol 780, ACS Symposium Series, American Chemical Society, pp 1–13
10. Perloff R, Sternberg RJ, Urbina S (1996) Intelligence: knowns and unknowns. Am Psychol 51
11. Ebara M, Kikuchi A, Sakai K, Okano T (2004) Fast shrinkable materials. In: Yui N, Mrsny RJ, Park K (eds) Reflexive Polymers and Hydrogels: Understanding and Designing Fast Responsive Polymeric Systems, CRC Press, pp 219–244
12. Heskins M, Guillet JE (1968) Solution properties of poly(N-isopropylacrylamide). J Macromol Sci Pure Appl Chem 2:1441–1455
13. Smidsrod O, Guillet JE (1969) Study of polymer-solute interactions by gas chromatography. Macromolecules 2:272–277

14. Hoffman AS (1987) Applications of thermally reversible polymers and hydrogels in therapeutics and diagnostics. J Control Rel 6:297–305
15. Monji N, Hoffman AS (1987) A novel immunoassay system and bioseparation process based on thermal phase-separating polymers. Appl Biochem Biotechnol 14:107–120
16. Chen G, Hoffman AS (1995) Graft copolymers that exhibit temperature-induced phase transitions over a wide range of pH. Nature 373:49–52
17. Ebara M, Yamato M, Hirose M, Aoyagi T, Kikuchi A, Sakai K, Okano T (2003) Copolymerization of 2-carboxyisopropylacrylamide with *N*-isopropylacrylamide accelerates cell detachment from grafted surfaces by reducing temperature. Biomacromol 4:344–349
18. Uenoyama S, Hoffman AS (1988) Synthesis and characterization of acrylamide-N-isopropylacrylamide copolymer grafts on silicone rubber substrates. Radia Phys Chem 32:605–608
19. Lahann J, Langer R (2005) Smart materials with dynamically controllable surfaces. MRS Bull 30:185–188
20. Stayton PS, Shimoboji T, Long C, Chilkoti A, Chen G, Harris JM, Hoffman AS (1995) Control of protein-ligand recognition using a stimuli-responsive polymer. Nature 378:472–474
21. Ebara M, Yamato M, Aoyagi T, Kikuchi A, Sakai K, Okano T (2004) Temperature-responsive cell culture surfaces enable on-off" affinity control between cell integrins and RGDS ligands. Biomacromol 5:505–510
22. Aoyagi T, Ebara M, Sakai K, Sakurai Y, Okano T (2000) Novel bifunctional polymer with reactivity and temperature sensitivity. J Biomater Sci Polym Edn 11:101–110
23. Ebara M, Aoyagi T, Sakai K, Okano T (2001) The incorporation of carboxylate groups into temperature-responsive poly(*N*-isopropylacrylamide)-based hydrogels promotes rapid gel shrinking. J Polym Sci Part A: Polym Chem 39:335–342
24. Ebara M, Aoyagi T, Sakai K, Okano T (2000) Introducing reactive carboxyl side chains retains phase transition temperature sensitivity in *N*-isopropylacrylamide copolymer gels. Macromolecules 33:8312–8316
25. Yoshida T, Aoyagi T, Kokufuta E, Okano T (2003) Newly designed hydrogel with both sensitive thermo-response and biodegradability. J Polym Sci Part A: Polym Chem 41:779–787
26. Maeda T, Yamamoto K, Aoyagi T (2006) Importance of bound water in hydration-dehydration behavior of hydroxylated poly(N-isopropylacrylamide). J Colloid Inter Sci 302:467–474
27. Okano T, Bae YH, Jacobs H, Kim SW (1990) Thermally on–off switching polymers for drug permeation and release. J Control Rel 11:255–265
28. Yoshida R, Sakai K, Okano T, Sakurai Y, Bae YH, Kim SW (1991) Surfacemodulated skin layer of thermal responsive hydrogels as on–off switches. I Drug release. J Biomater Sci Polym Ed 3:155–162
29. Yoshida R, Sakai K, Okano T, Sakurai Y (1992) Surface-modulated skin layer of thermal responsive hydrogels as on-off switches. II. Drug permeation. J Biomater Sci Polym Ed 3:243–252
30. Omura T, Ebara M, Lai JJ, Yin X, Hoffman AS, Stayton PS (2014) Design of smart nanogels that respond to physiologically relevant pH values and temperatures. J Nanosci Nanotech 14:2557–2562
31. Garbern JC, Hoffman AS, Stayton PS (2010) Injectable pH- and temperature-responsive poly(N-isopropylacrylamide-co-propylacrylic acid) copolymers for delivery of angiogenic growth factors. Biomacromol 11:1833–1839
32. Techawanitchai P, Ebara M, Idota N, Aoyagi T (2012) Light-induced spatial control of pH-jump reaction at smart gel interface. Colloids Surf B: Biointerfaces 99:53–59
33. Techawanitchai P, Idota N, Uto K, Ebara M, Aoyagi T (2012) A smart hydrogel-based time bomb triggers drug release mediated by pH-jump reaction. Sci Technol Adv Mater 13:064202
34. Matsumoto A, Ikeda S, Harada A, Kataoka K (2003) Glucose-responsive polymer bearing a novel phenylborate derivative as a glucose-sensing moiety operating at physiological pH conditions. Biomacromolecules 4:1410–1416
35. Matsumoto A, Yoshida R, Kataoka K (2004) Glucose-responsive polymer gel bearing phenylborate derivative as a glucose-sensing moiety operating at the physiological pH. Biomacromolecules 5:1038–1045

36. Kim YJ, Ebara M, Aoyagi T (2012) Temperature-responsive electrospun nanofibers for 'on-off' switchable release of dextran. Sci Technol Adv Mater 13:064203
37. Kim YJ, Ebara M, Aoyagi T (2013) A smart hyperthermia nanofiber with switchable drug release for inducing cancer apoptosis. Adv Funct Mater 23:5753–5761
38. Maeda T, Kim YJ, Aoyagi T, Ebara M (2017) The design of temperature-responsive nanofiber meshes for cell storage applications. Fibers 5:13
39. Kim YJ, Ebara M, Aoyagi T (2012) A smart nanofiber web that captures and release cells. Angew Chem Intl Ed 51:10537–10541
40. Niiyama E, Uto K, Lee CM, Sakura K, Ebara M (2018) Alternating magnetic field-triggered switchable nanofiber mesh for cancer thermo-chemotherapy. Polymers 10:1018
41. Ebara M, Hoffman JM, Hoffman AS, Stayton PS (2006) Switchable surface traps for injectable bead-based chromatography in PDMS microfluidic channels. Lab Chip 6:843–848
42. Lai JJ, Hoffman JM, Ebara M, Hoffman AS, Estournes C, Wattiaux A, Stayton PS (2007) Dual magnetic-/temperature-responsive nanoparticles for microfluidic separations and assays. Langmuir 23:7385–7391
43. Lai JJ, Nelson KE, Nash MA, Hoffman AS, Yager P, Stayton PS (2009) Dynamic bioprocessing and microfluidic transport control with smart magnetic nanoparticles in laminar-flow devices. Lab Chip 9:1997–2002
44. Ebara M, Yamato M, Aoyagi T, Kikuchi A, Sakai K, Okano T (2008) The effect of extensible PEG tethers on shielding between grafted thermo-responsive polymer chains and integrin–RGD binding. Biomaterials 29:3650–3655
45. Ebara M, Yamato M, Aoyagi T, Kikuchi A, Sakai K, Okano T (2008) A novel approach to observing synergy effects of PHSRN on integrin-RGD binding using intelligent surfaces. Adv Mater 20:3034–3038

Geometrical and Mechanical Nanoarchitectonics at Interfaces Bridging Molecules with Cell Phenotypes

Jun Nakanishi and Shota Yamamoto

1 Introduction

The establishment of induced pluripotent stem cells (iPS) cells and disease-specific iPS cells has opened doors to rebuild physiological and malignant tissues in any some laboratories [1, 2]. To apply these useful cell resources for regenerative medicines or drug screening, it is crucial to develop methods to keep their stemness, selectively induce their differentiation, and assemble them into physiologically relevant tissue structures. The knowledges are accumulating on the recipes when and how much soluble factors, like cytokines and growth factors, should be added in culture media [3, 4]. However, the processes are also highly dependent on chemical and mechanical properties of their substrata and their relationships are yet-to-be-elucidated from much more fundamental sides.

Cell adhesion to substrates starts from the molecular interactions between transmembrane integrins and specific motifs in extracellular matrix (ECM) proteins. The integrin molecules are existed as heterodimers of an α and β subunits in the plasma membranes. So far, more than twenty different heterodimers have been identified, each has its own selectivity against various ECM proteins [5]. The engagement of the ECM ligands to integrin induces clustering of the transmembrane proteins, accumulating various signaling and adaptor proteins, such as focal adhesion kinase (FAK), paxillin, talin, and vinculin, to the intracellular space in between integrin and actin cytoskeletal networks (Fig. 1a). These large protein clusters are called focal adhesion or focal complex, depending on their degree of maturation. Such accumulation process of multiple proteins in response to extracellular signals is like the activation processes of receptor tyrosine kinase cascades against soluble factors

J. Nakanishi (✉) · S. Yamamoto
International Center for Materials Nanoarchitectonics (WPI-MANA), National Institute for Materials Science (NIMS), 1–1 Namiki, Tsukuba 305-0044, Ibaraki, Japan
e-mail: NAKANISHI.Jun@nims.go.jp

Y. Wakayama and K. Ariga (eds.), *System-Materials Nanoarchitectonics*,
NIMS Monographs, https://doi.org/10.1007/978-4-431-56912-1_16

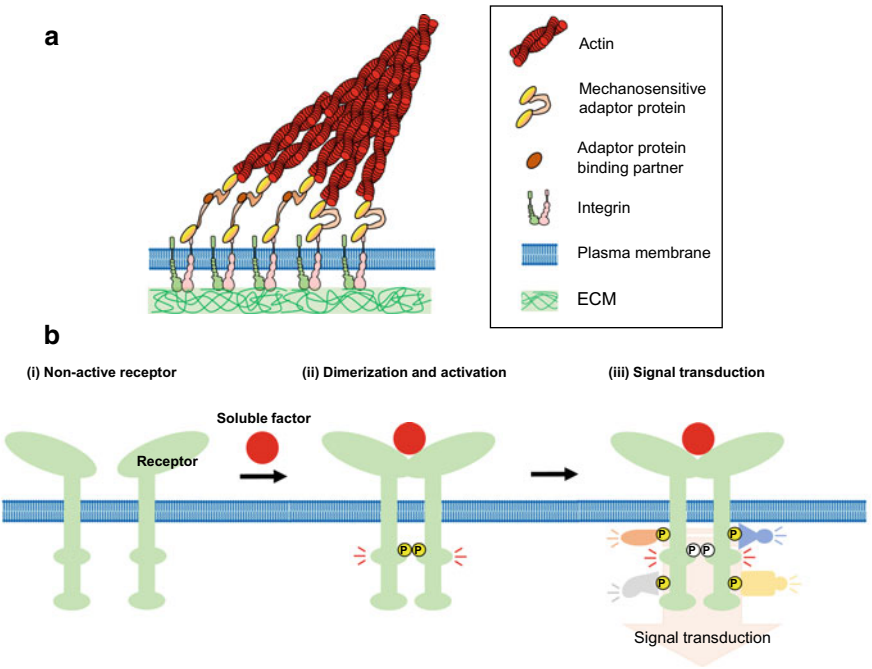

Fig. 1 Schematic representations of signaling centers and activation processes of **a** integrin and **b** receptor tyrosine kinase signaling

(Fig. 1b). However, due to the non-diffusive nature of the ECM ligands, the intensity of the signals is determined by the nanoscopic clustering of the ligands, rather than the concentration of the ligands. Especially, native ECMs have nanometer range textures, therefore nanoscopic control of ECM ligands is physiologically relevant [6]. Another important feature of focal adhesions is that they serve not only as hubs of biochemical signal transduction, but also as the mechanical supports against cellular traction force applied from actomyosin cytoskeletal structures. Therefore, in addition to local biochemical signal transduction occurring nearby the focal adhesions, we should pay attentions to reactions at distal sites mechanically transmitted through the cytoskeletal networks. Such features increase additional complexity compared to those of soluble ligands-mediated signaling, thereby intriguing researchers to an emerging discipline, *mechanobiology*. In this chapter, we will briefly overview how cells sense their surrounding nanoscopic and mechanical cues and integrate the information to adapt themselves to specific phenotypes, especially focusing on key materials and technologies useful to resolve the complex cellular system. The readers will notice conceptual similarity, in terms of nanoarchitectonics, to the other chapters of this book.

2 Geometrical Nanoarchitectonics

One of the straightforward approaches, to look at the impact of cell-ECM interactions on cellular responses, is to control the surface density of entire ECM proteins or their fragments immobilized to the substrate surface. Conventionally, the relationships have been studied by simply changing the amount of physically adsorbed proteins or the composition of mixed self-assembled monolayers (Fig. 2a). However, this strategy makes cells exposed to non-homogenous ligand distribution, especially in the molecular-scale nanoscopic resolutions, thereby the cellular phenotypes become the products of broad ranges of inter-ligand spacing with obscured causal relationship between them (Fig. 2b(i)). In addition, the scale which integrin molecule recognizes are in the order of tens of nanometer, which are difficult to be produced by conventional photolithography. To tackle this technical difficulty, Spatz et al. developed block copolymer nanolithography (Fig. 2c) [7]. This method is based on the

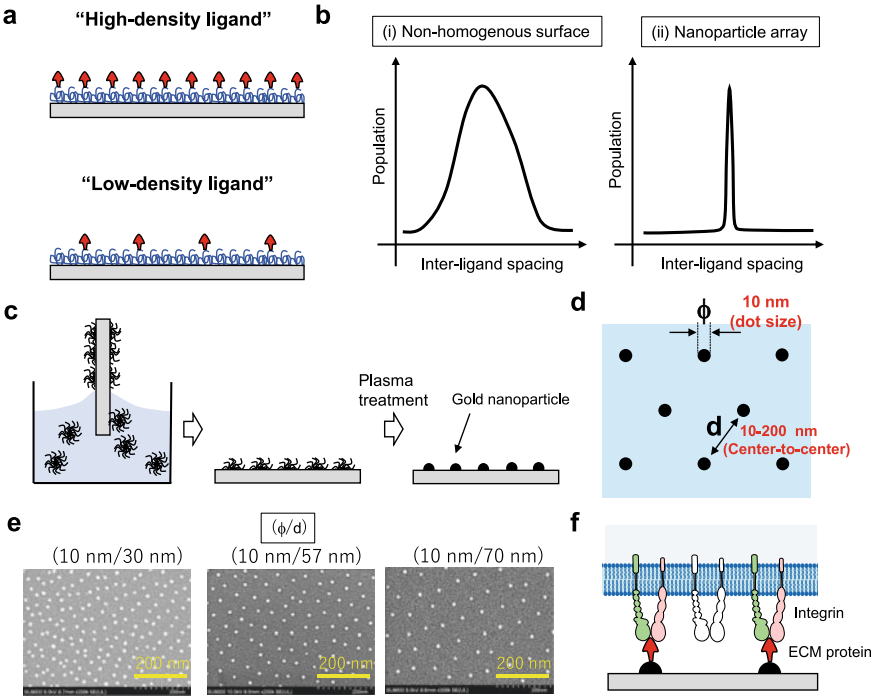

Fig. 2 Approaches to manipulate cell-ECM interactions. **a** A simple dilution method to control surface ligand density. **b** Conceptual diagram of distribution of the distance between neighboring ligands on the methods based on methods shown in (i) A and (ii) C. **c** The procedure of block copolymer nanolithography. **d** Schematic illustration of a gold nanoparticle array in hexagonal arrangement. **e** Scanning electron micrograph images of gold nanoparticle arrays with different interparticle separations. **f** The nanopatterned substrate activates integrin heterodimers corresponding to the distance between arrayed nanoparticles

self-assembly of reverse micelles entrapping $HAuCl_4$ at the substrate surface by dip-coating or spin-coating. The following plasma treatment burns out the organic shells and reduces the gold salt into gold nanoparticles embedded in the substrate surface in a hexagonal arrangement. Subsequent modification of the gold nanoparticles with an ECM ligand via the thiol-gold chemistry and passivation of surrounding glass regions by poly(ethylene glycol) silane, the surface presents the ECM ligand corresponding to the gold nanoparticle arrays. The configuration of gold nanoparticle arrays can be tuned by the amount of the gold salt as well as the chain length of hydrophobic/hydrophilic segments of the block copolymer, ranging from 1 to 12 nm nanoparticles with 10–200 nm interparticle separations (Fig. 2d, e). Especially, when the gold nanoparticles size is designed to be in the single nanometer order, each nanoparticle can accommodate single integrin heterodimer, thereby allowing to precisely control the separation between ligand-engaged (thus activated) integrin heterodimers corresponding to the distance among arrayed nanoparticles (Fig. 2b(ii) and f). By using the nanopatterned substrates, the threshold of integrin heterodimers clusters required for the focal adhesion maturation has been identified to be around 60 nm [8]. This threshold is universal to various cell types at least the cells are attached to the rigid substrates, like glass. However, a recent study demonstrated that the threshold dynamically changes depending on the stiffness of the matrices [9]. Another important aspects of this research strategy is that the size of nanopatterned substrate can be enlarged up to several cm^2 scale, enabling studies of cellular phenotypes by standard biochemical analyses, such as reverse transcription polymerase chain reaction (RT-PCR) and western blotting. It is a remarkable feature that normal top-down approaches lack.

Block copolymer nanolithography gives quantitative and molecular-level control of cell-ECM interactions. When this technology was combined with other conventional top-down processes, nanoarchitectonic feature of focal adhesion maturation can be addressed quantitatively. Arnold et al. used the electron-beam (EB) lithography to prepare hierarchical structures with several hundred nanometer islands made of arrayed gold nanoparticles and found the bridging of paxillin-rich nascent adhesions across non-adhesive spacing through actin bundles [10]. On the other hand, Shimizu and coworkers introduced photocleavable poly(ethylene glycol) (PEG) together with cRGD ligand (Fig. 3a) [11]. On this substrate, the cRGD ligand is covered by PEG brushes, therefore the nanopatterned ECM ligand becomes only addressable upon photoirradiation. They utilized this photoactivatable nanopatterned substrate to confine HeLa cells in a given circular cluster and induce their migration by releasing the geometrical confinements (Fig. 3b). What they found in this study was detachment of cell–cell cohesion and loss of collective feature on the nanopatterned substrate. Such phenotypes was associated to hampering of FAK phosphorylation signaling between Y397 and Y861. This study demonstrated the effect of nanoscopic molecular clustering leads to cell–cell cohesion, or further to collective migration, highlighting the nanoarchitectonic aspects of cell adhesion and collective behaviors.

Besides the clustering of integrin molecules, the existence of another larger geometrical feature at the cell-ECM interface was identified by different studies. Garcia and coworkers combined the substrates bearing hundreds of nanometer scale

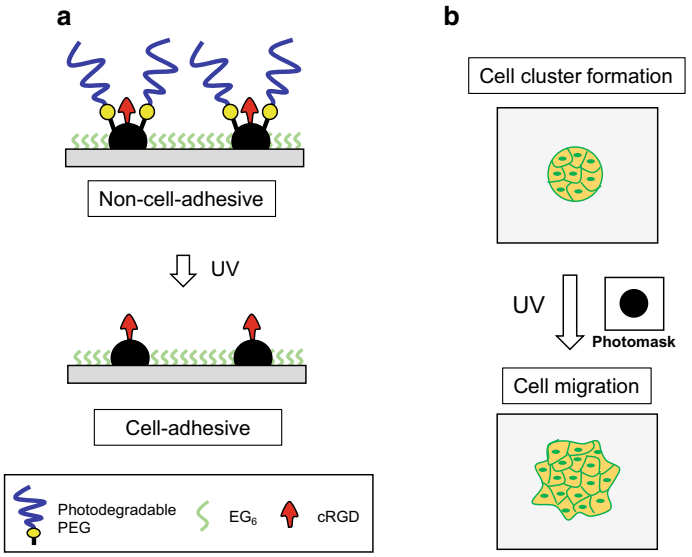

Fig. 3 Study of collective cell migration on photoactivatable nanopatterned substrate. Schematic illustration of **a** the surface functionalization strategy and **b** the procedure to study collective migration behaviors of a circular cluster formed on the substrate

gold regions (250, 333, 500, and 1000 nm), prepared by means of EB lithography, and the biochemical manipulation of adhesive force, cytoskeletal tension, and molecules that link integrin and cytoskeleton (Fig. 4a) [12]. This study demonstrated that geometrical area required for the focal adhesion maturation was not constant, rather it is determined by the balance between cell-ECM adhesion force and cytoskeletal tension (Fig. 4b). Also, Gautrot used colloidal lithography [13] to investigate the effect of geometrical frustration (confinements) on wider range of

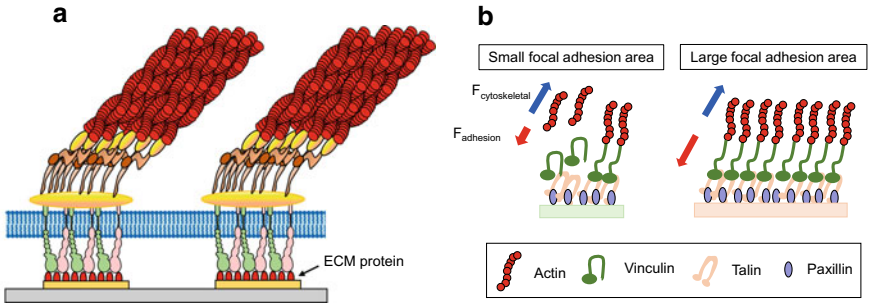

Fig. 4 Manipulation of cell-ECM interactions at the scale around nascent adhesion. **a** Schematic illustration of the cell adhesion machinery formed within hundreds of nm scale geometrical gold regions. **b** The focal adhesion maturation is determined by a balance of cell-ECM adhesion force and cytoskeletal tension

adhesion-associated proteins, including integrin β1, paxillin, talin, FAK, cortactin, and vinculin in the spreading of endothelial stem cells [14]. It is concluded that this range of nanoscopic areas change the dynamics of vinculin, which is involved in mechanical coupling in between the substrate and cytoskeletal tension, but show no effect on the proteins involved in initial step focal adhesion formation. Furthermore, a later super-resolution microscopy study demonstrated that large micrometer-size focal adhesions contains ample smaller adhesion structures with several hundred nm size below the diffraction limit [15]. Therefore, it is indicated the micrometer size matured focal adhesions are actually grown up from such small adhesions, upon fulfilling the biochemical and mechanical criteria discussed above.

The impact of nanotopography surfaces with nano-scale features has been also extensively studied [16]. These substrates not only provide similar-scale 2D geometrical frustration to those on nanogeometrical surfaces, but also manipulate curvature of basal membranes due to the 2.5D feature of the substrates. Therefore, additional unique cellular responses can be imposed by the membrane curvature sensor signaling [17].

3 Mechanical Nanoarchitectonics

In living system, cells encounter various mechanical stimuli, like blood flow, hydrostatic pressures, and the elasticity of surrounding matrices. Especially for the last one, Young's modulus ranges from tens of pascal in the softest brain to gigapascals in the stiffest bone tissues (Fig. 5) [18]. These variations play an important role in keeping homeostasis of different tissues, but also in drastically changing cellular fates, such as stem cell differentiation [19] and malignant phenotypes of cancer cells [20]. For example, a pioneering study by Engler et al. demonstrated that the differentiation lineage of mesenchymal stem cells is determined by the stiffness of underlying matrices, committing them to the lineage corresponding to the tissue-level elasticity [21]. In particular, the shape of each cell varies from round to flat spread shapes as increasing the stiffness of these substrates in a fashion reminiscent of stem cells attached on surfaces with different micrometer-size adhesive regions [22]. Interestingly, the lineages impacted by surface stiffness and micro-patterned structures are closely correlated and those two processes are commonly regulated by the changes in the cytosolic/nuclear localization of hippo-family transcription cofactors YAP (Yes-associated protein) and TAZ [23, 24]. These facts indicate that the overall cell morphology is critical for the fate decision of stem cells and the cells feel their own changes from the bending of cytoskeletal structures or nucleus (Fig. 6a).

Besides such global mechanical sensing, the substrate rigidity is sensed at the molecular levels, as well. In particular, various mechanosensing molecules have been identified in extracellular matrices, integrins, and focal adhesion-related proteins [25]. One common force sensing mechanism is traction-induced unfolding at some parts of their protein structures (Fig. 6b). Such structural changes result in exposing cryptic binding sites to allow them to polymerize or interact with other proteins [26].

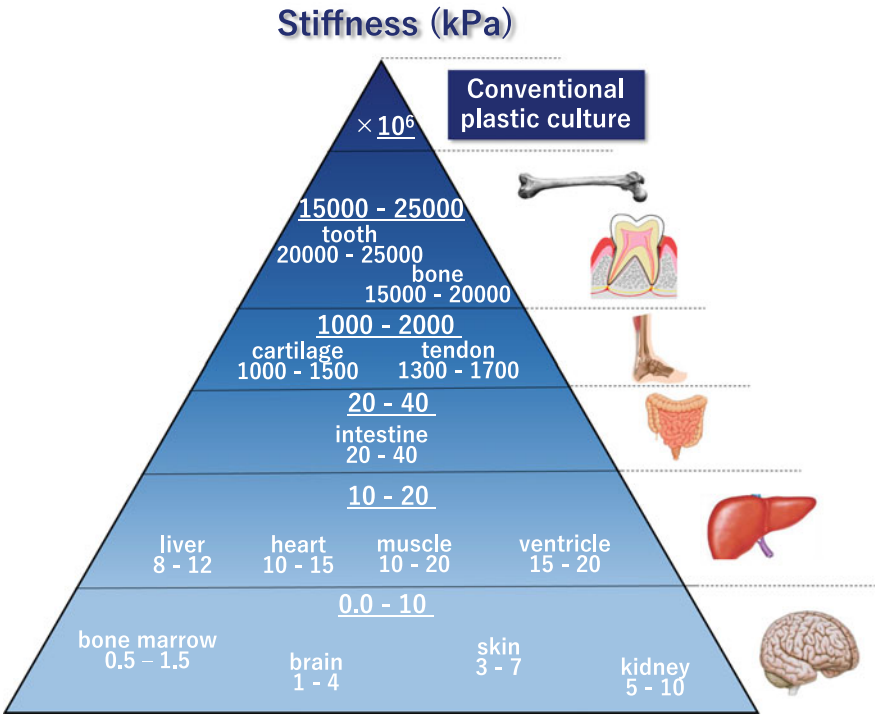

Fig. 5 Elastic modulus of biomedical tissues

The existence of these molecular-level mechanosensors adds further complexity to mechanotransdution, such as their dependence on the type of integrin-ECM complex [27] and the time frame [28]. Therefore, t is important to consider nanoarchitectonics of mechanobiological responses to surrounding mechanical stimuli both from physiochemical and mechanical aspects.

In most earlier studies, simple linear elastic materials, such as polyacrylamide hydrogels [29] and polydimethylsiloxane (PDMS), were utilized as substrates because of their facile preparation and easy-to-analyze. However, it has been noticed that the ways of tethering ECM ligands to these substrates affect cellular mechanosensing [30, 31], which intrigues another issue either cells sense stress or strain [32]. Moreover, native extracellular matrices have *visco*-elastic property, and in fact, some ECM proteins, like collagen, show stress-stiffening nature due to their fibrous structures [33]. Therefore, recent trends are moving to develop synthetic substrates that mimic mechanical characteristics or fibrous structures of natural ECM [34]. To focus on the impact of viscosity on cellular responses, Cameron et al. elaborated a series of polyacrylamide hydrogels with a constant storage modulus with varied loss moduli, by carefully choosing monomer and crosslinker ratios [35, 36].

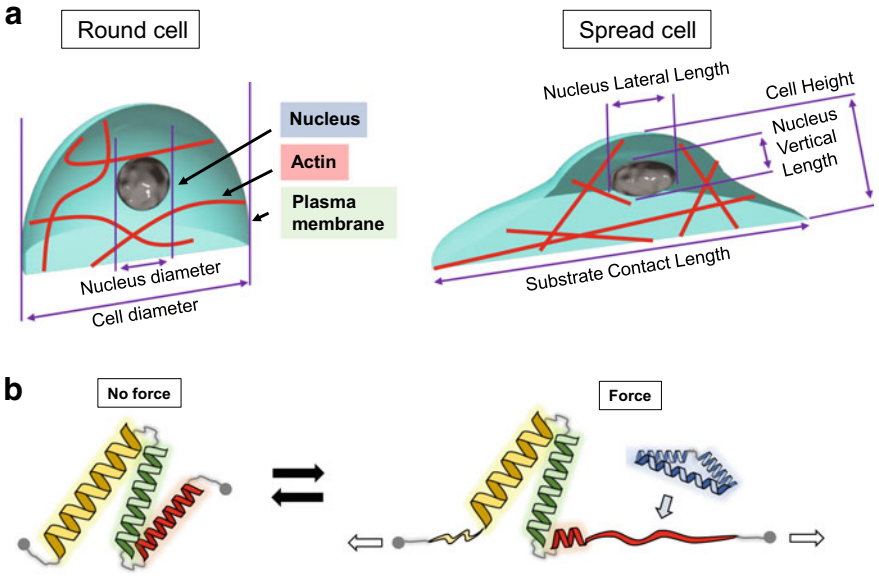

Fig. 6 The hierarchical feature of mechanical sensing. **a** Cellular level mechanosensing based on in response to the global change of cellular shape, which is sensed by the changes in the bending of actin cytoskeleton or nucleus. **b** A molecular-level mechanosensing based on a protein that exposes a cryptic binding site toward another target protein

Uto et al. tuned the crosslinking as well as crystalline/non-crystalline state of poly(ε-caprolactone)-based polymers and demonstrated the effect of fluidity as well as elasticity on cell spreading and cell senescence [37, 38]. On the other hand, Chaudhuri et al. introduced ionic bonds into alginate-based hydrogels to investigate the impact of stress relaxation on cell spreading and differentiation (Fig. 7a) [39, 40]. The stress relaxation properties of the alginate gels crosslinked by calcium can be modulated owing to the changes in connectivity and entanglement in the network depending on molecular weight of the polymers. To make ECM ligands more mobile, Yui et al. developed polyrotaxane-based polymeric surfaces composed of cyclodextrin threaded onto the PEG block (Fig. 7b). The dynamicity of the ECM ligand accelerates the initial interactions with integrin [41] and eventual stem cell differentiation [42]. Alternatively, amphiphilic block copolymers [43] or lipid bilayers [44, 45] can be used as a platform with tunable ligand mobility (viscosity) by changing their compositions (Fig. 7c). In the direction of focusing on the effect of viscosity (or fluidity) of matrices on cellular responses, the most extreme case is to use water-immiscible and denser liquids, like perfluorocarbon, as culture substrates (Fig. 7d). Conventionally, such liquid–liquid interface has been considered too dissipative to bear cellular traction force. However, when reactive surfactants, like pentafluorobenzyl chloride, were added to the organic phase, protein nanosheets, with sufficiently high shear modulus, were developed at the liquid–liquid interface [46, 47]. Furthermore, by choosing an

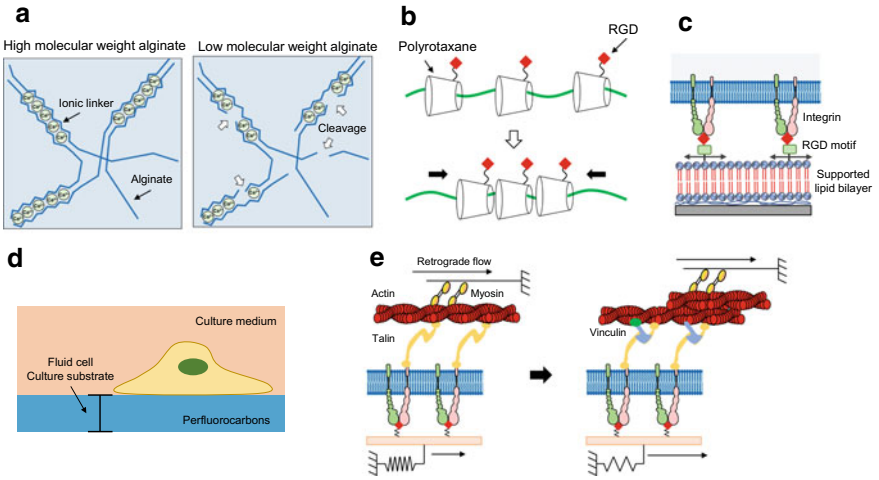

Fig. 7 Viscoelastic materials designed for study of cellular mechanosensing. **a** Alginate-based hydrogels with ionic linkages to modulate stress relaxation properties. **b** Polyrotaxane-based polymeric surfaces to control the ECM ligands mobility. **c** Supported lipid bilayers capable of regulating ligand mobility in 2D. **d** Liquid–liquid interface culture with extremely high fluidity properties. **e** Schematic drawing of the molecular clutch model

appropriate perfluorocarbon species, robust protein nanosheets were formed by the self-assembly process [48, 49]. Even though the elasticity of the protein nanosheets is within the super-physiological level, cells seemed to feel differently the mechanics of the protein nanosheets, it is shifted to upward range due to larger strain of free-standing protein layers. Furthermore, the liquid–liquid interface culture system is expected as an ideal platform for 3D bioreactors, when they were applied to the oil droplets in microfluidic systems [50].

Above studies used various terms (viscosity, mobility, stress relaxation, fluidity, etc.) for representing the *visco*-elastic feature of substrates. Among them, stress-relaxation becomes nowadays the most widely-used word because it is a reasonable parameter to discuss how cells respond to mechanical stimuli based on the framework of molecular clutch model (Fig. 7e) [51]. In this model, actin retrograde flow driven by cellular intrinsic contractility is modulated by dynamic linkage of adhesion machinery between substrate and actin cytoskeleton [51]. Currently, molecular clutch model is mainly used to discuss the cellular mechanobiology at cell-ECM interfaces mediated by integrins, but it is expected to be generalizable to cell–cell cohesion and adhesions mediated by other proteins.

4 Concluding Remarks

Here, we overviewed geometrical and mechanical nanoarchitectonics in cell adhesion machinery, whose comprehensive understanding is crucial for reproducing physiologically relevant tissues in various biomedical applications. In spite of recent progress through the development of sophisticated materials with nanomechanical features, their molecular level understanding of *dynamic* behaviors are still in the immature state and await for future work by the combination of these materials and advanced high-resolution imaging techniques.

References

1. Takahashi K, Yamanaka S (2006) Induction of pluripotent stem cells from mouse embryonic and adult fibroblast cultures by defined factors. Cell 126:663
2. Robinton DA, Daley GQ (2012) The promise of induced pluripotent stem cells in research and therapy. Nature 481:295
3. Takahashi K, Okita K, Nakagawa M, Yamanaka S (2007) Induction of pluripotent stem cells from fibroblast cultures. Nat Protocols 2:3081
4. Ohnuki M, Takahashi K, Yamanaka S (2009) Generation and characterization of human induced pluripotent stem cells. Curr Protocols Stem Cell Biol 9:4A.2.1
5. Hynes R (2002) Integrins: bidirectional, review allosteric signaling machines. Cell 110:673
6. Kim D-H, Provenzano PP, Smith CL, Levchenko A (2012) Matrix nanotopography as a regulator of cell function. J Cell Biol 197:351
7. Lohmuller T, Aydin D, Schwieder M, Morhard C, Louban I, Pacholski C, Spatz JP, MR1 (2011) Nanopatterning by block copolymer micelle nanolithography and bioinspired applications. Biointerphases 6
8. Arnold M, Cavalcanti-Adam EA, Glass R, Blummel J, Eck W, Kantlehner M, Kessler, Spatz JP (2004) Activation of integrin function by nanopatterned adhesive interfaces. Chemphyschem 5:383
9. Oria R, Wiegand T, Escribano J, Elosegui-Artola A, Uriarte JJ, Moreno-Pulido C, Platzman I, Delcanalem P, Albertazzi L, Navajas D, Trepat X, García-Aznar JM, Cavalcanti-Adam EA, Roca-Cusachs P (2017) Force loading explains spatial sensing of ligands by cells. Nature 552:219
10. Arnold M, Schwieder M, Blummel J, Cavalcanti-Adam EA, Lopez-Garcia M, Kessler H, Geiger B, Spatz JP (2009) Cell interactions with hierarchically structured nano-patterned adhesive surfaces. Soft Matter 5:72
11. Shimizu Y, Boehm H, Yamaguchi K, Spatz JP, Nakanishi J (2014) A photoactivatable nanopatterned substrate for analyzing collective cell migration with precisely tuned cell-extracellular matrix ligand interactions. Plos One 9:e91875
12. Coyer SR, Singh A, Dumbauld DW, Calderwood DA, Craig SW, Delamarche E, Garcia AJ (2012) Nanopatterning reveals an ECM area threshold for focal adhesion assembly and force transmission that is regulated by integrin activation and cytoskeleton tension. J Cell Sci 125:5110
13. Malmström J, Lovmand J, Kristensen S, Sundh M, Duch M, Sutherland DS (2011) Focal complex maturation and bridging on 200 nm vitronectin but not fibronectin patches reveal different mechanisms of focal adhesion formation. Nano Lett 11:2264
14. Gautrot JE, Malmström J, Sundh M, Margadant C, Sonnenberg A, Sutherland DS (2014) The nanoscale geometrical maturation of focal adhesions controls stem cell differentiation and mechanotransduction. Nano Lett 14:3945

15. van Hoorn H, Harkes R, Spiesz EM, Storm C, van Noort D, Ladoux B, Schmidt T (2014) The nanoscale architecture of force-bearing focal adhesions. Nano Lett 14:4257
16. Chen W, Shao Y, Li X, Zhao G, Fu J (2014) Nanotopographical surfaces for stem cell fate control: engineering mechanobiology from the bottom. Nano Today 9:759
17. Jarsch IK, Daste F, Gallop JL (2016) Membrane curvature in cell biology: an integration of molecular mechanisms. J Cell Biol 214:375
18. Butcher DT, Alliston T, Weaver VM (2009) A tense situation: forcing tumour progression. Nat Rev Cancer 9:108
19. Discher DE, Janmey P, Wang Y-I (2005) Tissue cells feel and respond to the stiffness of their substrate. Sci 310:1139
20. Paszek MJ, Zahir N, Johnson KR, Lakins JN, Rozenberg GI, Gefen A, Reinhart-King CA, Margulies SS, Dembo M, Boettiger D, Hammer DA, Weaver VM (2005) Tensional homeostasis and the malignant phenotype. Cancer Cell 8:241
21. Engler AJ, Sen S, Sweeney HL, Discher DE (2006) Matrix elasticity directs stem cell lineage specification. Cell 126:677
22. McBeath R, Pirone DM, Celeste MN, Bhadriraju K, Chen CS (2004) Cell shape, cytoskeletal tension, and RhoA regulate stem cell lineage commitment. Dev Cell 6:483
23. Low BC, Pan CQ, Shivashankar GV, Bershadsky A, Sudol M, Sheetz M (2014) YAP/TAZ as mechanosensors and mechanotransducers in regulating organ size and tumor growth. FEBS Lett 588:2663
24. Panciera T, Azzolin L, Cordenonsi M, Piccolo S (2017) Mechanobiology of YAP and TAZ in physiology and disease. Nat Rev Mol Cell Biol 18:758
25. Jansen KA, Donato DM, Balcioglu HE, Schmidt T, Danen EHJ, Koenderink GH (2015) A guide to mechanobiology: where biology and physics meet. Biochim Biophys Acta 1853:3043
26. Orr AW, Helmke BP, Blackman BR, Schwartz MA (2006) Mechanisms of mechanotransduction. Dev Cell 10:11
27. Seong J, Tajik A, Sun J, Guan J-L, Humphries MJ, Craig SE, Shekaran A, García AJ, Lu S, Lin MZ, Wang N, Wang Y (2013) Distinct biophysical mechanisms of focal adhesion kinase mechanoactivation by different extracellular matrix proteins. Proc Nat Acad Sci USA 110:19372
28. Roca-Cusachs P, Gauthier NC, del Rio A, Sheetz MP (2009) Clustering of $\alpha_5\beta_1$ integrins determines adhesion strength whereas $\alpha_v\beta_3$ and talin enable mechanotransduction. Proc Nat Acad Sci USA 106:16245
29. Fischer RS, Myers KA, Gardel ML, Waterman CM (2012) Stiffness-controlled three-dimensional extracellular matrices for high-resolution imaging of cell behavior. Nat Protocols 7:2056
30. Trappmann B, Gautrot JE, Connelly JT, Strange DGT, Li Y, Oyen ML, Cohen Stuart MA, Boehm H, Li B, Vogel V, Spatz JP, Watt FM, Huck WTS (2012) Extracellular-matrix tethering regulates stem-cell fate. Nat Mater 11:642
31. Wen JH, Vincent LG, Fuhrmann A, Choi YS, Hribar KC, Taylor-Weiner H, Chen S, Engler AJ (2014) Interplay of matrix stiffness and protein tethering in stem cell differentiation. Nat Mater 13:979
32. Yip AK, Iwasaki K, Ursekar C, Machiyama H, Saxena M, Chen H, Harada I, Chiam K-H, Sawada Y (2013) Cellular response to substrate rigidity is governed by either stress or strain. Biophys J 104:19
33. Han YL, Ronceray P, Xu G, Malandrino A, Kamm RD, Lenz M, Broedersz CP, Guo M (2018) Cell contraction induces long-ranged stress stiffening in the extracellular matrix. Proc Natl Acad Sci U.S.A. 115:4075
34. Baker BM, Trappmann B, Wang WY, Sakar MS, Kim IL, Shenoy VB, Burdick JA, Chen CS (2015) Cell-mediated fibre recruitment drives extracellular matrix mechanosensing in engineered fibrillar microenvironments. Nat Mater 14:1262
35. Cameron AR, Frith JE, Cooper-White JJ (2011) The influence of substrate creep on mesenchymal stem cell behaviour and phenotype. Biomaterials 32:5979

36. Cameron AR, Frith JE, Gomez GA, Yap AS, Cooper-White JJ (2014) The effect of time-dependent deformation of viscoelastic hydrogels on myogenic induction and Rac1 activity in mesenchymal stem cells. Biomaterials 35:1857
37. Uto K, Mano SS, Aoyagi T, Ebara M (2016) Substrate fluidity regulates cell adhesion and morphology on poly(ε-caprolactone)-based materials. ACS Biomater Sci Eng 2:446
38. Mano SS, Uto K, Ebara M (2017) Material-induced senescence (MIS): fluidity induces senescent type cell death of lung cancer cells via insulin-like growth factor binding protein 5. Theranostics 7:4658
39. Chaudhuri O, Gu L, Darnell M, Klumpers D, Bencherif SA, Weaver JC, Huebsch N, Mooney DJ (2015) Substrate stress relaxation regulates cell spreading. Nat Commun 6:6365
40. Chaudhuri O, Gu L, Klumpers D, Darnell M, Bencherif SA, Weaver JC, Huebsch N, Lee H-P, Lippens E, Duda GN, Mooney DJ (2016) Hydrogels with tunable stress relaxation regulate stem cell fate and activity. Nat Mater 15:326
41. Seo J-H, Kakinoki S, Inoue Y, Yamaoka T, Ishihara K, Yui N (2013) Inducing rapid cellular response on RGD-binding threaded macromolecular surfaces. J Am Chem Soc 135:5513
42. Seo J-H, Kakinoki S, Yamaoka T, Yui N (2015) Directing stem cell differentiation by changing the molecular mobility of supramolecular surfaces. Adv Healthc Mater 4:215
43. Kourouklis AP, Lerum RV, Bermudez H (2014) Cell adhesion mechanisms on laterally mobile polymer films. Biomaterials 35:4827
44. Yu C-H, Law JBK, Suryana M, Low HY, Sheetz MP (2011) Early integrin binding to Arg-Gly-Asp peptide activates actin polymerization and contractile movement that stimulates outward translocation. Proc Natl Acad Sci USA 108:20585
45. Bennett M, Cantini M, Reboud J, Cooper JM, Roca-Cusachs P, Salmeron-Sanchez M (2018) Molecular clutch drives cell response to surface viscosity. Proc Nat Acad Sci USA 115:1192
46. Kong D, Nguyen KDQ, Megone W, Peng L, Gautrot JE (2017) The culture of HaCaT cells on liquid substrates is mediated by a mechanically strong liquid–liquid interface. Faraday Discuss 204:367
47. Kong D, Megone W, Nguyen KDQ, Di Cio S, Ramstedt M, Gautrot JE (2018) Protein nanosheet mechanics controls cell adhesion and expansion on low-viscosity liquids. Nano Lett 18:1946
48. Minami K, Mori T, Nakanishi W, Shigi N, Nakanishi J, Hill JP, Komiyama M, Ariga K (2017) Suppression of myogenic differentiation of mammalian cells caused by fluidity of a liquid–liquid interface. ACS Appl Mater Interf 9:30553
49. Jia X, Minami K, Uto K, Chang AC, Hill JP, Ueki T, Nakanishi J, Ariga K (2019) Modulation of mesenchymal stem cells mechanosensing at fluid interfaces by tailored self-assembled protein monolayers. Small 15:1804640
50. Kong D, Peng L, Di Cio S, Novak P, Gautrot JE (2018) Stem cell expansion and fate decision on liquid substrates are regulated by self-assembled nanosheets. ACS Nano 12
51. Elosegui-Artola A, Trepat X, Roca-Cusachs P (2018) Control of mechanotransduction by molecular clutch dynamics. Trends Cell Biol 28:356

Emerging Methods

Electrical Measurement by Multiple-Probe Scanning Probe Microscope

Yoshitaka Shingaya and Tomonobu Nakayama

1 Introduction

To measure the physical properties of new nanomaterials that are formed using nanoarchitectonics technology is extremely important. Therefore, we have developed a multiple-probe scanning probe microscope (MP-SPM) to measure the properties of new nanomaterials, especially the electrical conductivity, in nanoscale. The aim of this technology is to enable the measurement of the electrical properties of nanomaterials at designated positions by increasing the number of probes in a scanning probe microscope to two, three, and four. Since scanning probe microscopes have very high resolution at the atomic scale [1–3], each probe of multiple-probe SPM has also high spatial resolution. Therefore, it is possible to place probes on nanomaterials with very high positional accuracy. If the resistance between any two points on a nanowire is measured using two probes of a double-probe SPM, the resistivity of the nanowire can be obtained. By using the three probes of triple-probe SPM, the electrical characteristics of a nanotransistor can be measured. Furthermore, if the four probe of quadruple-probe SPM with four probes is used, the resistivity of nanosheets can be measured by the "four-probe method" without being influenced by contact resistance. As mentioned above, multiple-probe SPM is a novel technique that can accurately determine the electrical properties of nanomaterials that have been difficult to measure at the nanoscale in the past, and is an indispensable measurement technology in order to develop the nanomaterials and nanosystem constructions.

Y. Shingaya (✉) · T. Nakayama
International Center for Materials Nanoarchitectonics (WPI-MANA), National Institute for Materials Science (NIMS), 1-1 Namiki, Tsukuba 305-0044, Ibaraki, Japan
e-mail: SHINGAYA.Yoshitaka@nims.go.jp

T. Nakayama
University of Tsukuba, Ibaraki 305-0044, Japan

Y. Wakayama and K. Ariga (eds.), *System-Materials Nanoarchitectonics*,
NIMS Monographs, https://doi.org/10.1007/978-4-431-56912-1_17

2 Development of Double-Probe Scanning Tunneling Microscope System

Figure 1a shows the world's first double-probe scanning tunneling microscope (DP-STM) that actually worked [4]. This apparatus is composed of a load lock chamber, a sample preparation chamber, and STM observation chamber. In the apparatus, all process such as the cleaning sample substrate, producing a nanostructure to be measured, and STM observation can be performed in an ultrahigh-vacuum environment. Figure 1b shows measurement stage of DP-STM. Both probes are attached to a cylindrical piezo actuator, and fine scanning is possible. Moreover, they are attached to a coarse motion stage which is driven by an inertia motion drive system, and the probes can be arranged at an arbitrary position on the sample surface. Each probe is bent at an angle of about 50° with respect to the sample surface so that the tips can approach each other. The STM observation is carried out at room temperature. After the development of the first DP-STM of our system, various designs of the MP-SPM have been reported by various research groups [5–21]. Figure 2 shows an

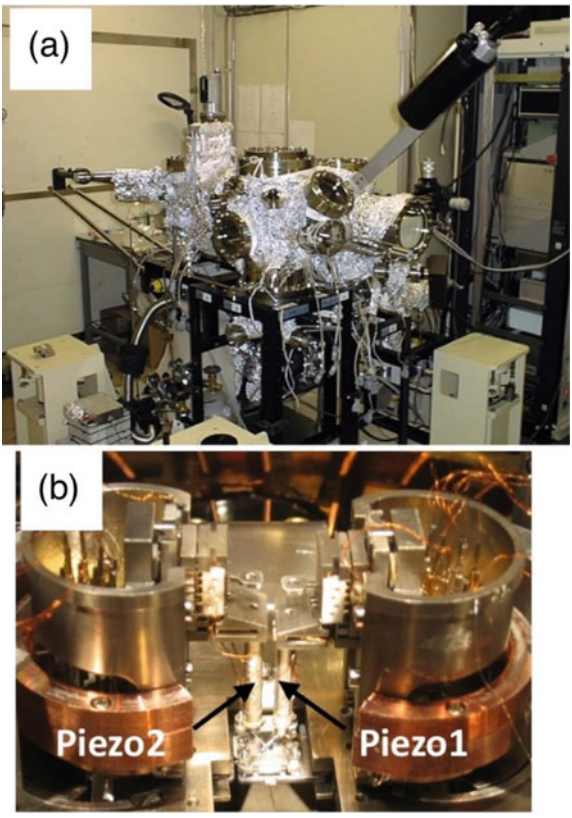

Fig. 1 **a** Photograph of world's first UHV DP-STM equipped with a sample preparation chamber and a long-focus optical microscope with a CCD camera. **b** Photograph of measurement stage of DP-STM. Tilted tungsten tips were attached to the cylindrical piezo actuators. Reproduced from [34], with the permission of Wiley Publishing

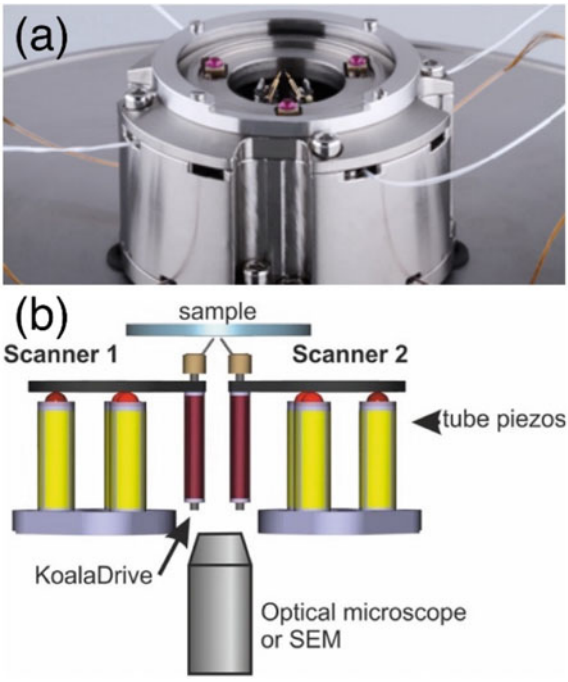

Fig. 2 **a** Photograph of the ultracompact TetraProbe multitip scanning probe microscope. Four independent STM units are integrated within a diameter of 50 mm, resulting in unsurpassed mechanical stability, enabling atomic-resolution imaging with each tip. **b** Schematic side view of the internal structure of the TetraProbe instrument. Reproduced from [22] with the authors' permission

ultracompact multitip STM developed by Cherepanov et al. [16, 22] Cherepanov and co-researchers have developed an original system, in which four independent STM units are integrated on a diameter of 50 mm. The heart of this STM is a new type of piezoelectric coarse approach called KoalaDrive [23]. The compactness of KoalaDrive allows the fabrication of a four-tip STM as small as a single-tip STM with a drift of less than 0.2 nm/min at room temperature and lowest resonance frequencies of 2.5 kHz (xy) and 5.5 kHz (z).

In measurement by using two-probe system, we should include influence of the contact resistance between the measured sample and the probe. Generally, the resistance at a certain probe distance L can be written as $R(L)$. $R(L)$ is constant when the object to be measured is a three-dimensional conductor, $\mathrm{R}(L) \propto \ln L$ when it is a two-dimensional conductor, and $R(L) \propto L$ when it is a one-dimensional conductor. After that, a finite contact resistance Rc is added, finally the total measured resistance is expressed as $R(L) + Rc$. In the case of a three-dimensional conductor, $R(L)$ and Rc cannot be obtained by two-probe resistance measurement, but for two-dimensional and one-dimensional conductors, $R(L)$ and Rc can be obtained when the resistance is measured while changing the distance between probes. In DP-STM measurements, the resistivity of the nanomaterial and the contact resistance between the probes and the nanomaterial are obtained by measuring the interprobe distance dependence of the resistance.

3 Elemental Technology for Realizing Double-Probe Scanning Tunneling Microscope

3.1 Development of Ultrasharp Probe

In MP-SPM measurement, the shape of the probe is very important. This is because the minimum distance between the probes is limited by the shape of the probe apex, that is, the radius of curvature of the probe apex. Figure 3a shows the schematic diagram of this. Some reseach groups have already reported a carbon nanotube (CNT) probe, a CNT attached to the apex of a tungsten tip can be used as a sharp probe of SPM [24–29]. However, the CNT probe has a problem in the reproducibility of the contact resistance between the CNT and the metal probe. Therefore, although it can be used as a probe with an SPM for observing the shape, it cannot be used as a probe for electrical measurement. Konishi and co-researchers have reported that a metal coating can be applied to the CNT probe so that it can be used as a probe for electrical measurement [30]. However, the thichness of metal layer is not so small. Here, we have developed ultrasharp probes with conductive oxide nanorods as an

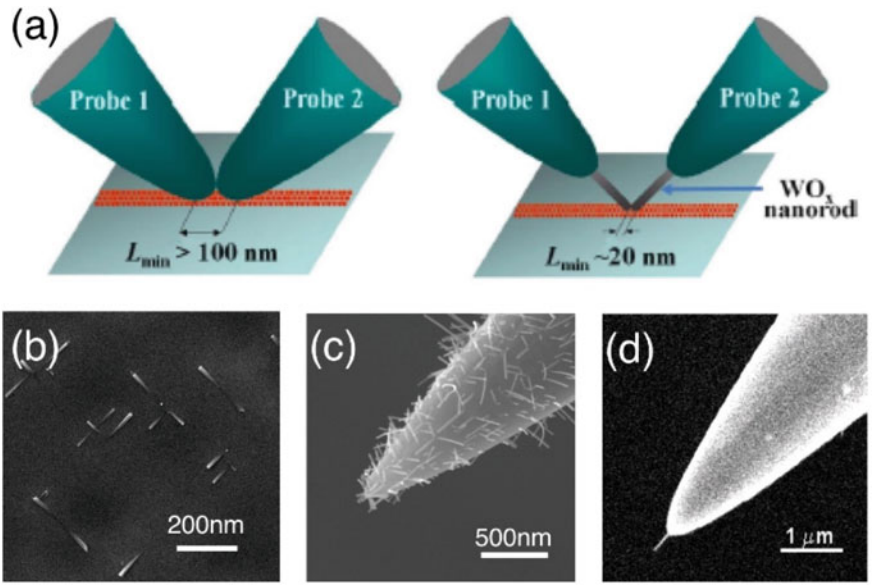

Fig. 3 **a** Schematic diagram of the minimum interprobe distance L_{min} between two probes: two conventional tungsten probes and two WO_x nanorod probes grown at apexes of two W probes. **b** SEM image of WO_x nanorods grown on W(001) surface. The aligned WO_x nanorods indicate that they were epitaxially grown on the tungsten substrate. **c** SEM image of WO_x nanorods directly grown on tungsten tip. **d** SEM image of WO_x nanorod on tungsten tip. Amorphous carbon is deposited by locally irradiating an electron beam to the portion where the nanorod growth is to be inhibited using an SEM. Reproduced from [34], with the permission of Wiley Publishing

alternative to CNT probes. The nanorods were grown directly on a metal probe [31]. Tungsten oxide was deposited on a tungsten tip by heating a tungsten filament in an ultrahigh-vacuum chamber at an oxygen partial pressure of 10^{-3} to 10^{-4} Pa. By heating the tungsten tip to about 600 to 700 °C, a tungsten oxide rod of 10 to 100 nm diameter can be grown. Tungsten oxide is known to form intermediate oxides of various compositions, but it has been clarified that intermediate oxides with a [001] crystallographic shear (CS) structure mainly form under these growth conditions. Since this structure has metallic electric conduction, it can be used as an STM probe and an electric conduction measurement probe. When using an ultrasharp probe with a nanomaterial having such a high aspect ratio attached to the tip for electrical conduction measurement, in addition to the electrical conduction characteristics of the nanomaterial, the part in contact with the nanomaterial and the metal probe often becomes problematic. Here, since the conductive tungsten oxide nanorods are grown directly on the tungsten tip, the contact resistance can be kept small. Actually, it has been revealed that the crystal orientation of a grown nanorod shows epitaxial growth having a certain relationship with the crystal orientation of the substrate [32]. Figure 3b is an SEM image of WO_x nanorods grown on a single-crystal (001) plane of tungsten. It can be seen that the nanorods grow in a certain direction on the single-crystal substrate. This indicates that WO_x is grown with a certain epitaxial relationship with the substrate. Therefore, the part in contact with the nanorod and the substrate is highly reproducible, and good electrical contact is always guaranteed.

Although a conductive nanorod probe has good electrical contact with the support substrate, simply growing it on a tungsten tip will cause many nanorods to form on the tip as shown in Fig. 3c, By using these probes, we cannot approach two probes at the close position to each other. Therefore, we have developed a method in order to locally inhibit nanorod growth as follows. First, amorphous carbon is deposited by locally irradiating an electron beam to the portion where the nanorod growth is to be inhibited using an SEM. The vicinity of the apex of probe is not deposited. Next, the tungsten tip is dipped into a hydrogen fluoride solution immediately before the nanorod growth. By the treatment with hydrogen fluoride solution, the natural oxide film is removed, and the nanorod can be epitaxially grown. Since the natural oxide film is not removed by dipping in the hydrogen fluoride solution when the amorphous carbon is deposited, nanorods do not grow on that portion. Figure 3d shows an amorphous carbon coating preliminarily applied in the vicinity of the apex of a tungsten tip and then treated with hydrogen fluoride solution. Here, a single nanorod can be selectively grown near the apex by preventing amorphous carbon from coating most of the apex of the probe. This shape of the probe is optimum structure for measuring the electrical conductivity of nanostructures.

3.2 Electrical Measurement by Using Ultrasharp Probe

This ultrasharp nanoprobe was actually introduced into the DP-STM system, and the electrical measurement of a nanostructure was performed to estimate the shortest

interprobe distance that could be realized. Although WO_3 unit is a semiconductor, WO_x has metallic electrical conductivity because it is considered that the oxygen-deficient part has conductivity. Therefore, when the nanostructure to be measured is very small, the contact resistance varies markedly. This is because that the contact resistance is depend on which part of the nanorod surface contact with the sample. As described above, in the electrical conductivity measurement by the DP-STM, it is necessary to repeatedly measure electrical conductivity by changing the distance between the probes while keeping the contact resistance constant. Here, for that purpose, the surface of the WO_x nanorod was coated with 3 to 6-nm-thick platinum and used as a probe for STM and electrical measurement. An $ErSi_2$ nanowire was used as the measurement target. $ErSi_2$ nanowires were formed by the thermal evaporation of Er on a Si (001) surface heated to 650 °C. Figure 4a is an STM image of $ErSi_2$ nanowires after electrical conductivity measurements using the DP-STM. The nanowire has a width of 2.1 nm and a height of 0.66 nm. Probes were placed at both ends of the nanowire, and the *I*–*V* curve was measured after placing the probe in contact with the nanowire as shown in Fig. 4b. Thereafter, both probes were moved 10–20 nm in opposite direction to bring them closer together, and then, placed in contact with the nanowires again to perform *I*–*V* curve measurement. This operation was repeated to obtain 12 *R*–*L* plots as shown in Fig. 4c. From this method, it was found that the resistivity of the nanowire was 0.27 mΩcm. The shortest distance between probes that could be used for electrical measurement was 72 nm. After the electrical measurement was performed with a probe distance of 72 nm, when the distance between the probes was further reduced to 65 nm, the two probes came in contact with each other. This result indicates that the use of an ultrasharp probe with

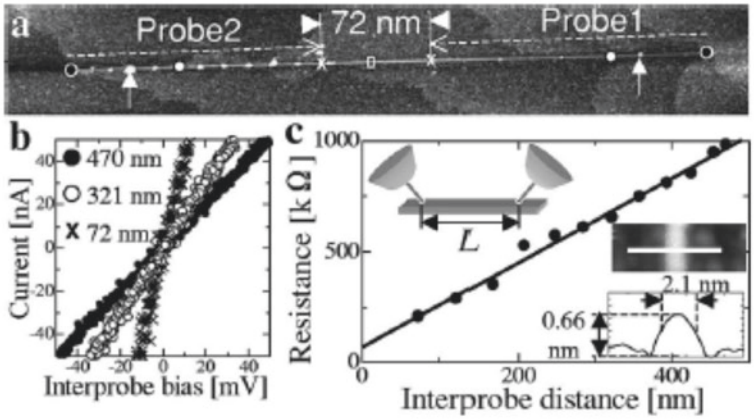

Fig. 4 **a** STM image (546 × 109 nm^2) of $ErSi_2$ NW obtained with a Pt/WO_x nanorod probe after electrical resistance measurement using the DP-STM. **b** *I*–*V* curves obtained with three different L values. **c** Measured resistances as a function of L. The lower-right inset is a magnified STM image corresponding to the part indicated by a white rectangle in (**a**) and its STM profile along the white line indicated in the magnified image. Reproduced from [31], with the permission of AIP Publishing

tungsten oxide nanorods enabled electric measurement with a probe distance of less than 100 nm, which could not be realized with a conventional metal probe.

Using this ultrasharp nanoprobe, it is not only we can reduce the distance between probes, but also we can keep the contact area small and constant when the probe is brought into contact with the nanostructure. Because the nanorod is very thin, the area in contact with the nanostructure for measurement does change little even if the position of the probe shifts in the Z direction. In addition, since the nanorod is flexible, even if the position fluctuates in the Z direction, an excessive force is not applied to the measurement target.

Next, we measured the electrical conductivity of $ErSi_2$ nanowires consisting of four segments with different thicknesses using the ultrasharp nanoprobe. When $ErSi_2$ nanowires are brought into contact with a probe, nanoparticles are always formed at the contact position which is considered to be derived from the probe. The probe cannot again be placed in contact at the same place where a nanoparticle is formed. Generally, the size of the nanoparticles is about 1 to 2 nm by using an ultrasharp probe. Therefore, precise electrical measurement is possible by bringing the probe into contact with the nanowire at 5 nm intervals. Figure 5a is an STM image of $ErSi_2$ nanowires after DP-STM measurement. The four segments have different cross-sectional shapes. The schematic diagram shows the cross-sectional shape and size of each segment. Probe 2 moved over segments iv, iii, and ii. On the other hand, probe 1 moved only over segment i. Figure 5b is a plot of the resistance between probes versus the probe distance. A different slope was obtained for each segment. This is due to the change in the cross-sectional area of the nanowire. By performing electrical measurement using a very sharp nanoprobe and maintaining a constant contact condition, it was possible to detect a very small change in the cross-sectional area with a width of 0.6 nm and a height of 0.33 nm as a slope change in the *R–L* plot. This result shows that DP-STM measurement, which can accurately measure distance-dependent resistance, is a powerful tool for determining the local resistance of nanomaterials. More interesting results have been obtained by performing such precise distance-dependent resistance measurements. The location where the change in the slope of the distance-dependent resistance in Fig. 5b occurred was found to shift from the point where the cross-sectional area actually changed. The distance of this deviation was 27 ± 10 nm. The model as shown in Fig. 5c has been proposed to explain why this phenomenon occurred. When a voltage is applied to the $ErSi_2$ nanowire and electrons are injected, the electrons move within the nanowire for a distance corresponding to the mean free path without being scattered. However, if the distance exceeds the mean free path, the conduction becomes diffusive and a resistance component is generated. When the probe approaches the thick segment of the nanowire, it is considered that the influence of the cross-sectional area starts to appear in the resistance change from a distance of about the mean free path to the position where the cross-sectional area change occurs, and the slope changes. Such precise local resistance measurement was made possible for the first time by the MP-SPM equipped with an ultrasharp nanoprobe.

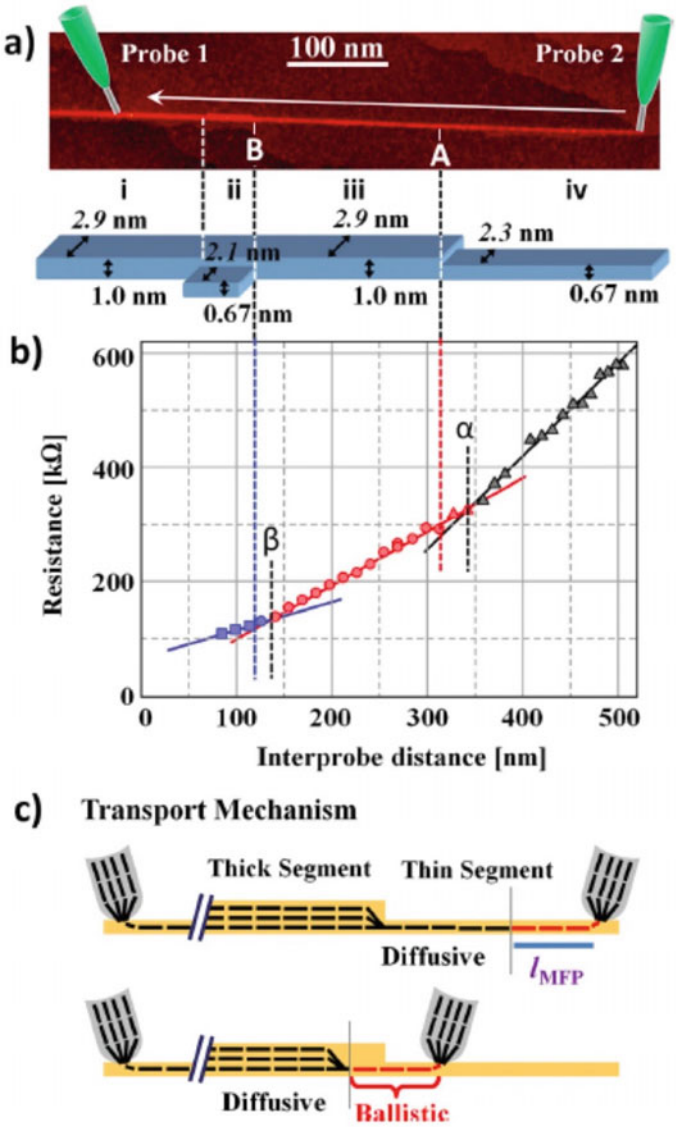

Fig. 5 **a** STM image (600 × 133 nm^2) of $ErSi_2$ NW, on which resistance measurements were performed using WO_x nanorod probes. A schematic illustration of this NW is shown below the image. The cross-sectional area of the NW changes at positions A and B. **b** *R–L* curve measured on the NW shown in (**a**). The points in the *R–L* curve where the slope changes (α and β) are not aligned with points A and B where the cross section changes, respectively. **c** Schematic diagrams of possible transport mechanism. Red broken lines indicate ballistic transport, which is considered to occur near the point of contact of the probe, whereas black broken lines indicate diffusive transport. Reproduced from [34], with the permission of Wiley Publishing

4 Development of Quadruple-Probe Atomic Force Microscope System

Inspired by the unprecedented measurement results provided by the DP-STM, quadruple-probe conductive atomic force microscopes (QP-c-AFMs) were developed to further expand the range of objects of measurement to more general materials [33–35]. An atomic force microscope adopts a self-sensing-type force sensor that uses a quartz tuning fork. This eliminates the need for optical axis adjustment required in the optical cantilever system. The self-sensing method is advantageous for increasing the number of probes to two, three, and four. The tuning fork uses the qPlus method, in which one of the two prongs is fixed and the other vibrates [36]. A tungsten wire of 0.1 mm diameter and 2–4 mm length whose tip was sharpened by electrochemical etching was attached to the end of the prong to be vibrated. As a result of attaching such a long wire, the tips of the four probes can be brought closer between the tuning fork assemblies without interfering with each other. A tube-type piezo actuator is attached to the sample, and the actuator is possible to scan the sample in the XY directions. The feedback in the Z direction can be performed independently using tube-type piezo actuators attached to each probe. Therefore, four different images can be obtained simultaneously by scanning the sample in the XY directions. By comparing the four image patterns, the relative positional relationship among the probes can be obtained. In addition, since the piezo actuators attached to the probes can be used for XY scanning, potential mapping can also be performed during current flow through a fixed probe [35]. In this case, one of the four probes is used for a Kelvin probe force microscope. In such measurement, the four probes need to be operated in conjunction. To enable such probe control, a four-probe integrated control system and dedicated control software were developed.

Figure 6 shows a photograph of one of the QP-c-AFM systems. The QP-c-AFM measures not only individual nanostructures but also nanosystems constructed by combining nanostructures. In the measurement of a nanosystem, there are many cases where the target structure is formed only in a limited region on the sample surface. Therefore, it is advantageous to combine the QP-c-AFM with other microscopes that can observe a wide range quickly. The QP-c-AFM has an arrangement in which the sample surface to be observed is located near the top of the system, making it possible to bring the objective lens of an optical microscope or scanning electron microscope closer to the sample surface. These microscopes can be used to easily search for specific nanosystems or markers by approaching them.

5 Electrical Measurement of Nanosystem with QP-c-AFM

An example of an actual measurement of a nanosystem using a QP-c-AFM is shown. A network of conductive polyaniline nanofibers was measured [37]. Polyaniline nanofibers were produced by a catalyst-free method using H_2O_2, and a network

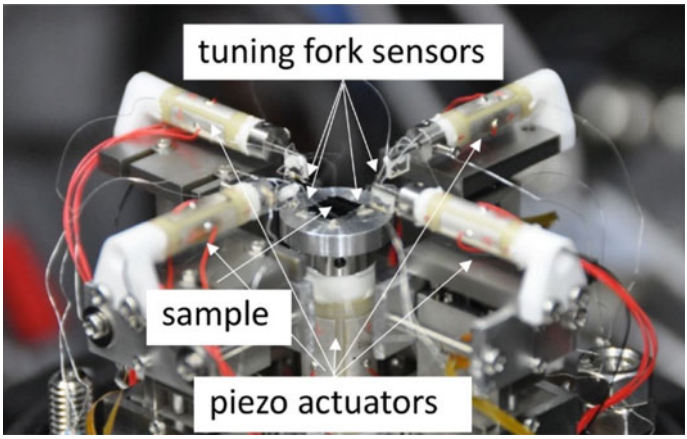

Fig. 6 Photograph of a QP-c-AFM. Four tube-type piezo actuators with tuning fork sensors were installed horizontally. The sample surface to be observed is located near the top of the system. This arrangement makes it possible to bring the objective lens of an optical microscope or scanning electron microscope closer to the sample surface

structure was formed on the SiO_2 substrate by drop casting. The typical length of a nanofiber is 5 μm and the diameter is 50 nm. It is important to clarify the electrical properties of individual components in the characterization of nanosystems. First, the resistivity of a single polyaniline nanofiber was determined by two-probe distance-dependent measurement. Figure 7a is an AFM image of the measured polyaniline. *I*–*V* curves were measured at each measurement point. Figure 7b shows a typical *I*–*V* curve. From the slope of the resistance–distance plot shown in Fig. 7c and the fiber diameter, the resistivity of the single nanofiber was determined to be 196 Ωcm. Next, to obtain information on the resistance between the components, which is important in the analysis of the nanosystem, the resistance of a single crossing point of the nanofibers was obtained using a QP-c-AFM. Figure 8a shows an AFM image of the crossing point of polyaniline nanofibers measured by two-probe distance-dependent measurements. First, the fiber was cut to isolate a single crossing point from the network. AFM probes can also be used for nanostructure processing. Here, the portion indicated by the dashed line in Fig. 8a was cut using the third probe, which was not used for measurement. While probe 1 moved on the fiber across the crossing point, probe 2 performed measurement at a nearly fixed position. In this case, the probe moved on the overlying fiber. A large resistance jump was observed across the crossing point as shown in Fig. 8b. The resistance at the crossing point was found to be 2.1 GΩ from the difference in resistance at this time. On the other hand, when the probe moved on the underlying fiber, a large variation in resistance was observed. Figure 8c shows an AFM image of the measured fiber crossing point. While probe 1 moved on the underlying fiber before the crossing point, the resistance greatly increased and decreased, but when probe 1 moved on the same fiber as probe 2 beyond the crossing point, the resistance became stable, as shown in Fig. 8d,

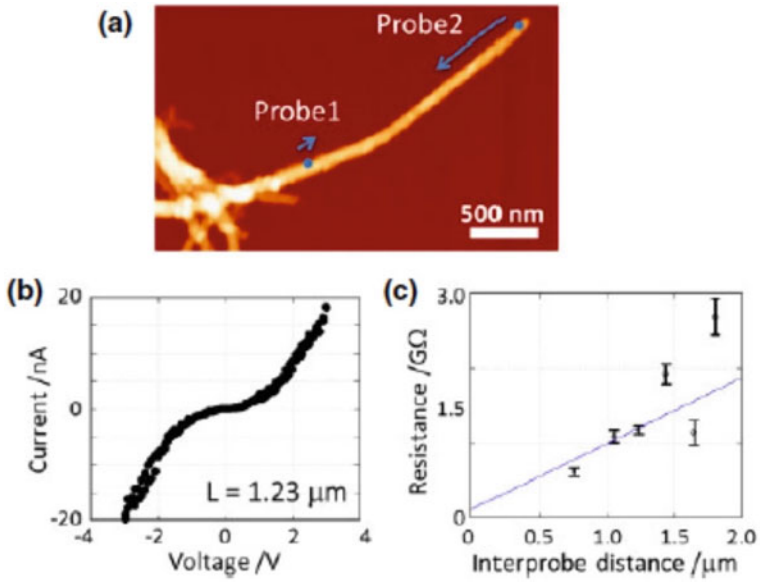

Fig. 7 **a** AFM image of single PANI fiber. Blue dots indicate the initial positions of the probes and arrows indicate the direction of the tip shift. **b** Typical *I*–*V* curve of single PANI fiber, which was measured at an interprobe distance of 1.23 μm. **c** Resistance of single PANI fiber as a function of interprobe distance. Reproduced with permission from [37], Copyright (2016) The Japan Society of Applied Physics

and the *R*–*L* plot formed a straight line. This result revealed that nanomechanical stimulation by the probe destabilized the contact between the fibers and induced large fluctuations in the resistance. Thus, it has been shown that by using an QP-c-AFM, the electrical characteristics of a single component of a nanosystem and the electrical characteristics of the contacts between the components can be clarified.

6 Summary

The development of an MP-SPM started from a DP-STM and has evolved into a QP-c-AFM. The QP-c-AFM, which can measure the potential distribution in a designated area with current flowing between two designated points, is an indispensable technology for the characterization of nanosystems such as neuromorphic networks. As future work, there are two targets. In nanosystems, the interaction among components is expected to change sensitively with environmental changes. Therefore, one target is that the development of an MP-SPM that can be operated under temperature control and atmosphere control is expected. The other target is about probes. It is also important for the MP-SPM to further reduce the accessible size. For that purpose, it

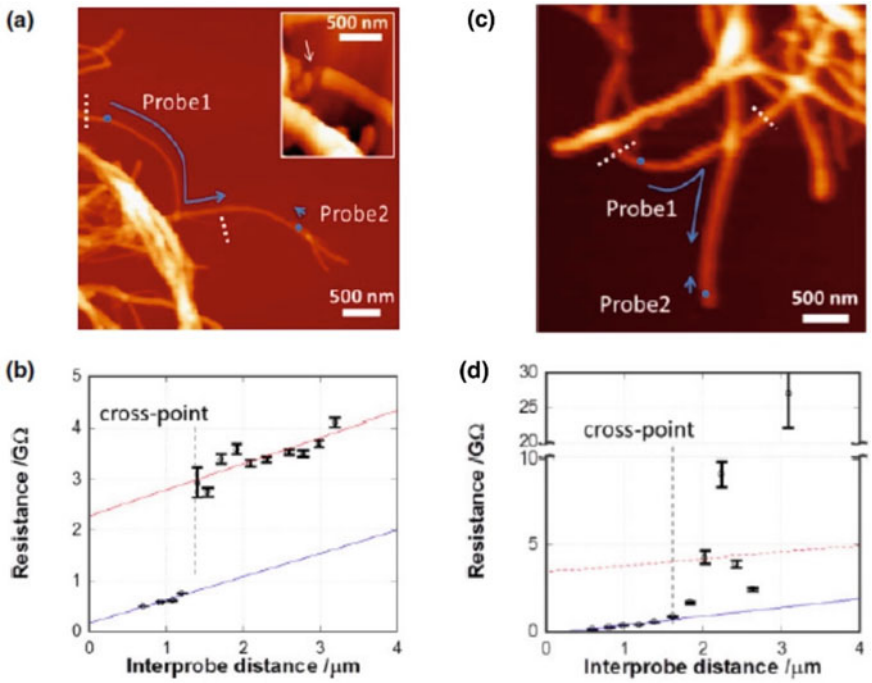

Fig. 8 **a** AFM image of PANI fibers including a crossing point. Probe 1 was shifted from the overlying fiber to the underlying fiber across the junction. White dashed lines in the image indicate the position where the fiber was cut using the probe before resistance measurement. The inset shows a AFM image of the cut fiber. **b** Resistance of PANI fibers with crossing point as a function of interprobe distance. **c** AFM image of PANI fibers including a crossing point. Probe 1 was shifted from the underlying fiber to the overlying fiber across the junction. **d** Resistance of PANI fibers with crossing point as a function of interprobe distance. Reproduced with permission from [37], Copyright (2016) The Japan Society of Applied Physics

is important to develop further sharper conductive nanoprobe that can be used for an SPM and electrical conductance measurement.

References

1. Binnig G, Rohrer H (1982) Scanning tunneling microscopy. Helv Phys Acta 55:726
2. Binnig G, Rohrer H, Gerber C, Weibel E (1983) 7×7 Reconstruction on Si(111) resolved in real space. Phys Rev Lett 50:120
3. Binnig G, Quate CF, Gerber C (1986) Atomic force microscope. Phys Rev Lett 5:930
4. Aono M, Jiang C-S, Nakayama T, Okuda T, Qiao S, Sakurai M, Thirstrup M, Wu Z-H (1998) How to measure the nanoscale physical properties of materials? Oyo Butsuri 67:1361
5. Okamoto H, Chen D (2001) An ultrahigh vacuum dual-tip scanning tunneling microscope operating at 4.2 K. Rev Sci Instrum 72:4398

6. Grube H, Harrison BC, Jia JF, Boland JJ (2001) Stability, resolution, and tip-tip imaging by a dual-probe scanning tunneling microscope. Rev Sci Instrum 72:4388
7. Watanabe H, Manabe C, Shigematsu T, Shimizu M (2001) Dual-probe scanning tunneling microscope: measuring a carbon nanotube ring transistor. Appl Phys Lett 78:2928
8. Shiraki I, Tanabe F, Hobara R, Nagao T, Hasegawa S (2001) Independently driven four-tip probes for conductivity measurements in ultrahigh vacuum. Surf Sci 493:633
9. Takami K, Akai-Kasaya M, Saito A, Aono M, Kuwahara Y (2005) Construction of independently driven double-tip scanning tunneling microscope. Jpn J Appl Phys 44:L120
10. Guise O, Marbach H, Yates JT, Jung M-C, Levy J, Ahner J (2005) Development and performance of the nanoworkbench: a four-tip STM for conductivity measurements down to submicrometer scales. Rev Sci Instrum 76:045107
11. Yi W, Kaya II, Altfeder IB, Appelbaum I, Chen DM, Narayanamurti V (2005) Dual-probe scanning tunneling microscope for study of nanoscale metal-semiconductor interfaces. Rev Sci Instrum 76:063711
12. Jaschinsky P, Coenen P, Pirug G, Voigtländer B (2006) Design and performance of a beetle-type double-tip scanning tunneling microscope. Rev Sci Instrum 77:093701
13. Xu JF, Thibado PM, Ding Z (2006) 4K, ultrahigh vacuum scanning tunneling microscope having two orthogonal tips with tunnel junctions as close as a few nanometers. Rev Sci Instrum 77:093703
14. Matsui A, Shigeta Y (2007) Development of probe-to-probe approach method for an independently controlled dual-probe scanning tunneling microscope. Rev Sci Instrum 78:106107
15. Kim T-H, Wang Z, Wendelken JF, Weitering HH, Li W, Li A-P (2007) A cryogenic Quadraprobe scanning tunneling microscope system with fabrication capability for nanotransport research. Rev Sci Instrum 78:123701
16. Cherepanov V, Zubkov E, Junker H, Korte S, Blab M, Coenen P, Voigtlander B (2012) Ultra compact multitip scanning tunneling microscope with a diameter of 50 mm. Rev Sci Instrum 83:033707
17. Onoe J, Nakayama T, Aono M, Hara T (2003) Structural and electrical properties of an electron-beam-irradiated C-60 film. Appl Phys Lett 82:595
18. Higuchi S, Kuramochi H, Laurent O, Komatsubara T, Machida S, Aono M, Obori K, Nakayama T (2010) Multiple-scanning-probe tunneling microscope with nanoscale positional recognition function. Rev Sci Instrum 81:073706
19. Satoh N, Tsunemi E, Miyato Y, Kobayashi K, Watanabe S, Fujii T, Matsushige K, Yamada H (2007) Multi-probe atomic force microscopy using piezoelectric cantilevers. Jpn J Appl Phys 46:5543
20. Tsunemi E, Satoh N, Miyato Y, Kobayashi K, Matsushige K, Yamada H (2007) Multi-probe atomic force microscopy with optical beam deflection method. Jpn J Appl Phys 46:5636
21. Voigtlander B, Cherepanov V, Korte S, Leis A, Cuma D, Just S, Lupke F (2018) Invited review article: multi-tip scanning tunneling microscopy: experimental techniques and data analysis. Rev Sci Instrum 89:101101
22. https://www.fz-juelich.de/pgi/pgi-3/EN/Forschung/Nanostructures/Multi_tip_STM_development/artikel.html
23. Cherepanov V, Coenen P, Voigtlander B (2012) A nanopositioner for scanning probe microscopy: the KoalaDrive. Rev Sci Instrum 83:023703
24. Dai H, Hafner JH, Rinzler AG, Colbert DT, Smalley RE (1996) Nanotubes as nanoprobes in scanning probe microscopy. Nature 384:147
25. Nishijima H, Kamo S, Akita S, Nakayama Y, Hohmura KI, Yoshimura SH, Takeyasu K (1999) Carbon-nanotube tips for scanning probe microscopy: preparation by a controlled process and observation of deoxyribonucleic acid. Appl Phys Lett 74:4061
26. Hafner JH, Cheung CL, Lieber CM (1999) Growth of nanotubes for probe microscopy tips. Nature 398:761
27. Barwich V, Bammerlin M, Baratoff A, Bennewitz R, Guggisberg M, Loppacher C, Pfeiffer O, Meyer E, Güntherodt H-J, Salvetat J-P, Bonard J-M, Forró L (2000) Carbon nanotubes as tips in non-contact SFM. Appl Surf Sci 157:269

28. Shimizu T, Tokumoto H, Akita S, Nakayama Y (2000) Stable atomic imaging of Si(111)-7× 7 surface by scanning tunneling microscope with carbon nanotube tip. Surf Sci 486:L455
29. Xu J, Shingaya Y, Zhao Y, Nakayama T (2015) In situ, controlled and reproducible attachment of carbon nanotubes onto conductive AFM tips. Appl Surf Sci 335:11
30. Konishi H, Murata Y, Wongwiriyapan W, Kishida M, Tomita K, Motoyoshi K, Honda S, Katayama M, Yoshimoto S, Kubo K, Hobara R, Matsuda I, Hasegawa S, Yoshimura M, Lee JG, Mori H (2007) High-yield synthesis of conductive carbon nanotube tips for multiprobe scanning tunneling microscope. Rev Sci Instrum 78:013703
31. Kubo O, Shingaya Y, Nakaya M, Aono M, Nakayama T (2006) Epitaxially grown WO_x nanorod probes for sub-100 nm multiple-scanning-probe measurement. Appl Phys Lett 88:254101
32. Shingaya Y, Nakayama T, Aono M (2004) Epitaxial growth of WO_x nanorod array on W(001). Sci Technol Adv Mater 5:647
33. Higuchi S, Kubo O, Kuramochi H, Aono M, Nakayama T (2011) A quadruple-scanning-probe force microscope for electrical property measurements of microscopic materials. Nanotechnology 22:285205
34. Nakayama T, Kubo O, Shingaya Y, Higuchi S, Hasegawa T, Jiang CS, Okuda T, Kuwahara Y, Takami K, Aono M (2012) Development and application of multiple-probe scanning probe microscopes. Adv Mater 24:1675
35. Nakayama T, Shingaya Y, Aono M (2016) Multiple-probe scanning probe microscopes for nanoarchitectonic materials science. Jpn J Appl Phys 55:1102A7
36. Giessibl FJ (2000) Atomic resolution on Si(111)-(7×7) by noncontact atomic force microscopy with a force sensor based on a quartz tuning fork. Appl Phys Lett 76:1470
37. Higuchi R, Shingaya Y, Nakayama T (2016) Resistance of single polyaniline fibers and their junctions measured by double-probe atomic force microscopy. Jpn J Appl Phys 55:08NB9

Large-Scale First-Principles Calculation Technique for Nanoarchitectonics: Local Orbital and Linear-Scaling DFT Methods with the CONQUEST Code

Tsuyoshi Miyazaki, Ayako Nakata, and David R. Bowler

1 Introduction

Detailed microscopic information of atomic and electronic structures is necessary to understand the unique functionalities or highly efficient properties of nanostructured devices or materials. First-principles calculations based on density functional theory (DFT) have been playing important roles in clarifying such information at the atomic scale for various materials [1], and they should be useful for investigating nanostructured materials. However, a DFT study of nanostructured materials is very difficult or almost impossible because of its computational cost.

The computational cost of conventional DFT methods, especially with the most widely used plane-wave basis set, is very high for large systems. There are two main reasons for this. First, we need many CPUs to employ large-scale DFT calculations, but the efficiency of plane-wave DFT calculations strongly depends on the performance of fast Fourier transforms (FFTs) and it is difficult to achieve high efficiency for FFTs on massively parallel supercomputers. Second, the computation time of usual DFT methods increases cubically with the number of atoms (N) in the target system. If we need to double the system size, the computation cost will increase by eight times.

Because of these difficulties, it is very expensive to treat systems of more than a thousand atoms by the conventional DFT methods. However, for the study of complex nanostructured materials, we often need to treat large systems containing many thousands of atoms. To realize DFT studies of complex nanostructured systems, we have

T. Miyazaki (✉) · A. Nakata · D. R. Bowler
International Center for Materials Nanoarchitectonics (WPI-MANA), National Institute for Materials Science (NIMS), 1-1 Namiki, Tsukuba 305-0044, Ibaraki, Japan
e-mail: MIYAZAKI.Tsuyoshi@nims.go.jp

T. Miyazaki · D. R. Bowler
Department of Physics and Astronomy, University College London (UCL), Gower Street, London WC1E 6BT, UK

Y. Wakayama and K. Ariga (eds.), *System-Materials Nanoarchitectonics*,
NIMS Monographs, https://doi.org/10.1007/978-4-431-56912-1_18

to overcome this size limitation in the DFT method. To achieve this goal, we have developed a large-scale DFT code, CONQUEST (Concurrent O(N) QUantum Electronic Structure Technique) [2–5]. The code is based on two calculation techniques: the local orbital method and the linear-scaling or O(N) method [6, 7]. It is also important that the code has a high parallel efficiency on massively parallel supercomputers. Using the code, we can realize DFT calculations for large systems consisting of many thousands of atoms and can treat systems having a length scale of 10–100 nm. In this chapter, we present an overview of the code and a brief explanation of the calculation methods, introduce the local orbital method called the multisite support function method, which is useful especially for large-scale metallic systems, show the parallel efficiency and possible system size using the linear-scaling method with the code, and present examples of first-principles molecular dynamics and electronic structure analysis, together with some applications of the code.

2 Calculation Methods Used in CONQUEST

In this section, we give an outline of the calculation methods used in CONQUEST.

Local orbitals (support functions) for Kohn–Sham orbitals and density matrix

In CONQUEST, Kohn–Sham orbitals (wave functions) or the Kohn–Sham density matrix is expressed by local orbitals called support functions $\phi_{i\alpha}$ (**r**), which are localized at each atom i with the orbital index α. The nth eigenfunction of the Kohn–Sham equation in DFT, i.e., the Kohn–Sham orbital ψ_n, is expressed using the support function,

$$\psi_n(\mathbf{r}) = \sum\nolimits_{i\alpha} c_n(i\alpha)\, \phi_{i\alpha}(\mathbf{r})$$

with the coefficients c_n ($i\alpha$).

In the linear-scaling method, the Kohn–Sham density matrix defined by

$$\rho(\mathbf{r}, \mathbf{r}') = \sum\nolimits_n f_n \psi_n(\mathbf{r}) \psi_n^*(\mathbf{r}')$$

is calculated without calculating $\{\psi_n\}$ explicitly. Using the support function $\phi_{i\alpha}$, this density matrix is expressed by

$$\rho(\mathbf{r}, \mathbf{r}') = \sum\nolimits_{i\alpha, j\beta} \phi_{i\alpha}(\mathbf{r}) K_{i\alpha, j\beta} \phi_{j\beta}^*(\mathbf{r}')$$

Here, K is the density matrix in the support function basis. The electron density is calculated from $\rho(\mathbf{r}, \mathbf{r})$, and the Kohn–Sham Hamiltonian $H_{i\alpha, j\beta}$ in the support basis and the total energy E_{DFT} within DFT can be calculated from the density

matrix ρ using the local density approximation (LDA) or the generalized gradient approximation (GGA).

In CONQUEST, the density matrix $K_{i\alpha,\,j\beta}$ can be calculated from the Kohn–Sham orbitals ψ_n, which are obtained by diagonalizing $H_{i\alpha,\,j\beta}$ with the computation time proportional to the cube of the number of atoms N or by the density matrix minimization (DMM) method [8] in the linear-scaling or O(N) mode, which is explained in the end of this section.

PAO basis set for support functions

Support functions are expressed by local basis sets. With the use of the pseudopotential technique, two types of local basis sets are provided in CONQUEST: B-splines on regular grids [9] and pseudo atomic orbitals (PAOs) [10]. The former basis set, called blips, has a considerable advantage because its accuracy can be improved systematically similarly to the plane-wave basis set. However, the number of basis functions is large, especially for hard pseudopotentials, and the cost of optimizing the support functions is high in some cases. On the other hand, with a PAO basis set, the number of basis functions required is normally much smaller than the number required with a blip basis set, and the cost of the calculations is lower. The PAO basis set consists of several numerical radial functions (ζ functions) and analytical spherical harmonic functions (s, p, d, …) for valence electrons. We often include additional functions called polarization functions, whose azimuthal quantum numbers are larger than those of valence orbitals. Although systematic improvement is difficult, the accuracy of the PAO basis set can be modified by increasing the number of basis functions. With the PAO basis functions of the orbital μ for atom i, $\{\chi_{i\mu}(\mathbf{r})\}$, support functions are expressed by

$$\phi_{i\alpha}(\mathbf{r}) = \sum\nolimits_{\mu} b_{i\alpha}(\mu)\chi_{i\mu}(\mathbf{r})$$

with the coefficients $b_{i\alpha}(\mu)$.

CONQUEST can use the pseudopotentials and PAOs generated by the Siesta code [11, 12]. In addition, we have recently developed our own code to generate the PAO basis sets compatible with the norm-conserving pseudopotentials made by the ONCVPSP code [13, 14]. As a result, freely available pseudopotential databases such as PseudoDojo [15] and SG15 [16], which were obtained by the ONCVPSP code, can be used in CONQUEST. We have recently reported tests of PAO basis sets obtained using the PAO generation code in CONQUEST with the PseudoDojo pseudopotentials, and compared the results with the fully converged plane-wave results [17]. The results show that the large PAO basis set (triple ζ with triple polarization functions (TZTP) or sometimes even double ζ with single polarization functions (DZP)) can be as accurate as the converged plane-wave calculations for most systems.

It is important that the large PAO basis sets having multiple ζ functions are sufficiently accurate. However, if each PAO is used as a support function as in many other local orbital DFT codes ($b_{i\alpha}(\mu) = 1$ for $\mu = \alpha$; otherwise 0), the cost of the calculations increases proportionally to the cube of the number of PAOs in either

diagonalization or the linear-scaling mode. If we use many ζ functions, the cost can be very high even with the PAO basis set. In the next section, we introduce the "multi-site method" used in CONQUEST to solve this problem. By this method, we can reduce the number of support functions to a minimal basis set size while keeping the accuracy of the primitive multiple-ζ basis set [18, 19].

Linear-scaling or O(N) method

In the linear-scaling or O(N) mode, we use the density matrix minimization (DMM) method, which was proposed by Li, Nunes, and Vanderbilt [8]. As in other linear-scaling methods, this method also uses the locality of the density matrix, which depends on the properties of the electronic structure. If the electronic structure has an energy gap, the amplitude of the matrix element $K_{i\alpha,\,j\beta}$ decays exponentially with the distance between two atoms i and j.

In the DMM method, we first introduce the auxiliary density matrix L to satisfy the idempotency ($\rho^2 = \rho$), where we express the real density matrix K as

$$K = 3LSL - 2LSLSL,$$

to make use of purification transformation of McWeeny [20]. Here, S is the overlap matrix between support functions. Owing to the purification transformation, if the matrix L is close to idempotency, K is closer to idempotency than L. To use the locality of the density matrix, we introduce a cutoff R_L for the matrix elements of L, that is,

$$L_{i\alpha,\,j\beta} = 0 \text{ when } R_{i,\,j} > R_L,$$

where $R_{i,\,j}$ is the distance between two atoms i and j. Then, the matrix L becomes sparse and the nonzero elements of L are calculated to minimize the DFT total energy using minimization techniques, such as a residual minimization method. More details of the method were explained in our previous papers [3–5]. Considering the near-sightedness principle [21], the value of R_L for accurate calculations should not depend on the system size, and thus the number of nonzero elements of $L_{i\alpha,\,j\beta}$ is only proportional to N.

One of the important advantages of the DMM method is that it satisfies a variational principle, and the accuracy of the method can be controlled solely by changing R_L. A comparison of the total energy between the exact diagonalization and DMM methods is shown in Fig. 1 for a Si(001) surface. Note that, in most cases, we only need the difference in the total energy of two or more structures. Thus, we can expect error cancellation, and sufficient accuracy is obtained with a relatively small R_L. For example, the cutoff of 8.5 Å is satisfactory for Si surface systems. The accuracy in the study of strained Ge systems was investigated in Ref. [22] for Ge/Si systems.

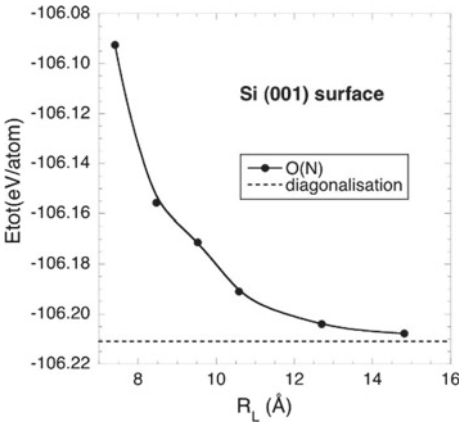

Fig. 1 Cutoff dependence of the total energy of a silicon surface, Si(001) calculated by the O(*N*) method. The energy calculated by the exact diagonalization technique is also shown by the dotted line

3 Accurate and Efficient Local Orbital Method in CONQUEST

As mentioned in the last section, we have to increase the number of ζ functions in the PAO basis set if we need to perform very accurate calculations. In such cases, the cost of the calculations increases significantly since the computation time and memory requirements scale with the cube and square of the basis size, respectively. This is one of the reasons why the local-orbital DFT calculations of relatively large systems (say, 1,000–10,000 atom systems) are already very expensive. This problem can be overcome by the recently developed multi-site support function (MSSF) method, which was originally proposed by Rayson and Briddon [23], and CONQUEST uses this method with some modification [18, 19]. In this method, while keeping the accuracy of original (or primitive) multiple-ζ basis set calculations, we can reduce the number of support functions to the same size as a minimal basis set. The cost of the calculations is thus considerably reduced by this method.

In the MSSF method, support functions for each atom are expressed by a linear combination of not only the PAOs belonging to the target atom but also those of the neighbor atoms,

$$\phi_{i\alpha}(\mathbf{r}) = \sum_k \sum_{\mu \in k} b_{i\alpha}(k\mu)\chi_{k\mu}(\mathbf{r})$$

Here, $\chi_{k\mu}$ $(\mathbf{r})$ is the PAO of the orbital μ for atom k, and the summation on k runs over neighbor atoms that are within the cutoff (r_{SF}) region from the target atom i. The coefficients $b_{i\alpha}$ $(k\mu)$ can be determined using the local filter diagonalization (LFD) method [18, 23] or the numerical optimization method [19]. In the LFD method, we first consider the local region near the target atom, defined by the cutoff r_{LFD}, which is equal to or larger than r_{SF}. Then, we construct and diagonalize the local Hamiltonian corresponding to the region, and generate the MSSF using the obtained occupied eigen orbitals through a projection technique.

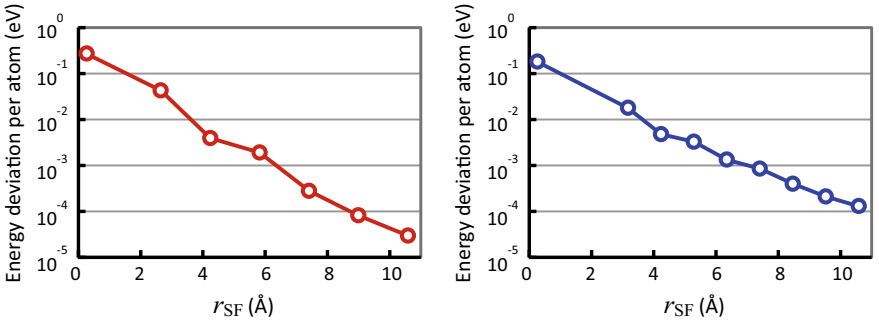

Fig. 2 Deviation of total energy per atom of **a** crystalline Si and **b** Al with the MSSF method from the primitive PAO results with respect to the cutoff for the support functions r_{SF}. In these calculations, the cutoff of LFD is set to $r_{SF} = r_{LFD}$. Modified with permission from Ref. [18]. Copyright (2014) American Chemical Society

Using the obtained MSSF, the electronic structure of the whole system is calculated by the exact diagonalization or O(N) method. This procedure is iterated until the self-consistent charge density is obtained. The accuracy of the method depends on r_{SF} and r_{LFD}. One of the advantages is that the error of the method decreases exponentially with the increase in the cutoffs for both insulating (or semiconducting) and metallic systems. Figure 2a, b show the r_{SF} dependence of the energy difference between the MSSF and the primitive (original) PAO calculations for crystalline silicon and aluminum systems, respectively. We can see that the difference decreases exponentially with increasing r_{SF} in both cases.

With the LFD method, the energy deviation of the MSSF calculation from the primitive PAO result is large for small r_{SF}. However, if we determine the coefficients by the numerical optimization method, the accuracy of the MSSF with small r_{SF} is significantly improved, meaning that we can reduce r_{SF} for accurate calculations. The energy–volume curve obtained by the numerical optimization and LFD methods is shown in Fig. 3 for crystalline silicon, and we can see that even for an MSSF with small r_{SF} (5.0 bohr), the optimized volume is almost the same as the result obtained by primitive PAO calculation.

When the electronic structure is calculated by diagonalizing the Hamiltonian matrix $H_{i\alpha,\,j\beta}$, the diagonalization is the most expensive part for large systems. In the calculations using the TZDP (three ζ functions for s and p, and two polarization functions for d) basis set for Si systems, for example, the number of support functions for each atom can be reduced from 22 to 4 by the MSSF method. Then, we can reduce the computation time of the diagonalization part by about $(22/4)^3 \sim 166$ times. Although we need the procedure to calculate the support functions for each atom, its cost is basically negligible when treating large systems. In addition, the part of calculating the MSSF can be parallelized very efficiently.

Using this advantage of the MSSF method, we can perform accurate DFT calculations of relatively large and complex systems, even by the exact diagonalization method. One of the examples is a corrugated graphene on a Rh(111) surface [24],

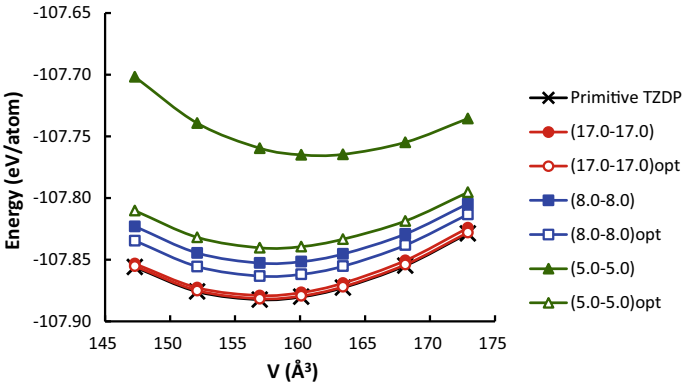

Fig. 3 Energy–volume curve of crystalline Si, calculated by primitive TZDP PAO basis (black line with crosses) and MSSF calculations (lines with circles, squares, and triangles). For the MSSF calculations, the results by LFD and numerical optimization methods are shown by closed and open symbols, respectively. We used the same cutoffs for r_{SF} and r_{LFD} in these calculations, and they are 5.0 (triangles), 8.0 (squares), and 17.0 (circles) bohr. Reproduced from Ref. [19] with permission from the PCCP Owner Societies

shown in Fig. 4, containing 3,088 atoms. We calculated the electronic structure of the system by the MSSF method using 36 nodes of the supercomputer SGI ICE X (Intel Xeon E5-2680V3 (12 cores, 2.5 GHz) × 2 and 128 GB memory per node) at NIMS. The computation time was about 66 times faster than those of primitive PAO (rhodium: DZP, carbon: TZDP) calculations using 72 nodes. Furthermore, for a smaller graphene on the Rh (111) surface system, we also calculated the density of states using the MSSF and primitive PAO methods, and compared them with the plane-wave results. We found that both the MSSF and primitive PAO results agree

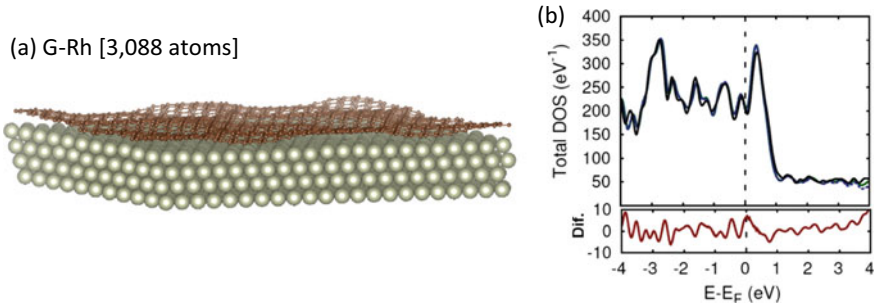

Fig. 4 **a** Structure of corrugated graphene on Rh (111). **b** Upper panel: Density of states determined by primitive PAO (green solid line), MSSF (blue dotted line), and plane-wave (black lines) calculations. Plane-wave calculations were carried out using the VASP code. Lower panel: Difference in the DOS between primitive PAO and MSSF calculations. (**b** is from Ref. [24] (https://doi.org/10.1088/1361-648X/aaec4c).)

very well with the plane-wave results, meaning that the MSSF calculations are quite accurate (Fig. 4b).

The MSSF method is powerful for relatively large systems, even without using the linear-scaling method. We can treat systems containing several thousand atoms if we are able to use about 100 CPU nodes. The diagonalization method can be applied to metallic systems as well as semiconducting or insulating systems.

4 Million-Atom DFT Calculations Using a Linear-Scaling Method

Although the MSSF method is powerful for large-scale DFT calculations, the computation time is still proportional to the cube of the number of atoms if the method is used with the exact diagonalization technique. For systems containing more than 10,000 atoms, we need to use a linear-scaling method.

As the DMM method in the linear-scaling mode uses the locality of the electronic structure, it also has an advantage in terms of parallelization efficiency. Figure 5 shows the wall-clock time to calculate the density matrix and atomic forces of crystalline silicon with various sizes [25]. The calculations were carried out on the K computer, which was the fastest supercomputer in the top 500 list [26] in 2011 (June and November), having 88,128 CPUs and more than 700,000 cores (each CPU had eight cores). The lines in Fig. 5 show the wall-clock time when the number of atoms per core is fixed. This data shows so-called weak-scaling parallel efficiency. On the other hand, we can determine strong parallel efficiency by comparing the timings of

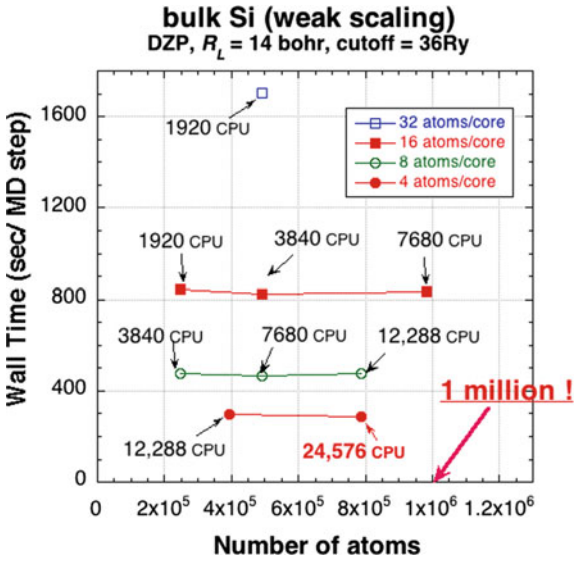

Fig. 5 Wall-clock time to calculate the density matrix (electronic structure) and atomic forces of crystalline Si having various numbers of atoms, using different numbers of CPUs of the K computer. The number of CPUs used for each calculation is also shown in the graph. Each line shows the wall-clock time of calculations having the same number of atoms per core (Ref. [25])

different lines. This comparison shows how we can reduce the wall-clock time for the calculations of the same system by increasing the number of CPUs.

In the test of weak-scaling parallel efficiency in Fig. 5, we can see that the wall-clock time does not change when increasing the system size. Even when we double the system size, the wall-clock time is almost the same if we use twice the number of CPUs. This result first indicates that the computational cost using the linear-scaling method is proportional to the number of atoms. Second, the ideal weak-parallel efficiency is achieved even when using such a large number of CPUs (about 25,000 CPUs or 200,000 cores). Strong scaling parallel efficiency is also good if there are at least four atoms per core. Finally, it is worth noting that the wall clock time for the 786,432-atom system using 24,576 CPUs is only 289.0 s. Considering the ideal weak-scaling parallel efficiency, one step of MD or structure relaxation in the DFT calculation on a million-atom system should be shorter than five minutes if we will use more than about 32,000 CPUs. We can conclude that one million atom DFT calculations are now possible with the CONQUEST code.

Using this capability of CONQUEST, we performed a theoretical study of Ge 3D nanoscale islands on a Si(001) surface, including structure relaxation [27, 28]. One of the biggest systems that we calculated is shown in Fig. 6a, which contains about 200,000 atoms. In this study, to investigate the initial process in the formation of new facets during the growth of the 3D nanoscale island, we calculated the energy of a single Ge dimer adsorbed at various positions on the facets of the island. The results suggest that (i) the adsorption energy depends on the adsorption site, (ii) the top or edges of the facets are more stable sites, and (iii) the higher sites are more favorable than the lower sites. We also calculated the total energy of the structures with imperfect facets and those with two and three adsorbed dimers, and discussed the initial process in the growth of the 3D nanostructure, which is very difficult to observe experimentally (for more details, see Ref. [28]).

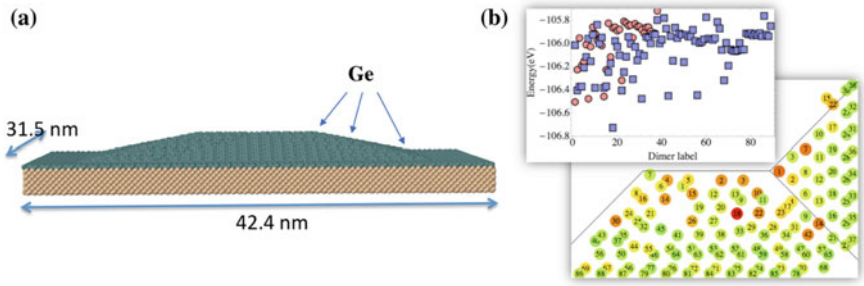

Fig. 6 **a** Largest system whose atomic positions were optimized in our linear-scaling DFT study of Ge 3D islands on a Si(001) surface. It contains about 200,000 atoms with a substrate area of 31.5 × 42.4 nm^2. **b** bottom: Adsorption energy map of single Ge dimers adsorbed on the {105} facets. The disks show the position of a given dimer on a facet projected on the *x*–*y* plane. The dimers are labeled according to their height. The adsorption energy of dimers increases from red to green. top: Energy values of single Ge dimers on small (circles) and large (rectangles) facets (Ref. [29])

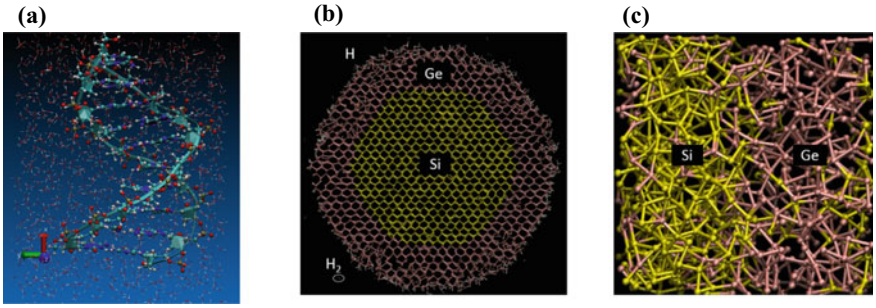

Fig. 7 Snapshots of the linear-scaling first-principles MD. **a** DNA in water from the NVE simulation, **b** Si/Ge core–shell nanowire [34], and **c** interface of Si/Ge. The MD simulations for (**b**) and (**c**) were NVT simulations at 3,000 K using the Nose–Hoover chain method (Refs. [29, 32])

5 Molecular Dynamics with CONQUEST

Considering the O(N) method mentioned above, we expect that first-principles molecular dynamics (FPMD) simulations based on the linear-scaling DFT methods can be realized for large and complex nanoscale materials. However, we observed a problematic energy drift in the MD simulations if the density matrix was not strictly optimized. Owing to this problem, it was difficult to perform efficient and accurate MD simulations by the O(N) method. We solved this problem [30] by combining the DMM method with the extended Lagrangian Born–Oppenheimer molecular dynamics (XLBOMD) method proposed by Niklasson [31]. We investigated the reliable calculation conditions in constant energy (NVE) simulations and demonstrated that it is possible to perform practical, reliable self-consistent FPMD simulations of large systems containing more than 10,000 atoms. We applied this method to 32,768-atom bulk silicon [30] and ten base pairs of a DNA molecule in water [32] (Fig. 7a) and observed that the constant of motion in the NVE calculations was almost perfectly conserved, which indicates that these MD simulations were fairly accurate. The method was extended to the case of constant temperature (NVT) simulations [33], and recently, to constant pressure–constant temperature (NPT) simulations. We have recently applied this method to Si/Ge core–shell nanowires (introduced in Sect. 2.3), Si/Ge interfaces, and the modeling of an amorphous structure.

6 Electronic Structure Analysis

So far, we have shown that the CONQUEST code can be used to perform reliable and accurate structure optimization or MD simulations of very large systems using the MSSF and/or linear-scaling methods. After we determine the self-consistent charge density for the optimized structure, or some important snapshot structures during

the MD, it is often useful or necessary to analyze the eigenvalues (band energy) and Kohn–Sham wave functions near the Fermi level, as in the usual DFT calculations.

However, the MSSF method, especially when the MSSFs are calculated by numerical optimization, may not have good accuracy for the unoccupied states. This is because MSSFs are optimized only for the accurate description of occupied Kohn–Sham orbitals or the density matrix. However, even in such cases, the calculated ground-state charge density obtained by the MSSF method is accurate and we can evaluate the Hamiltonian matrix with the primitive PAO basis set using the charge density. We have recently shown [35] that, for this sparse Hamiltonian matrix, we can use an efficient interior eigenproblem solver called the Sakurai–Sugiura (SS) method [36] and can calculate the eigenvalues and eigenfunctions in a given energy window. Here, we show the performance of this method for the hydrated DNA system, shown in the final section (Fig. 7a).

By following the procedure explained above, the accuracy of the unoccupied states can be recovered. The red line in Fig. 8a shows the DOS calculated by the SS method using the Hamiltonian matrix, which is evaluated using the charge density obtained in the MSSF calculation, with the primitive PAO basis set. We can see

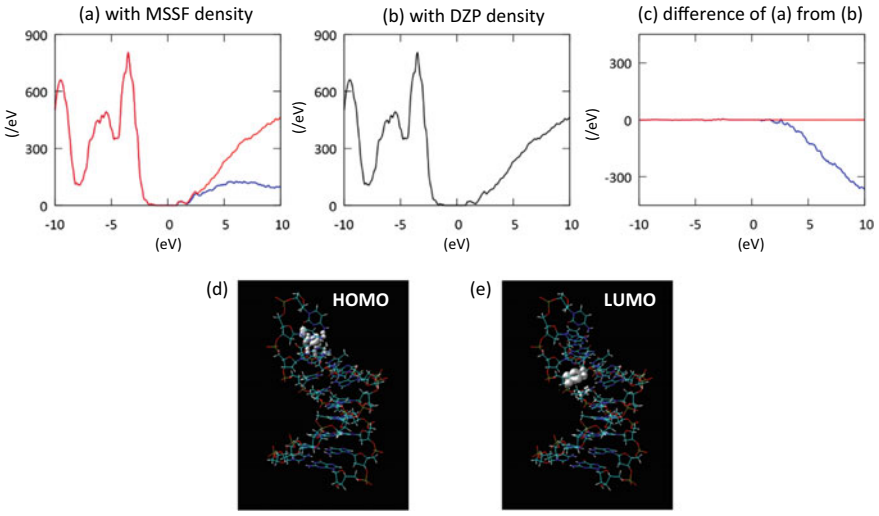

Fig. 8 **a** Density of states (DOS) of the hydrated DNA system calculated with the MSSFs (blue line), although the data in the occupied region (<0 eV) are covered by the red line. **b** DOS calculated using the primitive DZP PAO basis set. The difference between these results is shown in (**c**) with the blue line. We can see that while the difference in the occupied states is very small (the fractional difference is around 0.001), it becomes much larger in higher-lying unoccupied states. The red line in (**a**) shows the DOS calculated by the Sakurai–Sugiura method using the Hamiltonian with the primitive PAO basis, but the matrix elements are evaluated using the charge density obtained by the MSSF calculation. The difference in the DOS, i.e., the difference between the red lines in (**a**) and (**b**), is shown by the red line in (**c**), which is very small in the whole energy range. **d** and **e** Distributions of the HOMO and LUMO of the hydrated DNA system, respectively. Reprinted with permission from Ref. [35]. Copyright (2017) American Chemical Society

that the DOS of the red line in Fig. 8a is almost the same as that of the primitive PAOs (Fig. 8b), which can be confirmed by the red line shown in Fig. 8c, which is the difference between these two DOSs. This demonstrates the high accuracy of the charge density calculated by the MSSF method and that of the eigenvalues calculated by the SS method. Figure 8d, e show the HOMO and LUMO distributions of the hydrated DNA system calculated by the SS method, respectively. We confirmed that the energy levels and distributions of molecular orbitals determined by the SS method are almost the same as those determined by the primitive PAO calculations (Ref. [35]). Note that the dimension of the reconstructed Hamiltonian in the primitive PAO basis (27,883 for the DNA system) is much larger than that of the Hamiltonian in the MSSF basis (7,447). The diagonalization in the primitive PAO basis is often difficult even if it is possible in the MSSF basis. Thus, the combination of MSSF and SS methods is a very useful technique to calculate the unoccupied states accurately and efficiently.

On the other hand, in the case of linear-scaling calculations, no eigenvalues or Kohn–Sham orbitals are calculated during the structure relaxation or MD. However, again using the SS method, we can calculate them near the Fermi level as a postprocess analysis of the linear-scaling DFT calculations.

Using this technique, we can analyze the electronic structure of nanoscale materials [35]. Figure 9 shows the electronic structure near the Fermi level of the Ge 3D nanoisland on a Si(001) substrate containing 23,737 atoms. The electron distribution shown in Fig. 9 is the sum of the squares of the eigenstates (orbital density) in the energy window [−0.01: +0.02] eV around the Fermi level. Here, we first calculated the Kohn–Sham Hamiltonian using the self-consistent charge density obtained for the optimized atomic positions. During the structure optimization, we need to calculate the self-consistent charge density and atomic forces many times, which is possible only by the linear-scaling method. On the other hand, a one-shot calculation is enough for the calculation of eigenstates. Even a one-shot calculation is extremely difficult with standard, exact diagonalization techniques for such large systems. However, it is possible by the SS method. For the system shown in Fig. 9, the computation time was 146 s when using 64 CPUs of the K computer. Furthermore, we also calculated the eigenstates of the much larger system shown in Fig. 6a, containing about 200,000

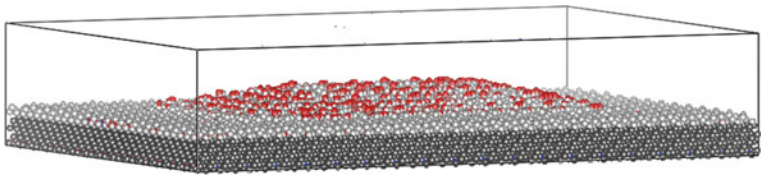

Fig. 9 Distribution of the electron density obtained from the eigen orbitals near the Fermi level [−0.01 eV: +0.02 eV] of the Ge hut cluster on a Si(001) substrate. The isosurface with the density of 2×10^{-4} (electron/bohr^3) is drawn in red. The area of the substrate is 15.2×20.6 nm^2 and the system contains 23,737 atoms. The Kohn–Sham Hamiltonian was evaluated with the SZP basis set using the self-consistent charge density, which was obtained by a linear-scaling DFT method using CONQUEST (Ref. [29])

atoms using 6,400 CPUs of the K computer; the computation time was 2,399 s. By such analyses of the eigenstates, we can examine the physical and material properties, such as the electron transport and optoelectronic properties, of very large nanoscale systems.

7 Summary

Owing to the size restrictions of conventional methods, it has been impossible until now to study large, complex nanostructured systems with length scales over 10 nm using DFT. However, using our linear-scaling DFT code CONQUEST, we can now perform DFT calculations on realistic models of systems with similar sizes to those studied experimentally. We have performed DFT studies of 3D Ge nanoislands on a Si substrate [27, 28], Si/Ge and Ge/Si core–shell nanowires [34, 37], complex biological systems [32, 38], metallic nanoparticles [39], and others [40]. The code has recently been released publicly with the open-source MIT license [41]. We hope that it will contribute significantly to future research on nanostructured materials and towards the implementation of nanoarchitectonics.

Acknowledgements The results for Si/Ge systems shown in this paper were obtained in collaboration with Dr. J. Lin and Dr. S. Arapan. The development of the CONQUEST code is performed jointly by the groups of University College London (Prof. D. R. Bowler), National Institute for Materials Science (first-principles simulation group), and University of Bordeaux (Dr. L. Truflandier). The electronic structure analyses using the Sakurai–Sugiura method were carried out in collaboration with Dr. Y. Futamura and Prof. T. Sakurai at the University of Tsukuba. For the study of Si/Ge or Ge/Si core-shell nanowires, we acknowledge Dr. N. Fukata for fruitful discussions.

This work was supported by "World Premier International Research Center Initiative (WPI Initiative) on Materials Nanoarchitectonics", JSPS Grants-in-Aid for Scientific Research (Grant Numbers 26246021, 15H01052, 17H05224, and 18H01143), and by the Priority Issue 7 "Creation of new functional devices and high-performance materials to support next-generation industries (CDMSI)" in the social and scientific priority issues to be tackled by using the post-K computer and "Exploratory Challenge on Post-K computer" by MEXT, Japan. Calculations were performed on the Numerical Materials Simulator at NIMS, the supercomputer HA8000 system at Kyushu University, and by using the computational resources of the K computer provided by the RIKEN Advanced Institute for Computational Science through the HPCI System Research project (Project IDs: hp160129, hp170264, hp180175, hp180226, and hp190096).

References

1. Martin RM (2004) Electronic structure: basic theory and practical methods. Cambridge University Press
2. http://www.linear-scaling.org
3. Hernández E, Gillan MJ, Goringe CM (1996) Linear-scaling density-functional-theory technique: the density-matrix approach. Phys Rev B 53:7147

4. Bowler DR, Miyazaki T, Gillan MJ (2002) Recent progress in linear scaling *ab initio* electronic structure techniques. J Phys: Condens Matter 14:2781
5. Bowler DR, Choudhury R, Gillan MJ, Miyazaki T (2006) Recent progress with large-scale ab initio calculations: the CONQUEST code. Phys Status Solidi B 243:989
6. Goedecker S (1999) Linear scaling electronic structure methods. Rev Mod Phys 71:1085
7. Bowler DR, Miyazaki T (2012) *O*(*N*) methods in electronic structure calculations. Rep Prog Phys 75:036503
8. Li XP, Nunes RW, Vanderbilt D (1993) Density-matrix electronic-structure method with linear system-size scaling. Phys Rev B 47:10891
9. Hernandez E, Gillan MJ, Goringe CM (1997) Basis functions for linear-scaling first-principles calculations. Phys Rev B 55:13485
10. Torralba AS, Todorović M, Brázdová V, Choudhury R, Miyazaki T, Gillan MJ, Bowler DR (2008) Pseudo-atomic orbitals as basis sets for the *O*(*N*) DFT code CONQUEST. J Phys: Condens Matter 20:294206
11. https://departments.icmab.es/leem/siesta/
12. Soler JM, Artacho E, Gale JD, García A, Junquera J, Ordejón P, Sánchez-Portal D (2002) The SIESTA method for *ab initio* order-*N* materials simulation. J Phys: Condens Matter 14:2745
13. http://www.mat-simresearch.com
14. Hamann DR (2013) Optimized norm-conserving Vanderbilt pseudopotentials. Phys Rev B 88:085117
15. http://www.pseudo-dojo.org
16. http://www.quantum-simulation.org/potentials/sg15_oncv/
17. Bowler D, Baker J, Poulton J, Mujahed S, Lin J, Yadav S, Raza Z, Miyazaki T (2019) Highly accurate local basis sets for large-scale DFT calculations in conquest. Jpn J Appl Phys 58:100503
18. Nakata A, Bowler DR, Miyazaki T (2014) Efficient calculations with multisite local orbitals in a large-scale DFT code CONQUEST. J Chem Theory Comput 10:4813
19. Nakata A, Bowler DR, Miyazaki T (2015) Optimized multi-site local orbitals in the large-scale DFT program CONQUEST. Phys Chem Chem Phys 17:31427
20. McWeeny R (1960) Some recent advances in density matrix theory. Rev Mod Phys 32:335
21. Kohn W (1996) Density functional and density matrix method scaling linearly with the number of atoms. Phys Rev Lett 76:3168
22. Miyazaki T, Bowler DR, Choudhury R, Gillan MJ (2007) Density functional calculations of Ge(105): local basis sets and *O(N)* methods. Phys Rev B 76:115327
23. Rayson MJ, Briddon PR (2009) Highly efficient method for Kohn-Sham density functional calculations of 500–10000 atom systems. Phys Rev B 80:205104
24. Romero-Muñiz C, Nakata A, Pou P, Bowler DR, Miyazaki T, Pérez R (2018) High-accuracy large-scale DFT calculations using localized orbitals in complex electronic systems: the case of graphene-metal interfaces. J Phys: Condens Matter 30:505901
25. Arita M, Arapan S, Bowler DR, Miyazaki T (2014) Large-scale DFT simulations with a linear-scaling DFT code CONQUEST on K-computer. J Adv Simul Sci Eng 1:87
26. http://www.top500.org
27. Miyazaki T, Bowler DR, Gillan MJ, Ohno T (2008) The energetics of hut-cluster self-assembly in Ge/Si(001) from linear-scaling DFT calculations. J Phys Soc Jpn 77:123706
28. Arapan S, Bowler DR, Miyazaki T, A linear scaling DFT study of the growth of a new {105} facet layer on a Ge hut cluster. arXiv:1510.00526
29. Miyazaki T (2018) Large-scale DFT study of Ge/Si 3D nanoislands and core-shell nanowires. ECS Trans 86:269
30. Arita M, Bowler DR, Miyazaki T (2014) Stable and efficient linear scaling first-principles molecular dynamics for 10000+ atoms. J Chem Theory Comput 10:5419
31. Niklasson AMN (2008) Extended Born-Oppenheimer molecular dynamics. Phys Rev Lett 100:123004
32. Otsuka T, Taiji M, Bowler DR, Miyazaki T (2016) Linear-scaling first-principles molecular dynamics of complex biological systems with the Conquest code. Jpn J Appl Phys 55:1102B1

33. Hirakawa T, Suzuki T, Bowler DR, Miyazaki T (2017) Canonical-ensemble extended Lagrangian Born–Oppenheimer molecular dynamics for the linear scaling density functional theory. J Phys: Condens Matter 29:405901
34. Lin J, Bowler DR, Miyazaki T, in preparation
35. Nakata A, Futamura Y, Sakurai T, Bowler DR, Miyazaki T (2017) Efficient calculation of electronic structure using O(N) density functional theory. J Chem Theory Comput 13:4146
36. Sakurai T, Sugiura H (2003) A projection method for generalized eigenvalue problems using numerical integration. J Comput Appl Math 159:119
37. O'Rourke C, Mujahed SY, Kumarasinghe C, Miyazaki T, Bowler DR (2018) Structural properties of silicon–germanium and germanium–silicon core–shell nanowires. J Phys: Condens Matter 30:465303
38. Todorovi M, Bowler DR, Gillan MJ, Miyazaki T (2013) Density-functional theory study of gramicidin A ion channel geometry and electronic properties. J R Soc Interface 10:20130547
39. Nakata A, Miyazaki T, in preparation
40. Li Y, Buerkle M, Li G, Rostamian A, Wang H, Wang Z, Bowler DR, Miyazaki T, Xiang L, Asai Y, Zhou G, Tao N (2019) Gate controlling of quantum interference and direct observation of anti-resonances in single molecule charge transport. Nat Mater 18:357
41. https://github.com/OrderN/CONQUEST-release

Machine Learning Approaches in Nanoarchitectonics

Ryo Tamura and Gaku Imamura

1 Introduction

Recently, diverse fields in materials science, including nanoarchitectonics, have shown interest in materials informatics, which is an emerging approach that utilizes machine learning (ML) for materials research. If ML technique is applied to materials dataset, for example, optimizing to obtain the desired property, predicting of physical quantities, understanding of materials, and upgrading of measurement technologies can be realized (Fig. 1). Researches on ML methods started around 1950s, and various methods have been developed so far [1]. ML methods can be roughly divided into two categories: unsupervised learning and supervised learning. Unsupervised learning uses only features (explanatory variables) of given training data to extract the underlying data structure. This category includes clustering and dimensionality reduction. On the other hand, supervised learning searches for a function to express the relationship between features (explanatory variables) and labels (objective variables). This category includes classification and regression. In materials science, features are often determined by composition of elements, structure of materials, and process of manufacturing, and the label is the parameter to be predicted such

R. Tamura (✉) · G. Imamura
International Center for Materials Nanoarchitectonics (WPI-MANA), National Institute for Materials Science (NIMS), 1-1 Namiki, Tsukuba 305-0044, Ibaraki, Japan
e-mail: TAMURA.Ryo@nims.go.jp

R. Tamura
Research and Services Division of Materials Data and Integrated System (MaDIS), National Institute for Materials Science (NIMS), 1-1 Namiki, Tsukuba 305-0044, Ibaraki, Japan

Graduate School of Frontier Sciences, The University of Tokyo, 5-1-5 Kashiwa-no-ha, Kashiwa 277-8561, Chiba, Japan

G. Imamura
Graduate School of Information Science and Technology, Osaka University, 1-5 Yamadaoka, Suita 565-0871, Osaka, Japan

Y. Wakayama and K. Ariga (eds.), *System-Materials Nanoarchitectonics*,
NIMS Monographs, https://doi.org/10.1007/978-4-431-56912-1_19

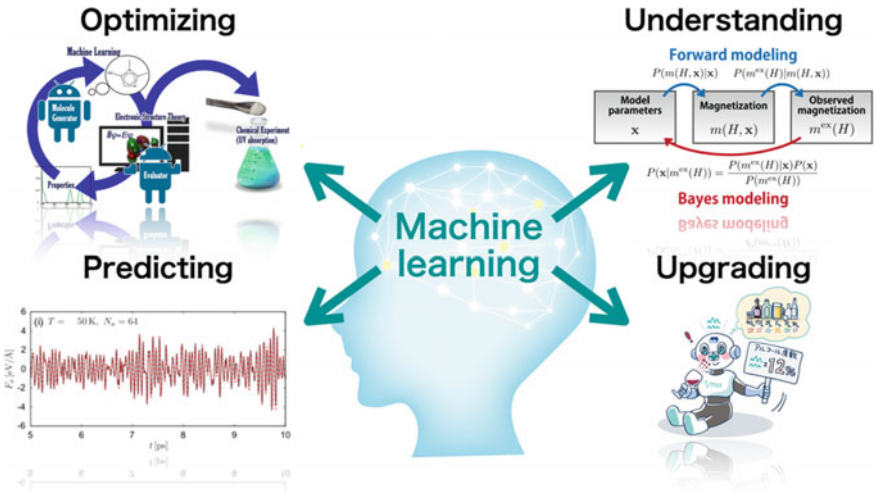

Fig. 1 Roles of machine learning in materials science. The optimization, prediction, understanding, and upgrading in materials science can be realized with the aid of machine learning

as physical property. Although both categories of ML methods are applicable to materials science, supervised learning is more likely to be used than unsupervised learning because most of materials informatics studies aim to predict the properties of unknown materials. In fact, in all topics covered in this chapter, supervised learning method is utilized.

In this chapter, we will introduce studies using ML for materials nanoarchitectonics. The following four topics will be discussed: (i) design of functional molecules based on artificial intelligence as an example of optimization by ML, (ii) effective model estimation of magnetic materials by Bayesian statistics as an example of understanding by ML, (iii) efficient estimation of the force field by ML as an example of prediction, and (iv) upgrading of gas sensor systems that utilize ML. Finally, we will discuss the perspective of materials science combined with ML.

2 Novel Organic Molecule Development Based on Artificial Intelligence

Computational techniques for automatically generating molecules with desired properties have been attracting much attention. The recent development of artificial intelligence (AI) technology by deep learning—an ML method based on multilayer neural networks—has enabled computers to learn complex rules of molecules automatically [2–5]. Sumita, Ishihara, Tamura, and colleagues prepared an AI-assisted chemistry platform to discover new photofunctional molecules (Fig. 2) [6]. Photofunctional organic molecules have received attention in green chemistry and molecular sensing.

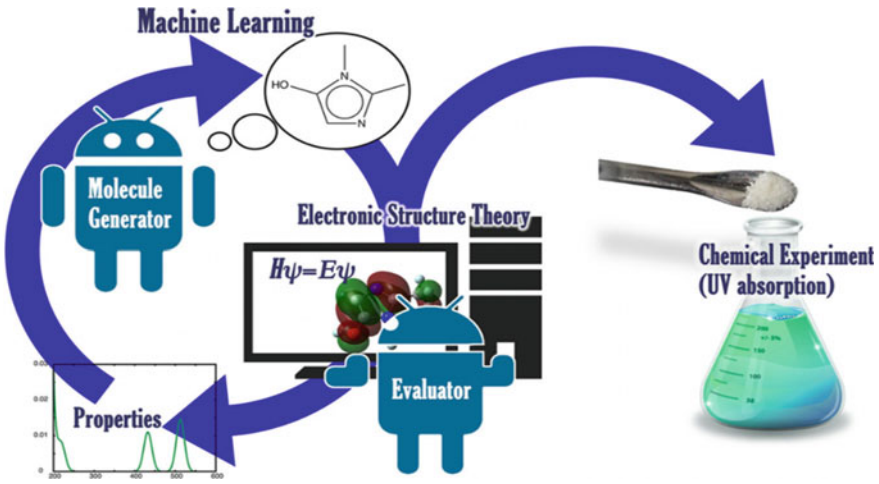

Fig. 2 Schematic of an AI-assisted chemistry platform to discover new functional molecules. (Reprinted from [6], Copyright 2018, with permission from American Chemical Society)

In these molecules, light induces transition between electronic states. If molecules with the desired level of excited states from their ground states can be designed, these can be used in various applications such as organic light-emitting diodes, organic photovoltaic cells, photofunctional sensors, and UV filters. Our prepared platform consists of ChemTS (a molecule generator) [7] and GAUSSIAN (a density functional theory (DFT) simulator). ChemTS utilizes a recurrent neural network (RNN) to learn complex rules of molecules and a Monte Carlo tree search (MCTS) to optimize the properties of functional molecules. ChemTS is available on GitHub (https://github.com/tsudalab/ChemTS).

Using this platform, the authors generated molecules that have their first excited states at desired wavelengths, which are labels in the algorithm. Here, the RNN is trained with a set of simplified molecular input line entry system (SMILES) strings of 13,000 molecules that contain only H, O, N, and C elements from the PubChemQC database (http://pccdb.org). This SMLIES is used as features in the algorithm. To design various molecules with different lowest excitation level, five runs of AI-assisted molecule generation were performed where the target excitation level in each run is given as 200, 300, 400, 500, and 600 nm. Each run was performed on a 12-core server (Intel Xeon E5-2689v3 CPU) for 2 days. In this computation, over 1000 DFT calculations were performed and this part takes a lot of time. In these molecule generations, 86 potential photofunctional molecules were obtained (the breakdown is 34, 26, 13, 12, and 1 for 200, 300, 400, 500, and 600 nm, respectively). Among them, six molecules were experimentally synthesized. UV spectral measurements indicated that five of these molecules reproduced the DFT predictions, showing the potential of AI-assisted chemistry to discover ready-to-synthesize novel molecules without using supercomputers [6]. The authors concluded that the AI-assisted chemistry

platform will accelerate the development of new functional molecules for solar cells and organic electroluminescence.

3 Effective Model Estimation of Magnetic Materials by Bayesian Statistics

Magnetic materials are used in many devises such as switch, sensor, and memory. Furthermore, magnetism in materials induces a lot of useful effects such as magnetoelectric and magnetocaloric effects. To understand these effects and interpret the microscopic properties of magnetic materials, a spin Hamiltonian as an effective model is often derived. Many methods have been proposed to determine spin Hamiltonians, and they are divided into two groups: (i) ab initio electronic structure calculation and (ii) fitting by data-driven technique [8–11]. To obtain an effective model from experimental results, Tamura et al. developed a new method that utilizes an ML technique based on Bayesian statistics (Fig. 3) [12], which is categorized into second group.

3.1 Construction of the Posterior Distribution by Bayesian Statistics

The inverse problem, in which an effective model explaining the given experimental results is the target to be derived, is considered. Notice that the first step in the forward

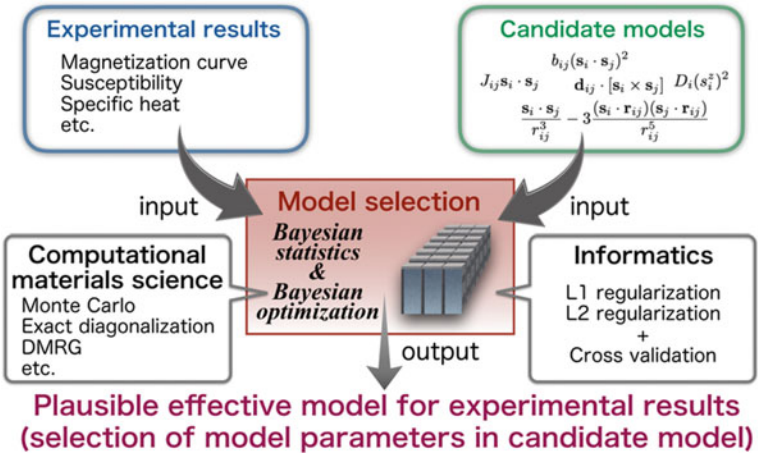

Fig. 3 Strategy to estimate an effective model from the experimental results by ML based on Bayesian statistics

problem involving conventional theoretical research on magnetic materials should determine an effective model. Since Bayesian statistics is useful for solving an inverse problem, the authors proposed a method of estimating an effective model from a given physical quantity by ML based on Bayesian statistics. Furthermore, using Bayesian statistics, idea of the prior distribution can be incorporated into model estimation. In the estimation method, plausible model parameters that explain the given physical quantity are determined by maximizing the posterior distribution, which is defined as

$$P(\mathbf{x}|\mathbf{y}^{\mathrm{ex}}) \propto \exp[-E(\mathbf{x})], \tag{1}$$

where the energy function $E(\mathbf{x})$ as a function of model parameters $\mathbf{x}$ is given by

$$E(\mathbf{x}) = \frac{1}{2\sigma^2}(\mathbf{y}^{\mathrm{ex}} - \mathbf{y}^{\mathrm{cal}}(\mathbf{x}))^2 - \log P(\mathbf{x}), \tag{2}$$

where $\mathbf{y}^{\mathrm{ex}}$ and $\mathbf{y}^{\mathrm{cal}}(\mathbf{x})$ are sets of physical quantities obtained by experiments and those calculated from the effective model characterized by $\mathbf{x}$, respectively. Furthermore, $P(\mathbf{x})$ is the prior distribution, which expresses the prior knowledge of model parameters $\mathbf{x}$. For example, this prior distribution can be regarded as the regularization terms in the minimization problem. The most common are L1 and L2 regularizations and each form is $P(\mathbf{x}) = \exp(-\lambda|\mathbf{x}|)$ and $P(\mathbf{x}) = \exp(-\lambda\|\mathbf{x}\|^2)$, respectively. Here, λ determines the strength of regularization. This method is categorized as supervised learning where the features are model parameters and label is physical quantities.

On the basis of Bayesian statistics, it is expected that both relevant and redundant terms are effectively selected from a candidate model Hamiltonian with the help of the ML technique by using a sparse prior of $P(\mathbf{x})$ and cross-validation. The efficiency of the estimation method can be tested with synthetic magnetization curve data obtained using the classical Heisenberg model. The results showed that the proposed method correctly estimated the model parameters in the effective Hamiltonian [12]. Furthermore, using our technique, we determined an effective model of $KCu_4P_3O_{12}$ from the experimentally observed magnetic susceptibility and magnetization curves with various temperatures under high magnetic fields [13]. It should be emphasized that the framework of this estimation method is not limited to magnetization curves but is applicable to any measured data.

3.2 Bayesian Optimization for Computationally Extensive Probability Distributions

To accelerate the estimation of an effective model, an efficient method of finding a preferable maximizer of the computationally expensive probability distributions is proposed on the basis of a Bayesian optimization technique [14]. In informatics and

materials science, the Bayesian optimization using ML prediction model has recently attracted much attention as a method of searching for the maximizer/minimizer of a black-box function. In the Bayesian optimization, by using the information of prediction value and standard deviation calculated by ML prediction model, the efficient optimization is realized. The Bayesian optimization technique developed by the authors was applied to the posterior distribution in the effective model estimation given by Eq. (1). Instead of searching for the maximizer of the posterior distribution, the minimizer of the energy function defined by Eq. (2) is searched. Even when the number of sampling points on the energy function is small, the Bayesian optimization provides a better minimizer of the energy function than those provided by the random search method, the steepest descent method, or the Monte Carlo method (Fig. 4). In this demonstration, the quantum Heisenberg model is used as the target Hamiltonian and the temperature dependence of the specific heat is inputted. Furthermore, the Bayesian optimization combined with the steepest descent method efficiently improved the results. Note that the candidate selection by Bayesian optimization takes a long time compared to that by random search and steepest descent methods. However, this selection time is shorter enough than the evaluation time of $E(\mathbf{x})$, and thus there is almost no difference in calculation times of whole optimization for each optimization methods.

In this study, we demonstrated that the Bayesian optimization is a powerful tool to search for a preferable maximizer of a computationally expensive probability

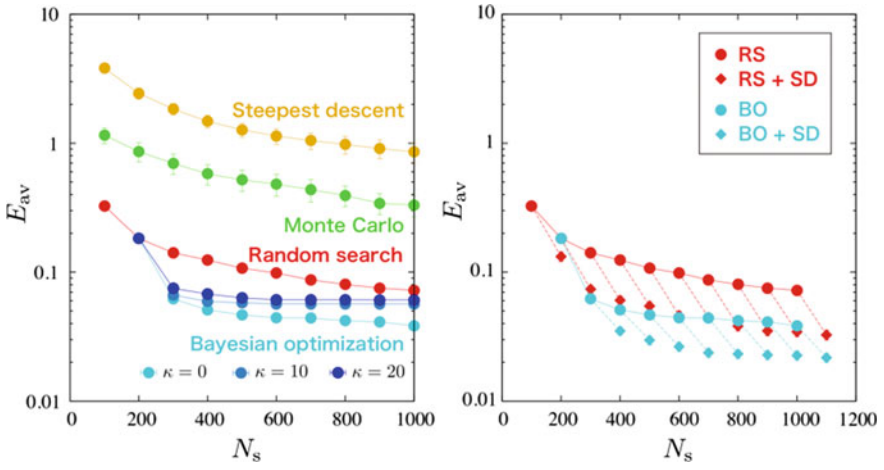

Fig. 4 Results of the average $E_{\rm av}$ of the minimum values of the energy function obtained from 100 independent runs in the effective model estimation. (Left) $E_{\rm av}$ as a function of sampling number $N_{\rm s}$ obtained from the random search method, the steepest descent method, the Monte Carlo method, and the Bayesian optimization. The value of κ is the strength of the effect of the standard deviation corresponding to the uncertainty in the Bayesian optimization. (Right) Results from the random search method (RS), the Bayesian optimization (BO), the random search method with the steepest descent method (RS + SD), and the Bayesian optimization with the steepest descent method (BO + SD). (Reprinted from [14], Copyright 2018, The Authors licensed under CC BY 4.0)

distribution [14]. The authors concluded that since the maximizer of the probability distribution is searched in many scientific fields, this method will play a prominent role in improving the efficiency of scientific studies.

4 Force-Field Estimation by Machine Learning

One of the important issues in materials informatics research is to predict atomic forces by ML techniques [15–18]. Classical molecular dynamics (MD) simulations using empirical classical force fields have been playing an important role to understand various phenomena in materials at the atomic scale. However, the reliability of the force fields is often a problem. On the other hand, DFT calculations can provide reliable atomic forces. Since the computational cost of DFT calculations is much more expensive than that of classical force fields, both the system size and simulation time of DFT-MD simulations are limited. If ML can predict atomic forces with accuracies comparable to DFT calculation, the cost of the force calculations will be significantly decreased, leading to long-time MD simulations for large systems. Thus, such ML-based force-field estimation will expand the scope of computational materials science.

Tamura, Miyazaki, and colleagues provided a simple, intuitive prescription to train robust ML forces that are applicable to a wide range of temperatures [19, 20]. The prescription consists of MD simulations and the construction of ML models. First, MD simulations are performed on the basis of DFT with a canonical ensemble at a very high temperature in each phase. The training data are sampled randomly from this MD simulation. Then, an ML model is constructed to predict the forces by a regression technique. Here, the atomic fingerprint proposed in Ref. [19] is used to express the local structure around a target atom. In this work, the authors trained a force component along a randomly selected direction (the unit vector is denoted as $\mathbf{e}$) for each training data. The force component and the atomic fingerprint of the i th atom are expressed as

$$F_i(\mathbf{e}) = \mathbf{F}_i \cdot \mathbf{e}, \tag{3}$$

$$X_i(\mathbf{e}; \eta_k) = \sum_{j \neq i} \frac{(\mathbf{r}_j - \mathbf{r}_i) \cdot \mathbf{e}}{r_{ij}} \exp[-(r_{ij}/\eta_k)^2] f(r_{ij}). \tag{4}$$

$\mathbf{F}_i$ and $\mathbf{r}_i$ are the atomic force and position of the i th atom, respectively. In Eq. (4), $r_{ij} = |\mathbf{r}_j - \mathbf{r}_i|$ is the distance between the atom i and its neighbor atom j, and $\eta_k (k = 1, \ldots, K)$ is the decay rate for this distance. A cutoff function is denoted as $f(r_{ij})$. By considering K types of decay rates, the K-dimensional fingerprint vector corresponding to features in ML is obtained as

$$\mathbf{X}_i(\mathbf{e}) = (X_i(\mathbf{e}; \eta_1), \ldots, X_i(\mathbf{e}; \eta_K))^{\mathrm{T}}. \tag{5}$$

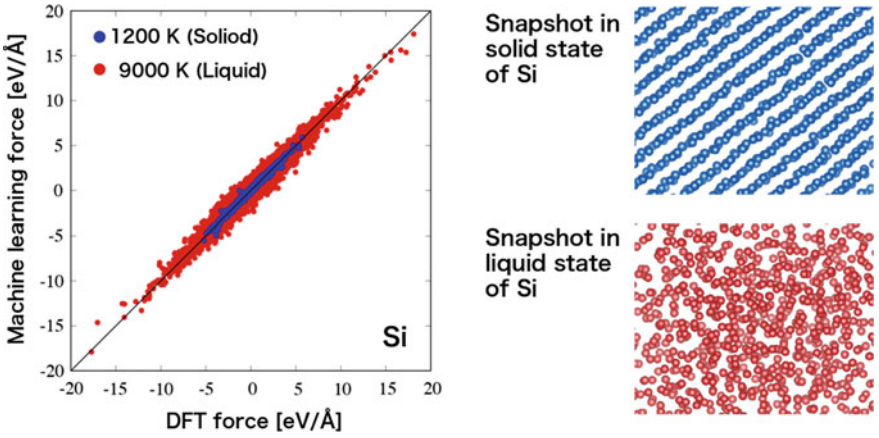

Fig. 5 Parity plot of the DFT force and the predicted force by the ML model for 1200 K solid state and 3000 K liquid state in the silicon system. Snapshots in solid and liquid states are also shown

Many $(F_i(\mathbf{e}), \mathbf{X}_i(\mathbf{e}))$ were collected as the training data, and Gaussian process regression was employed as a regression technique. Here, $\mathbf{X}_i(\mathbf{e})$ and $F_i(\mathbf{e})$ are the features and label in the supervised learning.

As a demonstration, the authors focused on a single-component system consisting of silicon atoms. The trained ML model exhibits noticeably small force prediction errors in the solid and liquid phases as shown in Fig. 5. Furthermore, we confirmed that the transferability of the ML model in terms of temperature and system size is satisfactory in the same phase. The authors concluded that the present ML forces already have sufficient generalization performance for many applications in computational materials science.

5 Machine Learning Approaches in Gas Sensor Systems

As an example of applications of materials science combined with informatics, here we will show several studies using nanomechanical sensors, namely, Membrane-type Surface stress Sensors (MSS) [21], which were introduced in Chap. 15. Since multidimensional data are obtained through gas-sensing measurements with MSS, informatics plays an essential role in sensor data analysis.

5.1 *Classification Models from Gas Sensor Signals Toward Artificial Olfaction*

Artificial olfaction is one of the most challenging issues in gas sensor systems. The definition of artificial olfaction is a gas sensor system that identifies odors—complex mixtures of gases—from sensing signals. The basic procedure for gas identification (i.e., classification of gases) is depicted in Fig. 6. First, sensing signals are obtained through gas-sensing measurements. In a common gas-sensing measurement, a sample gas and a carrier gas are alternately injected to a sensor array by using gas flow control units such as pumps and mass flow controllers. Second, the obtained sensing signals are preprocessed for subsequent analysis: offset subtraction, smoothing, normalization, and so on. Then, signal features that are intrinsic to gas species are extracted from the sensing signals. Typically, geometrical parameters of the signals such as slope, area, and peak height are used as features. Feature selection and dimensionality reduction are often adopted for the extracted features when the total number of extracted features is excessively large; high-dimensional datasets can deteriorate classification accuracy in some classification algorithms. As a typical dimensionality reduction algorithm, principal component analysis (PCA) is often used; high-dimensional data are projected to a lower dimensional space composed of principal components (PCs). Finally, gas species are classified from the extracted features through a classification algorithm for supervised learning including support vector machines (SVMs), random forests, and neural networks.

On the basis of this basic procedure, Imamura, Shiba, and Yoshikawa demonstrated the odor identification of spices and herbs by using MSS as a sensing platform [22]. The odors of spices and herbs, which are the headspace gases in glass vials in which samples are placed, were carried to an MSS chip with pure nitrogen. The MSS chip was then purged with pure nitrogen. In this study, the authors used a four-channel MSS chip coated with four different polymers. From the obtained sensing signals,

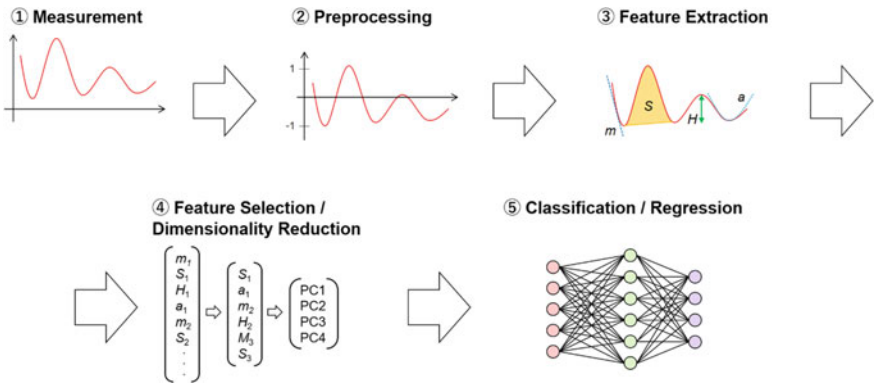

Fig. 6 Basic data-processing procedure for developing ML classification/regression models from sensing signals

the authors extracted two kinds of features that correspond to static and dynamic information: the signal intensity ratio and decay time constant. The signal intensity ratio reflects the chemical affinity of each channel to the gas species. On the basis of the signal intensity ratio, one can identify gas species through pattern recognition regardless of the concentration. In contrast, the decay time constant represents the dynamic behaviors of the gas sensors; the transient response of the decay curve (sensing signals obtained from the purge part) reflects the dynamics of gas desorption and the consequent changes in viscoelastic properties [23, 24]. PCA was performed on the dataset of these features to visualize the data by projecting each data point to a two-dimensional plane composed of the first and second principal components. The results are shown in Fig. 7. The data points obtained from the same sample form a cluster, and the clusters are separated from each other. It is noteworthy that the result reflects the chemical composition of the odors of spices and herbs. The spices and herbs that contain similar volatile organic compounds appear in close proximity on the plane; the odors of the spices and herbs categorized into groups I, II, and III in Fig. 7 contain thiols, terpenes, and aromatic aldehydes as their main components, respectively.

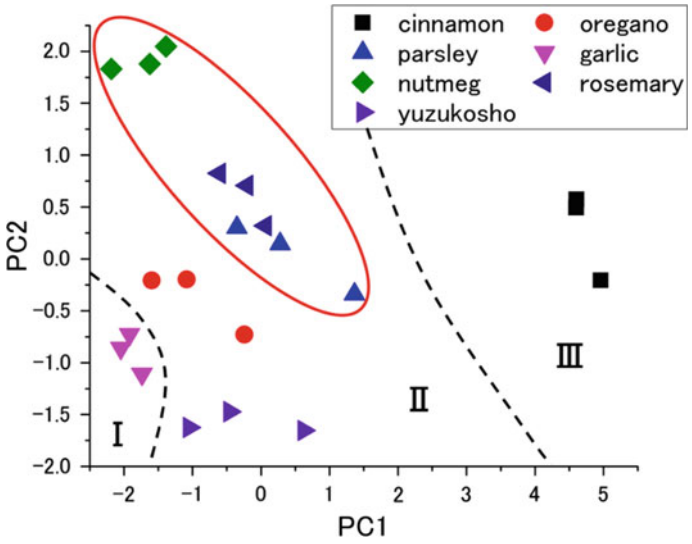

Fig. 7 PCA scatter plot for odor identification of spices and herbs. The spices and herbs are categorized into three groups: I, II, and III. In particular, the spices and herbs marked in the ellipse contain pinene, which is a kind of terpene. (Reprinted from [22], The Authors licensed under CC BY 4.0)

6 Analysis Method Based on System Identification

Such a basic gas identification protocol is often employed to identify odors from sensing signals. However, signal features such as the signal intensity ratio and decay time constant strongly depend on gas input patterns (e.g., gas flow control). Thus, gas input patterns must be strictly fixed for every measurement; otherwise, the measurement data cannot be compared with each other. To resolve this issue, data analysis methods used in system identification have been developed. In these methods, a gas sensor system is considered to be an input–output system; for example, the flow rate of the sample gas and the resultant sensing signals correspond to the input and output, respectively. To identify gas species, these methods focus on the relationship between the inputs and the outputs. A transfer function is one of the representations for the input–output relationship. The mathematical definition of a transfer function $h_g(t)$ for an input $x(t)$ and an output $y(t)$ is as follows:

$$y(t) = \int_0^t h_g(\tau)x(t-\tau)d\tau. \tag{6}$$

Note that t and g denote the time and gas species, respectively. As $h_g(t)$ is intrinsic to the combination of the gas species and sensor, gas species can be identified by $h_g(t)$. One of the biggest advantages of using $h_g(t)$ as a feature for gas identification is that $h_g(t)$ is independent of $x(t)$; hence, measurement data obtained through different gas input patterns become comparable. By applying the Fourier transform, the frequency-domain expression for Eq. (6) is obtained as the following formula:

$$Y(f) = H_g(f)X(f), \tag{7}$$

where $X(f)$, $Y(f)$, and $H_g(f)$ are the frequency-domain expressions for the input, output, and transfer function, respectively. In the frequency domain, the transfer function can be more easily calculated than in the time domain. Note that Eqs. (6) and (7) are mathematically equivalent; no information is lost by the Fourier transform.

While several studies that utilize transfer functions have been reported since the 1990s [25, 26], advanced data analysis becomes possible by combining the transfer functions with ML techniques, which were intensively developed in the 2010s. Here, we introduce one of the studies performed by Imamura, Yoshikawa et al. [27]. The authors conducted gas-sensing measurements with a polymer-coated MSS and utilized uniform-random gas input patterns as shown in Fig. 8. The authors measured headspace gases of solvent vapors with random gas input patterns and evaluated the transfer function for each measurement. On the basis of the dataset of the transfer functions, the authors developed ML models by using logistic regression and SVMs as a classifier. The models were optimized and evaluated through nested cross-validation. The results are summarized in Table 1. The authors achieved classification accuracies of 0.94 ± 0.04 and 0.98 ± 0.03 with a logistic-regression-based model and an SVM-based model, respectively. The authors also demonstrated the

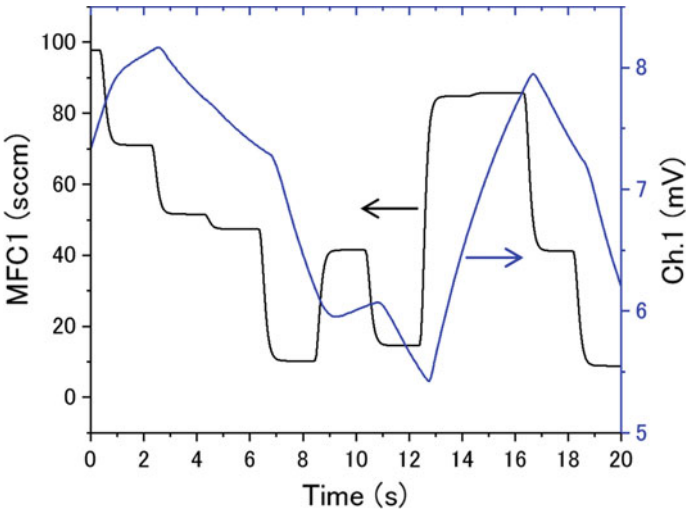

Fig. 8 Uniform-random gas input pattern (gas flow rate of the mass flow controller) and resultant sensing signal

Table 1 Classification accuracy of the models

Samples	Classifiers	
	Logistic regression	Support vector machine
Four solvent vapors (Uniform-random gas injection pattern)	0.94 ± 0.04	0.98 ± 0.03
Four solvent vapors (Four different gas injection patterns)	0.92 ± 0.06	0.97 ± 0.06
Four spices and herbs (Uniform-random gas injection pattern)	0.87 ± 0.08	0.94 ± 0.04

robustness of transfer functions to gas input patterns by measuring the solvent vapors with four types of different gas input patterns including a rectangular injection pattern (cycles of sample gas injection and carrier gas purge). Classification models based on transfer functions were developed from the measurement data obtained with the four different gas input patterns, resulting in high classification accuracies of 0.92 ± 0.06 and 0.97 ± 0.06 for a logistic-regression-based model and an SVM-based model, respectively.

The authors demonstrated the odor identification of spices and herbs (i.e., cinnamon, spearmint, rosemary, and thyme) with the uniform-random gas input pattern. The results are summarized in Table 1, showing that the data analysis methods focusing on transfer functions are also effective for such practical samples of odor identification. Thus, their study indicates that constraints on gas input patterns can be eliminated by using the transfer functions as features for ML; gas species or odors can be identified regardless of gas input patterns. An advanced application that

utilizes data analysis methods focusing on transfer functions was also reported by Imamura, Shiba, Yoshikawa et al. [28].

6.1 Regression Models for Quantitative Analysis with Gas Sensor Systems

In addition to the classification of odors, regression is another important method of analysis for sensor systems. Regression models predict continuous values whereas classification models predict discrete labels. In gas sensor systems, regression models are often used to estimate the concentration of target gas species such as toxic gases, oxygen, and water (humidity). However, estimating the concentration of a specific gas species from sensing signals is difficult because of the effect of interfering gases; even when samples contain the same amount of a target gas species, different sensing signals can be obtained from the samples if they have different gas compositions.

Toward resolving this issue, Shiba, Tamura, Imamura, and Yoshikawa reported the estimation of the alcohol content from the odors of drinks [29]. In this study, the authors measured the headspace gases of several kinds of drinks such as water, teas, and liquors with a gas measurement device equipped with an MSS chip. The MSS chip was coated with four different functional silica/titania hybrid nanoparticles (STNPs): aminopropyl-STNPs, vinyl-STNPs, C18-STNPs, and phenyl-STNPs. The measurements were performed through cycles of sample gas injection and carrier gas purging. From the sensing signals, four kinds of parameters were extracted for each measurement as features. Then, prediction models for the alcohol content were constructed from the dataset of the extracted features by kernel ridge regression. To optimize the combination of parameters that are used for developing regression models, the authors first trained regression models for each channel of the MSS chip. Although the prediction models developed from channels coated with C18-STNPs and phenyl-STNPs successfully predict the alcohol content, the models developed from the channel coated with aminopropyl-STNPs and vinyl-STNPs show large prediction errors. This result indicates that hydrophobic STNPs are more suitable for the receptor materials than hydrophilic ones in order to estimate the alcohol content. Then, the authors replaced the aminopropyl-STNPs and vinyl-STNPs with hydrophobic polymers, namely, polysulfone and polycaprolactone. On the basis of the sensing signals obtained with the four hydrophobic materials as receptor materials, the authors developed the regression model by using the parameters selected from each channel. The result is shown in Fig. 9. The prediction accuracy for both known and unknown samples markedly improved. Thus, the authors succeeded in estimating specific information, that is, the alcohol content, from sensing signals, which were obtained from the optimized combination of receptor materials through the data-driven approach.

Shiba, Tamura, Imamura, Yoshikawa et al. also reported another quantitative analysis for gas sensor systems based on ML [30]. In this study, the authors measured

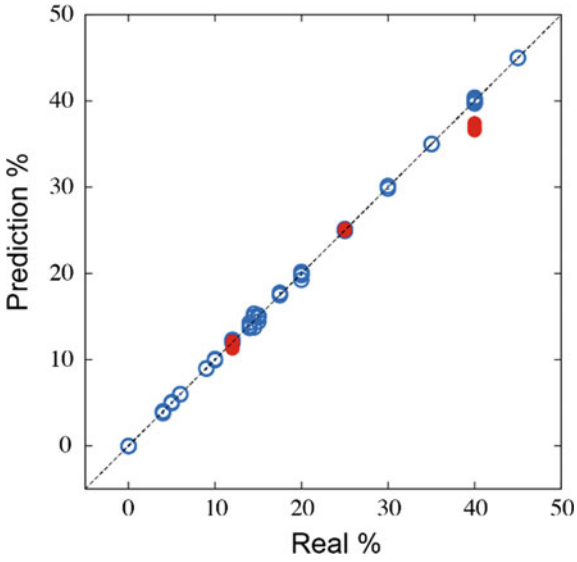

Fig. 9 Parity plot of predicted alcohol content versus real alcohol content. The open (blue) and solid (red) circles represent the training and validation samples, respectively. (Reprinted from [29], The Authors licensed under CC BY 4.0)

the vapors of a ternary mixture consisting of water, ethanol, and methanol. From the sensing signals, the authors constructed regression models that predict the concentration of each component. STNPs and silica nanoparticles (SNPs) were used as a receptor material platform for the MSS; the surfaces of the nanoparticles (NPs) were functionalized with aminopropyl, hydroxyl, phenyl, and octadecyl groups. The authors synthesized the following functional NPs: $NH_2(1) - OH(3) -$ SNPs, $NH_2 -$ STNPs, $C18(1) - NH_2(1) -$ STNPs, $C18 -$ STNPs, $Ph -$ STNPs, $Ph(1) - OH(3) -$ SNPs, $C18(4) - NH_2(1) -$ STNPs, and $C18(1) - NH_2(4) -$ STNPs. The values in parenthesis denote the molar ratio of each functional group. Note that the real molar ratios for the functional NPs are different from the denoted ratios. The vapors of the ternary mixtures with different concentration ratios were measured with MSS coated with the functional NPs through cycles of sample gas injection and carrier gas purging. The authors developed regression models based on the Gaussian process from the extracted parameters, which are the same as in the case of alcohol content estimation [29]. After the optimization of feature selection, the authors successfully estimated the concentration of each component (Fig. 10). This study indicates that the estimation of the concentration of each component is possible by combining the NP-coated MSS and ML techniques.

7 Summary

In this chapter, we have shown that machine learning techniques are useful in various fields of materials science. Machine learning techniques will not only enhance

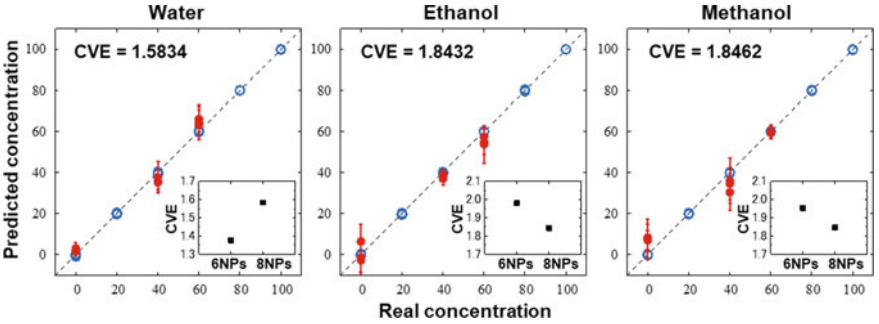

Fig. 10 Parity plots of predicted concentration versus real concentration. The open (blue) and solid (red) circles represent the training and validation samples, respectively. The cross-validation error is also denoted as CVE, and the inset is the dependence of CVE on the number of NPs used. (Reprinted from [30], Copyright 2018, with permission from the American Chemical Society)

the efficiency of materials research but also have the potential to discover new phenomena. In fact, machine learning has realized optimization of property in functional molecules, understanding of microscopic property in magnetic materials, prediction of atomic forces for molecular dynamics simulations, and upgrading of the gas sensor system. Thus, we believe that the fusion of machine learning and materials science, especially nanoarchitectonics, will be used to explore a new field of science and expand the scope of materials science. On the other hand, in many materials informatics researches, existing machine learning methods purely developed in informatics have been applied. But, the material dataset is characterized by the physical laws behind it, although the number of data is not large. Thus, a development of machine learning methods suitable for material science, which positively utilizes these characteristics in materials dataset, will be the future important perspective. If this can be developed, material science will be further speeded up and sophisticated with the aid of machine learning.

Acknowledgements We thank Prof. Koji Hukushima (The University of Tokyo), Dr. Shinsuke Ishihara (NIMS), Dr. Jianbo Lin (NIMS), Dr. Kosuke Minami (NIMS), Dr. Tsuyoshi Miyazaki (NIMS), Dr. Huynh Thien Ngo (NIMS), Dr. Kota Shiba (NIMS), Dr. Masato Sumita (RIKEN), Dr. Teppei Suzuki (ex NIMS), Prof. Koji Tsuda (The University of Tokyo), Prof. Takashi Washio (Osaka University), and Dr. Genki Yoshikawa (NIMS) for their collaboration in this research.

References

1. Bishop CM (2006) Pattern recognition and machine learning. Springer
2. Segler MHS, Kogej T, Tyrchan C, Waller MP (2018) Generating focused molecule libraries for drug discovery with recurrent neural networks. ACS Cent Sci 4:120–131. https://doi.org/10.1021/acscentsci.7b00512

3. Gómez-Bombarelli R et al (2018) Automatic chemical design using a data-driven continuous representation of molecules. ACS Central Sci 4:268–276. https://doi.org/10.1021/acscentsci.7b00572
4. Kusner MJ, Paige B, Hernández-Lobato JM (2017) Grammar variational autoencoder. In: Proceedings of the 34th international conference on machine learning, vol 70, pp 1945–1954
5. Ikebata H, Hongo K, Isomura T, Maezono R, Yoshida R (2017) Bayesian molecular design with a chemical language model. J Comput Aided Mol Des 31:379–391. https://doi.org/10.1007/s10822-016-0008-z
6. Sumita M, Yang X, Ishihara S, Tamura R, Tsuda K (2018) Hunting for organic molecules with artificial intelligence: molecules optimized for desired excitation energies. ACS Cent Sci 4:1126–1133. https://doi.org/10.1021/acscentsci.8b00213
7. Yang X, Zhang J, Yoshizoe K, Terayama K, Tsuda K (2017) ChemTS: an efficient python library for de novo molecular generation. Sci Technol Adv Mater 18:972–976. https://doi.org/10.1080/14686996.2017.1401424
8. Fujita H, Nakagawa YO, Sugiura S, Oshikawa M (2018) Construction of Hamiltonians by supervised learning of energy and entanglement spectra. Phys Rev B 97:075114.https://doi.org/10.1103/PhysRevB.97.075114
9. Takenaka H, Nagata K, Mizokawa T, Okada M (2016) Bayesian approach to effective model of $NiGa_2S_4$ triangular lattice with Boltzmann factor. J Phys Soc Jpn 85:124003. https://doi.org/10.7566/JPSJ.85.124003
10. Tamura R, Kawashima N, Yamamoto T, Tassel C, Kageyama H (2011) Random fan-out state induced by site-random interlayer couplings. Phys Rev B 84:214408. https://doi.org/10.1103/PhysRevB.84.214408
11. Tamura R, Kawashima N (2008) First-order transition to incommensurate phase with broken lattice rotation symmetry in frustrated Heisenberg model. J Phys Soc Jpn 77:103002. https://doi.org/10.1143/JPSJ.77.103002
12. Tamura R, Hukushima K (2017) Method for estimating spin-spin interactions from magnetization curves. Phys Rev B 95:064407. https://doi.org/10.1103/PhysRevB.95.064407
13. Tamura R, Hukushima K, Matsuo A, Kindo K, Hase M (2020) Data-driven determination of the spin Hamiltonian parameters and their uncertainties: the case of the zigzag-chain compound $KCu_4P_3O_{12}$. Phys Rev B 101:224435. https://doi.org/10.1103/PhysRevB.101.224435
14. Tamura R, Hukushima K (2018) Bayesian optimization for computationally extensive probability distributions. PLOS ONE 13:e0193785. https://doi.org/10.1371/journal.pone.0193785
15. Kobayashi R, Giofré D, Junge T, Ceriotti M, Curtin WA (2017) Neural network potential for Al-Mg-Si alloys. Phys Rev Mater 1:053604. https://doi.org/10.1103/PhysRevMaterials.1.053604
16. Li W, Ando Y, Watanabe S (2017) Cu diffusion in amorphous Ta_2O_5 studied with a simplified neural network potential. J Phys Soc Jpn 86:104004. https://doi.org/10.7566/JPSJ.86.104004
17. Pham TL, Kino H, Terakura K, Miyake T, Dam HC (2016) Novel mixture model for the representation of potential energy surfaces. The J Chem Phys 145:154103. https://doi.org/10.1063/1.4964318
18. Behler J, Parrinello M (2007) Generalized neural-network representation of high-dimensional potential-energy surfaces. Phys Rev Lett 98:146401. https://doi.org/10.1103/PhysRevLett.98.146401
19. Suzuki T, Tamura R, Miyazaki T (2017) Machine learning for atomic forces in a crystalline solid: transferability to various temperatures. Int J Quantum Chem 117:33–39. https://doi.org/10.1002/qua.25307
20. Tamura R, Lin J, Miyazaki T (2019) Machine learning forces trained by Gaussian process in liquid states: transferability to temperature and pressure. J Phys Soc Jpn 88:044601. https://doi.org/10.7566/JPSJ.88.044601
21. Yoshikawa G, Akiyama T, Gautsch S, Vettiger P, Rohrer H (2011) Nanomechanical membrane-type surface stress sensor. Nano Lett 11:1044. https://doi.org/10.1021/nl103901a

22. Imamura G, Shiba K, Yoshikawa G (2016) Smell identification of spices using nanomechanical membrane-type surface stress sensors. Jpn J Appl Phys 55:1102B3. https://doi.org/10.7567/JJAP.55.1102B3
23. Wenzel MJ, Josse F, Heinrich SM, Yaz E, Datskos PG (2008) Sorption-induced static bending of microcantilevers coated with viscoelastic material. J Appl Phys 103:064913. https://doi.org/10.1063/1.2902500
24. Imamura G, Shiba K, Yoshikawa G, Washio T (2018) Analysis of nanomechanical sensing signals; physical parameter estimation for gas identification. AIP Adv 8:075007. https://doi.org/10.1063/1.5036686
25. Davide FAM et al (1995) Dynamic calibration of QMB polymer-coated sensors by Wiener kernel estimation. Sens Actuators, B Chem 27:275–285. https://doi.org/10.1016/0925-4005(94)01601-D
26. Hines EL, Llobet E, Gardner JW (1999) Electronic noses: a review of signal processing techniques. IEE Proc -Circuits Devices Syst 146:297–310. https://doi.org/10.1049/ip-cds:19990670
27. Imamura G, Yoshikawa G, Washio T (2018) Development of machine learning models for gas identification based on transfer functions. In: 17th international meeting on chemical sensors—IMCS 2018, pp 225–226. https://doi.org/10.5162/IMCS2018/AR1.1
28. Imamura G, Shiba K, Yoshikawa G, Washio T (2019) Free-hand gas identification based on transfer function ratios without gas flow control. Sci Rep 9:9768. https://doi.org/10.1038/s41598-019-46164-1
29. Shiba K, Tamura R, Imamura G, Yoshikawa G (2017) Data-driven nanomechanical sensing: specific information extraction from a complex system. Sci Rep 7:3661. https://doi.org/10.1038/s41598-017-03875-7
30. Shiba K et al (2018) Functional nanoparticles-coated nanomechanical sensor arrays for machine learning-based quantitative odor analysis. ACS Sensors 3:1592–1600. https://doi.org/10.1021/acssensors.8b00450

Correction to: Wavelength-Selective Photothermal Infrared Sensors

Tadaaki Nagao, Dao Duy Thang, Doan Tung Anh, Satoshi Ishii, and Toshihide Nabatame

Correction to:
Chapter "Wavelength-Selective Photothermal Infrared Sensors" in: Y. Wakayama and K. Ariga (eds.), *System-Materials Nanoarchitectonics*, NIMS Monographs, https://doi.org/10.1007/978-4-431-56912-1_5

In the original version of the book, the following belated corrections have been incorporated in chapter "Wavelength-Selective Photothermal Infrared Sensors". Figure copyright information has been included in figure 1, and figure citation "10c" has been corrected as "9c" in Page number 84.

The correction chapter and the book has been updated with changes.

The updated version of this chapter can be found at
https://doi.org/10.1007/978-4-431-56912-1_5

Y. Wakayama and K. Ariga (eds.), *System-Materials Nanoarchitectonics*,
NIMS Monographs, https://doi.org/10.1007/978-4-431-56912-1_20

Epilogue: Today's Nanotechnology, Future Nanoarchitectonics

"Arrange the atoms the way we want; the very atoms, all the way down!", Professor Richard Phillips Feynman said in his famous speech entitled "There's Plenty of Room at the Bottom" in 1959 at California Institute of Technology. Nowadays, this is well known as a very foresighted message and recognized as a takeoff point of today's nanotechnology. After that, Japanese scientists made great contributions in this field: exploratory works on metal nanoparticles by Prof. Ryogo Kubo in 1962, invention of the superlattice by Prof. Leo Esaki in 1969, and a new concept of nanotechnology introduced by Prof. Norio Taniguchi in 1974. However, this historical information is only well known among scientists. We needed to wait until 2000 for nanotechnology to attract popular attention. An epoch-making speech was made again at California Institute of Technology in 2000. However, the speaker was not a scientist but a politician, President Bill Clinton, who announced the National Nanotechnology Initiative as a national strategic plan of the United States. Since then, the word nanotechnology has been widely popularized. However, in my opinion, it was not Clinton's speech in 2000 but the end of the roadmap of Moore's law in the 2010s that allowed us to notice the real significance and emergence of nanotechnology. The size of electronic elements has already reached the order of sub-10 nm, which can no longer be achieved by the simple extension of conventional lithographic techniques. As such, we at WPI-MANA of NIMS proposed a new concept, that is, "nanoarchitectonics". Here, nanoscale materials are assembled to generate new functionalities that cannot be attained solely by reducing the size of each material. Difficulties in this concept are still encountered, particularly in selecting and assembling materials for specific functions, such as electricity, photonics, electronics, ionics, sensors, and so on. Here, we would like to emphasize the urgency of the breakaway from the classical trial-and-error style of tackling these difficulties. The importance of computational science has been increasing. Machine learning, materials informatics, and theoretical

Y. Wakayama and K. Ariga (eds.), *System-Materials Nanoarchitectonics*,
NIMS Monographs, https://doi.org/10.1007/978-4-431-56912-1

prediction will offer a clear direction in finding solutions. In this special issue, we proposed potential ways of addressing these difficulties by both experimental and computational approaches as inseparable aspects. We believe that these approaches can prepare a path for promoting future nanoarchitectonics.

Yutaka Wakayama